



AFRL-RQ-WP-TR-2021-0055

THERMAL MANAGEMENT OF ELECTROMECHANICAL MACHINES FOR AEROSPACE SYSTEMS

**John P. Kizito, Jose Juan Corona, Jr., Augustine A. Kwarteng, and Kamal A. Kaddoura
North Carolina A&T State University Performing Company Name**

**Louis Chow, Osama Mesalhy, Mohamed Elsayed, and Yeong-ren Lin
University of Central Florida**

**AUGUST 2021
Final Report**

**DISTRIBUTION STATEMENT A. Approved for public release. Distribution is unlimited.
AFRL-2023-0859; Cleared 02/17/2023.**

**AIR FORCE RESEARCH LABORATORY
AEROSPACE SYSTEMS DIRECTORATE
WRIGHT-PATTERSON AIR FORCE BASE, OH 45433-7542
AIR FORCE MATERIEL COMMAND
UNITED STATES AIR FORCE**

NOTICE PAGE

Using Government drawings, specifications, or other data included in this document for any purpose other than Government procurement does not in any way obligate the U.S. Government. The fact that the Government formulated or supplied the drawings, specifications, or other data does not license the holder or any other person or corporation; or convey any rights or permission to manufacture, use, or sell any patented invention that may relate to them.

This paper was cleared for public release by AFRL Public Affairs, AFRL/PA and is available to the general public, including foreign nationals.

Copies may be obtained from the Defense Technical Information Center (DTIC)
(<https://discover.dtic.mil>).

AFRL-RQ-WP-TR-2021-0055 has been reviewed and is approved for publication in accordance with assigned distribution statement.

This paper is published in the interest of scientific and technical information exchange and its publication does not constitute the Government's approval or disapproval of its ideas or findings.

REPORT DOCUMENTATION PAGE

Form Approved
OMB No. 0704-0188

The public reporting burden for this collection of information is estimated to average 1 hour per response, including the time for reviewing instructions, searching existing data sources, gathering and maintaining the data needed, and completing and reviewing the collection of information. Send comments regarding this burden estimate or any other aspect of this collection of information, including suggestions for reducing this burden, to Department of Defense, Washington Headquarters Services, Directorate for Information Operations and Reports (0704-0188), 1215 Jefferson Davis Highway, Suite 1204, Arlington, VA 22202-4302. Respondents should be aware that notwithstanding any other provision of law, no person shall be subject to any penalty for failing to comply with a collection of information if it does not display a currently valid OMB control number. **PLEASE DO NOT RETURN YOUR FORM TO THE ABOVE ADDRESS.**

1. REPORT DATE (DD-MM-YY) 20210817	2. REPORT TYPE Final	3. DATES COVERED (From - To) 20 October 2017 – 3 August 2020
--	--------------------------------	--

4. TITLE AND SUBTITLE THERMAL MANAGEMENT OF ELECTROMECHANICAL MACHINES FOR AEROSPACE SYSTEMS	5a. CONTRACT NUMBER FA8650-17-2-2230
	5b. GRANT NUMBER
	5c. PROGRAM ELEMENT NUMBER 62201F

6. AUTHOR(S) John P. Kizito, Jose Juan Corona, Jr., Augustine A. Kwarteng, and Kamal A. Kaddoura (North Carolina A&T State University) Louis Chow, Osama Mesalhy, Mohamed Elsayed, and Yeong-ren Lin (University of Central Florida)	5d. PROJECT NUMBER 6206WF
	5e. TASK NUMBER
	5f. WORK UNIT NUMBER Q1X7

7. PERFORMING ORGANIZATION NAME(S) AND ADDRESS(ES) North Carolina A&T State University 1601 E Market Street Greensboro, NC 27411-0001	University of Central Florida Department of Mechanical and Aerospace Engineering Orlando, FL 32816-2450
---	---

9. SPONSORING/MONITORING AGENCY NAME(S) AND ADDRESS(ES) Air Force Research Laboratory Aerospace Systems Directorate Wright-Patterson Air Force Base, OH 45433-7542 Air Force Materiel Command United States Air Force	8. PERFORMING ORGANIZATION REPORT NUMBER
	10. SPONSORING/MONITORING AGENCY ACRONYM(S) AFRL/RQQM

11. SPONSORING/MONITORING AGENCY REPORT NUMBER(S) AFRL-RQ-WP-TR-2021-0055

12. DISTRIBUTION/AVAILABILITY STATEMENT DISTRIBUTION STATEMENT A. Approved for public release. Distribution is unlimited.

13. SUPPLEMENTARY NOTES PA Clearance Number: (Number).
14. ABSTRACT In making the transition towards electric aircraft, electro-mechanical actuators (EMAs) have been used to move the flight control surfaces. This has numerous advantages such as (a) reduction in weight and volume of power transmission; (b) reliability and safety improvement; (c) less maintenance and lower operating costs; (d) better dynamic characteristics; and (e) higher energy efficiency. An EMA contains four main parts: electric motor, electronic box, gearbox, and drive train.

15. SUBJECT TERMS electric aircraft, electro-mechanical actuators (EMAs)
--

16. SECURITY CLASSIFICATION OF:			17. LIMITATION OF ABSTRACT: SAR	18. NUMBER OF PAGES 388	19a. NAME OF RESPONSIBLE PERSON (Monitor) Quinn H. Leland
a. REPORT Unclassified	b. ABSTRACT Unclassified	c. THIS PAGE Unclassified			
					19b. TELEPHONE NUMBER (Include Area Code) 937-255-3060

TABLE OF CONTENTS

Section	Page
1 Executive Summary.....	1
2 Methods, Assumptions and Procedures.....	2
2.1 Fan Loop Testing Experimental Design	2
2.1.1 Construction and Experimental Setup.....	3
2.1.2 Calibration of Venturi Flowmeter.....	8
2.1.3 Results and Discussion.....	9
2.1.4 Experimental Results	14
2.2 Numerical Modeling of the Experimental Loop	17
2.2.1 Boundary and Initial Conditions	19
2.3 Grid Independent Study	19
2.3.1 Timestep Independence.....	19
2.3.2 Steady State Results	20
2.4 Transient State Results.....	22
2.5 Experimental Setup of Straight Pipe Experiments.....	27
2.6 EMA & Thermal Box Setup	47
2.7 EMA SIMULANT CAD DESIGNS.....	58
3 results and discussion	61
3.1 EMA Experimental Work	61
3.2 Experimental Procedure.....	62
3.3 Results and Discussion.....	68
3.4 Temperature Profile for Heating conditions	70
3.5 Numerical Simulations.....	73
3.6 Design Modifications.....	76
3.6.1 Option A: Extending the housing and installing a fan inside the motor	76
3.6.2 Option B: Incorporating internal recirculation through heat exchanger pipes..	81
3.7 CAD design and prototype build of EMA Heat Exchanger Setup.....	84
4 Thermosiphon Heat Pipe	86
4.1 Theory	87
4.2 Experimental Setup	88
4.3 Results and analysis:	91

4.3.1	The Effect of Screen Layers:	91
4.3.2	The Effect of Orientation	93
5	Sintered Heat Pipes.....	96
5.1	Experimental Setup	97
5.2	Results and Discussion.....	99
5.3	Normal Gravity Condition (+g)	102
5.4	Against Gravity Condition.....	106
6	Heat Pipe Applications on EMA Technology	108
6.1	Materials and Methods.....	109
6.2	Results and Discussion.....	115
7	Two Fan Comparison Work for EMA Simulant Cooling	125
7.1	Experimental setup.....	127
7.1.1	Equipment used for experimental setup.....	127
7.1.2	Fans tested.....	131
7.2	Theory	133
7.2.1	Hydrodynamic equations	133
7.2.2	3.2. Electrical component equations	133
7.3	Error Analysis	134
8	Results & discussion.....	135
8.1	Validation of the experiment.....	135
8.2	Fan 1 test results.....	136
5.3.	Fan 2 Test Results	138
9	Conclusion	143
10	Future Work on Thermal Box.....	144
	REFERENCES	145
	Appendix A.....	153
	Appendix B.....	162
	Appendix C.....	178
	Appendix D.....	186
	Appendix E	197
	Appendix F	208
	Appendix G.....	230
	Appendix H.....	234
	Appendix J.....	270

Appendix K.....	281
Appendix L.....	289
Appendix N.....	339
Appendix O.....	353
Appendix P.....	380

LIST OF FIGURES

Figure	Page
Figure 1. The Fan and Butyrate Clear Tube Assembly	3
Figure 2. Flow Loop-based	4
Figure 3. DC Power supply	4
Figure 4. Data of the Pressure in the Loop after 123 Seconds with the Vacuum Pump ON	5
Figure 5. The Vacuum Pump Used in the Loop.....	5
Figure 6. Loop's Capacity to Keep the Vacuum once the Vacuum Pump is Turned OFF	6
Figure 7. The PASCO 850 Universal Interface.....	6
Figure 8. The PASCO Quad Pressure Sensor	7
Figure 9. The CAD Design of the Venturi Meter Used in the Test Loop	7
Figure 10. Measurement of the Air Velocity using the Probe (Red box)	8
Figure 11. The Flow Straightener Used	8
Figure 12. Calibration of the Venturi Flowmeter.....	9
Figure 13. Fan Curves at 0.97 atm	9
Figure 14. Fan Curves Demonstrating Fan Scaling Laws with Variable Fan Speed	10
Figure 15. Fan Curves at Various Ambient Pressure Conditions with Constant Fan Speed	11
Figure 16. Fan curves Scaled with the Variable Ambient Pressure under Three Different Conditions with Constant Fan Speed.....	11
Figure 17. Comparison of the Two Geometrically Different Fans	12
Figure 18. Current Experimental Rig in the Laboratory	13
Figure 19. Pressure Taps in the Simulation are Placed in Identical Positions as the Experimental Taps	14
Figure 20. The Installation of the Two-stage Axial Fan into the Butyrate Tube	15
Figure 21. Fan Performance Curve Determined Experimentally with a Single Fan at 20000 rpm ...	15
Figure 22. AMETEK Rotron Propimax2 Geometric Features.....	16
Figure 23. Demonstrates the Rapid Fluctuations in Fluid Velocity Measured with the Testo 405i ..	16
Figure 24. CAD Design of the Loop	17
Figure 25. Flow straightener used in the simulation	18
Figure 26. The CAD of the venturi flowmeter used for simulation results.....	18
Figure 27. Demonstrates the Boundary Conditions Used to Model the Behavior within the Loop ..	18
Figure 28. Flow Trajectories within the Loop Simulating the Free Delivery of the Fan.....	20
Figure 29. Demonstrates the Flow Straightener's Effect on the Fluid Particles.....	21
Figure 30. Flow trajectories of the loop at the shutoff condition.	21

Figure 31. Fan Performance Curve that Compares the Experimental and SOLIDWORKS Flow Simulation Results.....	22
Figure 32. Comparison of the numerical and experimental pressures at the start.....	22
Figure 32. Comparison of the Numerical and Experimental Pressures at the Start	23
Figure 33. Volumetric Flow Rates Determined by SOLIDWORKS at Different Re when the Butterfly Valve is Fully Closed.....	23
Figure 34. Flow Trajectories around the Valve when Halfway Open.....	24
Figure 35. Vorticity around the Valve when Simulated at the Midway Position at $t=0.07s$	25
Figure 36. Isometric View of the Vortices in the Top Section of the Loop.....	26
Figure 37. Demonstrates the Entire Experimental Setup in Determining the Calibration	27
Figure 38. Zero Location was Carefully Determined in each Test	28
Figure 39. Water Level was Determined by Carefully Reading the Level at the Meniscus	28
Figure 40. Pressure Calibration Curve of the 493205 Pressure Transducer Unit	29
Figure 41. Demonstrates the Calibration Curve of the 492970 Gauge Transducer	29
Figure 42. Calibration Curve of the Differential Pressure Transducer	30
Figure 43. Demonstrates the 5 Points NIST Absolute Pressure Transducer Calibration Curve	30
Figure 44. Without Forcing the Curves to go through Zero.....	31
Figure 45. Demonstrates the Linear Fit Forced through the Point Zero-zero on the Plot.....	31
Figure 46. (b) Newport Super meter multi-meter used in monitoring the voltage output of the pressure transducer.	32
Figure 47. Differential pressure transducer calibration curve with linear fit function forced through the origin.....	33
Figure 48.(a) 5-bladed Delta Fan.	33
Figure 49. Arduino Circuit to Control the Fan Speed.....	34
Figure 50. The experimental loop that incorporates the butterfly valve as the flow restriction device and in the test loop laying flat on the table (experimental setup 1).....	35
Figure 51. 3D printed cone used for restricting the flow to obtain the fan performance curve	36
Figure 52. Demonstrates the manufacturer’s curve plotted against the experimental data obtained with the second experimental setup, cone valve, and demonstrates that a quadratic fit closely follows the trend of the manufacturer’s curve.....	37
Figure 53. The experimental setup used to develop the fan performance curves when using the cone as the flow restricting device (experimental setup 2).....	37
Figure 54. Compares the results of the single 7-bladed fan with the two different experimental setups.	38
Figure 55. The efficiency curves of the single 7-bladed fan for the two experimental setups.....	39
Figure 56. Single 7-bladed fan power vs volumetric flow rate curve for the two different experimental setups.	39

Figure 57. Fan performance curves of the three cases when using the cone valve experimental setup	40
Figure 58. Power vs volumetric flow rate determined while using experimental setup 2 at 13000 rpm.....	40
Figure 59. The efficiency vs volumetric flow rate for the three cases using experimental setup 2 at 13000 rpm.....	41
Figure 60. Displays the experimental setup where the pitot-tube is tested upstream of the venturi flowmeter.....	41
Figure 61. (a). 3D printed PLA venturi, $\beta = 0.51$	42
Figure 62. Demonstrates the average volumetric flow rates determined using the two venturi flowmeters and the pitot tube.	44
Figure 63. Demonstrates the fan performance curve with the error bars in the volumetric flow rate and the static pressure in the experimental data and a direct comparison to the numerical results. ..	46
Figure 64. Demonstrates the test rig.....	47
Figure 65. Pressure within the vacuum box after 30 minutes of testing.	48
Figure 66. The pipe fittings from the pump to the vacuum box.....	48
Figure 67. Experimental setup of the square stator testing within the wing-bay simulant.	49
Figure 68. Demonstrates the PLA 3D printed stand that was engineered to place the square stator within the box.....	50
Figure 69. A top view of the experimental setup with the DAQ system by MC Computing	51
Figure 70. Demonstrates the location of the K-type thermocouples used in the experiment.....	51
Figure 71. Temperatures of the stator core at the locations demonstrated in figure 70 for 1atm.....	52
Figure 72. The temperature of the copper end winding at various pressures.....	53
Figure 73. The temperature of the copper embedded winding at various pressures.	53
Figure 74. The ambient temperature of the test bay at various pressures.	54
Figure 75. The temperature of the laminated core at various pressures.....	55
Figure 76. The temperature of the end winding during the heating of the stator core	55
Figure 77. The temperature of the embedded windings during the heating of the stator core.....	56
Figure 78. The temperature of the laminated core during heating of the stator core.	56
Figure 79. The ambient temperature of the wing bay during heating of the stator core.	57
Figure 80. Demonstrates the aluminum housing of the EMA simulant.....	58
Figure 81. The temperature rise of the EMA to the average ambient temperature for different fin counts.....	59
Figure 82. Demonstrates the difference in temperature rises amongst the different fin counts at various thermal power settings.....	59
Figure 83. Transmotec Motor DMA-24-5-B-102-IP65	62
Figure 84. PA 003 Motor	63

Figure 85. DMA-24-5-B-IP65 Motor parts and experimental setup.....	66
Figure 87. An electrical circuit for the experiment.	67
Figure 86. Demonstrates the current vs load.....	67
Figure 88. Power consumption and dissipation profile at no external load.	69
Figure 89. Power consumption and dissipation at full Static load.	69
Figure 90. The air temperature inside DMA24motor housing at full static load and no-load (free spinning conditions)	71
Figure 91. The transient temperature profile of PA-003 at Q=60.12W. (b). The temperature probe locations.....	72
Figure 92. 80 s heating at Q=66W followed by cooling by natural convection.....	73
Figure 93. Mesh for the thermal study of the original motor	74
Figure 94 Transient thermal profile of the original motor	76
Figure 95. Demonstrates the redesigned outer housing with the fan source for convective cooling.77	
Figure 96. ETRI Fan temperature probes placed at and around the motor at a steady state.	78
Figure 97. Temperature contours using the ETRI Fan at steady-state conditions.	78
Figure 98. Temperature probe measurements at and around the motor using the Mechatronics Fan at a steady state.....	79
Figure 99. Temperature contour of the motor being cooled by Mechatronics Fan at a steady state..79	
Figure 100. Temperature probe measurements	80
Figure 101. The internal fan within the EMA	81
Figure 102. Temperature contours with velocity streamlines and quiver plots	82
Figure 103. Temperature contour within the system, and shows the distribution across the recirculating system.....	82
Figure 104. Demonstrates the hot spots within the rotor piece of the EMA; furthermore, the hotspot (red) is seen in the end windings with a temperature of 86.65°C along the backside of the motor. ..	83
Figure 105. Side view of the CAD demonstrating the interior of the fan assembly.	84
Figure 106. (a) Demonstrates the physical assembly of the fan HX concept. (b) Demonstrates the physical fan that was 3D printed that will be used for the testing of the HX concept.	85
Figure 107. The experimental setup	90
Figure 108. The variation of the temperature difference across the pipes as a function of heat input.	91
Figure 109. Thermal resistivity of the pipes as a function of the heat input.	92
Figure 110. The Nusselt number of pipes at different heat loads.....	93
Figure 111. The temperature difference across the pipes at different orientations.	94
Figure 112. The Nusselt Number of the pipes at different orientations.	95
Figure 113. Schematic of a general heat pipe showing its sections and component [61]	96

Figure 114. Pipe 3, un-sintered copper powder wick heat pipe	98
Figure 115. Experimental set-up for normal gravity condition (+g).....	99
Figure 116. Experimental set-up for against gravity (-g) condition.....	99
Figure 117. (a). SEM image of un-sintered copper wick; magnification 400. (b) SEM image of the un-sintered copper wick, magnification 1200.	100
Figure 118. SEM image of the sintered copper wick, magnification 1200.....	101
Figure 119. The behavior of un-sintered wick heat pipe at 5W heat load	102
Figure 120. The steady-state temperature difference between evaporator and condenser (ΔT) vs. heat load.	103
Figure 121. Total thermal resistance vs. heat load	104
Figure 122. Heat transfer coefficient vs. heat load.....	104
Figure 123. Steady-state evaporator temperature vs. heat input for un-sintered and sintered wick heat pipe.	105
Figure 124. Steady-state condenser temperature vs. heat input for un-sintered and sintered wick heat pipes.....	105
Figure 125. Evaporator and condenser temperatures of un-sintered and sintered wick heat pipes in against gravity condition.	107
Figure 126. The total thermal resistance of un-sintered and sintered wick heat pipes in normal gravity and against gravity conditions.....	107
Figure 127. Original motor in holding the position, Inside view of motor shows copper windings embedded in rotor core and separated by a clearance and PA 03 EMA with 5 heat pipes extending through the cover.....	111
Figure 128. Circuit diagram for the experiment.....	111
Figure 129. Inside view of motor showing heat pipe evaporators	112
Figure 130. Porous Fins.....	115
Figure 131. The temperature profile of the original motor at a heating rate of $Q=20.5$ Watts	116
Figure 132. The temperature profile of motor at a heating rate of $Q=20.5$ Watts with 5 heat pipes, δT of heat pipes = 1.20C	116
Figure 133. The temperature profile of motor at a heating rate of $Q=20.5$ Watts with 8 heat pipes, δT of heat pipes = 1.320C	117
Figure 134. The temperature profile of motor at a heating rate of $Q=20.5$ Watts with 10 heat pipes δT of heat pipes = 0.840C	117
Figure 135. The temperature of windings at the heating rate of $Q=20.5$ Watts.....	118
Figure 136. The air temperature inside motor housing at a heating rate of $Q=20.5$ Watts	118
Figure 137. The temperature of windings at a heating rate of $Q=28.2$ Watts	119
Figure 138. Air Temperature inside the housing at a heating rate of $Q=28.2$ Watts.	119
Figure 139. Reduction in temperature of windings vs the number of heat pipes.....	120

Figure 140. Temperature profile of windings 20.5 W when EMA was modified with heat pipes and porous fins.	121
Figure 141. The temperature profile of inside air at 20.5 W when EMA was modified with heat pipes and porous fins.....	121
Figure 142. The temperature profile of windings at 28.2 W when EMA was modified with heat pipes and porous fins.	122
Figure 143. The temperature profile of inside air at 28.2 W when EMA was modified with heat pipes and porous fins.....	123
Figure 144. Reduction in temperature of windings vs the number of heat pipes in finned configuration	123
Figure 145. Reduction in winding temperature with 5 heat pipes at different configurations.....	124
Figure 146. Structural diagram (top) with experimental loop (bottom).....	128
Figure 147. The 3D printed ABS Venturi, $\beta = 0.51$	129
Figure 148. The Pitot tube incorporated into the tube to determine the volumetric flow rate.	129
Figure 149. Demonstrates the calibration of the 3D printed Venturi flowmeter.....	130
Figure 150.(a) Arduino hardware setup (red arrow) that is used to read the fan (green arrow) speed from the signal wire (brown), the red and black wire are positive and ground, respectively. (b) The Protmex non-contact tachometer used to verify the fan’s rotational speed.	130
<i>Figure 151. The vacuum pump utilized to change the ambient pressure within the loop.</i>	<i>131</i>
Figure 152. Integration of the nylon and fan assembly to secure the 2-bladed fan, Fan 1.....	132
Figure 153. The Delta dual fan system and its incorporation into the clear tube, Fan 2.....	132
Figure 154. Validation of the experimental loop testing the 2-bladed fan.....	135
Figure 155. The fan performance of Fan 1 at various ambient conditions.....	136
Figure 156. Dimensionless performance curve for Fan 1.	137
Figure 157. The efficiency of Fan 1 at various ambient pressure conditions	138
Figure 158. The results of the single 7-bladed fan at various ambient pressures.....	139
Figure 159. The nondimensional fan performance of Fan 2 at variable ambient pressures.....	140
Figure 160. The fan efficiency for the Fan 2, 7-bladed fan at various ambient conditions.	140
Figure 161. Compares the nondimensional fan performance curves extreme pressure conditions.	141
Figure 162. Fan efficiencies at various ambient pressures.....	142

LIST OF TABLES

TABLE	PAGE
Table 1. The Fan Scaling Analysis with Varying Pressures and Constant Fan Speed.....	12
Table 2. The Fan Scaling of Power Consumption with Varying Pressures and Constant Fan Speed.	12
Table 3. Percent Difference between Different Grid Sizes Compared to the Densest Mesh.....	19
Table 4. Demonstrates the Time Step Independence of the Simulation.....	20
Table 5. Linear Equations of Best Fit for the Two Test Runs for 492970 Pressure Transducer	31
Table 6. The 4-wire arrangement of the 7-bladed Delta fan.	35
Table 7. The diameter ratio of each venturi is demonstrated.	43
Table 8. Demonstrates the degrees of freedom and the confidence interval used in the statistical analysis.	45
Table 9. The pressure transducer overall uncertainties for the units used in the experimental setup.	45
Table 10. Demonstrates a comparison of the temperature rise of the EMA to the ambient air compared to the 72 finned optimal cases.	60
Table 11. Manufacturer supplied specifications of DMA-24-5-B-IP65 (Source product catalog: www.transmotec.com) and PA 003 (source: progressiveautomations.com).....	63
Table 12. Mesh details.....	73
Table 13. Shows the various average heat transfer coefficients determined by SOLIDWORKS Flow Simulation.	77
Table 14. Heat Pipes Studied.	88
Table 15. Pipes Characteristics [59].....	89
Table 16. Water Thermo fluid Characteristics.	89
Table 17. Mesh Screen Characteristics.	90
Table 18. The temperature difference across the pipes.	91
Table 19. The heat transfer coefficient across heat pipes.....	92
<i>Table 20. Showing steady-state evaporator temperature of sintered and un-sintered heat pipes for against gravity condition.....</i>	<i>106</i>
Table 21. Manufacturer supplied data for PA 03-10-600 EMA.....	109

1 EXECUTIVE SUMMARY

In making the transition towards electric aircraft, electro-mechanical actuators (EMAs) have been used to move the flight control surfaces. This has numerous advantages such as (a) reduction in weight and volume of power transmission; (b) reliability and safety improvement; (c) less maintenance and lower operating costs; (d) better dynamic characteristics; and (e) higher energy efficiency. An EMA contains four main parts: electric motor, electronic box, gearbox, and drive train. One of the main issues in the use of EMAs in aircraft is the potential overheating that occurs in the electric motors and power electronics due to the high heat dissipation in them. In aerospace applications, air-cooling is preferable compared to liquid cooling because of the state instability (freezing) of liquids in a working environment, which could often become harsh. Besides, liquid cooling adds more weight and complication to the cooling system. Wing-bay air represents an attractive and economical medium for cooling. Using axial fans, this wing-bay air can be pushed/sucked over/through the heat sinks that cover the electric motor and electronics. The project was a collaboration between NCAT and UCF where we have focused on thermal management of EMA through the following items:

- Testing of A Cooling Fan for Wing-Bay Electro-Mechanical Actuators. The study closely observed the results obtained experimentally with that of the fan scaling analysis.
- Simulating the Effects of Turbulence on Pressure Tap Measurements. The main objective of this paper is to study the effects of turbulence in collecting pressure tap measurements under high Reynolds number flows.
- Effect of Screen Layers and Orientations on Mesh Wicked Heat Pipes. An experimental study was carried to compare the thermal performance of an empty copper pipe, a traditional thermosiphon, and two wicked heat pipes with different number of mesh screen layers.
- Performance of a Gravity Independent Heat Pipe. Experimental work on empty pipe, a thermosiphon, an un-sintered wick, and a sintered wick heat pipe, was considered for comparison.
- Thermal Management of PA-03-10-600 Linear Electromechanical Actuator End Windings Using Straight Circular Heat Pipes and Porous Fins. A thermal study on a linear electromechanical actuator (EMA) PA 03-10-600 with the goal of managing the temperatures of the windings when the motor is in operation.
- Comparison of Two Axial Fans for Cooling of Electromechanical Actuators at Variable Pressure. Two cooling fans were tested experimentally to determine the effects of the blade count and ambient pressure on the fan performance and efficiency.
- Studying the performance of an axial fan in cooling a heat sink attached to the electric motor housing.
- Studying the effect of using partial-shield/guide-plate on a parallel plate fin heat sink (PPFHS) attached on the electronics of an EMA.
- Studying the availability of using two fans in series to add redundancy to the cooling system and increase its reliability.

2 METHODS, ASSUMPTIONS AND PROCEDURES

2.1 Fan Loop Testing Experimental Design

The first action item that was conducted was to construct a viable experimental setup to determine fan performance curves accurately. Development methods to cool both the EMA electric machines together with their power electronics. Our collaboration between NCAT and UCF uses CFD and experimental methods to accomplish the specific tasks outlined in the project. The scaling laws express the relationship between the fan static pressure head, volume flow rate, air density, rotational speed, fan diameter, and power. The fans were characterized using the following equations [3]:

Volumetric flow rate:

$$Q = k_Q n d^3 \quad (1)$$

Static pressure head:

$$p = k_p \rho n^2 d^2 \quad (2)$$

Power:

$$P = k_P \rho n^3 d^5 \quad (3)$$

where

k: constants for geometrically and dynamically similar conditions

n: fan speed (rpm)

d: fan diameter

ρ : air density

Using these conditions, it is possible to determine another fan condition compared to that of a baseline.

The fan scaling laws are derived in the following manner [3]:

$$Q_2 = Q_1 \frac{n_2}{n_1} \quad (4)$$

$$p_2 = p_1 \left(\frac{n_2}{n_1} \right)^2 \quad (5)$$

$$P_2 = P_1 \left(\frac{n_2}{n_1} \right)^3 \quad (6)$$

where the only variable changing is the fan speed, and the diameter of the fan and density is held constant. Consequently, the fan scaling laws can be obtained for varying the density while keeping the fan diameter and fan speed at a constant:

$$Q_2 = Q_1 \quad (7)$$

$$p_2 = p_1 \frac{\rho_2}{\rho_1} \quad (8)$$

$$P_2 = P_1 \frac{\rho_2}{\rho_1} \quad (9)$$

The equations for determining the scaled volume flow rate (4), (7); scaled static pressure head (5), (8); and for scaled fan power (6), (9), are presented above with their corresponding

parameters held either constant or variable. Similarly, from Ockert, et al., the equations for the fan scaling laws were derived identically [1].

2.1.1 Construction and Experimental Setup

The loop was built using piping with 4” inner diameter (ID) and 4.5” outer diameter (OD) also known as Schedule 40 PVC. The joints used are cast plastic by the company Fernco [11]. To regulate the resistance of the system, a control valve was placed into the loop. The control valve used is the NIBCO butterfly valve with two flanges surrounding the valve. The hardware used to maintain the joints and the flanges to prevent the leakage of the system. Figure 1 shows the current configuration of the system. The joints are the black components of the system, and the butterfly valve can be seen at the bottom of the loop in blue. Venturi flow meter was positioned within the loop as shown in a red box.

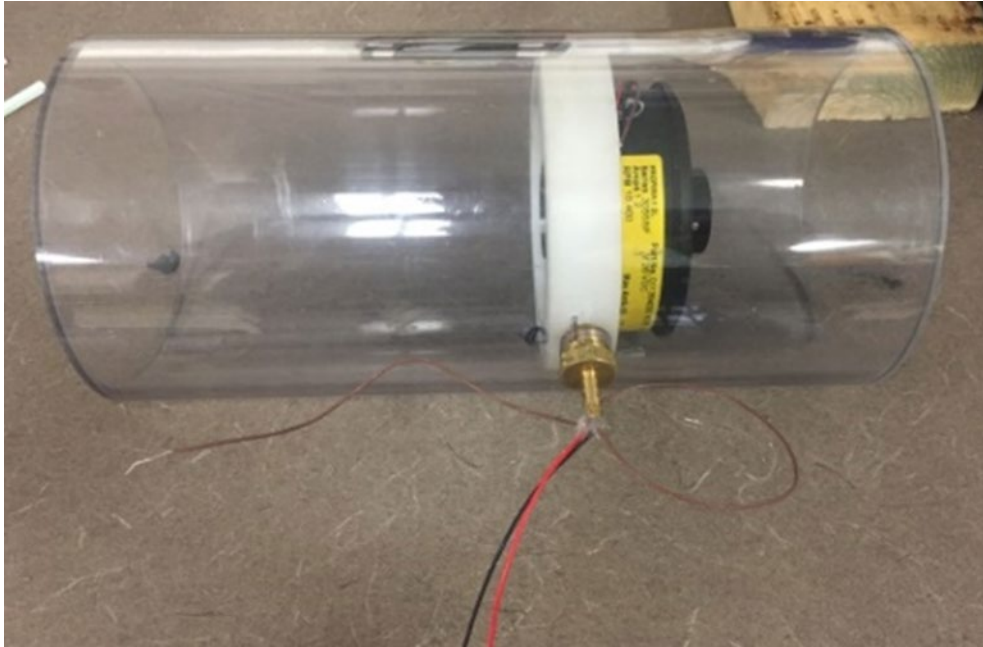


Figure 1. The Fan and Butyrate Clear Tube Assembly

The current test fan in the placed into the loop was an AMETEK PROPIMAX 2 [4] with an optimized fan speed of 18,400 RPM. There was a great deal of machining involved to embed the fan into the clear tube. The material of the clear tube is Butyrate (from Busada) which managed to withstand the vacuum needed for this experiment. Figure 2 shows how the fan was inserted into the butyrate tube.



Figure 2. Flow Loop-based

To achieve the various fan speeds, the fan is directly connected to a power supply. The voltage is then regulated to either increase or decrease the speed of the fan. The power supply used is the VOLTEQ DC Power Supply [6], shown in Figure 3.

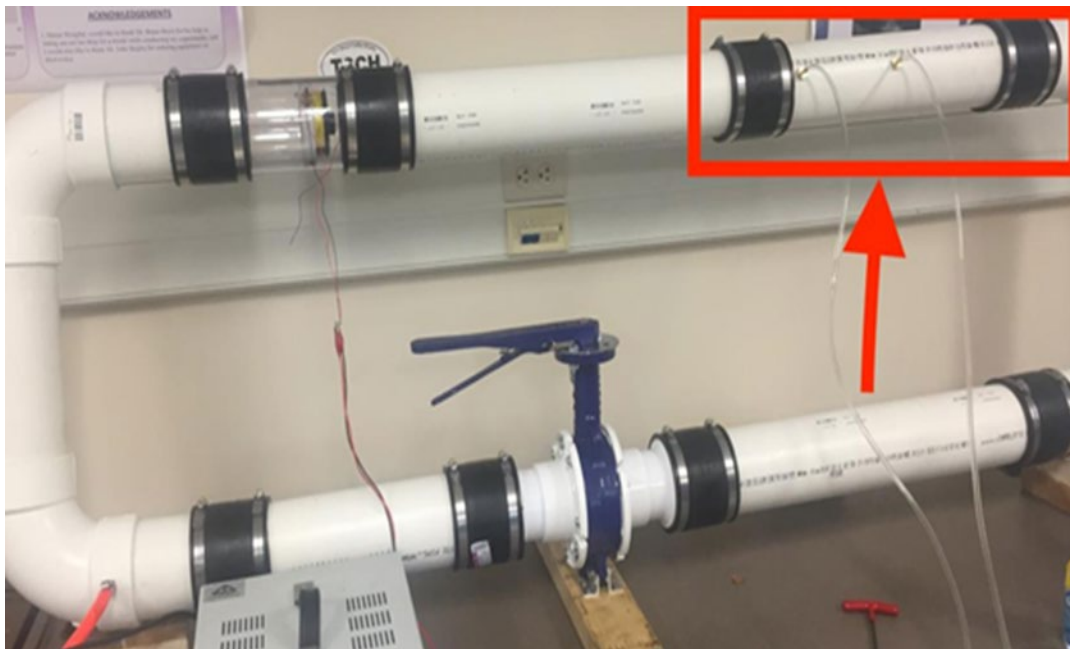


Figure 3. DC Power supply

After assembly, the loop was held under vacuum to simulate conditions at the high altitudes. The vacuum pump was tested multiple times, and with the current configuration, the pump could lower the pressure in the loop to 17950 Pa (which is approximately 20% of atmospheric pressure). The results shown in Figure 4 show the effectiveness of the vacuum pump to lower the pressure to 17950 Pa. Figure 5 shows the vacuum used in the experiment. The loop was tested for pressure leaks. Figure 6 shows the ability of the loop to maintain pressure after the pump has been turned OFF.

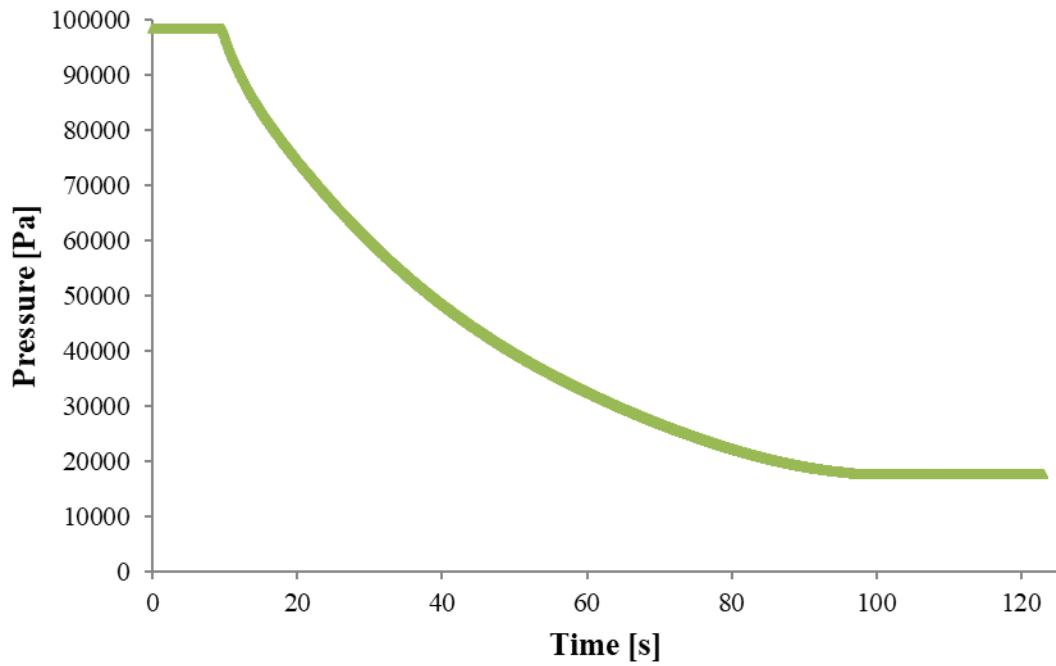


Figure 4. Data of the Pressure in the Loop after 123 Seconds with the Vacuum Pump ON



Figure 5. The Vacuum Pump Used in the Loop

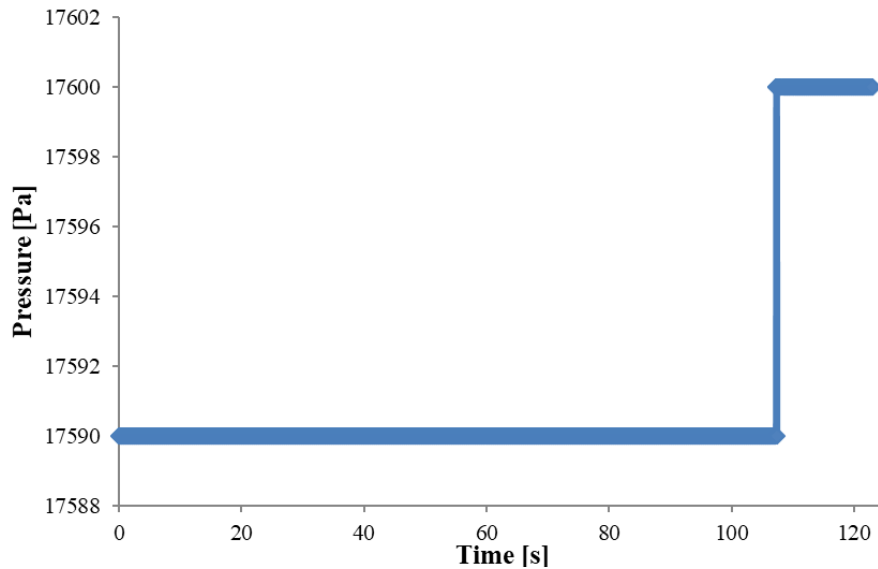


Figure 6. Loop's Capacity to Keep the Vacuum once the Vacuum Pump is Turned OFF

The pressure measurements were attained with the use of PASCO instruments. The PASCO devices used in the experiment are 850 Universal Interface [7], PS-2164 Quad Pressure Sensor [8], and PASCO's Capstone software. Figures 7 and 8 show the PASCO Interface and the PASCO pressure sensor respectively.



Figure 7. The PASCO 850 Universal Interface



Figure 8. The PASCO Quad Pressure Sensor

To measure the volumetric flow rate of the air within the loop, a Venturi meter was machined to measure the pressure drop across two set points. In doing so, we can calculate the air velocity generated by the fan. The Venturi meter machined was based upon the ISO-5167-4 [2]. The Venturi meter was positioned within the loop as shown by a red box in figure 1. In figure 9, a CAD was developed to represent the Venturi used in the loop to determine the volumetric flow rate within the test rig.

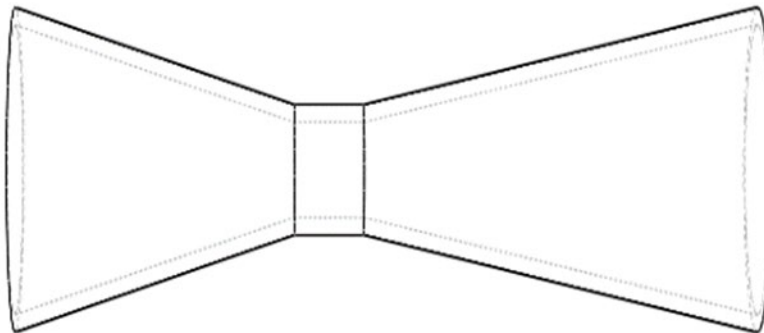


Figure 9. The CAD Design of the Venturi Meter Used in the Test Loop

The measured flow velocity was compared with a single point velocity probe using hot-wire anemometer, Testo 405i [10]. Both the probe and Venturi were exposed to the same fan speed. The Testo 405i was used to get the fluid's velocity at the center of the clear tube; since this is the point where the velocity of the probe will equal that of twice the Venturi's measured velocity. This device is a hot-wire anemometer that has the capacity to determining the fluid velocity by detecting a temperature difference between the passing fluid and the heated wire. Testo claims that their devices are reliable and calibrated to achieve fluid velocity measurements. The experiments operating range was well within the probe's range. The device was placed behind the tube as shown in figure 10, and the following figure shows the results obtained with this device.

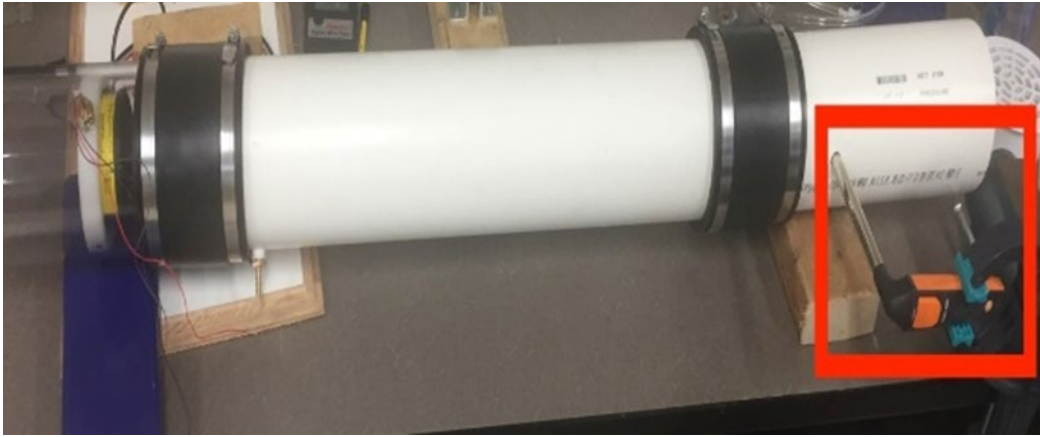


Figure 10. Measurement of the Air Velocity using the Probe (Red box)

To obtain a measurement with a closer agreement with the device and Venturi meter, a flow straightener was necessary. Figure 11 shows the flow straightener used in the experiment from Sioux Chief Mfg.



Figure 11. The Flow Straightener Used

2.1.2 Calibration of Venturi Flowmeter

The data shows the velocity based on this probe is $V_p = (10.07 \pm 0.09)$ m/s. The data associated with the figure above was taken for a total of 150 seconds. Thus, the Venturi meter can be calibrated. After several tests run under the same conditions, the probe's data and the Venturi meter data demonstrated consistency. Figure 12 demonstrates both of the velocity measuring devices and their corresponding data sets.

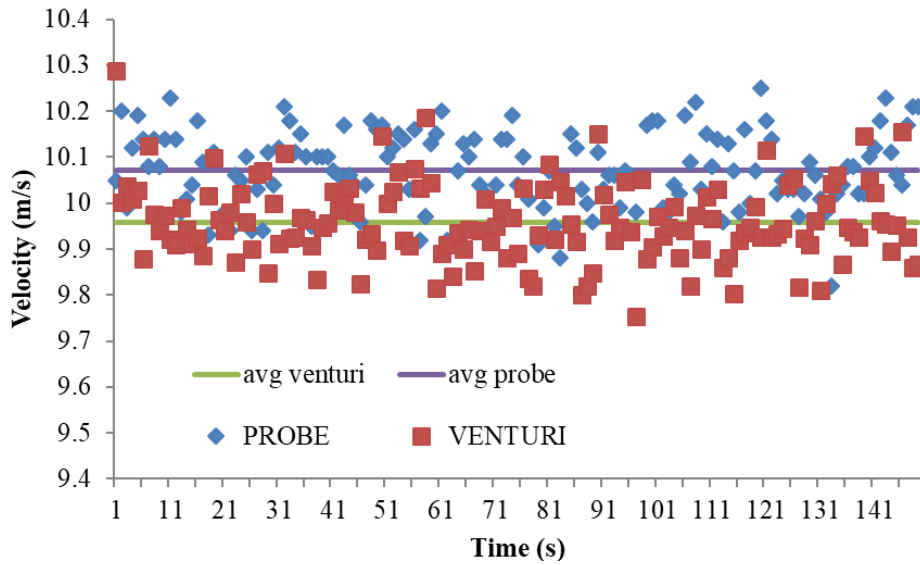


Figure 12. Calibration of the Venturi Flowmeter

2.1.3 Results and Discussion

The fan tested in the loop has delivered results at two fan speeds: 20,000 and 15,000 rpm. Figure 13 shows the data of the fan curve attained at atmospheric pressure.

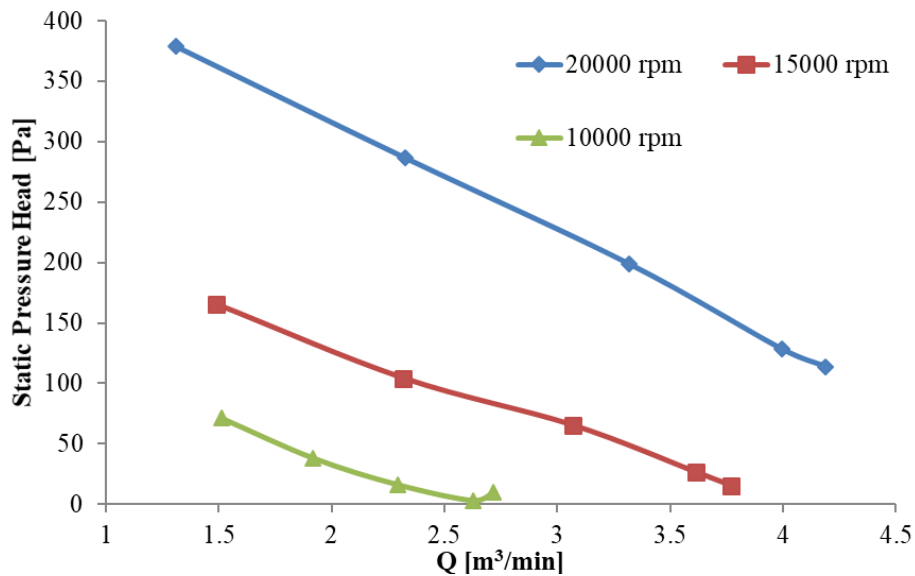


Figure 13. Fan Curves at 0.97 atm

Figure 14 uses the results obtained from the previous figure to prove the accuracy of fan scaling at variable rotational speeds. The baseline fan speed chosen was 20,000 rpm; consequently, the 15,000-rpm fan curve was scaled accordingly. With the use of the fan scaling laws [3], the fan curve for 15,000 rpm was altered. The static pressure at 15,000 rpm was decreased by a factor of 1.33^2 and the volumetric flow rate was also decreased by 1.33 ($20,000/15,000 = 1.33$). The scaling was also performed for the 10,000 rpm and the following factors were used for the static pressure head and volume flow rate, respectively 2^2 and 2 ($20,000/10,000 = 2$). From Figure 14, the scaling laws show validity at 15,000 rpm but lack consistency when trying to approximate the behavior at 10,000 rpm.

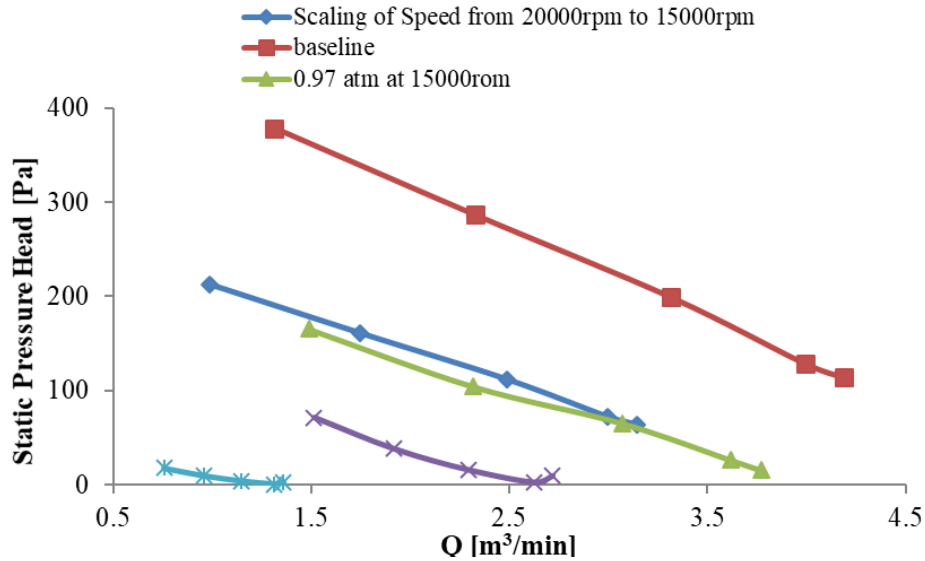


Figure 14. Fan Curves Demonstrating Fan Scaling Laws with Variable Fan Speed

These two rotational speeds have been tested at two other pressures within the test loop. There have been various experiments conducted at 0.7 atm. and 0.5 atm. The power supply has allowed for the adjustment of the voltage, which affects the rotational speeds of the fan throughout these experiments. To increase the resistance of the system, the butterfly valve was gradually closed; thus, the fan curves were obtained (the butterfly valve was closed at five intermittent points: 9, 7, 5, 3, 1 which are labeled).

Further experiments were conducted to test the fan at different pressures. Figure 15 shows the fan curves at 0.97 atm., 0.7 atm., and 0.5 atm. These experiments were carried out to determine the scaling laws of the fan under varying ambient pressures. The flow rate was not adjusted since it is independent of pressure as shown in equation (7). The static pressure was scaled with the use of equation (8) and is the ratio of densities. For the scaling of 0.97 atm. to 0.7 atm. the factor is $(0.8903/1.1486 = 0.7751)$. Consequently, a similar analysis was conducted for determining the scaling of the fan to 0.5 atm., which resulted in the following density ratio $(0.6798/1.1486 = 0.5918)$. The only parameter being changed under these conditions was the pressure within the loop; furthermore, the rotational speed of the fan was held constant at 20,000 rpm. Figure 16 has the results of the scaling, and the curves demonstrate the use of the scaling laws for density at 0.5 atm. and 0.7 atm.

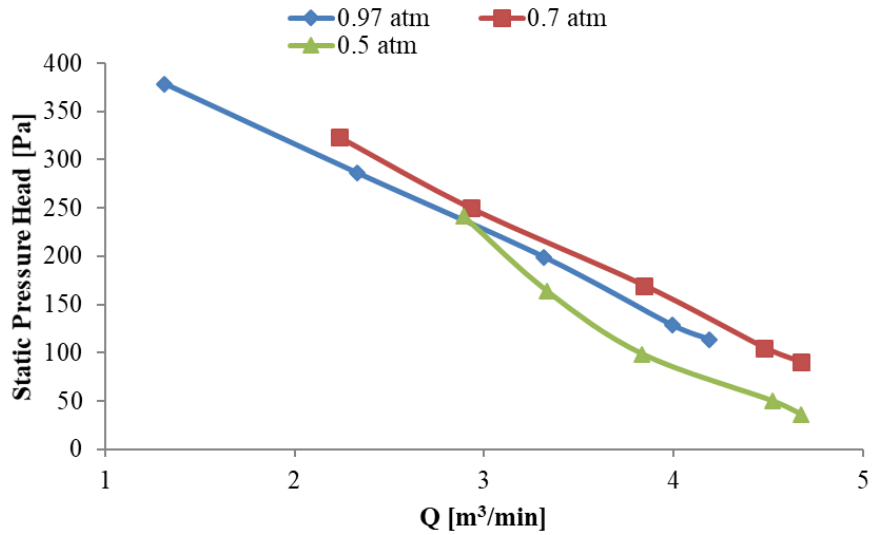


Figure 15. Fan Curves at Various Ambient Pressure Conditions with Constant Fan Speed

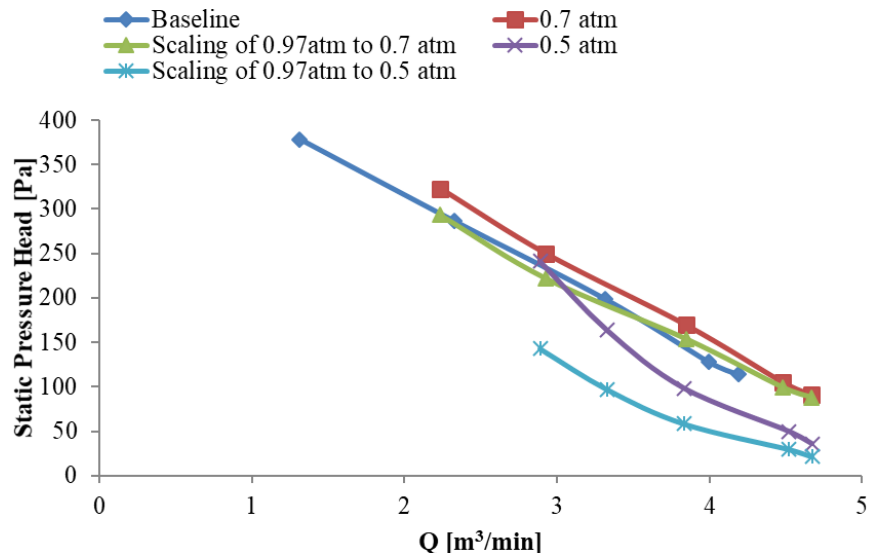


Figure 16. Fan curves Scaled with the Variable Ambient Pressure under Three Different Conditions with Constant Fan Speed

The scaled fan curve will follow the behavior of the baseline curve chosen. Moreover, the pressure did not scale as expected using the equations presented above. Further testing should be conducted to conclude this behavior.

Table 1 shows the data of power consumed by the fan along with the scaling of the fan speed as the variable parameter. The power consumption of the fan is provided in detail based upon the various pressures inside the test loop. Taking the fan speed of 20,000 rpm and atmospheric pressure as the baseline fan curve, the scaling laws [3] can be used again to approximate the power consumption and compare that the actual power consumption. Fan scaling shows that power consumption is reduced by the factors shown below. Equation (6) shows the factor is raised to the third power.

Table 1. The Fan Scaling Analysis with Varying Pressures and Constant Fan Speed

Fan Speed [rpm]	Power [W]	Scaled Power [W]	Scaling Factor
20000	25.6	n/a	Baseline
15000	10.68	10.8	0.422
10000	3.39	3.2	0.125

The scaling was performed comparably to that of the fan's speed and pressure scaling presented earlier. The fan is kept at a constant speed of 20,000 rpm to perform the analysis. Table 2 shows how the scaling and the actual power consumption behave under various ambient pressures.

Table 2. The Fan Scaling of Power Consumption with Varying Pressures and Constant Fan Speed

Pressure [atm.]	Power [W]	Scaled Power [W]	Scaling Factor
0.97	25.6	n/a	Baseline
0.7	23.04	19.84	0.775
0.5	20.48	15.15	0.592

The factors were used to scale the power accordingly since it is just the density ratio. The discrepancy in the power consumption can be due to the fan specifications since this fan is optimized to work at 18,400 rpm under an atmospheric pressure of 1 atm. Due to our environmental conditions, the atmosphere in the lab was 0.97 atm. In experimental procedures, other factors can play a role in this calculation as well, such as mechanical deficiencies in the fan (i.e., bearings and electric motor loss) [3]. The fan scaling laws show closer proximity to the actual conditions for the varying fan speeds, but do not show the same level of accuracy for the changes in pressure.

A different fan was then used for further testing. A 12-bladed fan by Freewing was tested to compare the results obtained by the 2-bladed AMETEK fan. Figure 17 shows the fan performance curves for the two different fans. We can see that the Freewing 12-bladed fan does not behave as the AMETEK fan. There have been numerous tests conducted on the 12-bladed fan. The trend discussed here is still under further investigation to determine what is physically happening in the test rig.

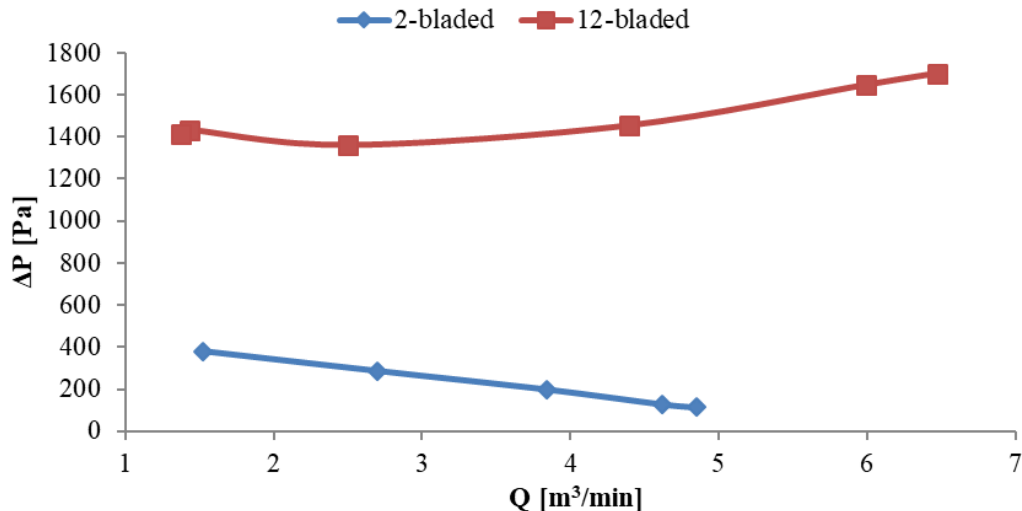


Figure 17. Comparison of the Two Geometrically Different Fans

The AMETEK PROPIMAX 2 fan has been tested for three ambient pressures of 0.97 atm., 0.7 atm., and 0.5 atm. Under these varying conditions, the fan performance curve has been determined for two fan speeds 20,000 rpm and 15,000 rpm. These fan scaling laws have been proven to accurately determine the curve using 20,000 rpm as the baseline fan curve. The experimental data and the scaling laws have been verified to show the proper nature of the fan curve when varying the fan speed and holding the pressure, and fan diameter constant. The scaling analysis for the varying pressures and constant fan speed and fan diameter does not show the same level of fidelity. Further tests will be conducted to obtain fan performance curves at 0.17 atm. for the current fan. Also, the tests that have been discussed thus far will be conducted with a completely different fan to test the scaling laws further.

This study is a continuation of an already existing experiment. In that paper, the affinity laws were experimentally confirmed to accurately predict the performance curve of a single fan at various rotational speeds and pressures, but once tested under extreme pressure conditions (i.e., 0.2 atm.) the fan scaling laws were unable to predict accurately the fan curves [12]. Figure 18 demonstrates the current experimental setup used in that paper.



Figure 18. Current Experimental Rig in the Laboratory

The objective is to enhance the cooling performance of electro-mechanical actuators used in aerospace applications. Electro-mechanical actuators act as a heat source within a wing-bay; therefore, the test loop has been simulating sub-atmospheric conditions and the performance of axial fans under these environmental conditions. According to the literature, fans in a series formation increase the static pressure across n number of fans; on the other hand, for fans in a parallel arrangement the volume flow rate is the parameter that increases [13]. Extensive studies have been conducted for parallel systems around Water Distributions Systems (WDS). The affinity laws have been studied for various applications to accurately predict the best point of operation [14,15]. According to Koor et al., they investigated the best efficiency point (BEP) of variable speed pumps (VSPs) using the Levenberg-Marquardt algorithm (LMA); furthermore, they discovered that for identical pumps the efficiency is optimized at equal discharge rates [16]. Borsting et al modeled various methods of grouping VSP's and optimization techniques [17]. The automotive industry also is heavily investing time in discovering better cooling mechanisms. In Filho et al, they studied how installing parallel fans are beneficial to cooling a system used for

buses. The electrical fan system was more efficient, less noisy, more controllable, and easier to maintain [18]. Researchers have worked extensively in understanding the characteristics of axial fans.

Chow et. al have performed studies of fan performance curves at various ambient pressures [19, 20]. In evaluating fan performance, computational fluid dynamics (CFD) and experimentation have been combined by many researchers. Lin et al utilized ANSYS to combine numerical results and experimental results for improving the performance of fan design [21]. Additional methods of cooling have been studied. Combining both series and parallel arrangements to cooling heat generation enclosures have been investigated. These studies evaluated small fans function well for areas of localized heat generation, and large fans dissipate heat effectively in large areas [22]. Other methods of cooling have been proposed, such as using the working principles within heat pipes to transfer localized areas of heat to the ambient for cooling of electrical machines [23].

Using fans to cool the electronic components has the capability of stirring the ambient air within the system. Thus, this mixing can introduce eddies which can enhance the heat transfer within the structure. Studies of turbulent pipe flow have been extensively studied since Osborne Reynolds proposed the idea. Researchers have studied the methods to disrupt turbulence within pipe flow [24]. Other studies have centralized their work on studying the behavior of pipe flow at low Reynolds numbers with the use of various turbulence solvers and experimentation [25, 26].

The high Reynolds number flows within the pipe could potentially provide erroneous pressure measurements at the taps. Xu et al have performed numerical studies on errors of pressure measurements related to orifice flowmeters [27]. The objective of this paper is to explore whether the pressure measurements have been compromised by the turbulent flow within the system. The physics of the flow within the test loop will provide insight into improving the cooling capabilities.

2.1.4 Experimental Results

The fan performance was determined experimentally for the fan operating at standard pressure and temperature conditions while rotating at a constant speed of 20,000 rpm. The performance of a fan can be determined by measuring the pressure differential across the fan and a flow measurement device. We have chosen a venturi flowmeter to determine the volumetric flow rate within the loop. The pressure tap positions are demonstrated in figure 19; moreover, the taps at the fan are position 2'' before and after the fan. The Nylon was machined to mount the fan into the butyrate tube displayed in figure 20. The fan performance curve obtained with the AMETEK Rotron two-stage fan is shown in figure 21. Figure 22 demonstrates the geometry of the AMETEK fan in closer detail.



Figure 19. Pressure Taps in the Simulation are Placed in Identical Positions as the Experimental Taps



Figure 20. The Installation of the Two-stage Axial Fan into the Butyrate Tube

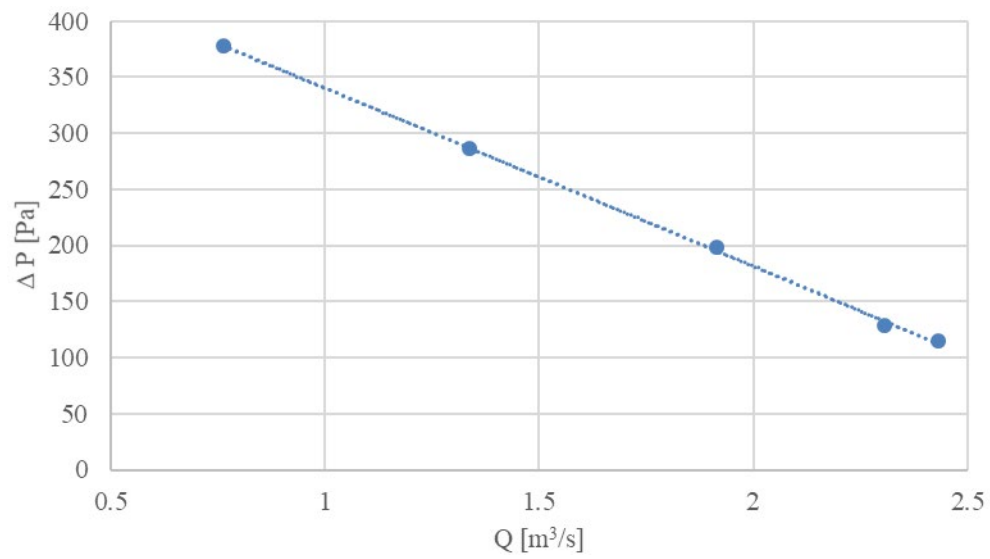


Figure 21. Fan Performance Curve Determined Experimentally with a Single Fan at 20000 rpm



Figure 22. AMETEK Rotron Propimax2 Geometric Features

The equation for the volume flow rate of an obstruction flowmeter can be obtained by combining Bernoulli's equation with continuity to yield [28, 29],

$$Q = C_d A_t \sqrt{\frac{2(\Delta p)}{\rho(1 - \beta^4)}} \quad (10)$$

where Δp is the differential pressure in the throat and upstream of the venturi, ρ is the density, $\beta = d/D$ the diameter ratio of the throat to upstream diameter, A_t is the cross-sectional area in the throat of the flowmeter, and C_d is the discharge coefficient.

A hot-wire anemometer by Testo 405i was used to determine the fluid velocity experimentally. In figure 23 the results demonstrate rapid fluctuations in the values recorded by this unit.

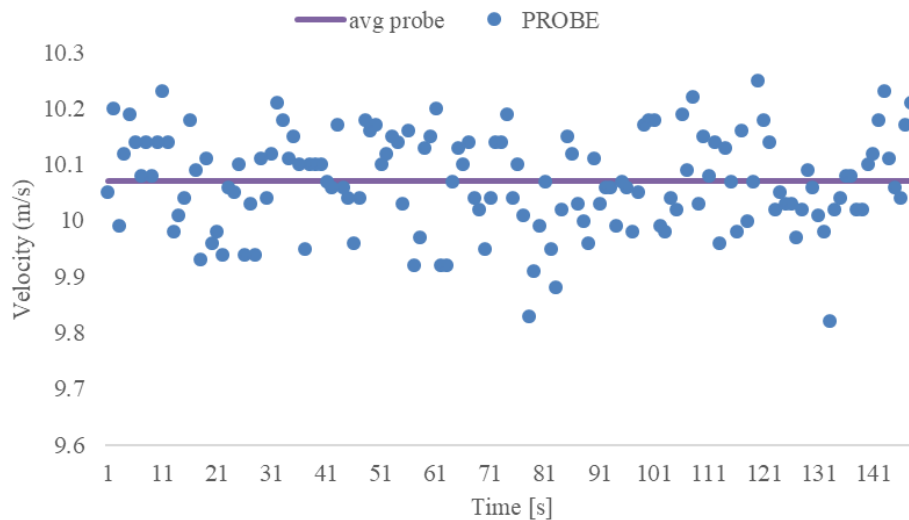


Figure 23. Demonstrates the Rapid Fluctuations in Fluid Velocity Measured with the Testo 405i

This data was recorded 26 inches downstream of the fan. When testing at the shutoff condition of the fan; furthermore, with the use of SOLIDWORKS flow simulation, we will explore those effects. The shutoff condition is experimentally obtained when the flow is constrained with the use of a flow regulating devices such as a ball valve or butterfly valve. For our experiments, we selected the latter by NIBCO. Using such a device with rough edges will introduce areas of eddies within the flow.

When the valve is fully closed, the flow is forced to bounce back from the valve. This condition provokes a back-pressure buildup, which could introduce wall shear stresses that could potentially lead to erroneous data collection. In tapping holes for pressure measurement, it is important to properly deburr the area since it may lead to flow disturbances.

2.2 Numerical Modeling of the Experimental Loop

In this paper, the experimental loop shown in figure 24 was modeled in SOLIDWORKS to closely represent the effects within the testing loop. The turbulence model that is used in the SOLIDWORKS flow simulation is the Lam-Bremhorst $k-\epsilon$ turbulence model.

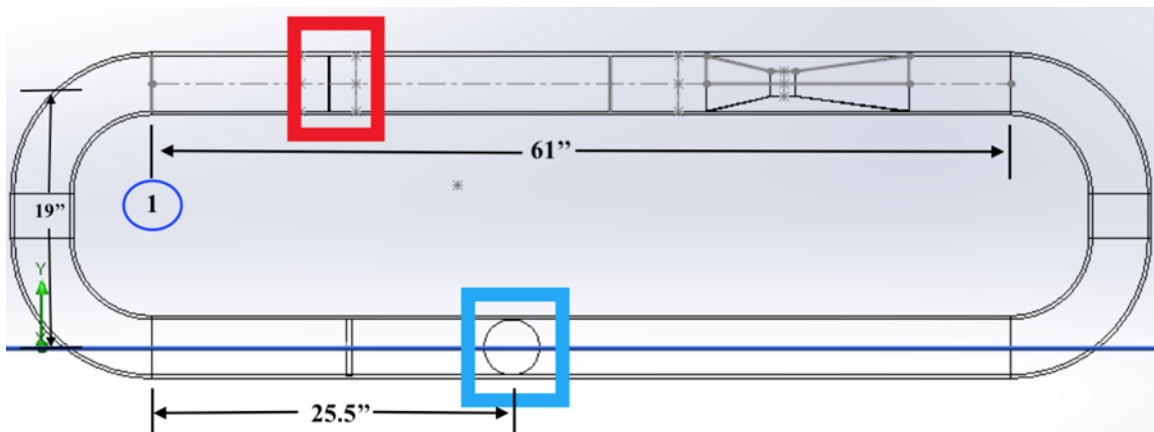


Figure 24. CAD Design of the Loop

The source term was placed at the red region of the simulation and the blue box indicates the location of the butterfly valve shown in figure 25. The two-stage axial fan is located 11.75" downstream of point one shown in figure 26. In the simulation, the rotational effects of the fan were modeled, and those results are observed in the flow trajectories shown in the following sections of this manuscript. The valve was simulated for four different positions in steady-state, and up to this point has been simulated for two positions under transient conditions.



Figure 25. Flow straightener used in the simulation

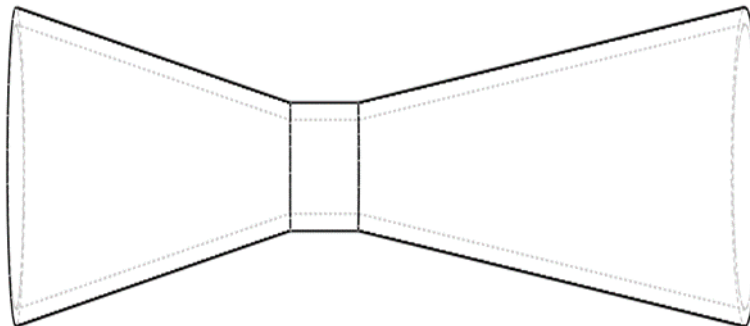


Figure 26. The CAD of the venturi flowmeter used for simulation results

Additionally, there is a flow straightener downstream of the fans. This straightener is located 2.5 inches upstream of the venturi flowmeter.

The drawings provided in figures 27 and 28 have been carefully constructed to meet specific sizes of the physical components in the test loop. The venturi flowmeter has been constructed in-house and follows the specifications of machine venturi from ISO-5167 [30].

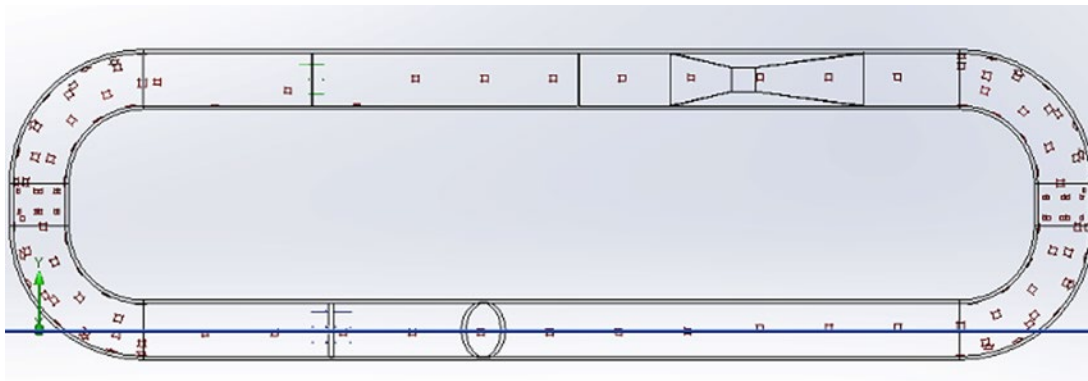


Figure 27. Demonstrates the Boundary Conditions Used to Model the Behavior within the Loop

2.2.1 Boundary and Initial Conditions

The preliminary numerical results obtained in this study were conducted through SOLIDWORKS Flow Simulation software. These preliminary results served to provide initial thoughts on the physics of the flow within the loop.

Steady-state, gravitational effects in the y-direction, standard temperature and pressure within the loop, adiabatic conditions from the wall of the PVC to the environment, the roughness of the inner wall for PVC, and both laminar and turbulent flow regimes were the conditions considered for the simulation. Figure 29 demonstrates the boundary conditions assigned to simulate the environment within the test loop.

The red squares show the roughness assigned the wall ($\epsilon = 0.0015 \text{ mm}$), the blue arrows at the bottom are the pressure ambient pressure conditions ($P = 101325 \text{ Pa}$), and the green arrows are the momentum source term of the fan.

The simulation was conducted for four different valve positions. Those valve positions were simulated by rotating the bottom center circle about the x-z plane at 90° , 60° , 30° , and 0° . The 90° is the fully open condition (i.e., free delivery) and the 0° being the fully closed condition or shutoff.

The source term was specified by providing SOLIDWORKS with the fan performance curve indicated in figure 21. In the simulation, we are considering the fan to already have been initiated to 20,000 rpm at a time, $t = 0\text{s}$.

2.3 Grid Independent Study

The model was tested for grid independence. To guarantee that the model is grid-independent, a single valve position was tested with various mesh sizes provided in SOLIDWORKS. The mesh size was studied extensively, varying with differential meshing within the model and uniform meshing within the model. Initial results indicated that a denser mesh was required in the throat of the venturi to ensure consistent data. The denser the mesh, the more confident one can be in the results provided in the simulation; therefore, a differential grid sizing of 1^{-3}m and 1^{-6}m was taken as the most accurate result in the loop and throat of the venturi, respectively. The percent difference was calculated amongst the various mesh sizes and given in Table 3.

Table 3. Percent Difference between Different Grid Sizes Compared to the Densest Mesh

Pressure [Pa]	Non-uniform Grid	Uniform Grid Size 1 mm	Uniform mesh 0.5 mm
PG1_3	0.003903926	0.001454446	2.91E-08
PG2_3	0.054040662	0.016276622	1.12E-08
PG3_3	0.02231483	0.022195182	1.06E-08
PG4_3	0.138913646	0.040686807	4.74E-08

According to the results of table 3, the percent difference in the pressures between the different mesh settings is less than 1%; consequently, that indicates that the study was grid independent. The remainder of the valve settings were simulated at a mesh size with a uniform grid size of 1^{-3}m to save computation time.

2.3.1 Timestep Independence

To test if the numerical results are independent of the time step, we considered different time steps of $\Delta t = 0.1\text{s}$ and $\Delta t = 0.01\text{s}$ for a total time of $t = 0.5\text{s}$. The test loop condition considered was at the free delivery of the fan and standard pressure and temperature conditions within the loop.

Table 4. Demonstrates the Time Step Independence of the Simulation

Parameter	$\Delta t=0.1s$	$\Delta t=0.01s$	%Difference
PG1_3	101303.7	101304.4	7.16739E-06
PG2_3	101498.6	101509.8	0.000109894
PG3_3	101414.3	101429.6	0.000151266
PG4_3	101157.8	101189.6	0.000314195

The size of the time steps demonstrates similar results for the two cases studied; therefore, the results obtained in the transient results section will be conducted at the smallest time step in table 4. Preliminary results were obtained at $\Delta t = 0.001s$ but will be further tested to verify that we are capturing the physics of the flow and that the results presented here are accurate.

2.3.2 Steady State Results

First, we considered the flow within the system to be independent of time. The flow trajectories within the loop can provide insight as to what the flow characteristics appear to be in the experimental rig. The simulation was tested in the case where the valve is fully open to allow minimal flow resistance within the loop.

Figure 28 shows that the greatest velocity is seen at the throat of the venturi and that the flow becomes twisted as soon as it passes through the fan. The flow straightener can eliminate the rotational characteristics of the flow; but due to its small length in the axial direction, the flow becomes twisted shortly after as demonstrated in figure 29.

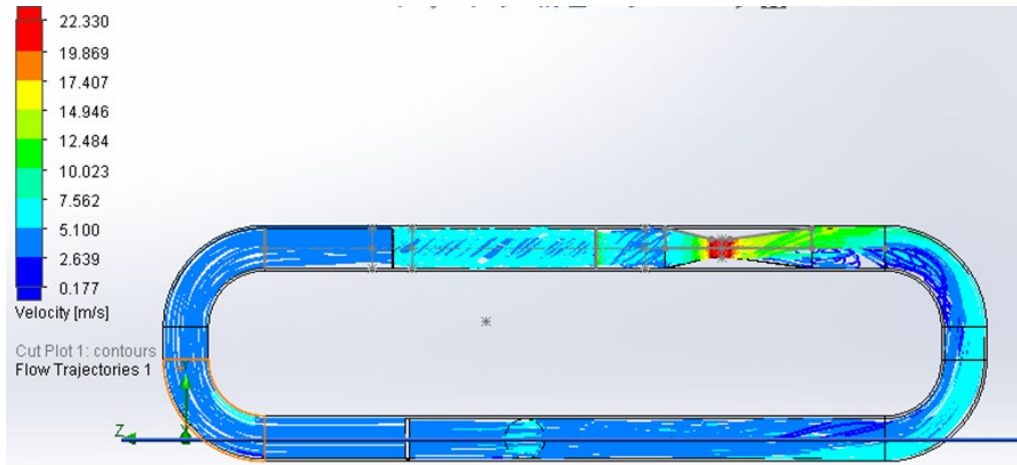


Figure 28. Flow Trajectories within the Loop Simulating the Free Delivery of the Fan

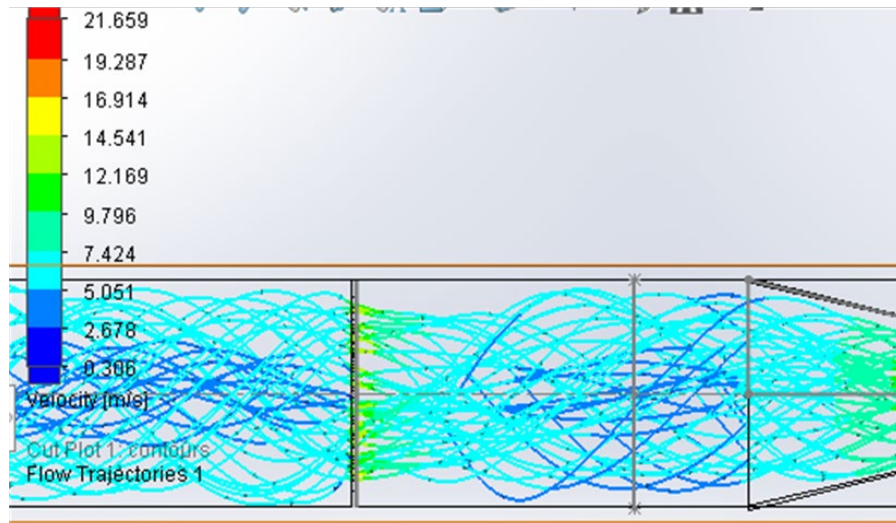


Figure 29. Demonstrates the Flow Straightener's Effect on the Fluid Particles

Perhaps including a second flow straightener in the loop, a set distance from the first could disrupt the flow and make it straighter. Next, the simulation of the closed valve system was simulated to study the flow particles in the loop. The steady-state result yield that enough time has been allotted to the system. This indicates that the pressure has built up significantly, and the flow has become stagnant within the system which is shown in figure 30.

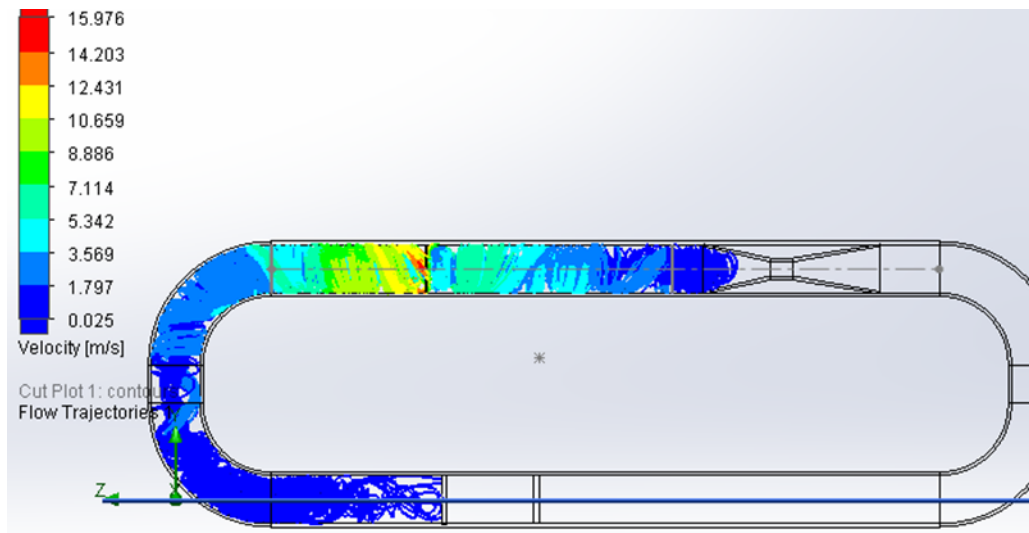


Figure 30. Flow trajectories of the loop at the shutoff condition.

The highest velocity determined in the simulation is higher in this case than the case mentioned previously. Furthermore, the highest velocity is located in the region around the fan. This behavior can be explained by the fact that the flow has stagnated and is continuously being supplied with kinetic energy by the fan.

Recall that the pressure taps of the loop are labeled in figure 31. The difference between PG1 and PG2 will provide the static pressure rise of the fan, and the differential pressure of the PG3 and PG4 will give the volumetric flow rate. Due to lack of time restrictions, the fan performance curve was not obtained at a uniform mesh of 1 mm, but initial results were obtained with the coarser, non-uniform mesh.

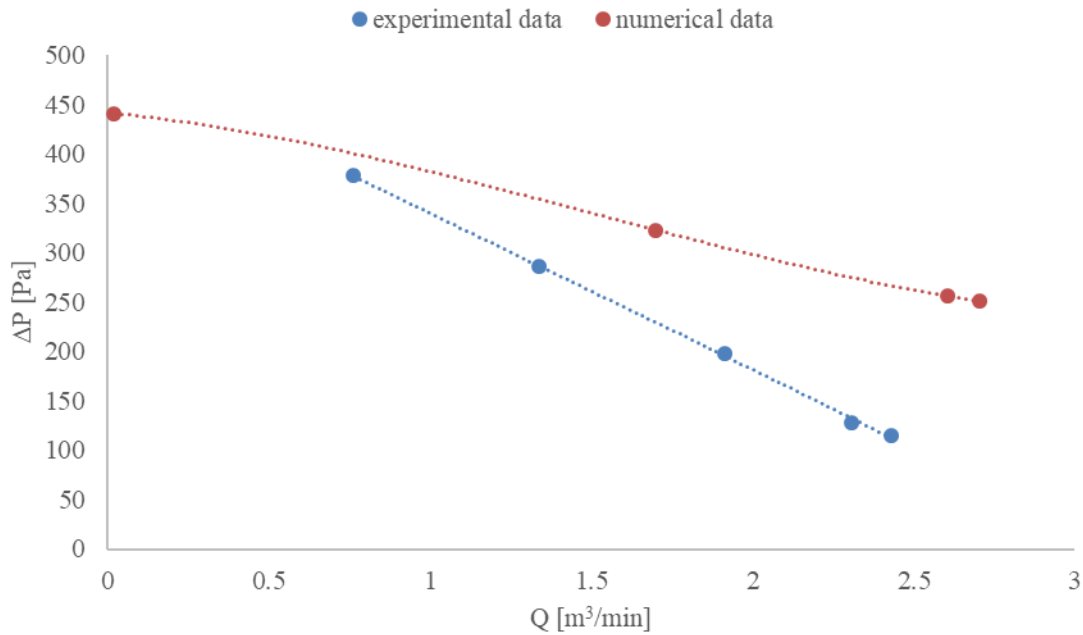


Figure 31. Fan Performance Curve that Compares the Experimental and SOLIDWORKS Flow Simulation Results

The results demonstrate that the numerical results closely approximate the experimental results at low volumetric flow rates. On the other hand, the higher volume flow rates show greater differences in the data among the two scenarios shown in figure 33. Lam-Bremhorst turbulence models are typically utilized for low-Re flow simulations; nonetheless, if the grid is carefully accounted for then the simulations can be conducted with this turbulence model even at high Reynolds numbers.

2.4 Transient State Results

We consider the transient effects in the loop mainly for the condition of the fully closed butterfly valve; furthermore, under this condition, the experimental results demonstrate complications. These difficulties in collecting the data could be a result of flow reversals in the loop causing undesirable shear stress at the wall taps. The transient state results were tested taking the time step to be 0.01s, the results were tested for a duration of 1s. The following graphs demonstrate the pressure at the wall for the different locations of the point measurements in the testing loop. The results yield that a minimum of 0.45s should be given for startup time. Once that time has elapsed, the pressure readings are steady across every point where the pressure is determined experimentally.

From figure 32, the comparison between the numerical and experimental pressures are demonstrated from the start of the test runs. The data acquisition system in the lab can obtain five points per second, which are indicated by the dashed lines; on the other hand, SOLIDWORKS flow simulation has the capacity a much higher rate of values within that same time frame. All the numerical results overestimate the experimental values by 155 Pa, 189 Pa, 149 Pa, and 242 Pa for points PG 1, PG 2, PG 3, and PG 4, respectively. The figure also demonstrates that numerically, the pressure achieves a convergence point past approximately 45 seconds. The experimental and numerical data shown in figure 15 are at the same conditions (i.e., 20000 rpm and free delivery condition).

Figure 32. Comparison of the numerical and experimental pressures at the start.

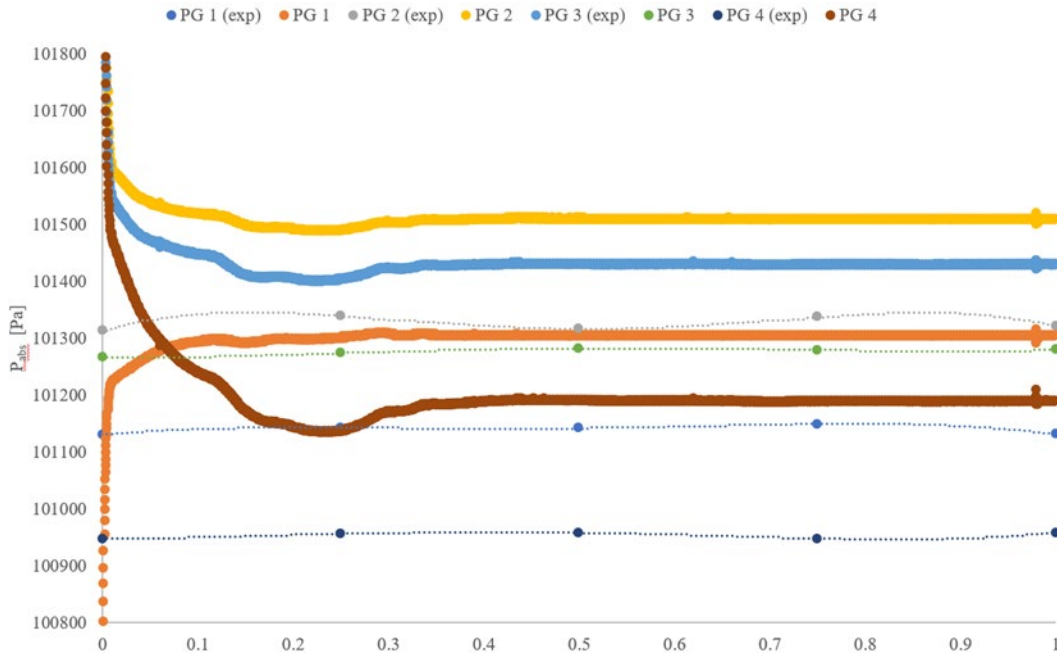


Figure 33. Comparison of the Numerical and Experimental Pressures at the Start

The Reynolds number within the system varies as the butterfly valve is rotated to restrict the flow. The higher Reynolds number shows a higher volumetric flow rate, and that is shown in figure 33 to be consistent throughout the time elapsed in the plot. Additionally, the difference is widened as time progressed. Nonetheless, both conditions still demonstrate that more time needs to progress for steady-state results.

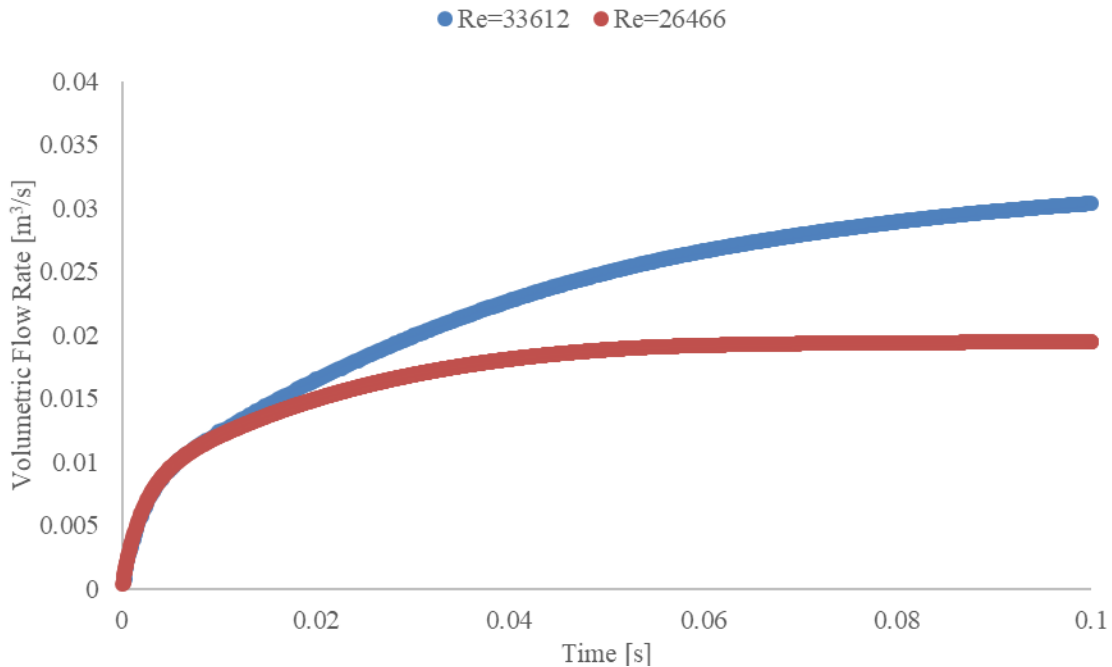


Figure 34. Volumetric Flow Rates Determined by SOLIDWORKS at Different Re when the Butterfly Valve is Fully Closed

Figure 33 demonstrates that the higher Reynolds number would require more time for steady-state results. The numerical results obtained from SOLIDWORKS flow simulation demonstrate that after approximately 0.45s, the solutions demonstrate steady-state behavior for the fully open

valve condition. Therefore, we are confident in our experimental results for this fan curve since the Reynolds numbers are in a fully turbulent regime. Further analysis for higher Reynolds numbers will be tested to determine the time necessary for steady-state results.

The transient effects are to be closely examined when the valve is fully closed. The experimental results show that complications have been encountered when the flow is obstructed by the valve. The smallest time step did not demonstrate groundbreaking results when the fan is operating at the shutoff condition. The trajectories demonstrated similar results of stagnant flow conditions due to the back-pressure buildup.

Simulations were conducted when the system is at 30° and 60° flow resistances. Intermediate valve positions have presented complications in the experimental results, especially when the very minimal flow is allowed through the system. The current results have been tested for a time of $t = 0.1s$. This time was chosen due to the long computation times to obtain a solution. The geometry of the loop is very large, and due to the grid size combined with transient effects the run times are significant. The flow trajectories demonstrate chaotic behavior. The velocity of the particles increases around the edges of the valve and the wall. Along the right side of the valve, particles tend to follow a straight path. On the opposite side of the valve, the flow tends to recirculate, shown in figure 34. Figure 35 demonstrates a snapshot of the vorticity around the valve. The vorticity has rapid fluctuations in the small time that this parameter was studied. Allowing for a greater run time would reveal whether the fluctuations are to eventually vanish with time.

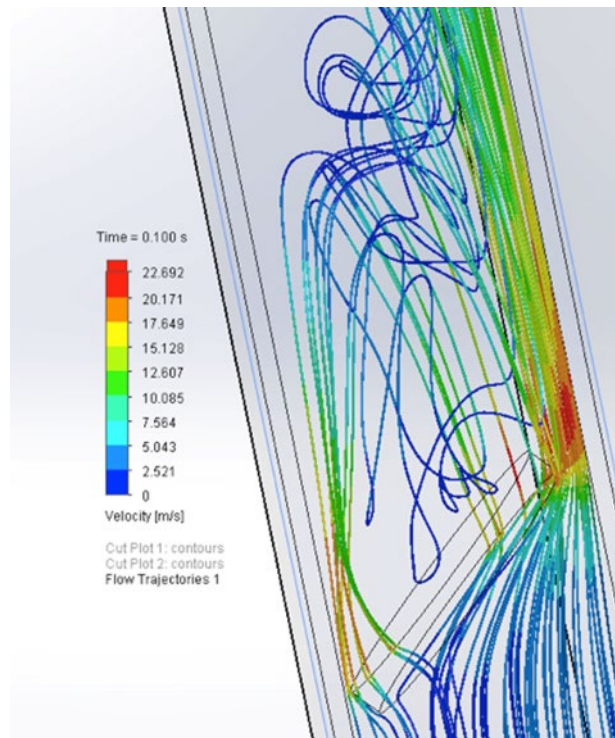


Figure 35. Flow Trajectories around the Valve when Halfway Open

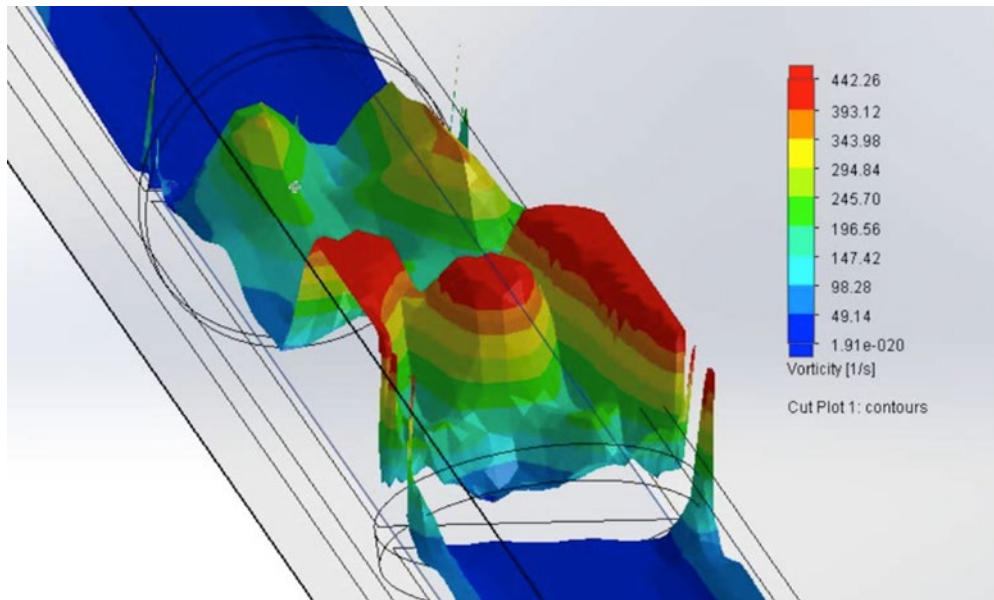


Figure 36. Vorticity around the Valve when Simulated at the Midway Position at $t=0.07s$

The high vorticities around the valve indicate that the flow has patches of strong rotation that is introduced by the valve. The vortices are greater near the wall and directly behind the valve.

A similar analysis was performed on the venturi to understand the flow in that section of the loop. Along the top, the high vorticity is due to the fan's kinetic energy stirring up the flow. As the flow goes downstream and time progresses, the vortices are translated towards the center of the pipe. The frictional effects at the wall cause the vortices to dissipate near the wall downstream of the fan. When the flow interacts with the straightener, vortices begin to form near the edges and the solid structure of the straightener. Nonetheless, those effects are negligible compared to the results shown in figure 36. The change in diameters from upstream of the venturi and in the throat causes vortices to form.

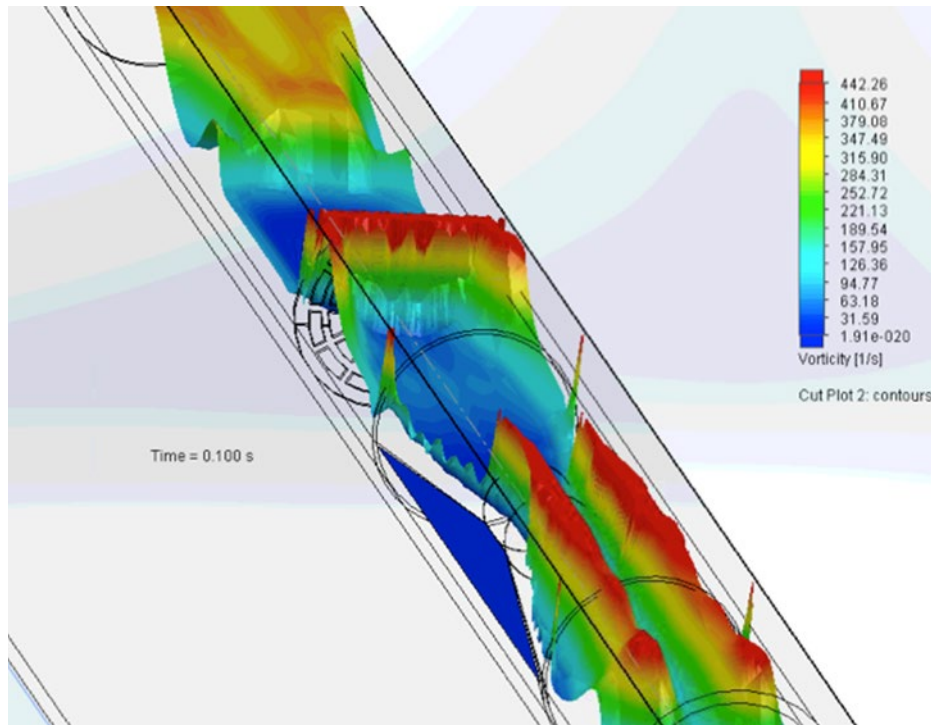


Figure 37. Isometric View of the Vortices in the Top Section of the Loop

Taking a smaller time step would demonstrate more gradual results in the vortices along with figure 36. Regardless, having such a small-time step will not aid our results in properly measuring the pressure at the taps since the results tend to achieve steady-state behavior after approximately half a second.

The simulations showed that the results achieve steady-state behavior approximately at $t > 0.45s$ for the fully open butterfly valve condition. This gives a strong indication that when taking the pressure measurements at the taps, we can be assured that the results are accurate at any point in the experiment.

The fan performance curve was determined numerically under steady-state conditions and follows the trend of the experimental results. The CAD simulations were drawn to mimic the actual experiment in every aspect. The boundary conditions and initial conditions are intended to model inherent properties within the experiment and environmental conditions within the testing facility. These preliminary results obtained from SOLIDWORKS flow simulation provide insight into the physics of the flow within the test rig. Due to the high Reynolds numbers in the pipe, we assume that turbulence exists; furthermore, the flow trajectories and vorticity contours we have confirmed our hypothesis. Also, with the simulation, we can pinpoint the locations where the vortices are concentrated. These pockets of vortices present a possible problem in accurately measuring pressures at the taps. We were able to explore the dynamics of the fluid particles around key components in the loop. We were able to find that the butterfly valve introduces wakes when the valve is being closed.

We will expand this work to include higher Reynolds numbers up to about 90,000. The interest in this is to determine if the pressure tap measurements will show greater variations in the pressures at higher Reynolds numbers and if the venturi flow gives accurate results for the volumetric flow rate.

2.5 Experimental Setup of Straight Pipe Experiments

An experiment was conducted to properly calibrate the pressure transducers used in this work. The PX-409 High-Accuracy Gauge Transducers were used to determine the fan performance curves accurately. The pressure transducers were calibrated using the following methodology of using a vertical clear tube that was filled to specific water levels. Once the water level is known as is shown displayed in figures 37 38 and 39, the pressure can be determined by reading the meniscus in the tube.



Figure 38. Demonstrates the Entire Experimental Setup in Determining the Calibration



Figure 39. Zero Location was Carefully Determined in each Test



Figure 40. Water Level was Determined by Carefully Reading the Level at the Meniscus

In figure 38 the initial point (zero) was accurately determined. From that point forward, the remaining 5 points along the curve are determined by reading the meniscus as shown in figure 39. The water was carefully dispensed into the tube and maintained approximately 2” intervals.

Multiple runs were conducted to verify that the calibration curves for the 4 pressure transducers were accurately determined. The pressure transducers come with a 5-point calibration from the National Institute of Standards and Technology (NIST). The NIST calibration was verified in the lab. Figures 40, 41, and 42, demonstrate the calibration curve of the three transducers tested using the experimental setup demonstrated in figure 37, 38, and 39.

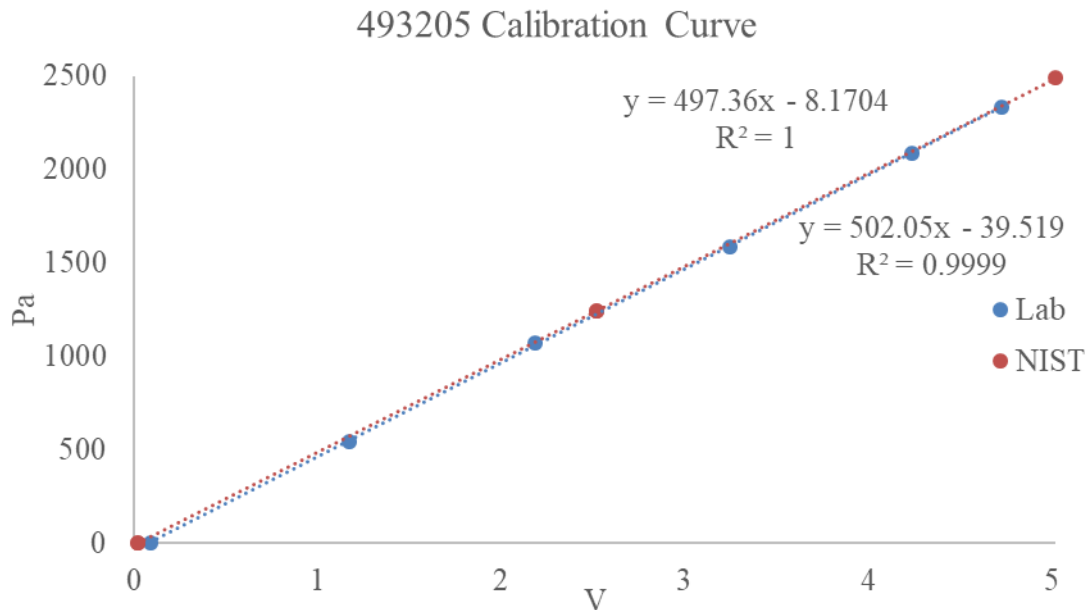


Figure 41. Pressure Calibration Curve of the 493205 Pressure Transducer Unit

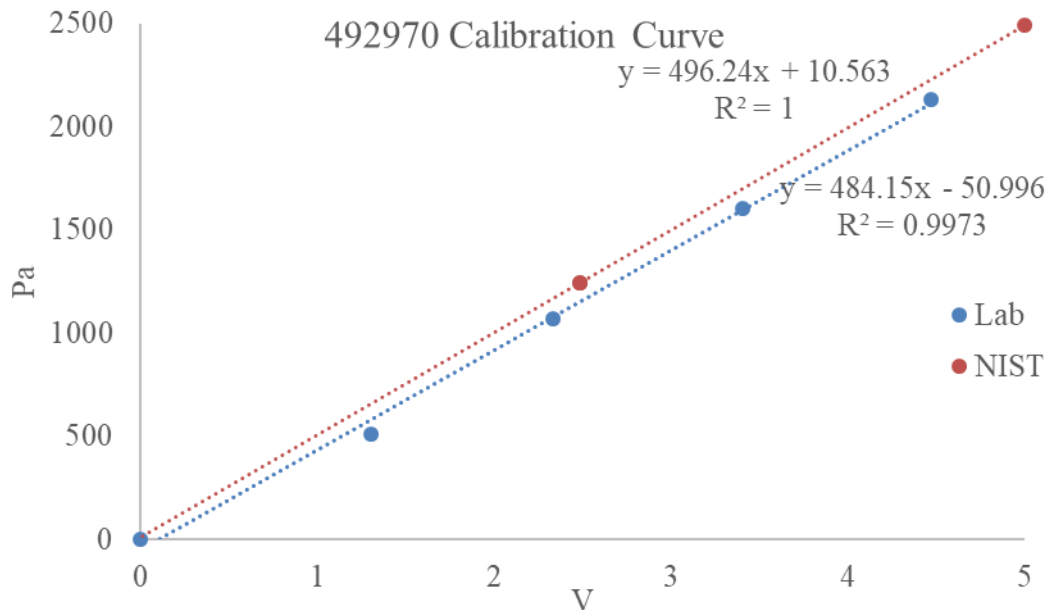


Figure 42. Demonstrates the Calibration Curve of the 492970 Gauge Transducer

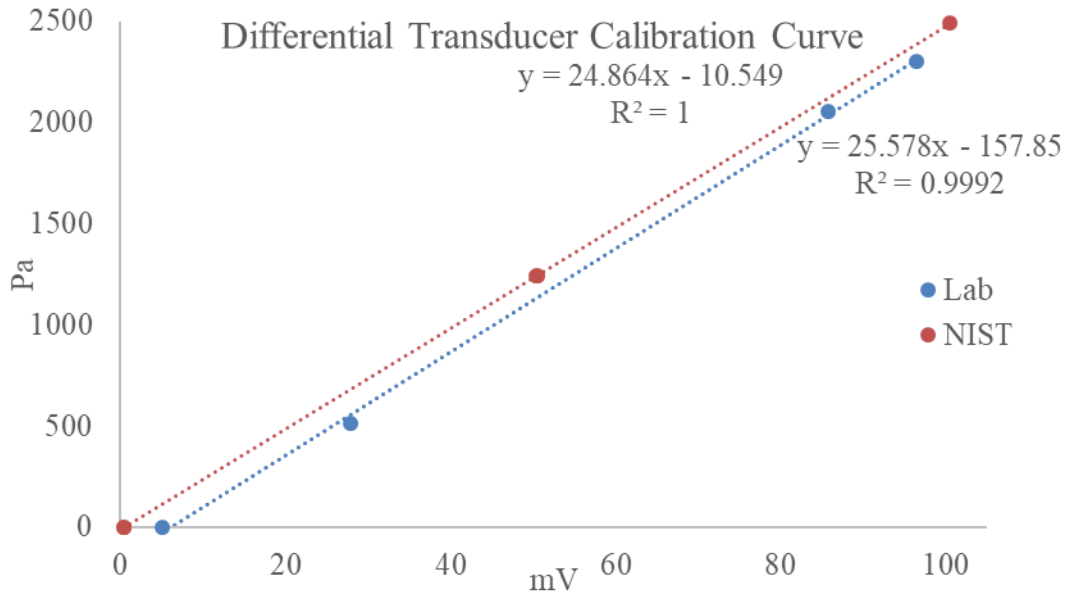


Figure 43. Calibration Curve of the Differential Pressure Transducer

A final pressure transducer was used in testing for the absolute pressure within the experimental loop. The 5-point NIST calibration provided by the manufacturer was used for this transducer since due to the lack of capability of verifying the calibration curve in the lab. Moreover, the lab results and NIST results for the other transducers demonstrated an acceptable set of data in which a high level of confidence was established in the manufacturer’s calibration.

In figure 43 and 44, the difference between fitting the curve with and without a forced zero linear fit function is revealed.

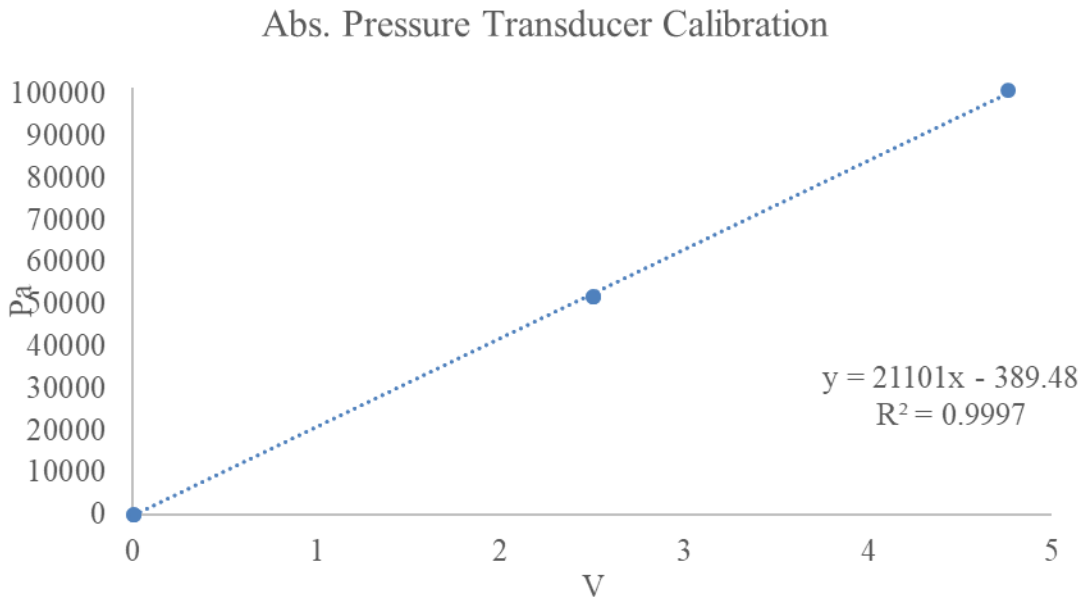


Figure 44. Demonstrates the 5 Points NIST Absolute Pressure Transducer Calibration Curve

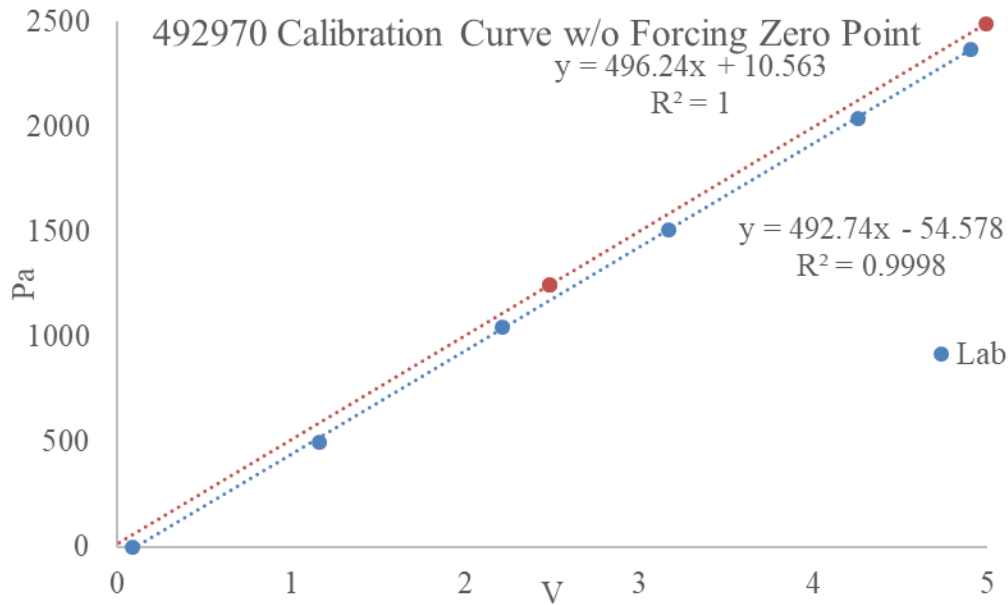


Figure 45. Without Forcing the Curves to go through Zero

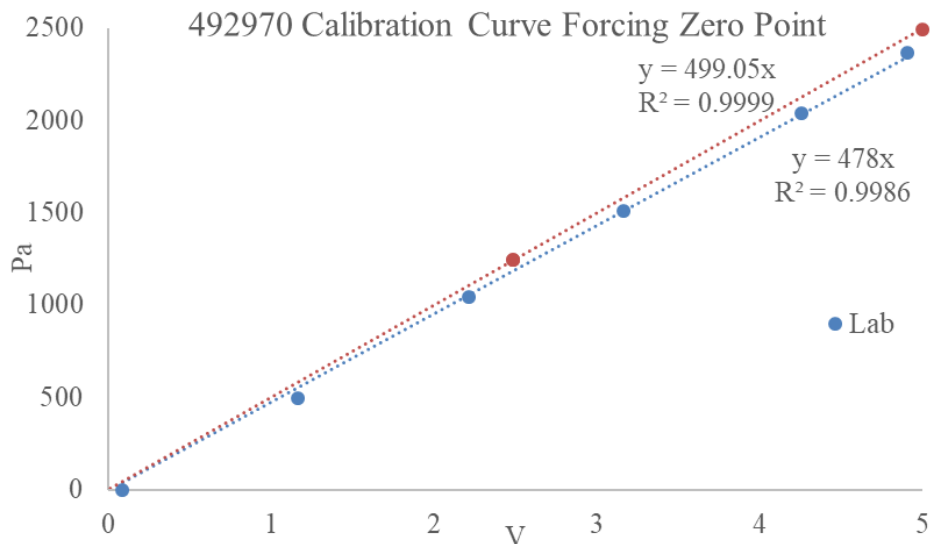


Figure 46. Demonstrates the Linear Fit Forced through the Point Zero-zero on the Plot

Forcing the zero in line of best fit does not affect the R^2 value, but drastically affects the slope of the curve obtained in the lab. The linear equations that fit the points are demonstrated in the following table.

Table 5. Linear Equations of Best Fit for the Two Test Runs for 492970 Pressure Transducer

Run	Lab	NIST	Forcing Through Zero in Lab Results
1	$Pa = 484.15 \times V - 50.996$ (not forced through zero)	$Pa = 496.24 \times V + 10.563$ (not forced through zero)	$Pa = 468.98 \times V$
2	$Pa = 492.74 \times V - 54.578$ (not forced through zero)	$Pa = 496.24 \times V + 10.563$ (not forced through zero)	$Pa = 478 \times V$

The line of best fit when the NIST calibration is forced through zero for this transducer is

$$Pa = 499.05 \times V \quad (11)$$

By not forcing the best fit line through zero gives a slope that is in close agreement with the NIST 5-point calibration curve. In the lab, the results demonstrate an offset of about 55~80 Pa. Even for the NIST calibration, it is not possible to a zero voltage, but in the lab, if we compensate for that small voltage acquired in the DAQ and make that point be the zero-pressure point. It is also seen that for two tests conducted in the lab, the equations that are determined demonstrate that the two sets of data show repeatability in the results. This small discrepancy in the results can be accounted for by the fact that pressure transducers are subject to zero error resulting from environmental and temperature changes. The devices used together in the measurement of the pressures are the following,

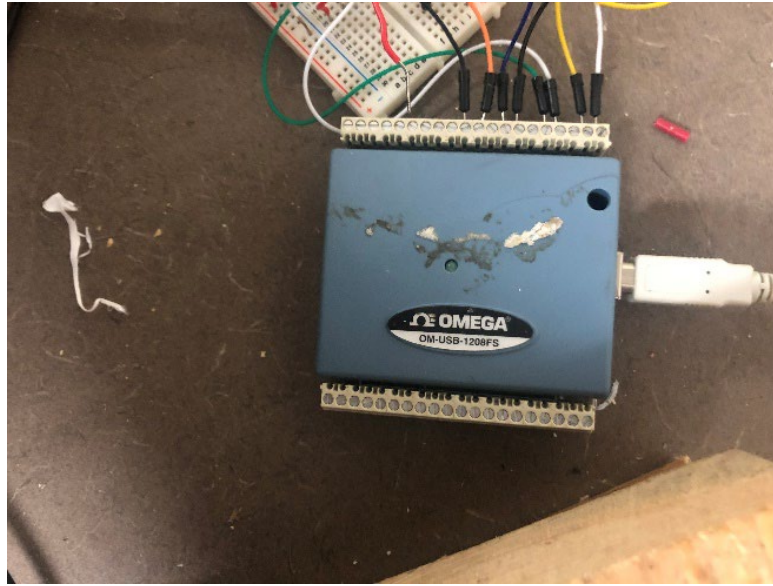


Figure 46 (a). OMEGA OM-USB-1208FS DAQ used in the results determined in the experiments.



Figure 47. (b) Newport Super meter multi-meter used in monitoring the voltage output of the pressure

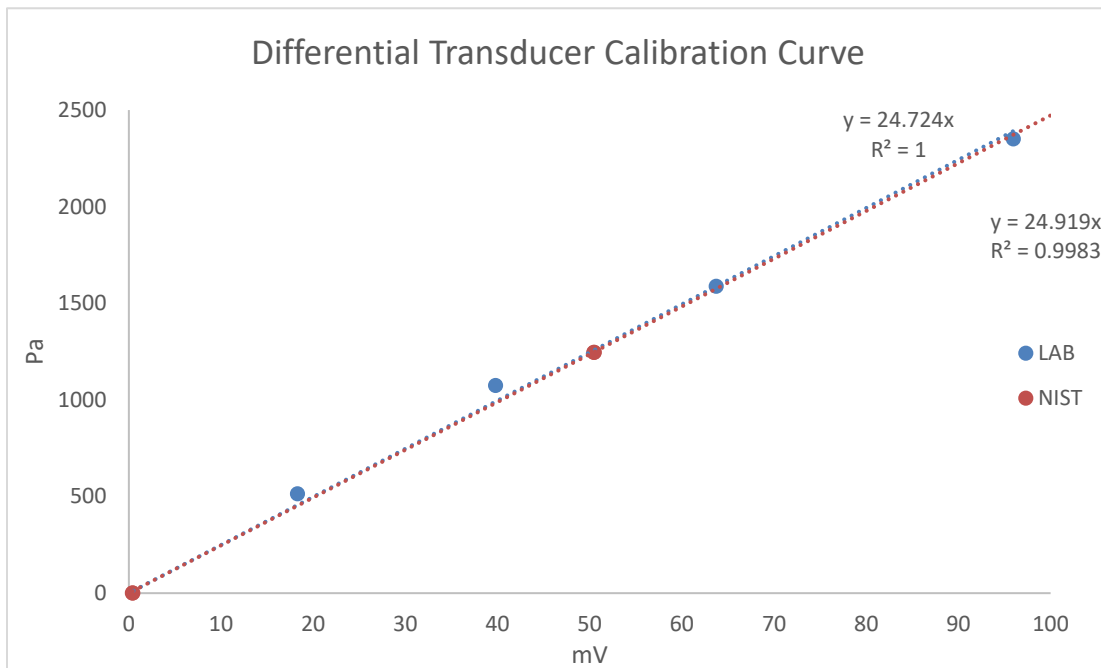


Figure 48. Differential pressure transducer calibration curve with linear fit function forced through the origin.

Both devices measured similar output voltages measured in the pressure transducer. Figure 47 is compared to that of figure 42, it is demonstrated that a better fit was found once the calibration curve was retested and forced through the zero-zero point; furthermore, any testing from this point forward the calibration curves with the forced zero linear fit function was utilized. There is a slight bias in the transducers, but it is insignificant and does not affect the results.

In further testing, a dual system was used to find an appropriate fan for cooling the electromechanical actuators. A 7 and 5 bladed fan system purchased from Delta was used for the remainder of this work. The two fans are demonstrated in figure 48(a) and (b); moreover, the order of the system is 7-bladed operates upstream of the 5-bladed fan.

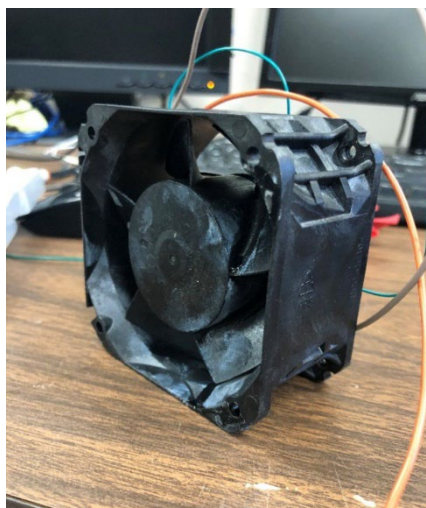


Figure 49.(a) 5-bladed Delta Fan.

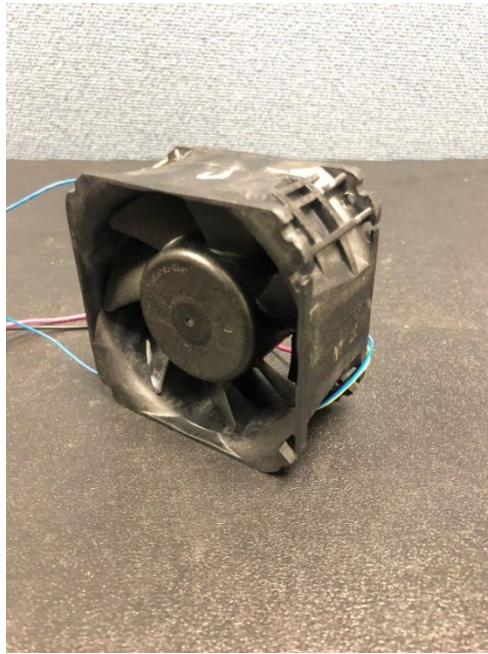


Figure 48(b). 7-bladed Delta Fan.

This dual fan system is a pulse width modulation (PWM) controlled fan. For the majority of the work, the single 7-bladed fan was utilized. In figure 63, an Arduino circuit was constructed to accurately control the fan's rotational speed. The fan speed was verified using a separate handheld tachometer. The variation in fan speed from the desired speed was approximately 30 rpm.

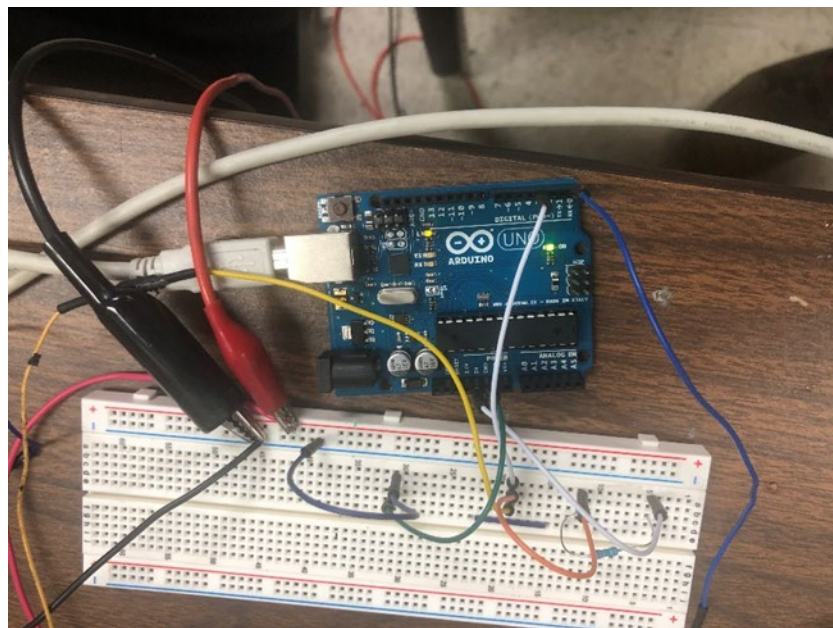


Figure 50. Arduino Circuit to Control the Fan Speed

In table 6, the different wire colors and their functions are outlined such that it was easily referenced for future work.

Table 6. The 4-wire arrangement of the 7-bladed Delta fan.

Color	Meaning
Red	+12V
Black	GRD
Blue	Speed Control
Yellow	PWM

In the initial stages of the project, the experimental loop was placed in a vertical position (standing) but later was changed into a horizontal position where the loop sits on the table flat. In figure 50, the new horizontal configuration is displayed. A new throttling device was constructed to eliminate some inherent turbulences developed inside of the test loop due to the butterfly valve's opening/closing mechanism. In figure 51(a), the additively manufactured cone is the device used to regulate the flow within the system. The procedure of manipulating the flow rate in the system is shown in 51(b) with the experimental setup of figure 52. Figure 52 is the straight pipe setup and results on the two systems are demonstrated.



Figure 51. The experimental loop that incorporates the butterfly valve as the flow restriction device and in the test loop laying flat on the table (experimental setup 1).



Figure 52. 3D printed cone used for restricting the flow to obtain the fan



Figure 51(b). Shows how the flow was regulated and the mounting structure to maintain the flow axisymmetric.



Figure 54. *The experimental setup used to develop the fan performance curves when using the cone as the flow restricting device (experimental setup 2).*

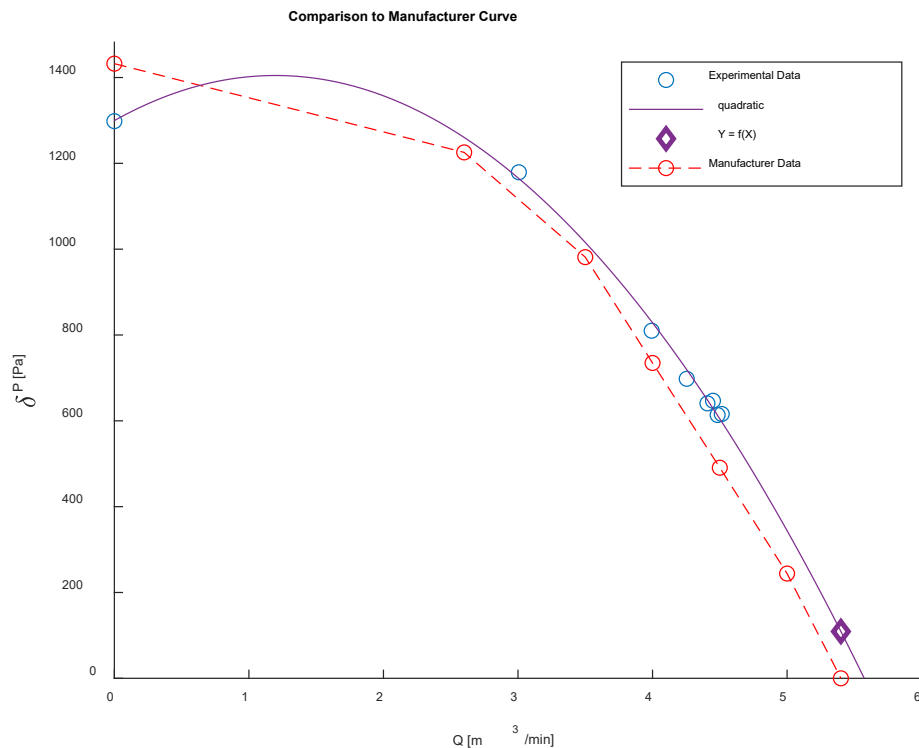


Figure 53. *Demonstrates the manufacturer’s curve plotted against the experimental data obtained with the second experimental setup, cone valve, and demonstrates that a quadratic fit closely follows the trend of the manufacturer’s curve*

The results were obtained to determine how the second experimental setup’s data (straight pipe set up) compared to that of the manufacturer’s curve, shown in figure 53. This fan configuration consists of the 7-bladed and 5-bladed fans placed back-to-back running together (i.e., the original specifications of the dual fan system).

The manufacturer's curve demonstrates that at $Q = 5.4 \text{ m}^3/\text{min}$ the head is zero, $\delta P = 0 \text{ Pa}$; on the other hand, the experimental results demonstrate that at that same volumetric flow rate, $\delta P = 109 \text{ Pa}$.

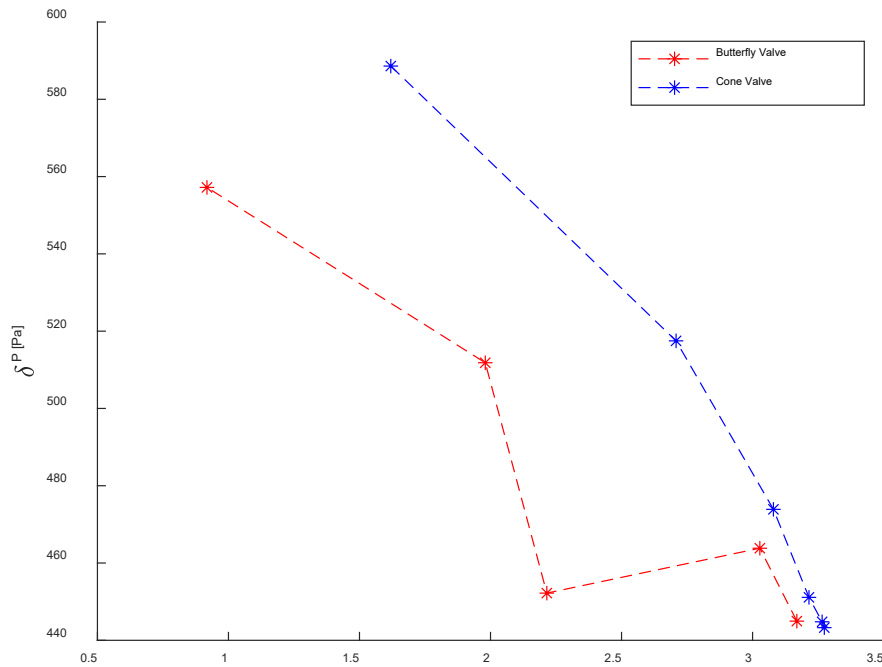


Figure 55. Compares the results of the single 7-bladed fan with the two different experimental setups.

In figure 54, the single 7 bladed fan configuration was tested. Comparing the previous results obtained in the loop setup and the straight pipe setup, we conclude that the discrepancy point around $Q \sim 2.2 \text{ m}^3/\text{min}$ that exists with the butterfly valve is eliminated in the cone valve setting. The blue curve demonstrates that the cone axisymmetric geometry gives a smoother trend in the data. The butterfly valve's opening mechanics do not allow a uniform flow to travel across the restricting device, which could lead to potential problems at certain volumetric flow rates.

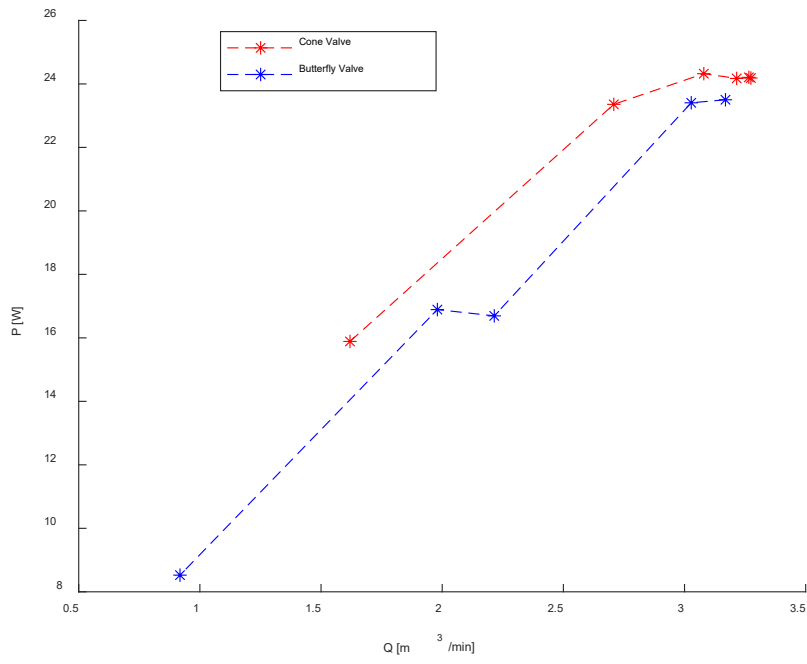


Figure 57. Single 7-bladed fan power vs volumetric flow rate curve for the two different experimental setups.

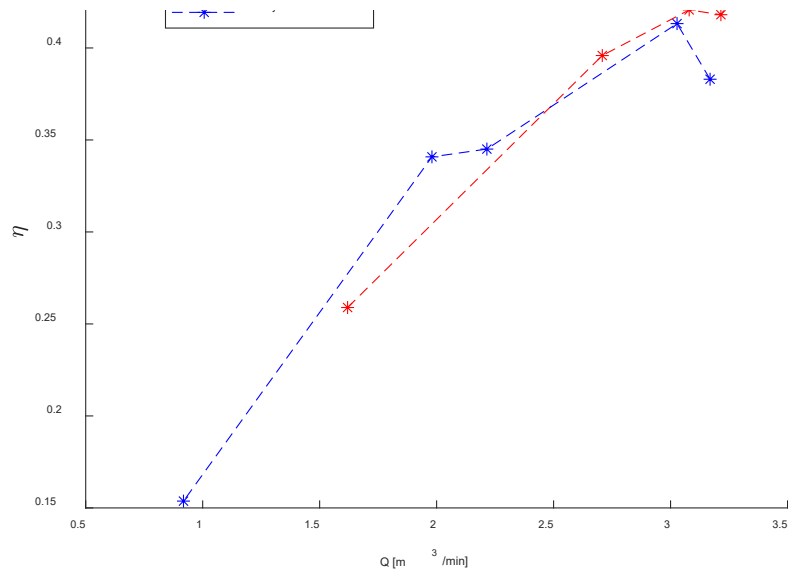


Figure 56. The efficiency curves of the single 7-bladed fan for the two experimental setups.

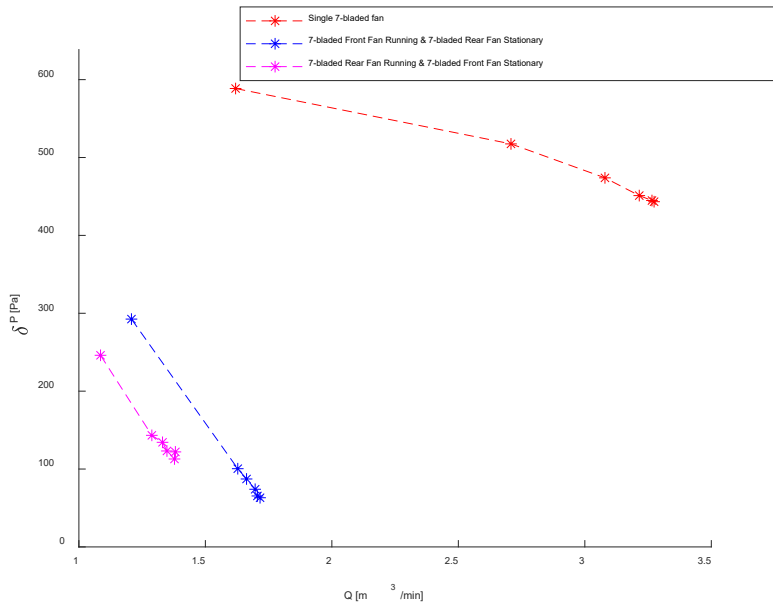


Figure 58. Fan performance curves of the three cases when using the cone valve experimental setup

We can see that the experimental results indicate that the second stationary fan whether downstream or upstream within the system drastically hinders the performance of the dual fan configuration. The rear running fan (purple curve) is the least performing setup of the three configurations. For reliability purposes, the front running fan should be used as the preferred option.

Case 1 is the red curve, single 7-bladed curve, case 2 is the blue curve, 7-bladed front running fan and rear fan stationary, and case 3 is the purple curve 7-bladed rear fan running and front stationary fan.

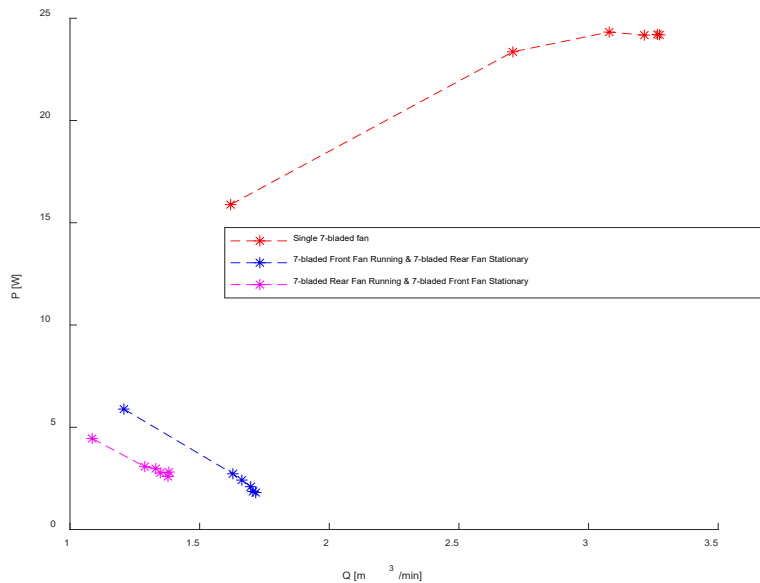


Figure 59. Power vs volumetric flow rate determined while using experimental setup 2 at 13000 rpm.

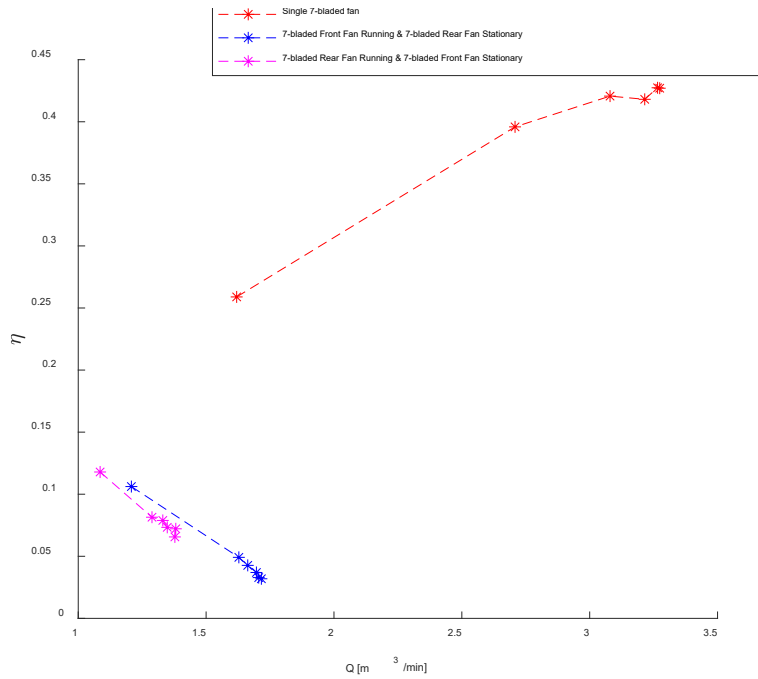


Figure 60. The efficiency vs volumetric flow rate for the three cases using experimental setup 2 at 13000 rpm.

In every case, the fan performance is drastically hindered by the inclusion of the second fan within the loop. In either position, the fan performance severely affected when the secondary fan is within the system and permanently fixed. The efficiency of the overall system is also greatly disturbed by the secondary fan as is demonstrated in figure 59.

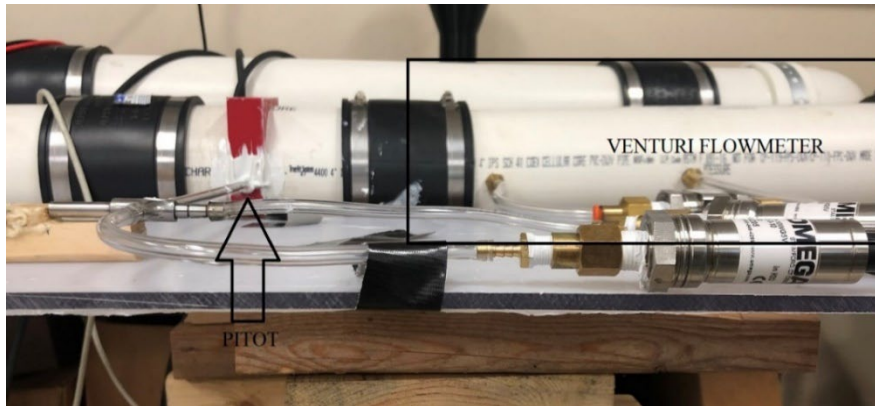


Figure 61. Displays the experimental setup where the pitot-tube is tested upstream of the venturi flowmeter.

In figure 60, the experimental setup of how the calibration was performed is shown. The pitot tube is placed upstream, and the venturi flowmeter is placed downstream in both cases. This configuration was chosen to reduce the restriction of the pressure drop in the venturi from

affecting the measurement in the pitot tube. It is expected that the pitot tube will have a negligible pressure drop due to its small construction.

Figure 61(a) and 61(b) demonstrate the two venturi flowmeters. The differences in the two venturi flowmeters are outlined in table 7.



Figure 62. (a). 3D printed PLA venturi, $\beta = 0.51$.



Figure 61 (b). Nylon machined venturi, $\beta = 0.46$

Table 7. The diameter ratio of each venturi is demonstrated.

Venturi	$\beta = d/D$
3D Printed Venturi (3V)	$\beta=0.51$
Machine Venturi (MV)	$\beta=0.46$

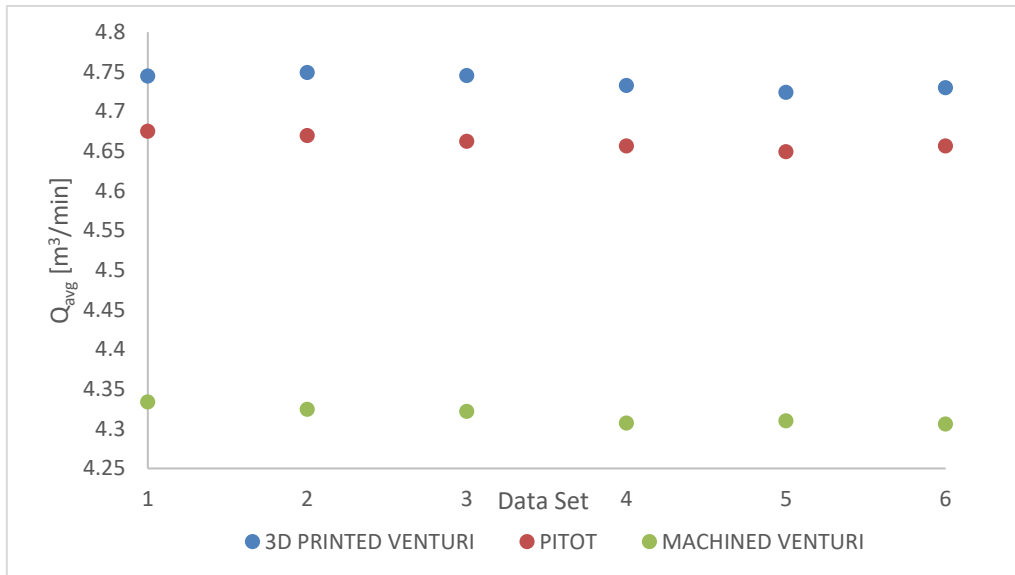


Figure 63. Demonstrates the average volumetric flow rates determined using the two venturi flowmeters and the pitot tube.

Assuming the data sets follow a normal distribution, performing statistical analysis of finite data sets the results are analyzed and demonstrate the following results,

$$Q_{avg,pitot} = (4.650 \pm 0.028) \text{ m}^3/\text{min}, \quad (12)$$

$$Q_{avg,MV} = (4.308 \pm 0.031) \text{ m}^3/\text{min}, \quad (13)$$

$$Q_{avg,3V} = (4.738 \pm 0.026) \text{ m}^3/\text{min}, \quad (14)$$

Where the data demonstrates the pressure loss of the system introduced in the diameter reduction of the throat in the venturi flowmeters. The greater the diameter difference from the throat to the overall tube diameter the greater the loss. That loss is reflected in the determination of the volumetric flow rate. The experiment has conducted an overall of 18 times in which the pitot tube was used every time, 12 measurements with the machined venturi, and 6 with the 3D printed venturi. The average difference among the pitot measurement and the venturi flowmeters is,

$$\Delta_{avg} = Q_{avg,pitot} - Q_{avg,venturi} \quad (15)$$

where the results demonstrate the greatest difference in volumetric flow rates is seen in the machined venturi $\Delta_{avg} = 0.0773 \text{ m}^3/\text{min}$ and $\Delta_{avg} = 0.336 \text{ m}^3/\text{min}$. The percent difference amongst the pitot tube and the two venturi flowmeters demonstrated that the 3D printed venturi agrees closely with the pitot tube as opposed to the machined venturi since the results were less than 2% and 8%, respectively. For the validation process of the simulation results, the 3D printed venturi flowmeter was utilized.

Table 8. Demonstrates the degrees of freedom and the confidence interval used in the statistical analysis.

N=	18
DOG=	17
(%P)	95
t=	2.110

The data is analyzed with a Student's t-Distribution and based upon the measurements the true value certainly lies within this range with a 95% confidence interval. For further testing, it was concluded that the additively manufactured venturi flowmeter was used since those results showed better results to that of what is expected. The larger diameter ratio of the 3D printed venturi imparted fewer pressure losses in the system.

To determine the volumetric flow rate, the following equation was [31],

$$Q = C_d A_t \sqrt{\frac{2\delta P}{\rho(1-\beta^4)}}, \quad (16)$$

where δP is the pressure drop within the venturi flowmeter, $\beta = d/D$ the diameter ratio of the throat of the venturi to the overall system, $\rho = P/RT$ the density of the air within the system, A_t the throat diameter, and C_d is the discharge coefficient that is only a function of the diameter ratio. All pressure measurement systems have inherent elemental errors that require consideration. The overall instrument error and instrument uncertainty is given [32],

$$u_p = [u_{BSL}^2 + u_z^2 + u_s^2]^{1/2}, \quad (17)$$

where the $u_{BSL} = 0.08\%$ best standard line (BSL) combines the linearity, hysteresis, and repeatability uncertainties of maximum value, $u_z = 0.5\% FS$ the zero-balance uncertainty, and $u_s = 0.5\% FS$ is the span setting uncertainty. For the differential unit used and the gauge transducers in the experiment range from $P = (0 - 2488.4) Pa$ and the absolute pressure transducer range from $P = (0 - 103421) Pa$. The instrument uncertainty of the pressure transducers is demonstrated in table 9.

Table 9. The pressure transducer overall uncertainties for the units used in the experimental setup.

Pressure Transducer [Pa]	δP	P_{abs}	P_1	P_2
u_c	17.71	735.96	17.71	17.71

Considering the overall uncertainty in our measurement, a CFD model was developed that was validated in the lab using these units and the experiment used in figure 52 (straight pipe). In figure 63, the validation of the CFD model with the experimental setup is demonstrated. The results are shown to demonstrate acceptable results for both configurations.

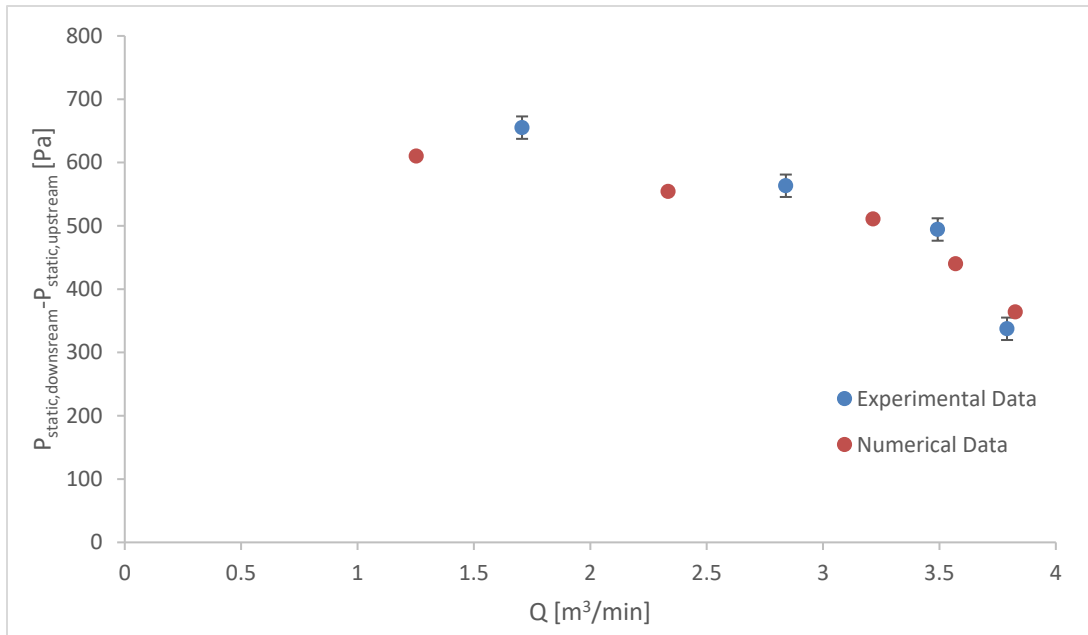


Figure 64. Demonstrates the fan performance curve with the error bars in the volumetric flow rate and the static pressure in the experimental data and a direct comparison to the numerical results.

2.6 EMA & Thermal Box Setup

In figure 64 the current configuration of the vacuum box (wing-bay simulant) is demonstrated. The box was constructed with aluminum extrusions on the inside and outside of the box. The inner extrusions provide structural rigidity so that the box does not collapse with the large pressure gradient within the box and atmospheric pressure of the lab. The outer extrusions are used to provide an equal pressure distribution along the top and bottom face to maintain the pressure of the chamber. The extrusions are denoted by the blue text in figure 64.

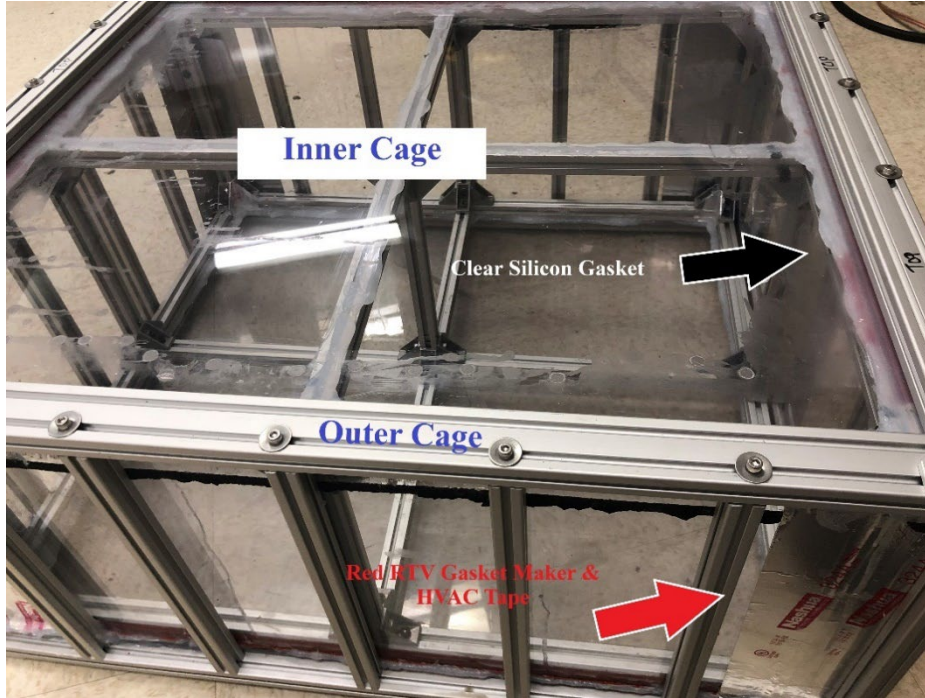


Figure 65. Demonstrates the test rig.

The sealant materials used for the pressure chamber are Red RTV gasket maker by Permatex and ordinary clear silicon by DAP; furthermore, both products are silicon-based. The red silicon was used along the four edges of the box along with HVAC tape (red arrow). For the top and bottom glass, the clear silicon was applied (black arrow). This product was used liberally on those faces and squeezed between the edge and faces. Application of soap on the contacting faces ensured that the top and bottom faces would not permanently adhere to the box; therefore, the two faces are free to move. The vacuum box can retain the pressure within the box as long as the necessary pressure is applied by the outer cage. The results of the current test rig configuration are demonstrated in figure 65.

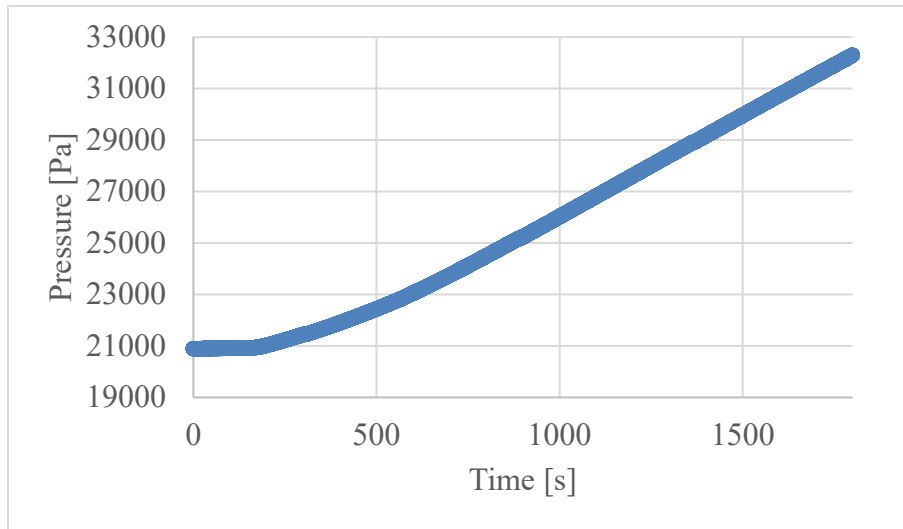


Figure 66. Pressure within the vacuum box after 30 minutes of testing.

From figure 65, the pressure within the box was tested for a total time of 30 minutes, which is the necessary testing time. The vacuum pump was shut off and the pressure was then recorded. From the graph, within that 30-minute lapse, approximately 12.3 kPa was lost. This demonstrates that there is a slight leak within the box; moreover, the data demonstrates that the pressure is lost at a rate of nearly 2 Pa/s. Nonetheless, with the current configuration, we are confident that the tests can be conducted. Figure 66 demonstrates the pipe fittings used such that the pressure within the vacuum box can be regulated to maintain the desired pressure.

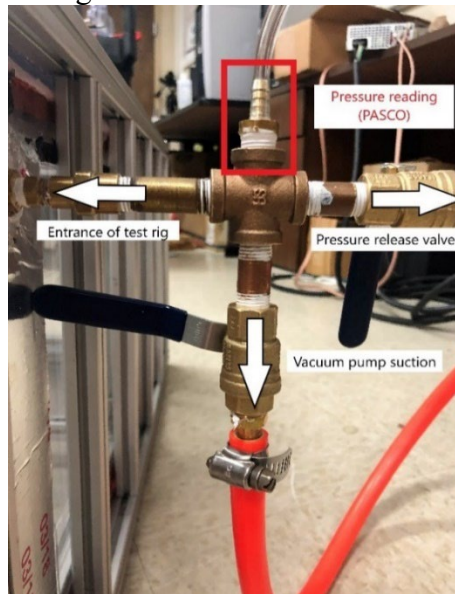


Figure 67. The pipe fittings from the pump to the vacuum box.

The pump can be used continuously. Carefully adjusting the valves to regulate the evacuation of the pressure within the box (bottom arrow) and the release valve (right arrow) to keep the pressure at the pressure being tested. The red box in figure 66 demonstrated the barbed fitting to read the pressure in real-time within the test rig.

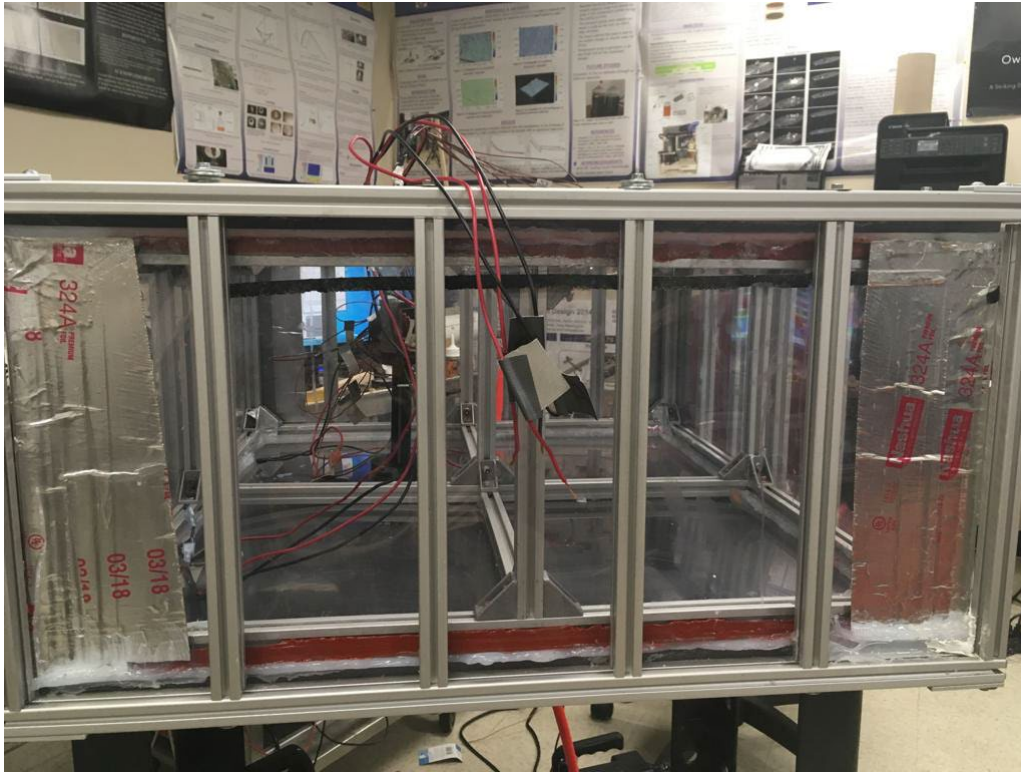


Figure 68. Experimental setup of the square stator testing within the wing-bay simulant.

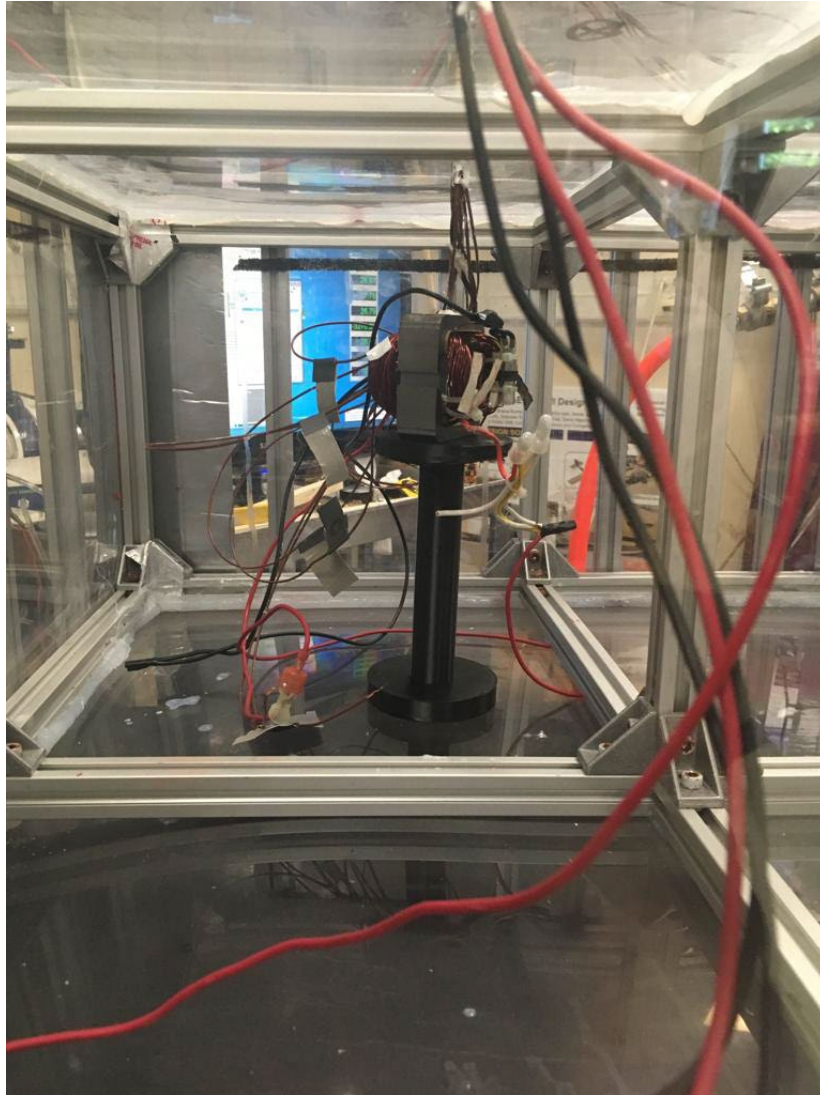


Figure 69. Demonstrates the PLA 3D printed stand that was engineered to place the square stator within the box.

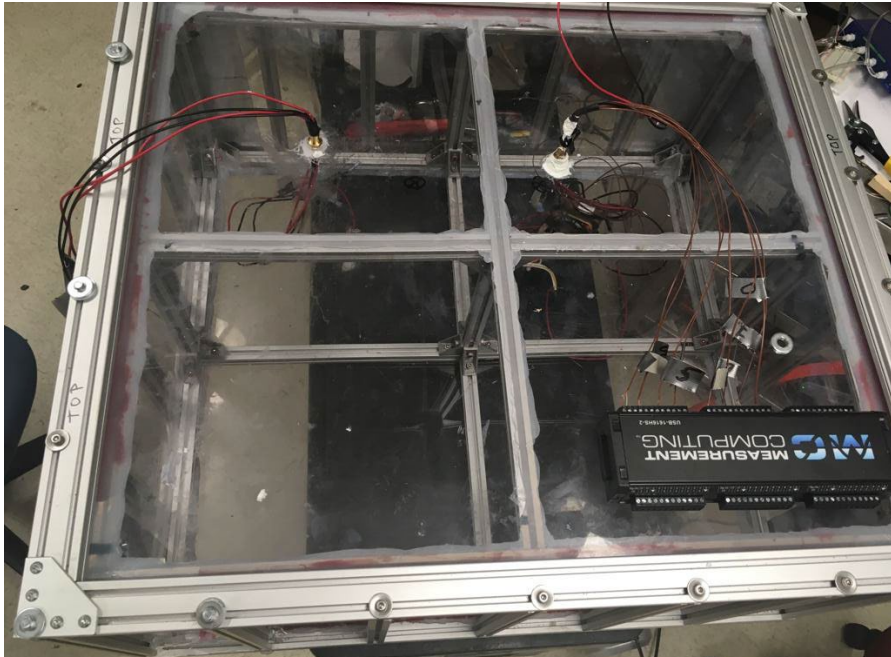


Figure 70. A top view of the experimental setup with the DAQ system by MC Computing

In figure 69, the location of the K-type thermocouples is demonstrated. The various points on the stator core have been labeled accordingly and are the same notation used in the plots demonstrated below. The points labeled EW indicate a point at the copper end windings. The points that demonstrate IW are the imbedded windings. There is a single thermocouple at the top of the laminated stator core and the point labeled AMB stands for the ambient temperature within the thermal box.

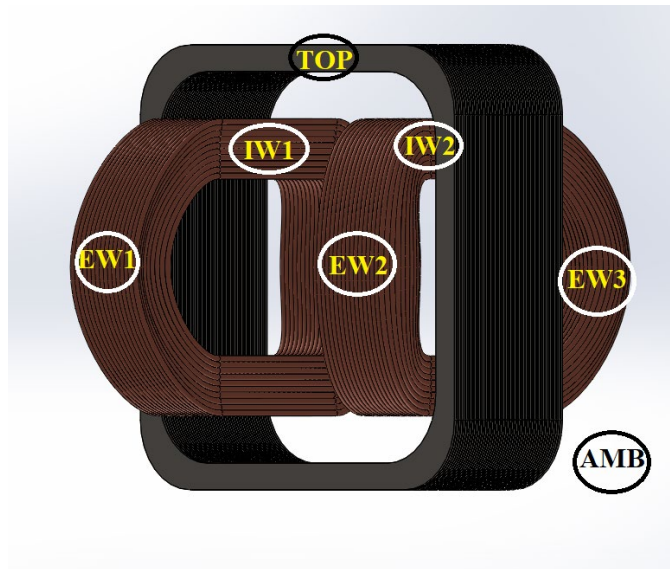


Figure 71. Demonstrates the location of the K-type thermocouples used in the experiment.

The electrical power supplied to the stator core winding is given by, $P = I^2R$ where the I is the electrical current flowing through the circuit and R is the electrical resistance of the core. The resistance measured was 1.6Ω .

The following procedure was followed in the data collection process:

1. First 30 seconds of the experiment were without any heating effects
2. In the following 60 seconds, the stator core was supplied with $179.78 W$ of electrical power to observe the heating.
3. For the following 240 seconds (i.e., 4 minutes) the power supply is turned off and the rate of cooling was observed.

The temperatures seen across the various locations of the stator core at 1 atm is seen in figure 71. The blue curves demonstrate the various end windings temperatures of the core, the red curves denote the embedded winding temperature, and top and ambient temperatures are given by the solid light blue and solid orange curves, respectively. It has been observed from previous experimentation that the highest temperature is seen at the end of windings since there is no available access to transfer the heat via conduction. The embedded windings have a preferred heat path due to the direct contact available with the laminated core. Therefore, for further analysis of the effects of pressure on the temperature curves, four points will be more closely observed: EW2 (highest end winding), IW2 (lowest embedded winding), TOP, and AMB.

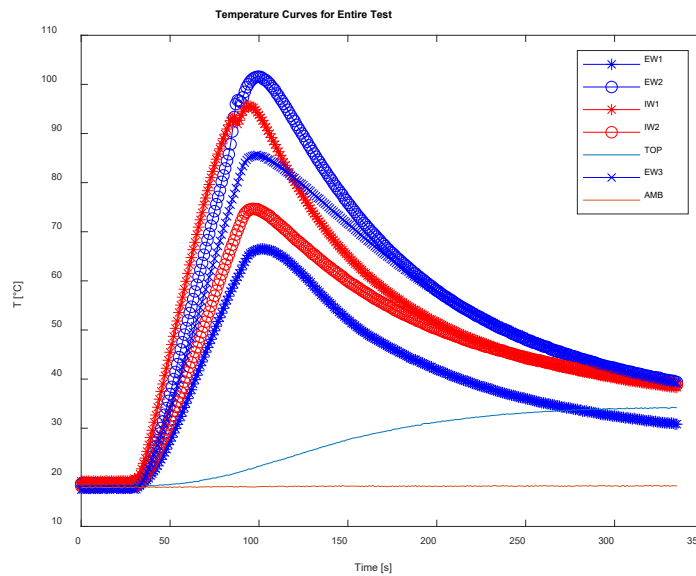


Figure 72. Temperatures of the stator core at the locations demonstrated in figure 70 for 1atm.

From figure 72, the location of the thermocouple is, in the end, winding at location EW2. The highest peak temperature is seen at the lowest pressure conditions, 0.2atm and the lowest peak

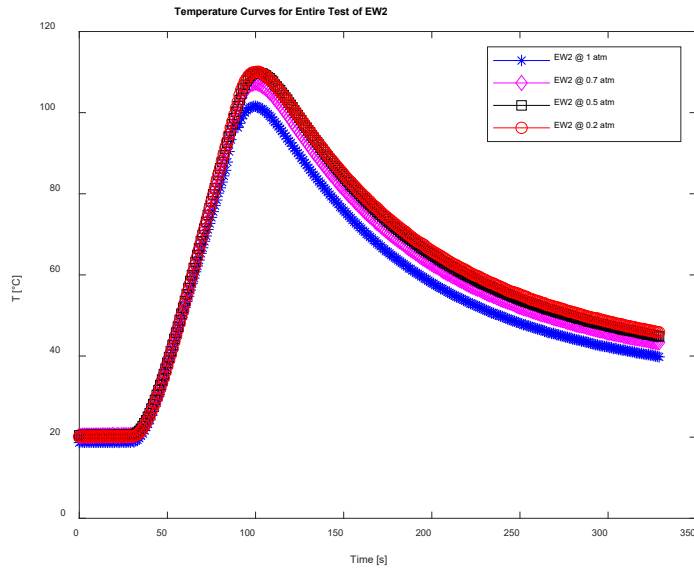


Figure 73. The temperature of the copper end winding at various pressures.

temperature occurred for the 1 atm pressure condition. The two intermediate pressure conditions, 0.7 atm and 0.5 atm, both fall in between and follow the trend of the inverse relationship between pressure and peak temperature. For figure 73, the temperature of the embedded windings was

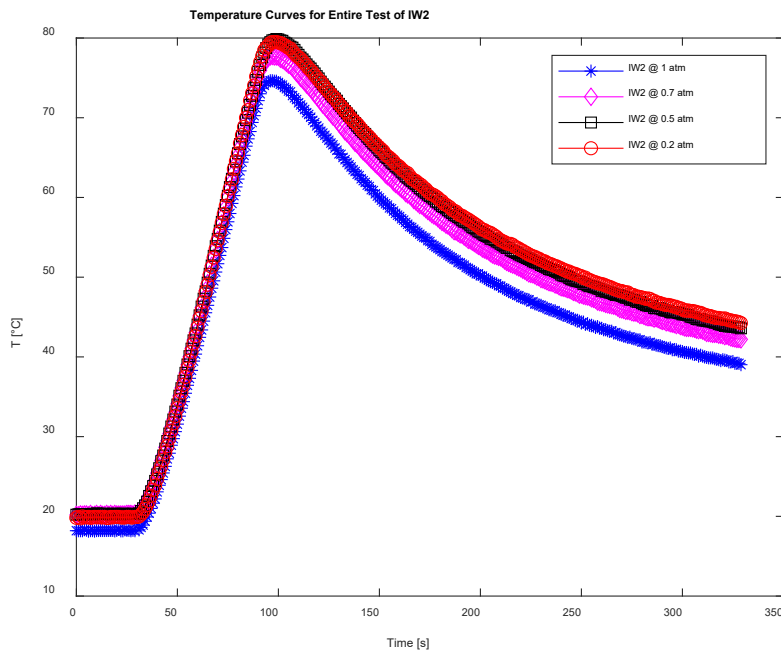


Figure 74. The temperature of the copper embedded winding at various pressures.

demonstrated for various pressures.

In figures 74 and 75, the ambient temperature of the thermal box and the temperature of the laminated core for the duration of the experiment are shown, respectively. In the following figures 76-79, the temperatures of the stator for various locations for the heating portion time-

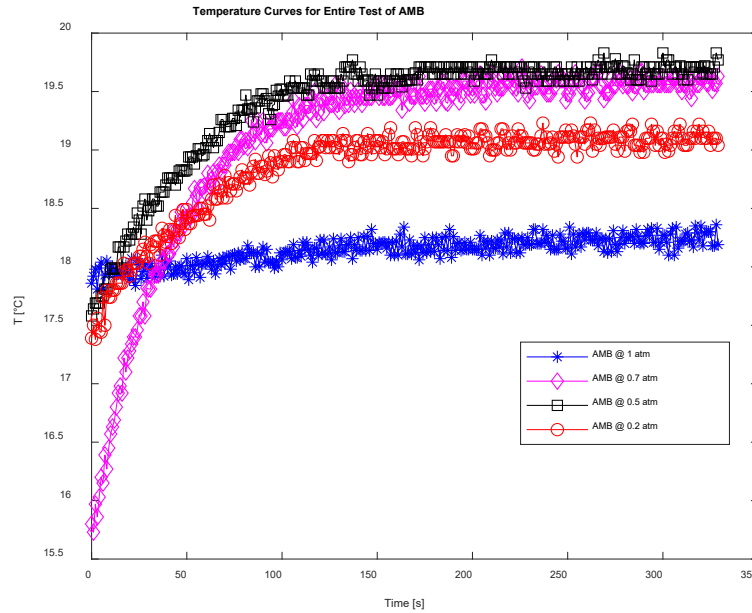


Figure 75. The ambient temperature of the test bay at various pressures.

lapse of the experiment are demonstrated for 1-100 seconds.

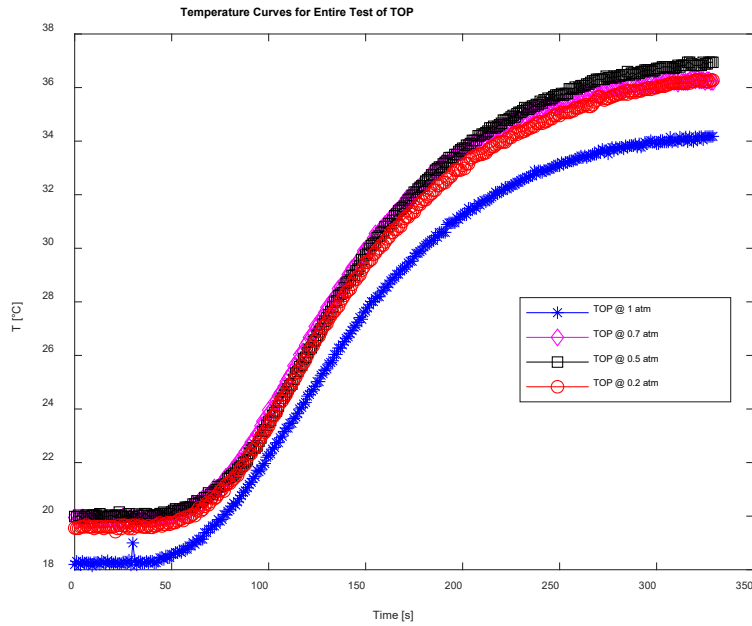


Figure 76. *The temperature of the laminated core at various pressures.*

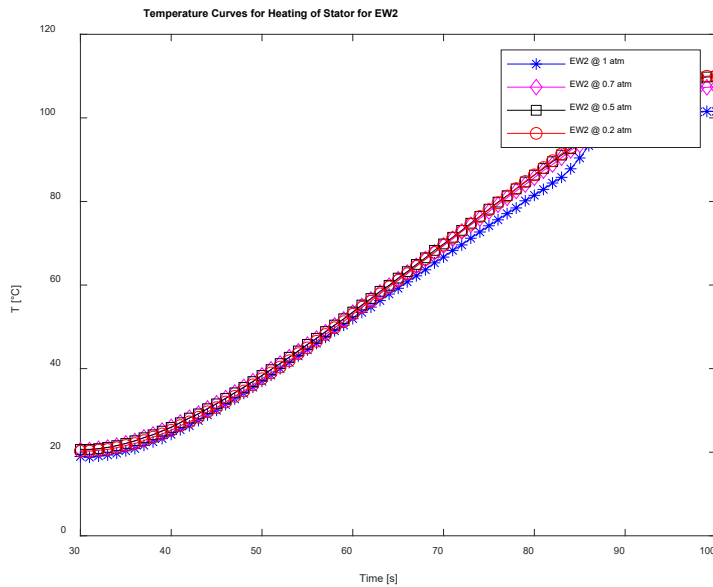


Figure 77. *The temperature of the end winding during the heating of the stator core*

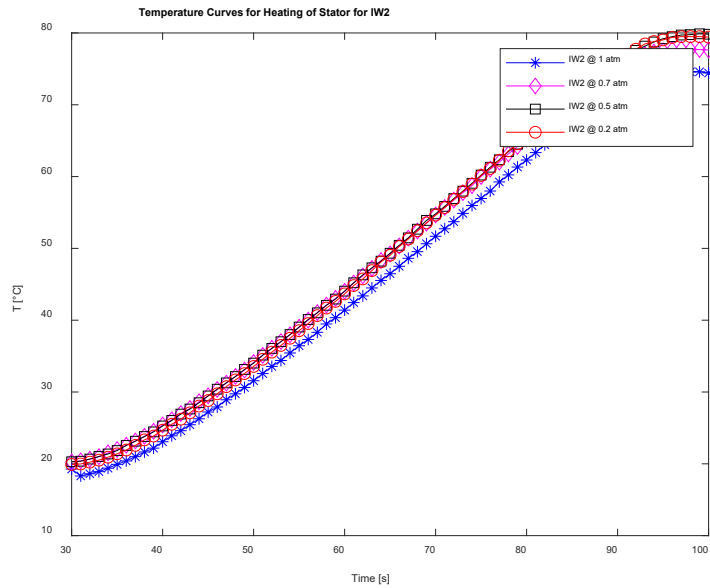


Figure 78. The temperature of the embedded windings during the heating of the stator core.

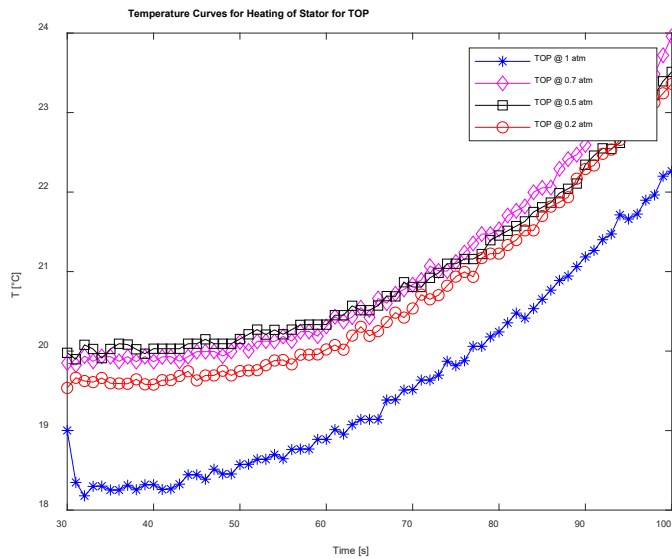


Figure 79. The temperature of the laminated core during heating of the stator core.

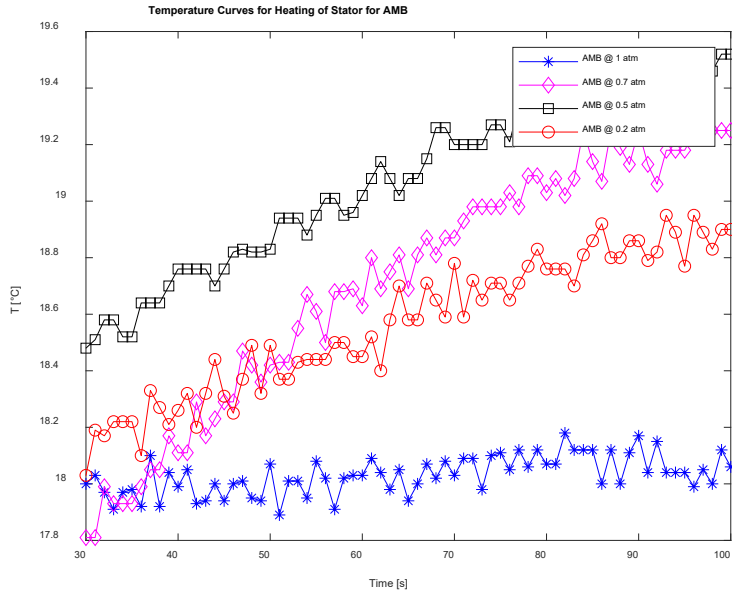


Figure 80. The ambient temperature of the wing bay during heating of the stator

2.7 EMA SIMULANT CAD DESIGNS

Further work was investigated into constructing an aluminum EMA simulant. The EMA simulant would have been comprised of finned structures such as shown in figure 80.

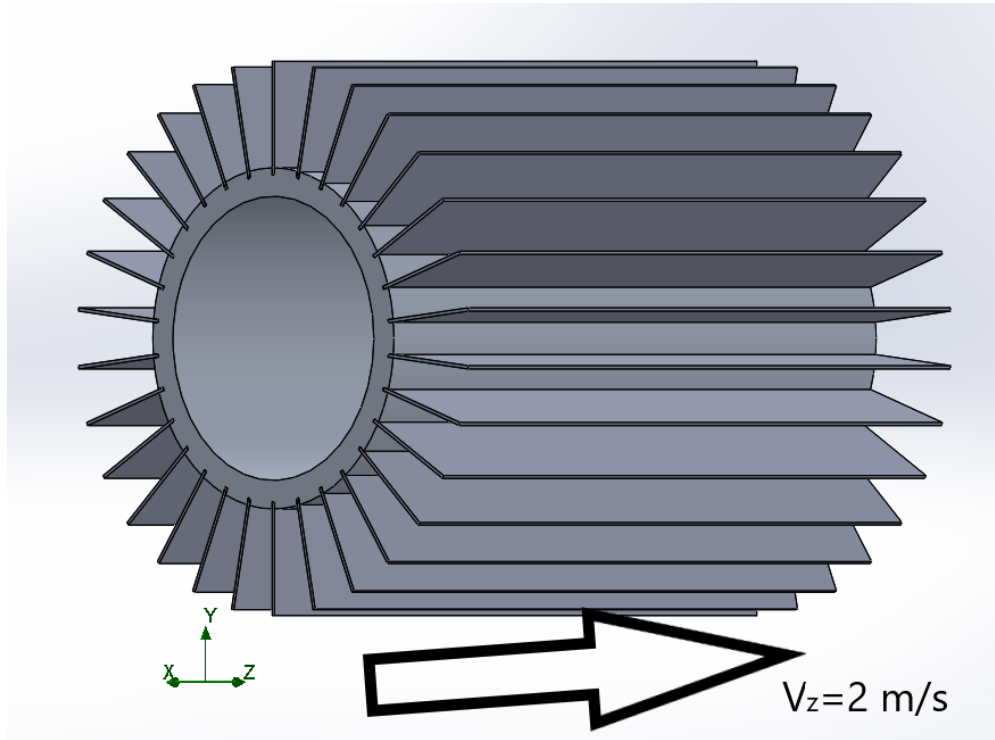


Figure 81. Demonstrates the aluminum housing of the EMA simulant.

In figure 80, the CAD demonstrates the geometry and the velocity of the air that assigned to study the effect of the convective cooling at a volumetric flow rate that is slightly less than one-meter cube per minute, $Q < 1m^3/min$. Standard pressure and temperature conditions were assigned in the simulation. Heat conduction is selected for the simulation. The bodies were selected given the thermal properties of aluminum for the study.

Heat sink specifications by the manufacturer provide information on the temperature rise of the heat sink to that of the ambient air that surrounds the structure. Taking a similar approach, the average global temperature of the fluid and the average total temperature of the EMA were goals calculated by the software. The temperature rises are displayed as a function of heating power given in figure 81.

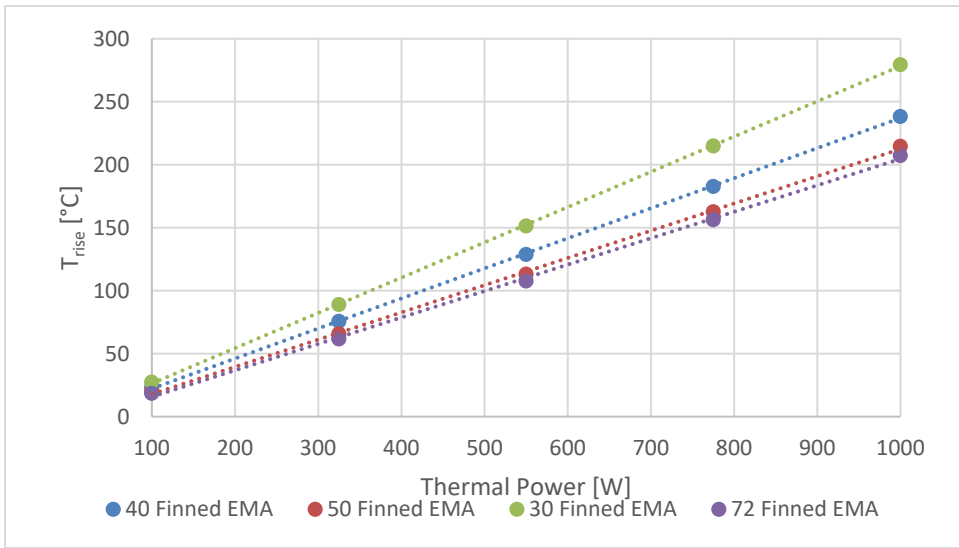


Figure 82. The temperature rise of the EMA to the average ambient temperature for different

In figure 81, the temperature increase amongst the EMA and the ambient temperature is shown as the fin count is varied across various thermal power settings. As expected, the least number of fins give to higher temperature rises; conversely, as the fin count is increased the temperature rise decreases.

Figure 82 compares the highest fin count, 72 fins, and is treated as the best-case scenario due to the fact the temperature rise is the least as shown in figure 2. Having 30 fins introduces a large temperature difference between the two-fin configuration. However, using a fin count of 50 is a suitable option since the temperature difference amongst the 72 and 50 finned cases is less than 10°C. The machining costs for 50, 40, and 30 fins are located in table 10. Table one demonstrates the maximum thermal power, 1000W and the costs to aid in making a judgment on which fin configuration to construct for the EMA simulant.

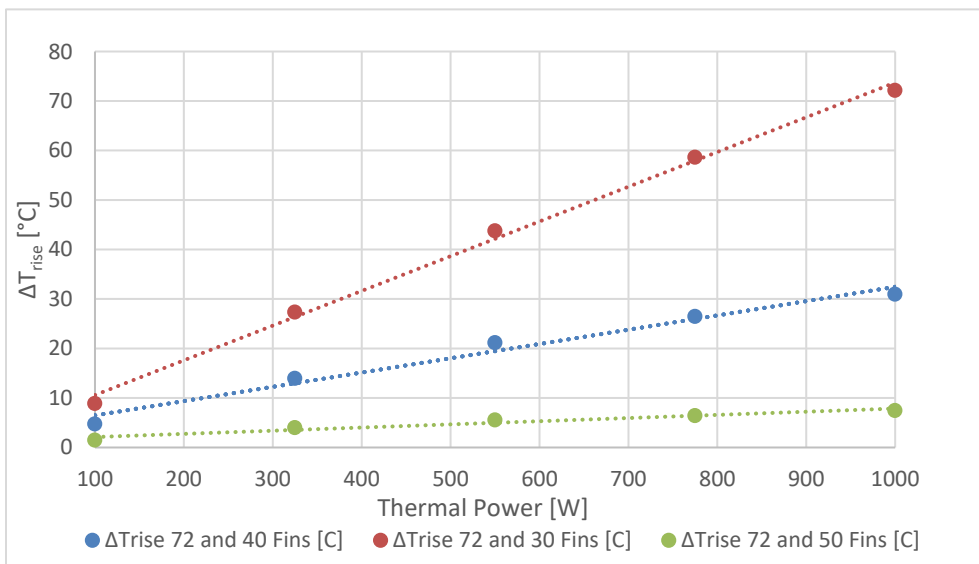


Figure 83. Demonstrates the difference in temperature rises amongst the different fin counts at various thermal power settings

Table 10. Demonstrates a comparison of the temperature rise of the EMA to the ambient air compared to the 72 finned optimal cases.

Fin Count	ΔT_{rise} [C]	Manufacturing Cost
30	72.1639038	\$ 480.49
40	30.97268113	\$ 532.63
50	7.466185163	\$ 586.35

In comparison to the three cases and for the price. The 50 finned cases would be the best option since there is a 23°C difference among the 40 and 50 finned cases for a price difference of \$53.72.

CFD results demonstrated the optimal results of the finned structures would be of a total of 72. Constructing a 72 finned EMA would have to be outsourced and the cost of approximately \$2000 at a local machine shop. Due to limited capabilities on campus, the work is not possible.

3 RESULTS AND DISCUSSION

3.1 EMA Experimental Work

EMA's form the backbone of reliable power-by-wire actuation systems for both aerospace applications and they present a formidable alternative to eliminate hydraulic systems from aircraft and spacecraft [33]. The benefits include improved safety, efficiency, reliability, and maintainability as well as overall weight reduction. Power by wire in "More Electric Aircraft" (MEA) concepts seeks to systematically substitute hydraulic actuators by EMA's [34].

EMAs eliminates the necessity for central and local hydraulic circuits because it transmits motor power to the load via mechanical reducers such as gearbox and nut-screw mechanisms [35]. Nevertheless, EMAs are yet to replace conventional hydraulic servo-actuators (HSA) in normal mode for safety-critical functions such as flight controls due to technical challenges such as weight and size constraints for integration, voltage spikes, and current transients effects on the stability of electrical networks, heat rejection for actuator thermal balance [35,36].

Thermal management of motor windings has been the focus of ongoing research in recent years. This effort is commensurate with the need for a well-controlled temperature for the performance and safety of the motors. High temperatures beyond the insulation class limit of the windings cause the enamel to melt away leading to a shorting of the wires. The suitable mode of cooling depends on the motor capacity [37] as well as the duty cycle, whether continuous or short cycle duty. In general, the cooling methods for a motor can be divided into air-cooling and liquid-cooling. In this current study, for instance, it was observed that proven cooling methods that were effective for continuously rotating motors would not necessarily work for the EMA's operating on short duty by default. The method of air-cooling mainly dissipates heat by fins on the surface of the casing and it is typical for low power machines, presenting the advantages of simple structure, low cost, and easy maintenance [38,39]. The operating temperature of an electrical machine such as EMA's is a balance between heat generation and removal rates, thus a good thermal management scheme is required to boost performance and enhance reliability [40,41].

Wang et al [41] proposed a novel thermal management approach with phase change material (PCM) for a permanent magnet synchronous motor (PMSM) applied in the actuator systems of aircraft using a numerical approach. They were able to show that when the conventional motor casing was replaced by a paraffin-based enclosure, the effective time for the PMSM temperature control could be prolonged by approximate 32.7% when the motor works under a continuous mode and dissipating 270 W. The peak temperature of the PMSM could be decreased by 7.82 °C when the PMSM operates under a duty cycle of 0.67. Sun et al. [42] applied potting silicone gelatin to reduce the end windings temperature of a 53kW permanent magnet synchronous motor, a modification that also altered the temperature distribution of the windings. For the original motor, the lowest temperature of the windings situated in the middle part of the windings which contacts the stator through the slot paper directly. The lowest temperature, however, moved towards the end when potting silicone gelatin was applied to the windings. They explained that the potting material enhances the heat transfer from the end windings because it offered a solid contact to the casing. The peak operating temperature of the windings reduced by 27.3°C.

The road map of this current study was to establish the temperature distribution inside the motor via experimental measurements and to devise an effective means of managing temperature hotspots in the windings. It worth stating that motors used in this research have permanent magnet stators and windings on the rotor. This design (having an air gap around the rotor) presents a high thermal resistance thus trapping heat generated in the rotor windings. and sending it out via the casing.

3.2 Experimental Procedure

The main purpose of the experimental procedure was to determine the power consumption, heat dissipation and temperature profile of the original EMA's at specified operating conditions. This was followed by systematic efforts to manage the temperature hotspots inside the equipment by introducing design modifications.

Two EMA's from different manufacturers were procured for initial testing. The models used are Transmotec DMA-24-5-B-102-IP65 and Progressive Automation PA-003. The two models are shown respectively in Figures 83 and 84. Measurements were made to determine the temperature at specific points inside the motor and housing using k-type thermocouples and were plotted over nine minutes. At the early phase of the study, it was sought to test the motors for the nine-minute duration to follow the typical aircraft landing cycle time, but the rated duty cycle of the motor meant that the nine minutes continuous run demanding on the motors. Thus, subsequent experiments are reverted to a limit of five minutes based on the manufacturer's recommended duty cycle for the two motors.



Figure 84. Transmotec Motor DMA-24-5-B-102-IP65

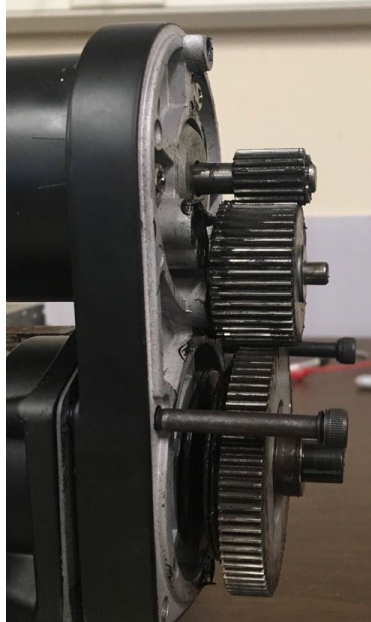


Figure 85. PA 003 Motor

Table 11. Manufacturer supplied specifications of DMA-24-5-B-IP65 (Source product catalog: www.transmotec.com) and PA 003 (source: progressiveautomations.com)

	Transmotec DMA-24-5-B-IP65	PA 003
Maximum Voltage	24 VDC	12 VDC
Current at Maximum Dynamic Load	14 A	7.6 A
Maximum force	2500 N	2670 N
Duty Cycle	25%	20%
Speed at maximum load	47 mm/s	--
Gear speed reduction	5	--
Stroke Length	102 mm	204 mm
Weight	4.6 kg	
Protection rating	IP65	IP54
Insulation class/ Maximum winding Temperature	F/ 150°C (Based on an ambient of 65°C)	F/ 150°C (Based on an ambient of 65°C)

The DMA24-5B is a brushed, two-pole 12-slot permanent magnet motor rated for 24 V and 14 A at peak dynamic load of 2500 N. It has a duty cycle of 25%, which stipulates that for every five minutes of continuous use it must be allowed to idle for not less than 15 minutes to get the temperature back within safe operating limits. The motor has a linear actuator that simultaneously spins about its axis as it extends or retracts. This motion is executed by a ball screw gearing set (figure 85c). When the motor is powered, and the actuator is held in a static position as in figure 85d, the dependent rotatory/linear motion of the actuator shaft is stopped, the motor shaft, as well as the associated gearing shown in figure 85a, also stays at rest without rotating. Hence the stopping mechanism which simulates a static load provides a braking force for the electrical motor. The PA-003 is a brushed, two-pole 10-slot configuration motor having a permanent magnet stator and the windings on the rotor. It is rated for 2670 N at 12 VDC.



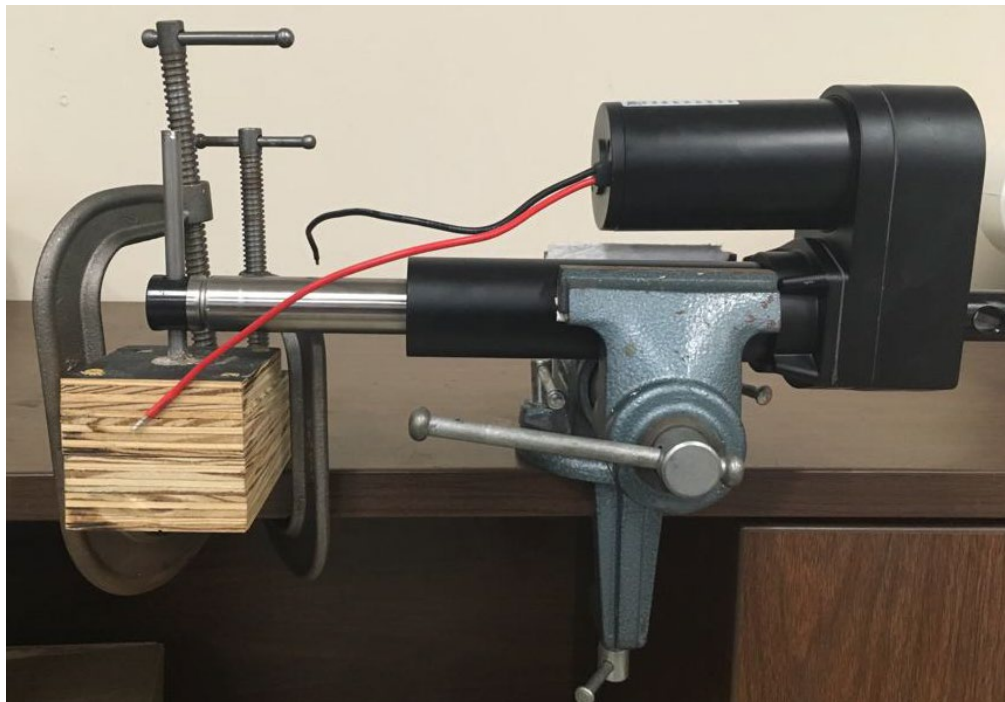
85(a) DMA-24 Gear arrangement



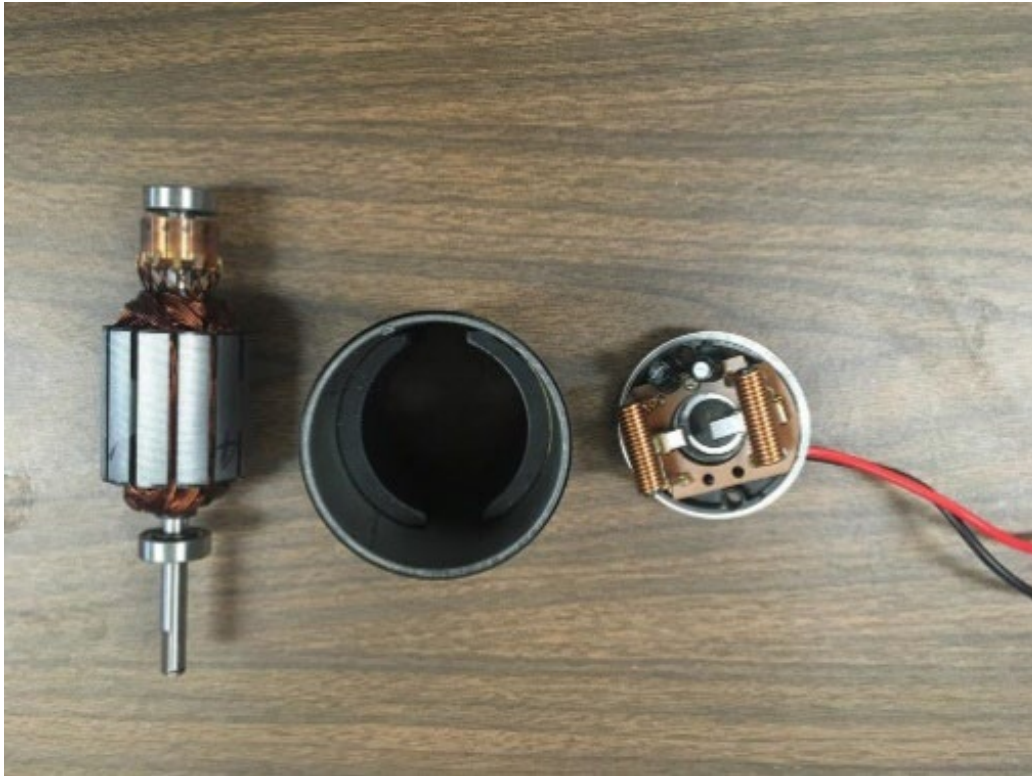
85(b) Ball Screw in the actuator



85(c) Rotor and stator assembly.



85(d) EMA in a jammed position.



85(e) Rotor, stator, and housing cover with commutator brushes.

Figure 86. DMA-24-5-B-IP65 Motor parts and experimental setup

The circuit was wired as shown in Figure 86. The voltage readings across a calibrated conductor and motor were logged on the data acquisition system for the duration of the experiment simultaneously with the temperature of the air inside the motor housing. The calibrated conductor had been previously calibrated to obtain a current-voltage curve before being used in the circuit in figure 85. The voltage V_c was used to calculate the instantaneous current going through the motor.

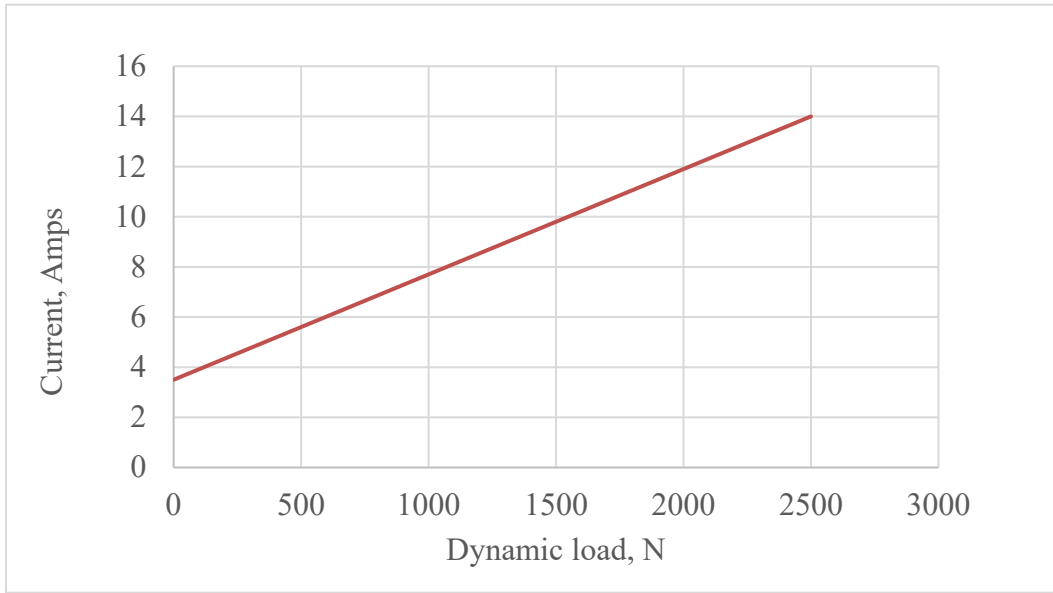


Figure 88. Demonstrates the current vs load.

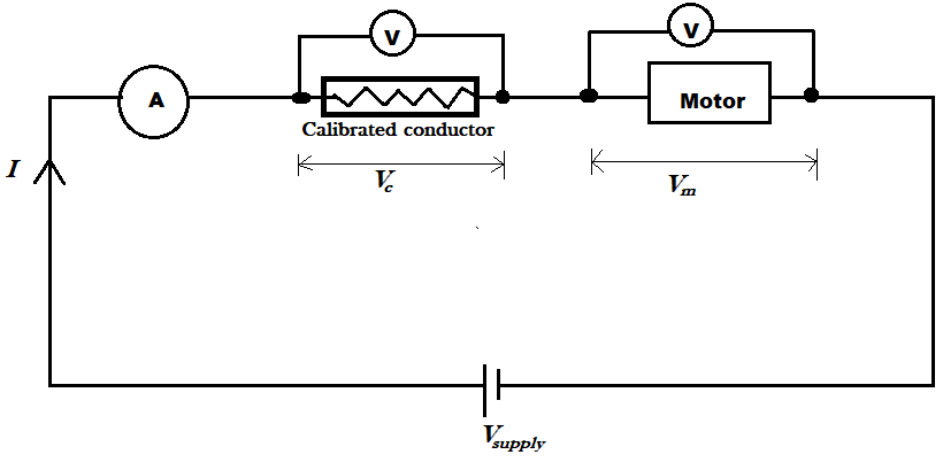


Figure 87. An electrical circuit for the experiment.

3.3 Results and Discussion

At no-load conditions, the DMA24 extends to full stroke actuator continues to spin at a full stroke without extending, which means it keeps delivering a mechanical work output drawing an average of 4.66 A at 21.3 V over a nine-minute duration. According to [43], the current drawn by the motor has a linear relationship with the force it delivers at stationary conditions or steady velocity, a trend which is also confirmed by plots from other manufacturers. Even though the manufacturer's catalog for this very motor (DMA 24-5B) does not provide such a plot, it gives the current and force at peak dynamic load which was used together with the values measured in this study to produce the plot in Figure 86.

When the actuator is in motion, a portion of the power supplied to the motor is used to provide motional emf E whilst the rest is dissipated as heat in driving currents through the coils as seen in figure 87. From the energy balance on the motor:

$$\text{electrical input power} = \text{rate of heat dissipation in the windings} + \text{mechanical power output} \quad (18)$$

$$V_m I = I^2 R + EI \quad (19)$$

The product EI which represents the power required to deliver the mechanical output is equal to *Force* \times *linear velocity* for a linear motion or *Torque* \times *angular velocity* for rotation. At stationary conditions, no motional emf is required, and the applied voltage only is what the circuit requires to drive current I through the circuit to provide static equilibrium between the motor and the mechanical load. The result of the latter is that all the electrical power supplied to the motor comes off as heat when the EMA is held in static equilibrium as illustrated by the plot in Figure 88.

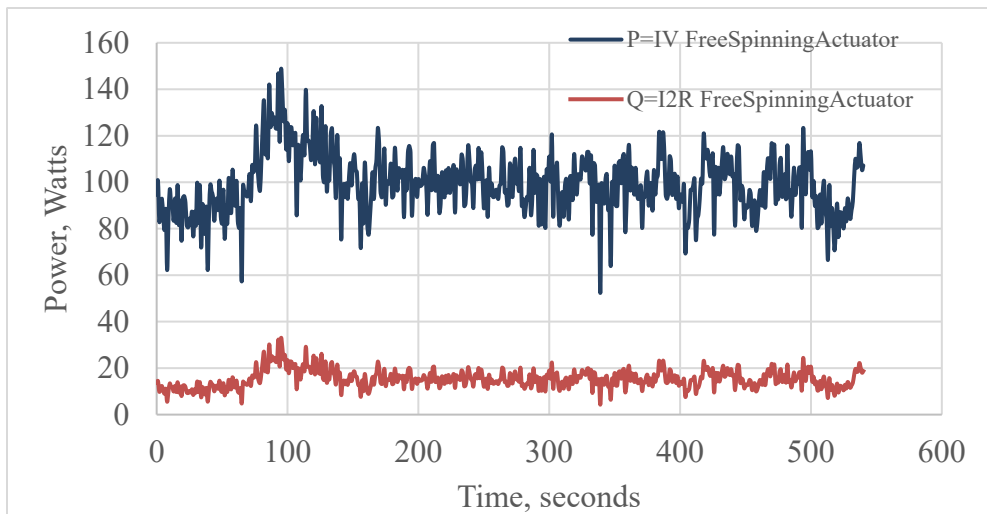


Figure 89. Power consumption and dissipation profile at no external load.

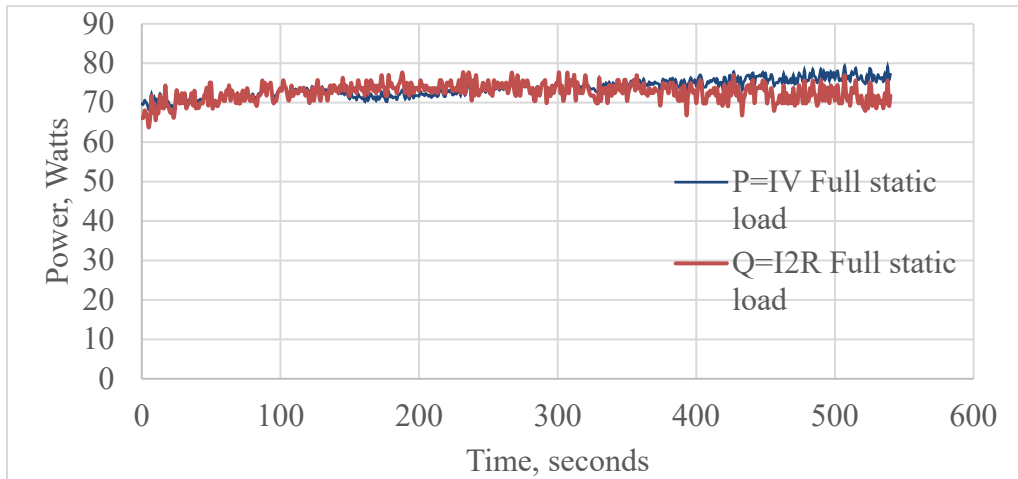


Figure 90. Power consumption and dissipation at full Static load.

The effect of having all the supplied power going to heat in stationary cases results in a rapidly rising temperature inside the motor as illustrated in figure 89. The measured electrical resistance of the DMA24 motor is 0.65 Ohms. Efficiency at no Load with actuator freely spinning the efficiency averaged at 84.7% and the remaining 15.3% was dissipated as heat. At maximum dynamic load approximately dissipated as the heat would be 127.4 W representing approximately 37.9% of the rated power. At static loading situations, the motor shaft and gearing mechanisms do not spin. Approximately 95-100% of the power drawn is dissipated as heat (up to 77 W). This represents 22.9% of the motor's rated power. PA-003 also gave plots of a similar trend of heat and power characteristics. With a rated power of 91.2W and measured electrical resistance of 0.6Ω , the maximum dissipation is 34.6 W, which evaluates as 38% of its rated 91.2 W power. Hence, a design to manage the heat dissipation of this motor should target about 38% of the rated power input as possible heat dissipation during peak operation.

3.4 Temperature Profile for Heating conditions

As expected, the loading situation that resulted in higher energy dissipation resulted in higher temperature rise as seen in figure 90. The temperature measured in this setup gives indicative values for simulating the model in solid works especially when modeling the effect of the air trapped inside the housing. The design of the DMA-24-5B motor and housing makes it highly inaccessible (IP 65) for the windings to be reached by thermocouples or directly via the infrared camera. It was only possible to pass one thermocouple lead through to measure the inside air temperature. To be able to present real-time temperature plots of the windings and other internal components of the motor as the experimental procedure is repeated with PA-003, which appears more accessible with an ingress protection of IP54.

The temperature profile for the PA-003 at an average heating rate of 60.12 W is shown in Figure 90. As seen from figure 90, the temperature at the two points on the end turns were the highest, reaching 129°C point 0 and 110°C for point 6 in nine minutes. The temperature of the embedded turns ranged between 80 and 100 °C, whilst the air trapped inside the motor housing warmed up to 50 °C. Figure 91 shows this transient plot as well as the corresponding temperature probe locations.

To ascertain the effective heat transfer path from the windings to the ambient via the enclosure the plot in Figure 92 was produced by including the stainless housing in the measurements. PA-003 was run at an average I^2R value of 66 W for 80 seconds and observed as it cooled over a 20-minute period. The high-temperature difference between the windings and inside air gives an indication of the high resistance to heat transfer to and across the air to the housing wall. Noting that the rotor becomes stationary when the EMA is holding a load in position implies that air trapped inside the housing remains stationary at this instant, making conduction the only effective means of heat transfer. The temperature of the housing, however, stayed very low – a few degrees above the ambient.

The high local thermal resistance posed by the air space between the rotor and the housing implies that an effective means of cooling the rotor must deal with the removal of heat from the windings. In effect, a local cooling that removes heat from the windings becomes a prerequisite before a global cooling (removal to the surroundings) becomes effective for this configuration of motors.

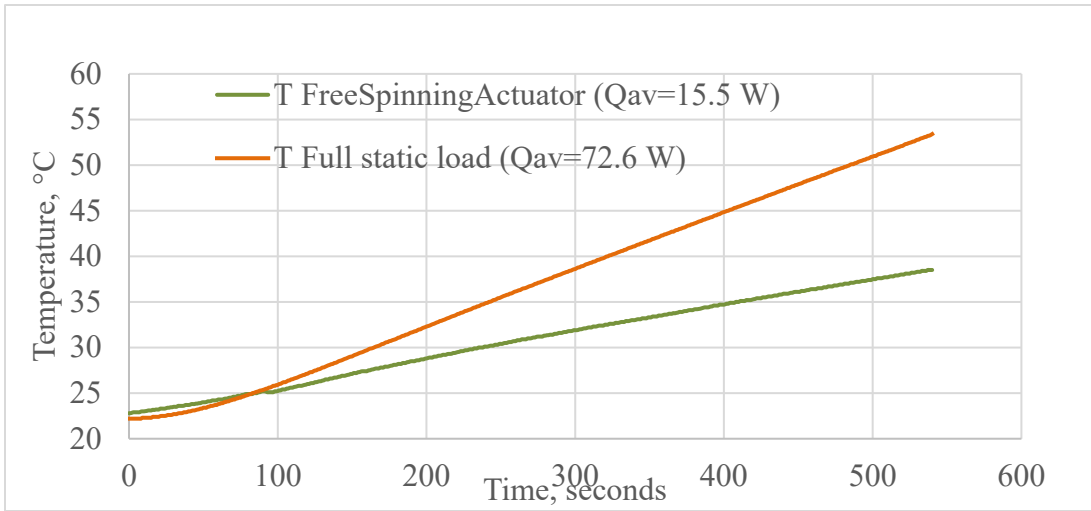
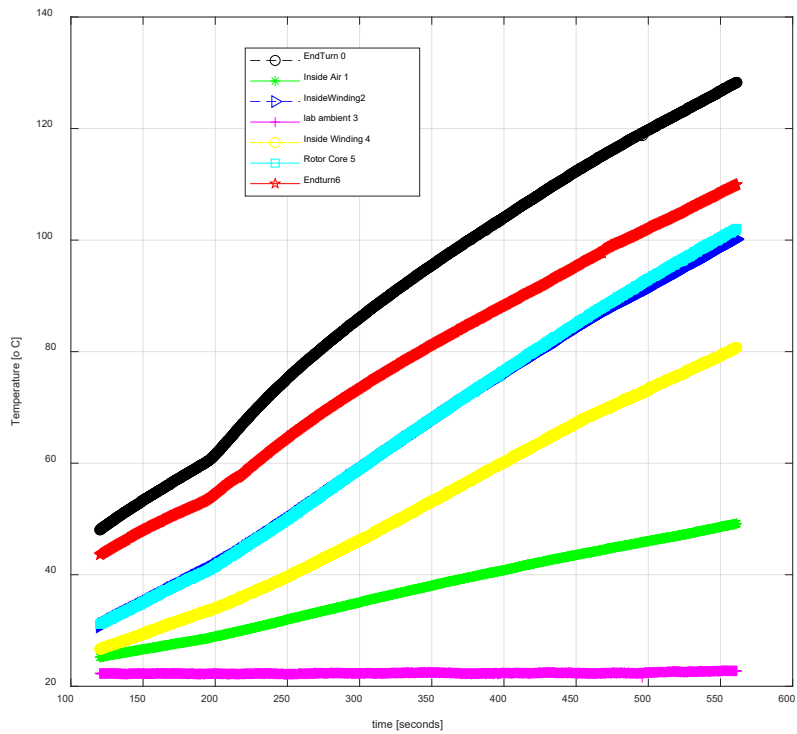
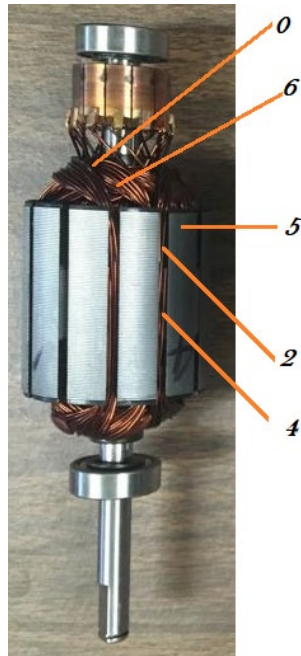


Figure 91. The air temperature inside DMA24 motor housing at full static load and no-load (free spinning conditions)



(a).



(b).

Figure 92. The transient temperature profile of PA-003 at $Q=60.12W$. (b). The temperature probe locations

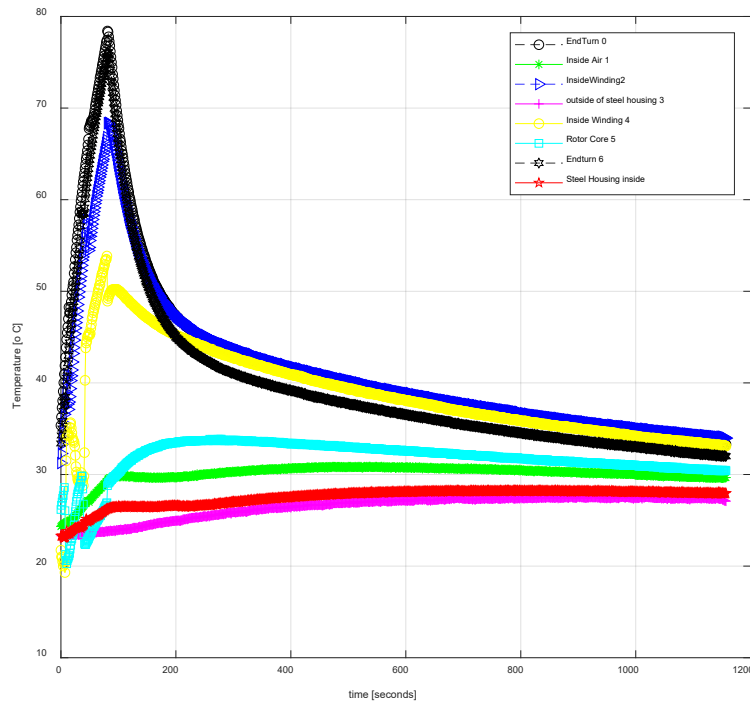


Figure 93. 80 s heating at $Q=66W$ followed by cooling by natural convection.

At peak load, the motor draws 336 W power and dissipates whilst moving against a dynamic load of 2500N (this takes place within 2.2 s). At holding the position, the motor draws a maximum 77 W and dissipates all of it at heat whilst resisting a static load. Thus, in a design to manage the heat generated by this EMA, we must consider a heat spike approximately **40%** of maximum rating and a then to constant dissipation of **23%** whilst holding on to the load.

3.5 Numerical Simulations

The motor was modeled in the SOLIDWORKS thermal solver in transient mode to simulate the performance of the original motor. A heat source term of 72.6 W was placed on the windings as a uniform volumetric heating and an approximate heat transfer coefficient of $h=5 \text{ W/m}^2\text{K}$ was used to represent the heat dissipation from the rotor. The mesh details are presented in Table 12.

Table 12. Mesh details

Total Nodes	36829
Total Elements	19393
Maximum Aspect Ratio	19.389
% of elements with aspect ratio <3	88.7
% of elements with aspect ratio >10	0.165

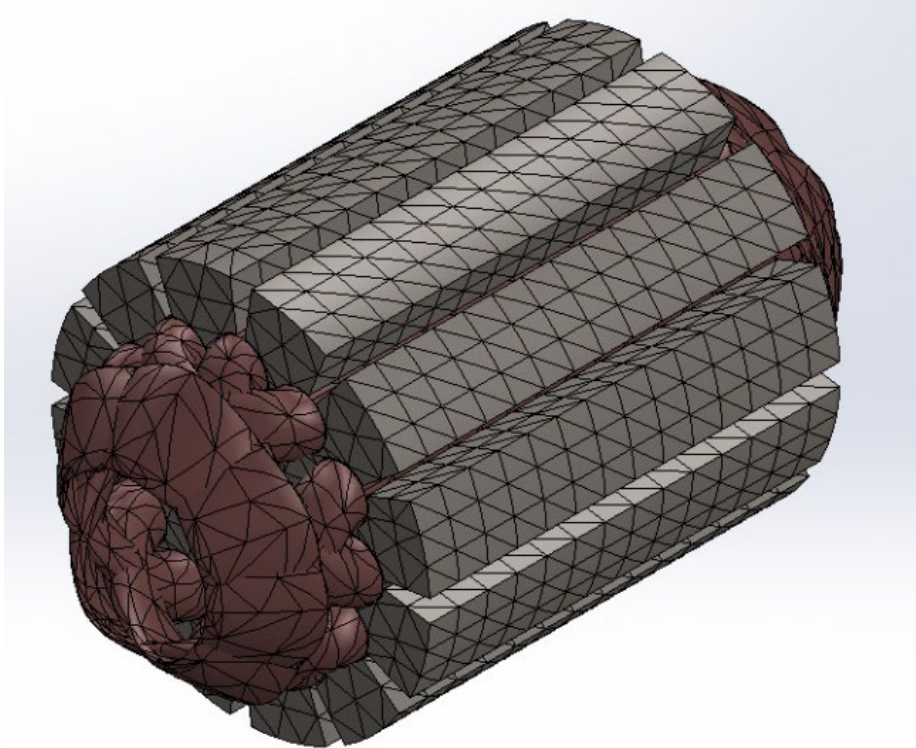
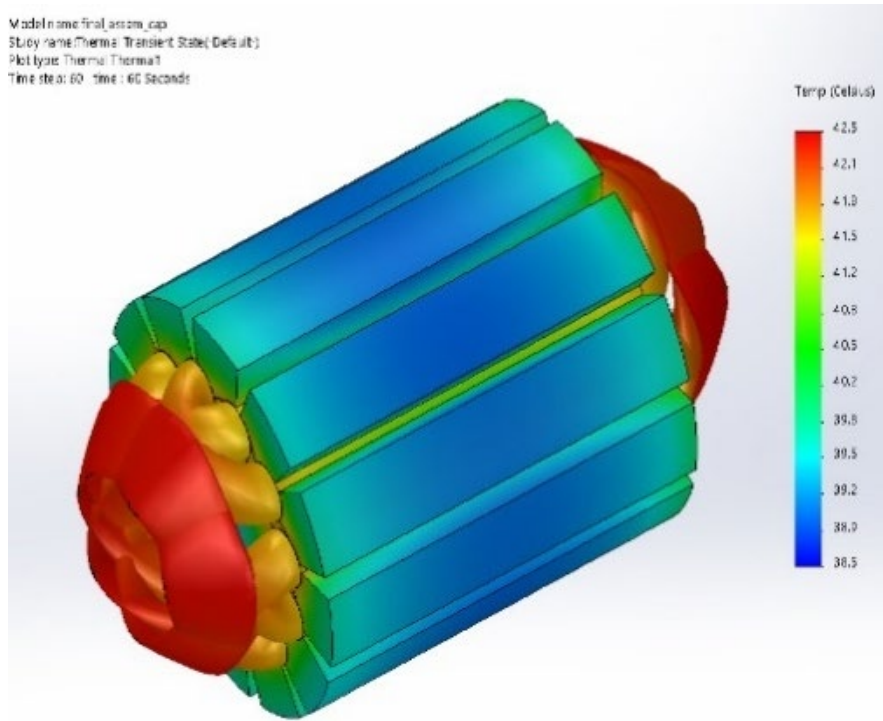
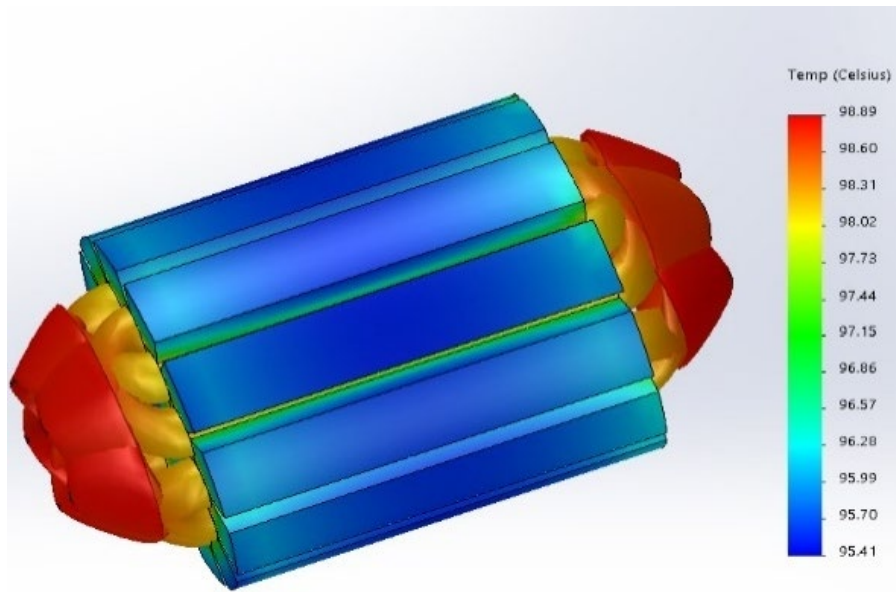


Figure 94. Mesh for the thermal study of the original motor

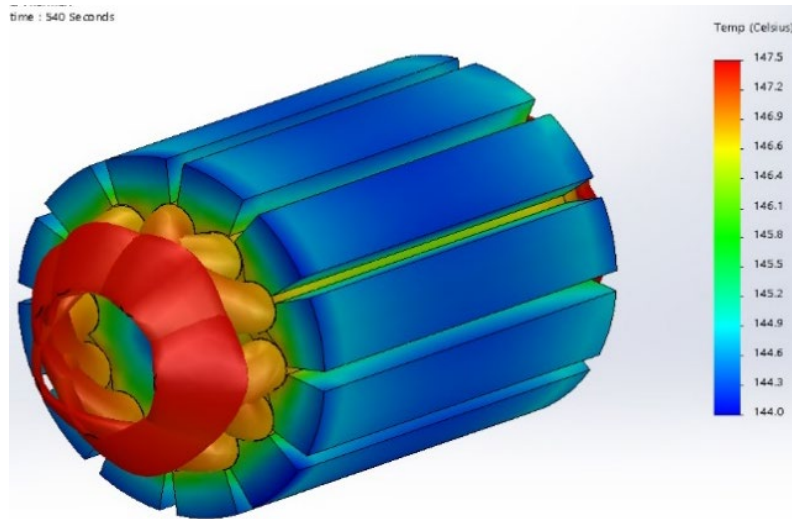
Model name: final_asm_cap
Study name: Thermal: Transient State (Default)
Plot type: Thermal: Temperature
Time step: 60 time : 60 Seconds



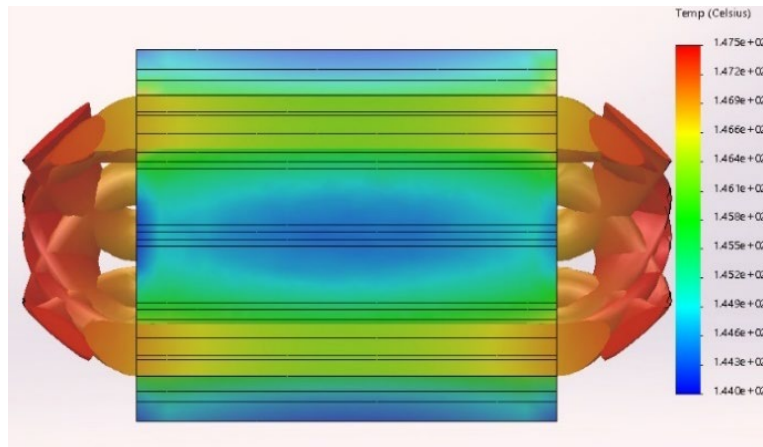
94a. Temperature distribution at 60 s



94b. Temperature distribution at 300 s



94c. Temperature distribution at 540 seconds



94d. Cutaway section through rotor at 540 second

Figure 95 Transient thermal profile of the original motor

3.6 Design Modifications

3.6.1 Option A: Extending the housing and installing a fan inside the motor

In figure 95 the new design of the outer casing is seen such that a ducted fan can be introduced into the case. The flow direction is indicated by the blue arrow and the fan source term is a circular cylinder that contains the fan curve used for the simulations. On the left-hand side of Figure 83, an opening has been designed such that air can enter the housing, and past the motor 12 circular holes of equal-sized diameters of 0.28 inches to allow for the air to exit the housing into the wing bay.

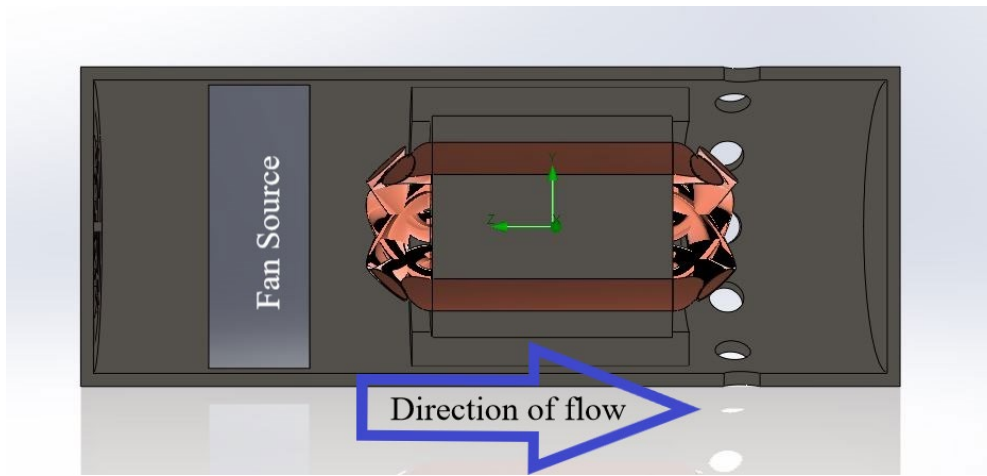


Figure 96. Demonstrates the redesigned outer housing with the fan source for convective cooling.

Carbon-Based stainless steel was assigned for the outer housing and for the interlamination material of the motor itself. The windings are assigned a pure copper property. In Figure 84, using compressed air as a method for cooling the EMA was proposed at various inlet pressures. The 12 outlets were kept at the same location as are shown in Figure 95.

The results are shown in Table 13 for the average heat transfer coefficient that was calculated numerically through the SOLIDWORKS flow simulation. The compressed air demonstrated higher average heat transfer coefficients than the two fans tested. The ETRI 280DH demonstrated a higher h which indicates a better cooling performance than the Mechatronics G4020. Since the compressed air is not a viable option for cooling the EMA, using the ETRI fan can cool EMA closely to that of flowing compressed air at 20 psi.

Table 13. Shows the various average heat transfer coefficients determined by SOLIDWORKS Flow Simulation.

Fan	Inlet Pressure [psi]	Avg. h [W/m ² /K]
n/a	20	24.8
n/a	25	25.7
n/a	30	26.4
n/a	35	28.1
n/a	40	29.0
n/a	50	32.6
ETRI 280DH	n/a	21.3
Mechatronics G4020	n/a	15.9

From figure 85, the ETRI fan demonstrates that at transient state the highest temperatures are approximately 157°C at the copper windings. Introducing the fan into the casing, the

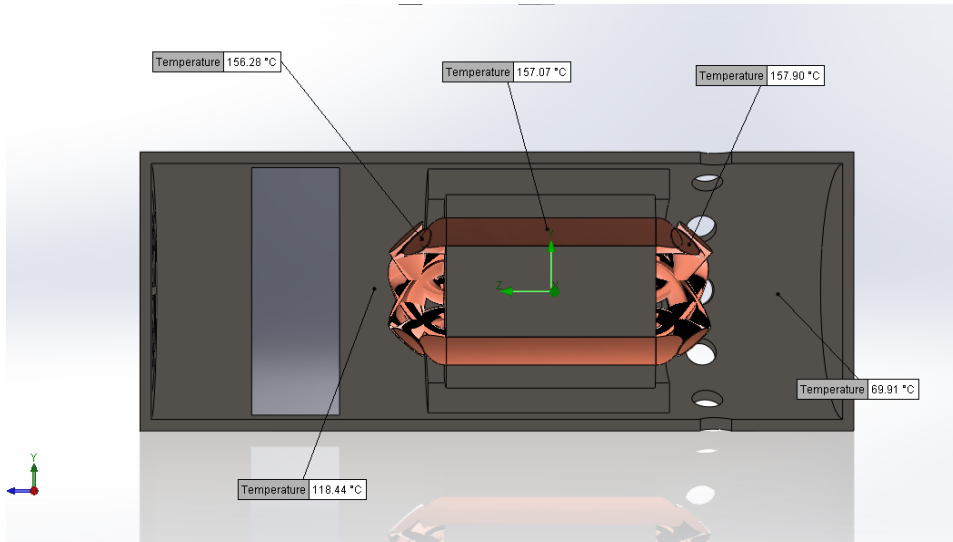


Figure 97. ETRI Fan temperature probes placed at and around the motor at a steady state.

temperatures are highest at the backside of the motor since the fan is not directly blowing that surface. The temperatures increase the farther that you move away from the fan. Figure 15 demonstrates the temperature contours and from the figure, we can see that the motor temperature is higher than the rated temperature of the motor. Figures 96 and 97 are both at steady-state results.

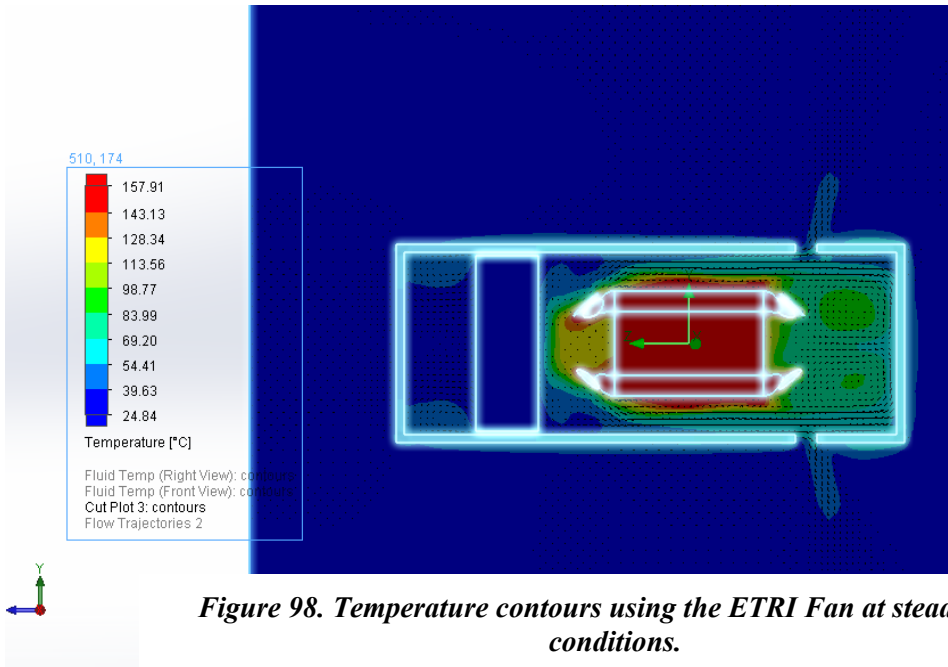


Figure 98. Temperature contours using the ETRI Fan at steady-state conditions.

Figures 98 and 99 demonstrate the same results of temperature probe measurements and temperature contours for the Mechatronics fan, respectively. The results of this particular fan are

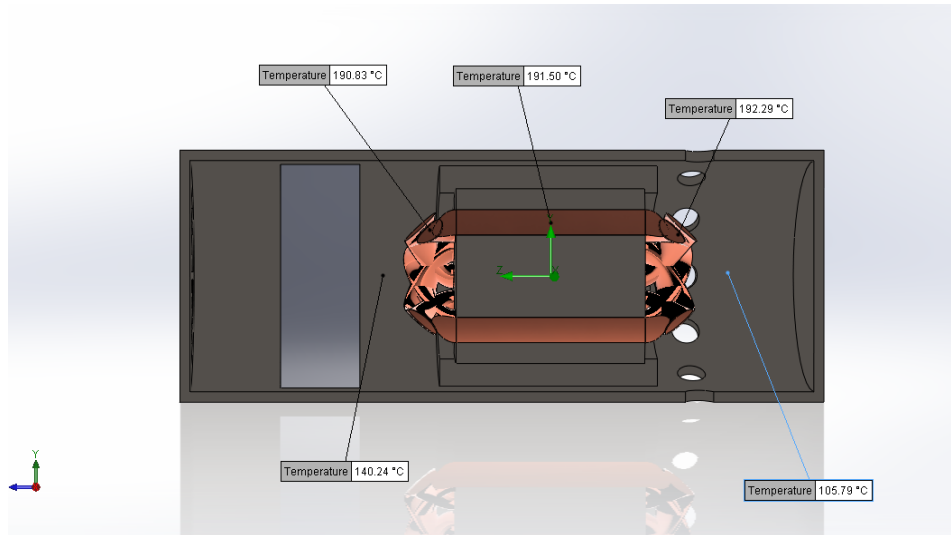


Figure 99. Temperature probe measurements at and around the motor using the Mechatronics Fan at a steady state.

not as beneficial for cooling the EMA as that of the ETRI fan. Using the Mechatronics fan, the results demonstrate that the maximum temperature seen within the motor is that of 192°C.

The normal operation of the EMA at the fully loaded condition is for a few minutes. Therefore, a transient study of the EMA was carefully studied when the ETRI fan is being used to cool the

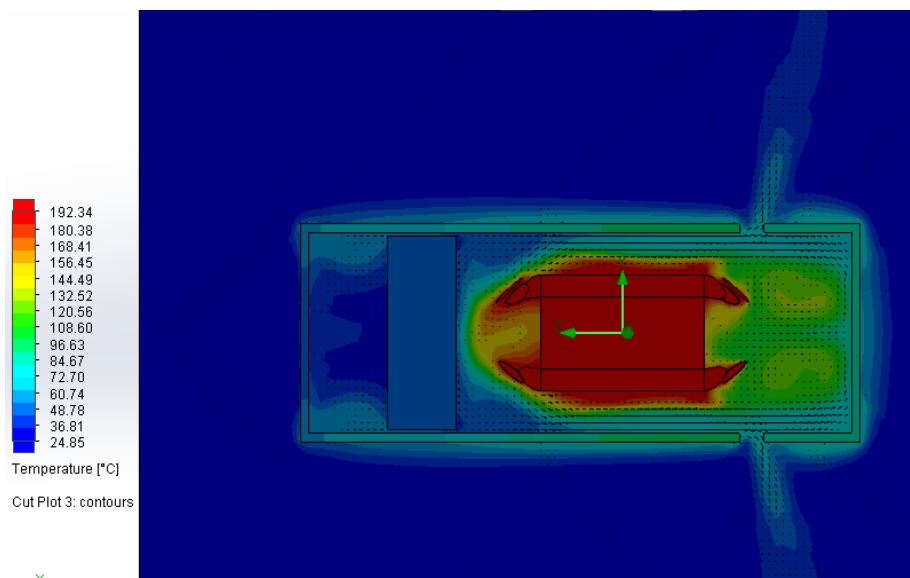
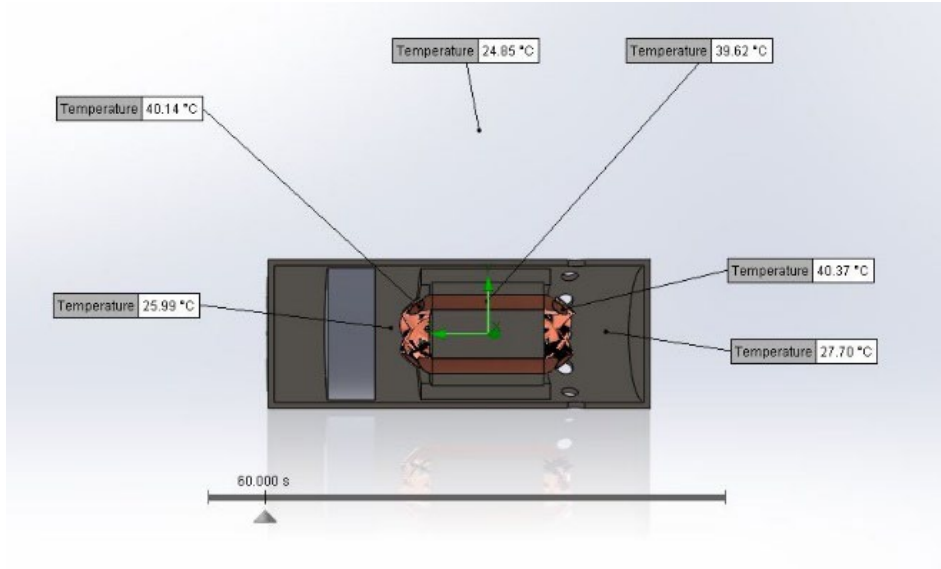


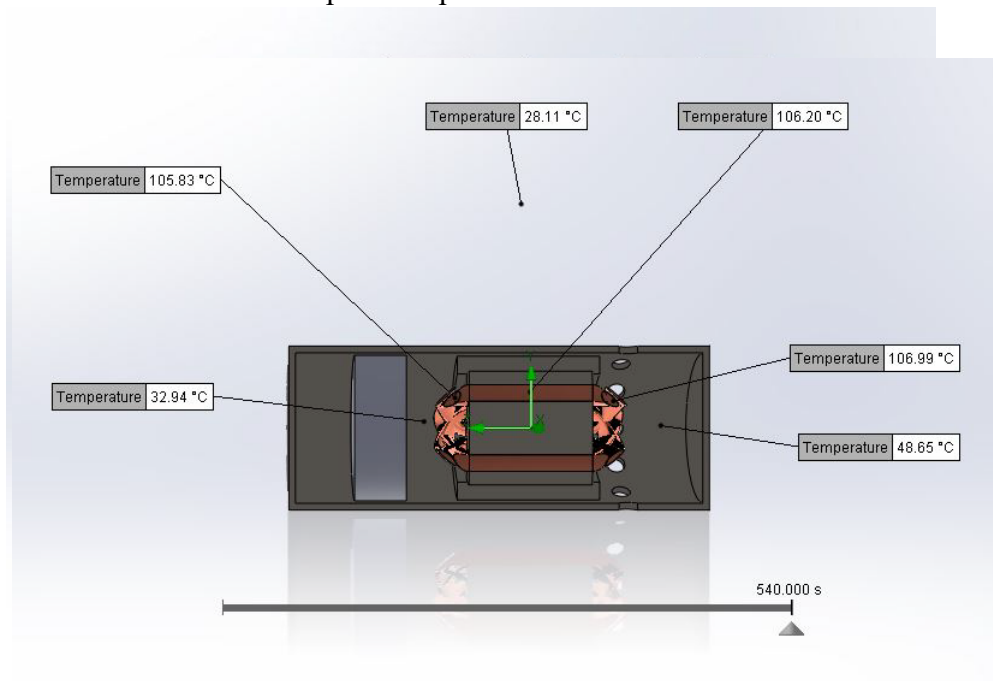
Figure 100. Temperature contour of the motor being cooled by Mechatronics Fan at a steady state.

motor. The temperature probe measurements are seen in figure 18a-c. At 9 minutes of operation, the maximum temperature at the copper windings is seen to reach temperatures of 106°C.



100a: Temperature probe measurements at $t=60s$

100b: Temperature probe measurements at $t=300s$



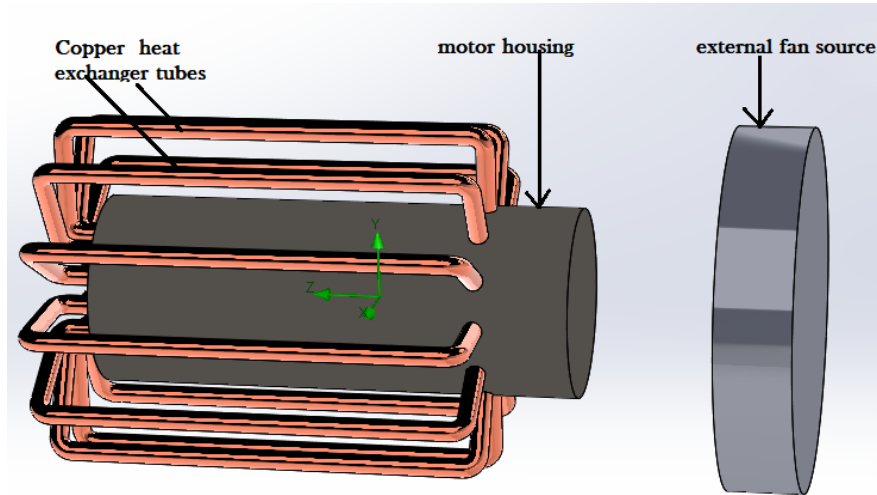
100c: Temperature probe measurements at $t=540s$.

Figure 101. Temperature probe measurements

The number of cells used in the simulation is demonstrated in table 13; moreover, figure 91 shows the location of those cells. The cells at the boundaries were given a higher level of refinement to capture the physics of the flow at the boundaries. SOLIDWORKS flow simulation is a software that uses a finite volume method. It can the ETRI fan demonstrated better performance for cooling the motor than the Mechatronics fan.

3.6.2 Option B: Incorporating internal recirculation through heat exchanger pipes

An alternative design having the same internally housed ETRI fan but cuts the motor air off from the wing bay by introducing copper heat exchanger tubes for recirculation (referred to as option B). An external fan blows air over the heat exchanger tubes as the motor housing air circulates in



it Figure 101.

Figure 101(a). An external image of the internal recirculation of the heat exchanger pipes.

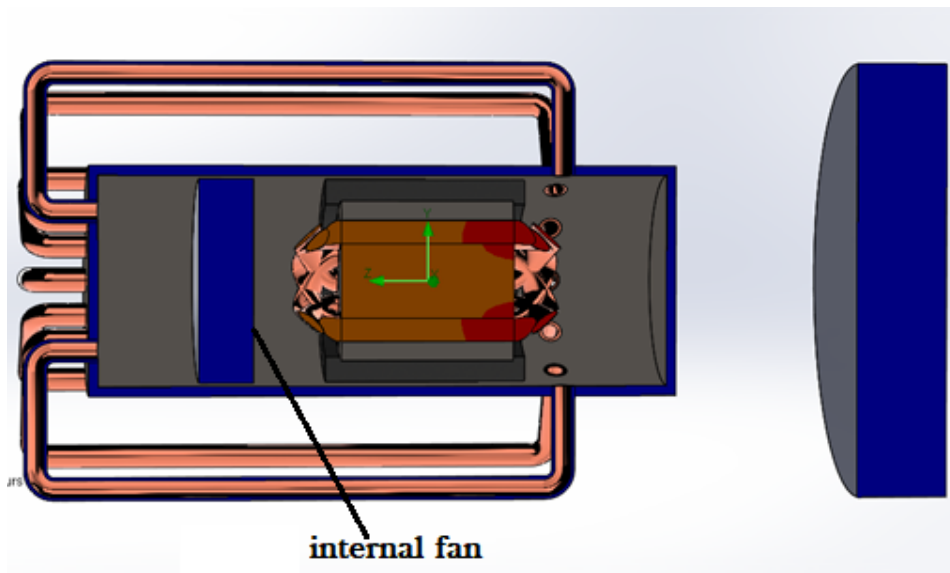


Figure 102. The internal fan within the EMA

101(b). An internal image of the heat exchanger demonstrating the internal fan within the EMA, with temperature contours demonstrating the hot spots (red).

Figure 102 shows flow streamlines and velocity quivers plotted on temperature contours of the air in and around the motor. The results presented in figure 103 and 104 are for the 300 seconds run. The highest temperature drops to 86.6°C compared to 98.9°C for the original case.

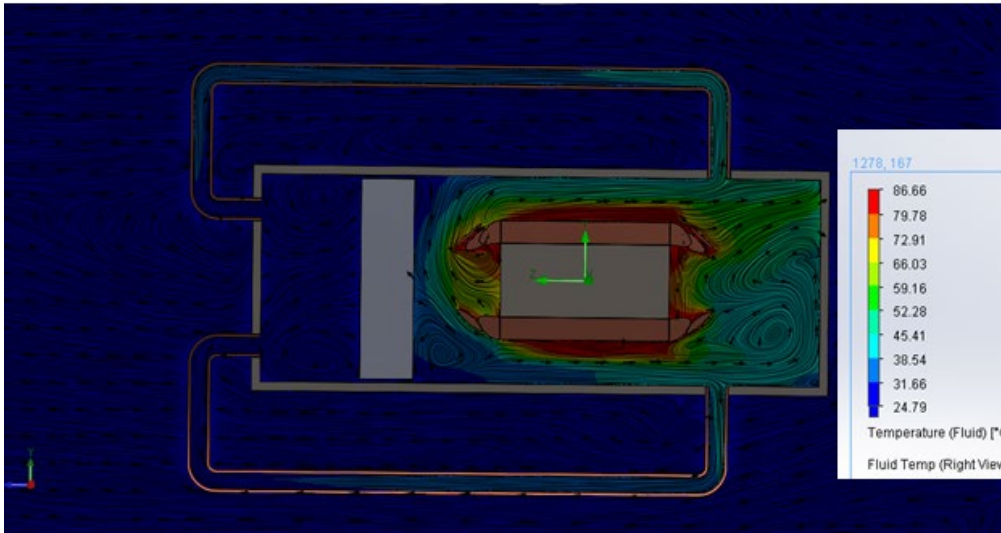


Figure 103. Temperature contours with velocity streamlines and quiver plots

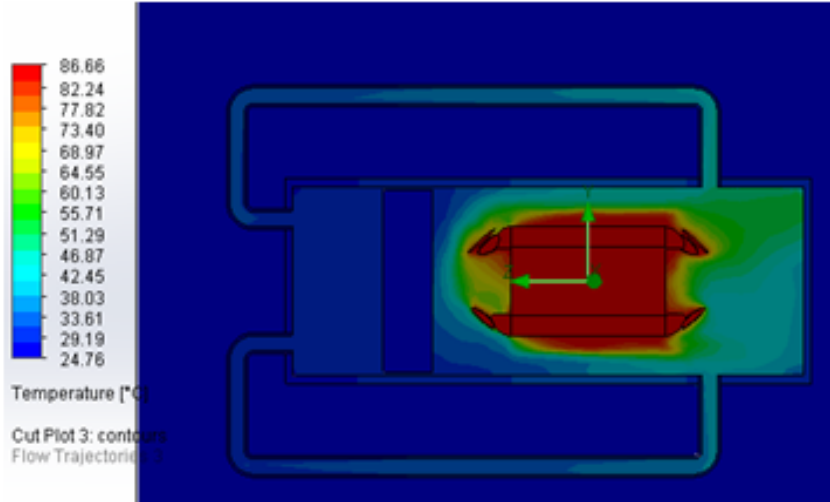


Figure 104. Temperature contour within the system, and shows the distribution across the

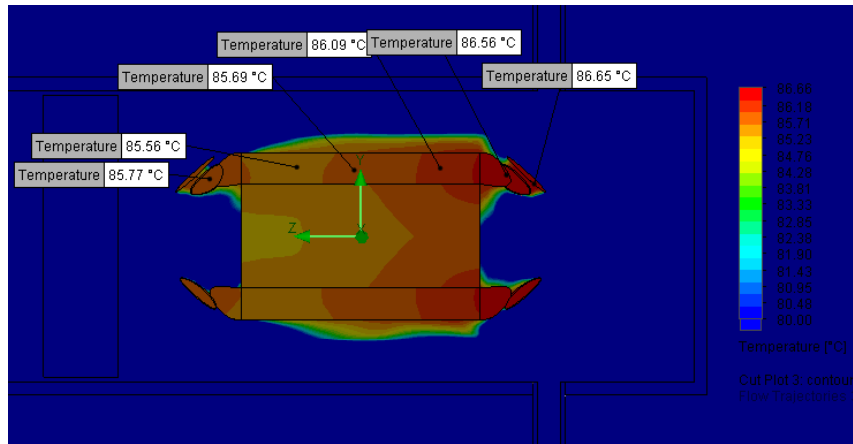


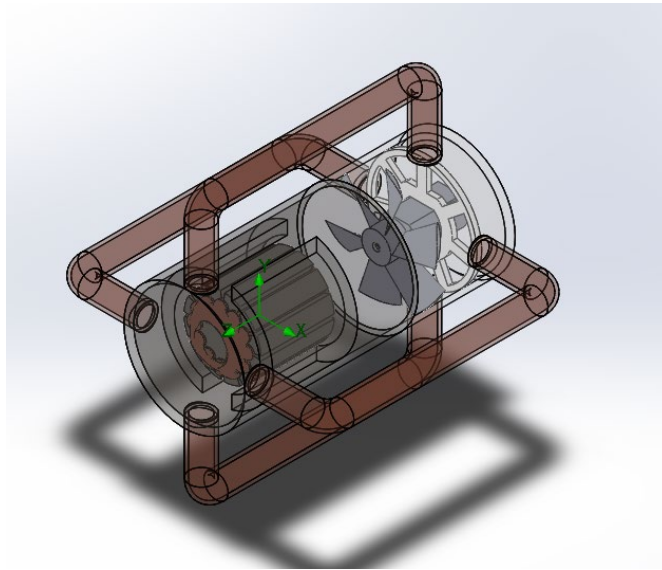
Figure 105. Demonstrates the hot spots within the rotor piece of the EMA; furthermore, the hotspot (red) is seen in the end windings with a temperature of 86.65°C along the backside of the motor.

Two viable designs have been proposed to solve the heating problem of the motors under study. The design using an internal recirculating fan and an external fan is preferred since it preserved the ingress protection of the motor against intrusion by moisture and particulates whilst having performance comparable with the other option A using through air-cooling.

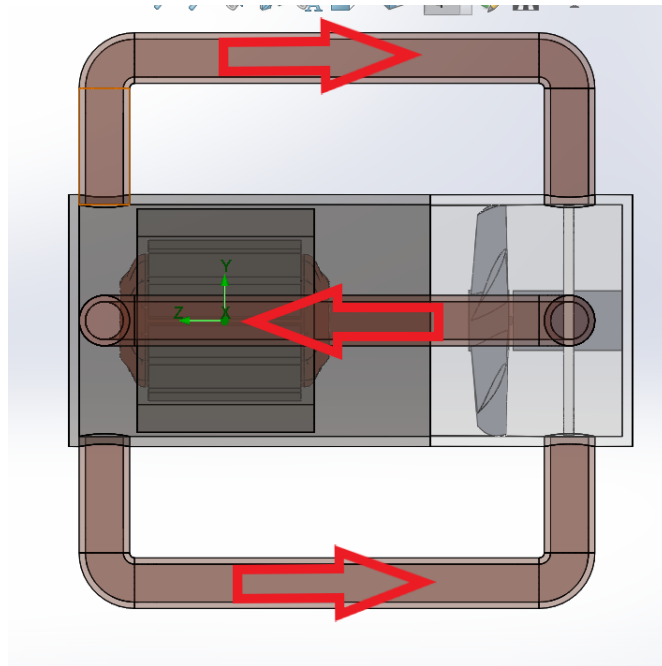
The design concepts, as well as the original motor, were simulated in SOLIDWORKS flow simulation software. The studies revealed that option A reduced the highest temperature spot by 40.5°C whilst option B brings a reduction of 37.5°C. In conclusion, the cooling performance of both systems are good and in a comparable range. Option A introduces fewer modifications to the original motor design, which would have been desirable but introduces a draw of air from which can potentially contaminate the internal motor components. Option B however, preserves the original ingress protection of the EMA even though it requires extra components. Subsequent simulations will be run to optimize the design and to ascertain its reliability by checking the thermal performance in case one of the fans is off.

Based on the CFD simulations, a conceptual design was devised to test this heat exchanger concept. The original CFD results were obtained with 12 copper sections, but was impractical; furthermore, the physical design contains four copper section. In figure 103, a clear CAD demonstrates the setup. The white section was 3D printed from PLA plastic. The fan inside of the concept was also 3D printed of the same material. The flow of the recirculating fluid is shown in figure 104. The internal fan needs to be able to generate enough motion within the EMA to transfer the heat from the end windings into the copper section. Figure 105 demonstrates the physical design that was manufactured. The internal structure of the fan within the system is displayed in figure 106.

3.7 CAD design and prototype build of EMA Heat Exchanger Setup



105 (a). Isometric view of the CAD assembly.



(b)

Figure 106. Side view of the CAD demonstrating the interior of the fan assembly.



(a)

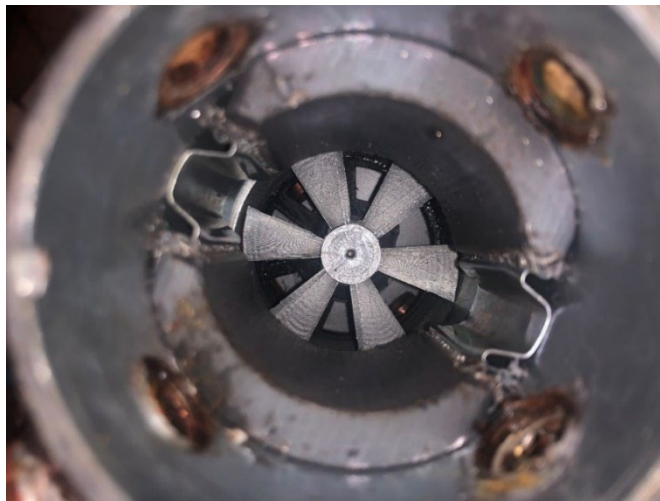


Figure 107. (a) Demonstrates the physical assembly of the fan HX concept. (b) Demonstrates the physical fan that was 3D printed that will be used for the testing of the HX concept.

The electromagnetics of the design was not considered carefully. When the internal fan was started, it was found that the electromagnetic strength of the magnetic stator caused a magnetic interference with the motor driving the impeller. This problem would cause the fan to not function. The design needs to be further studied to eliminate this electromagnetic problem.

4 THERMOSIPHON HEAT PIPE

Thermal management in hybrid emerging technologies is the main concern, in which local cooling becomes necessary to ensure the reliability of the electronic components by controlling the temperature and dissipation [44]. Heat pipes, in their simplest forms, are being utilized for their ability to carry large heat quantities across small sectional areas. The easiness of heat pipes' manufacturing, operation, and integration are attractive aspects when coupled with the simplicity of design and control [45]. Even though Perkins introduced their first thermosiphon in 1836, the scientific revolution in heat pipes did not climax until the 1960s [45, 46]. Thermosiphons, gravity-assisted heat pipes, impose many limitations including the inflexibility of orientation, shape modifications, and operational environment. Several scholars, including Swanson, expected the adoption of the heat pipe technology by NASA in 2007 [46]. However, in the absence of the gravitational effects, a thermosiphon becomes useless. Various techniques exist in which the manufactured heat pipes are made gravity independent. Internal wicks presented in the pipe assist the condensate return to the evaporator section, and it was first implemented by Graugler in 1944 [47]. Nowadays, wicks include a wider variety of homogeneous and composite shapes and sizes.

Mesh screens are simple wicks that substitute a mechanical pump by providing the capillary pressure needed to transport and distribute the working fluid in the heat pipe [48, 49]. Usually, screens are characterized by their high thermal conductivity, porosity, and wick permeability. The high thermal conductivity favors a more uniform temperature distribution across the wick and the heat pipe. In addition, the porosity of the wick represents the fraction of the void volume to the total volume of the screen [49]. The wick permeability is an empirical constant that describes the wick's resistance to axial liquid flow. The high permeability maintains small liquid pressure drops and better thermal performance [45].

The small size of the screen's opening induces high capillarity action to enhance the thermal cycle within the heat pipe. As the evaporator section is heated, the working fluid evaporates while the menisci recede into the wick. As the vapor pressure increases at the evaporator's section, bubbles grow and escape through the wick's structure. The latent heat of vaporization is released to the ambient as the vapor condenses at the condenser section. The pressure difference generated by the capillarity force pumps the condensate to the evaporator section through the wick's pores [45, 48, 52].

The maximum heat transfer and the effective thermal resistance contributed by the screen wick are common criteria to determine its performance [53]. The properties of the wick and the working fluid control the generated capillary pressure, which limits the heat transfer rate and thermal resistance of the heat pipe [54]. A commonly encountered limitation in capillary driven heat pipes is the inability to circulate the working fluid. Known as the capillary limit, the sum of the liquid and vapor pressure drops dominate the capillary pressure generated by the wick. The capillarity forces are insufficient to pump the condensate to the evaporator and the wick is no longer saturated. The dry out that occurs at the evaporator section causes a sudden increase in its corresponding temperature [45, 55].

The choice of the working fluid affects the performance of the used wick as well. For instance, water is characterized by its large heat of vaporization and high surface tension, which are favorable for the capillarity action [44, 45].

4.1 Theory

Shifting from thermosiphons to capillary driven heat pipes is beneficial when working in micro gravitational environments, like terrestrial applications. In such applications, inserting wicks is essential to drive the internal thermal cycle and achieve the desired thermal performance. However, the performance of the heat pipe relies on the performance of the wick's structure and working fluid.

Beyond the geometrical specifications of available screen meshes, the performance of the wick structure relies on various thermo fluid parameters. The thermal conductivity of mesh screens is given by [51] as,

$$k_{eff} = \frac{k_l[(k_l+k_w)-(1-\varepsilon)(k_l-k_w)]}{(k_l+k_w)+(1-\varepsilon)(k_l-k_w)}. \quad (20)$$

The effective thermal conductivity of mesh screens depends on the thermal conductivity of the wick material ' k_w ', the thermal conductivity of the working fluid ' k_l ', and the porosity of the wick's structure ' ε '.

The porosity of the wrapped screen meshes is also given by [51, 57, 58] as follows

$$\varepsilon = 1 - \frac{\pi FNd}{4}, \quad (21)$$

where F represents the crimping factor that is approximated to be 1.05 [56]. The mesh number and wire diameter are referred to as ' N ' and ' d ', respectively. Moreover, the unit of the diameter is inches in eq. (21) and (22).

Knowing the corresponding porosity of the wicked design is necessary to calculate its permeability, as the following equation shows [51, 58],

$$K = \frac{d^2 \varepsilon^3}{122(1-\varepsilon)^2}. \quad (22)$$

A general comparison could be formulated based on the previously mentioned parameters regarding the wick's material and working fluid. However, the main parameter to be considered is the capillary contribution of the screen mesh. For the wicking to occur, the capillary pressure must exceed the static pressure existing in the heat pipe. The general expression of the static pressure is

$$P_{static} = \rho g h \sin \theta, \quad (23)$$

where " ρ " corresponds to the density of the working fluid, " g " corresponds to the gravitational acceleration, " h " corresponds to the height of the fluid in the pipe, and " θ " corresponds to the angle of orientation.

On the other hand, the capillary pressure is defined as follows,

$$P_{cap} = \frac{2\sigma \cos \theta}{r_{eff}}, \quad (24)$$

where " σ " represents the surface tension of the working fluid and " r_{eff} " represents the effective radius of the wick. In case the wick is a wired screen, the effective radius is defined as follows [51]:

$$r_{eff} = \frac{w + d_w}{2}, \quad (25)$$

where " w " and " d_w " represent the wire spacing and diameter, respectively.

To avoid the dry-out and capillary limit, enough liquid must be introduced into the wick to ensure its saturation. In the presence of mesh screen wicks, it is more convenient to describe the fluid charge relative to the saturation of the wick. The following equation defines the 100% charge of the mesh screen wick [52],

$$100\% = V_{wick} * \varepsilon, \quad (26)$$

where “ V_{wick} ” represents the volume of the cylindrical mesh insert.

Various ways exist to understand the thermal performance of a heat pipe. The temperature difference describes how even the temperature is distributed along the heat pipe. The temperature difference between the evaporator’s and condenser’s section is defined as,

$$\delta T = T_e - T_c. \quad (27)$$

The small temperature difference indicates a better thermal distribution. Moreover, the thermal resistance of a heat pipe is directly related to the temperature difference, in which it is defined as follows,

$$R_{th} = \frac{\delta T}{Q}, \quad (28)$$

where “ Q ” corresponds to the heat load introduced at the evaporator section. The lower thermal resistance indicates better heat transport along the heat pipe. The thermal conductivity of a heat pipe describes its ability in transporting the heat along; it is inversely proportional to the thermal resistance [53]:

$$k_{hp} = \frac{\ln\left(\frac{r_o}{r_i}\right)}{2\pi R_{th} L}, \quad (29)$$

where “ r_o ” and “ r_i ” are the outer and inner radii of the heat pipe, and L is the effective heat pipe length.

In addition to the conductive behavior of the pipe, the presence of the fluid in heat pipes provides convective heat transfer that is described by the heat transfer coefficient as,

$$h = \frac{Q}{\delta T}. \quad (30)$$

Finally, the convective ability of the heat pipe is compared against its conductive capacity through the Nusselt Number as shown,

$$Nu = \frac{h \cdot D}{k_{air}}, \quad (31)$$

where “ D ” refers to the active diameter of the pipe.

4.2 Experimental Setup

Four heat pipes are designed, and their thermal performance is being studied. The following table shows the specification and labeling of the pipes.

Table 14. Heat Pipes Studied.

Pipe 1	Pipe 2	Pipe 3	Pipe 4
Empty	No wick	1-Mesh Layer	2-Mesh Layers

The common characteristics among all the manufactured pipes are shown below,

Table 15. Pipes Characteristics [59].

Material	Outer Diameter	Inner Diameter	Length	Thermal Conductivity
101Copper	0.0191 m	0.0174 m	0.2 m	391 W/m.K

The working fluid charged in the pipes is water. Water is characterized by the following thermo fluid properties,

Table 16. Water Thermo fluid Characteristics.

Density	Surface Tension	Thermal Conductivity
997 Kg/m ³	0.072 N/m	0.608 W/m.K

Finally, the characteristics of the mesh screen are tabulated below.



Figure 108. The experimental setup

Table 17. Mesh Screen Characteristics.

Material	Type	Mesh size	Opening Size	Wire Diameter
Copper	Wire Cloth	100x100	0.000152 m	0.0001143 m

Based on the characteristics presented in Table 17, the mesh’s porosity is calculated by eq. (21) to be 63%. Thus, the permeability of the mesh screen used is calculated by eq. (22) to be $3 \times 10^{-7} \text{ m}^2$. The effective thermal conductivity of the mesh screen used is 1.32 W/m.K , through eq. (20).

All pipe rigs possess similar geometrical properties, as presented in table 15. The internal volume of the heat pipes is $4.76 \times 10^{-5} \text{ m}^3$; therefore, each can hold up to 47.6 ml of water. Previous experiments and literature show that the optimum volume of working fluid for the best thermal performance is around 50% [60]. Thus, the heat pipes are charged with 50% working fluid, thus each pipe is filled with 23.8 ml of water. According to the porosity model described [56], 23.8 ml is enough to saturate the mesh screens inserted.

The saturation of the wick is necessary to avoid the dry out limit. Since the fluid occupies 50% of the total internal volume, the static pressure calculated using eq. (23) is 979 Pa. This pressure is competing against the capillary pressure that is calculated to be 1081 Pa through eq. (24) and (25). Since the capillary pressure exceeds the static pressure, wicking occurs.

An aluminum block holds the high-density heat cartridge and the heat pipe under study. The heating cartridge is connected to an adjustable voltage supply that reads the power introduced. To ensure that all heat flux is introduced to the evaporator section, the aluminum block is insulated. Five J-type thermocouples are evenly spaced and attached to the outer wall of the heat pipe using thermosensitive adhesive strips (Kapton™). Temperature readings are acquired with MCC DAQ. The following image shows the experimental setup, where two heat pipes are placed into the aluminum block and thermocouples are attached using Kapton tape.

First, the thermal performance of the heat pipes is studied at 5 different power ratings to understand the general behavior of mesh screen wicked heat pipes. Then, the performance of the heat pipes is studied under the effect of inclination to understand the wicking ability of screen meshes.

4.3 Results and analysis:

4.3.1 The Effect of Screen Layers:

The following table shows the temperature differences between the evaporator and condenser section of the pipes.

Table 18. The temperature difference across the pipes.

Power (Watts)	δT ($^{\circ}C$)			
	Pipe 1	Pipe 2	Pipe 3	Pipe 4
15	2.4	1.5	0.13	3.9
23.8	4.4	3.1	1.2	4
34.5	6.3	5.6	4.5	4.8
47.3	8.9	7.5	5.8	8
62	11.2	8.6	6.5	0.1

The following graph represents the trend of the temperature distribution as a function of heat

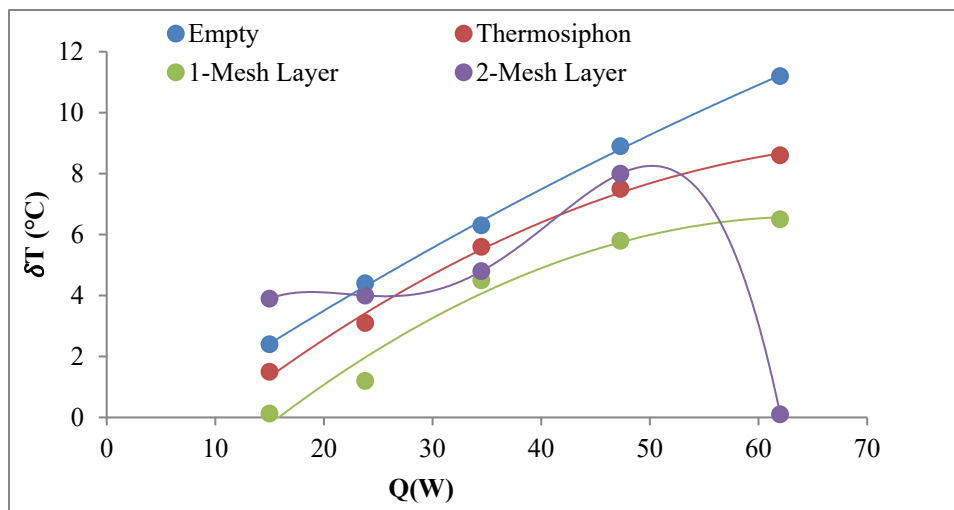


Figure 109. The variation of the temperature difference across the pipes as a function of heat load.

As shown by figure 108, the temperature difference generally increases across all the pipes as the heat input increases. However, the 1-Mesh layer heat pipe shows the lowest temperature difference. Moreover, the thermal resistivities of the pipes are plotted as follows.

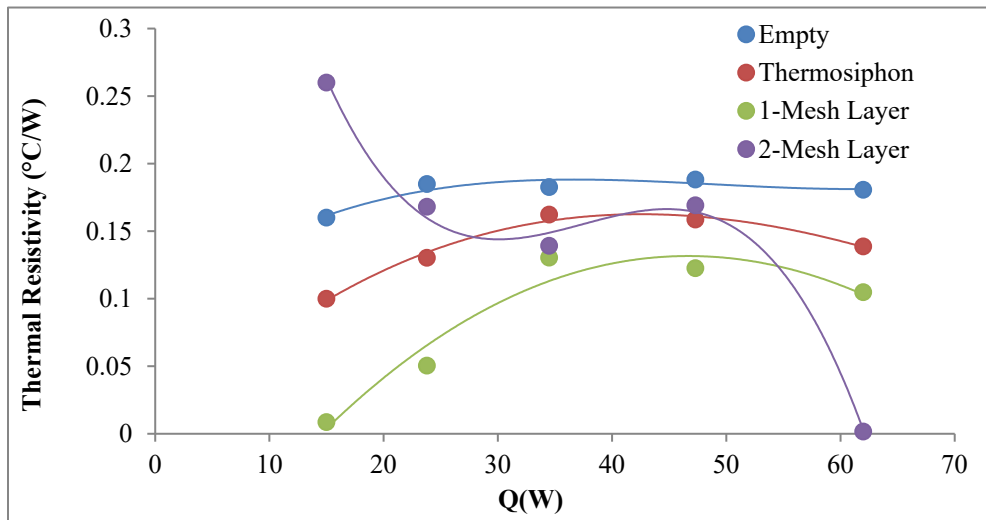


Figure 110. Thermal resistivity of the pipes as a function of the heat input.

As shown in fig.109, the 1-mesh layer heat pipe shows the least thermal resistivity across various powers. Generally, the thermal resistivity of all pipes follows the same trend except for the 2-mesh layer heat pipe which shows high thermal resistivities due to the presence of extra copper layers within it.

To understand the convective characteristics of the pipes at hand, the corresponding heat transfer coefficients are tabulated below.

Table 19. The heat transfer coefficient across heat pipes.

Power (Watts)	$h(W/°C)$			
	Pipe 1	Pipe 2	Pipe 3	Pipe 4
15	6.25	10	115.38	3.86
23.8	5.41	7.68	19.83	5.95
34.5	5.48	6.16	7.67	7.19
47.3	5.31	6.31	8.16	5.91

62	5.54	7.21	9.54	620
----	------	------	------	-----

As the power increases, the heat transfer coefficient of the 1-Mesh layer heat pipe remains the highest up until 47.3W. At 62 W, the heat transfer coefficient of the 2-Mesh layer heat pipe exceeds all pipes by 10 orders of magnitude.

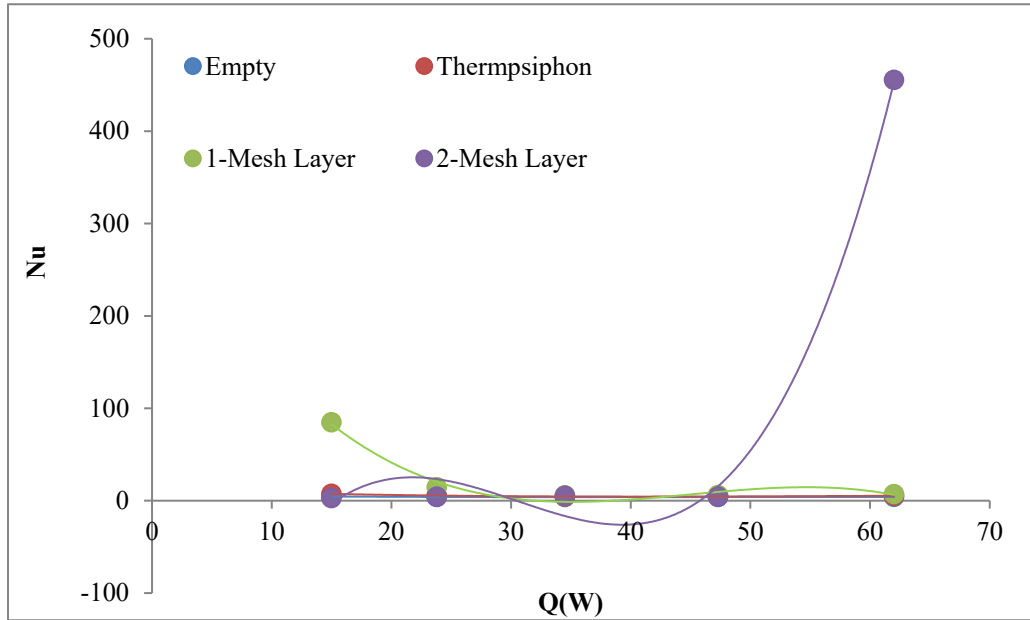


Figure 111. The Nusselt number of pipes at different heat loads.

As shown in figure110, the Nusselt number corresponding to the 1-Mesh layer heat pipe remains the highest as the power increases to 47.3 W. However, the Nusselt number of the 2-Mesh layer heat pipe exceeds all others by 10 orders of magnitude at 62 W.

4.3.2 The Effect of Orientation

After exploring the thermal performance of the heat pipes under vertical conditions, the study is extended to various orientations. The corresponding temperature differences are plotted as follows.

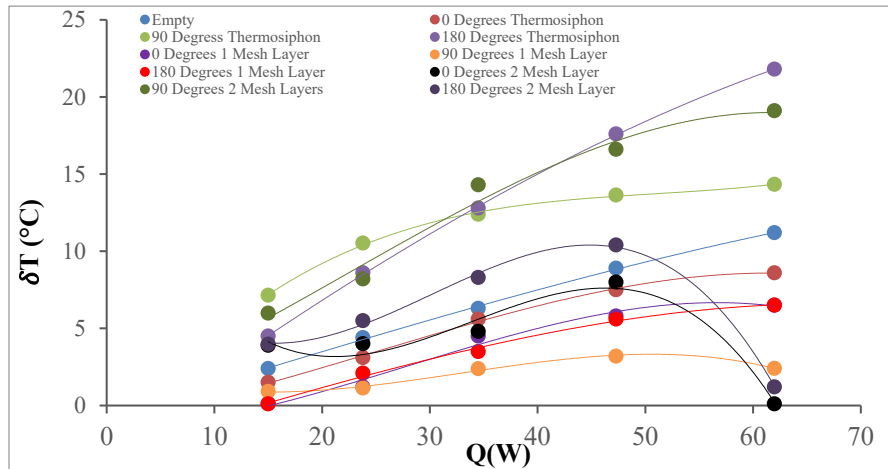


Figure 112. The temperature difference across the pipes at different orientations.

Based on figure 111, the thermosiphon shows the most uniform distribution when setting vertically and aligned with gravity (0 degrees). However, the thermosiphon does not perform effectively at different orientations nor against gravity (90 and 180 degrees, respectively) in which the empty pipe shows a better thermal performance. The 1-Mesh Layer and the 2-Mesh Layer show similar performance when oriented vertically in both directions, indicating their independency of gravity. Moreover, the 1-Mesh Layer shows the most uniform temperature distribution when oriented horizontally.

The Nusselt Number of the previous studies are plotted as

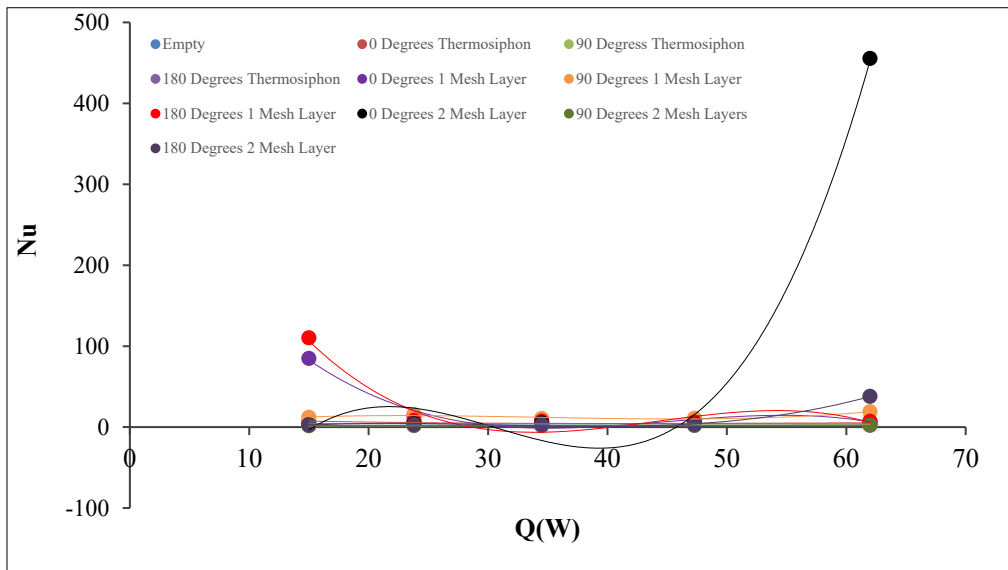


Figure 113. The Nusselt Number of the pipes at different orientations.

According to figure 112, the 1-Mesh Layer and 2- Mesh Layer heat pipes always perform better than the empty pipe. The 2-Mesh Layer heat pipe shows its cooling superiority at high heat loads, whereas the 1-Mesh Layer shows its cooling superiority at lower heat loads. However, the thermosiphon performs better than the empty pipe when oriented vertically aligned with gravity. All pipes show a convective trait of heat transfer where the Nusselt Number exceeds unity.

It was shown that utilizing capillarity using mesh screens enhances the performance of a heat pipe. A layer of mesh screen was enough to exceed the performance of a thermosiphon. As the number of layers increases, the performance of the meshed heat piped showed a delay where the effectiveness did not show until the thermal resistivity of the wall and screen layers were overcome. Thus, the number of layers affects the operation range of the heat pipe. If the heat pipe was to be operated at low heat inputs, fewer screen layers are needed and vice versa.

Moreover, the thermosiphon performs best when aligned with gravity, which fits its definition. If oriented otherwise, the thermosiphon shows its ineffectiveness in transporting heat. On the other hand, the 1-Mesh and 2-Mesh layer heat pipe showed their independency of gravity and showed the best performance when positioned horizontally.

5 SINTERED HEAT PIPES

Since their development in the late twentieth century, heat pipes have been employed for cooling applications in electric motors, blast furnaces, space systems and the electronic industry [61-81]. Heat pipes are capable of transferring heat over reasonable distances with a small temperature drop [64-68]. Besides, heat pipes require no power source for their operation.

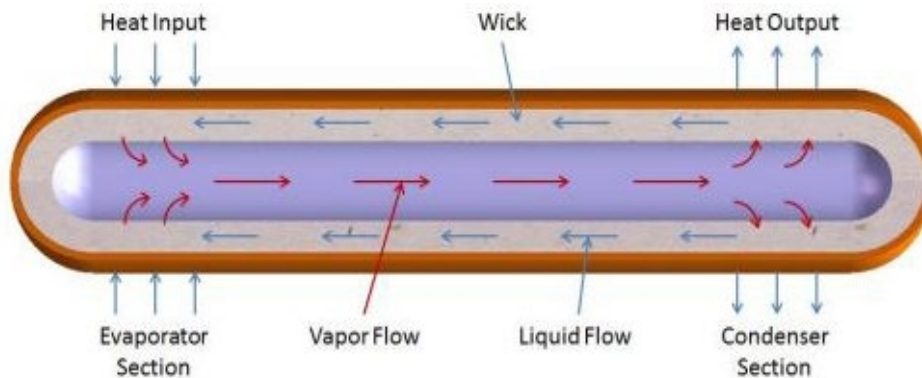


Figure 114. Schematic of a general heat pipe showing its sections and component [61]

The heat pipe has three sections, viz.: evaporator, condenser, and adiabatic section (the region between the evaporator and the condenser section). Heat pipes are normally filled with liquid containing its vapor. When heat is applied to the evaporator, liquid changes to vapor and is forced to move towards the relatively cooler condenser section. Here, the vaporized fluid relinquishes its latent heat of vaporization and changes back to liquid. Wicks are the inner layer of the tube. Condensate is re-directed towards the evaporator section by capillary action improved by a wick structure.

Wicks and working fluids are the two most important components of a heat pipe [62] and [63]. Different types of working fluids such as water, acetone, methanol, ammonia, or sodium can be used in heat pipes depending on the desired temperature range of operation [64]. Generally, the wicks for phase-change cooling devices include metal wire meshes, micro-grooves, sintered metal powder, metal foams, sintered metal fibers and composite wicks [65]. Wicks control capillarity pressure, permeability, and the working fluid's flow resistance.

Porous media allow fluid flow through its pores and have vast applications in thermal sciences, soil sciences, aerospace, and other engineering fields. A fluid-filled porous structure provides solid-liquid-vapor contact lines in the interstitial volumes between the solid particles where large capillary forces developed from interfacial tensions [66]. These forces pull the liquid through porous media by capillarity action. Porous materials, made from sintered metallic powder compacts, are used as wicks in heat pipes for continuous circulation of the working fluid.

To provide effective water supply, the porous structure must contain many pores so that enough water is supplied continuously from the condenser to the evaporator section. Also, the pore size must be small enough so that the capillary pressure is high enough to draw the water through the porous wick, even against gravity [67-69]. Lin et al, examined the effects of powder shape on heat dissipation of a heat pipe using gas atomized spherical powder, water atomized and electrolytic copper powder to create wick structure [67]. From the results, the gas atomized

spherical powder gave the utmost capillarity speed and permeability, hence the highest heat dissipation even though its porosity was the lowest. It was concluded that capillarity speed affects heat dissipation more than permeability. Jo, et al, demonstrated enhanced fluid transport through a multilayer, porous wick comprising a micro-porous structure [4]. Wicking is the process by which heat is dissipated because of increased surface area through morphology modification [70].

Homogeneous wicks are constructed with one type of material or machining technique [71]. Sintered wicks are made by stuffing particles between the inner heat pipe walls [64]. Even though they are difficult to make, their capillary pressure developed (capillary limit) is easily predicted. Sintered wicks are designed to have a small capillary radius if a large capillary difference is required.

The production of metallic parts by compacting metal powders in suitable dies and sintering them at elevated temperatures to obtain the desired density and strength is known as powder metallurgy [72]. The compaction process and escape of gases during sintering minimize the porosity in powder metallurgy. Besides having the necessary pore structure and size characteristics for fluid and heat transport, the wicks produced had to be mechanically rigid to be integrated into heat pipe [71-75].

This present study investigates the thermal properties of an empty pipe, thermosiphon, a sintered and an unsintered wick used in heat pipe at six different heat loads. The effect of gravity on these pipes is also investigated. Copper powder, 140 μm average diameter, from Atlantic Equipment Engineers, was used to construct the wick structure. Besides, copper 101 tubes, 200 mm long with 19.1 mm and 17.44 mm internal and external diameter respectively were used to make heat pipes.

5.1 Experimental Setup

Li et al compared the performance of three different ranges of copper powder: 80–110, 110–140 and 140–170 μm . Results indicated that wicks produced from sintering 140–170 μm cell size range copper powders had better binding strength, improved uniformity, greater capillary pumping force and a reduced amount of backflow resistance [67], [76-91].

Copper powder of 140 μm average diameter was selected to make wicks. 87% of the powder was mixed with 13% of the water-based binder to form a paste-like feedstock. Binder was made from polyvinyl alcohol supplied by the Carolina's. Binder and copper powder mixing ratios were imperative in obtaining a smooth and uniform feedstock. Inadequate binder in the mixture would cause high viscosity and formation of voids in the mixture while excess binder in the mixture would cause contraction of the sample during de-binding [72]. The wick was made in a stainless-steel mold by cold pressing. Two wick structures of 8.382 mm thickness were manufactured. Reports of the sintering process are well documented in the literature [73], [75] and [91-95].

Description of labels of the pipes used for the experiment are presented below.

1. Pipe 1- Empty Pipe
2. Pipe 2- Thermosiphon (no wick structure)
3. Pipe 3-Un-sintered copper powder wick heat pipe
4. Pipe 4- Sintered copper powder wick heat pipe



Figure 115. Pipe 3, un-sintered copper powder wick heat pipe

Wick structure should be compatible with working fluid. The high surface tension of distilled water beside its compatibility with a wick made it suitable for use as a working fluid. Distilled water also can increase capillary pressure [91]. Pipes 2, 3 and 4 were filled with 50% of working fluid.

The experimental setup comprises an aluminum block with three drilled holes, two for accommodating heat pipes, the remaining middle for holding a high-density heater cartridge. The cartridge is heated by connecting to a power source that allows variation in current and voltage. Desired power can be obtained from the equation below.

$$Q = IV \quad (32)$$

where Q, I and V are heat load, current and voltage respectively.

Ultra-high temperature ceramic tape obtained from McMaster Carr was used for insulation to create the adiabatic section. The block was held in place by an insulated vice and connected to a DAQ system (data acquisition system) via K-type thermocouples. Using thermo-sensitive adhesive strips two K-type thermocouples were fixed to the outer wall of the pipes, one at the evaporator section and the other at the condenser section. Data collected from the DAQ system is analyzed with computers. The data acquisition device system collects data every 0.01 laps and displays the data on the computer. Experiments were performed in normal gravity conditions, (+g) and in against gravity condition, (-g). Fig 3 and fig 4 shows the experimental set-up for normal gravity and against gravity conditions with pipe 3 and pipe 4. The error related to the K-type thermocouple was 0.1⁰C. Uncertainty in power measurement was 0.2%.

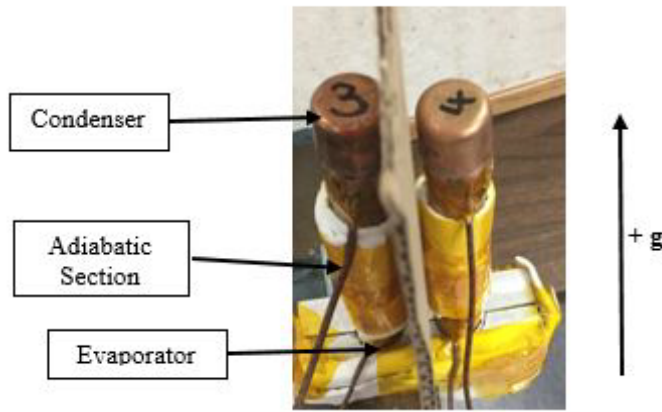


Figure 116. Experimental set-up for normal gravity condition (+g).

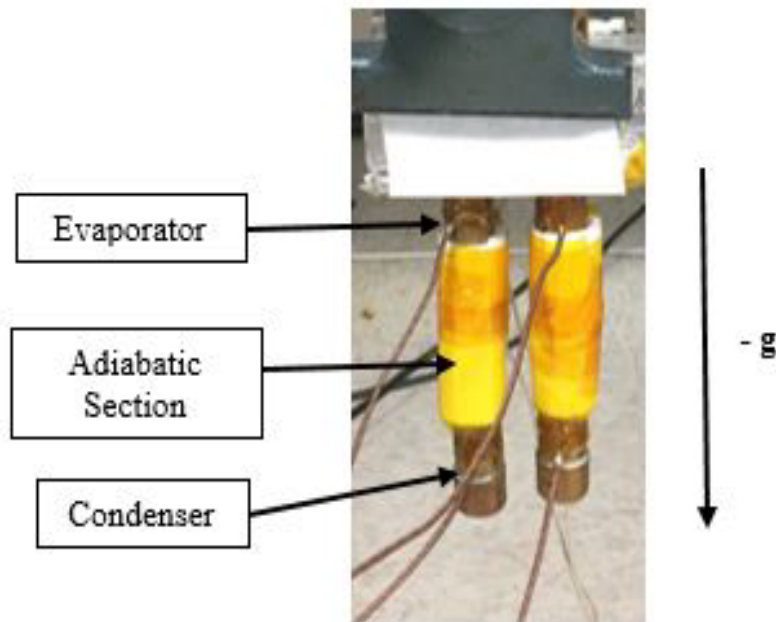
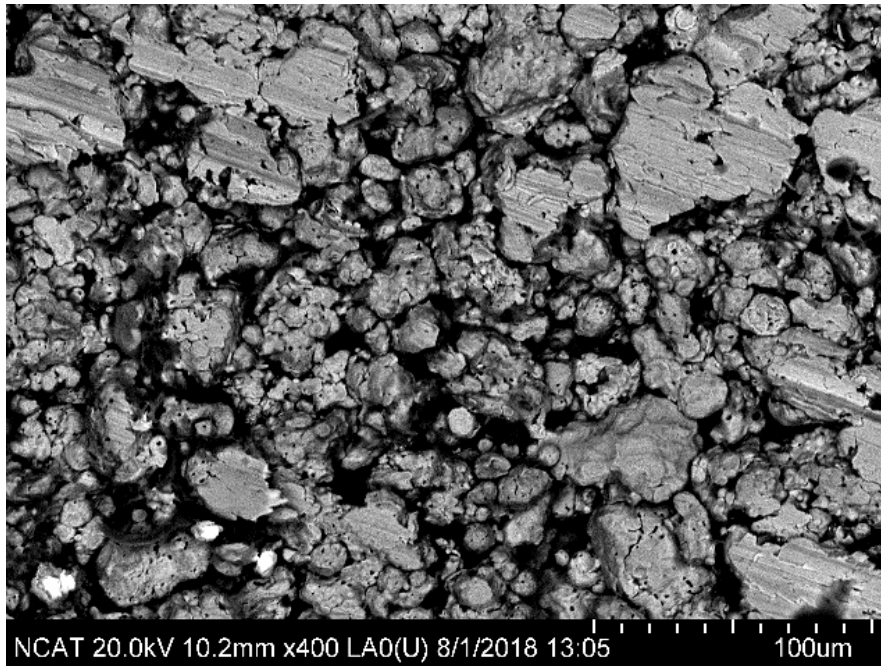


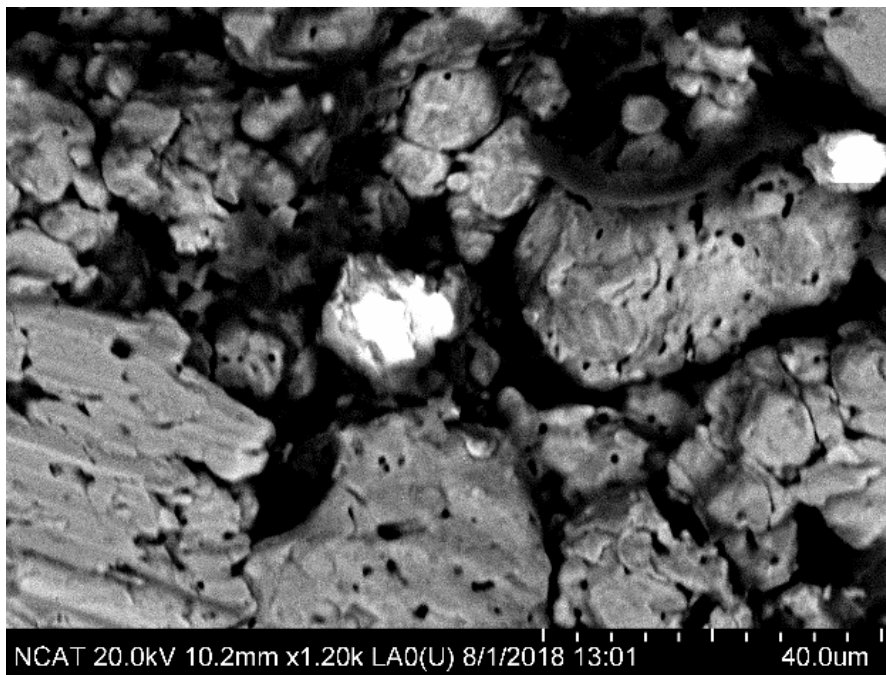
Figure 117. Experimental set-up for against gravity (-g) condition.

5.2 Results and Discussion

The performance of porous wicks is determined by pore sizes and porosity: with finer pore, the wick can provide higher capillary force; with higher porosity, the permeability of wick is larger, which means less resistance for fluid flowing in the wick [94] and [96-100]. Figure 117(a) and 117(b) shows an SEM image of un-sintered copper at 400 and 1200 magnification respectively. Also, fig 6 shows the SEM image of the sintered copper wick at 1200 magnification. It can be seen that powder particles bond together after the sintering process. Images also show reduced pore spaces after sintering.



(a)



(b)

Figure 118. (a). SEM image of un-sintered copper wick; magnification 400. (b) SEM image of the un-sintered copper wick, magnification 1200.

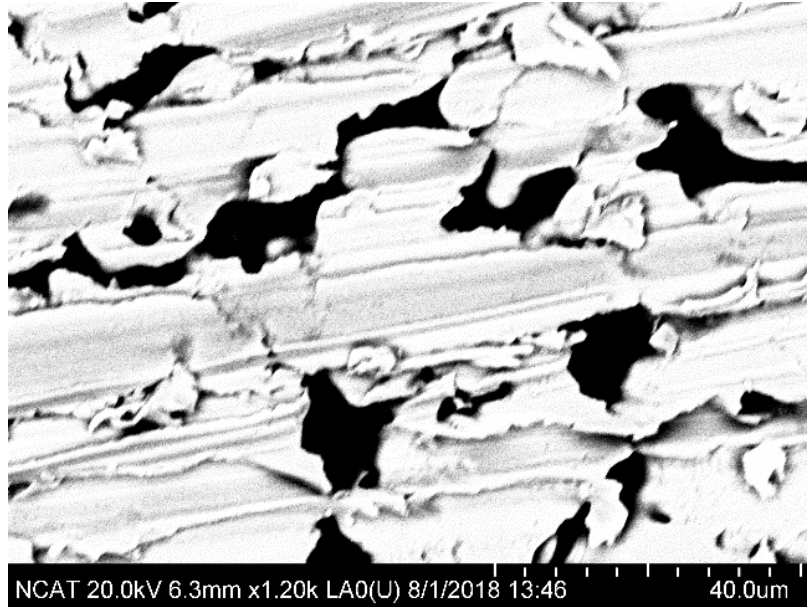


Figure 119. SEM image of the sintered copper wick, magnification 1200

Porosity is the ratio of the void's volume to the entire wick's volume. The porosity of fabricated sintered wick can be calculated by the mass-volume method [38].

$$\varepsilon = \left(1 - \frac{m}{\rho_w V}\right) * 100\% \quad (33)$$

where ε , m and V , are the porosity, mass, and volume of the wick structure, and ρ_w is the density of the copper powder sintered. The porosity of the sample is determined to be 40%. The mass was measured with a digital balance and the uncertainty in the measurement was 1%.

Permeability is a measure of the wicks' resistance to axial liquid flow [64]. For sintered wicks, the permeability is determined by the Carman-Kozeny equation [101]

$$K = \frac{\varepsilon^2 * d^2}{150 * (1 - \varepsilon)^2}, \quad (34)$$

Here, d is the effective diameter of the copper powder.

The capillary pumping force of the wick is calculated as [42]

$$\Delta P_c = \frac{2\sigma}{r} * \cos\theta, \quad (35)$$

where ΔP_c is the capillary pumping force of the porous wick structure, σ is the surface tension of the liquid, r is the radius of curvature, and θ is the contact angle between the liquid and the surface. Capillary forces increase as pore sizes decrease [70]

5.3 Normal Gravity Condition (+g)

First and foremost, the general performance of all the pipes used is studied. Experiments are performed with 5W, 10W, 15W, 25W, 35W and 50W heat input. Each experiment is performed twice for repeatability. The thermocouples acquire temperature readings every 100 seconds until a steady state is achieved.

Figure 119 denotes the temperature distribution across the un-sintered wick heat pipe at 5W power input. The applied heat to the evaporator section causes the vaporization of the working fluid. Phase-change occurs in the condenser section. The capillary pressure developed in the wick continuously circulates the working fluid in the heat pipe.

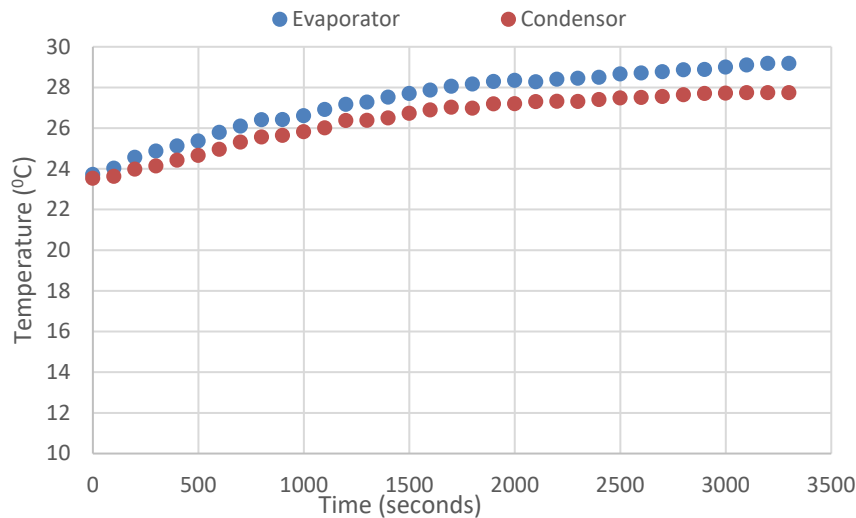


Figure 120. The behavior of un-sintered wick heat pipe at 5W heat load

Figure 119 shows that temperatures at the evaporator section increase at a higher rate as compared to temperatures at the condenser section. Both evaporator and condenser temperatures eventually reach a constant value which signifies a steady state.

The thermal characteristics of heat pipes are compared using the difference in temperature between the condenser and evaporator sections, ΔT . Heat pipes with smaller ΔT values have higher thermal performance [64] and [89], [103-105].

$$\Delta T = T_e - T_c \quad (36)$$

Here, T_e and T_c are the evaporator and condenser steady-state temperatures respectively.

Figure 120 shows a plot of ΔT against heat load. The empty pipe has the largest temperature difference. The empty pipe represents heat transfer by pure conduction. A phase change is introduced when working fluid is used in a pipe. Heat pipes make use of conduction and convection heat transfer hence making their thermal performance better than empty pipes. The

presence of a wick structure further reduces the temperature difference, ΔT , as depicted in the un-sintered heat pipe. The sintered heat pipe had the smallest temperature difference.

Sintering is a process in which powders are compacted and heated at appropriate temperatures and inappropriate atmospheres, with the results that powders are conglutinated [85]. Sintering reduces the porosity of the compacted powder. Small pores sizes increase the circulation of the working fluid by capillary action. Sintered wick heat pipe had the least value of ΔT .

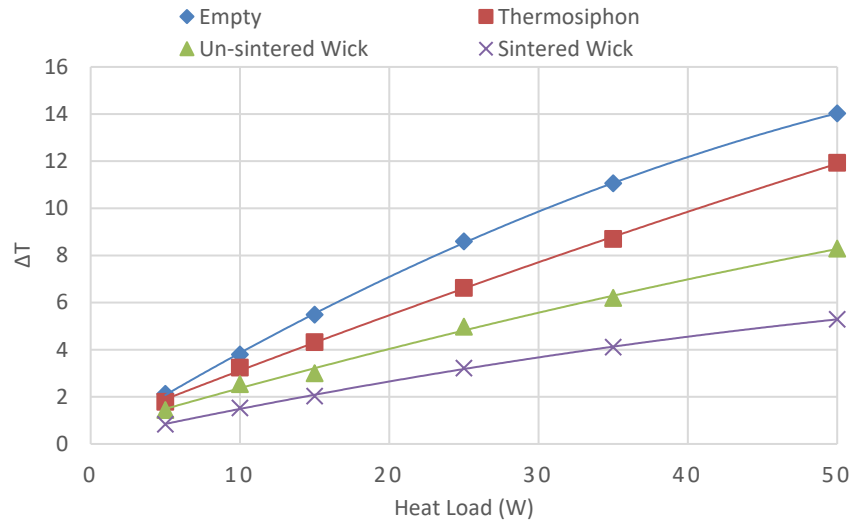


Figure 121. The steady-state temperature difference between evaporator and condenser (ΔT) vs. heat load.

The total thermal resistance of the pipes investigated at different heat loads is shown in Figure 121. To understand the thermal performance of a heat pipe, the total thermal resistance is determined.

$$R_{th} = \frac{T_e - T_c}{Q}, \quad (37)$$

Here, Q is the applied load at the evaporator section.

The thermal resistance offers an indication of heat flow resistance in a system. The total thermal resistance is reciprocal to the heat load. This implies that as the heat load increases, the total thermal resistance decreases. The maximum and minimum value of the total thermal resistance is $0.426 \text{ } ^\circ\text{C/W}$ and $0.1058 \text{ } ^\circ\text{C/W}$ and was recorded for an empty pipe and sintered wick heat pipe respectively. Therefore, these results demonstrate that the smaller the thermal resistance, the better the thermal performance.

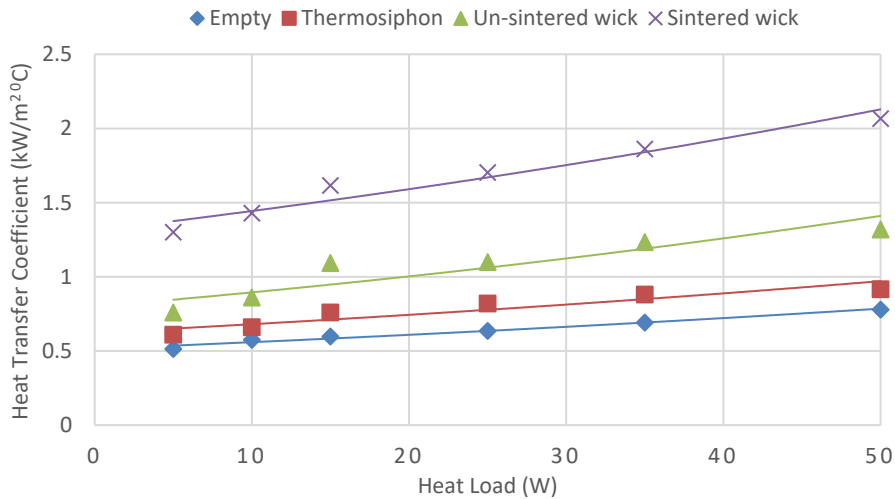


Figure 122. Total thermal resistance vs. heat load

The effectiveness of the thermal system is determined from the heat transfer coefficient as:

$$h = \frac{Q}{A_e(T_e - T_c)}, \quad (38)$$

where, A_e , is the active heated area of the evaporator.

Figure 122 shows a plot of the heat transfer coefficient at different heat loads. The figure points out a rise in the heat transfer coefficient as the heat load increases. The figure also demonstrates that higher heat transfer coefficients can be achieved at low thermal resistance and relatively high heat loads. The maximum and minimum values of the heat transfer coefficient in the

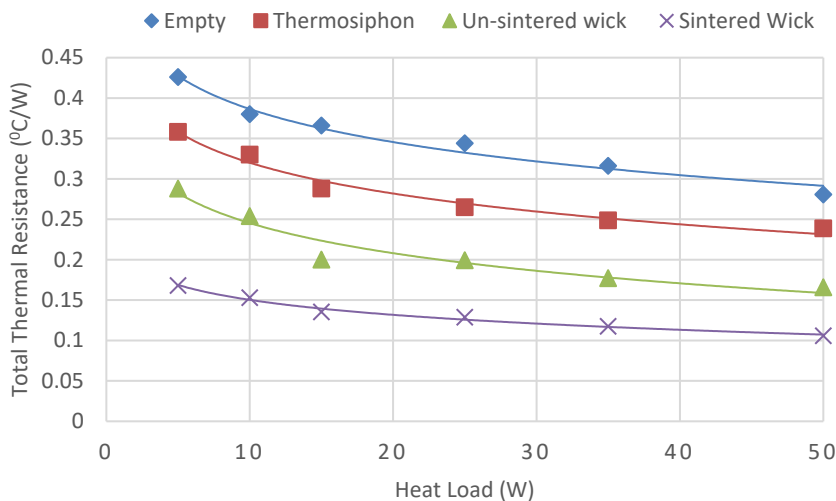


Figure 123. Heat transfer coefficient vs. heat load

sintered wick heat pipe are 2.067 kW/m² °C and 1.301 kW/m² °C for 50 and 5-Watt heat loads respectively.

Figure 123 shows the steady-state evaporator temperatures for pipes 3 and 4. From the plot, temperatures at the evaporator section increase with increasing heat load. This linear relationship demonstrates continuous conductance mode in these pipes. The plot also shows that the steady-state evaporator temperature of the un-sintered and sintered wick is identical for different heat loads.

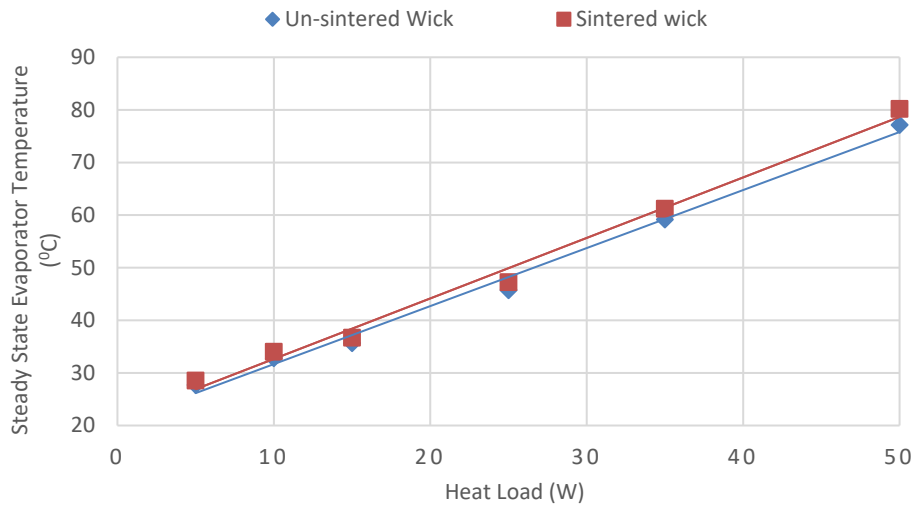


Figure 124. Steady-state evaporator temperature vs. heat input for un-sintered and sintered wick heat pipe.

The difference in the steady-state temperature for un-sintered and sintered wick at the condenser section is significant and can be seen in figure 124. The condenser temperature in pipe 4 is

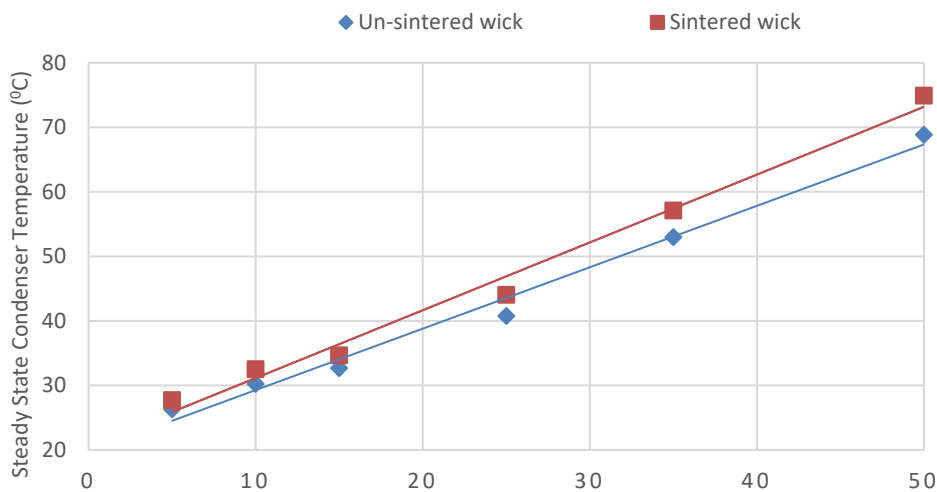


Figure 125. Steady-state condenser temperature vs. heat input for un-sintered and sintered wick heat pipes.

higher than in pipe 3. Due to this, Pipe 3, sintered wick heat pipe has a lower total thermal resistance, hence better thermal performance.

5.4 Against Gravity Condition

The general thermal behavior of the un-sintered and sintered wick heat pipes are studied at 5W, 10W, 15W, 25W, 35W and 50 W. Figure 125 shows the general behavior of evaporator and condenser temperatures of these pipes. The shape of the graph changes as power readings is increased. From the plot, the evaporator temperatures for un-sintered and sintered wick heat pipes are identical. It can be concluded that the evaporator temperatures for the un-sintered and sintered wick heat pipes are similar and not influenced by gravity. The table below compares the steady-state evaporator temperature for un-sintered and sintered pipes against gravity conditions. The data shows that the steady-state evaporator temperature for sintered and un-sintered heat pipes in against gravity conditions are identical.

Table 20. Showing steady-state evaporator temperature of sintered and un-sintered heat pipes for against gravity condition

Heat Load [W]	Sintered (-g) [°C]	Un-sintered (-g) [°C]
5	26.26	26.28
10	35.37	35.59
15	41.20	41.21
25	51.98	51.98
35	71.70	71.74
50	87.02	87.02
standard deviation	23.10777	23.07703

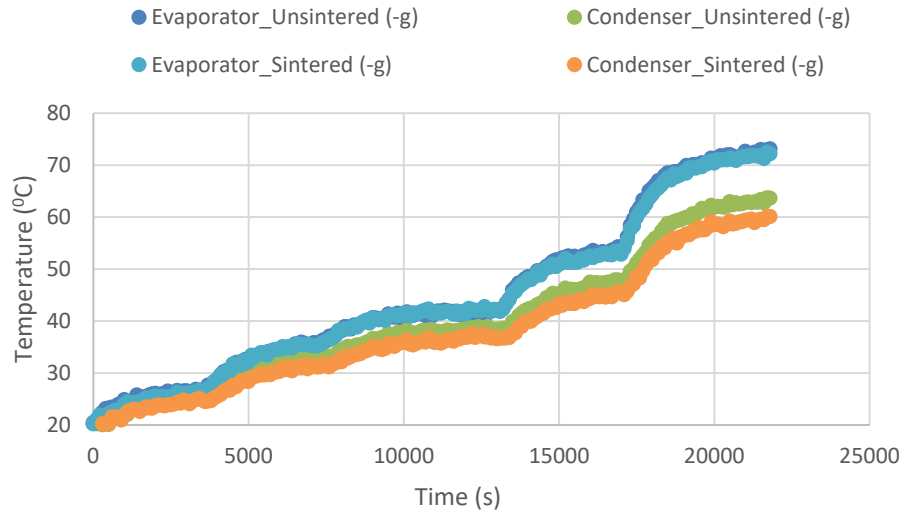


Figure 126. Evaporator and condenser temperatures of un-sintered and sintered wick heat pipes in against gravity condition.

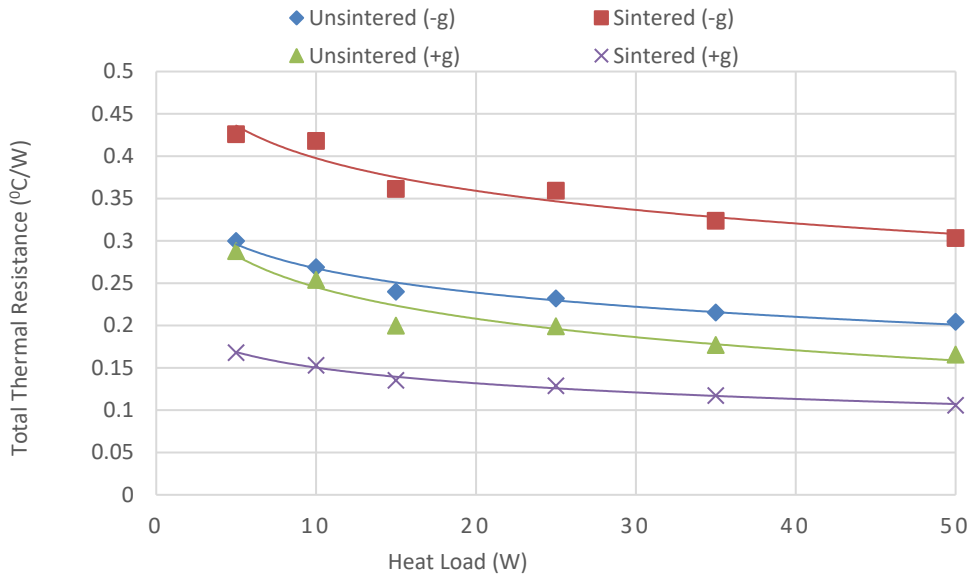


Figure 127. The total thermal resistance of un-sintered and sintered wick heat pipes in normal gravity and against gravity conditions.

Fig 126 compares the total thermal resistance of the un-sintered and sintered wick heat pipe in normal and against gravity conditions. Un-sintered wick heat pipe had a lower thermal resistance than the sintered wick heat pipe in against gravity condition. This implies that the un-sintered wick heat pipe will have much higher thermal performance than the sintered wick heat pipe.

An empty pipe, a thermosiphon, a sintered and an un-sintered heat pipe was fabricated from a 200mm long copper tube with 19.1mm diameter and 1.66mm thickness. 8.382 mm thick wicks were made from 140 μm average diameter copper powder.

In normal gravity conditions, the thermal performance of all heat pipes used was greater than the empty pipe. Heat pipes with wicks performed better when compared to the thermosiphon. Also, the thermal performance of the heat pipe with a wick structure increased when the wick was sintered. However, in against gravity conditions, the un-sintered wick had a higher thermal performance when compared to the sintered wick. The value of the evaporator temperature for the un-sintered and sintered heat pipe was identical either in normal gravity condition or in against gravity condition.

6 HEAT PIPE APPLICATIONS ON EMA TECHNOLOGY

However, the transition towards more intensive electronic technologies in aeronautical and ground vehicles presented intense heat flux problems affecting both the lifetime and reliability of the system [110-113]. In pursue of cooling the electromechanical actuators in hybrid airplanes and technologies, Corona et al explored pure forced convection using a fan in the wing bay [114]. Typically, electric motors have been cooled by mounting fans on outer housing [115]. However, Davin et al experimentally explored the cooling effect of lubricating oil on the motor [116]. Moreover, Lee et al used channels for forced convection on the housing and hollow shaft rotor cooling [117]. To avoid the complexity of manufacturing, operation, and integration Faghri emphasized the simplicity of designing and controlling heat pipes [118]. Heat pipes attracted the attention of thermal managers investigating cooling methods for hybrid technologies [119]. Heat pipes are passive cooling devices with a self-driven two-phase flow that collects waste heat energy and reject the latent heat energy of the working fluid into the ambient [120]. Heat pipes in their various forms are characterized by their low thermal resistivity and their ability to transport excessive amounts of heat through a small surface area [121]. Depending on the application, heat pipes vary in size, material, working fluid, and type. For instance, capillarity driven heat pipes showed better performance than gravity-driven heat pipes in the aeronautical application due to their independence of gravity [123]. The thermal performance could be enhanced in different manners as well. On the interior level, Putra et al. showed that the usage of biomaterial wicks and nanofluid particles enhances the performance of heat pipes [122-125]. On the other hand, improvements could also be done on the exterior level by adding fins and forced convection [116].

Typical thermal management methods rely on a well-defined conduction path between motor windings and the housing due to the location of convenient placement of the windings in the stator core right at the periphery of the motors. The current test piece, PA 03-10-600 motor, however, presents the challenge of high thermal resistance between the heat laden windings which happen to be at the center of the piece and separated from the stator and housing by air space.

Kwarteng et al. [125] established the temperature distribution inside the motor via experimental measurements noted that the hotspots in the motor occur at the end turns of the windings. Thus, the development of an effective means of managing the temperature at the end turns of the copper windings is the drive of the current study. Heat pipes are proposed as a possible means of managing the heating problem. Abotsi et al. [126] demonstrated the gravity independence of sintered heat pipes and their effectiveness in all orientations.

6.1 Materials and Methods

Materials used the study include the following: PA 03-10-600 linear actuator, power source, variac transformer, rectifier unit, voltmeter, ammeter, k-type thermocouples, sintered copper heat pipes (0.6 cm diameter, 7 cm long), 36-gage copper wire and an MCC DAQ data acquisition system. The PA-003-10-600 is a brushed, two-pole 10-slot configuration motor having a permanent magnet stator and copper windings on the rotor as shown in Figure 127. It is rated for 2670 N at 12 VDC with additional manufacturer-supplied data as provided in table 21.

Table 21. Manufacturer supplied data for PA 03-10-600 EMA

Maximum Voltage	12 VDC
Current at Maximum Dynamic Load	7.6 A
Maximum force	2670 N (600 lbs)
Duty Cycle	20%
Stroke Length	10 ”
Protection rating	IP54
Insulation class/ Maximum winding Temperature	F/ 150°C (Based on an ambient of 65°C)

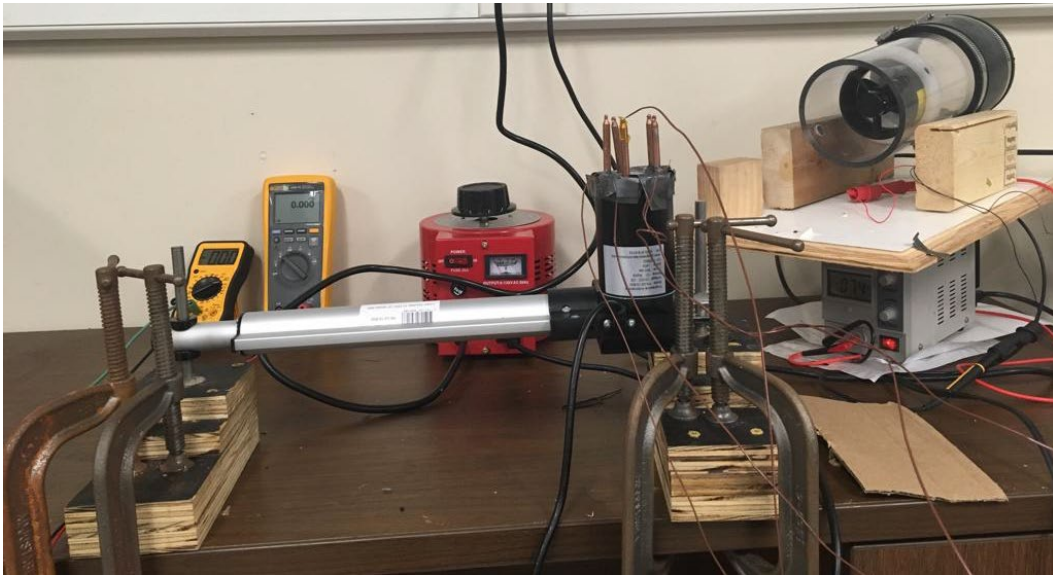
In dynamic mode, the linear actuator has a maximum speed of 0.39 inch/s (9.9 mm/s). When the motor is powered, and the actuator is held in a static position as in figure 127b, the linear motion of the actuator shaft is stopped, the motor shaft, as well as the associated drive gears, come to near zero rotational speeds. Hence the stopping mechanism which simulates a static load provides a braking force for the electrical motor. The temperature of selected positions on the copper windings and air trapped inside the housing is monitored and logged during the operation of the motor using the thermocouples and the MCC data acquisition system. The circuit diagram in Figure 128 shows how the set up was connected electrically.



127(a). Original motor in holding the position



127(b). Inside view of motor shows copper windings embedded in rotor core and separated by a clearance. The stator is a permanent magnet.



127c. PA 03 EMA with 5 heat pipes extending through the cover

Figure 128. Original motor in holding the position, Inside view of motor shows copper windings embedded in rotor core and separated by a clearance and PA 03 EMA with 5 heat pipes extending through the cover

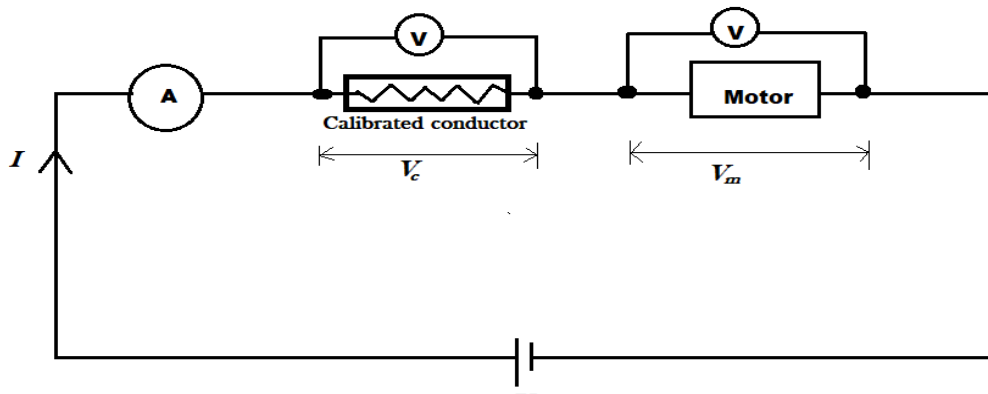


Figure 129. Circuit diagram for the experiment



Figure 130. Inside view of motor showing heat pipe evaporators

For seven minutes, the motor was run in extension mode at a nominal supply of 6.05 Amps corresponding to $Q = 20.5 \pm 1.2$ Watts, first without heat pipes and later with the varying number of heat pipes. The procedure was repeated with a supply of 7.10 Amps, corresponding to $Q = 28.2 \pm 2$ Watts. This allows the effects of heat pipes on the transient behavior of the EMA to be monitored as presented in the graphs in the next section.

To optimize the heat transfer enhancement of the heat pipes, a network of 36 gages enameled wire was interlaced in between the heat pipes at the evaporator section of the heat pipes. The 36 gages enameled copper wire has a diameter of 0.124 mm the total mass of the wire used in the mesh is approximately 3.48grams which is less than the mass of one heat pipe (5.27 g). Thus, it would be plausible to be able to cut down on the number of heat pipes required if the tradeoff is a few grams of wire mesh from the weigh savings point of view.

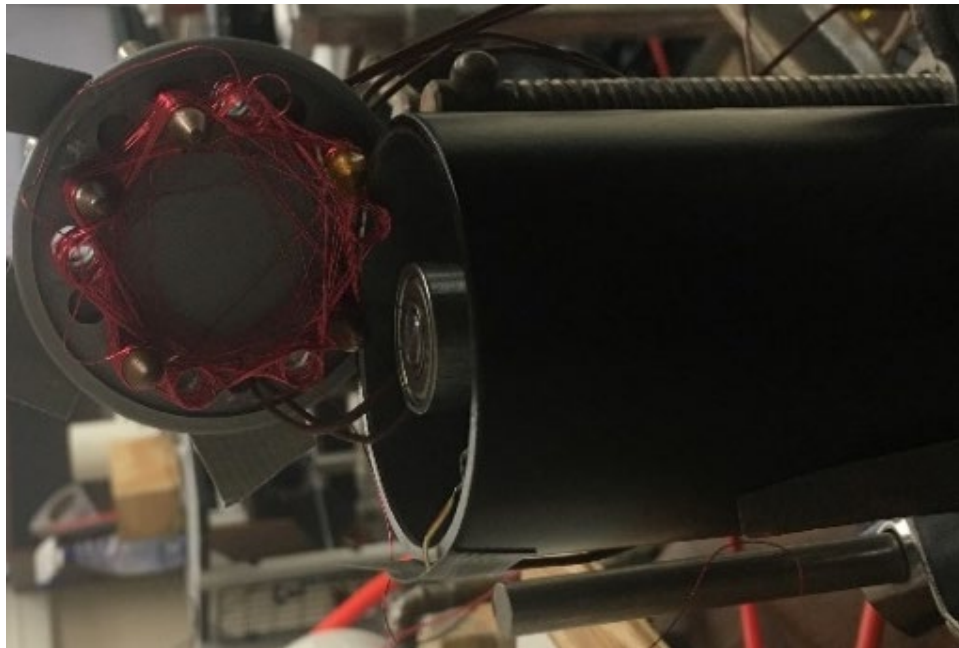
The addition of these woven structures is to increase the metallic presence in the housing area occupied by near-stagnant heated air, thereby improving the heat transfer path to the heat pipes for onward transference to the ambient. The addition of porous fins brought about an additional reduction in the temperature of the internal components of the EMA.



130(a). The network of porous fins heats pipes and motor cover.



130(b). Ten heat pipes in porous fins



130(c). Five heat pipes in porous fins



130(d). Two heat pipes in porous fins

Figure 131. Porous Fins

6.2 Results and Discussion

Figures 131 through 135 present the temperature at an EMA power setting of 20.5 Watts. Without heat pipes, the original EMA show a maximum winding temperature of 63.4°C and an internal air temperature of 30.5°C as seen in figure 131. The introduction of heat pipes through the top cover of the motor affected the temperature profile of both the windings and the inside air positively, bringing notable reduction in both temperatures at the end of the recording period. From Figures 134 and 135, the maximum winding temperature drops to 56.2°C whilst the air drops to 24.1°C. Figures 136 and 137 show the performance at a power setting of 28.2 W. whilst figure 138 summarizes the temperature reductions at various design points.

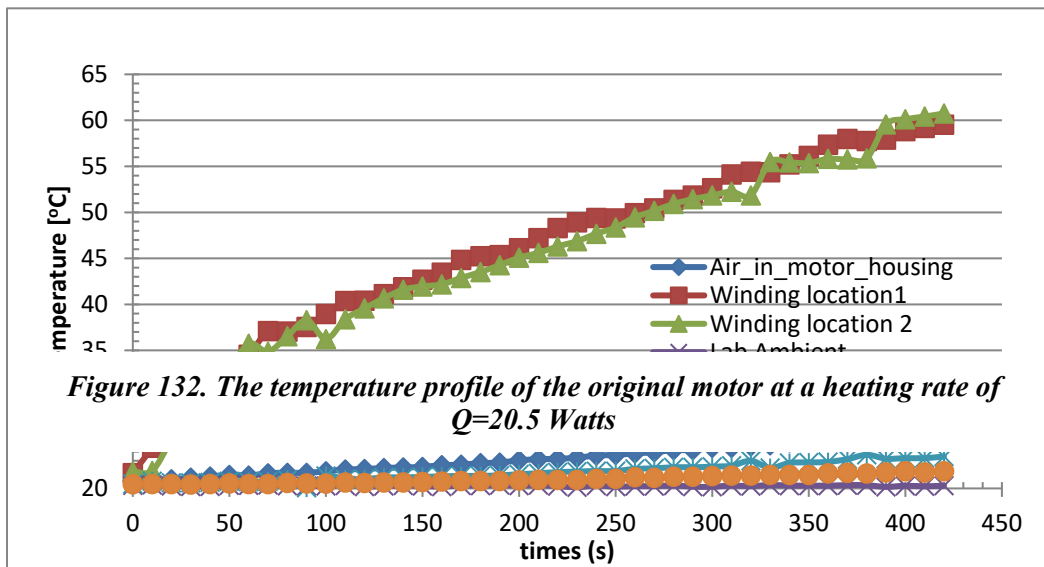
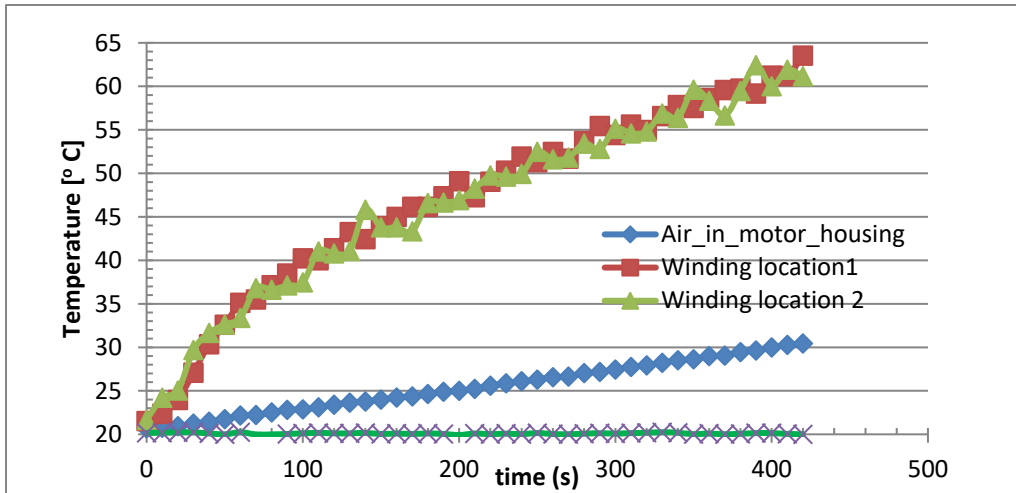


Figure 132. The temperature profile of the original motor at a heating rate of $Q=20.5$ Watts

Figure 133. The temperature profile of motor at a heating rate of $Q=20.5$ Watts with 5 heat pipes, δT of heat pipes = 1.2°C

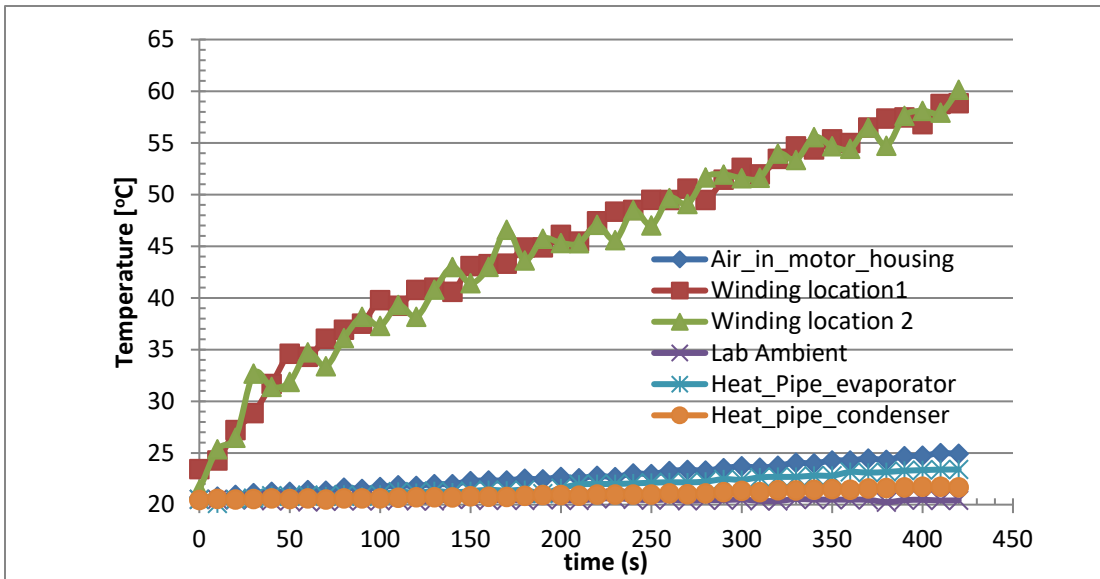


Figure 134. The temperature profile of motor at a heating rate of $Q=20.5$ Watts with 8 heat pipes, δT of heat pipes = $1.32^{\circ}C$

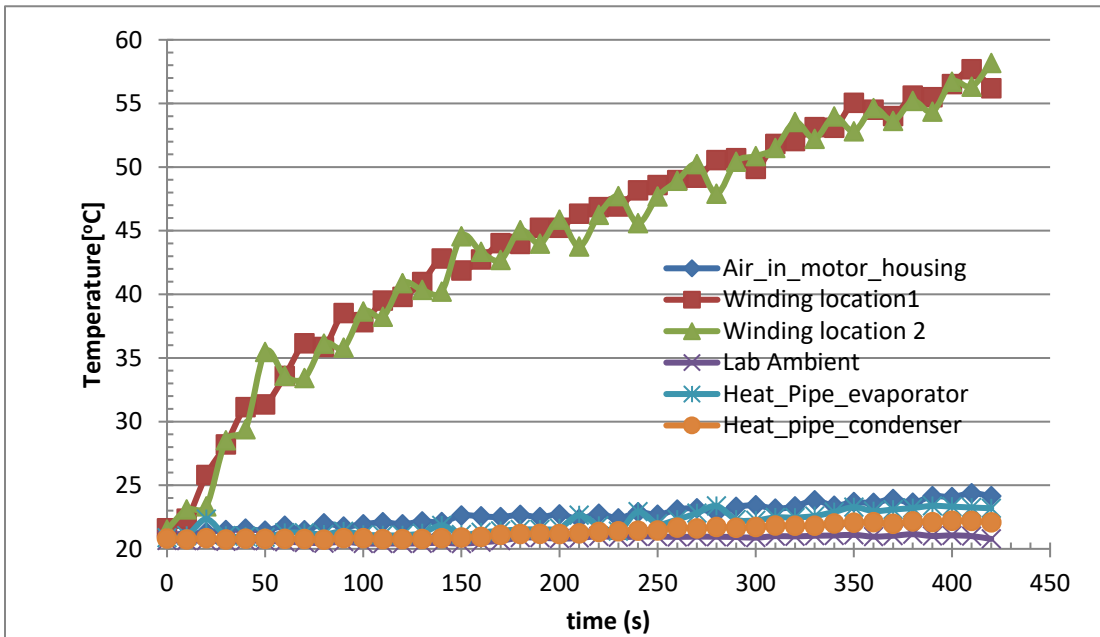


Figure 135. The temperature profile of motor at a heating rate of $Q=20.5$ Watts with 10 heat pipes δT of heat pipes = $0.84^{\circ}C$

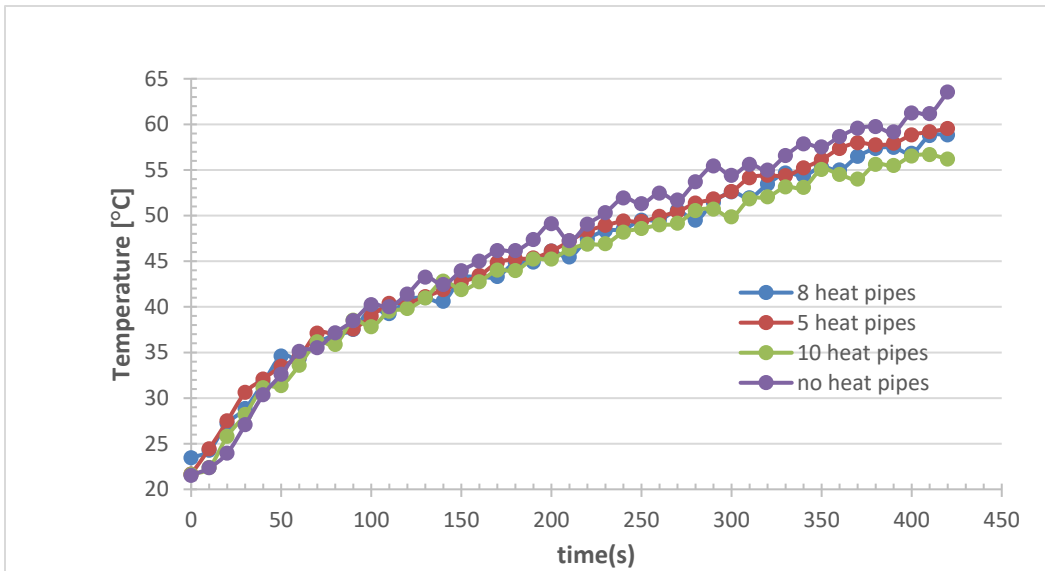


Figure 136. The temperature of windings at the heating rate of $Q=20.5$ Watts.

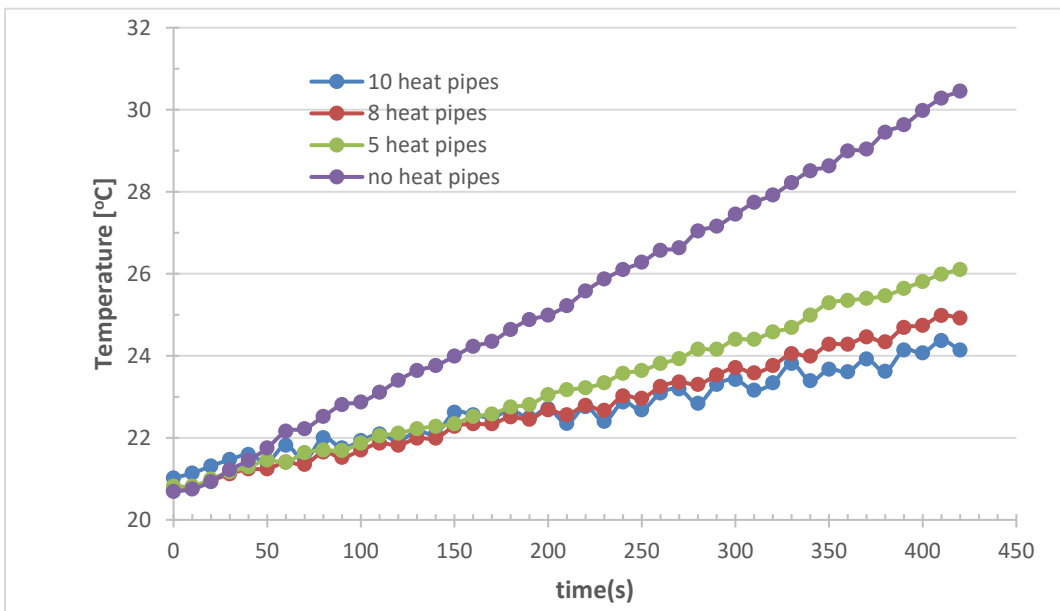


Figure 137. The air temperature inside motor housing at a heating rate of $Q=20.5$ Watts

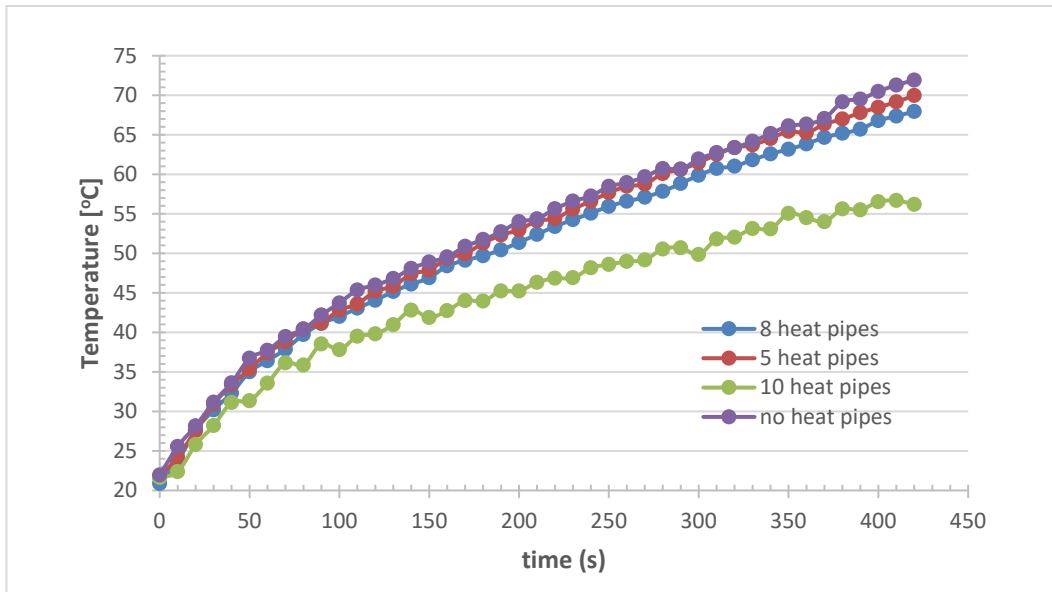


Figure 138. The temperature of windings at a heating rate of $Q=28.2$ Watts

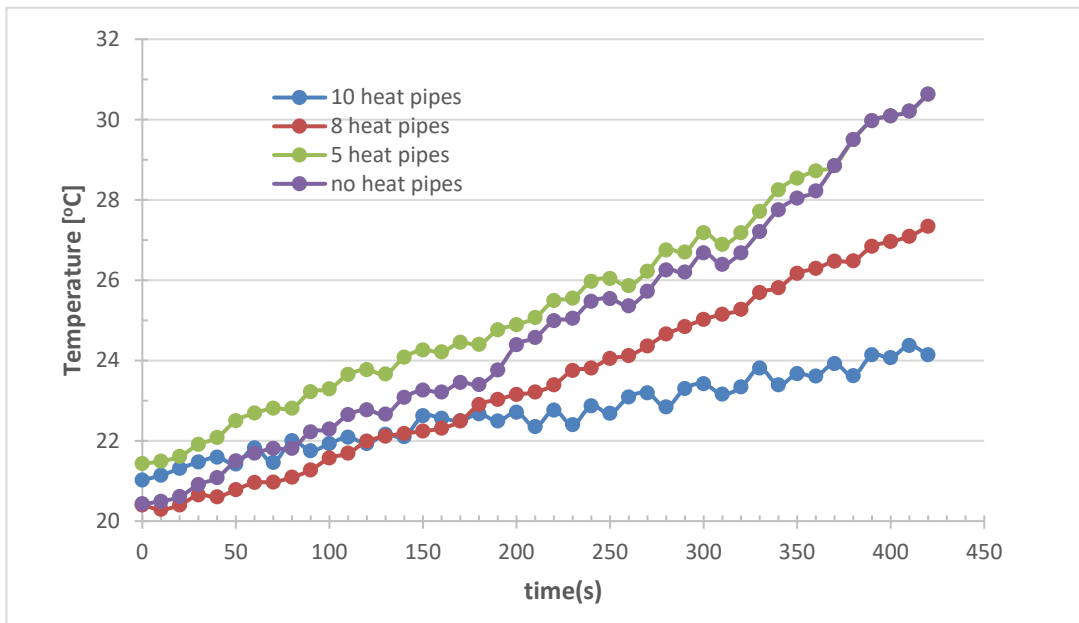


Figure 139. Air Temperature inside the housing at a heating rate of $Q=28.2$ Watts.

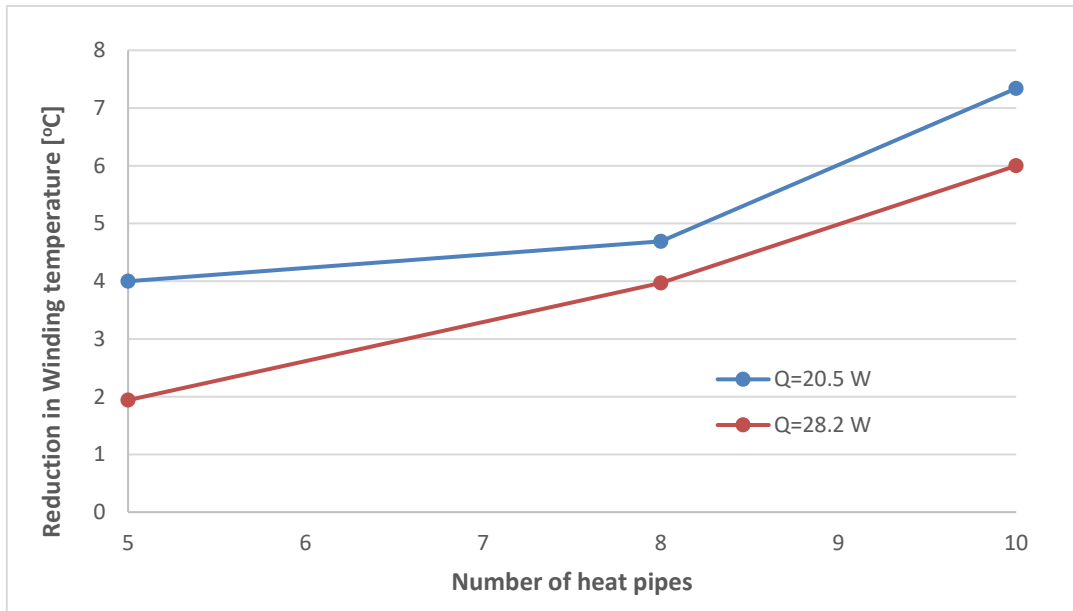


Figure 140. Reduction in temperature of windings vs the number of heat pipes

The matrix of heat pipes and meshed copper wires was seen to enhance the heat transfer characteristics of the EMA considerably as seen in Figures 140 through 143. At moderate power (nominal heating of 20.5 W), the reduction in winding temperature is 11.9°C with ten heat pipes and 11.6°C with five heat pipes, from which it can be inferred that the effect of changing between ten heat pipes was insignificant on the winding temperature. At high power (nominal heating of 28.2 W), this enhancement results in approximately 8°C drop-in in maximum winding temperature with ten heat pipes and downgrades to 6°C with five heat pipes.

High power modes of the EMA require higher heat transfer from within the device if the same level of thermal management is desired. This is consistent with the fact that five heat pipes working the 20.5 W setting are unable to achieve a comparable effect for the 28.2 W setting

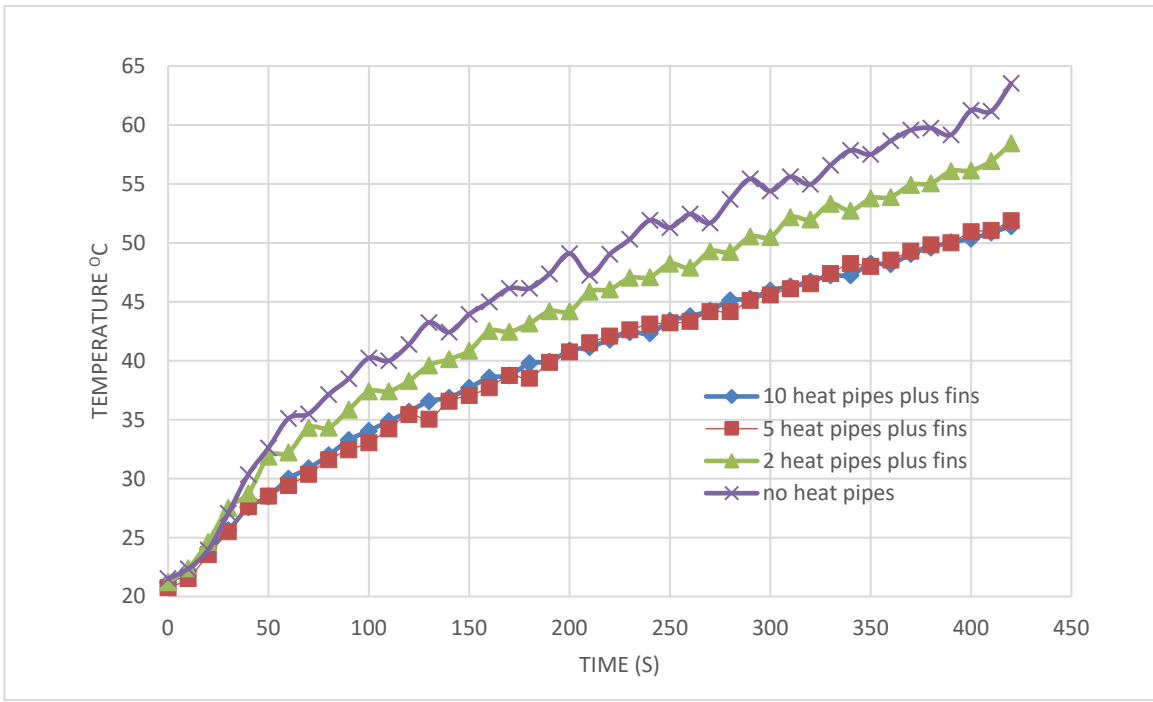


Figure 141. Temperature profile of windings 20.5 W when EMA was modified with heat pipes and porous fins.

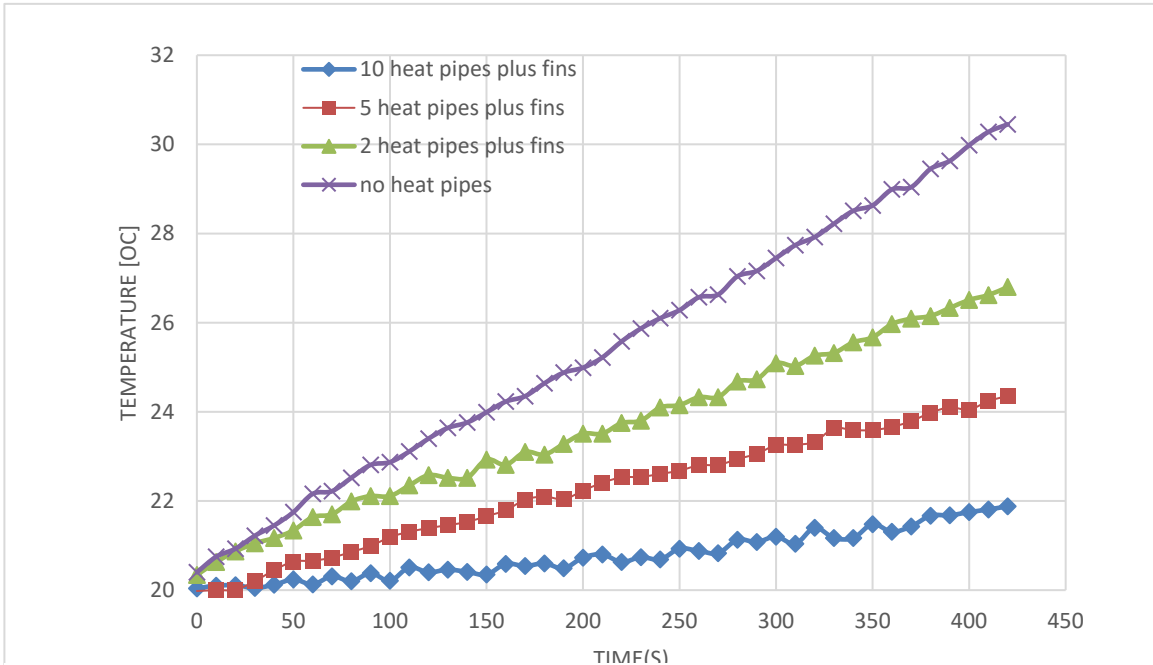


Figure 142. The temperature profile of inside air at 20.5 W when EMA was modified with heat pipes and porous fins

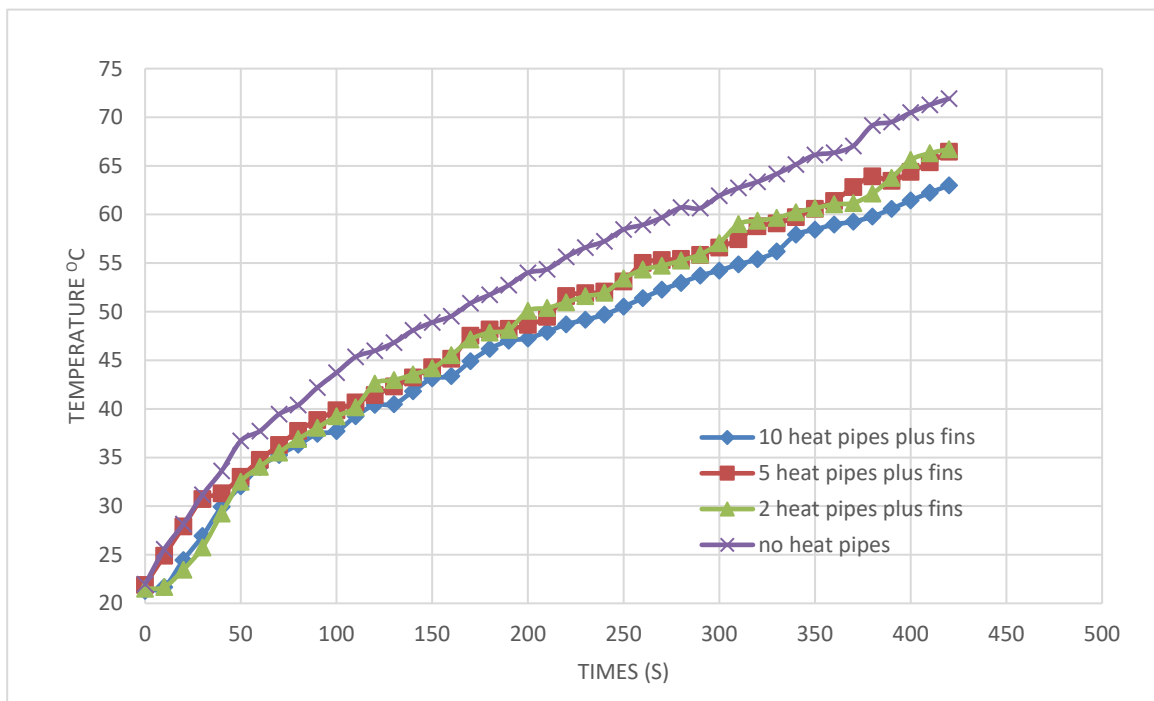


Figure 143. The temperature profile of windings at 28.2 W when EMA was modified with heat pipes and porous fins.

The maximum winding temperature at $Q=28.2$ W. At $Q=28.2$ W a temperature reduction of 9°C is obtained by using ten heat pipes and the porous fins formed by enameled copper wires. The use of two or five heat pipes resulted in a 5.2°C reduction of winding temperature.

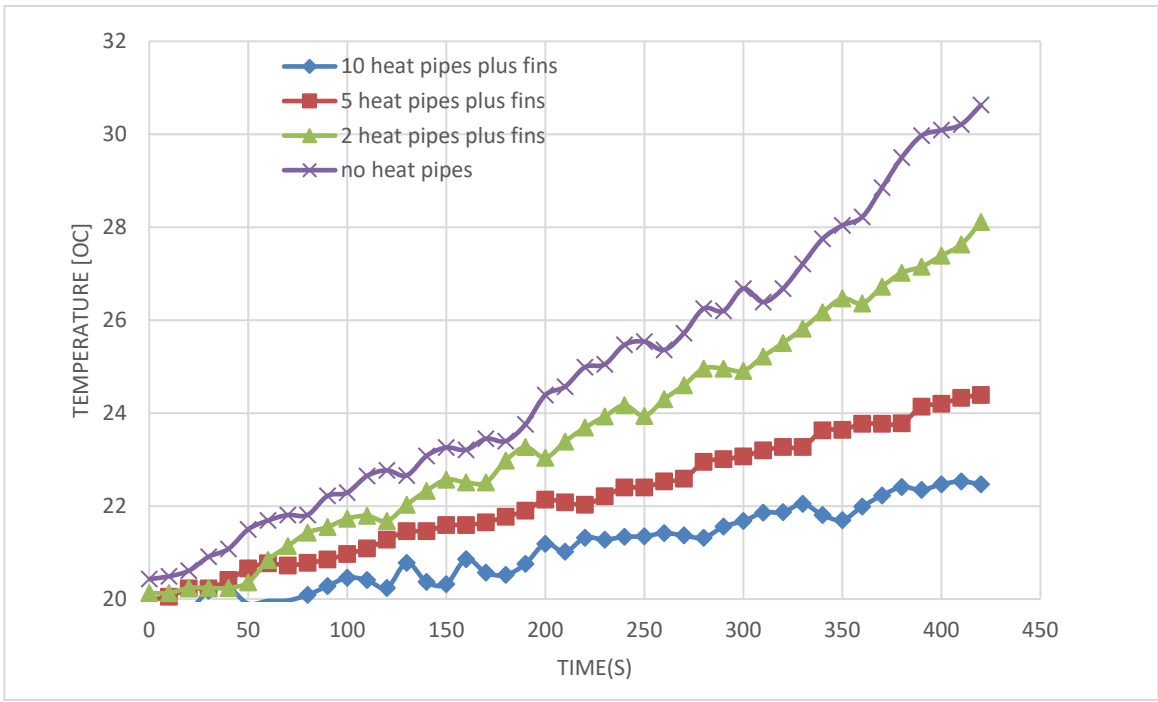


Figure 144. The temperature profile of inside air at 28.2 W when EMA was modified with heat pipes and porous fins

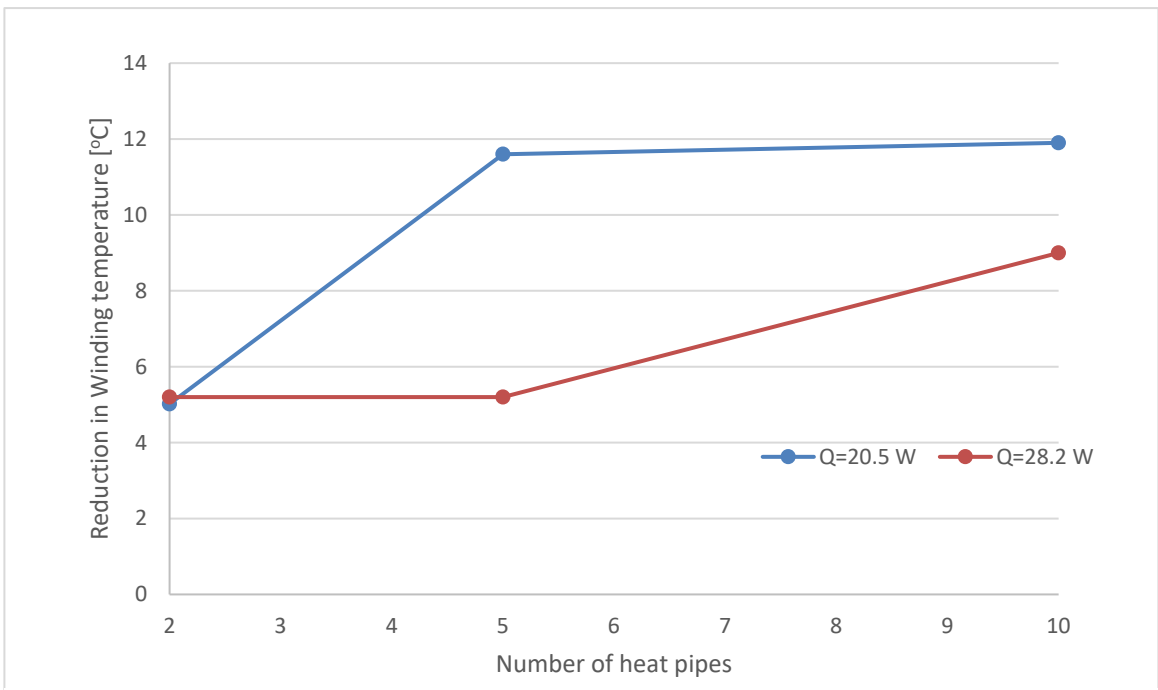


Figure 145. Reduction in temperature of windings vs the number of heat pipes in finned configuration

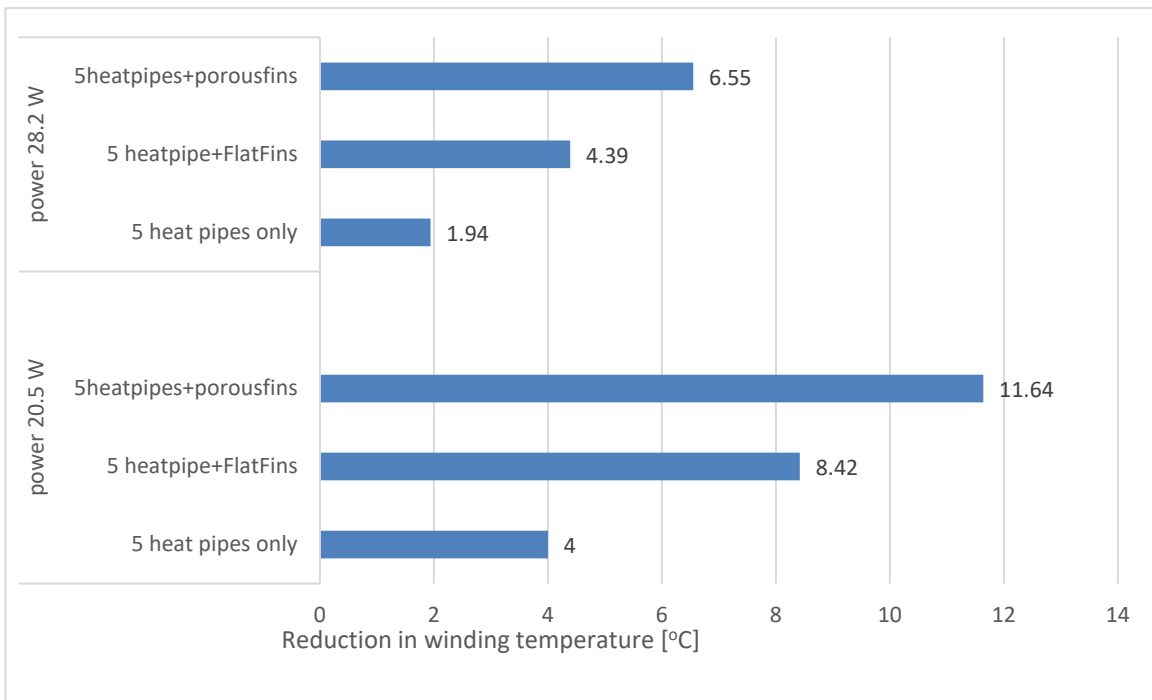


Figure 146. Reduction in winding temperature with 5 heat pipes at different configurations

The study showed that the use of only heat pipes resulted in lower temperatures for the copper windings. With ten heat pipes hanging in the device, a temperature reduction of 7.3°C and 6°C was recorded respectively at EMA power settings of 20.5 W and 28.2W. The temperature reduction effect is better with an increasing number of heat pipes and was further enhanced by interlacing the evaporator ends with the porous fins. The heat pipes also lowered the temperature of the air trapped in the motor housing. The reduction in air temperature is an effect of the introduction of heat pipes and serves as an intermediate causality for the observed lower winding temperatures.

Five heat pipes with porous fins proved to be the optimum operating point for the 20.5 W power setting whilst the 28.2 W power setting required more heat pipes to achieve a comparable thermal regulation. High power modes of the EMA require higher heat transfer from within the device if the same level of thermal management is desired. This is consistent with the fact that five heat pipes working the 20.5 W setting are unable to achieve a comparable effect for the 28.2 W setting. Subsequent studies will focus on the determination of novel ways of further enhancing the heat transfer path from the motor windings to the heat pipes.

7 TWO FAN COMPARISON WORK FOR EMA SIMULANT COOLING

In recent times there is a new demand for electromechanical actuation. Many works have been produced changing the current linear actuation systems to electromechanical units in aerospace applications. In Qiao et al., a direct comparison of the three main power-by-wire actuators is analyzed: electro-hydrostatic actuator (EHA), electromechanical actuator (EMA), and hydraulic servo actuators (HSA). EMA is the emerging technology that will be implemented in future years due to its safety and reliability improvement, and easily accessible maintenance [1]. EMA implementation is an emerging technology being studied for many types of air vehicles; which includes airplanes and vertical take-off and landing (VTOL) vehicles such as helicopters; moreover, Helicopter Electromechanical Actuation System (HEMAS) are also being analyzed for More Electric Aircraft (MEA) systems. The main electrical components of a helicopter were analyzed, and prototyping tests were conducted for thermal, electromagnetic, and rotor-dynamic studies [2]. Although EMA's have the potential to replace traditional actuation, there are critical safety concerns still that need to be addressed: limitations in weight and size, voltage spikes and current transients can affect the stability of electrical networks, thermal management of the system, dynamic performance of the actuator, reliability issues in the safety of the EMA from failing [3]. Interest for EMA in aerospace applications has been ongoing for several decades [4] and many researchers are currently attempting to implement design strategies that will ensure reliability by introducing multiple redundant actuator systems [5].

In the work presented, the focus is on the thermal management of the EMA. Multiple cooling strategies have been implemented. Heat pipe applications are widely used in electronics cooling, such as in computer workstations and any form of electronics that generates high heat loads [6]. The electric motor is permanent magnet synchronous motors that are extremely popular for hybrid electric vehicles; moreover, thermal management of these systems has been conducted using phase-changing heat pipes of various configurations. Heat pipes have emerged as a prominent technology in order to cool electronic components, and the working principle of such cooling structures is discussed in [7] and is a great option due to its compactness. According to Fang et. al, a straightly embedded module in an enclosure heat pipe significantly reduces peak temperature by about 22.3% under strenuous conditions of the EMA's operation [8]. Heat pipes can be used to cool heated sections of a system and distribute that heat to other parts needing higher temperatures [9]. Other researchers have implemented L-shaped heat pipes for cooling electric motors. Combining the L-shaped heat pipes with radial finned heat sinks demonstrated at 44% reduction in thermal resistance to that of the heat sink alone [10]. In Aprianingsih et al., using pulsating heat pipes with acetone as the working fluid and 50% infill within the heat pipe demonstrated to reduce the surface temperature of the electric motor by 55.3°C and minimizing the thermal resistance to 0.151°C/W [11].

Other cooling techniques have been analyzed for EMA cooling, such as thermal radiation studies have been conducted. In McCarthy et al, radiation studies are analyzed and demonstrate that it is the main mode of heat transfer to provide cooling to EMA's in a wing-bay enclosure of an aircraft [12]. Other researchers have demonstrated that natural convection and radiation is not sufficient to cool these high heat loads introduced by the electric motors [13]. Some researchers have focused on the fluid flow within microfluidic devices for design enhancements of such devices [14]. The use of holographic interference and smoke was used to determine heating of a confined space under natural convection effects [15]; moreover, the EMA also a heat source within a confined 3-dimensional space. Work in analyzing the effects of flow and thermal regimes have been conducted of the transitional flow regime; moreover, researchers found that the Reynolds number increased with increasing heat fluxes because of viscosity and temperature

[16]. Turbulent flows are of large interest due to the majority of natural flow phenomenon in nature occurs in the turbulent regime; furthermore, novel techniques of fluid flow and heat transfer have been studied extensively for winglet shapes [17] which can have applications of fan blade development.

For the current work, the forced convection cooling will be achieved by using axial fans. Many researchers have worked on improvements to axial fans have designed innovative techniques to improve their overall performance. In Li et al, the research entails designing rapid prototyping of a ducted fan with tip-jets. The researchers relied on the Coanda effect that causes the fluid to wrap around a solid body in order to push the blades forward. They claim that it has the nozzle functions under subsonic to supersonic conditions [18]. Other studies on the effect of tip clearance on the performance of an impeller. The varied the height of the tip clearance by 5%, 10%, and 15% to study the effect. Simulation results demonstrated that impeller trimming has adverse effects on fan performance; moreover, at the optimal flow rate fans without tip clearing change have better performance [19]. Studies of abnormal condition blades have been studied. Fan performance is lower than normal value and the noise rises. Varying the angle at which the abnormal blade is and obtained hydrodynamic and acoustic results for the undesired fan blade. The pressure contours demonstrate high pressures at localized points on the blade which could potentially cause severe problems [20]. Other studies have modified the tip of the fan by introducing grooves. A direct groove at the tip was superior over other groove designs [21]. In Wu et. al the idea of improving the reliability of the EMA cooling fan. The current fan EMA fan technology is a brushless direct current motor that powers the fan. Improvement of the meantime to failure (MTTF) of the fan from 5×10^4 to 2.5×10^9 hours of operation. The approach is to determine the possible causes of failure which are categorized into two failure mechanisms: (1) mechanical and (2) electrical failures. The solutions proposed to improve the reliability of the system are to include dual bearings, dual windings, and dual fans. They conclude that the utilizing a dual fan system is beneficial; other hand, implementing either a dual bearing or dual winding system alone does not drastically improve the reliability of the overall system [22] Previous researchers focus on developing a fan that can effectively cool an electromechanical actuator (EMA) for a wide range of ambient pressures; additionally, generating high static pressure head, high volumetric flow rate, and high efficiency over a wide operating range of rotational speed and ambient pressure. At maximum altitude aircraft experience, ambient pressures of 20% atmospheric; furthermore, the research focuses on fan design and optimization of the fan blades to operate from (0.2 – 1) atm. A commercially available fan by AMETEK is used for the analysis, specifically the Propimax 2 [22-28].

The design parameters that were varied in their work were to improve the performance of the commercially available fan are the setting angle, the blade root chord, and the blade end chord. CFD results were obtained indicate that a 1.81x improvement was obtained over that of the commercially available fan for a wide range of fan rotational speeds, (8,000 – 22,000) rpm, and ambient pressure conditions, (0.2 – 1) atm.; moreover, the pressure directly affects the density within the system [24, 29]. The Ametek Propimax 2 was used to test the fan scaling laws by varying all parameters except for one at a time. The conclusions yielded similar results to that of [27, 30] since a similar setup and fan were used. However, a high powered 12-bladed fan for RC aircraft was used to compare the performance curves of the 2-bladed vs 12-bladed fan. Adverse thermodynamic effects were measured within the system due to the high-power requirement of the 12-bladed fan. The air within the experimental setup was being heated due to the high heat generated by the motor of the 12-bladed ducted fan [28]; furthermore, using a lower-powered fan is tested in the current work. The system is a fully enclosed ducted system, the inherent losses of the system can affect the performance of fan. Convective heat transfer has been analyzed extensively for straight pipes; furthermore, work has been shown to have heat transfer and pressure loss improvements for helical as opposed to straight pipes [31].

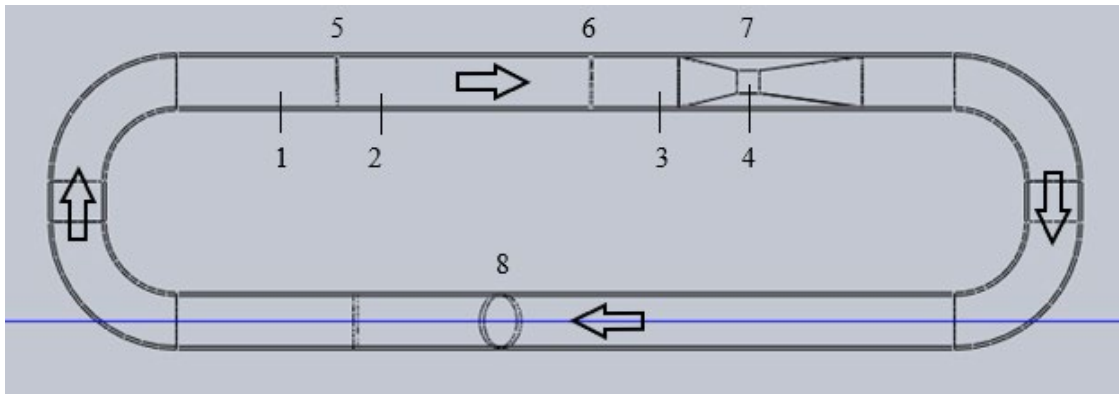
To the best of the authors' knowledge, the current work on studying the adverse effects of pressure on fan performance and fan efficiency is limited. Currently, the aim of the research is to focus on design and experimental rig that can effectively analyze fan performance of various axial fans. The only restriction of the experimental loop is the maximum diameter of the fan

cannot exceed 4in. First, the experimental setup and the equipment used is presented. Followed by calculations necessary to determine the fan performance curve and efficiencies of the systems. The error analysis of the measurements is determined using regression analysis and the main parameters that could lead to experimental error are considered in depth. The validation of the 2-bladed fan is demonstrated; moreover, two fans were experimentally tested at four ambient pressures, (1, 0.7, 0.5, 0.3) atm. The findings are discussed in the following sections and the results measured conclude that not only must the hydrodynamic performance of the fans can be considered, but also that the fan efficiency is critical in identifying a viable option in cooling EMAs at variable pressures.

7.1 Experimental setup

7.1.1 Equipment used for experimental setup

In Fig. 146 the experimental loop is depicted. The loop is comprised of various components to accurately determine the fan performance curve at various pressure conditions. The overall hydraulic diameter of the system is 4" PVC pipe. The pipe is a standard schedule 40 PVC pipe. The butterfly valve provides the ability to throttle the volumetric flow rate within the loop. There are two types of fixtures that mate the individual PVC pipes. The first is permanent joints that have been introduced to the elbows and around the butterfly valve. Secondly, the black coupling units provide the ability to give removable joints within the system. These joints are beneficial in cases where extensions/reductions are necessary for the system. Both methods of joining the components demonstrate the ability to maintain a vacuum.



1,2,3,4—pressure transducers; 5—fan with power supply and PC for fan speed measurement; 6—NEL Spearman; 7—Venturi flowmeter; 8—Butterfly valve

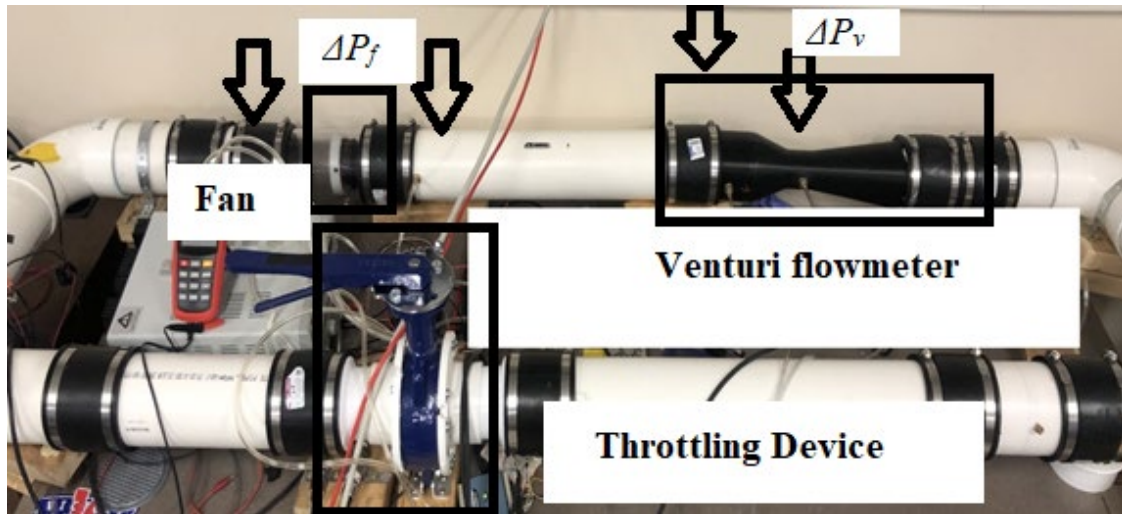


Figure 147. Structural diagram (top) with experimental loop (bottom)

All the pressure measurements are static pressures located at the wall of the pipe. The pressure taps across the fan determine static pressure rise across the fan ΔP_f , and the pressure drop in the Venturi flowmeter gives the volumetric system of the fluid within the system ΔP_v . The pipe tap distances and lengths all follow minimum length requirements followed by the Air Movement & Control Association and specific dimensions are specified in previous work [28, 32]. With the use of a butterfly valve, the system resistance is throttled to obtain the various points along the fan performance curves.

The Venturi flowmeter used to determine the volumetric flow rate within the system was additively manufactured of Acrylonitrile Butadiene Styrene (ABS). Enough infill percentage was used so that the Venturi would be able to withstand the large pressure gradient of the ambient conditions in the lab to the internal pressure of the experimental loop. The Venturi follows ISO Standard 5167-4 [33] with a diameter ratio, $\beta = 0.51$, and is demonstrated below in Fig. 147. The original Venturi flowmeter was fabricated by machining nylon but was replaced with the current design due to its smaller throat diameter and larger pressure loss within the system. The volumetric flow rate was tested with a secondary flow obstruction device, a pitot tube, and the volumetric flow rates determined from both devices. In Fig. 148, an image of the pitot tube is demonstrated to show the integration of the device into the flow loop, which must have been placed directly in the center of the tube to obtain the correct measurement of total pressure.



Figure 148. The 3D printed ABS Venturi, $\beta = 0.51$.



Figure 149. The Pitot tube incorporated into the tube to determine the volumetric flow

The Pitot tube gives us point measurement whereas a Venturi flow meter gives us the average flow rate. The Pitot tube is calibrated by the manufacturer; then we use the Pitot tube to calibrate the 3D printed (in-house) Venturi flowmeter. By calibrating the Venturi flowmeter with the Pitot tube there is high confidence in the measurement and determination of the volumetric flow rate. The experimental setup of the calibration performed is demonstrated in Fig. 149. The Pitot tube is placed upstream, and the Venturi flowmeter is placed downstream in both cases. The order of the flow measurement devices was chosen in that manner to reduce the restriction of the pressure drop in the Venturi from affecting the measurement in the Pitot tube. It is expected that the Pitot tube will have a negligible pressure drop due to its smaller size in obstructing the flow.

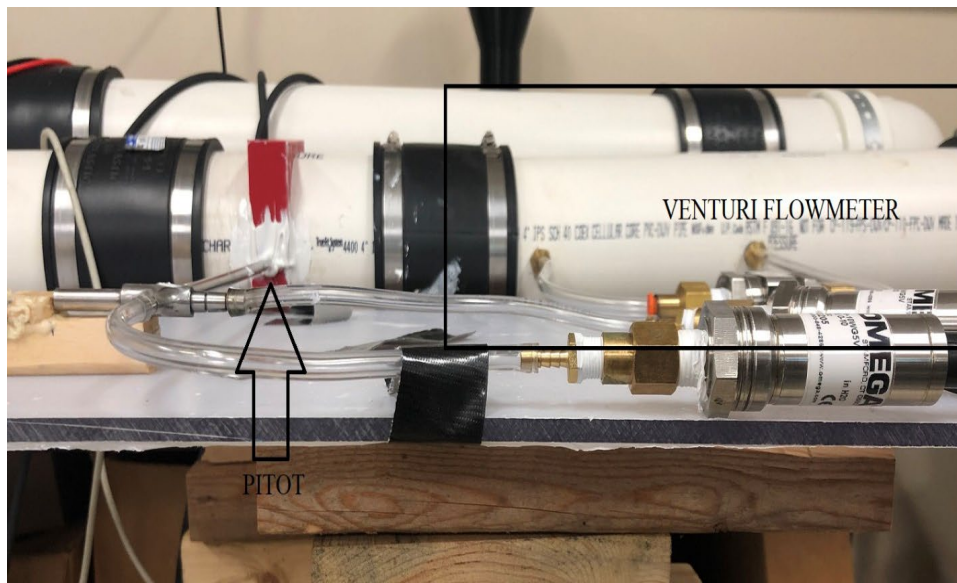
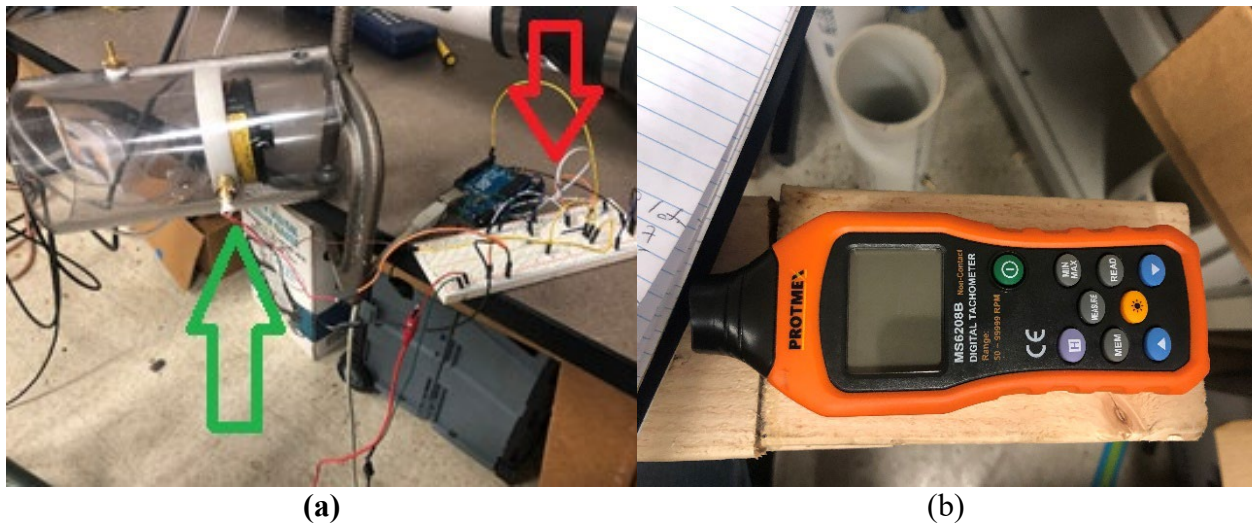


Figure 150. Demonstrates the calibration of the 3D printed Venturi flowmeter.

The pressure drops were measured using OMEGA’s High Accuracy PX-409 Pressure Transducers. The transducers feature a ¼ in. NPT thread is connected to barbed fittings followed by a flexible tube to be hooked into the loop. In Fig. 149, the transducers are pictured and their respective fittings.

The two fan systems use 3-wire and 4-wire cabling system and the three wires used are positive and negative to power the fans and the third wire is the signal wire to detect the frequency of the fan. Fig. 150a demonstrates the Arduino setup to read the fan’s rotational speed from the Hall Sensor inserted in the hub of the fans. A script was written in Arduino that determined the frequency in the electromagnetism within the brushless motor. A Hall Effect sensor inside the hub counts the frequency and that is then converted into angular velocity. The Protmex tachometer was used to verify the rotational speed of the fan as displayed in Fig. 150b. The accuracy of the tachometer is $50 - 99999 \pm (0.03\% + 2) \text{ rpm}$. The highest fan speed measured in the current work is 21,170 rpm; therefore, the maximum possible error in measurement is 8.4 rpm when operating at 21,170 rpm.

Figure 151.(a) Arduino hardware setup (red arrow) that is used to read the fan (green arrow) speed from the signal wire (brown), the red and black wire are positive and ground, respectively. (b) The Protmex non-contact tachometer used to verify the fan’s rotational speed.



To test for low-ambient pressure conditions within the loop, a two-stage vacuum pump by HFS with a suction rate of 12 cfm; moreover, the vacuum pump had enough suction capacity to obtain a pressure of 0.3 atm. The pump used for the test is pictured in Fig. 151. Previous tests in [23, 28] demonstrated that 20% atmospheric pressure condition posed difficulties in obtaining results of the performance curves at those conditions.



Figure 152. The vacuum pump utilized to change the ambient pressure within the loop.

7.1.2 Fans tested

The two geometrically different fans were selected in conducting the fan performance test. The first fan is a Propimax 2L by Ametek (Fan 1) [34], shown in Fig. 152. Fan 1 features a 2-bladed configuration with an optimized fan speed of 18,400 RPM. Fan 1 has a round shroud with an effective blade diameter of 77.33mm. The fan was inserted into a clear Butyrate tube, its

diameter of the fan is slightly smaller than the 4 in. duct; furthermore, to secure the fan in place nylon was machined with a locking screw to fasten the assembly into the tube.

The second fan system by Delta (Fan 2) is integrated in a similar manner. Fan 2 features a square shroud which makes mounting easier than the round configuration of Fan 1; in addition, black insulation foam was used to fix its position inside of the tube. In Fig. 153, the Delta dual fan system is presented in its 7-bladed and 5-bladed configuration [35], but in further testing in the comparison of the two fans only the entrance, 7-bladed, is used. Fan 2 has a blade diameter of 71.2mm.

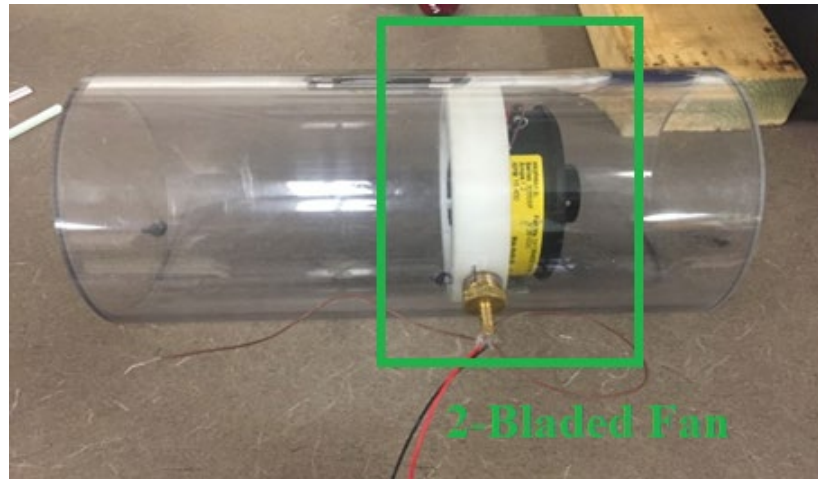


Figure 153. Integration of the nylon and fan assembly to secure the 2-bladed fan, Fan 1



Figure 154. The Delta dual fan system and its incorporation into the clear tube, Fan 2

7.2 Theory

7.2.1 Hydrodynamic equations

From Fig. 146, the experimental loop consists of pressure taps to obtain the fan performance. The volumetric flow rate within the system is determined from the Bernoulli energy equation of obstruction flow devices. The volumetric flow rate is given by,

$$Q = C_d A_t \left[\frac{2\Delta P_v}{\rho(1-\beta^4)} \right]^{1/2} \quad (38)$$

where C_d is the discharge coefficient, A_t throat cross-sectional area of the Venturi, ΔP_v is the pressure drop across the Venturi, $\rho = P/RT$ the density of the air within the system and the diameter ratio of the throat to the system is given by $\beta = d/D$. The discharge coefficient is given by [36, 37],

$$C_d \approx 0.9858 - 0.196\beta^{4.5} \quad (39)$$

which is a minor loss for Venturi flow meters unlike other obstruction devices in determining the volumetric flow rate; nonetheless is a factor that must be considered due to its dependence upon the diameter ratio.

The hydrodynamic power that is supplied by the axial flow fans was determined by,

$$\dot{W} = \Delta P_f Q \quad (40)$$

where ΔP_f is pressure rise across the fan. The Reynolds number is given by [38],

$$Re = \frac{\rho V D}{\mu} \quad (41)$$

where ρ is the fluid density, μ is the dynamic viscosity, V is the fluid velocity, and D is the hydraulic diameter of the system. From continuity, it is known that $Q = AV$, and plugging in that relationship into Eq. (41), the Reynolds number can be derived to,

$$Re = \frac{4\rho Q}{\mu\pi D} \quad (42)$$

thus, the Reynolds number can be determined directly from the volumetric flow rate determined by the measurement within the system.

7.2.2 3.2. Electrical component equations

The main concern in determining the fan performance curve is the physics of hydrodynamics related to the fan. Nonetheless, the fan must be supplied electrical power to drive the propeller; therefore, the input power to the fan is essential in determining the overall efficiency of the axial fan. The power input is determined experimentally by recording the voltage and current supplied to the fan. Hence, the efficiency of the fan yields [38],

$$\eta = \frac{\Delta P_f Q}{V_e I}, \quad (43)$$

where the numerator is the output power, fluid power, and the denominator denote the input power, the electrical power supplied to the fan; moreover, those parameters determine were used to determine the efficiency.

7.3 Error Analysis

Taking the root mean squares approach in determining the uncertainty in the volume flow rate as follows [39],

$$u_Q = \left[\left(\frac{\partial Q}{\partial \delta P} u_{\delta P} \right)^2 + \left(\frac{\partial Q}{\partial C_d} u_{C_d} \right)^2 + \left(\frac{\partial Q}{\partial A_t} u_{A_t} \right)^2 + \left(\frac{\partial Q}{\partial \beta} u_{\beta} \right)^2 + \left(\frac{\partial Q}{\partial \rho} u_{\rho} \right)^2 \right]^{1/2} \quad (44)$$

where the uncertainties in the independent variables $u_{\delta P}$, u_{C_d} , u_{β} , u_{ρ} , u_{A_t} contribute to the overall uncertainty in the volumetric flow rate. The following set of Eq. (45-49) are the partial derivatives for the volumetric flow rate as a function of the pressure drop measured, density determined, discharge coefficient, Venturi throat cross-sectional area, and the diameter ratio as follows,

$$\frac{\partial Q}{\partial \delta P} = \frac{C_d A_t}{\sqrt{2\rho(1-\beta^4)}} \left[\frac{\delta P}{\rho(1-\beta^4)} \right]^{-1/2} \quad (45)$$

$$\frac{\partial Q}{\partial \rho} = -\frac{C_d A_t \delta P}{\sqrt{2\rho^2(1-\beta^4)}} \left[\frac{\delta P}{\rho(1-\beta^4)} \right]^{-1/2} \quad (46)$$

$$\frac{\partial Q}{\partial C_d} = \sqrt{2} A_t \sqrt{\frac{\delta P}{\rho(1-\beta^4)}} \quad (47)$$

$$\frac{\partial Q}{\partial A_t} = \sqrt{2} C_d \sqrt{\frac{\delta P}{\rho(1-\beta^4)}} \quad (48)$$

$$\frac{\partial Q}{\partial \beta} = \frac{2^{3/2} C_d A_t \delta P \beta^3}{\rho(\beta^4-1)^2} \left[\frac{\delta P}{\rho(1-\beta^4)} \right]^{-1/2} \quad (49)$$

and can observe that the only variables necessary to consider are variables that require pressure measurements and geometrical quantities.

To determine the uncertainties in the pressure measurement and in the density; first, the determination of the uncertainty in the instruments used. The current work was executed using the OMEGA PX-409 high-accuracy pressure transducer. Pressure transducers experience elemental errors such as linearity, hysteresis, sensitivity, drift, and temperature changes within the working environment. Taking those elemental errors into consideration the overall instrument error and instrument uncertainty is given by [40],

$$u_P = [u_{BSL}^2 + u_z^2 + u_S^2]^{1/2} \quad (50)$$

where the $u_{BSL} = 0.08\%$ best standard line (BSL) combines the linearity, hysteresis, and repeatability uncertainties of maximum value, $u_z = 0.5\% FS$ the zero-balance uncertainty, and $u_S = 0.5\% FS$ is the span setting uncertainty. For the differential unit used and the gauge transducers in the experiment range from $P = (0 - 2488.4) Pa$ and the absolute pressure transducer range from $P = (0 - 103421) Pa$ [40].

8 RESULTS & DISCUSSION

8.1 Validation of the experiment

Firstly, the experimental setup was validated for Fan 146. The rotational speed of the fan from literature is tested at 21,170 rpm; moreover, the validation curve was tested for that rotational speed in the loop constructed in Fig. 146. The results of the experimental validation are demonstrated in Fig. 154.

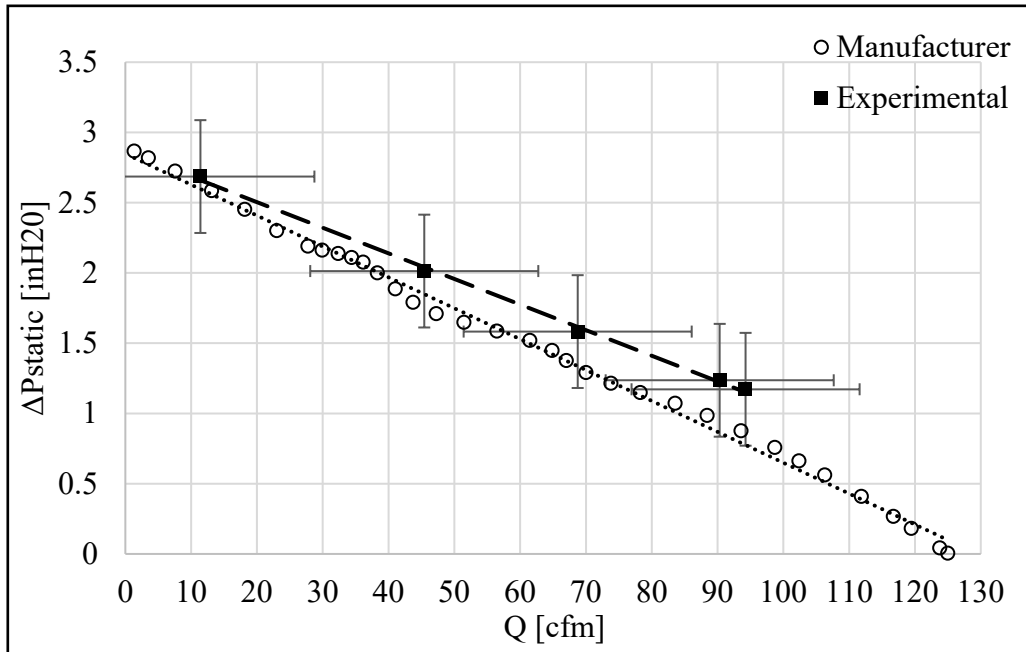


Figure 155. Validation of the experimental loop testing the 2-bladed fan.

Based upon the error analysis discussed previously, the various points along the fan performance curve demonstrate to reside within an agreeable margin of the manufacturer's specification. The experimental setup provided those points to be measured, and the curve lies in close proximity at the low volumetric flow rates, but as the valve is further opened, there is a higher deviation in the determined pressure rise and volume flow rates. The highest volumetric flow rate determined within the loop is 94.3 cfm. The stall pressure occurs at the zero volumetric flow rate condition. Also, at the stall condition the maximum back pressure generated by the fan is experienced. Due to the inherent nature of the fan loop system, there are slight losses within the 90° bends, the butterfly valve, a flow straightener located downstream of the fan before the Venturi, and the overall roughness of the PVC pipe itself.

The performance curve is determined for both fans under identical testing conditions. The testing conditions are the same experimental loop, but varying the pressures from (1-0.3) atm. These pressures are chosen to predict the behavior of the fans at high elevations (i.e., low-pressure conditions). All fan curves for the remainder of the experiments were conducted at the rotational speed of 13,000 rpm.

8.2 Fan 1 test results

The physics of pump performance curves demonstrates that there is an inverse relationship of the increasing pressure across the fan and decreasing the volumetric flow rate. In Fig. 10, Fan 1 is demonstrated at various pressures.

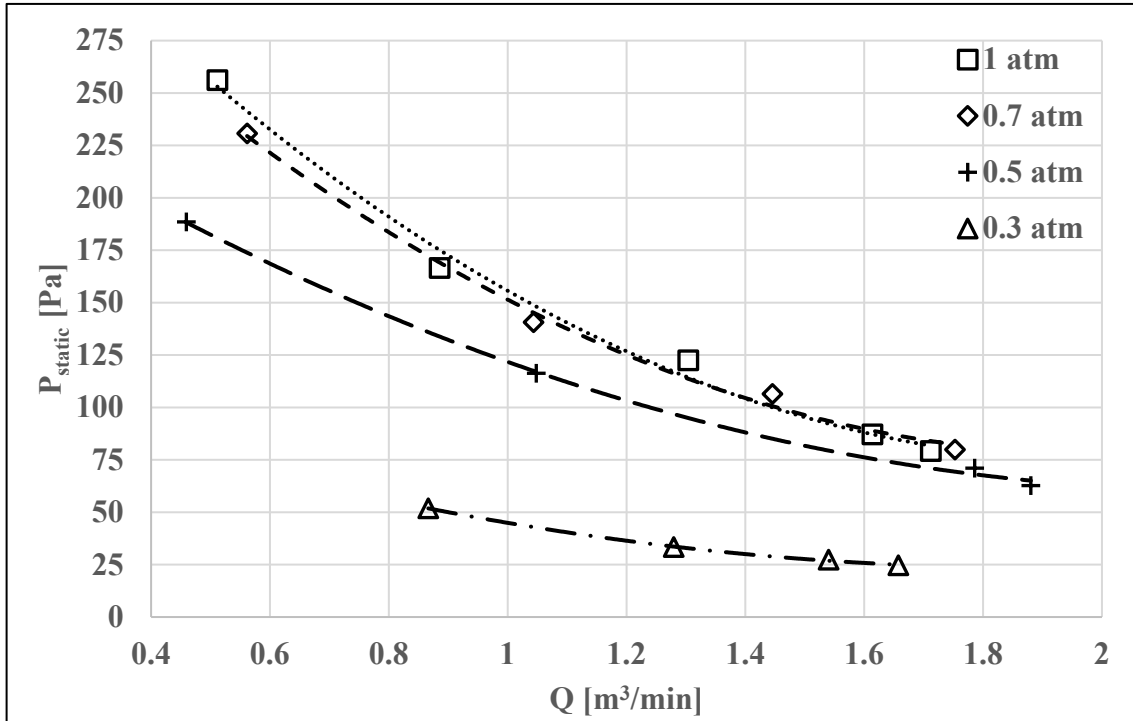


Figure 156. The fan performance of Fan 1 at various ambient conditions.

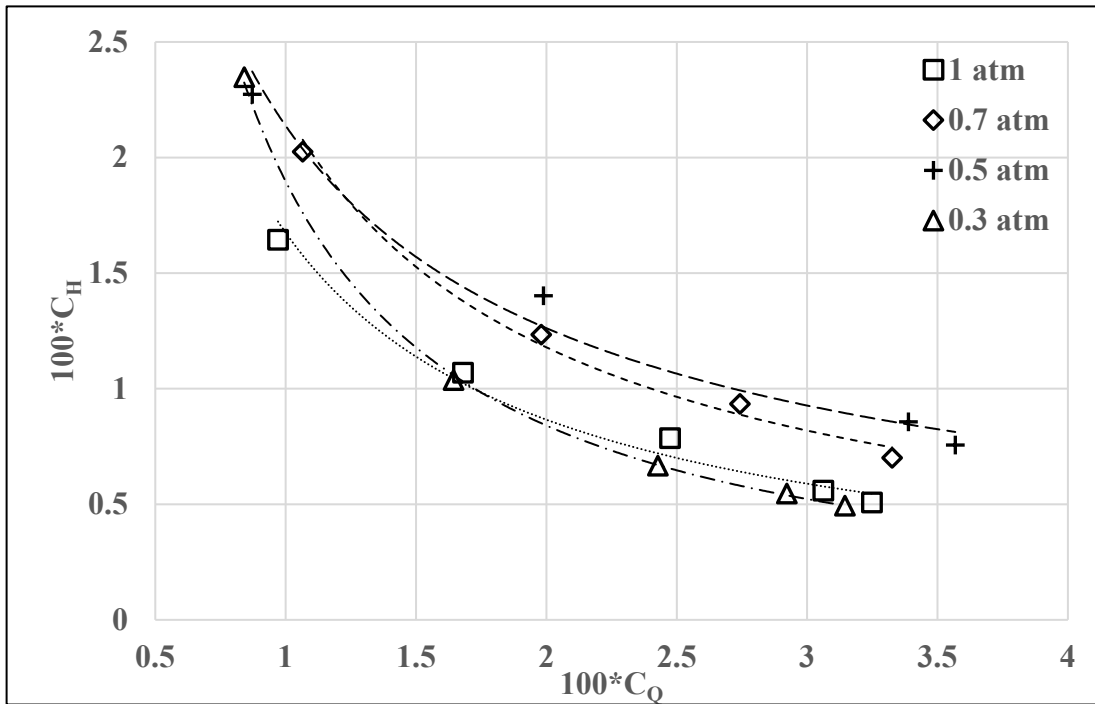


Figure 157. Dimensionless performance curve for Fan 1.

The dimensionless performance curve is demonstrated in Fig. 156. The equations were derived using traditional Buckingham Pi Theorem to determine the dimensionless curves of Fan 1 at variable pressure. The data demonstrates a correlation of $R^2 > 0.99$ for all pressure conditions. A power fitting curve is used for the data and given the high correlation value it is evident that the data behaves as a power function. The 1 atm. and 0.3 atm. pressure conditions perform nearly identically, whilst the 0.7 atm. and 0.5 atm. have very close trends. At near shutoff flow conditions, the fan at all pressure conditions perform the equivalently. A factor 100 is multiplied to the coefficient of head and coefficient of volumetric flow rate to easily view the trends of the data.

The fan performance at standard atmospheric pressure and 0.7 atm. is roughly the same; moreover, Fan 1 is not drastically affected by the slight change in ambient pressure. Once the pressure drops to 50% of atmospheric, the fan performance starts to deteriorate significantly. The difference in performance is drastic when the pressure of the system varies from 0.7 atm. to 0.5 atm. The performance deteriorates further at 30% atmospheric pressure. To compensate for the drastic loss in performance, the fan should be operated to a higher rotational speed in order to provide the same amount of performance to that of the ambient pressure condition. All four pressure cases demonstrate a high tendency for a quadratic behavior and using regression analysis all sets of data demonstrate the good correlations that indicate those relationships, $R^2 > 0.99$.

The maximum efficiency of the fan indicates the best efficiency point (BEP); moreover, with the BEP the optimal volumetric flow rate and pressure rise of the fan can be evaluated. To determine the BEP, the input power is determined by multiplying the pressure drop measured across the fan and the volumetric flow rate determined; furthermore, the input power is simply recorded from the digital display of the power supply used. The BEP indicates the point where the fan is

intended to operate. In Fig. 157, the efficiency of the fan for different ambient pressures within the loop is demonstrated.

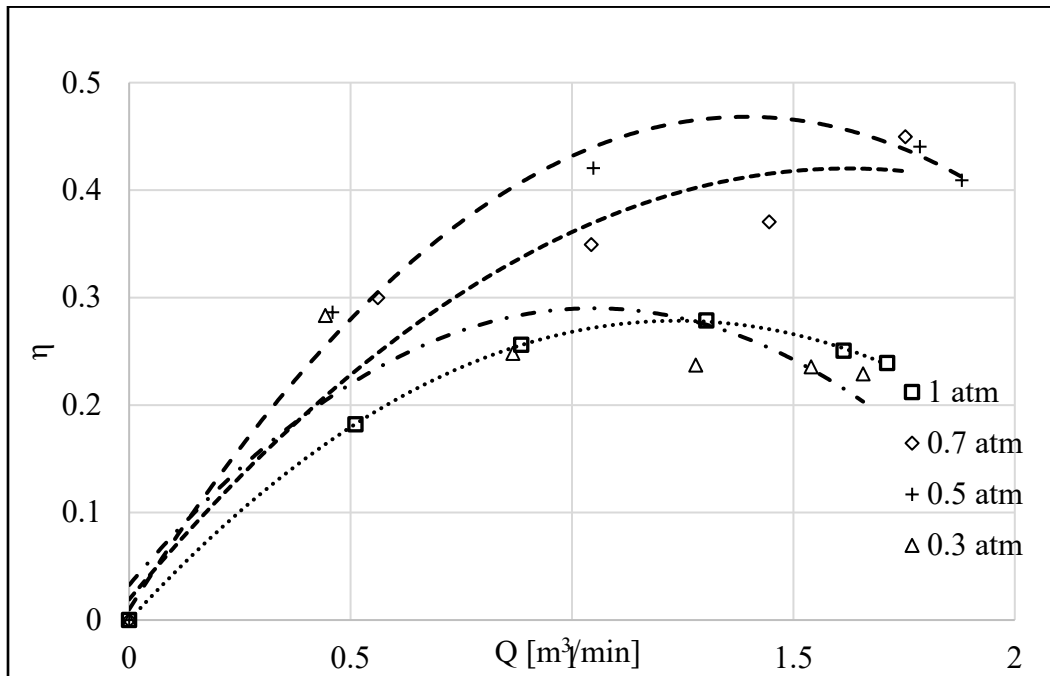


Figure 158. The efficiency of Fan 1 at various ambient pressure conditions

From Fig. 157, the highest efficiency was determined to be at 0.5 atm. with $Q = 1.4 \text{ m}^3/\text{min}$ and $\eta \approx 0.47$. The next highest efficiency pressure condition is determined at 0.7 atm. Next, the atmospheric condition peaked the maximum efficiency at approximately, $Q = 1.0 \text{ m}^3/\text{min}$ with an efficiency shy of $\eta = 0.3$. Lastly, the lowest BEP is for the lowest pressure condition with an apex slightly smaller than the atmospheric case; nonetheless, there is a considerable shift in volumetric flow rate between the two ambient conditions of approximately, $Q \approx 0.4 \text{ m}^3/\text{min}$.

5.3. Fan 2 Test Results

The second fan is a 7-bladed fan which is demonstrated in Fig. 153 by Delta. A similar analysis was conducted for Fan 2 with the same controls implemented to that of the Fan 1. In Fig. 158, Fan 2 was tested for various pressure conditions; moreover, similar trends were determined. The highest performance curve is measured in atmospheric pressure conditions. Consequently, as the pressure within the loop was dropped the performance of the fan was affected. The Delta fan has the same tendency to follow a quadratic fit, with all ambient pressure condition cases demonstrating an acceptable correlation of $R^2 > 0.99$ like that of the Fan 1.

Similarly, the analysis conducted for Fan 1 is also performed on Fan 2 in Fig. 159. In Fig. 159., the dimensionless performance curves of Fan 2 behave similarly to that of Fan 1 where a power function curve fits are the closest fitting trends to the data. The two extreme pressures (1 atm. and 0.3 atm.) demonstrate similar trends and the intermediate pressure conditions (0.7 atm. and 0.5 atm.) show comparable trends. Although the trends are the same, Fan 2 demonstrate much different performance for the two extreme ambient conditions since the 1 atm. clearly outperforms the 0.3 atm. unlike Fan 1. Moreover, 0.7 atm. also has a slightly higher performance than that of 0.5 atm.

In Fig. 160, the efficiency curves at the different pressure conditions are demonstrated. For Fan 2, the highest efficiency is measured at 0.3 atm. For all the lower pressure, (0.7, 0.5, 0.3) atm., the peak of the efficiency curve is observed at around a volumetric flow rate of, $Q \approx 3 \text{ m}^3/\text{min}$. Indicating that the fans must operate at higher flow conditions to find the BEP at those lower pressure conditions. On the other hand, the atmospheric pressure condition demonstrates the peak at a lower volumetric flow rate which indicates that it reaches its highest efficiency point at a lower flow condition.

Near free delivery conditions, (1, 0.7, 0.5) atm. perform similarly in exception to 0.3 atm that is lower in producing coefficient of head. At the higher system resistances the fan outperforms at 1 atm. The 1 atm. and 0.3 atm. pressure conditions exhibit nearly identical trends; furthermore, the 0.7 atm. and 0.5 atm. also produce nearly identical trends.

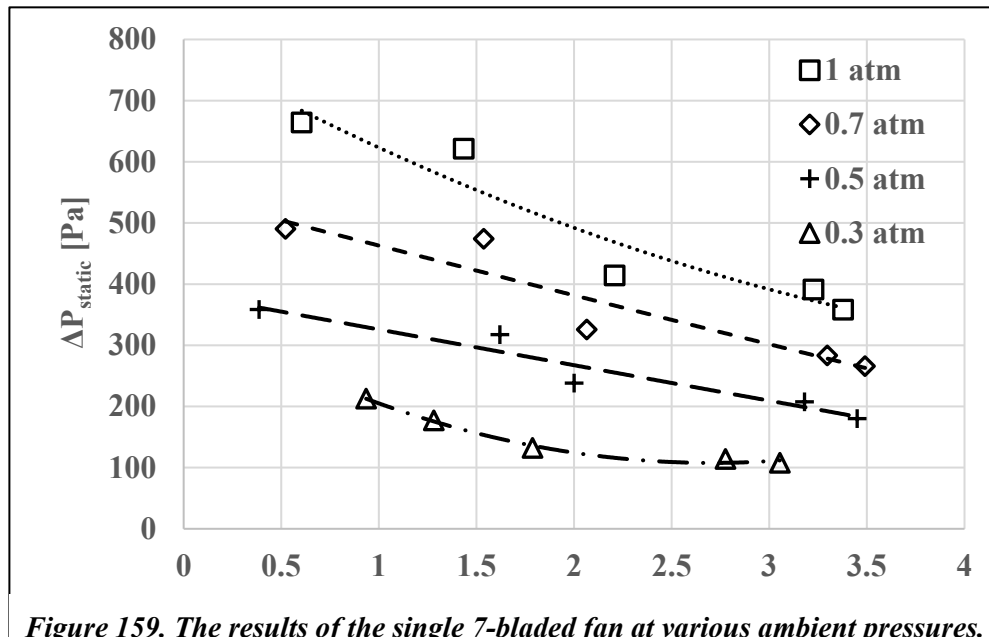


Figure 159. The results of the single 7-bladed fan at various ambient pressures.

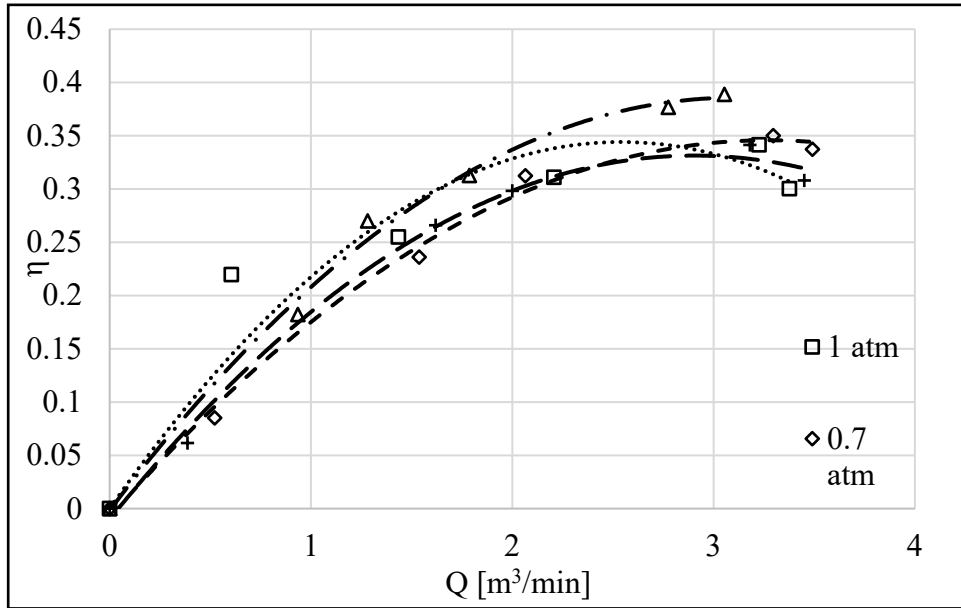


Figure 160. The nondimensional fan performance of Fan 2 at variable ambient pressures.

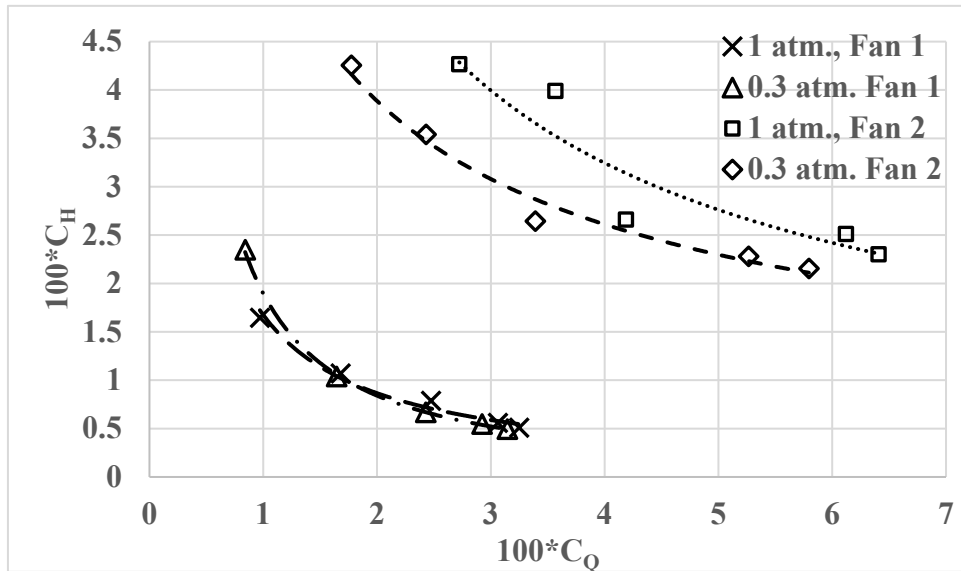


Figure 161. The fan efficiency for the Fan 2, 7-bladed fan at various ambient conditions.

In Fig. 161, the fan performance curves are compared for two extreme cases (1atm. and 0.3 atm.) of the Fan 1 and Fan 2 running at 13,000 rpm. Fan 2 performance curve clearly outshines that of Fan 1's performance. For both cases, Fan 2 has a higher volumetric flow rate even at the lowest pressure condition; moreover, it can still push more air through than Fan 1 at the atmospheric condition.

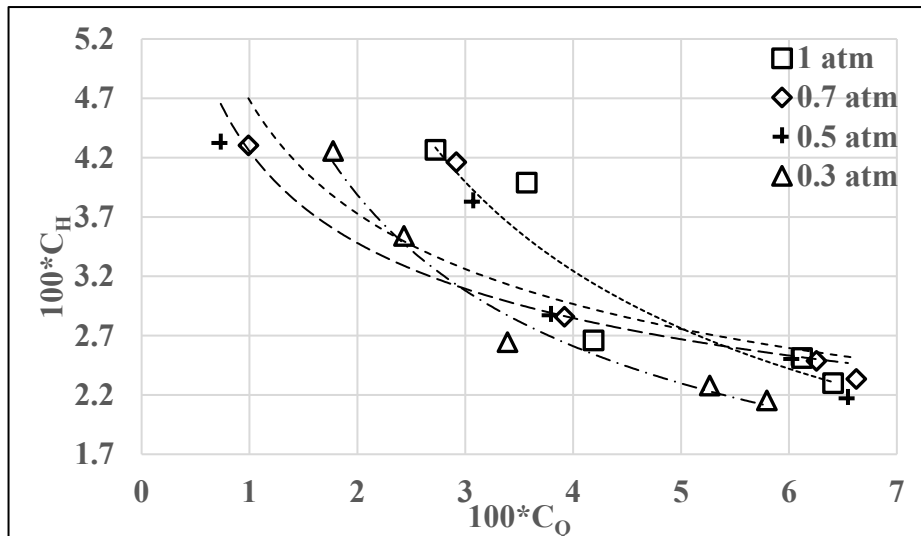


Figure 162. Compares the nondimensional fan performance curves extreme pressure conditions.

The gradient of the static pressure to flow rate is greater than the Fan 2 curves: thus, delivering lower maximum volumetric flow rates for Fan 1. For all cases, Fan 2 has a lower slope which in turn allows the performance of the fan to operate for a much large range of flow conditions. Using the nondimensional analysis Fan 2 is a higher performance fan comparatively to that of Fan 1. Fan 2 is the better choice in terms of fan performance to that of Fan 1 and airflow delivery. The results demonstrate that the fan scaling laws can be applied to Fan 1, but not to Fan 2 due to the overlap of the curves for fan 1 in Fig. 161.

The BEP of the two fans at the changing pressure conditions is determined in Fig. 162. Fan 2 demonstrates consistent efficiency across various pressure conditions. The range of efficiencies for Fan 2 is 5%. Fan 1 demonstrates a large range in BEP of 17% from the lowest to highest peak efficiencies. At the intermediate pressures (0.7 and 0.5) atm., Fan 1 has higher BEP's to that of Fan 2. The fan BEP is approximately 10% higher for Fan 1 over that of Fan 2 and does not exactly reflect that it outperforms the 7-bladed fan. The efficiency just demonstrates the fan's ability to convert electrical energy to mechanical energy. The higher BEP was determined in Fan 1 at these conditions since it does not require as much input power to drive the fan at 13,000 rpm as Fan 2. Lower electrical input power to the fan will lead to lower heat dissipated in the fan windings of the fan, which in turn, means less heat introduced to the system that would have to also be dissipated.

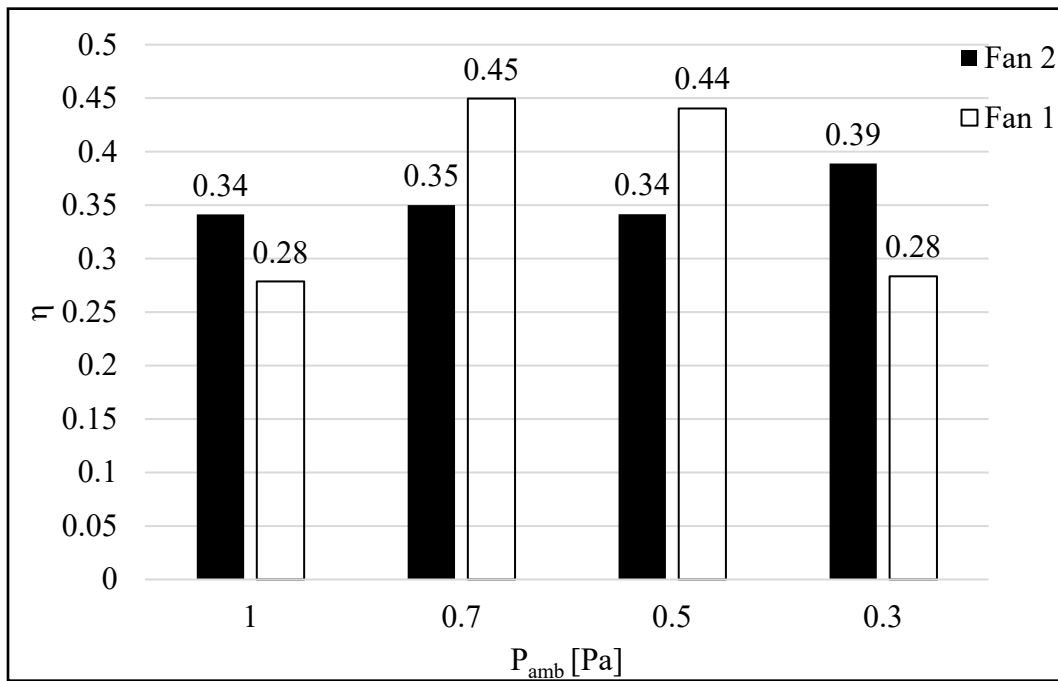


Figure 163. Fan efficiencies at various ambient pressures.

Regardless of the Fan 1 demonstrating higher efficiencies for the intermediate pressures, the inferior performance curves to that of Fan 2 does not justify its use for cooling in such a highly demanding application. The fan must be able to deliver enough forced convection to the EMA to direct the heat from the heated structure. The use of Fan 2 would be a better choice instead of Fan 1 since it can provide more air delivered to the EMA.

The Reynolds number was determined, to identify the type of flow within the system. For Fan 1, it is determined that at low-pressure conditions the flow is laminar, transitional, and turbulent since the Reynolds number ranges from $1882.7 < Re < 7040.8$. Also, for the case of 0.5 atm. for Fan 1, at low volumetric flow rates the flow goes from transitional to turbulent flow, $Re > 3254.3$. The higher ambient pressure conditions for Fan 1 demonstrate that the flow is fully turbulent. Fan 2 has a fully turbulent flow for (1, 0.7, 0.5) atm. Fan 2 nearly has a fully turbulent flow for 0.3 atm. except for the lowest volumetric flow rate determined. At the shutoff conditions of Fan 2 in 0.3 atm. of ambient pressure the flow is transitional with a Reynolds number of $Re = 3970.9$. In terms of cooling, the higher the Reynolds number indicates that the flow has regions of eddies; therefore, these pockets of eddies will provoke more mixing of the fluid and will provide better cooling for the EMA.

9 CONCLUSION

In the current work, an experimental test rig was constructed to compare fan performance curves at various ambient pressure conditions. The first set of experiments was conducted to consistently acquire the manufacturer's curve to validate the experimental setup and testing procedure. All performance curves for these fans demonstrated a strong quadratic correlation. Both fans were tested at 13,000 rpm. Fan 1 is a 2-bladed system with a slightly higher diameter but has a lower blade surface area due to its low blade count. Fan 2 is the 7-bladed fan with a slightly lowered tip-to-tip diameter, but the high blade count provides more surface area for the fluid to be driven. The performance curves and efficiencies at various pressures were determined experimentally. The fan performance curves for the fans deteriorated once the pressure within the system was lowered below atmospheric pressure. For both fans, the peak efficiencies occurred at higher volumetric flow rates. Fan 1 demonstrated higher efficiencies at (0.7, 0.5) atm. because of Fan 1 requiring lower power input to operate at that constant speed. The efficiencies in Fan 2 were consistent across all pressure conditions with peak efficiencies of 0.45 and 0.39 for Fan 1 and Fan 2, respectively. Demonstrating that a large amount of usable energy is being lost within the internal structure (i.e., mechanical and heat losses) of the fans. Finally, the higher blade counts provide higher performance curves with a loss in maximum efficiency due higher power consumptions necessary to operate the fan.

10 FUTURE WORK ON THERMAL BOX

For the future work, data collection within the thermal box was to be conducted on a cylindrical EMA simulant. The simulant was constructed of 6061 Aluminum Alloy. Experimental data of the heated simulant is to be determined at variable pressure conditions. The fans tested in the experimental loop are to be used for methods of cooling within the wing-bay configuration. Researching these cooling strategies will determine whether the fans are able to provide sufficient cooling to maintain the EMA within operating temperatures for the time that the EMA is intended to operate during take-off/landing. Furthermore, special emphasis will be analyzed under low ambient pressure conditions since the fan's flow rate is drastically reduced.

REFERENCES

- [1] Ockert P. H. Augustyn, Sybrand J. van der Spuy, and Theodor W. von Backström, "Numerical and experimental investigation into the accuracy of the fan scaling laws applied to large diameter axial flow fans," *Proceedings of the Institution of Mechanical Engineers, Part A: Journal of Power and Energy* 230 (5), 477-486 (2016);
- [2] ISO, "Measurement of fluid flow by means of pressure differential devices inserted in circular cross-section conduits running full— Part 4: Venturi tubes", (2003), Vol. ISO 5167-4:2003(E);
- [3] Wei Wu, Yeong-Ren Lin, Louis C. Chow, and Quinn Leland, "Fan Performance Characteristics at Various Rotational Speeds and Ambient Pressures", in SAE Technical Paper Series (2014).
- [4] AMETEKRotron's PROPIMAX 2
[fan/media/ametektrottron/products/digital%20library/table%20of%20contents/tubeaxial%20fans/04-26_propimax_2.pdf?la=en](http://www.ametekrottron.com/fan/media/ametektrottron/products/digital%20library/table%20of%20contents/tubeaxial%20fans/04-26_propimax_2.pdf?la=en)
- [5] Butterfly Valve - Cast Iron, International, Wafer, Bronze Disc, N200145
<http://www.nibco.com/resources/ProductSubmittalDocs/N2001BF.pdf>
- [6] VOLTEQ DC Power Supply HY3010D 30V 10A <http://www.mastechpowersupply.com/volteq-regulated-variable-dc-power-supply-hy3010d-30v-10a-new-model.html>
- [7] PASCO 850 Universal Interface – UI-5000 <https://www.pasco.com/prodCatalog/UI/UI-5000850-universal-interface/>
- [8] PASPORT Quad Pressure Sensor – PS-1264 <https://www.pasco.com/prodCatalog/PS/PS-2164-passport-quad-pressure-sensor/index.cfm>
- [9] Hobbico Digital Mini-Tach. 135-140.
- [10] Testo 405i – Hot-wire anemometer wireless Smart Probe <https://www.testo.com/en-US/testo-405i/p/0560-1405>
- [11] Fernco PVC Flexible Coupling <https://www.fernco.com/dimensional-drawings/plumbing/flexible-couplings/stock-couplings-1056/1056-44>
- [12] Corona, J. and Kwarteng, A. "Testing of a Cooling Fan for Wing-bay Electro-Mechanical Actuators." 5th *Joint US-European Fluids Engineering Division Summer Meeting*. ASME, no. FEDSM2018-83480 (2018).
- [13] Wright, Terry. 1999. *Fluid machinery: performance, analysis, and design*. Boca Raton, Florida: CRC Press.
- [14] Augustyn, Ockert P. H., Sybrand J. van der Spuy, and Theodor W. von Backström. "Numerical and Experimental Investigation into the Accuracy of the Fan Scaling Laws Applied to Large Diameter Axial Flow Fans." *Proceedings of the Institution of Mechanical Engineers, Part A: Journal of Power and Energy* 230, no. 5 (2016): 477-86.
- [15] Marchi, A. and Simpson, A.R. "Evaluating the Approximation of the Affinity Laws and Improving the Estimate of the Efficiency for Variable Speed Pumping." *Journal of Water Resources Planning and Management* 139, no. 12 (2013): 1314-17.
- [16] Koor, M., A. Vassiljev, and T. Koppel. "Optimization of Pump Efficiencies with Different Pumps Characteristics Working in Parallel Mode." *Advances in Engineering Software* 101 (2016): 69-76. (al., 2017; Koor, Vassiljev, & Koppel, 2016)
- [17] Borsting, Zhenyu Yang and Hakon. "Energy Efficient Control of a Boosting System with Multiple Variable-Speed Pumps in Parrallel." *49th IEEE Conference on Decision and Control* (December 15-17, 2010 2010).

- [18] Ivar José de Souza Filho, Adriano de Oliveira Francisco, Bruno Scarano Paterlini, Daniel Luna Ferreira da Silva, Marcello Cervini Procida Veissid, Paschoal Frederico Neto, and Ricardo Moreira Vaz. "Application Study of Electrical Fans Assemble Applied in Bus Cooling System." *SAE International 24th SAE Brasil International Congress and Display*, no. 0148-7191 (2015). (al., 2017)
- [19] Wu, Wei, Yeong-Ren Lin, Louis C. Chow, and Quinn Leland. "Fan Performance Characteristics at Various Rotational Speeds and Ambient Pressures." In *SAE Technical Paper Series*, 2014.
- [20] Wu, Wei, Yeong-Ren Lin, Louis Chow, Edmund Gyasi, John P. Kizito, and Quinn Leland. "Electromechanical Actuator Cooling Fan Blades Design and Optimization." In *SAE Technical Paper Series*, 2016.
- [21] Lin, Sheam-Chyun, Shen Ming-Chiou, Tso Hao-Ru, Yen Hung-Cheng, and Chen Yu-Cheng. "Numerical and Experimental Study on Enhancing Performance of the Stand Fan." [In English]. *Applied Sciences* 7, no. 3 (2017).
- [22] al., Barron et. "Parallel-Series Hybrid Fan Cooling Apparatus and Optimization." no. US 2017/0082112 A1 (2017).
- [23] Kabir, Rifat, Patrick McCluskey, and John P. Kizito. "Investigation of a Cooling System for a Hybrid Airplane." In 2018 AIAA/IEEE Electric Aircraft Technologies Symposium, p. 4991. 2018.
- [24] Kühnen, Jakob, Baofang Song, Davide Scarselli, Nazmi Burak Budanur, Michael Riedl, Ashley P. Willis, Marc Avila, and Björn Hof. "Destabilizing Turbulence in Pipe Flow." *Nature Physics* 14, no. 4 (2018): 386-90.
- [25] Avila, Marc, Ashley P. Willis, and BjÖRn Hof. "On the Transient Nature of Localized Pipe Flow Turbulence." *Journal of Fluid Mechanics* 646 (2010).
- [26] Kerstin Avila, David Moxey, Alberto de Lozar, Marc Avila, Dwight Barkley, Bjorn Hof. "The Onset of Turbulence in Pipe Flow." *SCIENCE* 333 (8 July, 2011 2011): 192-96.
- [27] YinQin Xu, Daniel Coxe, Yulia Peet, Taewoo Lee, . "Computational Modeling of Flow Rate Measurements Using an Orfice Flow Meter." American Society of Mechanical Engineers FEDSM2018 (2018)
- [28] White, Frank M. 1999. *Fluid mechanics*. Boston, Mass: WCB/McGraw-Hill.
- [29] Cengel, Yunus A., and John M. Cimbala. 2006. *Fluid mechanics: fundamentals and applications*. Boston: McGraw-Hill Higher Education.
- [30] ISO, "Measurement of fluid flow by means of pressure differential devices inserted in circular cross-section conduits running full— Part 4: Venturi tubes", (2003), Vol. ISO 5167-4:2003(E);
- [31] Jensen, S.C., G.D. Jenney, and D. Dawson. Flight test experience with an electromechanical actuator on the F-18 Systems Research Aircraft. in 19th DASC. 19th Digital Avionics Systems Conference. Proceedings (Cat. No.00CH37126). 2000.
- [32] Garcia, A., et al., Reliable electro-mechanical actuators in aircraft. *IEEE Aerospace and Electronic Systems Magazine*, 2008. 23(8): p. 19-25.
- [33] Fu, J., J.-C. Maré, and Y. Fu, Modelling and simulation of flight control electromechanical actuators with special focus on model architecting, multidisciplinary effects and power flows. *Chinese Journal of Aeronautics*, 2017. 30(1): p. 47-65.
- [34] Yu, X. and Y. Zhang, Design of passive fault-tolerant flight controller against actuator failures. *Chinese Journal of Aeronautics*, 2015. 28(1): p. 180-190.
- [35] Lim, D.H. and S.C. Kim, Thermal performance of oil spray cooling system for in-wheel motor in electric vehicles. *Applied Thermal Engineering*, 2014. 63(2): p. 577-587.

- [36] Davin, T., et al., Experimental study of oil cooling systems for electric motors. *Applied Thermal Engineering*, 2015. 75: p. 1-13.
- [37] Fawzal, A.S., et al., Air inlet/outlet arrangement for rotor cooling application of axial flux PM machines. *Applied Thermal Engineering*, 2018. 130: p. 1520-1529.
- [38] Kothari, D.P. and I.J. Nagrath, *Electric Machines*. 2004: Tata McGraw-Hill.
- [39] Tong, W., *Mechanical design of electric motors*. 2014, Boca Raton: CRC Press, Taylor & Francis Group. xxxiii, 702 pages illustrations.
- [40] Wang, S., et al., Transient cooling effect analyses for a permanent-magnet synchronous motor with phase-change-material packaging. *Applied Thermal Engineering*, 2016. 109: p. 251-260.
- [41] Sun, Y., et al., Applicability study of the potting material based thermal management strategy for permanent magnet synchronous motors. *Applied Thermal Engineering*, 2019. 149: p. 1370-1378.
- [42] Hughes, A. and W. Drury, *Electric Motors and Drives: Fundamentals, Types and Applications*. 2013: Elsevier Science.
- [44] Kizito, John, and Md Monir Hossain. "Experimental study of thermal performance of a flat loop heat pipe." *Frontiers in Heat Pipes (FHP)* 6.1 (2015).
- [45] Faghri, Amir. "Heat pipes: review, opportunities and challenges." *Frontiers in Heat Pipes (FHP)* 5.1 (2014).
- [46] Cotter, T. P. Theory of heat pipes. No. LA-3246. Los Alamos Scientific Lab., Univ. of California, N. Mex., 1965.
- [47] Swanson, Theodore D. "Thermal control technologies for complex spacecraft." (2004).
- [48] Gaugler, Richard S. "Heat transfer device." U.S. Patent No. 2,350,348. 6 Jun. 1944.
- [49] Nemeč, Patrik, Alexander Caja, and Milan Malcho. "Thermal performance measurement of heat pipe." *Global journal of technology and optimization* 2.1 (2011).
- [50] Reay, David, Ryan McGlen, and Peter Kew. *Heat pipes: theory, design and applications*. Butterworth-Heinemann, 2013.
- [51] Bejan, Adrian, and Allan D. Kraus. *Heat transfer handbook*. Vol. 1. John Wiley & Sons, 2003.
- [52] Wong, Shwin-Chung, and Yi-Huan Kao. "Visualization and performance measurement of operating mesh-wicked heat pipes." *International Journal of Heat and Mass Transfer* 51.17-18 (2008): 4249-4259.
- [53] Kempers, R., D. Ewing, and C. Y. Ching. "Effect of number of mesh layers and fluid loading on the performance of screen mesh wicked heat pipes." *Applied Thermal Engineering* 26.5-6 (2006): 589-595.
- [54] Faghri, Amir. *Heat pipe science and technology*. Global Digital Press, 1995.
- [55] Faghri, Amir, and S. Thomas. "Performance characteristics of a concentric annular heat pipe: Part I—Experimental prediction and analysis of the capillary limit." *Journal of heat transfer* 111.4 (1989): 844-850.
- [56] Marcus, Bruce David. "Theory and design of variable conductance heat pipes." (1972).
- [57] Kozai, Hiroaki, Hideaki Imura, and Yuji Ikeda. "The permeability of screen wicks." *JSME international journal. Ser. 2, Fluids engineering, heat transfer, power, combustion, thermophysical properties* 34.2 (1991): 212-219.
- [58] Mwaba, Misheck G., Xiao Huang, and Junjie Gu. "Influence of wick characteristics on heat pipe performance." *International journal of energy research* 30.7 (2006): 489-499.

- [59] Davis, Joseph R., ed. Copper and copper alloys. ASM international, 2001.
- [60] Kabir, Rifat, Kaddoura, Kamal, Patrick McCluskey, and John P. Kizito. "Investigation of a Cooling System for a Hybrid Airplane." 2018 AIAA/IEEE Electric Aircraft Technologies Symposium. 2018.
- [61] Modak, Y.A. (2016). CFD Analysis of vapor chamber with micro pillars as heat spreader for high power electronic devices. (Master's Thesis, University of Texas at Arlington).
- [62] Khairnasov, S., & Naumova, A. (2015). Heat pipes application in electronics thermal control systems. *Frontiers in Heat Pipes (FHP)*, 6(1).
- [63] Bodla, K. K., Murthy, J. Y., & Garimella, S. V. (2012). Direct simulation of thermal transport through sintered wick microstructures. *Journal of heat transfer*, 134(1), 012602.
- [64] Faghri, A. (2014). Heat pipes: review, opportunities and challenges. *Frontiers in Heat Pipes (FHP)*, 5(1).
- [65] Jung, S. M., Preston, D. J., Jung, H. Y., Deng, Z., Wang, E. N., & Kong, J. (2016). Porous Cu nanowire aerospunges from one-step assembly and their applications in heat dissipation. *Advanced Materials*, 28(7), 1413-1419.
- [66] Iverson, B. D., Davis, T. W., Garimella, S. V., North, M. T., & Kang, S. S. (2007). Heat and mass transport in heat pipe wick structures. *Journal of Thermophysics and Heat Transfer*, 21(2), 392-404.
- [67] Lin, Y. J., & Hwang, K. S. (2009). Effects of powder shape and processing parameters on heat dissipation of heat pipes with sintered porous wicks. *Materials transactions*, 50(10), 2427-2434.
- [68] Vafai, K. (Ed.). (2015). *Handbook of porous media*. Crc Press.
- [69] Kostornov, A. G., Moroz, A. L., Shapoval, A. A., Kabov, O., Strizhak, P., & Legros, J. C. (2015). Composite structures with gradient of permeability to be used in heat pipes under microgravity. *Acta Astronautica*, 115, 52-57
- [70] Jo, H. S., An, S., Nguyen, X. H., Kim, Y. I., Bang, B. H., James, S. C., ... & Yoon, S. S. (2018). Modifying capillary pressure and boiling regime of micro-porous wicks textured with graphene oxide. *Applied Thermal Engineering*, 128, 1605-1610.
- [71] Faghri, A. (1995). *Heat pipe science and technology*. Global Digital Press.
- [72] H.S. Jo, S. An, H.G. Park, M.-W. Kim, S.S. Al-Deyab, S.C. James, J. Choi, S.S. Yoon (2017). Enhancement of critical heat flux and superheat through controlled wettability of cuprous-oxide fractal-like Nano textured surfaces in pool boiling, *Int. J. Heat Mass Transfer* 107 105–111
- [73] Lin, Y. J., & Hwang, K. S. (2010). Swelling of copper powders during sintering of heat pipes in hydrogen-containing atmospheres. *Materials transactions*, 51(12), 2251-2258
- [74] Leong, K. C., Liu, C. Y., & Lu, G. Q. (1997). Characterization of sintered copper wicks used in heat pipes. *Journal of Porous Materials*, 4(4), 303-308.
- [75] Li, Z., Wu, Y., Zhuang, B., Zhao, X., Tang, Y., Ding, X., & Chen, K. (2017). Preparation of novel copper-powder-sintered frame/paraffin form-stable phase change materials with extremely high thermal conductivity. *Applied Energy*, 206, 1147-1157.
- [76] Udell, K. S. (1985). Heat transfer in porous media considering phase change and capillarity—the heat pipe effect. *International Journal of Heat and Mass Transfer*, 28(2), 485-495.
- [77] Reay, D., McGlen, R., & Kew, P. (2013). *Heat pipes: theory, design and applications*. Butterworth-Heinemann.
- [78] Vasiliev, L. L. (2008). Micro and miniature heat pipes—Electronic component coolers. *Applied Thermal Engineering*, 28(4), 266-273.

- [79] Wang, B., Hong, Y., Hou, X., Xu, Z., Wang, P., Fang, X., & Ruan, X. (2015). Numerical configuration design and investigation of heat transfer enhancement in pipes filled with gradient porous materials. *Energy Conversion and Management*, 105, 206-215.
- [80] Ling, W., Zhou, W., Liu, R., Qiu, Q., & Ke, Y. (2017). Operational characteristics of loop heat pipes with porous copper fiber sintered sheet as wick. *Applied Thermal Engineering*, 122, 398-408.
- [81] Ji, X., Li, H., Xu, J., & Huang, Y. (2017). Integrated flat heat pipe with a porous network wick for high-heat-flux electronic devices. *Experimental Thermal and Fluid Science*, 85, 119-131.
- [82] Ingham, D. B., & Pop, I. (1998). *Transport phenomena in porous media*. Elsevier.
- [83] Nield, D. A., Bejan, A., & Nield-Bejan... (2006). *Convection in porous media (Vol. 3)*. New York: Springer.
- [84] Chen, X., Ye, H., Fan, X., Ren, T., & Zhang, G. (2016). A review of small heat pipes for electronics. *Applied Thermal Engineering*, 96, 1-17.
- [85] De Schampheleire, S., De Kerpel, K., Deruyter, T., De Jaeger, P., & De Paepe, M. (2015). Experimental study of small diameter fibres as wick material for capillary-driven heat pipes. *Applied Thermal Engineering*, 78, 258-267.
- [86] Yao, S., Lei, L., Deng, J. W., Lu, S., & Zhang, W. (2015). Heat transfer mechanism in porous copper foam wick heat pipes using nanofluids. *International journal of heat and technology*, 33(3), 133-138.
- [87] Li, X. B., Tang, Y., Li, Y., Zhou, S. Z., & Zeng, Z. X. (2010). Sintering technology for micro heat pipe with sintered wick. *Journal of Central South University of Technology*, 17(1), 102-109.
- [88] Wang, Y., Cen, J., Jiang, F., Cao, W., & Guo, J. (2016). LHP heat transfer performance: A comparison study about sintered copper powder wick and copper mesh wick. *Applied Thermal Engineering*, 92, 104-110.
- [89] Atabaki, N., & Baliga, B. R. (2007). Effective thermal conductivity of water-saturated sintered powder-metal plates. *Heat and Mass Transfer*, 44(1), 85-99.
- [90] Mantle, W. J., & Chang, W. S. (1991). Effective thermal conductivity of sintered metal fibers. *Journal of thermophysics and heat transfer*, 5(4), 545-549.

- [91] Kizito, J., & Hossain, M. M. (2015). Experimental study of thermal performance of a flat loop heat pipe. *Frontiers in Heat Pipes (FHP)*, 6(1).
- [92] Dominguez Espinosa, F. A., Peters, T. B. and Brisson, J. G., (2012), "Effect of Fabrication Parameters on the Thermophysical Properties of Sintered Wicks for Heat Pipe Applications," *International Journal of Heat and Mass Transfer*, 55(25–26), 7471-7486.
- [93] Pruzan, D. A., Klingensmith, L. K., Torrance, K. E., & Avedisian, C. T. (1991). Design of high-performance sintered-wick heat pipes. *International journal of heat and mass transfer*, 34(6), 1417-1427.
- [94] Early, J. G., Lenel, F. V., & Ansell, G. S. (1963). The material transport mechanism during sintering of copper powder compacts at high temperatures (No. TID-20324). Rensselaer Polytechnic Inst., Troy, NY
- [95] Li, H., Liu, Z., Chen, B., Liu, W., Li, C., & Yang, J. (2012). Development of biporous wicks for flat-plate loop heat pipe. *Experimental Thermal and Fluid Science*, 37, 91-97.
- [96] Tang, H., Tang, Y., Wan, Z., Li, J., Yuan, W., Lu, L. & Tang, K. (2018). Review of applications and developments of ultra-thin micro heat pipes for electronic cooling. *Applied Energy*, 223, 383-400.
- [97] Zhong, G., Ding, X., Tang, Y., Yu, S., Chen, G., Tang, H., & Li, Z. (2018). Various orientations research on thermal performance of novel multi-branch heat pipes with different sintered wicks. *Energy Conversion and Management*, 166, 512-521.
- [98] Tang Y, Tang H, Li J, Zhang S, Zhuang B, Sun Y. (2017) Experimental investigation of capillary force in a novel sintered copper mesh wick for ultra-thin heat pipes. *Appl Therm Eng*; 115: 1020–30.
- [99] Zhou, W., Xie, P., Li, Y., Yan, Y., & Li, B. (2017). Thermal performance of ultra-thin flattened heat pipes. *Applied Thermal Engineering*, 117, 773-781.
- [100] Tang, Y., Deng, D., Huang, G., Wan, Z., & Lu, L. (2013). Effect of fabrication parameters on capillary performance of composite wicks for two-phase heat transfer devices. *Energy conversion and management*, 66, 66-76.
- [101] Qu, Y., Zhou, K., Zhang, K. F., & Tian, Y. (2016). Effects of multiple sintering parameters on the thermal performance of bi-porous nickel wicks in Loop Heat Pipes. *International Journal of Heat and Mass Transfer*, 99, 638-646.
- [102] Ling, W., Zhou, W., Yu, W., & Chu, X. (2018). Capillary pumping performance of porous copper fiber sintered wicks for loop heat pipes. *Applied Thermal Engineering*, 129, 1582-1594

- [103] Mwaba, M. G., Huang, X., & Gu, J. (2006). Influence of wick characteristics on heat pipe performance. *International journal of energy research*, 30(7), 489-499.
- [104] Grissa, Kods, Adel M. Benselama, Zied Lataoui, Yves Bertin, and Abdelmajid Jemni. "Investigations of the thermal performance of a cylindrical wicked heat pipe." *International Journal of Energy Research* (2018).
- [105] Brahim, T., & Jemni, A. (2014). Effect of the heat pipe adiabatic region. *Journal of heat transfer*, 136(4), 042901.
- [106] Jensen, S.C., G.D. Jenney, and D. Dawson. Flight test experience with an electromechanical actuator on the F-18 Systems Research Aircraft. in 19th DASC. 19th Digital Avionics Systems Conference. Proceedings (Cat. No.00CH37126). 2000.
- [107] Garcia, A., et al., *Reliable electro-mechanical actuators in aircraft*. IEEE Aerospace and Electronic Systems Magazine, 2008. 23(8): p. 19-25.
- [108] Wang, Huawei, et al. "An integrated heat pipe coupling the vapor chamber and two cylindrical heat pipes with high anti-gravity thermal performance." *Applied Thermal Engineering* 159 (2019): 113816.
- [109] M. Arik, J. Petroski, S. Weaver, Thermal challenges in the future generation solid-state lighting applications: Light emitting diodes, in: Conference on Thermal & Thermomechanical Phenomena in Electronic Systems, 2002.
- [110] Zhirnov, Victor V., et al. "Limits to binary logic switch scaling-a gedanken model." *Proceedings of the IEEE* 91.11 (2003): 1934-1939.
- [111] L. Zhu, H. Tan, J. Yu, Analysis on optimal heat exchanger size of thermoelectric cooler for electronic cooling applications, *Energy Convers. Manage.* 76 (2013)685–690.
- [112] Corona, J. J., et al. "Testing of a Cooling Fan for Wing-Bay Electro-Mechanical Actuators." ASME 2018 5th Joint US-European Fluids Engineering Division Summer Meeting. American Society of Mechanical Engineers Digital Collection, 2018.
- [113] Putra, Nandy, and Bambang Ariantara. "Electric motor thermal management system using L-shaped flat heat pipes." *Applied Thermal Engineering* 126 (2017): 1156-1163.
- [114] T. Davin, J. Pellé, S. Harmand, R. Yu Experimental study of oil cooling systems for electric motors *Appl. Therm. Eng.*, 75 (2015), pp. 1-13.

- [115] Lee, Kea-Ho, Hyun-Rok Cha, and Young-Bae Kim. "Development of an interior permanent magnet motor through rotor cooling for electric vehicles." *Applied Thermal Engineering* 95 (2016): 348-356.
- [116] Faghri, Amir. "Heat pipes: review, opportunities and challenges." *Frontiers in Heat Pipes (FHP)* 5.1 (2014).
- [117] Kabir, Rifat, et al. "Investigation of a Cooling System for A Hybrid Airplane." 2018 AIAA/IEEE Electric Aircraft Technologies Symposium. 2018.
- [118] Chen, Xianping, et al. "A review of small heat pipes for electronics." *Applied Thermal Engineering* 96 (2016): 1-17.
- [119] K. Kaddoura, Abosti, O.Y.W., and J.P. Kizito, EFFECT OF SCREEN LAYERS AND ORIENTATIONS ON MESH WICKED HEAT PIPES, in *Proceedings of the 18th Annual Early Career Technical Conference*. 2018, School of Engineering, University of Alabama Birmingham: Birmingham, Alabama.
- [120] Putra, Nandy, and Wayan Nata Septiadi. "Improvement of heat pipe performance through integration of a coral biomaterial wick structure into the heat pipe of a CPU cooling system." *Heat and Mass Transfer* 53.4 (2017): 1163-1174.
- [121] Putra, Nandy, et al. "Thermal performance of biomaterial wick loop heat pipes with water-base Al₂O₃ nanofluids." *International Journal of Thermal Sciences* 76 (2014): 128-136.
- [122] Putra, Nandy, et al. "Thermal performance of screen mesh wick heat pipes with nanofluids." *Experimental thermal and fluid science* 40 (2012): 10-17.
- [123] Akuoko Kwarteng, A., et al., Thermal management of Electromechanical Actuator Motor by circulating air inside the housing, in *International Mechanical Engineering Congress and Exposition*. 2019, ASME: Salt Lake City, Utah.
- [124] Abosti, O.Y.W., K. Kaddoura, and J.P. Kizito, *Performance of Gravity Independent Heat pipe*, in *Proceedings of the 18th Annual Early Career Technical Conference*. 2018, School of Engineering, University of Alabama Birmingham: Birmingham, Alabama. p. 3-10.

APPENDIX A

Proceedings of the ASME 2018 5th Joint US-European Fluids Engineering Summer Conference
July 15-20, 2018, Montreal, Quebec, Canada
FEDSM2018-83480

TESTING OF A COOLING FAN FOR WING-BAY ELECTRO-MECHANICAL ACTUATORS

J. J. Corona Jr.^a, A. A. Kwarteng^a, G. Warwick^a, K. Kaddoura^a, O. Mesalhy^{b,c}, Q.H. Leland^d,
L.C. Chow^b, J.P. Kizito^{a*},

^aDepartment of Mechanical Engineering, North Carolina Agricultural and Technological State University, Greensboro, NC 27411, USA

^bDepartment of Mechanical and Aerospace Engineering, University of Central Florida, Orlando, FL 32816, USA

^cDepartment of Mechanical Power Engineering, Zagazig University, Zagazig, 44159 Egypt

^dPower and Control Division, Aerospace Systems Directorate, Air Force Research Laboratory, Wright-Patterson AFB, OH 45433

*Email: jpkizito@ncat.edu

Abstract

The scope of the work is to develop a cooling system which uses wing-bay air to cool the Electro-Mechanical Actuators (EMA). The wing-bay is enclosed. The system will operate between 20% and 100% of atmospheric pressure. Using high speed fans as a means of cooling the EMAs it is important to understand the characteristics of the fan. The study also closely observed the results obtained experimentally with that of the fan scaling analysis. The fan laws can be derived from dimensionless analysis of volumetric flow rate, static pressure, and power equations. Considering the current experimental data, the fan scaling laws can be used to verify the proper nature of the fan curves when using a certain measurement at the baseline. In this study, the results have been verified for various rotational speeds and ambient pressure conditions. Consequently, there are two fans that have been tested within the loop. The first fan is a 2 bladed fan whereas the other fan has a 12 bladed propeller. The fan performance curves will determine the cooling capacities of each and provide a means to compare geometrically different fans.

Key Words: fan performance, low pressure testing, fan curves, Electro-mechanical Actuators (EMA), Calibration, Scaling, Fan Curves.

INTRODUCTION

This current submission covers the progress of the study and results obtained so far. We are developing methods to cool both the EMA electric machines together with their power electronics. Our collaboration between NCAT and UCF uses CFD and experimental methods to accomplish the specific tasks set forth in the project. The scaling laws express the relationship between the fan static pressure head, volume flow rate, air density, rotational speed, fan diameter, and power. The fans were characterized using the following equations [3]:

Volumetric flow rate:

$$Q = k_q n d^3 \dots \dots \dots (1)$$

Static pressure head:

$$p = k_p \rho n^2 d^2 \dots \dots \dots (2)$$

Power:

$$P = k_p \rho n^3 d^5 \dots \dots \dots (3)$$

where

k: constants for geometrically and dynamically similar conditions

n: fan speed (rpm)

d: fan diameter

ρ: air density

Using these conditions, it is possible to determine another fan condition compared to that of a baseline.

The fan scaling laws are derived in the following manner [3]:

$$Q_2 = Q_1 \frac{n_2}{n_1} \dots \dots \dots (4)$$

$$p_2 = p_1 \left(\frac{n_2}{n_1} \right)^2 \dots \dots \dots (5)$$

$$P_2 = P_1 \left(\frac{n_2}{n_1} \right)^3 \dots \dots \dots (6)$$

where the only variable changing is the fan speed and the diameter of the fan and density is held constant. Consequently, the fan scaling laws can be obtained for varying the density while keeping the fan diameter and fan speed at a constant:

$$Q_2 = Q_1 \dots \dots \dots (7)$$

$$p_2 = p_1 \frac{\rho_2}{\rho_1} \dots \dots \dots (8)$$

$$P_2 = P_1 \frac{\rho_2}{\rho_1} \dots \dots \dots (9)$$

The equations for determining the scaled volume flow rate (4), (7); scaled static pressure head (5), (8); and for scaled fan power (6), (9), are presented above with their corresponding parameters held either constant or variable. Similarly, from Ockert, et al., the equations for the fan scaling laws were derived identically [1].

CONSTRUCTION AND EXPERIMENTAL SETUP

The loop was built using piping with 4” inner diameter (ID) and 4.5” outer diameter (OD) also known as Schedule 40 PVC. The joints used are cast plastic by the company Fernco [11]. To regulate the resistance of the system, a control valve was placed into the loop. The control valve used is the NIBCO butterfly valve with two flanges surrounding the valve. The hardware used to maintain the joints and the flanges to prevent the leakage of the system. Figure 1 shows the current configuration of the system. The joints are the black components of the system, and the butterfly valve can be seen in the bottom of the loop in blue. Venturi flow meter was positioned within the loop as shown in a red box.



Figure 1. Flow loop based.

The current test fan in the placed into the loop was an AMETEK PROPIMAX 2 [4] with an optimized fan speed of 18,400 RPM. There was a great deal of machining involved to imbed the fan into the clear tube. The material of the clear tube is Butyrate (from Busada) which managed to withstand the vacuum needed for this experiment. Figure 2 shows how the fan was inserted into the butyrate tube.



Figure 2. The fan and butyrate clear tube assembly.

To achieve the various fan speeds, the fan is directly connected to a power supply. The voltage is then regulated to either increase or decrease the speed of the fan. The power supply used is the VOLTEQ DC Power Supply [6], shown in Figure 3.



Figure 3. DC Power supply

After assembly, the loop was held under vacuum to simulate conditions at the high altitudes. The vacuum pump was tested multiple times, and with the current configuration, the pump could lower the pressure in the loop to 17950 Pa (which is approximately 20% of atmospheric pressure). The

results shown in Figure 4 show the effectiveness of the vacuum pump to lower the pressure to 17950 Pa. Figure 5 shows the vacuum used in the experiment. The loop was tested for pressure leaks. Figure 6 shows the ability of the loop to maintain pressure after the pump has been turned OFF.

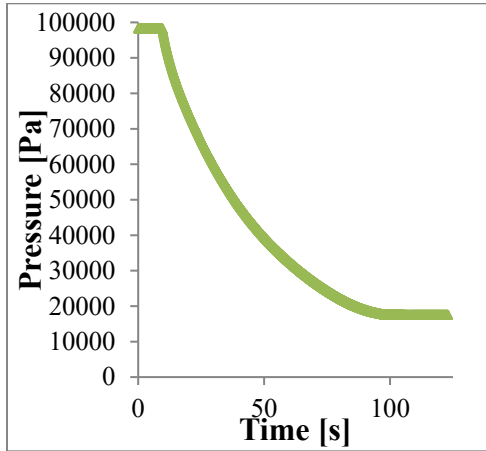


Figure 4. Data of the pressure in the loop after 123 seconds with the vacuum pump ON



Figure 5. The vacuum pump used in the loop.

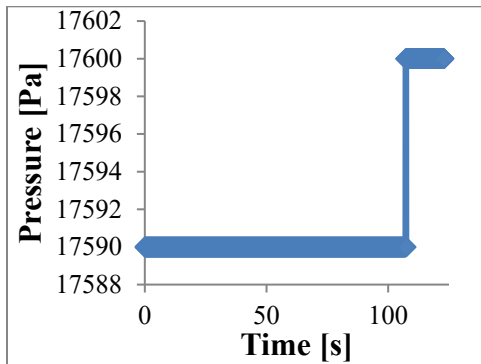


Figure 6. Loop's capacity to keep the Vacuum once the vacuum pump is turned OFF

The pressure measurements were attained with the use of PASCO instruments. The PASCO devices used in the experiment are: 850 Universal Interface [7], PS-2164 Quad Pressure Sensor [8], and PASCO's Capstone software. Figures 7 and 8 show the PASCO Interface and the PASCO pressure sensor respectively.



Figure 7. The PASCO 850 Universal Interface.



Figure 8. The PASCO Quad Pressure Sensor.

To measure volumetric flow rate of the air within the loop, a Venturi meter was machined to measure the pressure drop across two set points. In doing so, we can calculate the air velocity generated by the fan. The Venturi meter machined was based upon the ISO-5167-4 [2]. The Venturi meter was positioned within the loop as shown by red box in the Figure 1. In Figure 9, a CAD was developed to represent the Venturi used in the loop to determine the volumetric flow rate within the test rig.

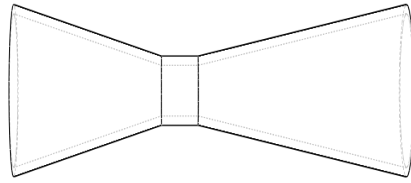


Figure 9. The CAD Design of the Venturi meter used in the test loop.

The measured flow velocity was compared with a single point velocity probe using hot wire anemometer, Testo 405i [10]. Both the probe and Venturi were exposed to the same fan speed.

The Testo 405i was used to get the fluid's velocity at the center of the clear tube; since this is the point where the velocity of the probe will equal that of twice the Venturi's measured velocity. This device is a hot-wire anemometer that has the capacity of determine the fluid velocity by detecting a temperature difference between the passing fluid and the heated wire. Testo claims that their devices are reliable and calibrated to achieve the fluid velocity measurement. The experiments operating range was well within the probe's range. The device was placed behind the tube as shown Figure 10, and the following figure shows the results obtained with this device.



Figure 10. Measurement of the air velocity using the probe (red box).

To obtain a measurement with closer agreement with the device and Venturi meter, a flow straightener was necessary. Figure 11 shows the flow straightener used in the experiment from Sioux Chief Mfg.



Figure 11. The flow straightener used.

CALIBRATION OF VENTURIMETER

The data shows the velocity based on this probe is $V_p = (10.07 \pm 0.09)$ m/s. The data associated with the figure above was taken for a total of 150 seconds. Thus, the Venturi meter can be calibrated. After several test runs under the same conditions, the probe's data and the Venturi meter data demonstrated consistency. Figure 12 demonstrates both velocity measuring devices and their corresponding data sets.

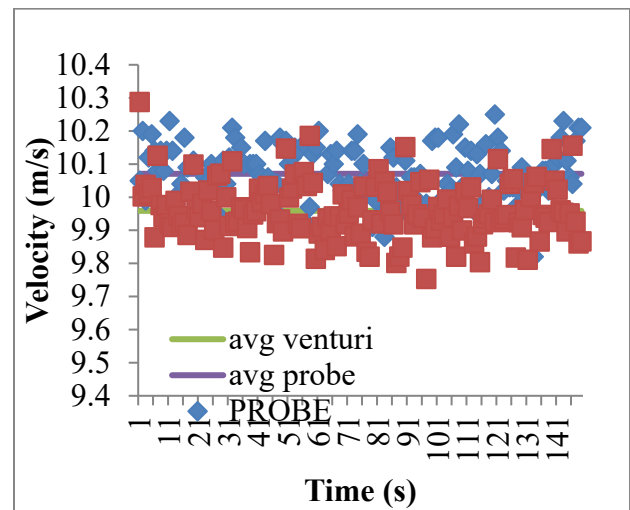


Figure 12. Calibration of the Venturi flowmeter.

RESULTS AND DISCUSSIONS

The fan tested in the loop has delivered results at two fan speeds: 20,000 and 15,000 rpm. Figure 13 shows the data of fan curve attained at atmospheric

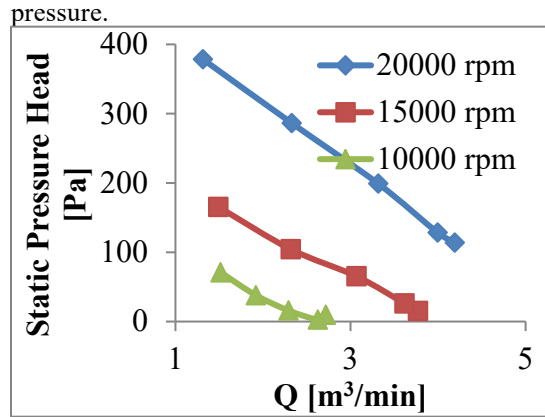


Figure 13. Fan Curves at 0.97 atm

Figure 14 uses the results obtained from the previous figure to prove the accuracy of fan scaling at variable rotational speeds. The baseline fan speed chosen was 20,000 rpm; consequently, the 15,000-rpm fan curve was scaled accordingly. With the use of the fan scaling laws [3] the fan curve for 15,000 rpm was altered. The static pressure at 15,000 rpm was decreased by a factor of 1.33^2 and the volumetric flow rate was also decreased by 1.33 ($20,000/15,000 = 1.33$). The scaling was also performed for the 10,000 rpm and the following factors were used for the static pressure head and volume flow rate, respectively 2^2 and 2 ($20,000/10,000 = 2$). From Figure 14, the scaling laws show validity at 15,000 rpm, but lack consistency when trying to approximate the behavior at 10,000 rpm.

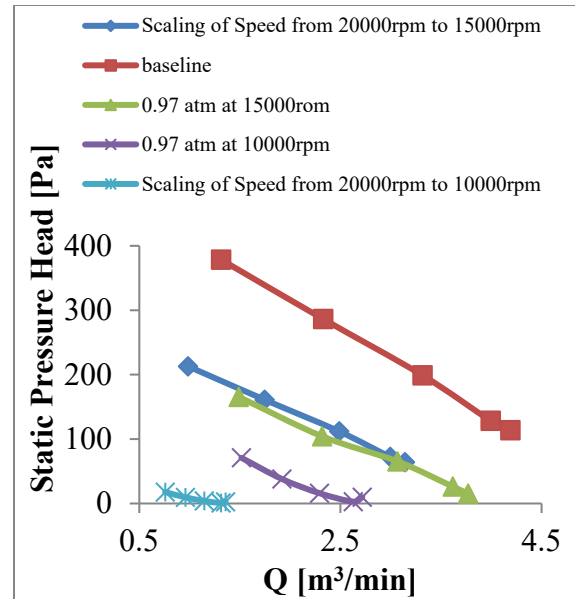


Figure 14. Fan Curves demonstrating fan scaling laws with variable fan speed.

These two rotational speeds have been tested at two other pressures within the test loop. There have been various experiments conducted at 0.7 atm. and 0.5 atm. The power supply has allowed for the adjustment of the voltage, which affect the rotational speeds of the fan throughout these experiments. To increase the resistance of the system, the butterfly valve was gradually closed; thus, the fan curves were obtained (the butterfly valve was closed at five intermittent points: 9, 7, 5, 3, 1 which are labeled).

Further experiments were conducted to test the fan at different pressures. Figure 15 shows the fan curves at 0.97 atm., 0.7 atm., and 0.5 atm. These experiments were carried out to determine the scaling laws of the fan under varying ambient pressures. The flow rate was not adjusted since it is independent of pressure as shown in equation (7). The static pressure was scaled with the use of equation (8) and is the ratio of densities. For the scaling of 0.97 atm. to 0.7 atm. the factor is $(0.8903/1.1486 = 0.7751)$. Consequently, a similar analysis was conducted for determining the scaling of the fan to 0.5 atm., which resulted in the following density ratio $(0.6798/1.1486 = 0.5918)$. The only parameter being changed under these conditions was the pressure within the loop; furthermore, the rotational speed of the fan was held

constant at 20,000 rpm. Figure 16 has the results of the scaling, and the curves demonstrate the use of the scaling laws for density at 0.5 atm. and 0.7atm.

It is evident that the scaled fan curve will follow the behavior of the baseline curve chosen. Moreover, pressure did not scale as expected using the equations presented above. Further testing should be conducted to make a conclusion on this behavior.

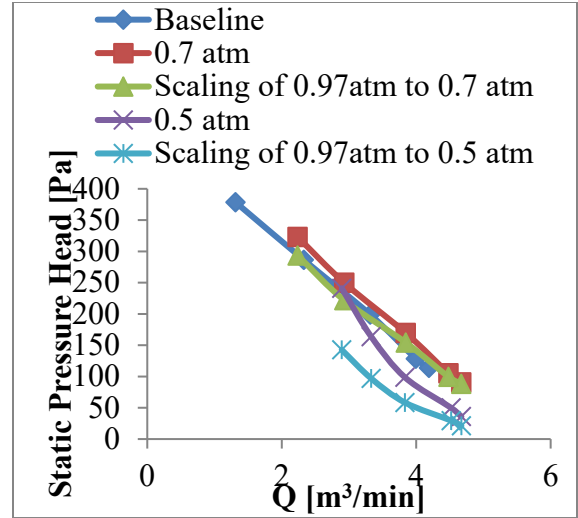


Figure 16. Fan curves scaled with the variable ambient pressure under three different conditions with constant fan speed.

Pressure [atm.]	Power [W]	Scaled Power [W]	Scaling Factor
0.9	5.6	n/a	Baseline
0.7	3.04	19.8	0.77
0.5	0.48	15.1	0.59

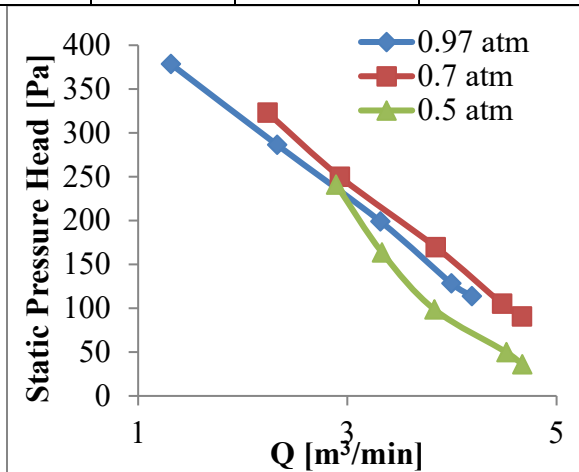


Figure 15. Fan Curves at various ambient pressure conditions with constant fan speed

Table 1 shows the data of power consumed by the fan along with the scaling of the fan speed as the variable parameter. The power consumption of the fan is provided in detail based upon the various pressures inside the test loop. Taking the fan speed of 20,000 rpm and atmospheric pressure as the baseline fan curve, the scaling laws [3] can be used again to approximate the power consumption and compare that the actual power consumption. The fan scaling shows that the power consumption is reduced by the factors shown below. Equation (6) shows the factor is raised to the third power.

Table 1. The fan scaling analysis with varying the pressures and constant fan speed.

The scaling was performed in a comparable manner to that of the fans speed and pressure

scaling presented earlier. The fan is kept at a constant speed of 20,000 rpm to perform the analysis. Table 2 shows how the scaling and the actual power consumptions behave under various ambient pressures.

Table 2. The fan scaling of the power consumption with varying fan speed and constant pressure.

The factors were used to scale the power accordingly, since it is just the density ratio. The discrepancy in the power consumption can be due to the fan specifications since this fan is optimized to work at 18,400 rpm under an atmospheric pressure of 1 atm. Due to our environmental conditions, the atmosphere in the lab was 0.97 atm. In experimental procedures other factors can play a role in this calculation as well, such as mechanical deficiencies in the fan (i.e., bearings and electric motor loss) [3]. The fan scaling laws show closer proximity to the actual conditions for the varying fan speeds, but do not show the same level of accuracy for the changes in pressure.

A different fan was then used for further testing. A 12-bladed fan by Freewing was tested to compare the results obtained by the 2-bladed AMETEK fan. The following figure shows the fan performance curves for the two different fans.

In figure 17, we can see that the Freewing 12-bladed fan does not behave as the AMETEK fan. There have been numerous tests conducted on the 12-bladed fan. The trend discussed here is still under further investigation to determine what is physically happening in the test rig.

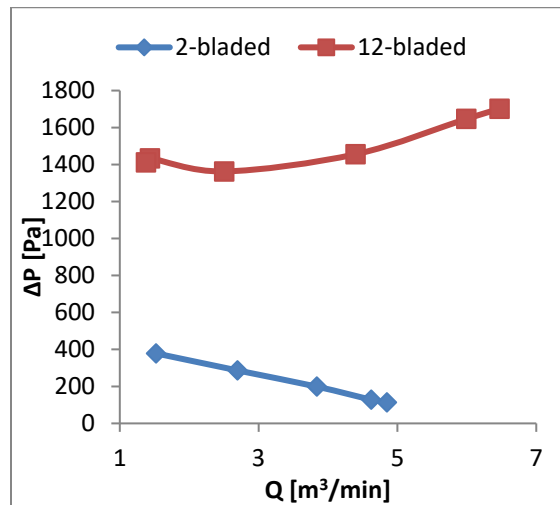


Figure 17: Comparison of the two geometrically different fans

CONCLUSION

Fan Speed [rpm]	Power [W]	Scaled Power [W]	Scaling Factor
200	25.6	n/a	Baseline
150	10.68	10.8	0.4
100	3.39	3.2	0.1

The AMETEK PROPIMAX 2 fan has been tested for three ambient pressures of 0.97 atm., 0.7 atm., and 0.5 atm. Under these varying conditions, the fan performance curve has been determined for two fan speeds 20,000 rpm and 15,000 rpm. These fan scaling laws have been proven to accurately determine the curve using 20,000 rpm as the baseline fan curve. The experimental data and the scaling laws have been verified to show the proper nature of the fan curve when varying the fan speed and holding the pressure, and fan diameter constant. The scaling analysis for the varying pressures and constant fan speed and fan diameter does not show the same level of fidelity. Further tests will be conducted to obtain fan performance curves at 0.17 atm. for the current fan. Also, the tests that have been discussed thus far will be conducted with a completely different fan to test the scaling laws further.

Acknowledgements and Disclaimers

"This material is based on research sponsored by the United States Air Force under agreement number FA8650-17-2-2226. The U.S. Government is authorized to reproduce and distribute reprints for Governmental purposes notwithstanding any copyright notation thereon."

"The views and conclusions contained herein are those of the authors and should not be interpreted as FA8650-17-2-2230 necessarily representing the official policies or endorsements, either expressed or implied, of the United States Air Force or the U.S. Government."

- 1 Ockert P. H. Augustyn, Sybrand J. van der Spuy, and Theodor W. von Backström, "Numerical and experimental investigation into the accuracy of the fan scaling laws applied to large diameter axial flow fans," Proceedings of the Institution of Mechanical Engineers, Part A: Journal of Power and Energy 230 (5), 477-486 (2016);
- 2 ISO, "Measurement of fluid flow by means of pressure differential devices inserted in circular cross-section conduits running full—Part 4: Venturi tubes", (2003), Vol. ISO 5167-4:2003(E);
- 3 Wei Wu, Yeong-Ren Lin, Louis C. Chow, and Quinn Leland, "Fan Performance Characteristics at Various Rotational Speeds and Ambient Pressures", in SAE Technical Paper Series (2014).
- 4 AMETEK Rotron's PROPIMAX 2 fan http://www.rottron.com/-/media/ametektortron/products/digital%20library/table%20of%20content_s/tubeaxial%20fans/04-26_propimax_2.pdf?la=en
- 5 Butterfly Valve - Cast Iron, International, Wafer, Bronze Disc, N200145 <http://www.nibco.com/resources/ProductSubmittalDocs/N2001BF.pdf>
- 6 VOLTEQ DC Power Supply HY3010D 30V 10A <http://www.mastechpowersupply.com/volteq-regulated-variable-dc-power-supply-hy3010d-30v-10a-new-model.html>
- 7 PASCO 850 Universal Interface – UI-5000 <https://www.pasco.com/prodCatalog/UI/UI-5000850-universal-interface/>
- 8 PASPORT Quad Pressure Sensor – PS-1264 <https://www.pasco.com/prodCatalog/PS/PS-2164-passport-quad-pressure-sensor/index.cfm>
- 9 Hobbico Digital Mini-Tach <http://manuals.hobbico.com/hca/cap0401-manual.pdf> 135-140.
- 10 Testo 405i – Hot-wire anemometer wireless Smart Probe <https://www.testo.com/en-US/testo-405i/p/0560-1405>
- 11 Fernco PVC Flexible Coupling <https://www.fernco.com/dimensional-drawings/plumbing/flexible-couplings/stock-couplings-1056/1056-44>

APPENDIX B

**Eighteenth Annual Early Career Technical Conference
The University of Alabama, Birmingham ECTC 2018**

November 3 - 4, 2018 - Birmingham, Alabama USA

SIMULATING THE EFFECTS OF TURBULENCE ON PRESSURE TAP MEASUREMENTS

Jose J Corona Jr.

North Carolina Agricultural & Technical
State University
Greensboro, NC, USA

Dr. John P. Kizito

North Carolina Agricultural & Technical
State University
Greensboro, NC, USA

Abstract

The main objective of this paper is to study the effects of turbulence in collecting pressure tap measurements under high Reynolds number flows. The Reynolds numbers have been determined experimentally for free delivery of a 2-bladed fan to range from its free delivery condition to the shutoff condition respectively, $10540 < Re_D < 33,612$. For internal flow, the results indicate that the experimental rig is experiencing turbulence.

The fan performance curve was determined numerically under steady state conditions and follows the trend of the experimental results. The CAD simulations were drawn to represent the actual experiment. The boundary conditions and initial conditions are intended to model inherent properties within the experiment and environmental conditions. These preliminary results obtained from SOLIDWORKS flow simulation provide insight on the physics of the flow within the test rig. Due to the high Reynolds numbers in the pipe, we assume that turbulence exists; furthermore, the flow trajectories and vorticity contours have confirmed such behavior. Also, with the simulation we can pinpoint the locations where the vortices are concentrated. These pockets of vortices present a possible problem in accurately measuring pressures at the taps. The key components in the loop, such as the venturi flow meter, butterfly valve and the axial fan, have been our primary focus in this study. The flow characteristics around these items are studied extensively. We were able to find that the butterfly valve introduces wakes when the valve is being closed. Additionally, the venturi flowmeter also can have effects of vorticity at certain fan conditions.

We will expand this work to include higher Reynolds numbers up to about 90,000. The interest in this is to determine if the pressure tap measurements will show greater variations in the pressures.

Key Words: Electro-mechanical Actuators (EMAs), fan performance curves, numerical simulations, turbulence, internal flow

INTRODUCTION

This study is a continuation of an already existing experiment. In that paper, the affinity laws were experimentally confirmed to accurately predict the performance curve of a single fan at various rotational speeds and pressures [1]. Figure 1 demonstrates the current experimental setup used in that paper.

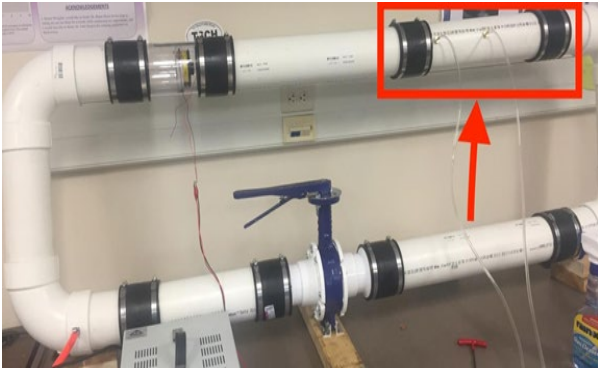


Figure 1. Current experimental rig in the laboratory.

The objective is to enhance the cooling performance of electro-mechanical actuators used in aerospace applications. Electro-mechanical actuators act as a heat source within a wing-bay; therefore, the test loop has been simulating sub atmospheric conditions, and the performance of axial fans under these environmental conditions. According to the literature, fans in a series formation increase the static pressure across n number of fans; on the other hand, for fans in a parallel arrangement the volume flow rate is the parameter that increases [2]. Extensive studies have been conducted for parallel systems around Water Distributions Systems (WDS). The affinity laws have been studied for various applications to accurately predict the best point of operation [3,4]. According to Koor et al., they investigated the best efficiency point (BEP) of variable speed pumps (VSPs) using Levenberg-Marquardt algorithm (LMA); furthermore, they discovered that for identical pumps the efficiency is optimized at equal discharge rates [5]. Borsting et al modeled various methods of grouping VSP's and optimization techniques [6]. The automotive industry also is heavily investing time to discovering better cooling mechanisms. In Filho et al, they studied how installing parallel fans is beneficial to cooling a system used for buses. The electrical fan system was more efficient, less noisy, more controllable, and easier to maintain [7]. Researchers have worked extensively in understanding the characteristics of axial fans. Chow et. al have performed studies of fan performance curves at various ambient pressures [8, 9]. In evaluating fan performance, computational fluid dynamics (CFD) and experimentation have been combined by many researchers. Lin et al utilized ANSYS to combine numerical results and experimental results for improving performance of fan design [10]. Additional methods of cooling have been studied. Combining both series and parallel arrangements to cooling heat generation enclosures have been investigated. These studies evaluated small fans function well for areas of localized heat generation, and large fans dissipate heat effectively in large areas [11]. Other methods of cooling have been proposed, such as using the working principles within heat pipes to transfer localized areas of heat to the ambient for cooling of electrical machines [12].

Using fans to cool the electronic components has the capability of stirring the ambient air within the system. Thus, this mixing can introduce eddies which can enhance the heat transfer within the structure. Studies of turbulent pipe flow have been extensively studied since Osborne Reynolds proposed the idea. Researchers have studied the methods to disrupt turbulence within pipe flow [13]. Other studies have centralized their work on studying the behavior of pipe flow at low Reynolds numbers with the use of various turbulence solvers and experimentation [14,15]. (Avila, Willis, & Hof, 2010; Kerstin Avila, 2011; YinQin Xu, 2018)

The high Reynolds number flows within the pipe could potentially provide erroneous pressure measurements at the taps. Xu et al have performed numerical studies on errors of pressure measurements related to orifice flowmeters [16]. The objective of this paper is to explore whether the pressure measurements have been compromised by the turbulent flow within the system. The physics of the flow within the test loop will provide insight into improving the cooling capabilities.

EXPERIMENTAL RESULTS

The fan performance was determined experimentally for the fan operating at standard pressure and temperature conditions while rotating at a constant speed of 20,000 rpm. The performance of a fan can be determined by measuring the pressure differential across the fan and a flow measurement device. We have chosen a venturi flowmeter to determine the volumetric flow rate within the loop. The pressure tap positions are demonstrated in figure 2; moreover, the taps at the fan are positioned 2'' before and after the fan. The Nylon was machined to mount the fan into the butyrate tube displayed in figure 3. The fan performance curve obtained with the AMETEK Rotron two-stage fan is shown in figure 4. Figure 5 demonstrates the geometry of the AMETEK fan in closer detail.



Figure 2. Pressure taps in the simulation are placed in identical positions as the experimental taps.



Figure 3. The installation of the two-stage axial fan into the butyrate tube.

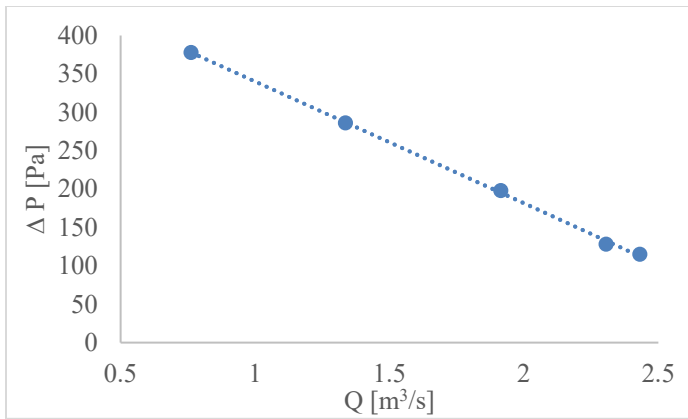


Figure 4. Fan performance curve determined experimentally with a single fan at 20000 rpm.



Figure 5. AMETEK Rotron Propimax2 geometric features.

The equation for the volume flow rate of an obstruction flowmeter can be obtained by combining Bernoulli's equation with continuity to yield [17,18],

$$Q = C_d A_t \sqrt{\frac{2(\Delta p)}{\rho(1-\beta^4)}}, \quad (1)$$

where Δp is the differential pressure in the throat and upstream of the venturi, ρ is the density, $\beta = d/D$ the diameter ratio of throat to upstream diameter, A_t is the cross-sectional area in the throat of the flowmeter, and C_d is the discharge coefficient.

A hot-wire anemometer by Testo 405i was used to determine the fluid velocity experimentally. In figure 6 the results demonstrate rapid fluctuations in the values recorded by this unit.

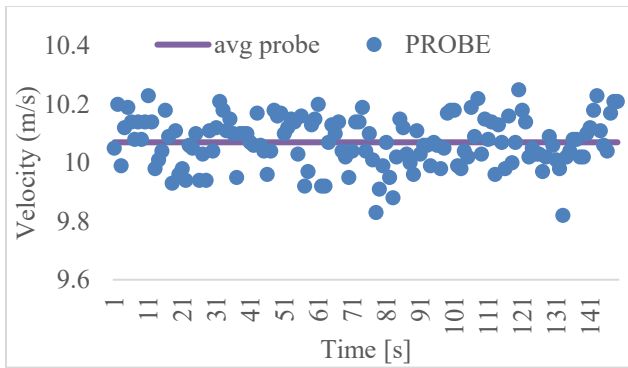


Figure 6. Demonstrates the rapid fluctuations in fluid velocity measured with the Testo 405i.

This data was recorded 26 inches downstream of the fan.

We encountered interesting results in collecting data at the shutoff condition of the fan; furthermore, with the use of SOLIDWORKS flow simulation we will explore those effects. The shutoff condition is experimentally obtained when the flow is constrained with the use of a flow regulating device such as ball valve or butterfly valve. For our experiments we selected the latter by NIBCO. Using such a device with rough edges will introduce areas of eddies within the flow.

When the valve is fully closed, the flow is forced to bounce back from the valve. This condition provokes a back-pressure buildup, which could introduce wall shear stresses that could potentially lead to erroneous data collection. In tapping holes for pressure measurement, it is important to properly deburr the area since it may lead to flow disturbances.

CAD DESIGN OF THE LOOP

In this paper, the experimental loop shown in figure 1 was modeled in SOLIDWORKS to closely represent the effects within the testing loop. The turbulence model that is used in SOLIDWORKS flow simulation is the Lam-Bremhorst $k-\epsilon$ turbulence model.

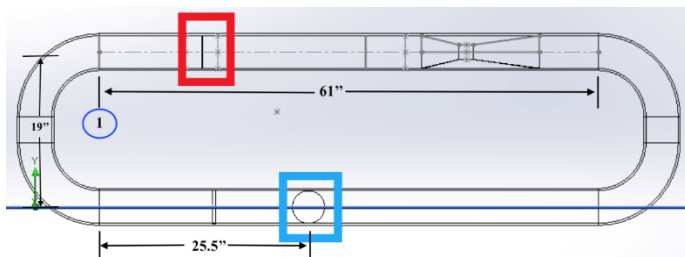


Figure 7. CAD design of the loop.

The source term was placed at the red region of the simulation and the blue box indicates the location of the butterfly valve shown in figure 7. The two-stage axial fan is located 11.75'' downstream of point one shown in the figure 7. In the simulation, the rotational effects of the fan were modeled, and those results are observed in the flow trajectories shown in the following sections of this manuscript. The valve was simulated for four different positions in steady state, and up to this point has been simulated for two positions under transient

conditions. Additionally, there is a flow straightener downstream of the fans. This straightener is located 2.5 inches upstream of the venturi flowmeter.



Figure 8. Flow straightener used in the simulation.

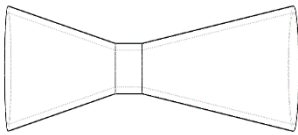


Figure 9. CAD of the venturi flowmeter used for simulation results.

The drawings provided in figure 8 and 9 have been carefully constructed to meet specific sizes of the physical components in the test loop. The venturi flowmeter has been constructed in-house and follows the specifications of machine venturi from ISO-5167 [19].

BOUNDARY AND INITIAL CONDITIONS

The preliminary numerical results obtained in this study were conducted through SOLIDWORKS Flow Simulation software. These preliminary results served to provide initial thoughts on the physics of the flow within the loop.

Steady state, gravitational effects in the y-direction, standard temperature and pressure within the loop, adiabatic conditions from the wall of the PVC to the environment, roughness of the inner wall for PVC, and both laminar and turbulent flow regimes were the conditions considered for the simulation. Figure 10 demonstrates the boundary conditions assigned to simulate the environment within the test loop.

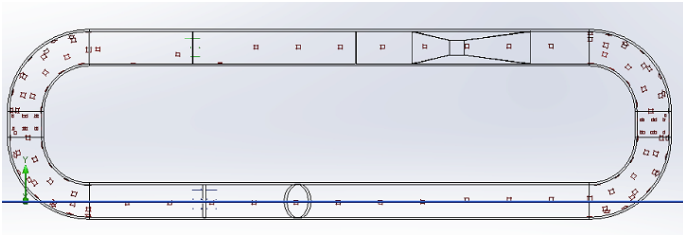


Figure 10. Demonstrates the boundary conditions used to model the behavior within the loop.

The red squares show the roughness assigned the wall ($\epsilon = 0.0015 \text{ mm}$), the blue arrows at the bottom are the pressure ambient pressure conditions ($P = 101325 \text{ Pa}$), and the green arrows are the momentum source term of the fan.

The simulation was conducted for four different valve positions. Those valve positions were simulated by rotating the bottom center circle about the x-z plane at 90° , 60° , 30° , and 0° . The 90° is the fully open condition (i.e., free delivery) and the 0° being the fully closed condition or shutoff.

The source term was specified by providing SOLIDWORKS with the fan performance curve indicated in figure 2. In the simulation we are considering the fan to already have been initiated to 20,000 rpm at time, $t = 0\text{s}$.

GRID INDEPENDENT STUDY

The model was tested for grid independence. To guarantee that the model is grid independent, a single valve position was tested with various mesh sizes provided in SOLIDWORKS. The mesh size was studied extensively, varying with differential meshing within the model and uniform meshing within the model. Initial results indicated that a denser mesh was required in the throat of the venturi to ensure consistent data. The denser the mesh, the more confident one can be in the results provided in the simulation; therefore, a differential grid sizing of 1^{-3}m and 1^{-6}m was taken as the most accurate result in the loop and throat of the venturi, respectively. The percent difference was calculated amongst the various mesh sizes and given in the following table.

Table 1. The percent difference between the different grid size compared to the densest mesh.

Pressure [Pa]	Non-uniform Grid	Uniform Grid Size 1mm	Uniform mesh 0.5mm
PG1_3	0.003903926	0.001454446	2.9104E-08
PG2_3	0.054040662	0.016276622	1.12067E-08
PG3_3	0.02231483	0.022195182	1.06329E-08

PG4_3	0.138913646	0.040686807	4.74084E-08
-------	-------------	-------------	-------------

According to the results of table 1, the percent difference of the pressures between the different mesh settings is less than 1%; consequently, that indicates that the study was grid independent. The remainder of the valve settings were simulated at a mesh size with uniform grid size of $1^{-3}m$ to save computation time.

TIME STEP INDEPENDENCE

To test if the numerical results are independent of the time step, we considered different time steps of $\Delta t = 0.1s$ and $\Delta t = 0.01s$ for a total time of $t = 0.5s$. The test loop condition considered was at free delivery of the fan and standard pressure and temperature conditions within the loop.

Table 2. Demonstrates the time step independence of the simulation.

Parameter	$\Delta t=0.1s$	$\Delta t=0.01s$	%Difference
PG1_3	101303.7	101304.4	7.16739E-06
PG2_3	101498.6	101509.8	0.000109894
PG3_3	101414.3	101429.6	0.000151266
PG4_3	101157.8	101189.6	0.000314195

The size of the time steps demonstrates similar results for the two cases studied; therefore, the results obtained in the transient results section will be conducted at the smallest time step in table 2. Preliminary results were obtained at $\Delta t = 0.001s$, but will be further tested to verify that we are capturing the physics of the flow and that the results presented here are accurate.

STEADY STATE RESULTS

First, we considered the flow within the system to be independent of time. The flow trajectories within the loop can provide insight as to what the flow characteristics appear to be in the experimental rig. The simulation was tested in the case where the valve is fully open to allow minimal flow resistance within the loop.

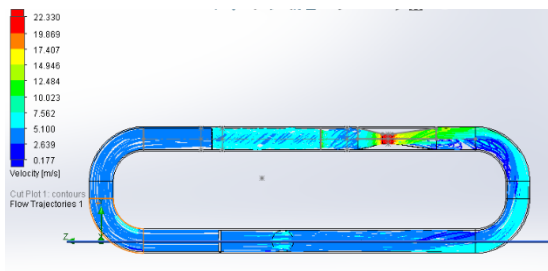


Figure 11. Flow trajectories within the loop simulating free delivery of the fan.

Figure 11 above shows that the greatest velocity is seen at the throat of the venturi, and that the flow becomes twisted as soon as it passes through the fan. The flow straightener has the ability of eliminating the rotational characteristics of the flow; but due its small length in the axial direction, the flow becomes twisted shortly after as demonstrated in figure 12.

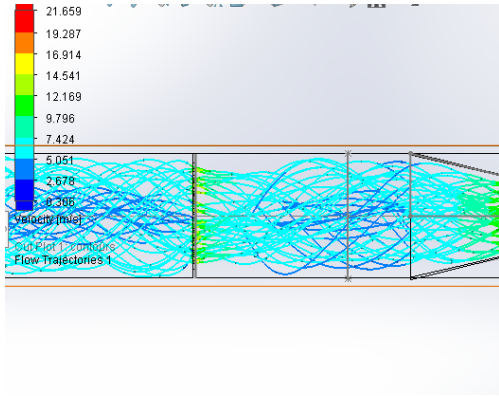


Figure 12. Demonstrates the flow straighteners effect on the fluid particles.

Perhaps including a second flow straightener in the loop a set distance from the first could disrupt the flow and make it straighter.

Next, the simulation of the closed valve system was simulated to study the flow particles in the loop. The steady state result yield that enough time has been allotted to the system. This indicates that the pressure has built up significantly, and the flow has become stagnant within the system which is shown in figure 13.

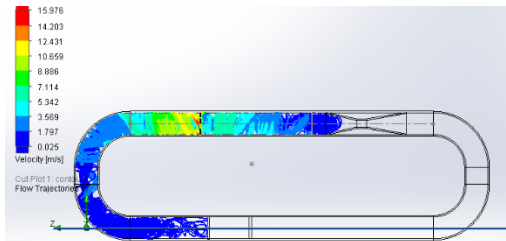


Figure 13. Flow trajectories of the loop at the shutoff condition.

The highest velocity determined in the simulation is higher in this case than the case mentioned previously. Furthermore, the highest velocity is in the region around the fan. This behavior can be explained by the fact that the flow has stagnated and is continuously being supplied with kinetic energy by the fan.

Recall that the pressure taps of the loop are labeled in figure 2. The difference of PG1 and PG2 will provide the static pressure rise of the fan, and the differential pressure of the PG3 and PG4 will give the volumetric flow rate. Due to lack of time restrictions, the fan performance curve was not obtained at a uniform mesh of 1mm, but initial results were obtained with the coarse, non-uniform mesh.

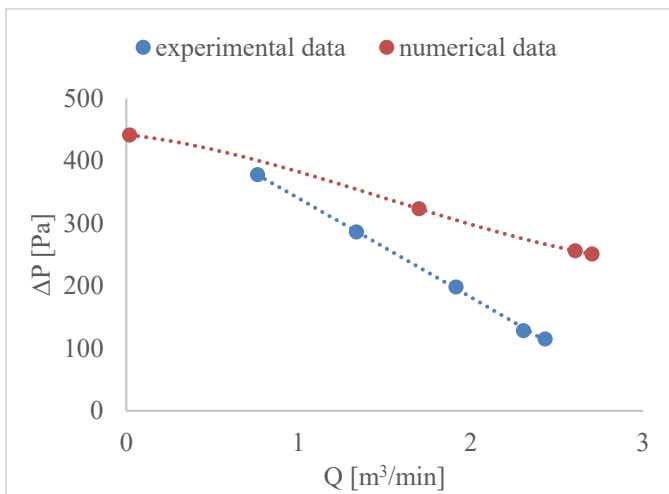


Figure 14. Fan performance curve that compares the experimental and SOLIDWORKS flow simulation results.

The results demonstrate that the numerical results closely approximate the experimental results at low volumetric flow rates. On the other hand, the higher volume flow rates show greater differences in the data among the two scenarios shown in figure 14. Lam-Bremhorst turbulence models are typically utilized for low-Re flow simulations; nonetheless, if the grid is carefully accounted for then the simulations can be conducted with this turbulence model even at high Reynolds numbers.

TRANSIENT STATE RESULTS

We consider the transient effects in the loop mainly for the condition of the fully closed butterfly valve; furthermore, under this condition, the experimental results demonstrate complications. These difficulties in collecting the data could be because of flow reversals in the loop causing undesirable shear stress at the wall taps. The transient state results were tested taking the time step to be 0.01s, the results were tested for duration of 1s. The following graphs demonstrate the pressure at the wall for the different locations of the point measurements in the testing loop. The results yield that a minimum of 0.45s should be given for startup time. Once that time has elapsed, the pressure readings are steady across every point where the pressure is determined experimentally.

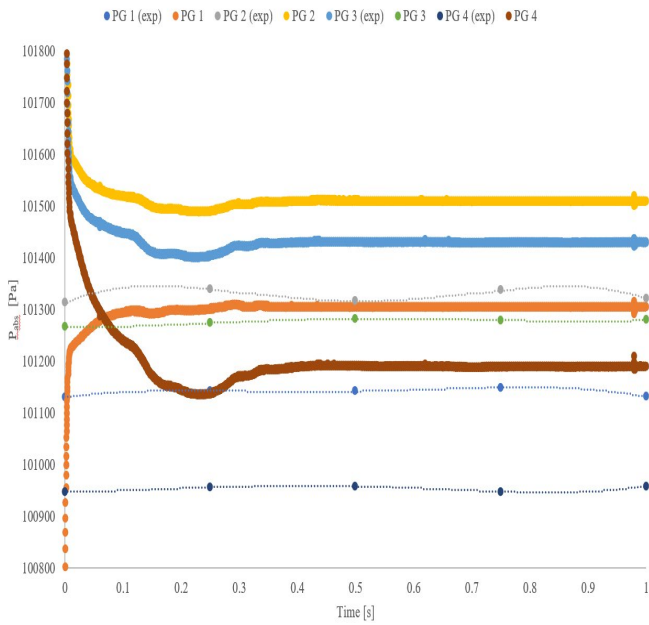


Figure 15. Comparison of the numerical and experimental pressures at the start.

From figure 15, the comparison between the numerical and experimental pressures are demonstrated from the start of the test runs. The data acquisition system in the lab has the ability of obtaining five points per second, which are indicated by the dashed lines; on the other hand, SOLIDWORKS flow simulation has the capacity a much higher rate of values within that same time frame. All the numerical results overestimate the experimental values by 155 Pa, 189 Pa, 149 Pa, and 242 Pa for points PG 1, PG 2, PG 3, and PG 4, respectively. The figure also demonstrates that numerically, the pressure achieves a convergence point past approximately 45 seconds. The experimental and numerical data shown in figure 15 are at the same conditions (i.e., 20000 rpm and free delivery condition).

The Reynolds number within the system varies as the butterfly valve is rotated to restrict the flow. The higher Reynolds number shows higher volumetric flow rate, and that is shown in figure 16 to be consistent throughout the time elapsed in the plot. Additionally, the difference is widened as time progressed. Nonetheless, both conditions still demonstrate that more time needs to progress for steady state results.

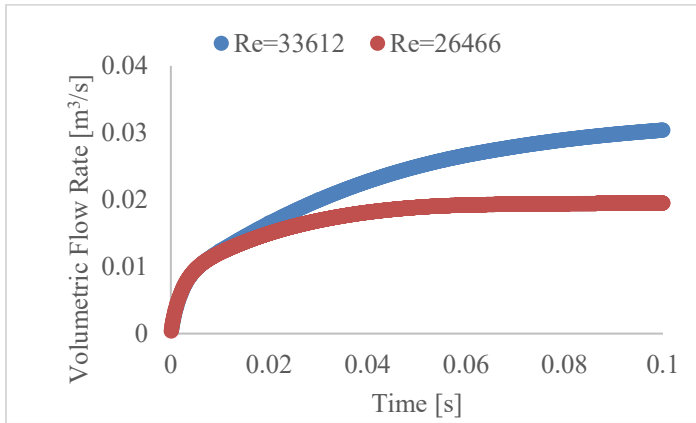


Figure 16. Volumetric flow rates determined by SOLIDWORKS at different Re when butterfly valve is fully closed.

Figure 16 demonstrates that the higher Reynolds number would require a more time for steady state results.

The numerical results obtained from SOLIDWORKS flow simulation demonstrate that after approximately 0.45s, the solutions demonstrate steady state behavior for the fully open valve condition. Therefore, we are confident in our experimental results for this fan curve since the Reynolds numbers are in a fully turbulent regime. Further analysis for higher Reynolds numbers will be tested to determine the time necessary for steady state results.

The transient effects are to be closely examined for when the valve is fully closed. The experimental results show that complications have been encountered when the flow is obstructed by the valve. The smallest time step did not demonstrate groundbreaking results when the fan is operating at the shutoff condition. The trajectories demonstrated similar results of stagnant flow conditions due to the back-pressure buildup.

Simulations were conducted when the system is in 30° and 60° flow resistances. Intermediate valve positions have presented complications in the experimental results, especially when very minimal flow is allowed through the system. The current results have been tested for a time of $t = 0.1s$. This time was chosen due to long computation times to obtain a solution. The geometry of the loop is very large, and due to the grid size combined with transient effects the run times are significant. The flow trajectories demonstrate chaotic behavior. The velocity of the particles increases around the edges of the valve and the wall. Along the right side of the valve, particles tend to follow a straight path. On the opposite side of the valve the flow tends to recirculate, shown in figure 17. Figure 18 demonstrates a snapshot of the vorticity around the valve. The vorticity has rapid fluctuations in the small time that this parameter was studied. Allowing for a greater run time would reveal whether the fluctuations are to eventually vanish with time.

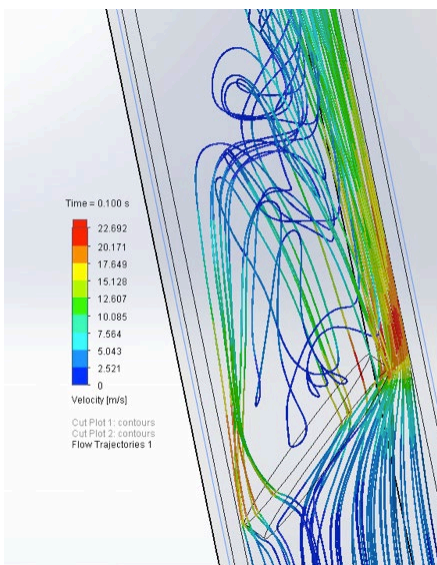


Figure 17. Flow trajectories around the valve when halfway open.

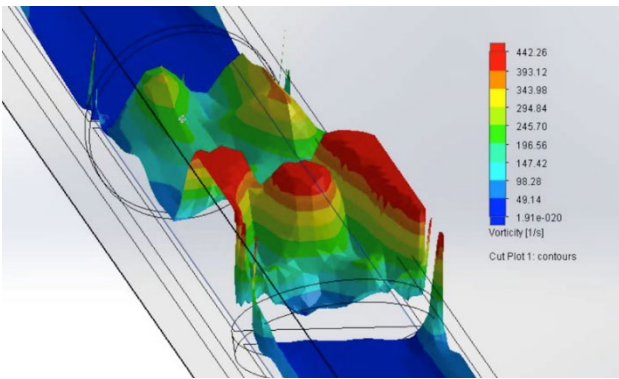


Figure 18. Vorticity around the valve when simulated at the midway position at $t = 0.07s$.

The high vorticities around the valve indicate that the flow has patches of strong rotation that is introduced by the valve. The vortices are greater near the wall and directly behind the valve.

A similar analysis was performed on the venturi to understand the flow in that section of the loop. Along the top the high vorticity is due to the fan's kinetic energy stirring up the flow. As the flow goes downstream and time progresses, the vortices are translated towards the center of the pipe. The frictional effects at the wall cause the vortices to dissipate near the wall downstream of the fan. When the flow interacts with the straightener, vortices begin to form near the edges and the solid structure of the straightener. Nonetheless, those are effects are negligible compared to the results shown in figure 10. The change in diameters from upstream of the venturi and in the throat causes vortices to form.

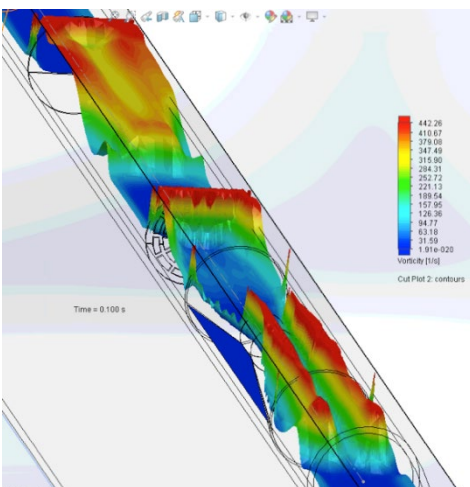


Figure 19. Isometric view of the vortices in the top section of the loop.

Taking a smaller time step would demonstrate more gradual results in the vortices along figure 19. Regardless, having such a small-time step will not aid our results in properly measuring the pressure at the taps since the results tend to achieve steady state behavior after approximately half a second.

CONCLUSIONS

The simulations showed that the results achieve steady state behavior approximately at $t > 0.45s$ for the fully open butterfly valve condition. This gives a strong indication that when taking the pressure measurements at the taps, we can be assured that the results are accurate at any point of the experiment.

The fan performance curve was determined numerically under steady state conditions and follows the trend of the experimental results. The CAD simulations were drawn to mimic the actual experiment in every aspect. The boundary conditions and initial conditions are intended to model inherent properties within the experiment and environmental conditions within the testing facility. These preliminary results obtained from SOLIDWORKS flow simulation provide insight on the physics of the flow within the test rig. Due to the high Reynolds numbers in the pipe, we assume that turbulence exists; furthermore, the flow trajectories and vorticity contours we have confirmed our hypothesis. Also, with the simulation we can pinpoint the locations where the vortices are concentrated. These pockets of vortices present a possible problem in accurately measuring pressures at the taps. We were able to explore the dynamics of the fluid particles around key components in the loop. We were able to find that the butterfly valve introduces wakes when the valve is being closed.

We will expand this work to include higher Reynolds numbers up to about 90,000. The interest in this is to determine if the pressure tap measurements will show greater variations in the pressures at higher Reynolds numbers, and if the venturi flow gives accurate results for volumetric flow rate.

REFERENCES

[1] Corona, J. and Kwarteng, A. "Testing of a Cooling Fan for Wing-bay Electro-Mechanical Actuators." 5th Joint US-European Fluids Engineering Division Summer Meeting. ASME, no. FEDSM2018-83480 (2018).

[2] Wright, Terry. 1999. Fluid machinery: performance, analysis, and design. Boca Raton, Florida: CRC Press.

[3] Augustyn, Ockert P. H., Sybrand J. van der Spuy, and Theodor W. von Backström. "Numerical and Experimental Investigation into the Accuracy of the Fan Scaling Laws Applied to Large Diameter Axial Flow Fans." Proceedings of the Institution of Mechanical Engineers, Part A: Journal of Power and Energy 230, no. 5 (2016): 477-86.

[4] Marchi, A. and Simpson, A.R. "Evaluating the Approximation of the Affinity Laws and Improving the Estimate of the Efficiency for Variable Speed Pumping." Journal of Water Resources Planning and Management 139, no. 12 (2013): 1314-17.

[5] Koor, M., A. Vassiljev, and T. Koppel. "Optimization of Pump Efficiencies with Different Pumps Characteristics Working in Parallel Mode." Advances in Engineering Software 101 (2016): 69-76.

(al., 2017; Koor et al., 2016)

- [6] Borsting, Zhenyu Yang and Hakon. "Energy Efficient Control of a Boosting System with Multiple Variable-Speed Pumps in Parallel." 49th IEEE Conference on Decision and Control (December 15-17, 2010 2010).
- [7] Ivar José de Souza Filho, Adriano de Oliveira Francisco, Bruno Scarano Paterlini, Daniel Luna Ferreira da Silva, Marcello Cervini Procida Veissid, Paschoal Frederico Neto, and Ricardo Moreira Vaz. "Application Study of Electrical Fans Assemble Applied in Bus Cooling System." SAE International 24th SAE Brasil International Congress and Display, no. 0148-7191 (2015). (al., 2017)
- [8] Wu, Wei, Yeong-Ren Lin, Louis C. Chow, and Quinn Leland. "Fan Performance Characteristics at Various Rotational Speeds and Ambient Pressures." In SAE Technical Paper Series, 2014.
- [9] Wu, Wei, Yeong-Ren Lin, Louis Chow, Edmund Gyasi, John P. Kizito, and Quinn Leland. "Electromechanical Actuator Cooling Fan Blades Design and Optimization." In SAE Technical Paper Series, 2016.
- [10] Lin, Sheam-Chyun, Shen Ming-Chiou, Tso Hao-Ru, Yen Hung-Cheng, and Chen Yu-Cheng. "Numerical and Experimental Study on Enhancing Performance of the Stand Fan." [In English]. Applied Sciences 7, no. 3 (2017).
- [11] al., Barron et. "Parrallel-Series Hybrid Fan Cooling Apparatus and Optimization." no. US 2017/0082112 A1 (2017).
- [12] Kabir, Rifat, Patrick McCluskey, and John P. Kizito. "Investigation of a Cooling System for a Hybrid Airplane." In 2018 AIAA/IEEE Electric Aircraft Technologies Symposium, p. 4991. 2018.
- [13] Kühnen, Jakob, Baofang Song, Davide Scarselli, Nazmi Burak Budanur, Michael Riedl, Ashley P. Willis, Marc Avila, and Björn Hof. "Destabilizing Turbulence in Pipe Flow." Nature Physics 14, no. 4 (2018): 386-90.
- [14] Avila, Marc, Ashley P. Willis, and BjÖRn Hof. "On the Transient Nature of Localized Pipe Flow Turbulence." Journal of Fluid Mechanics 646 (2010).
- [15] Kerstin Avila, David Moxey, Alberto de Lozar, Marc Avila, Dwight Barkley, Bjorn Hof. "The Onset of Turbulence in Pipe Flow." SCIENCE 333 (8 July, 2011 2011): 192-96.
- [16] YinQin Xu, Daniel Coxe, Yulia Peet, Taewoo Lee, . "Computational Modeling of Flow Rate Measurements Using an Orifice Flow Meter." American Society of Mechanical Engineers FEDSM2018 (2018)
- [17] White, Frank M. 1999. Fluid mechanics. Boston, Mass: WCB/McGraw-Hill.

[18] Cengel, Yunus A., and John M. Cimbala. 2006. Fluid mechanics: fundamentals and applications. Boston: McGraw-Hill Higher Education.

[19] ISO, "Measurement of fluid flow by means of pressure differential devices inserted in circular cross-section conduits running full— Part 4: Venturi tubes", (2003), Vol. ISO 5167-4:2003(E).

APPENDIX C

Eighteenth Annual Early Career Technical Conference

The University of Alabama, Birmingham ECTC 2018

November 3 - 4, 2018 - Birmingham, Alabama USA

EFFECT OF SCREEN LAYERS AND ORIENTATIONS ON MESH WICKED HEAT PIPES

K. Kaddoura, O.Y.W. Abotsi

North Carolina A&T State University
Greensboro, NC, USA

J.P. Kizito

North Carolina A&T State University
Greensboro, NC, USA

Abstract

Thermosiphons utilize gravity, thermal conduction, and convection to achieve desired cooling. On the other hand, wicked heat pipes are different versions of heat pipes that employ capillarity to overcome any gravitational limitations. Mesh screens provide additional pumping to enhance the thermal cycle within the heat pipe.

In this paper, an experimental study is carried to compare the thermal performance of an empty copper pipe, a traditional thermosiphon, and two wicked heat pipes with different number of mesh screen layers. The comparison of the thermal performance is done through measuring the thermal resistivity, thermal conductivity, and heat transfer coefficient of the pipes at steady state. Then, the corresponding non-dimensional parameter, Nusselt number, is calculated to relate the conductive and convective abilities of the pipes. With an identical percentage fill of 50%, the heat pipes are subjected to five different heat loads and five different orientations.

Theoretically, the layers of mesh screens enhance the heat transfer, and the pipes perform best at

the vertical position. The wicked heat pipes perform better than the copper tube and thermosiphon at any orientation. Furthermore, the mesh wicked heat pipes show an identical performance when they are rotated by 180°.

Key Words: Thermosiphon, Heat Pipe, Mesh Screen, Capillarity, Capillary Limit, Dry-out Limit.

INTRODUCTION

Thermal management in hybrid emerging technologies is a main concern, in which local cooling becomes necessary to ensure the reliability of the electronic components by controlling the temperature and dissipation [1]. Heat pipes, in their simplest forms, are being utilized for their ability of carrying large heat quantities across small sectional areas. The easiness of heat pipes' manufacturing, operation, and integration are attractive aspects when coupled with the simplicity of design and control [2]. Even though Perkins introduced their first thermosiphon in 1836, the scientific revolution in heat pipes didn't climax until 1960s [2, 3]. Thermosiphons, gravity assisted heat pipes, impose many limitations including the

inflexibility of orientation, shape modifications, and operational environment. Several scholars, including Swanson, expected the adoption of the heat pipe technology by NASA in 2007 [4]. However, in the absence of the gravitational effects, a thermosiphon becomes useless. Various techniques exist in which the manufactured heat pipes are made gravity independent. Internal wicks presented in the pipe assist the condensate return to the evaporator section, and it was first implemented by Graugler in 1944 [5].

Nowadays, wicks include a wider variety of homogeneous and composite shapes and sizes.

Mesh screens are simple wicks that substitute a mechanical pump by providing the capillary pressure needed to transport and distribute the working fluid in the heat pipe [6, 7]. Usually, screens are characterized by their high thermal conductivity, porosity, and wick permeability. The high thermal conductivity favors a more uniform temperature distribution across the wick and the heat pipe. Also, porosity of the wick represents the fraction of the void volume to the total volume of the screen [8]. The wick permeability is an empirical constant that describes the wick's resistance to axial liquid flow. The high permeability maintains small liquid pressure drops and better thermal performance [2].

The small size of the screen's opening induces high capillarity action to enhance the thermal cycle within the heat pipe. As the evaporator section is heated, the working fluid evaporates while the menisci recede into the wick. As the vapor pressure increases at the evaporator's section, bubbles grow and escape through the wick's structure. The latent heat of vaporization is released to the ambient as the vapor condenses at the condenser section. The pressure difference generated by the capillarity force pumps the condensate to the evaporator section through the wick's pores [2, 6, 9].

The maximum heat transfer and the effective thermal resistance contributed by the screen wick are common criteria to determine its performance

[10]. The properties of the wick and the working fluid control the generated capillary pressure, which limits the heat transfer rate and thermal resistance of the heat pipe [11]. A commonly encountered limitation in capillary driven heat pipes is the inability to circulate the working fluid. Known as the capillary limit, the sum of the liquid and vapor pressure drops dominates the capillary pressure generated by the wick. The capillarity forces are insufficient to pump the condensate to the evaporator and the wick is no longer saturated. The dry out that occurs at the evaporator section causes a sudden increase in its corresponding temperature [2, 12].

The choice of the working fluid affects the performance of the used wick as well. For instance, water is characterized by its large heat of vaporization and high surface tension, which are favorable for the capillarity action [1, 2].

THEORY

Shifting from thermosiphons to capillary driven heat pipes is beneficial when working in micro gravitational environments, like terrestrial applications. In such applications, inserting wicks is essential to drive the internal thermal cycle and achieve the desired thermal performance. However, the performance of the heat pipe relies on the performance of the wick's structure and working fluid.

Beyond the geometrical specifications of available screen meshes, the performance of the wick structure relies on various thermo fluid parameters. The thermal conductivity of mesh screens is given by [8] as

$$k_{eff} = \frac{k_l[(k_l + k_w) - (1 - \varepsilon)(k_l - k_w)]}{(k_l + k_w) + (1 - \varepsilon)(k_l - k_w)}. \quad (1)$$

The effective thermal conductivity of mesh screens depends on the thermal conductivity of the wick material ' k_w ', thermal conductivity of the working fluid ' k_l ', and the porosity of the wick's structure ' ε '.

The porosity of the wrapped screen meshes is also given by [8, 14, 15] as follows

$$\varepsilon = 1 - \frac{\pi F N d}{4}, \quad (2)$$

where F represents the crimping factor that is approximated to be 1.05 [13]. The mesh number and wire diameter are referred to as ' N ' and ' d ', respectively. Moreover, the unit of the diameter is inches in eq. (2) and (3).

Knowing the corresponding porosity of the wick design is necessary to calculate its permeability, as the following equation shows [8, 15],

$$K = \frac{d^2 \varepsilon^3}{122(1 - \varepsilon)^2}. \quad (3)$$

A general comparison could be formulated based on the previously mentioned parameters regarding the wick's material and working fluid. However, the main parameter to be considered is the capillary contribution of the screen mesh. For the wicking to occur, the capillary pressure must exceed the static pressure existing in the heat pipe. The general expression of the static pressure is

$$P_{static} = \rho g h \sin \theta, \quad (4)$$

where " ρ " corresponds to the density of the working fluid, " g " corresponds to the gravitational acceleration, " h " corresponds to the height of the fluid in the pipe, and " θ " corresponds to the angle of orientation.

On the other hand, the capillary pressure is defined as follows,

$$P_{cap} = \frac{2\sigma \cos \theta}{r_{eff}}, \quad (5)$$

where " σ " represents the surface tension of the working fluid and " r_{eff} " represents the effective radius of the wick. In case the wick is a wired screen, the effective radius is defined as follows [8]:

$$r_{eff} = \frac{w + d_w}{2}, \quad (6)$$

where " w " and " d_w " represent the wire spacing and diameter, respectively.

To avoid the dry-out and capillary limit, enough liquid must be introduced into the wick to ensure its saturation. In the presence of mesh screen wicks, it is more convenient to describe the fluid charge relative to the saturation of the wick. The following equation defines the 100% charge of the mesh screen wick [9],

$$100\% = V_{wick} * \varepsilon, \quad (7)$$

where " V_{wick} " represents the volume of the cylindrical mesh insert.

Various ways exist to understand the thermal performance of a heat pipe. The temperature difference describes how even the temperature is distributed along the heat pipe. The temperature difference between the evaporator's and condenser's section is defined as,

$$\delta T = T_e - T_c. \quad (8)$$

The small temperature difference indicates a better thermal distribution. Moreover, the thermal resistance of a heat pipe is directly related to the temperature difference, in which it is defined as follows,

$$R_{th} = \frac{\delta T}{Q}, \quad (9)$$

where " Q " corresponds to the heat load introduced at the evaporator section. The lower thermal resistance indicates a better heat transport along the heat pipe. The thermal conductivity of a heat pipe describes its ability in transporting the heat along; it is inversely proportional to the thermal resistance [10]:

$$k_{hp} = \frac{\ln \left(\frac{r_o}{r_i} \right)}{2\pi R_{th} L}, \quad (10)$$

where " r_o " and " r_i " are the outer and inner radii of the heat pipe, and L is the effective heat pipe length.

In addition to the conductive behavior of the pipe, the presence of the fluid in heat pipes provides convective heat transfer that is described by the heat transfer coefficient as,

$$h = \frac{Q}{\delta T}. \quad (11)$$

Finally, the convective ability of the heat pipe is compared against its conductive capacity through the Nusselt Number as shown,

$$Nu = \frac{h \cdot D}{k_{air}}, \quad (12)$$

where “D” refers to the active diameter of the pipe.

EXPERIMENTAL SETUP

Four heat pipes are designed, and their thermal performance is be studied. The following table shows the specification and labeling of the pipes.

Table.1. Heat Pipes Studied.

Pipe 1	Pipe 2	Pipe 3	Pipe 4
Empty	No wick	1- Mesh Layer	2- Mesh Layers

The common characteristics among all the manufactured pipes are shown below,

Table.2. Pipes Characteristics [16].

Material	Outer Diameter	Inner Diameter	Length	Thermal Conductivity
101 Copper	0.0191 m	0.0174 m	0.2 m	391 W/m.K

The working fluid charged in the pipes is water. Water is characterized by the following thermo fluid properties,

Table.3. Water Thermo fluid Characteristics.

Density	Surface Tension	Thermal Conductivity
997 Kg/m ³	0.072 N/m	0.608 W/m.K

997 Kg/m ³	0.072 N/m	0.608 W/m.K
-----------------------	-----------	-------------

Finally, the characteristics of the mesh screen are tabulated below.

Table.4. Mesh Screen Characteristics.

Material	Type	Mesh size	Opening Size	Wire Diameter
Copper	Wire Cloth	100x100	0.000152 m	0.0001143 m

Based on the characteristics presented in table 4, the mesh’s porosity is calculated by eq. (2) to be 63%. Thus, the permeability of the mesh screen used is calculated by eq. (3) to be $3 \times 10^{-7} \text{ m}^2$. The effective thermal conductivity of the mesh screen used is 1.32 W/m.K, through eq. (1).

All pipe rigs possess similar geometrical properties, as presented in table 2. The internal volume of the heat pipes is $4.76 \times 10^{-5} \text{ m}^3$; therefore, each can hold up to 47.6 ml of water. Previous experiments and literature show that that the optimum volume of working fluid for the best thermal performance is around 50% [17]. Thus, the heat pipes are charged with 50% working fluid, thus each pipe is filled with 23.8 ml of water. According to the porosity model described [13], 23.8 ml is enough to saturate the mesh screens inserted.

The saturation of the wick is necessary to avoid the dry out limit. Since the fluid occupies 50% of the total internal volume, the static pressure calculated using eq. (4) is 979 Pa. This pressure is competing against the capillary pressure that is calculated to be 1081 Pa through eq. (5) and (6). Since the capillary pressure exceeds the static pressure, wicking occurs.

An aluminum block holds the high-density heat cartridge and the heat pipe under study. The heat cartridge is connected to an adjustable voltage supply that reads the power introduced. To ensure that all heat fluxes are introduced to the

evaporator section, the aluminum block is insulated. Five J-type thermocouples are evenly spaced and attached to the outer wall of the heat pipe using thermo sensitive adhesive strips (Kapton™). Temperature readings are acquired with MCC DAQ. The following image shows the experimental setup, where two heat pipes are placed into the aluminum block and to thermocouples are attached using Kapton tape.



Fig.1. The experimental setup.

First, the thermal performance of the heat pipes is studied at 5 different power ratings to understand the general behavior of mesh screen wicked heat pipes. Then, the performance of the heat pipes is studied under the effect of inclination to understand the wicking ability of screen meshes.

RESULTS AND ANALYSIS:

A. The Effect of Screen Layers:

The following table shows the temperature differences between the evaporator and condenser section of the pipes.

Table.5. The temperature difference across the pipes.

Power (Watts)	δT (°C)
15	2.4, 1.5, 0.13, 3.9
23.8	4.4, 3.1, 1.2, 4
34.5	6.3, 5.6, 4.5, 4.8
47.3	8.9, 7.5, 5.8, 8
62	11.2, 8.6, 6.5, 0.1

Power (W)	Pipe 1	Pipe 2	Pipe 3	Pipe 4
15	2.4	1.5	0.13	3.9
23.8	4.4	3.1	1.2	4
34.5	6.3	5.6	4.5	4.8
47.3	8.9	7.5	5.8	8
62	11.2	8.6	6.5	0.1

The following graph represents the trend of the temperature distribution as a function of heat load.

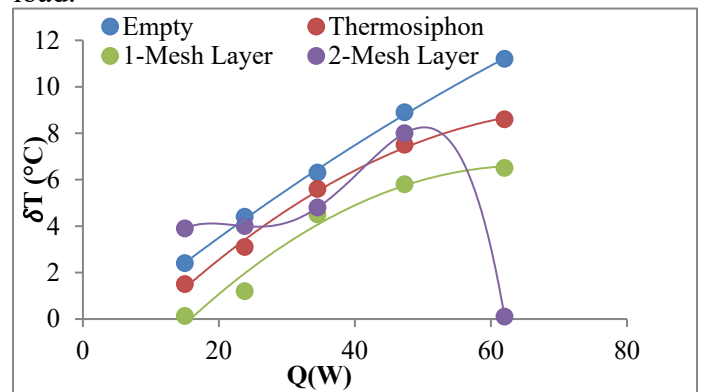


Fig.2. The variation of temperature difference across the pipes as a function of heat input.

As shown by Fig.2, the temperature difference generally increases across all the pipes as the heat input increases. However, the 1-Mesh layer heat pipe shows the lowest temperature difference. Moreover, the thermal resistivities of the pipes are plotted as follows.

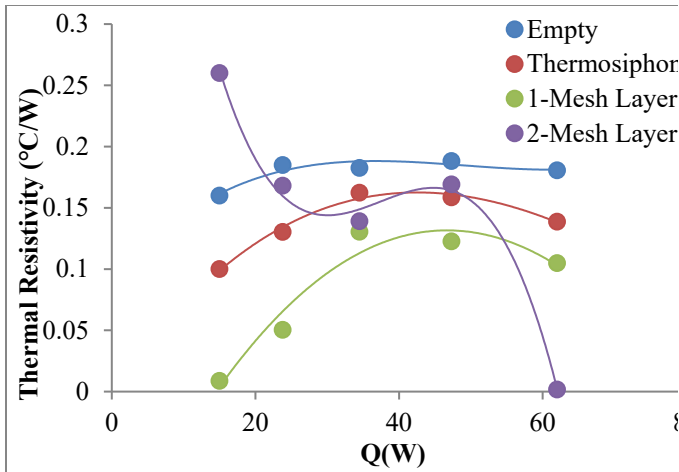


Fig.3. Thermal resistivity of the pipes as a function of the heat input.

As shown in fig.3, the 1-mesh layer heat pipe shows the least thermal resistivity across various powers. Generally, the thermal resistivity of all pipes follows the same trend except for the 2-mesh layer heat pipe which shows high thermal resistivities due to the presence of extra copper layers within it.

To understand the convective characteristics of the pipes at hand, the corresponding heat transfer coefficients are tabulated below.

Table.6. The heat transfer coefficient across heat pipes.

Power (Watts)	$h(W/°C)$			
	Pipe 1	Pipe 2	Pipe 3	Pipe 4
15	6.25	10	115.38	3.8
23.8	5.41	7.68	19.83	5.9
34.5	5.48	6.16	7.67	7.1

47.3	5.3	6.3	8.16	5.9
	1	1		1
62	5.5	7.2	9.54	62
	4	1		0

As the power increases, the heat transfer coefficient of the 1-Mesh layer heat pipe remains the highest up until 47.3 W. At 62 W, the heat transfer coefficient of the 2-Mesh layer heat pipe exceeds all pipes by 10 orders of magnitude.

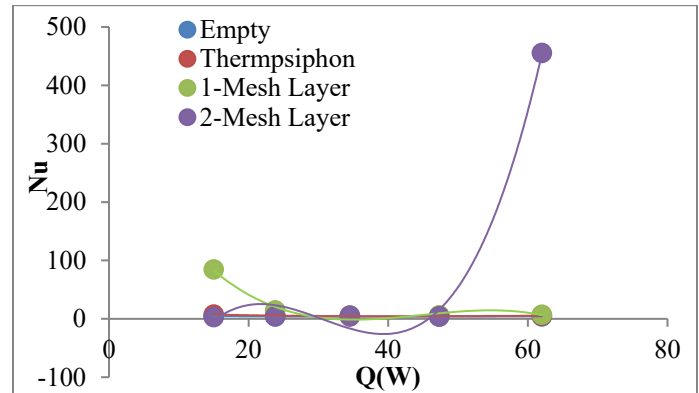


Fig.4. The Nusselt number of the pipes at different heat loads.

As shown in fig.4, the Nusselt number corresponding to the 1-Mesh layer heat pipe remains the highest as the power increases to 47.3 W. However, the Nusselt number of the 2-Mesh layer heat pipe exceeds all others by 10 orders of magnitude at 62 W.

B. The Effect of Orientation

After exploring the thermal performance of the heat pipes under vertical conditions, the study is extended to various orientations. The corresponding temperature differences are plotted as follows.

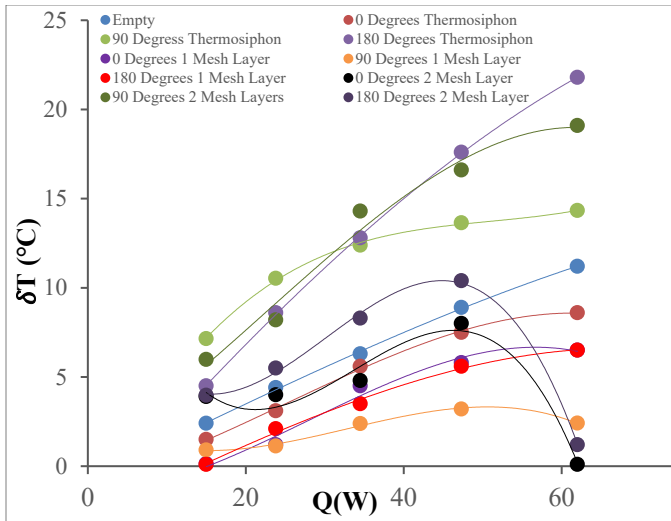


Fig.5. The temperature difference across the pipes at different orientations.

Based on fig.5, the thermosiphon shows the most uniform distribution when set vertically and aligned with gravity (0 degrees). However, the thermosiphon does not perform effectively at different orientations nor against gravity (90 and 180 degrees, respectively) in which the empty pipe shows a better thermal performance. The 1-Mesh Layer and the 2-Mesh Layer show similar performance when oriented vertically in both directions, indicating their independency of gravity. Moreover, the 1-Mesh Layer shows the most uniform temperature distribution when oriented horizontally.

The Nusselt Number of the previous studies are plotted as

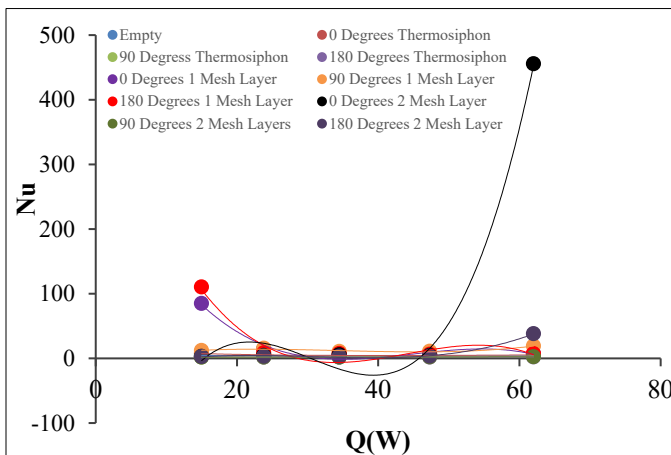


Fig.6. The Nusselt Number of the pipes at different orientations.

According to fig.6, the 1-Mesh Layer and 2-Mesh Layer heat pipes always perform better than the empty pipe. The 2-Mesh Layer heat pipe shows its cooling superiority at high heat loads, whereas the 1-Mesh Layer shows its cooling superiority at lower heat loads. However, the thermosiphon performs better than the empty pipe when oriented vertically aligned with gravity. All pipes show a convective trait of heat transfer where the Nusselt Number exceeds unity.

CONCLUSION

In this paper, it was shown that utilizing capillarity using mesh screens enhances the performance of a heat pipe. A layer of mesh screen was enough to exceed the performance of a thermosiphon. As the number of layer increases, the performance of the meshed heat piped showed a delay where the effectiveness did not show until the thermal resistivity of the wall and screen layers were overcome. Thus, the number of layers affects the operation range of the heat pipe. If the heat pipe was to be operated at low heat inputs, less screen layers are needed and vice versa.

Moreover, the thermosiphon performs best when aligned with gravity, which fits its definition. If oriented otherwise, the thermosiphon shows its ineffectiveness in transporting heat. On the other hand, the 1-Mesh and 2-Mesh layer heat pipe showed their independency of gravity and showed the best performance when positioned horizontally.

ACKNOWLEDGEMENTS

We acknowledge the support from NASA NNH16ZEA001N: Electric Propulsion: Challenges and Opportunities.

REFERENCES

- [1] Kizito, John, and Md Monir Hossain. "Experimental study of thermal performance of a flat loop heat pipe." *Frontiers in Heat Pipes (FHP)* 6.1 (2015).
- [2] Faghri, Amir. "Heat pipes: review, opportunities and challenges." *Frontiers in Heat Pipes (FHP)* 5.1 (2014).
- [3] Cotter, T. P. *Theory of heat pipes*. No. LA-3246. Los Alamos Scientific Lab., Univ. of California, N. Mex., 1965.
- [4] Swanson, Theodore D. "Thermal control technologies for complex spacecraft." (2004).
- [5] Gaugler, Richard S. "Heat transfer device." U.S. Patent No. 2,350,348. 6 Jun. 1944.
- [6] Nemec, Patrik, Alexander Caja, and Milan Malcho. "Thermal performance measurement of heat pipe." *Global journal of technology and optimization* 2.1 (2011).
- [7] Reay, David, Ryan McGlen, and Peter Kew. *Heat pipes: theory, design and applications*. Butterworth-Heinemann, 2013.
- [8] Bejan, Adrian, and Allan D. Kraus. *Heat transfer handbook*. Vol. 1. John Wiley & Sons, 2003.
- [9] Wong, Shwin-Chung, and Yi-Huan Kao. "Visualization and performance measurement of operating mesh-wicked heat pipes." *International Journal of Heat and Mass Transfer* 51.17-18 (2008): 4249-4259.
- [10] Kempers, R., D. Ewing, and C. Y. Ching. "Effect of number of mesh layers and fluid loading on the performance of screen mesh wicked heat pipes." *Applied Thermal Engineering* 26.5-6 (2006): 589-595.
- [11] Faghri, Amir. *Heat pipe science and technology*. Global Digital Press, 1995.
- [12] Faghri, Amir, and S. Thomas. "Performance characteristics of a concentric annular heat pipe: Part I—Experimental prediction and analysis of the capillary limit." *Journal of heat transfer* 111.4 (1989): 844-850.
- [13] Marcus, Bruce David. "Theory and design of variable conductance heat pipes." (1972).
- [14] Kozai, Hiroaki, Hideaki Imura, and Yuji Ikeda. "The permeability of screen wicks." *JSME international journal. Ser. 2, Fluid's engineering, heat transfer, power, combustion, thermophysical properties* 34.2 (1991): 212-219.
- [15] Mwaba, Misheck G., Xiao Huang, and Junjie Gu. "Influence of wick characteristics on heat pipe performance." *International journal of energy research* 30.7 (2006): 489-499.
- [16] Davis, Joseph R., ed. *Copper and copper alloys*. ASM international, 2001.
- [17] Kabir, Rifat, Kaddoura, Kamal, Patrick McCluskey, and John P. Kizito. "Investigation of a Cooling System for a Hybrid Airplane." 2018 AIAA/IEEE Electric Aircraft Technologies Symposium. 2018.

APPENDIX D

Eighteenth Annual Early Career Technical Conference
The University of Alabama, Birmingham ECTC 2018
November 3 - 4, 2018 - Birmingham, Alabama USA

PERFORMANCE OF A GRAVITY INDEPENDENT HEAT PIPE

O.Y.W. Abotsi, K. Kaddoura

North Carolina A&T State University
Greensboro, NC, USA

J.P. Kizito

North Carolina A&T State University
Greensboro, NC, USA

Abstract

Heat pipes are two phase cooling devices which provide one dimensional heat flow. Passive transport of working fluid continually in heat pipes is enhanced by wicks which exploit wicking through capillary action.

In the present study, an empty pipe, a thermosiphon, an un-sintered wick, and a sintered wick heat pipe, was considered for comparison. The thermal behavior, total thermal resistance and heat transfer coefficient of these pipes were investigated at 5W, 10W, 15W, 25W, 35W and 50W. Thermosiphon performed better than the empty pipe due to the introduction of working fluid exchanging heat by phase change. The presence of a wick structure proved to further increase the thermal performance of the heat pipe. Sintering reduced pore spaces and increased the wicking ability and hence the thermal performance. Wicks were manufactured from 140 μm average diameter copper powder. Results show that

temperatures at the evaporator section for the un-sintered and sintered wick heat pipe were identical.

The performance of the un-sintered and the sintered wick heat pipe were also investigated in against gravity conditions. The results portrayed that their evaporator temperatures were alike. However, the un-sintered wick heat pipe performed better than sintered wick heat pipe.

KEY WORDS: Heat pipe, wick, gravity, thermal resistance, thermal performance, thermosiphon, sintering

INTRODUCTION

Since their development in the late twentieth century, heat pipes have been employed for cooling applications in electric motors, blast furnaces, space systems and the electronic industry [1-20]. Heat pipes are capable of transferring heat over reasonable

distance with small temperature drop [4-8]. In addition, heat pipes require no power source for their operation.

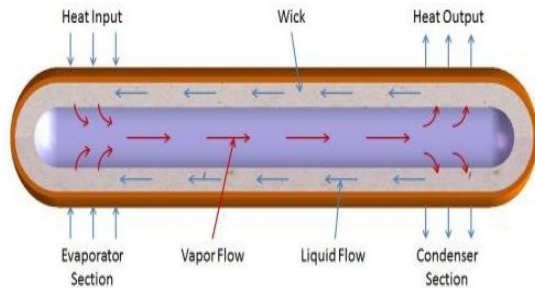


Fig. 1. Schematic of a general heat pipe showing its sections and component [1]

Heat pipes have three sections, viz.; evaporator, condenser and adiabatic section (the region between the evaporator and the condenser section). Heat pipes are normally filled with liquid containing its own vapor. When heat is applied to the evaporator, liquid changes to vapor and is forced to move towards the relatively cooler condenser section. Here, the vaporized fluid relinquishes its latent heat of vaporization and changes back to liquid. Wicks are the inner layer of the tube. Condensate is re-directed towards evaporator section by capillary action improved by a wick structure.

Wicks and working fluids are the two most important components of a heat pipe [2] and [3]. Different types of working fluids such as water, acetone, methanol, ammonia, or sodium can be used in heat pipes depending on the desired temperature range of operation [4]. Generally, the wicks for phase-change cooling devices include metal wire meshes, micro-grooves, sintered metal powder, metal foams, sintered metal fibers and composite wicks [5]. Wicks control capillary pressure, permeability, and the working fluid's flow resistance.

Porous media allow fluid flow through its pores and have vast applications in thermal sciences, soil sciences, aerospace, and other engineering fields. A fluid-filled porous structure provides solid-liquid-vapor contact lines in the interstitial volumes between the solid particles where large capillary forces developed from interfacial tensions [6]. These forces pull the liquid through porous media by capillary action. Porous materials, made from sintered metallic powder compacts, are used as wicks in heat pipes for continuous circulation of working fluid.

To provide effective water supply, the porous structure must contain large number of pores so that

enough water is supplied continuously from the condenser to the evaporator section. In addition, the pore size must be small enough so that the capillary pressure is high enough to draw the water through the porous wick, even against gravity [7-9]. Lin et al, examined the effects of powder shape on heat dissipation of a heat pipe using gas atomized spherical powder, water atomized and electrolytic copper powder to create wick structure [7]. From the results, the gas atomized spherical powder gave the utmost capillarity speed and permeability, hence highest heat dissipation even though its porosity was the lowest. It was concluded that capillarity speed affects heat dissipation more than permeability. Jo, et al, demonstrated enhanced fluid transport through a multilayer, porous wick comprising a micro-porous structure [4]. Wicking is the process by which heat is dissipated because of increased surface area through morphology modification [10]

Homogeneous wicks are constructed with one type of material or machining technique [11]. Sintered wicks are made by stuffing particles between the inner heat pipe walls [4]. Even though they are difficult to make, their capillary pressure developed (capillary limit) is easily predicted. Sintered wicks are designed to have small capillary radius if a large capillary difference is required.

The production of metallic parts by compacting metal powders in suitable dies and sintering them at elevated temperatures to obtain the desired density and strength is known as powder metallurgy [12]. Compaction process and escape of gases during sintering minimize the porosity in powder metallurgy. Besides having the necessary pore structure and size characteristics for fluid and heat transport, the wicks produced had to be mechanically rigid to be integrated into heat pipe [11-15].

This present study investigates the thermal properties of an empty pipe, thermosiphon, a sintered and an unsintered wick used in heat pipe at six different heat loads. The effect of gravity on these pipes are also investigated. Copper powder, 140 μm average diameter, from Atlantic Equipment Engineers was used to construct the wick structure. In addition, copper 101 tubes, 200 mm long with 19.1 mm and 17.44 mm internal and external diameter respectively were used to make heat pipes.

EXPERIMENTAL SETUP

Li et al compared the performance of three different ranges of copper powder: 80–110, 110–140 and 140–

170 μm. Results indicated that wicks produced from sintering 140–170 μm cell size range copper powders had better binding strength, improved uniformity, greater capillary pumping force and a reduced amount of back flow resistance [7], [16-30].

Copper powder of 140 μm average diameter was selected to make wicks. 87% of the powder was mixed with 13% of water-based binder to form a paste like feedstock. Binder was made from polyvinyl alcohol supplied by the Carolina's. Binder and copper powder mixing ratios were imperative in obtaining a smooth and uniform feedstock. Inadequate binder in the mixture would cause high viscosity and formation of voids in the mixture while excess binder in the mixture would cause contraction of the sample during de-binding [12]. The wick was made in a stainless-steel mold by cold pressing. Two wick structures of 8.382 mm thickness were manufactured. Reports of sintering process are well documented in the literature [13], [15] and [31-35].

Description of labels of the pipes used for experiment are presented below.

Pipe 1- Empty Pipe

Pipe 2- Thermosiphon (no wick structure)

Pipe 3- Un-sintered copper powder wick heat pipe

Pipe 4- Sintered copper powder wick heat pipe



Fig. 2. Pipe 3, un-sintered copper powder wick heat pipe

Wick structure should be compatible with working fluid. High surface tension of distilled water besides its compatibility with wick made it suitable for use as working fluid. Distilled water also has the capability to increase the capillary pressure [31].

Pipes 2, 3 and 4 was filled with 50% of working fluid.

The experimental setup comprises an aluminum block with three drilled holes, two for accommodating heat pipes, the remaining middle for holding a high-density heater cartridge. The cartridge is heated by connecting to a power source that allows variation in current and voltage. Desired power can be obtained from the equation below.

$$Q = IV \quad (1)$$

Where Q, I and V are heat load, current and voltage respectively

Ultra-high temperature ceramic tape obtained from McMaster Carr was used for insulation to create the adiabatic section. The block was held in place by an insulated vice and connected to a DAQ system (data acquisition system) via K-type thermocouples. Using thermo-sensitive adhesive strips two K-type thermocouples were fixed to the outer wall of the pipes, one at the evaporator section and the other at the condenser section. Data collected from the DAQ system is analyzed with computers. The data acquisition device system collects data every 0.01 laps and displays the data on the computer. Experiments were performed in normal gravity conditions, (+g) and in against gravity condition, (-g). Fig 3 and fig 4 shows the experimental set-up for normal gravity and against gravity conditions with pipe 3 and pipe 4. Error related to K-type thermocouple was 0.10C. Uncertainty in power measurement was 0.2%.

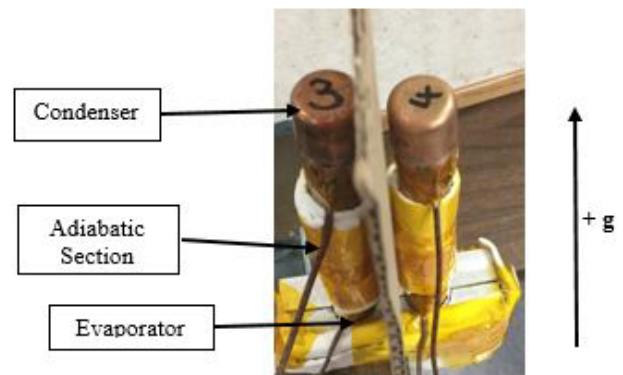


Fig. 3. Experimental set-up for normal gravity condition (+g)

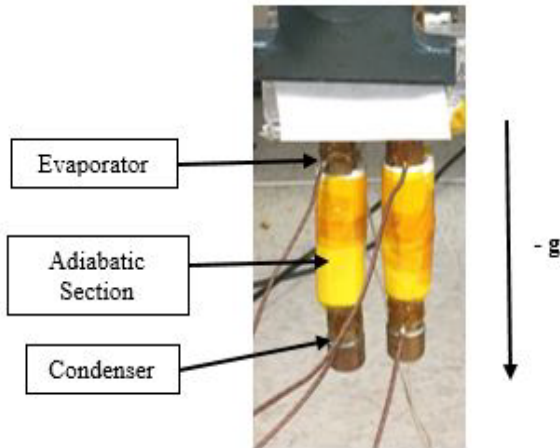


Fig. 4. Experimental set-up for against gravity (-g) condition

RESULTS AND DISCUSSION

The performance of porous wicks is determined by pore sizes and porosity: with finer pore, the wick can provide higher capillary force; with higher porosity, the permeability of wick is larger, which means less resistance for fluid flowing in the wick [34] and [36-40]. Fig 5(a) and 5(b) shows SEM image of un-sintered copper at 400 and 1200 magnification respectively. Also, fig 6 shows the SEM image of the sintered copper wick at 1200 magnification. Powder particles bond together after the sintering process. Images also show reduced pore spaces after sintering.

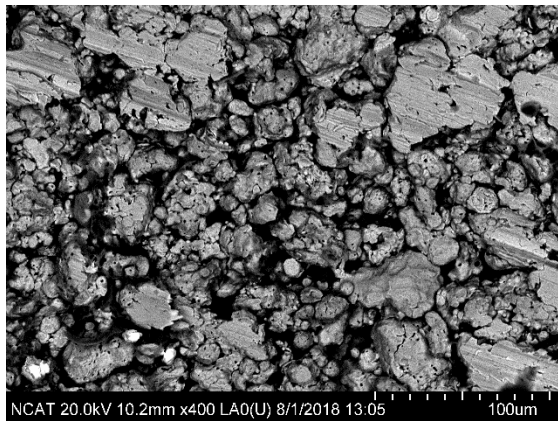


Fig. 5 (a). SEM image of un-sintered copper wick; magnification 400

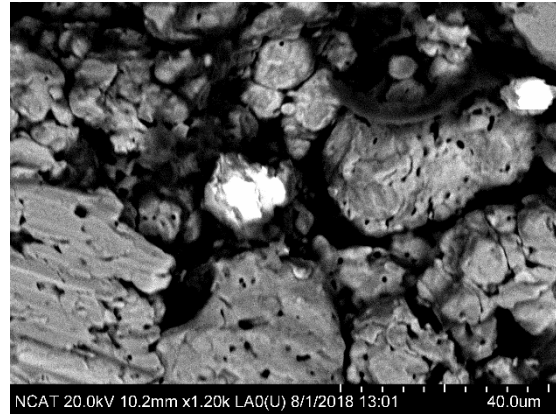


Fig. 5 (b). SEM image of un-sintered copper wick, magnification 1200

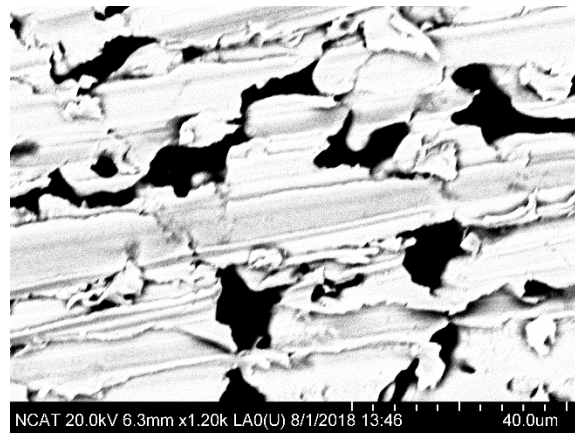


Fig. 6. SEM image of sintered copper wick, magnification 1200

Porosity is the ratio of the void's volume to the entire wick's volume. The porosity of fabricated sintered wick can be calculated by the mass-volume method [38].

$$\varepsilon = \left(1 - \frac{m}{\rho_w V}\right) * 100\% \quad (2),$$

where ε , m and V , are the porosity, mass, and volume of the wick structure, and ρ_w is the density of the copper powder sintered. The porosity of the sample is determined to be 40%. The mass was measured with a digital balance and the uncertainty in the measurement was 1%.

Permeability is a measure of the wick's resistance to axial liquid flow [4]. For sintered wicks, the permeability is determined by the Carman-Kozeny equation [41]

$$K = \frac{\epsilon^2 * d^2}{150 * (1 - \epsilon)^2} \quad (3)$$

Here, d is the effective diameter of the copper powder.

The capillary pumping force of the wick is calculated as [42]

$$\Delta P_c = \frac{2\sigma}{r} * \cos\theta \quad (4)$$

where ΔP_c is the capillary pumping force of the porous wick structure, σ is the surface tension of the liquid, r is the radius of curvature, and θ is the contact angle between the liquid and the surface. Capillary forces increase as pore sizes decrease [10]

NORMAL GRAVITY CONDITION (+g)

First and foremost, the general performance of all the pipes used is studied. Experiments are performed with 5W, 10W, 15W, 25W, 35W and 50W heat input. Each experiment is performed twice for repeatability. The thermocouples acquire temperature readings every 100 seconds until steady state is achieved.

Fig. 7, denotes the temperature distribution across un-sintered wick heat pipe at 5W power input. The applied heat to the evaporator section causes vaporization of working fluid. Phase-change occurs at the condenser section. The capillary pressure developed in the wick continuously circulates the working fluid in the heat pipe.

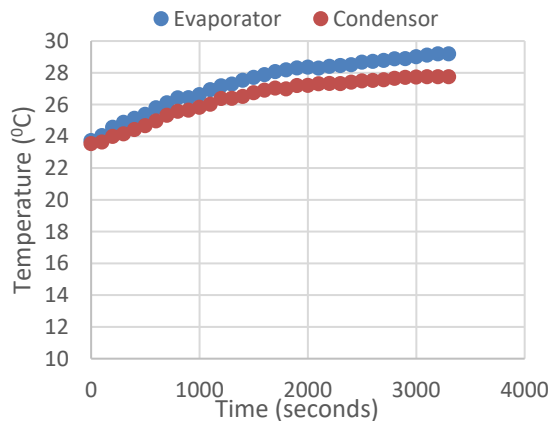


Fig. 7. Behavior of un-sintered wick heat pipe at 5W heat load

Fig. 7 shows that, temperatures at the evaporator section increases at a higher rate as compared to temperatures at the condenser section. Both evaporator and condenser temperature eventually reach a constant value which signifies steady state.

The thermal characteristics of heat pipes are compared using the difference in temperature between the condenser and evaporator sections, ΔT . Heat pipes with smaller ΔT values have higher thermal performance [4] and [29], [43-45].

$$\Delta T = T_e - T_c \quad (5)$$

Here, T_e and T_c are the evaporator and condenser steady state temperatures respectively.

Fig. 8 shows a plot of ΔT against heat load. The empty pipe has the largest temperature difference. The empty pipe represents heat transfer by pure conduction. Phase change is introduced when working fluid is used in pipe. Heat pipes make use of conduction and convection heat transfer hence making their thermal performance better than empty pipes. The presence of a wick structure further reduces the temperature difference, ΔT , as depicted in un-sintered heat pipe. The sintered heat pipe had the smallest temperature difference.

Sintering is a process in which powders are compacted and heated at appropriate temperatures and in appropriate atmospheres, with the results that powders are conglutinated [25]. Sintering reduces the porosity of the compacted powder. Small pores sizes increase circulation of working fluid by capillary action. Sintered wick heat pipe had the least value of ΔT .

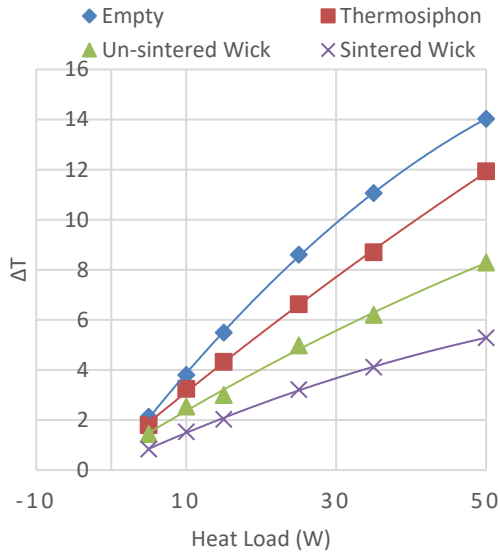


Fig. 8. Steady state temperature difference between evaporator and condenser (ΔT) vs. heat load

The total thermal resistance of the pipes investigated at different heat loads is shown in Fig 9. To understand the thermal performance of a heat pipe, the total thermal resistance is determined.

$$R_{th} = \frac{T_e - T_c}{Q}, \quad (6)$$

Here, Q is the applied load at the evaporator section.

The thermal resistance offers an indication of heat flow resistance in a system. The total thermal resistance is reciprocal to the heat load. This implies that as the heat load increases, the total thermal resistance decreases. The maximum and minimum value of the total thermal resistance is $0.426 \text{ } ^\circ\text{C/W}$ and $0.1058 \text{ } ^\circ\text{C/W}$ and was recorded for an empty pipe and sintered wick heat pipe respectively. Therefore, these results demonstrate that the smaller the thermal resistance, the better the thermal performance.

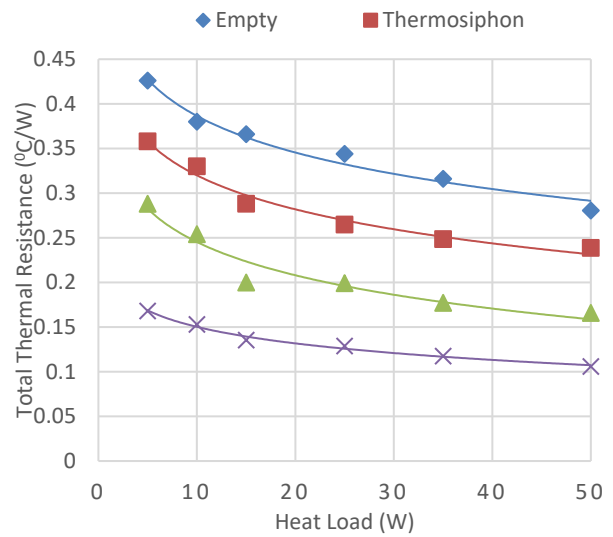


Fig. 9. Total thermal resistance vs. heat load

The effectiveness of the thermal system is determined from the heat transfer coefficient as:

$$h = \frac{Q}{A_e(T_e - T_c)} \quad (7)$$

where, A_e , is the active heated area of the evaporator

Fig. 10 shows a plot of the heat transfer coefficient at different heat loads. The figure points out a rise in heat transfer coefficient as the heat load increases. The figure also demonstrates that higher heat transfer coefficients can be achieved at low thermal resistance and relatively high heat loads. The maximum and minimum values of the heat transfer coefficient in the sintered wick heat pipe are $2.067 \text{ kW/m}^2 \text{ } ^\circ\text{C}$ and $1.301 \text{ kW/m}^2 \text{ } ^\circ\text{C}$ for 50 and 5-Watt heat load respectively.

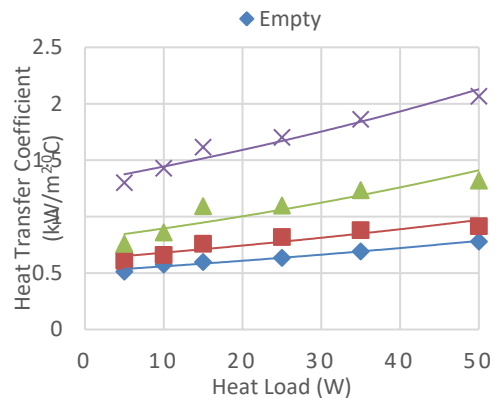


Fig. 10. Heat transfer coefficient vs. heat load

Fig. 11 shows the steady state evaporator temperatures for pipes 3 and 4. From the plot, temperatures at evaporator section increases with increasing heat load. This linear relationship demonstrates continuous conductance mode in these pipes. Plot also show that the steady state evaporator temperature of un-sintered and sintered wick is identical for different heat loads.

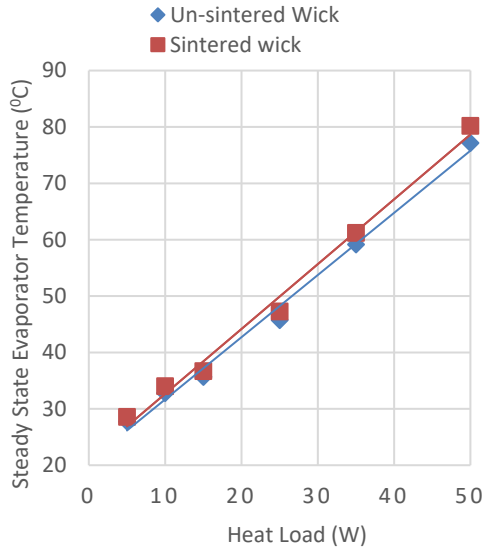


Fig. 11. Steady state evaporator temperature vs. heat input for un-sintered and sintered wick heat pipe

The difference in the steady state temperature for un-sintered and sintered wick at the condenser section is significant and can be seen in fig 12. The condenser temperature in pipe 4 is higher than in pipe 3. Due to this, Pipe 3, sintered wick heat pipe has a lower total thermal resistance, hence a better thermal performance.

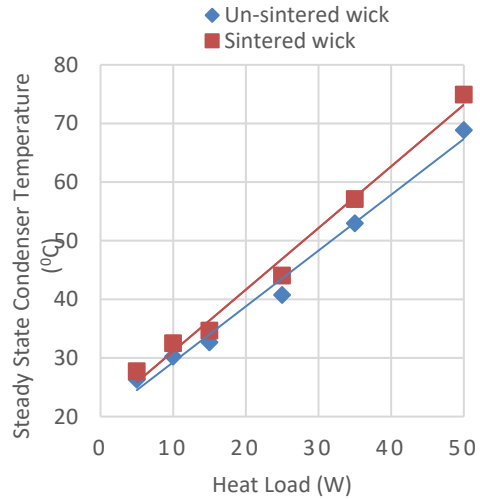


Fig. 12. Steady state condenser temperature vs. heat input for un-sintered and sintered wick heat pipes

AGAINST GRAVITY CONDITION

The general thermal behavior of the un-sintered and sintered wick heat pipes are studied at 5W, 10W, 15W, 25W, 35W and 50 W. Fig 13 shows the general behavior of evaporator and condenser temperatures of these pipes. The shape of graph changes as power readings are increased. From the plot, the evaporator temperatures for un-sintered and sintered wick heat pipes are identical. It can be concluded that the evaporator temperatures for the un-sintered and sintered wick heat pipes are similar and not influenced by gravity. The table below compares the steady state evaporator temperature for un-sintered and sintered pipes in against gravity conditions. The data shows that the steady state evaporator temperature for sintered and un-sintered heat pipes in against gravity conditions are identical.

Table showing steady state evaporator temperature of sintered and un-sintered heat pipes for against gravity condition

Heat Load [W]	Sintered (-g) [0C]	Un-sintered (-g) [0C]
5	26.26	26.28
10	35.37	35.59
15	41.20	41.21

25	51.98	51.98
35	71.70	71.74
50	87.02	87.02
standard deviation	23.10777	23.07703

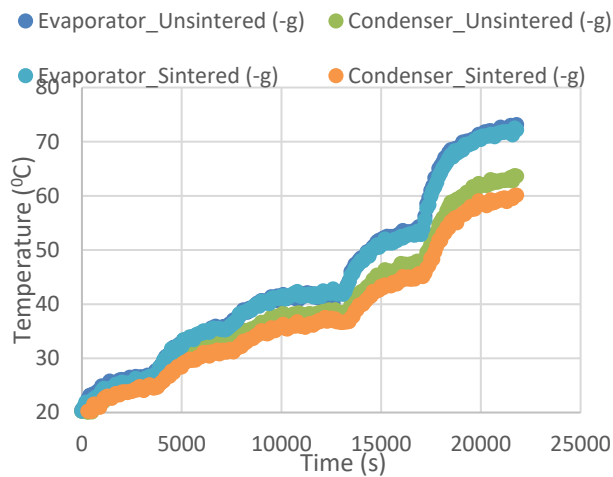


Fig. 13. Evaporator and condenser temperatures of un-sintered and sintered wick heat pipes in against gravity condition

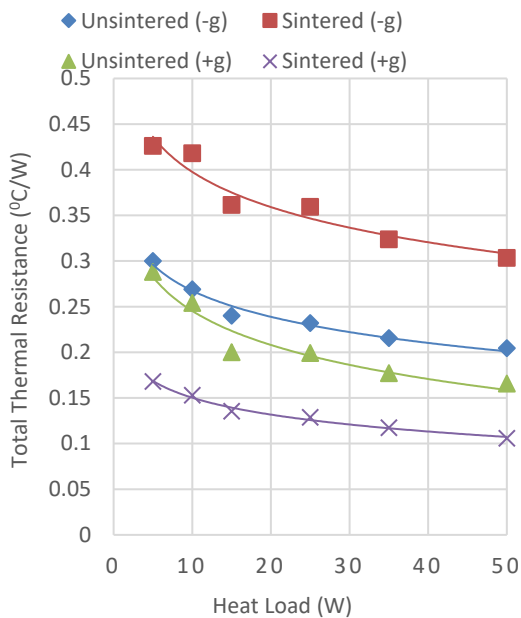


Fig. 14. Total thermal resistance of un-sintered and sintered wick heat pipes in normal gravity and against gravity conditions.

Fig 14 compares the total thermal resistance of the un-sintered and sintered wick heat pipe in normal and against gravity conditions. Un-sintered wick heat pipe had a lower thermal resistance than the sintered wick heat pipe in against gravity condition. This implies that the un-sintered wick heat pipe will have much higher thermal performance than the sintered wick heat pipe.

CONCLUSION

An empty pipe, a thermosiphon, a sintered and an un-sintered heat pipe was fabricated from 200mm long copper tube with 19.1mm diameter and 1.66mm thickness. 8.382 mm thick wicks were made from 140 μm average diameter copper powder.

In normal gravity conditions, the thermal performance of all heat pipes used was greater than the empty pipe. Heat pipes with wicks performed better when compared to the thermosiphon. In addition, the thermal performance of the heat pipe with wick structure increased when wick was sintered. However, in against gravity conditions, the un-sintered wick had a higher thermal performance when compared to the sintered wick. The value of the evaporator temperature for the un-sintered and sintered heat pipe were identical either in normal gravity condition or in against gravity condition.

ACKNOWLEDGEMENT

We acknowledge the support from NASA NNH16ZEA001N: Electric Propulsion: Challenges and Opportunities.

REFERENCES

- [1] Modak, Y.A. (2016). CFD Analysis of vapor chamber with micro pillars as heat spreader for high power electronic devices. (Master's Thesis, University of Texas at Arlington).
- [2] Khairnasov, S., & Naumova, A. (2015). Heat pipes application in electronics thermal control systems. *Frontiers in Heat Pipes (FHP)*, 6(1).
- [3] Bodla, K. K., Murthy, J. Y., & Garimella, S. V. (2012). Direct simulation of thermal transport through sintered wick microstructures. *Journal of heat transfer*, 134(1), 012602.
- [4] Faghri, A. (2014). Heat pipes: review, opportunities and challenges. *Frontiers in Heat Pipes (FHP)*, 5(1).
- [5] Jung, S. M., Preston, D. J., Jung, H. Y., Deng, Z., Wang, E. N., & Kong, J. (2016). Porous Cu nanowire aerospunges from one-step assembly and their applications in heat dissipation. *Advanced Materials*, 28(7), 1413-1419.
- [6] Iverson, B. D., Davis, T. W., Garimella, S. V., North, M. T., & Kang, S. S. (2007). Heat and mass transport in heat pipe wick structures. *Journal of Thermophysics and Heat Transfer*, 21(2), 392-404.
- [7] Lin, Y. J., & Hwang, K. S. (2009). Effects of powder shape and processing parameters on heat dissipation of heat pipes with sintered porous wicks. *Materials transactions*, 50(10), 2427-2434.
- [8] Vafai, K. (Ed.). (2015). *Handbook of porous media*. Crc Press.
- [9] Kostornov, A. G., Moroz, A. L., Shapoval, A. A., Kabov, O., Strizhak, P., & Legros, J. C. (2015). Composite structures with gradient of permeability to be used in heat pipes under microgravity. *Acta Astronautica*, 115, 52-57
- [10] Jo, H. S., An, S., Nguyen, X. H., Kim, Y. I., Bang, B. H., James, S. C., ... & Yoon, S. S. (2018). Modifying capillary pressure and boiling regime of micro-porous wicks textured with graphene oxide. *Applied Thermal Engineering*, 128, 1605-1610.
- [11] Faghri, A. (1995). *Heat pipe science and technology*. Global Digital Press.
- [12] H.S. Jo, S. An, H.G. Park, M.-W. Kim, S.S. Al-Deyab, S.C. James, J. Choi, S.S. Yoon (2017). Enhancement of critical heat flux and superheat through controlled wettability of cuprous-oxide fractal-like Nano textured surfaces in pool boiling, *Int. J. Heat Mass Transfer* 107 105–111
- [13] Lin, Y. J., & Hwang, K. S. (2010). Swelling of copper powders during sintering of heat pipes in hydrogen-containing atmospheres. *Materials transactions*, 51(12), 2251-2258
- [14] Leong, K. C., Liu, C. Y., & Lu, G. Q. (1997). Characterization of sintered copper wicks used in heat pipes. *Journal of Porous Materials*, 4(4), 303-308.
- [15] Li, Z., Wu, Y., Zhuang, B., Zhao, X., Tang, Y., Ding, X., & Chen, K. (2017). Preparation of novel copper-powder-sintered frame/paraffin form-stable phase change materials with extremely high thermal conductivity. *Applied Energy*, 206, 1147-1157.
- [16] Udell, K. S. (1985). Heat transfer in porous media considering phase change and capillarity—the heat pipe effect. *International Journal of Heat and Mass Transfer*, 28(2), 485-495.

- [17] Reay, D., McGlen, R., & Kew, P. (2013). Heat pipes: theory, design and applications. Butterworth-Heinemann.
- [18] Vasiliev, L. L. (2008). Micro and miniature heat pipes—Electronic component coolers. *Applied Thermal Engineering*, 28(4), 266-273.
- [19] Wang, B., Hong, Y., Hou, X., Xu, Z., Wang, P., Fang, X., & Ruan, X. (2015). Numerical configuration design and investigation of heat transfer enhancement in pipes filled with gradient porous materials. *Energy Conversion and Management*, 105, 206-215.
- [20] Ling, W., Zhou, W., Liu, R., Qiu, Q., & Ke, Y. (2017). Operational characteristics of loop heat pipes with porous copper fiber sintered sheet as wick. *Applied Thermal Engineering*, 122, 398-408.
- [21] Ji, X., Li, H., Xu, J., & Huang, Y. (2017). Integrated flat heat pipe with a porous network wick for high-heat-flux electronic devices. *Experimental Thermal and Fluid Science*, 85, 119-131.
- [22] Ingham, D. B., & Pop, I. (1998). Transport phenomena in porous media. Elsevier.
- [23] Nield, D. A., Bejan, A., & Nield-Bejan... (2006). *Convection in porous media* (Vol. 3). New York: Springer.
- [24] Chen, X., Ye, H., Fan, X., Ren, T., & Zhang, G. (2016). A review of small heat pipes for electronics. *Applied Thermal Engineering*, 96, 1-17.
- [25] De Schampheleire, S., De Kerpel, K., Deruyter, T., De Jaeger, P., & De Paepe, M. (2015). Experimental study of small diameter fibres as wick material for capillary-driven heat pipes. *Applied Thermal Engineering*, 78, 258-267.
- [26] Yao, S., Lei, L., Deng, J. W., Lu, S., & Zhang, W. (2015). Heat transfer mechanism in porous copper foam wick heat pipes using nanofluids. *International journal of heat and technology*, 33(3), 133-138.
- [27] Li, X. B., Tang, Y., Li, Y., Zhou, S. Z., & Zeng, Z. X. (2010). Sintering technology for micro heat pipe with sintered wick. *Journal of Central South University of Technology*, 17(1), 102-109.
- [28] Wang, Y., Cen, J., Jiang, F., Cao, W., & Guo, J. (2016). LHP heat transfer performance: A comparison study about sintered copper powder wick and copper mesh wick. *Applied Thermal Engineering*, 92, 104-110.
- [29] Atabaki, N., & Baliga, B. R. (2007). Effective thermal conductivity of water-saturated sintered powder-metal plates. *Heat and Mass Transfer*, 44(1), 85-99.
- [30] Mantle, W. J., & Chang, W. S. (1991). Effective thermal conductivity of sintered metal fibers. *Journal of thermophysics and heat transfer*, 5(4), 545-549.
- [31] Kizito, J., & Hossain, M. M. (2015). Experimental study of thermal performance of a flat loop heat pipe. *Frontiers in Heat Pipes (FHP)*, 6(1).
- [32] Dominguez Espinosa, F. A., Peters, T. B. and Brisson, J. G., (2012), "Effect of Fabrication Parameters on the Thermophysical Properties of Sintered Wicks for Heat Pipe Applications," *International Journal of Heat and Mass Transfer*, 55(25–26), 7471-7486.
- [33] Pruzan, D. A., Klingensmith, L. K., Torrance, K. E., & Avedisian, C. T. (1991). Design of high-performance sintered-wick heat pipes. *International journal of heat and mass transfer*, 34(6), 1417-1427.
- [34] Early, J. G., Lenel, F. V., & Ansell, G. S. (1963). The material transport mechanism during sintering of copper powder compacts at high temperatures (No. TID-20324). Rensselaer Polytechnic Inst., Troy, NY
- [35] Li, H., Liu, Z., Chen, B., Liu, W., Li, C., & Yang, J. (2012). Development of biporous wicks for flat-plate loop heat pipe. *Experimental Thermal and Fluid Science*, 37, 91-97.
- [36] Tang, H., Tang, Y., Wan, Z., Li, J., Yuan, W., Lu, L. & Tang, K. (2018). Review of applications and developments of ultra-thin micro heat pipes for electronic cooling. *Applied Energy*, 223, 383-400.

- [37] Zhong, G., Ding, X., Tang, Y., Yu, S., Chen, G., Tang, H., & Li, Z. (2018). Various orientations research on thermal performance of novel multi-branch heat pipes with different sintered wicks. *Energy Conversion and Management*, 166, 512-521.
- [38] Tang Y, Tang H, Li J, Zhang S, Zhuang B, Sun Y. (2017) Experimental investigation of capillary force in a novel sintered copper mesh wick for ultra-thin heat pipes. *Appl Therm Eng*; 115: 1020–30.
- [39] Zhou, W., Xie, P., Li, Y., Yan, Y., & Li, B. (2017). Thermal performance of ultra-thin flattened heat pipes. *Applied Thermal Engineering*, 117, 773-781.
- [40] Tang, Y., Deng, D., Huang, G., Wan, Z., & Lu, L. (2013). Effect of fabrication parameters on capillary performance of composite wicks for two-phase heat transfer devices. *Energy conversion and management*, 66, 66-76.
- [41] Qu, Y., Zhou, K., Zhang, K. F., & Tian, Y. (2016). Effects of multiple sintering parameters on the thermal performance of bi-porous nickel wicks in Loop Heat Pipes. *International Journal of Heat and Mass Transfer*, 99, 638-646.
- [42] Ling, W., Zhou, W., Yu, W., & Chu, X. (2018). Capillary pumping performance of porous copper fiber sintered wicks for loop heat pipes. *Applied Thermal Engineering*, 129, 1582-1594
- [43] Mwaba, M. G., Huang, X., & Gu, J. (2006). Influence of wick characteristics on heat pipe performance. *International journal of energy research*, 30(7), 489-499.
- [44] Grissa, Kods, Adel M. Benselama, Zied Lataoui, Yves Bertin, and Abdelmajid Jemni. "Investigations of the thermal performance of a cylindrical wicked heat pipe." *International Journal of Energy Research* (2018).
- [45] Brahim, T., & Jemni, A. (2014). Effect of the heat pipe adiabatic region. *Journal of heat transfer*, 136(4), 042901.

APPENDIX E

Nineteenth Annual Early Career Technical Conference

The University of Alabama, Birmingham ECTC 2019

November 2 - 3, 2019 - Birmingham, Alabama USA

THERMAL MANAGEMENT OF PA-03-10-600 LINEAR ELECTROMECHANICAL ACTUATOR END WINDINGS USING STRAIGHT CIRCULAR HEAT PIPES AND POROUS FINs

Augustine Akuoko
Kwarteng

North Carolina A&T State
University

Greensboro, North
Carolina, USA.

University of Mines &
Technology

Tarkwa, WR, Ghana.
Quinn H. Leland

Air Force Research
Laboratory

Dayton, OH, USA

Kamal Kaddoura

North Carolina A&T State University
Greensboro, North Carolina, USA.

Louis Chow

University of Central Florida, Orlando,
Florida, USA

Jose Corona Jr

North Carolina A&T State
University

Greensboro, North Carolina,
USA.

John Kizito

North Carolina A&T State
University

Greensboro, North Carolina,
USA.

Abstract

The following presents a thermal study on a linear electromechanical actuator

(EMA) PA 03-10-600 with the goal of managing the temperatures of the windings when the motor is in operation. The study replicates the actuation of flaps and other

flight controls surfaces using EMA's in revolutionary concepts more electrical aircraft (MEA) designs. The motor configuration having with current-carrying copper windings, embedded in a silicon steel rotor core, separated by a clearance from the stator and the housing presents high resistance to heat transfer from internal components of the device. The result of the latter is high operating temperatures which tend to compromise the safety, reliability, and operational time of the EMA because of possible delamination of the winding and subsequent short-circuiting.

Concepts proposed and experimentally tested in the current work have achieved up to 11.9°C reduction in the maximum winding temperature of the EMA. The proposed design achieves the state level thermal control by introducing sintered copper heat pipes interlaced with porous fins into the airspace in close proximity with the windings whilst avoiding a direct physical contact with the motor windings.

KEY WORDS: Electromechanical actuators, cooling motor windings, thermal management, heat pipes, porous fins

INTRODUCTION

EMA's are essential to the operation of reliable power-by-wire actuation systems for aerospace applications, and they present a formidable alternative to replace hydraulic systems from aircraft and spacecraft [1]. The benefits of using EMA's include improved safety, efficiency, reliability, and maintainability as well as overall weight reduction. Power by wire in "More Electric Aircraft" (MEA) concepts seeks to systematically substitute hydraulic actuators by EMA's [2].

However, the transition towards more intensive electronic technologies in aeronautical and ground vehicles presented intense heat flux problems affecting both the lifetime and reliability of the system [3-6]. In pursue of cooling the electromechanical actuators in hybrid airplanes and technologies, Corona et al explored pure forced convection using a fan in the wing bay [7]. Typically, electric motors have been cooled by mounting fins on the outer housing [8]. However, Davin et al experimentally explored the cooling effect of lubricating oil on the motor [9]. Moreover, Lee et al used channels for forced convection on the housing and hollow shaft rotor cooling [10]. To avoid the complexity of manufacturing, operation, and integration Faghri emphasized the simplicity of designing and controlling of heat pipes [11]. Heat pipes attracted the attention of thermal managers investigating cooling methods for hybrid technologies [12]. Heat pipes are passive cooling devices with self-driven two-phase flow that collects waste heat energy and reject the latent heat energy of the working fluid into the ambient [11]. Heat pipes in their various forms are characterized by their low thermal resistivity and their ability of transporting excessive amount of heat through a small surface area [13]. Depending on the application, heat pipes vary in size, material, working fluid, and type. For instance, capillarity driven heat pipes showed better performance than gravity driven heat pipes in the aeronautical application due to their independence of gravity [14]. The thermal performance could be enhanced in different manners as well. On the interior level, Putra et al. showed that the usage of biomaterial wicks and nanofluid particles enhance the performance of heat pipes [15-17]. On the other hand, improvements could also be done on the

exterior level by adding fins and forced convection [8].

Typical thermal management methods rely on a well-defined conduction path between motor windings and the housing due to the location of convenient placement of the of the windings in the stator core right at the periphery of the motors. The current test piece, PA 03-10-600 motor, however, presents the challenge of high thermal resistance between the heat laden windings which happen to be at the center of the piece and separated from the stator and housing by air space.

Kwarteng et al. [12] established the temperature distribution inside the motor via experimental measurements noted that the hotspots in the motor occur at the end turns of the windings. Thus, the development of an effective means of managing temperature at the end turns of the copper windings is the drive of the current study. Heat pipes is proposed as a possible means of managing the heating problem. Abotsi et al. [13] demonstrated the gravity independence of sintered heat pipes and their effectiveness in all orientations.

MATERIALS AND METHODS

Materials used the study include the following: PA 03-10-600 linear actuator, power source, variac transformer, rectifier unit, voltmeter, ammeter, k-type thermocouples, sintered copper heat pipes (0.6 cm diameter, 7 cm long), 36-gage copper wire and an MCC DAQ data acquisition system. The PA-003-10-600 is a brushed, two-pole 10-slot configuration motor having a permanent magnet stator and copper windings on the rotor as shown in

Figure 1. It is rated for 2670 N at 12 VDC with additional manufacturer supplied data as provided in table 1.

Table 1: Manufacturer supplied data for PA 03-10-600 EMA

Maximum Voltage	12 VDC
Current at Maximum Dynamic Load	7.6 A
Maximum force	2670 N (600 lbs)
Duty Cycle	20%
Stroke Length	10 ”
Protection rating	IP54
Insulation class/ Maximum winding Temperature	F/ 150°C (Based on an ambient of 65°C)

In dynamic mode, the linear actuator has a maximum speed of 0.39 inch/s (9.9 mm/s). When the motor is powered, and the actuator is held in a static position as in Figure 1 b, the linear motion of the actuator shaft is stopped, the motor shaft as well as the associated drive gears come to near zero rotational speeds. Hence the stopping mechanism which simulates a static load provides a breaking force for the electrical motor. The temperature of selected positions on the copper windings and air trapped inside the housing are monitored and logged during the operation of the motor using the thermocouples and the MCC data acquisition system. The circuit diagram in Figure 2 shows how the set up was connected electrically.



a. Original motor in holding position



b. Inside view of motor shows copper windings embedded in rotor core and separated by a clearance. Stator is a permanent magnet



c. PA 03 EMA with 5 heat pipes extending through the cover

Figure 1: PA 03 EMA with 5 heat pipes extending through the cover

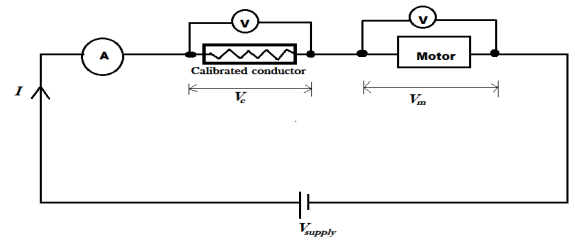


Figure 2: Circuit diagram for the experiment



Figure 3: inside view of motor showing heat pipe evaporators

For a period of seven minutes the motor was run in extension mode at a nominal supply of 6.05 Amps corresponding to $Q=20.5\pm 1.2$ Watts, first without heat pipes and later with varying number of heat pipes. The procedure was repeated with a supply of 7.10 Amps, corresponding to $Q=28.2\pm 2$ Watts. This allows the effects of heat pipes on the transient behavior of the EMA to be monitored as presented in the graphs in the next section.

To optimize the heat transfer enhancement of the heat pipes, a network of 36 gage enameled wire was interlaced in between the heat pipes at the evaporator section of the heat pipes. The 36-gage enameled copper wire has diameter of 0.124 mm the total mass of the wire used in the mesh is approximately 3.48grams which is less than the mass of one heat pipe (5.27 g). Thus, it would be plausible to be able to cut down on the number of heat pipes required if the tradeoff is a few grams of wire mesh from the weigh savings point of view.

The addition of these woven structures is to increase the metallic presence in the housing area occupied by near-stagnant heated air, thereby improving the heat transfer path to the heat pipes for onward transference to the ambient. The addition of porous fins brought about additional reduction in temperature of the internal components of the EMA.



a. Network of porous fins heat pipes and motor cover



b. Ten heat pipes in porous fins



c. Five heat pipes in porous fins



d. Two heat pipes in porous fins

Figure 4: interlaced copper wires form a network of porous fins enhancing heat transfer from trapped air to the heat pipes

RESULTS AND DISCUSSION

Figures 5 through 10 present the temperature at an EMA power setting of 20.5 Watts. Without heat pipes the original EMA show a maximum winding temperature of 63.4°C and internal air temperature of 30.5°C as seen in figure 5. The introduction of heat pipes through the top cover of the motor affected the temperature profile of both the windings and the inside air positively, bringing notable reduction in both temperatures at the end of the recording period. From Figures 9 and 10 the maximum winding temperature drops to 56.2°C whilst the air drops to 24.1°C. Figures 11 and 12 show the performance at a power setting of 28.2 W. whilst Figure 13 summarizes the temperature reductions at various design points.

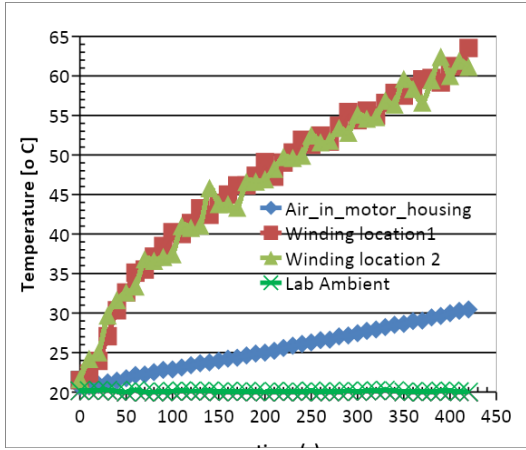


Figure 5: Temperature profile of original motor at heating rate of $Q=20.5$ Watts

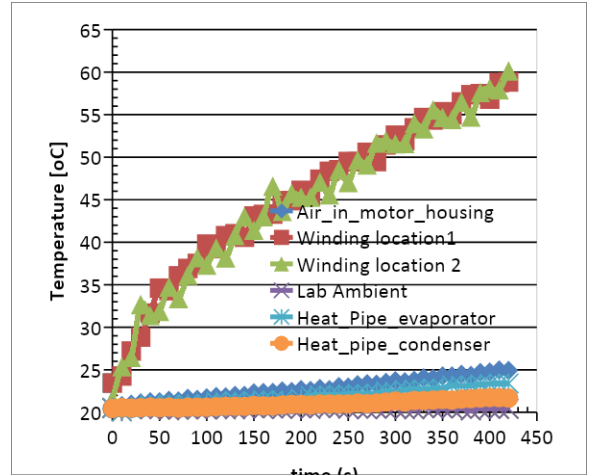


Figure 7: Temperature profile of motor at heating rate of $Q=20.5$ Watts with 8 heat pipes, δT of heat pipes = $1.32^\circ C$

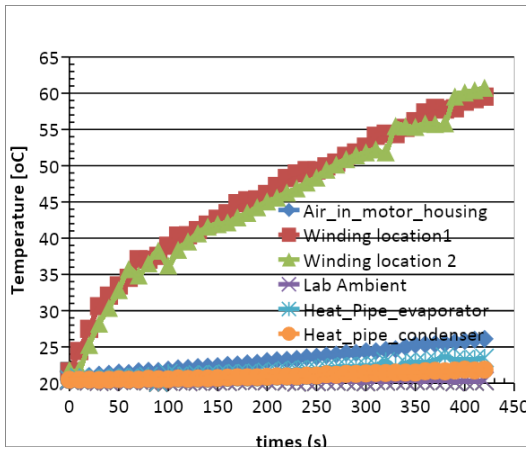


Figure 6: Temperature profile of motor at heating rate of $Q=20.5$ Watts with 5 heat pipes, δT of heat pipes = $1.20^\circ C$

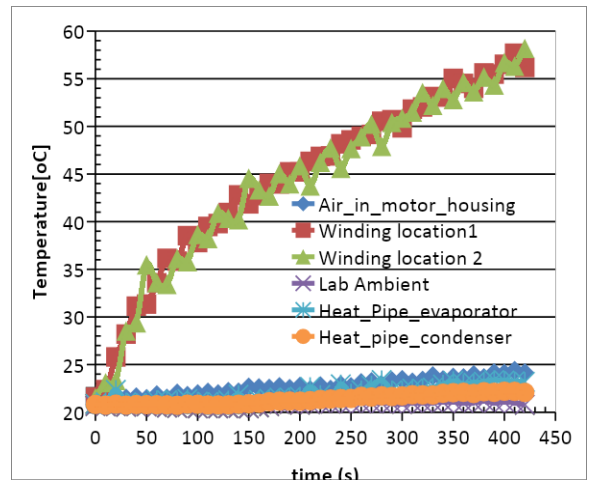


Figure 8: Temperature profile of motor at heating rate of $Q=20.5$ Watts with 10 heat pipes δT of heat pipes = $0.84^\circ C$

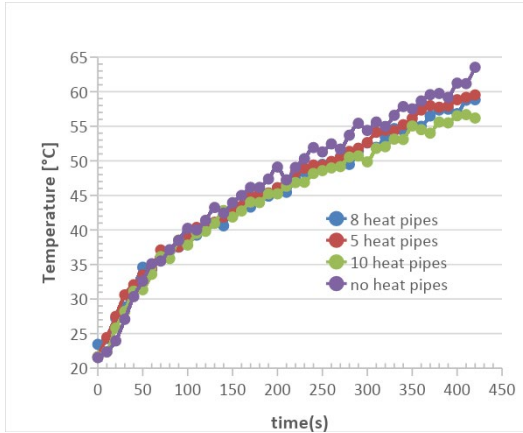


Figure 9: Temperature of windings at heating rate of $Q=20.5$ Watts

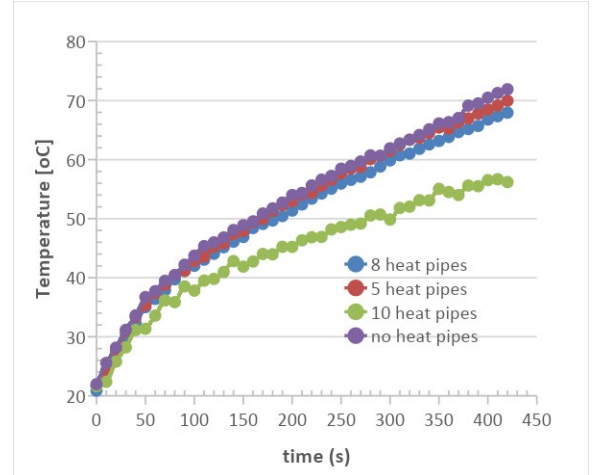


Figure 11: Temperature of windings at heating rate of $Q=28.2$ Watts

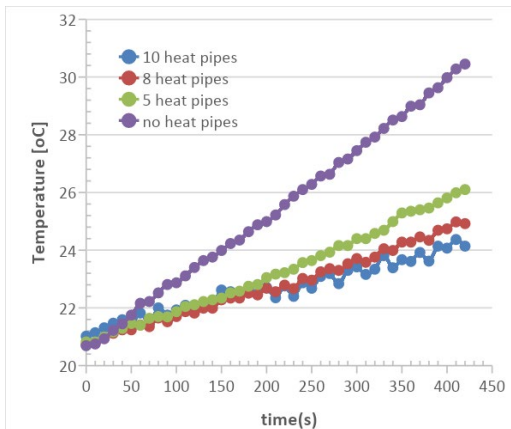


Figure 10: Air temperature inside motor housing at heating rate of $Q=20.5$ Watts

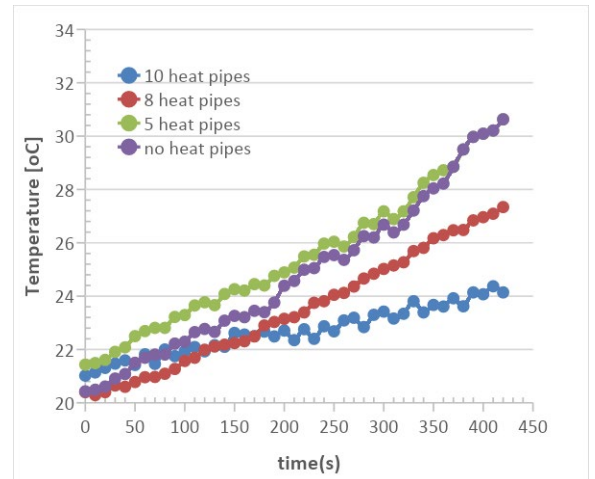


Figure 12: Air Temperature inside housing at heating rate of $Q=28.2$ Watts

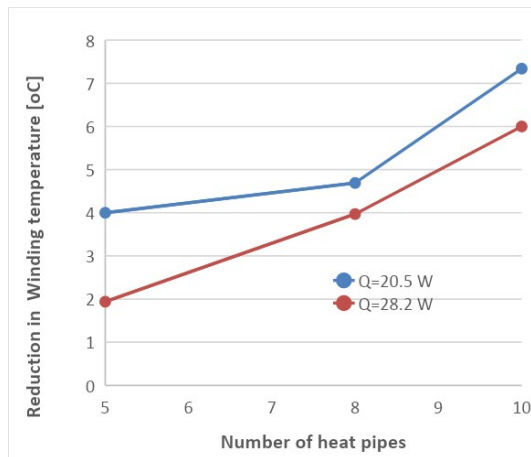


Figure 13: Reduction in temperature of windings vs number of heat pipes

The matrix of heat pipes and meshed copper wires was seen to enhance on the heat transfer characteristics of the EMA considerably as seen in Figures 14 through 17. At moderate power (nominal heating of 20.5 W), the reduction in winding temperature is 11.9°C with ten heat pipes and 11.6°C with five heat pipes, from which it can be inferred that the effect of changing between ten heat pipes was insignificant on the winding temperature. At high power (nominal heating of 28.2 W), this enhancement results in approximately 8°C drop in in maximum winding temperature with ten heat pipes and downgrades to 6°C with five heat pipes.

High power modes of the EMA require higher heat transfer from within the device if the same level of thermal management is desired. This is consistent with the fact that five heat pipes working the 20.5 W setting is unable to achieve a comparable effect for the 28.2 W setting

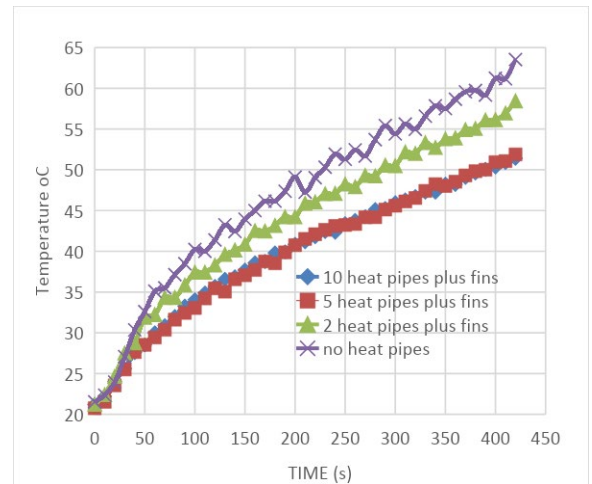


Figure 14: Temperature profile of windings 20.5 W when EMA was modified with heat pipes and porous fins

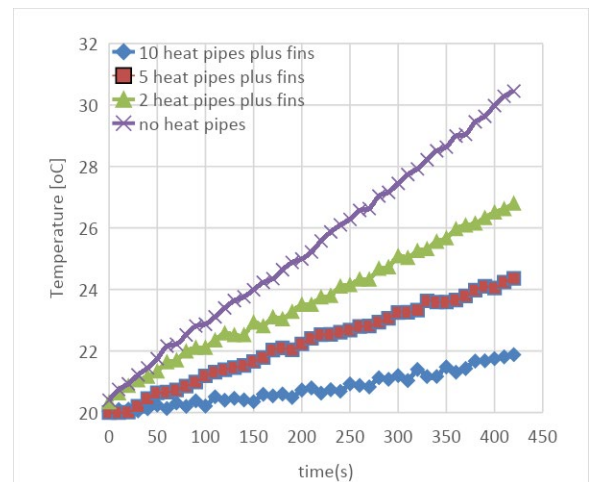


Figure 15: Temperature profile of inside air at 20.5 W when EMA was modified with heat pipes and porous fins

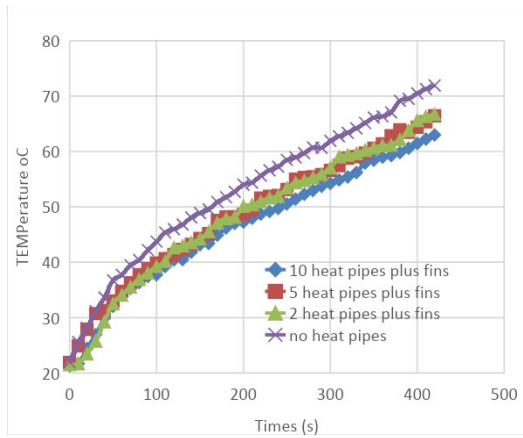


Figure 16: Temperature profile of windings at 28.2 W when EMA was modified with heat pipes and porous fins

Maximum winding temperature at $Q=28.2$ W

At $Q=28.2$ W a temperature reduction of 9°C is obtained by using ten heat pipes and the porous fins formed by enameled copper wires. The use of two or five heat pipes resulted in a 5.2°C reduction of winding temperature.

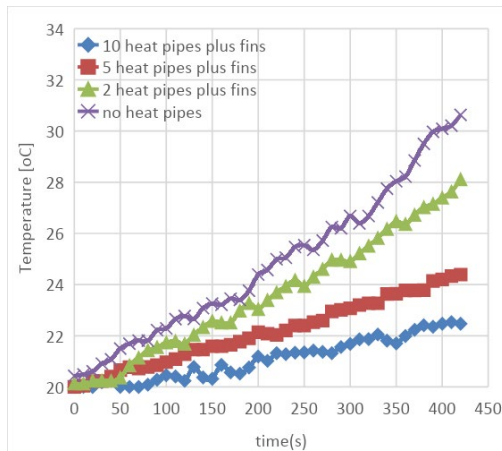


Figure 17: Temperature profile of inside air at 28.2 W when EMA was modified with heat pipes and porous fins

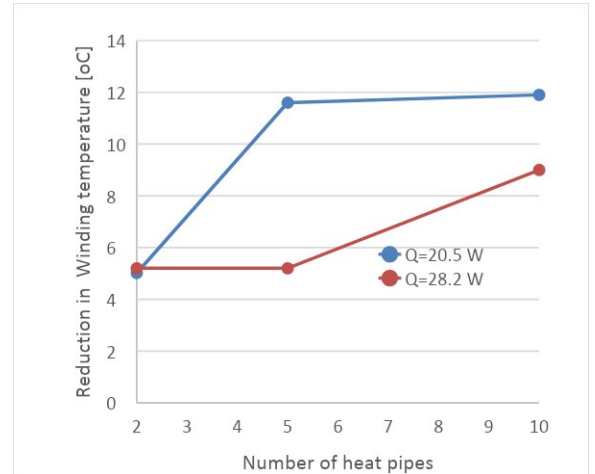


Figure 18: Reduction in temperature of windings vs number of heat pipes in finned configuration

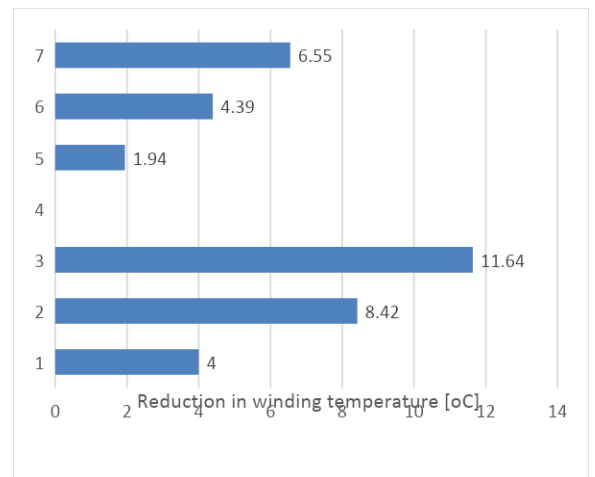


Figure 19: Reduction in winding temperature with 5 heat pipes at different configurations

CONCLUDING REMARKS

The study showed that the use of only heat pipes resulted in lower temperatures for the copper windings. With

ten heat pipes hanging in the device, a temperature reduction of 7.3°C and 6°C was recorded respectively at EMA power settings of 20.5 W and 28.2W. The temperature reduction effect is better with increasing number of heat pipes and was further enhanced by interlacing the evaporator ends with the porous fins. The heat pipes also lowered the temperature of the air trapped in the motor housing. The reduction in air temperature is an effect of the introduction of heat pipes and serves as an intermediate causality for the observed lower winding temperatures.

Five heat pipes with porous fins proved to be the optimum operating point for the 20.5 W power setting whilst the 28.2 W power setting required more heat pipes to achieve a comparable thermal regulation. High power modes of the EMA require higher heat transfer from within the device if the same level of thermal management is desired. This is consistent with the fact that five heat pipes working the 20.5 W setting is unable to achieve a comparable effect for the 28.2 W setting. Subsequent studies will focus on the determination of novel ways of further enhancing the heat transfer path from the motor windings to the heat pipes.

Acknowledgements

The authors are grateful to the US Airforce for funding this research.

References

1. Jensen, S.C., G.D. Jenney, and D. Dawson. Flight test experience with an electromechanical actuator on the F-18 Systems Research Aircraft. in 19th DASC.

19th Digital Avionics Systems Conference. Proceedings (Cat. No.00CH37126). 2000.

2. Garcia, A., et al., *Reliable electro-mechanical actuators in aircraft*. IEEE Aerospace and Electronic Systems Magazine, 2008. 23(8): p. 19-25.

3. Wang, Huawei, et al. "An integrated heat pipe coupling the vapor chamber and two cylindrical heat pipes with high anti-gravity thermal performance." *Applied Thermal Engineering* 159 (2019): 113816.

4. M. Arik, J. Petroski, S. Weaver, Thermal challenges in the future generation solid-state lighting applications: Light emitting diodes, in: Conference on Thermal & Thermomechanical Phenomena in Electronic Systems, 2002.

5. Zhirnov, Victor V., et al. "Limits to binary logic switch scaling-a gedanken model." *Proceedings of the IEEE* 91.11 (2003): 1934-1939.

6. L. Zhu, H. Tan, J. Yu, Analysis on optimal heat exchanger size of thermoelectric cooler for electronic cooling applications, *Energy Convers. Manage.* 76 (2013)685–690.

7. Corona, J. J., et al. "Testing of a Cooling Fan for Wing-Bay Electro-Mechanical Actuators." ASME 2018 5th Joint US-European Fluids Engineering Division Summer Meeting. American Society of Mechanical Engineers Digital Collection, 2018.

8. Putra, Nandy, and Bambang Ariantara. "Electric motor thermal management system using L-shaped flat

heat pipes." *Applied Thermal Engineering* 126 (2017): 1156-1163.

9. T. Davin, J. Pellé, S. Harmand, R. Yu Experimental study of oil cooling systems for electric motors *Appl. Therm. Eng.*, 75 (2015), pp. 1-13.

10. Lee, Kea-Ho, Hyun-Rok Cha, and Young-Bae Kim. "Development of an interior permanent magnet motor through rotor cooling for electric vehicles." *Applied Thermal Engineering* 95 (2016): 348-356.

11. Faghri, Amir. "Heat pipes: review, opportunities and challenges." *Frontiers in Heat Pipes (FHP)* 5.1 (2014).

12. Kabir, Rifat, et al. "Investigation of a Cooling System for A Hybrid Airplane." 2018 AIAA/IEEE Electric Aircraft Technologies Symposium. 2018.

13. Chen, Xianping, et al. "A review of small heat pipes for electronics." *Applied Thermal Engineering* 96 (2016): 1-17.

14. K. Kaddoura, Abosti, O.Y.W., and J.P. Kizito, EFFECT OF SCREEN LAYERS AND ORIENTATIONS ON MESH WICKED HEAT PIPES, in *Proceedings of the 18th Annual Early Career Technical Conference*. 2018, School of Engineering, University of Alabama Birmingham: Birmingham, Alabama.

15. Putra, Nandy, and Wayan Nata Septiadi. "Improvement of heat pipe performance through integration of a coral biomaterial wick structure into the heat pipe of a CPU cooling system." *Heat and Mass Transfer* 53.4 (2017): 1163-1174.

16. Putra, Nandy, et al. "Thermal performance of biomaterial wick loop heat

pipes with water-based Al₂O₃ nanofluids." *International Journal of Thermal Sciences* 76 (2014): 128-136.

17. Putra, Nandy, et al. "Thermal performance of screen mesh wick heat pipes with nanofluids." *Experimental thermal and fluid science* 40 (2012): 10-17.

18. Akuoko Kwarteng, A., et al., Thermal management of Electromechanical Actuator Motor by circulating air inside the housing, in *International Mechanical Engineering Congress and Exposition*. 2019, ASME: Salt Lake City, Utah.

19. Abosti, O.Y.W., K. Kaddoura, and J.P. Kizito, *Performance of Gravity Independent Heat pipe*, in *Proceedings of the 18th Annual Early Career Technical Conference*. 2018, School of Engineering, University of Alabama Birmingham: Birmingham, Alabama. p. 3-10.

APPENDIX F

Comparison of Two Axial Fans for Cooling of Electromechanical Actuators at Variable Pressure

Jose J. Corona Jr.^{a,1}, Kamal A. Kaddoura^a, Augustine A. Kwarteng^a, Osama Mesalhy^{b,c}, Louis C. Chow^b, Quinn H. Leland^d, John P. Kizito^{a,*}

^a*Department of Mechanical Engineering, North Carolina Agricultural and Technological State University,
Greensboro, NC 27411, USA*

^b*Department of Mechanical and Aerospace Engineering, University of Central Florida, Orlando, FL 32816-2450,
USA*

^c*Department of Mechanical Power Engineering, Zagazig University, Zagazig 44519, Egypt*

^d*Power and Control Division, Aerospace Systems Directorate, Air Force Research Laboratory, Wright Patterson
Air Force Base, OH 45433, USA*

Abstract

Electro-Mechanical Actuators (EMAs) in the aerospace field will provide major benefits to reduce overall weight, cost, and easier maintenance when servicing the aircraft. In the present study, two cooling fans were tested experimentally to determine the effects of the blade count and ambient pressure on the fan performance and efficiency. Both fans were tested at the same rotational speed of 13,000 rpm and four pressure conditions, (1, 0.7, 0.5, 0.3) atm. The lowest ambient pressure tested was 0.3 atm. Typical commercial aircraft operate at this ambient pressure at cruising altitudes. Selecting a 2-bladed and 7-bladed fan accommodates for testing of the extrema in terms of solidity, fan performance, and efficiency. The 7-bladed fan yielded the best performance to the 2-bladed fan in terms of static pressure to the volumetric flow rate, but the 2-bladed fan demonstrated to operate more efficiently than the 7-bladed fan in some ambient pressure conditions. The 7-bladed fan demonstrated turbulent flow regimes with Reynolds numbers, $Re \gg 4000$, for all cases except for at the high resistance when operating at 0.3 atm.; on the other hand, the 2-bladed fan-operated in the laminar and transitional flow regimes for 0.3 atm. and during shutoff conditions at 0.5 atm. The higher Reynolds numbers allow for more air mixing which will, in turn, enhance the cooling of the system. In terms of volumetric flow rate delivery, the higher blade counts can deliver higher volumetric flow rates. The smaller blade counts perform more efficiently at (0.7, 0.5) atm which is due to lower power requirement to drive the blades. The current work addresses the effects of pressure on fan efficiency and performance. Both fans demonstrated higher efficiencies at pressure lower than ambient pressure due to the density changes at the lower pressure conditions.

Keywords: Forced convection, fan performance curves, Electro-Mechanical Actuator, Aerospace, Pressure effects

*Corresponding author.

E-mail: jpkizito@ncat.edu (John P. Kizito).

Introduction

In recent times there is a new demand for electromechanical actuation. Many works have been produced changing the current linear actuation systems to electromechanical units in aerospace applications. In Qiao et al., a direct comparison of the three main power-by-wire actuators is analyzed: electro-hydrostatic actuator (EHA), electromechanical actuator (EMA), and hydraulic servo actuators (HSA). EMA is the emerging technology that will be implemented in future years due to its safety and reliability improvement, and easily accessible maintenance [1]. EMA implementation is an emerging technology being studied for many types of air vehicles; which includes airplanes and vertical take-off and landing (VTOL) vehicles such as helicopters; moreover, Helicopter Electromechanical Actuation System (HEMAS) are also being analyzed for More Electric Aircraft (MEA) systems. The main electrical components of a helicopter were analyzed, and prototyping tests were conducted for thermal, electromagnetic, and rotor-dynamic studies [2]. Although EMA's have the potential to replace traditional actuation, there are critical safety concerns still that need to be addressed: limitations in weight and size, voltage spikes and current transients can affect the stability of electrical networks, thermal management of the system, dynamic performance of the actuator, reliability issues in the safety of the EMA from failing [3]. Interest for EMA in aerospace applications has been ongoing for several decades [4] and many researchers are currently attempting to implement design strategies that will ensure reliability by introducing multiple redundant actuator systems [5].

In the work presented, the focus is on the thermal management of the EMA. Multiple cooling strategies have been implemented. Heat pipe applications are widely used in electronics cooling, such as in computer workstations and any form of electronics that generates high heat loads [6]. The electric motor is permanent magnet synchronous motors that are extremely popular for hybrid electric vehicles; moreover, thermal management of these systems has been conducted using phase-changing heat pipes of various configurations. Heat pipes have emerged as a prominent technology in order to cool electronic components, and the working principle of such cooling structures is discussed in [7] and is a great option due to its compactness. According to Fang et. al, a straightly embedded module in an enclosure heat pipe significantly reduces peak temperature by about 22.3% under strenuous conditions of the EMA's operation [8]. Heat pipes can be used to cool heated sections of a system and distribute that heat to other parts needing higher temperatures [9]. Other researchers have implemented L-shaped heat pipes for cooling electric motors. Combining the L-shaped heat pipes with radial finned heat sinks demonstrated at 44% reduction in thermal resistance to that of the heat sink alone [10]. In Aprianingsih et al., using pulsating heat pipes with acetone as the working fluid and 50% infill within the heat pipe demonstrated to reduce the surface temperature of the electric motor by 55.3°C and minimizing the thermal resistance to 0.151°C/W [11].

Other cooling techniques have been analyzed for EMA cooling, such as thermal radiation studies have been conducted. In McCarthy et al, radiation studies are analyzed and demonstrate that it is the main mode of heat transfer to provide cooling to EMA's in a wing-bay enclosure of an aircraft [12]. Other researchers have demonstrated that natural convection and radiation is not sufficient to cool these high heat loads introduced by the electric motors [13]. Some researchers have focused on the fluid flow within microfluidic devices for design enhancements of such devices [14]. The

use of holographic interference and smoke was used to determine heating of a confined space under natural convection effects [15]; moreover, the EMA also a heat source within a confined 3-dimensional space. Work in analyzing the effects of flow and thermal regimes have been conducted of the transitional flow regime; moreover, researchers found that the Reynolds number increased with increasing heat fluxes because of viscosity and temperature [16]. Turbulent flows are of large interest due to the majority of natural flow phenomenon in nature occurs in the turbulent regime; furthermore, novel techniques of fluid flow and heat transfer have been studied extensively for winglet shapes [17] which can have applications of fan blade development.

For the current work, the forced convection cooling will be achieved by using axial fans. Many researchers have worked on improvements to axial fans have designed innovative techniques to improve their overall performance. In Li et al, the research entails designing rapid prototyping of a ducted fan with tip-jets. The researchers relied on the Coanda effect that causes the fluid to wrap around a solid body to push the blades forward. They claim that it has the nozzle functions under subsonic to supersonic conditions [18]. Other studies on the effect of tip clearance on the performance of an impeller. The varied the height of the tip clearance by 5%, 10%, and 15% to study the effect. Simulation results demonstrated that impeller trimming has adverse effects on fan performance; moreover, at the optimal flow rate fans without tip clearing change have better performance [19]. Studies of abnormal condition blades have been studied. Fan performance is lower than normal value and the noise rises. Varying the angle at which the abnormal blade is and obtained hydrodynamic and acoustic results for the undesired fan blade. The pressure contours demonstrate high pressures at localized points on the blade which could potentially cause severe problems [20]. Other studies have modified the tip of the fan by introducing grooves. A direct groove at the tip was superior over other groove designs [21]. In Wu et. al the idea of improving the reliability of the EMA cooling fan. The current fan EMA fan technology is a brushless direct current motor that powers the fan. Improvement of the meantime to failure (MTTF) of the fan from 5×10^4 to 2.5×10^9 hours of operation. The approach is to determine the possible causes of failure which are categorized into two failure mechanisms: (1) mechanical and (2) electrical failures. The solutions proposed to improve the reliability of the system are to include dual bearings, dual windings, and dual fans. They conclude that the utilizing a dual fan system is beneficial; other hand, implementing either a dual bearing or dual winding system alone does not drastically improve the reliability of the overall system [22] Previous researchers focus on developing a fan that can effectively cool an electromechanical actuator (EMA) for a wide range of ambient pressures; additionally, generating high static pressure head, high volumetric flow rate, and high efficiency over a wide operating range of rotational speed and ambient pressure. At maximum altitude aircraft experience, ambient pressures of 20% atmospheric; furthermore, the research focuses on fan design and optimization of the fan blades to operate from (0.2 – 1) atm. A commercially available fan by AMETEK is used for the analysis, specifically the Propimax 2 [22-28].

The design parameters that were varied in their work were to improve the performance of the commercially available fan are the setting angle, the blade root chord, and the blade end chord. CFD results were obtained indicate that a 1.81x improvement was obtained over that of the commercially available fan for a wide range of fan rotational speeds, (8,000 – 22,000) rpm, and ambient pressure conditions, (0.2 – 1) atm.; moreover, the pressure directly affects the density within the system [24, 29]. The Ametek Propimax 2 was used to test the fan scaling laws by

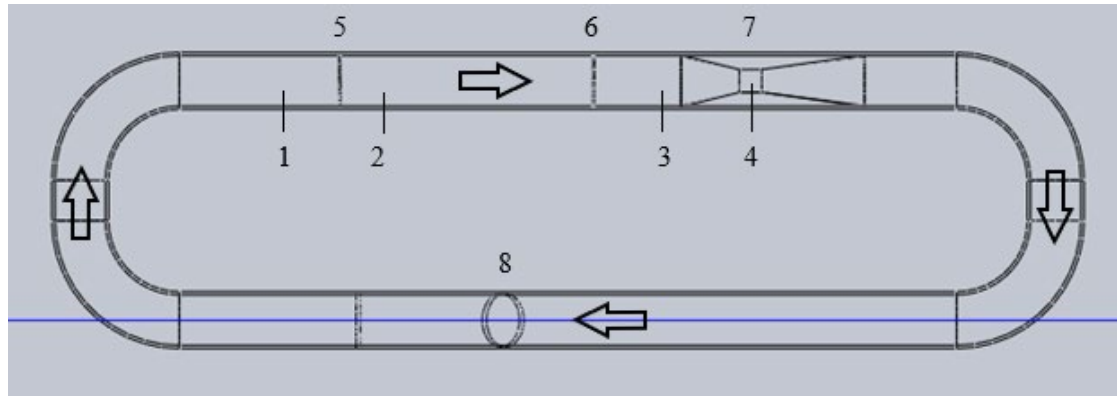
varying all parameters except for one at a time. The conclusions yielded similar results to that of [27, 30] since a similar setup and fan were used. However, a high powered 12-bladed fan for RC aircraft was used to compare the performance curves of the 2-bladed vs 12-bladed fan. Adverse thermodynamic effects were measured within the system due to the high-power requirement of the 12-bladed fan. The air within the experimental setup was being heated due to the high heat generated by the motor of the 12-bladed ducted fan [28]; furthermore, using a lower-powered fan is tested in the current work. The system is a fully enclosed ducted system, the inherent losses of the system can affect the performance of fan. Convective heat transfer has been analyzed extensively for straight pipes; furthermore, work has been shown to have heat transfer and pressure loss improvements for helical as opposed to straight pipes [31].

To the best of the authors' knowledge, the current work on studying the adverse effects of pressure on fan performance and fan efficiency is limited. Currently, the aim of the research is to focus on design and experimental rig that can effectively analyze fan performance of various axial fans. The only restriction of the experimental loop is the maximum diameter of the fan cannot exceed 4in. First, the experimental setup and the equipment used is presented. Followed by calculations necessary to determine the fan performance curve and efficiencies of the systems. The error analysis of the measurements is determined using regression analysis and the main parameters that could lead to experimental error are considered in depth. The validation of the 2-bladed fan is demonstrated; moreover, two fans were experimentally tested at four ambient pressures, (1, 0.7, 0.5, 0.3) atm. The findings are discussed in the following sections and the results measured conclude that not only must the hydrodynamic performance of the fans can be considered, but also that the fan efficiency is critical in identifying a viable option in cooling EMAs at variable pressures.

Experimental setup

2.1. Equipment used for experimental setup

In Fig. 1 the experimental loop is depicted. The loop is comprised of various components to accurately determine the fan performance curve at various pressure conditions. The overall hydraulic diameter of the system is 4" PVC pipe. The pipe is a standard schedule 40 PVC pipe. The butterfly valve provides the ability to throttle the volumetric flow rate within the loop. There are two types of fixtures that mate the individual PVC pipes. The first is permanent joints that have been introduced to the elbows and around the butterfly valve. Secondly, the black coupling units provide the ability to give removable joints within the system. These joints are beneficial in cases where extensions/reductions are necessary for the system. Both methods of joining the components demonstrate the ability to maintain a vacuum.



1,2,3,4—pressure transducers; 5—fan with power supply and PC for fan speed measurement; 6—NEL Spearman; 7—Venturi flowmeter; 8—Butterfly valve

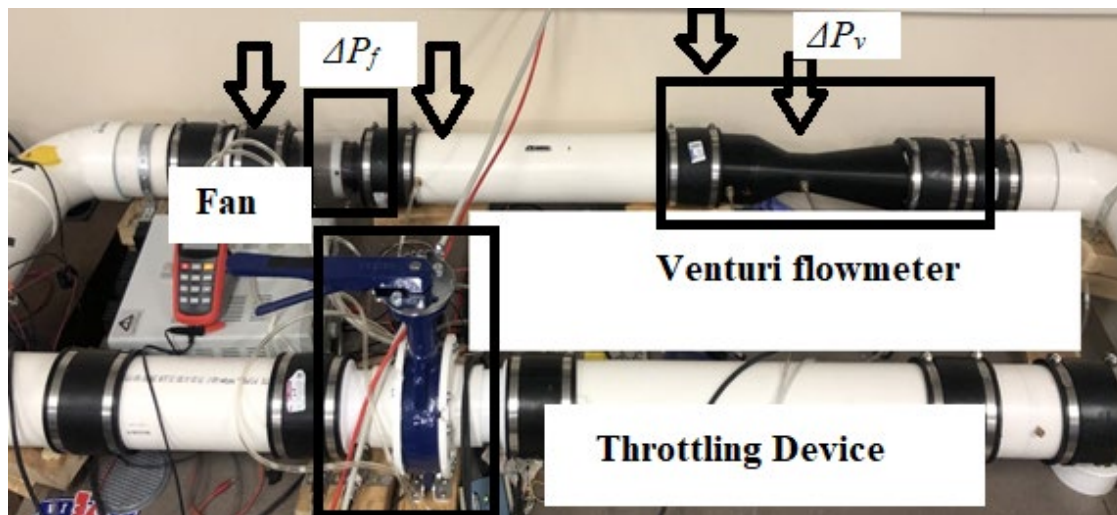


Fig. 1. Structural diagram (top) with experimental loop (bottom).

All the pressure measurements are static pressures located at the wall of the pipe. The pressure taps across the fan determine static pressure rise across the fan ΔP_f , and the pressure drop in the Venturi flowmeter gives the volumetric system of the fluid within the system ΔP_v . The pipe tap distances and lengths all follow minimum length requirements followed by the Air Movement & Control Association and specific dimensions are specified in previous work [28, 32]. With the use of a butterfly valve, the system resistance is throttled to obtain the various points along the fan performance curves.

The Venturi flowmeter used to determine the volumetric flow rate within the system was additively manufactured of Acrylonitrile Butadiene Styrene (ABS). Enough infill percentage was used so that the Venturi would be able to withstand the large pressure gradient of the ambient conditions in the lab to the internal pressure of the experimental loop. The Venturi follows ISO Standard 5167-4 [33] with a diameter ratio, $\beta = 0.51$, and is demonstrated below in Fig. 2. The original Venturi flowmeter was fabricated by machining nylon but was replaced with the current design due to its smaller throat diameter and larger pressure loss within the system. The volumetric flow rate was tested with a secondary flow obstruction device, a pitot tube, and the volumetric flow rates

determined from both devices. In Fig. 3, an image of the pitot tube is demonstrated to show the integration of the device into the flow loop, which must have been placed directly in the center of the tube to obtain the correct measurement of total pressure.



Fig. 2. The 3D printed ABS Venturi, $\beta = 0.51$.



Fig. 3. The Pitot tube incorporated into the tube to determine the volumetric flow rate.

The Pitot tube gives us point measurement whereas a Venturi flow meter gives us the average flow rate. The Pitot tube is calibrated by the manufacturer; then we use the Pitot tube to calibrate the 3D printed (in-house) Venturi flowmeter. By calibrating the Venturi flowmeter with the Pitot tube there is high confidence in the measurement and determination of the volumetric flow rate. The experimental setup of the calibration performed is demonstrated in Fig. 4. The Pitot tube is placed upstream, and the Venturi flowmeter is placed downstream in both cases. The order of the flow measurement devices was chosen in that manner to reduce the restriction of the pressure drop in the Venturi from affecting the measurement in the Pitot tube. It is expected that the Pitot tube will have a negligible pressure drop due to its smaller size in obstructing the flow.

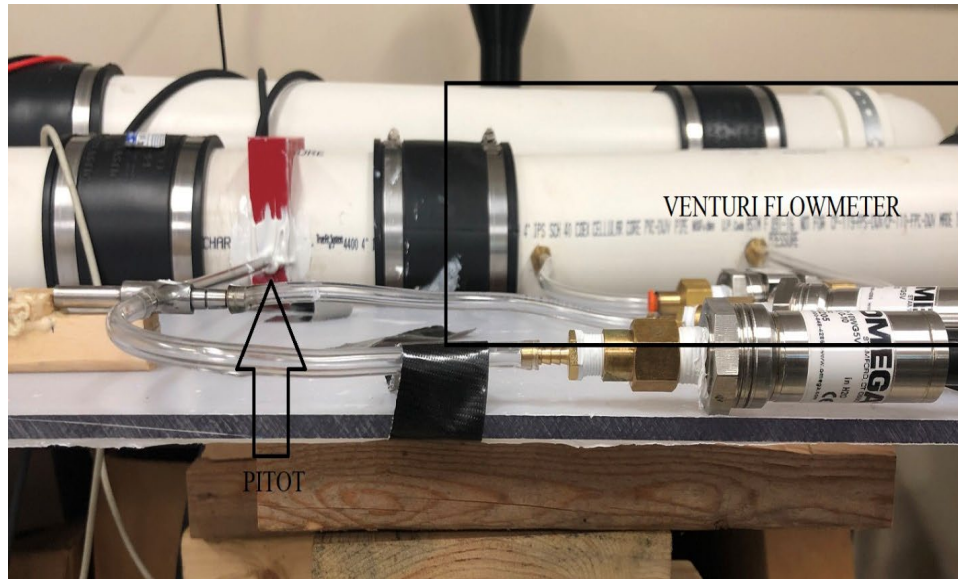


Fig. 4. Demonstrates the calibration of the 3D printed Venturi flowmeter.

The pressure drops were measured using OMEGA's High Accuracy PX-409 Pressure Transducers. The transducers feature a $\frac{1}{4}$ in. NPT thread is connected to barbed fittings followed by a flexible tube to be hooked into the loop. In Fig. 4, the transducers are pictured and their respective fittings.

The two fan systems use 3-wire and 4-wire cabling system and the three wires used are positive and negative to power the fans and the third wire is the signal wire to detect the frequency of the fan. Fig. 5a demonstrates the Arduino setup to read the fan's rotational speed from the Hall Sensor inserted in the hub of the fans. A script was written in Arduino that determined the frequency in the electromagnetism within the brushless motor. A Hall Effect sensor inside the hub counts the frequency and that is then converted into angular velocity. The Protmex tachometer was used to verify the rotational speed of the fan as displayed in Fig. 5b. The accuracy of the tachometer is $50 - 99999 \pm (0.03\% + 2) \text{ rpm}$. The highest fan speed measured in the current work is 21,170 rpm; therefore, the maximum possible error in measurement is 8.4 rpm when operating at 21,170 rpm.

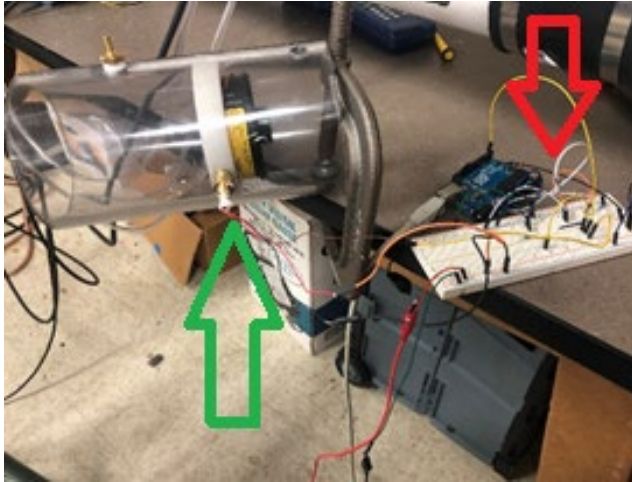


Fig. 5a. Arduino hardware setup (red arrow) that is used to read the fan (green arrow) speed from the signal wire (brown), the red and black wire are positive and ground, respectively.



Fig. 5b. The Protmex non-contact tachometer used to verify the fan's rotational speed.

To test for low-ambient pressure conditions within the loop, a two-stage vacuum pump by HFS with a suction rate of 12 cfm; moreover, the vacuum pump had enough suction capacity to obtain a pressure of 0.3 atm. The pump used for the test is pictured in Fig. 6. Previous tests in [23, 28] demonstrated that 20% atmospheric pressure condition posed difficulties in obtaining results of the performance curves at those conditions.



Fig. 6. The vacuum pump utilized to change the ambient pressure within the loop.

2.2. Fans tested

The two geometrically different fans were selected in conducting the fan performance test. The first fan is a Propimax 2L by Ametek (Fan 1) [34], shown in Fig. 7. Fan 1 features a 2-bladed configuration with an optimized fan speed of 18,400 RPM. Fan 1 has a round shroud with an

effective blade diameter of 77.33mm. The fan was inserted into a clear Butyrate tube, its diameter of the fan is slightly smaller than the 4 in. duct; furthermore, to secure the fan in place nylon was machined with a locking screw to fasten the assembly into the tube.

The second fan system by Delta (Fan 2) is integrated in a similar manner. Fan 2 features a square shroud which makes mounting easier than the round configuration of Fan 1; in addition, black insulation foam was used to fix its position inside of the tube. In Fig. 8, the Delta dual fan system is presented in its 7-bladed and 5-bladed configuration [35], but in further testing in the comparison of the two fans only the entrance, 7-bladed, is used. Fan 2 has a blade diameter of 71.2mm.

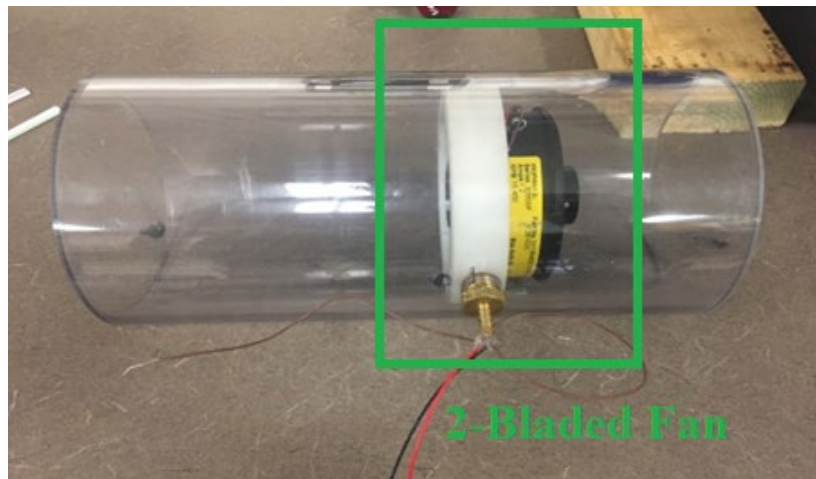


Fig. 7. Integration of the nylon and fan assembly to secure the 2-bladed fan, Fan 1.



Fig. 8. The Delta dual fan system and its incorporation into the clear tube, Fan 2.

Theory

3.1. Hydrodynamic equations

From Fig. 1, the experimental loop consists of pressure taps to obtain the fan performance. The volumetric flow rate within the system is determined from the Bernoulli energy equation of obstruction flow devices. The volumetric flow rate is given by,

$$Q = C_d A_t \left[\frac{2\Delta P_v}{\rho(1-\beta^4)} \right]^{1/2} \quad (1)$$

where C_d is the discharge coefficient, A_t throat cross-sectional area of the Venturi, ΔP_v is the pressure drop across the Venturi, $\rho = P/RT$ the density of the air within the system and the diameter ratio of the throat to the system is given by $\beta = d/D$. The discharge coefficient is given by [36, 37],

$$C_d \approx 0.9858 - 0.196\beta^{4.5} \quad (2)$$

which is a minor loss for Venturi flow meters unlike other obstruction devices in determining the volumetric flow rate; nonetheless is a factor that must be considered due to its dependence upon the diameter ratio.

The hydrodynamic power that is supplied by the axial flow fans was determined by,

$$\dot{W} = \Delta P_f Q \quad (3)$$

where ΔP_f is pressure rise across the fan. The Reynolds number is given by [38],

$$Re = \frac{\rho V D}{\mu} \quad (4)$$

where ρ is the fluid density, μ is the dynamic viscosity, V is the fluid velocity, and D is the hydraulic diameter of the system. From continuity, it is known that $Q = AV$, and plugging in that relationship into Eq. (4), the Reynolds number can be derived to,

$$Re = \frac{4\rho Q}{\mu\pi D} \quad (5)$$

thus, the Reynolds number can be determined directly from the volumetric flow rate determined by the measurement within the system.

3.2. Electrical component equations

The main concern in determining the fan performance curve is the physics of hydrodynamics related to the fan. Nonetheless, the fan must be supplied electrical power to drive the propeller; therefore, the input power to the fan is essential in determining the overall efficiency of the axial fan. The power input is determined experimentally by recording the voltage and current supplied to the fan. Hence, the efficiency of the fan yields [38],

$$\eta = \frac{\Delta P_f Q}{V_e I}, \quad (6)$$

where the numerator is the output power, fluid power, and the denominator denote the input power, the electrical power supplied to the fan; moreover, those parameters determine were used to determine the efficiency.

Error Analysis

Taking the root mean squares approach in determining the uncertainty in the volume flow rate as follows [39],

$$u_Q = \left[\left(\frac{\partial Q}{\partial \Delta P} u_{\Delta P} \right)^2 + \left(\frac{\partial Q}{\partial C_d} u_{C_d} \right)^2 + \left(\frac{\partial Q}{\partial A_t} u_{A_t} \right)^2 + \left(\frac{\partial Q}{\partial \beta} u_{\beta} \right)^2 + \left(\frac{\partial Q}{\partial \rho} u_{\rho} \right)^2 \right]^{1/2} \quad (7)$$

where the uncertainties in the independent variables $u_{\delta P}$, u_{C_d} , u_{β} , u_{ρ} , u_{A_t} contribute to the overall uncertainty in the volumetric flow rate. The following set of Eq. (8-12) are the partial derivatives for the volumetric flow rate as a function of the pressure drop measured, density determined, discharge coefficient, Venturi throat cross-sectional area, and the diameter ratio as follows,

$$\frac{\partial Q}{\partial \delta P} = \frac{C_d A_t}{\sqrt{2\rho(1-\beta^4)}} \left[\frac{\delta P}{\rho(1-\beta^4)} \right]^{-1/2} \quad (8)$$

$$\frac{\partial Q}{\partial \rho} = -\frac{C_d A_t \delta P}{\sqrt{2\rho^2(1-\beta^4)}} \left[\frac{\delta P}{\rho(1-\beta^4)} \right]^{-1/2} \quad (9)$$

$$\frac{\partial Q}{\partial C_d} = \sqrt{2} A_t \sqrt{\frac{\delta P}{\rho(1-\beta^4)}} \quad (10)$$

$$\frac{\partial Q}{\partial A_t} = \sqrt{2} C_d \sqrt{\frac{\delta P}{\rho(1-\beta^4)}} \quad (11)$$

$$\frac{\partial Q}{\partial \beta} = \frac{2^{3/2} C_d A_t \delta P \beta^3}{\rho(\beta^4-1)^2} \left[\frac{\delta P}{\rho(1-\beta^4)} \right]^{-1/2} \quad (12)$$

and can observe that the only variables necessary to consider are variables that require pressure measurements and geometrical quantities.

To determine the uncertainties in the pressure measurement and in the density; first, the determination of the uncertainty in the instruments used. The current work was executed using the OMEGA PX-409 high-accuracy pressure transducer. Pressure transducers experience elemental errors such as linearity, hysteresis, sensitivity, drift and temperature changes within the working environment. Taking those elemental errors into consideration the overall instrument error and instrument uncertainty is given by [40],

$$u_P = [u_{BSL}^2 + u_z^2 + u_S^2]^{1/2} \quad (13)$$

where the $u_{BSL} = 0.08\%$ best standard line (BSL) combines the linearity, hysteresis, and repeatability uncertainties of maximum value, $u_z = 0.5\%$ FS the zero-balance uncertainty, and $u_S = 0.5\%$ FS is the span setting uncertainty. For the differential unit used and the gauge transducers in the experiment range from $P = (0 - 2488.4) Pa$ and the absolute pressure transducer range from $P = (0 - 103421) Pa$ [40].

Results & discussion

5.1. Validation of the experiment

Firstly, the experimental setup was validated for Fan 1. The rotational speed of the fan from literature is tested at 21,170 rpm; moreover, the validation curve was tested for that rotational speed in the loop constructed in Fig. 1. The results of the experimental validation are demonstrated in Fig. 9.

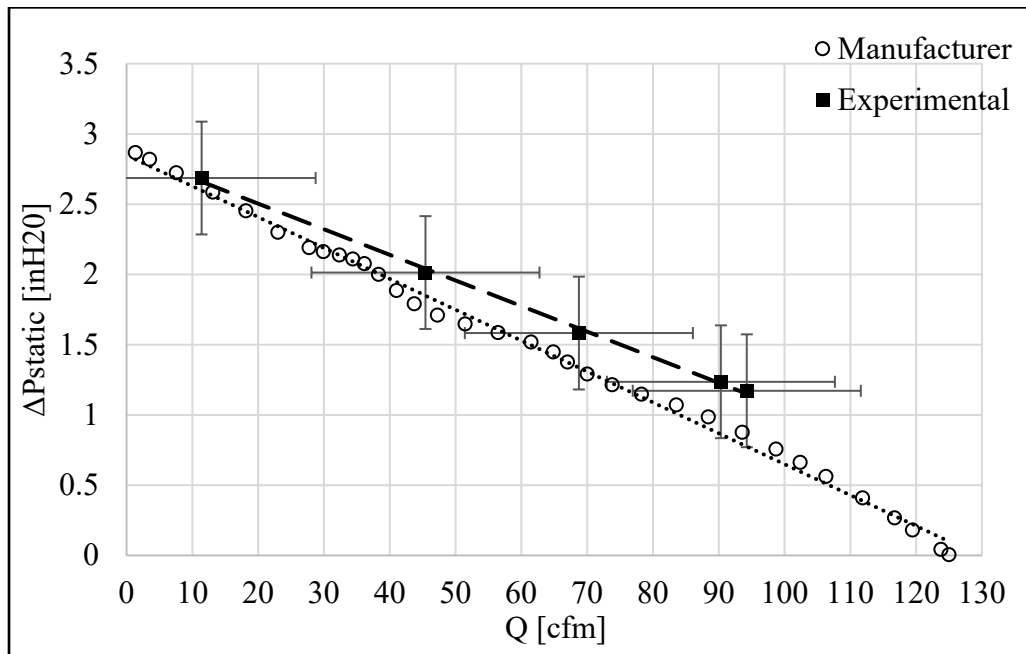


Fig. 9. Validation of the experimental loop testing the 2-bladed fan.

Based upon the error analysis discussed previously, the various points along the fan performance curve demonstrate to reside within an agreeable margin of the manufacturer's specification. The experimental setup provided those points to be measured, and the curve lies in proximity at the low volumetric flow rates, but as the valve is further opened, there is a higher deviation in the determined pressure rise and volume flow rates. The highest volumetric flow rate determined within the loop is 94.3 cfm. The stall pressure occurs at the zero volumetric flow rate condition. Also, at the stall condition the maximum back pressure generated by the fan is experienced. Due to the inherent nature of the fan loop system, there are slight losses within the 90° bends, the butterfly valve, a flow straightener located downstream of the fan before the Venturi, and the overall roughness of the PVC pipe itself.

The performance curve is determined for both fans under identical testing conditions. The testing conditions are the same experimental loop, but varying the pressures from (1-0.3) atm. These pressures are chosen to predict the behavior of the fans at high elevations (i.e., low-pressure conditions). All fan curves for the remainder of the experiments were conducted at the rotational speed of 13,000 rpm.

5.2. Fan 1 test results

The physics of pump performance curves demonstrates that there is an inverse relationship of the increasing pressure across the fan and decreasing the volumetric flow rate. In Fig. 10, Fan 1 is demonstrated at various pressures.

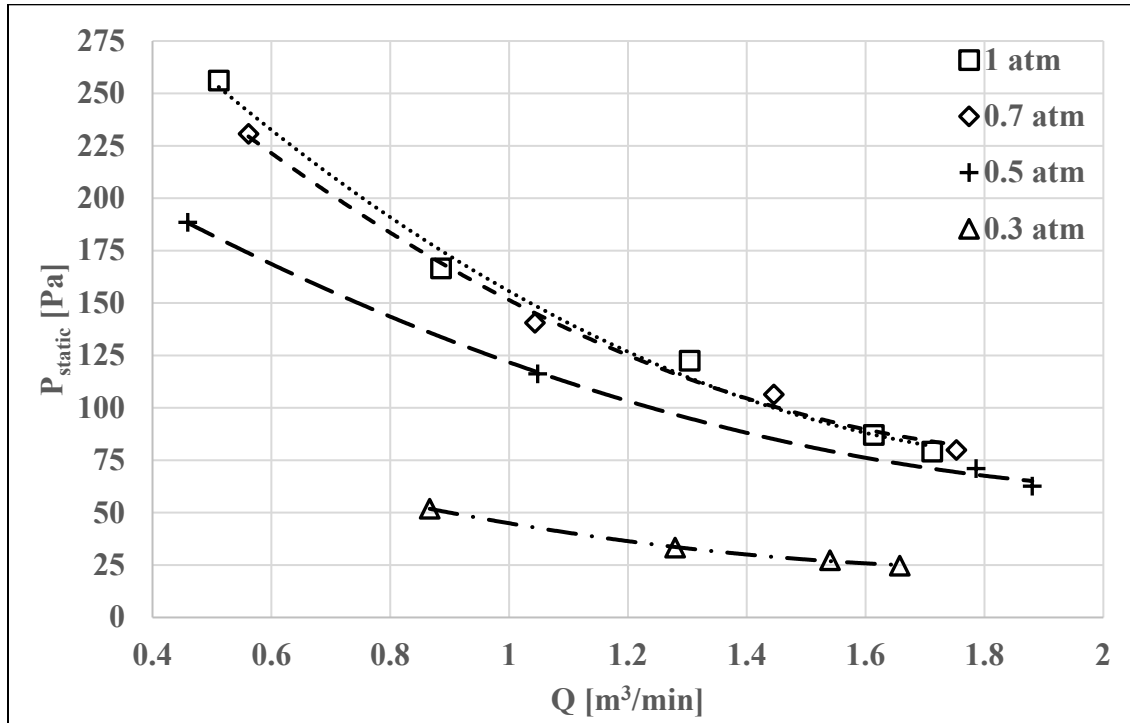


Fig. 10. The fan performance of Fan 1 at various ambient conditions.

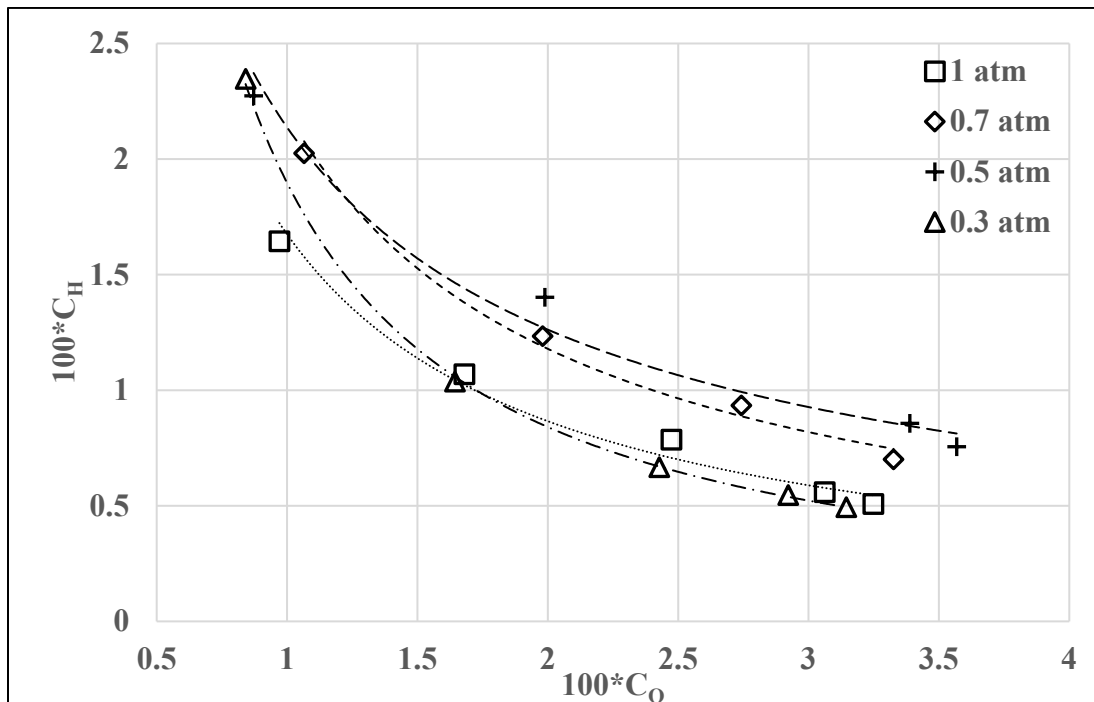


Fig. 11. Dimensionless performance curve for Fan 1.

The dimensionless performance curve is demonstrated in Fig. 11. The equations were derived using traditional Buckingham Pi Theorem to determine the dimensionless curves of Fan 1 at variable pressure. The data demonstrates a correlation of $R^2 > 0.99$ for all pressure conditions. A power fitting curve is used for the data and given the high correlation value it is evident that the data behaves as a power function. The 1 atm. and 0.3 atm. pressure conditions perform nearly identically, whilst the 0.7 atm. and 0.5 atm. have very close trends. At near shutoff flow conditions, the fan at all pressure conditions perform the equivalently. A factor 100 is multiplied to the coefficient of head and coefficient of volumetric flow rate to easily view the trends of the data.

The fan performance at standard atmospheric pressure and 0.7 atm. is roughly the same; moreover, Fan 1 is not drastically affected by the slight change in ambient pressure. Once the pressure drops to 50% of atmospheric, the fan performance starts to deteriorate significantly. The difference in performance is drastic when the pressure of the system varies from 0.7 atm. to 0.5 atm. The performance deteriorates further at 30% atmospheric pressure. To compensate for the drastic loss in performance, the fan should be operated to a higher rotational speed in order to provide the same amount of performance to that of the ambient pressure condition. All four pressure cases demonstrate a high tendency for a quadratic behavior and using regression analysis all sets of data demonstrate the good correlations that indicate those relationships, $R^2 > 0.99$.

The maximum efficiency of the fan indicates the best efficiency point (BEP); moreover, with the BEP the optimal volumetric flow rate and pressure rise of the fan can be evaluated. To determine the BEP, the input power is determined by multiplying the pressure drop measured across the fan and the volumetric flow rate determined; furthermore, the input power is simply recorded from the digital display of the power supply used. The BEP indicates the point where the fan is intended to operate. In Fig. 12, the efficiency of the fan for different ambient pressures within the loop is demonstrated.

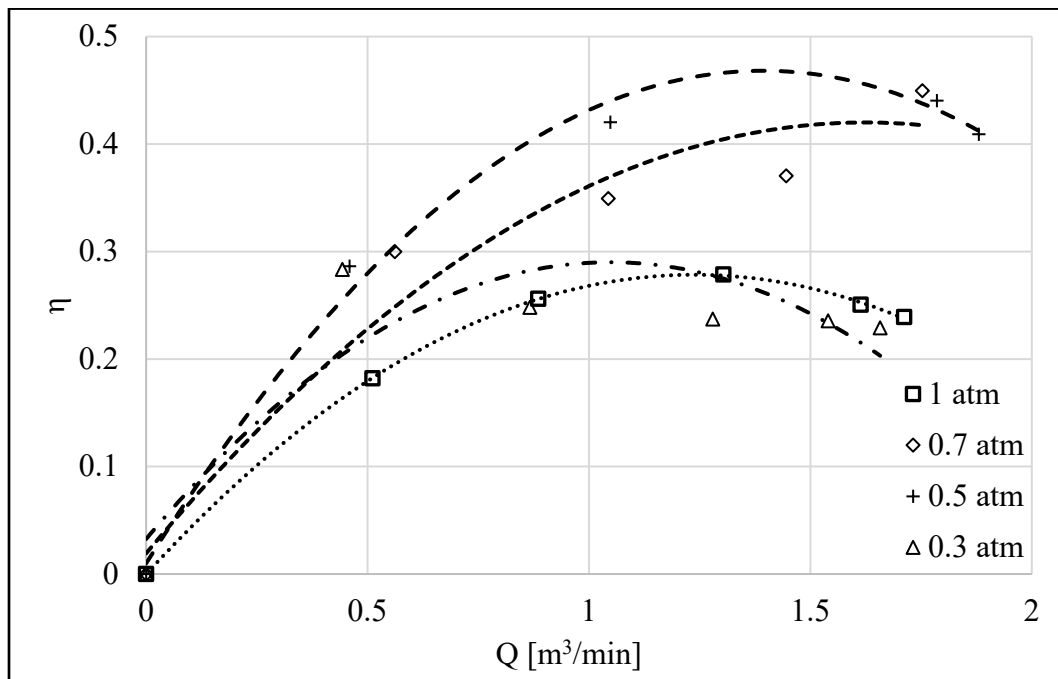


Fig. 12. The efficiency of Fan 1 at various ambient pressure conditions.

From Fig. 12, the highest efficiency was determined to be at 0.5 atm. with $Q = 1.4 \text{ m}^3/\text{min}$ and $\eta \approx 0.47$. The next highest efficiency pressure condition is determined at 0.7 atm. Next, the atmospheric condition peaked the maximum efficiency at approximately, $Q = 1.0 \text{ m}^3/\text{min}$ with an efficiency shy of $\eta = 0.3$. Lastly, the lowest BEP is for the lowest pressure condition with an apex slightly smaller than the atmospheric case; nonetheless, there is a considerable shift in volumetric flow rate between the two ambient conditions of approximately, $Q \approx 0.4 \text{ m}^3/\text{min}$.

5.3. Fan 2 Test Results

The second fan is a 7-bladed fan which is demonstrated in Fig. 8 by Delta. A similar analysis was conducted for Fan 2 with the same controls implemented to that of the Fan 1. In Fig. 13, Fan 2 was tested for various pressure conditions; moreover, similar trends were determined. The highest performance curve is measured in atmospheric pressure conditions. Consequently, as the pressure within the loop was dropped the performance of the fan was affected. The Delta fan has the same tendency to follow a quadratic fit, with all ambient pressure condition cases demonstrating an acceptable correlation of $R^2 > 0.99$ like that of the Fan 1.

Similarly, the analysis conducted for Fan 1 is also performed on Fan 2 in Fig. 14. In Fig. 14., the dimensionless performance curves of Fan 2 behave similarly to that of Fan 1 where a power function curve fits are the closest fitting trends to the data. The two extreme pressures (1 atm. and 0.3 atm.) demonstrate similar trends and the intermediate pressure conditions (0.7 atm. and 0.5 atm.) show comparable trends. Although the trends are the same, Fan 2 demonstrate much different performance for the two extreme ambient conditions since the 1 atm. clearly outperforms the 0.3 atm. unlike Fan 1. Moreover, 0.7 atm. also has a slightly higher performance than that of 0.5 atm.

In Fig. 15, the efficiency curves at the different pressure conditions are demonstrated. For Fan 2, the highest efficiency is measured at 0.3 atm. For all the lower pressure, (0.7, 0.5, 0.3) atm., the peak of the efficiency curve is observed at around a volumetric flow rate of, $Q \approx 3 \text{ m}^3/\text{min}$. Indicating that the fans must operate at higher flow conditions to find the BEP at those lower pressure conditions. On the other hand, the atmospheric pressure condition demonstrates the peak at a lower volumetric flow rate which indicates that it reaches its highest efficiency point at a lower flow condition.

Near free delivery conditions, (1, 0.7, 0.5) atm. perform similarly in exception to 0.3 atm that is lower in producing coefficient of head. At the higher system resistances the fan outperforms at 1 atm. The 1 atm. and 0.3 atm. pressure conditions exhibit nearly identical trends; furthermore, the 0.7 atm. and 0.5 atm. also produce nearly identical trends.

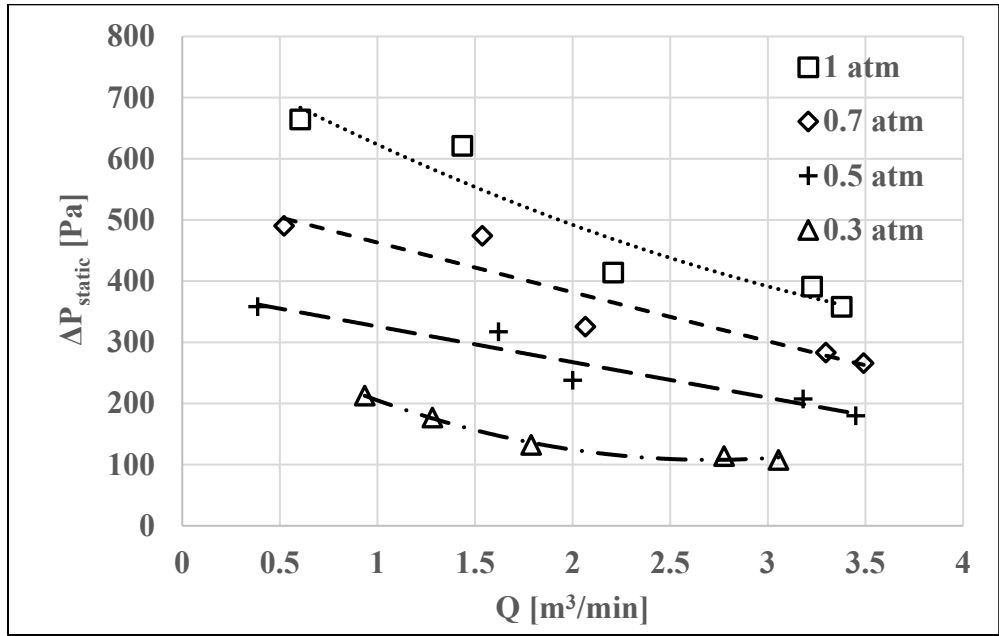


Fig. 13. The results of the single 7-bladed fan at various ambient pressures.

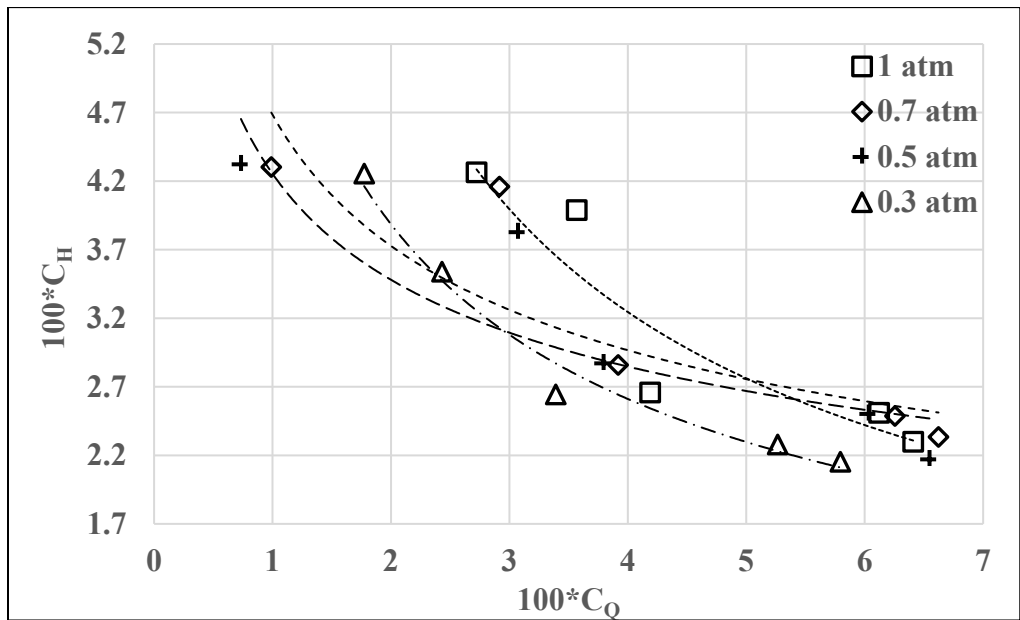


Fig. 14. The nondimensional fan performance of Fan 2 at variable ambient pressures.

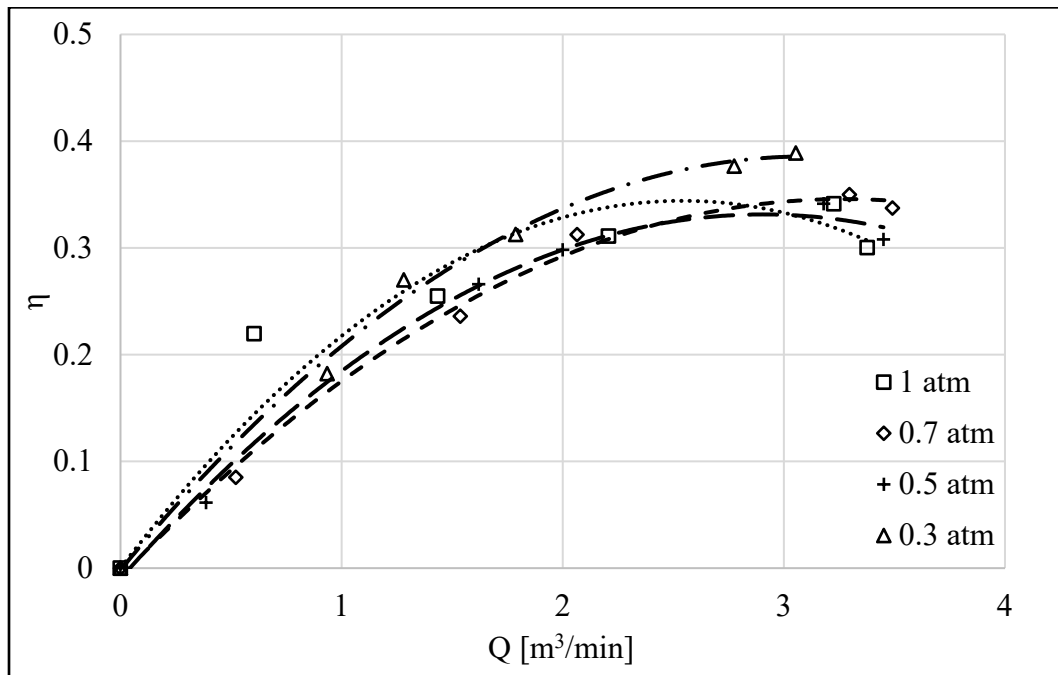


Fig. 15. The fan efficiency for the Fan 2, 7-bladed fan at various ambient conditions.

In Fig. 16, the fan performance curves are compared for two extreme cases (1atm. and 0.3 atm.) of the Fan 1 and Fan 2 running at 13,000 rpm. Fan 2 performance curve clearly outshines that of Fan 1's performance. For both cases, Fan 2 has a higher volumetric flow rate even at the lowest pressure condition; moreover, it can still push more air through than Fan 1 at the atmospheric condition.

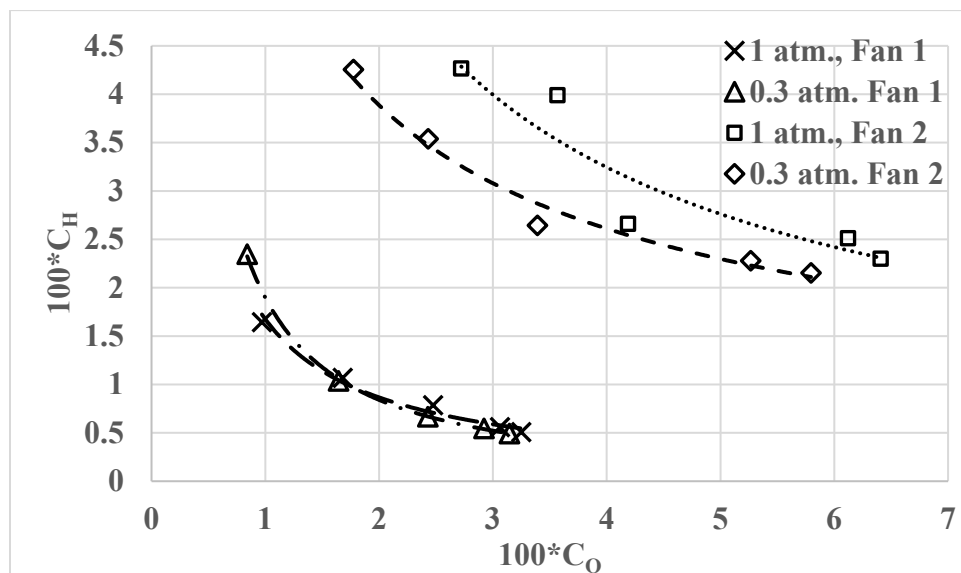


Fig. 16. Compares the nondimensional fan performance curves extreme pressure conditions.

The gradient of the static pressure to flow rate is greater than the Fan 2 curves; thus, delivering lower maximum volumetric flow rates for Fan 1. For all cases, Fan 2 has a lower slope which in

turn allows the performance of the fan to operate for a much large range of flow conditions. Using the nondimensional analysis Fan 2 is a higher performance fan comparatively to that of Fan 1. Fan 2 is the better choice in terms of fan performance to that of Fan 1 and airflow delivery. The results demonstrate that the fan scaling laws can be applied to Fan 1, but not to Fan 2 due to the overlap of the curves for fan 1 in Fig. 16.

The BEP of the two fans at the changing pressure conditions is determined in Fig. 17. Fan 2 demonstrates consistent efficiency across various pressure conditions. The range of efficiencies for Fan 2 is 5%. Fan 1 demonstrates a large range in BEP of 17% from the lowest to highest peak efficiencies. At the intermediate pressures (0.7 and 0.5) atm., Fan 1 has higher BEP's to that of Fan 2. The fan BEP is approximately 10% higher for Fan 1 over that of Fan 2 and does not exactly reflect that it outperforms the 7-bladed fan. The efficiency just demonstrates the fan's ability to convert electrical energy to mechanical energy. The higher BEP was determined in Fan 1 at these conditions since it does not require as much input power to drive the fan at 13,000 rpm as Fan 2. Lower electrical input power to the fan will lead to lower heat dissipated in the fan windings of the fan; which in turn, means less heat introduced to the system that would have to also be dissipated.

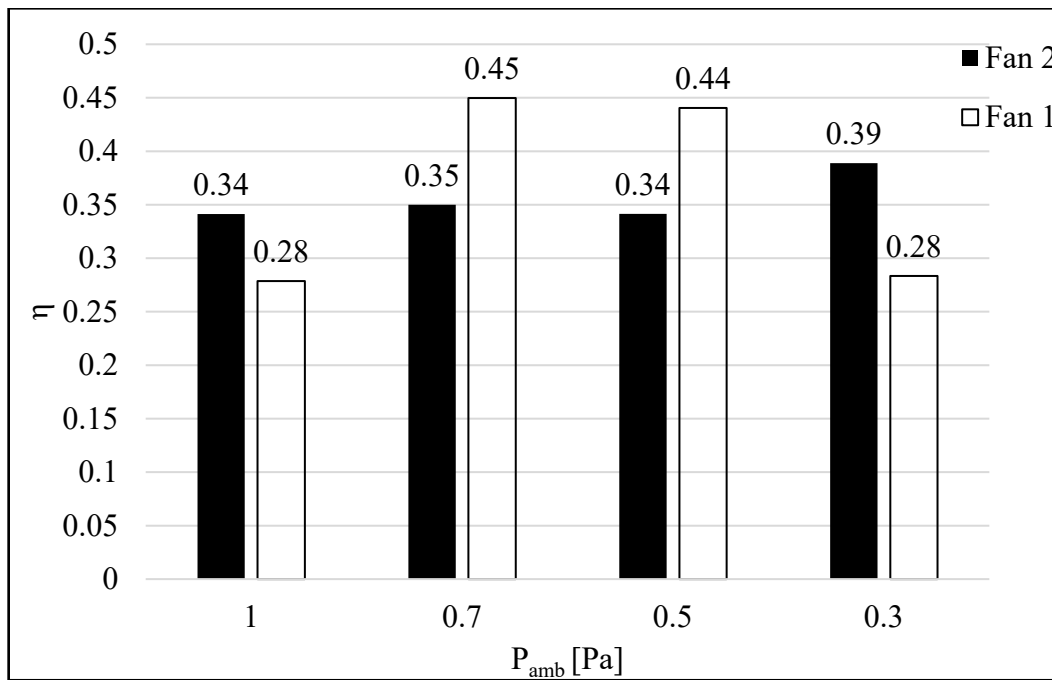


Fig. 17. Fan efficiencies at various ambient pressures.

Regardless of the Fan 1 demonstrating higher efficiencies for the intermediate pressures, the inferior performance curves to that of Fan 2 does not justify its use for cooling in such a highly demanding application. The fan must be able to deliver enough forced convection to the EMA to direct the heat from the heated structure. The use of Fan 2 would be a better choice instead of Fan 1 since it can provide more air delivered to the EMA.

The Reynolds number was determined, to identify the type of flow within the system. For Fan 1, it is determined that at low-pressure conditions the flow is laminar, transitional, and turbulent since

the Reynolds number ranges from $1882.7 < Re < 7040.8$. Also for the case of 0.5 atm. for Fan 1, at low volumetric flow rates the flow goes from transitional to turbulent flow, $Re > 3254.3$. The higher ambient pressure conditions for Fan 1 demonstrate that the flow is fully turbulent. Fan 2 has a fully turbulent flow for (1, 0.7, 0.5) atm. Fan 2 nearly has a fully turbulent flow for 0.3 atm. except for the lowest volumetric flow rate determined. At the shutoff conditions of Fan 2 in 0.3 atm. of ambient pressure the flow is transitional with a Reynolds number of $Re = 3970.9$. In terms of cooling, the higher the Reynolds number indicates that the flow has regions of eddies; therefore, these pockets of eddies will provoke more mixing of the fluid and will provide better cooling for the EMA.

Conclusion

In the current work, an experimental test rig was constructed to compare fan performance curves at various ambient pressure conditions. The first set of experiments was conducted to consistently acquire the manufacturer's curve to validate the experimental setup and testing procedure. All performance curves for these fans demonstrated a strong quadratic correlation. Both fans were tested at 13,000 rpm. Fan 1 is a 2-bladed system with a slightly higher diameter but has a lower blade surface area due to its low blade count. Fan 2 is the 7-bladed fan with a slightly lowered tip-to-tip diameter, but the high blade count provides more surface area for the fluid to be driven. The performance curves and efficiencies at various pressures were determined experimentally. The fan performance curves for the fans deteriorated once the pressure within the system was lowered below atmospheric pressure. For both fans, the peak efficiencies occurred at higher volumetric flow rates. Fan 1 demonstrated higher efficiencies at (0.7, 0.5) atm. because of Fan 1 requiring lower power input to operate at that constant speed. The efficiencies in Fan 2 were consistent across all pressure conditions with peak efficiencies of 0.45 and 0.39 for Fan 1 and Fan 2, respectively. Demonstrating that a large amount of usable energy is being lost within the internal structure (i.e., mechanical and heat losses) of the fans. Finally, the higher blade counts provide higher performance curves with a loss in maximum efficiency due higher power consumptions necessary to operate the fan.

Conflict of interest

The authors declare that there is no conflict of interest.

Acknowledgements

"The views and conclusions contained herein are those of the authors and should not be interpreted as FA8650-17-2-2230 necessarily representing the official policies or endorsements, either expressed or implied, of the United States Air Force or the U.S. Government.

References

- [1] G. Qiao, G. Liu, Z. H. Shi, Y. W. Wang, S. J. Ma, and T. C. Lim, "A review of electromechanical actuators for More/All Electric aircraft systems," *Proceedings of the Institution of Mechanical Engineers Part C-Journal of Mechanical Engineering Science*, vol. 232, no. 22, pp. 4128-4151, Nov 2018, doi: 10.1177/0954406217749869.
- [2] L. Papini, P. Connor, C. Patel, L. Empringham, C. Gerada, and P. Wheeler, "Design and testing of electromechanical actuator for aerospace applications," in 2018 25th International Workshop on Electric Drives: Optimization in Control of Electric Drives (IWED), 31 Jan.-2 Feb. 2018 2018, pp. 1-6, doi: 10.1109/IWED.2018.8321392. [Online]. Available: <https://ieeexplore.ieee.org/ielx7/8315075/8321363/08321392.pdf?tp=&arnumber=8321392&isnumber=8321363&ref=>
- [3] J. Fu, J.-C. Maré, and Y. Fu, "Modelling and simulation of flight control electromechanical actuators with special focus on model architecting, multidisciplinary effects and power flows," *Chinese Journal of Aeronautics*, vol. 30, no. 1, pp. 47-65, 2017/02/01/ 2017, doi: <https://doi.org/10.1016/j.cja.2016.07.006>.
- [4] C. R. Spitzer, "The All-Electric Aircraft: A Systems View and Proposed NASA Research Programs," *IEEE Transactions on Aerospace and Electronic Systems*, vol. AES-20, no. 3, pp. 261-266, 1984, doi: 10.1109/TAES.1984.310509.
- [5] A. M. Gollapudi, V. Velagapudi, and S. Korla, "Modeling and simulation of a high-redundancy direct-driven linear electromechanical actuator for fault-tolerance under various fault conditions," *Engineering Science and Technology, an International Journal*, 2020/01/09/ 2020, doi: <https://doi.org/10.1016/j.jestch.2019.12.007>.
- [6] J. Choi and M. Jeong, "Preliminary design on high-end workstation cooling system using loop heat pipes," *Thermal Science and Engineering Progress*, p. 100519, 2020/03/05/ 2020, doi: <https://doi.org/10.1016/j.tsep.2020.100519>.
- [7] A. Faghri, "Heat Pipes: Review, Opportunities and Challenges," *Frontiers in Heat Pipes*, vol. 5, no. 1, 2014, doi: 10.5098/fhp.5.1.
- [8] G. Y. Fang, W. Yuan, Z. G. Yan, Y. L. Sun, and Y. Tang, "Thermal management integrated with three-dimensional heat pipes for air-cooled permanent magnet synchronous motor," *Applied Thermal Engineering*, vol. 152, pp. 594-604, Apr 2019, doi: 10.1016/j.applthermaleng.2019.02.120.
- [9] W. Wu, Y.-R. Lin, and L. Chow, "A Heat Pipe Assisted Air-Cooled Rotary Wankel Engine for Improved Durability, Power and Efficiency," presented at the SAE Technical Paper Series, 2014.
- [10] N. Putra and B. Ariantara, "Electric motor thermal management system using L-shaped flat heat pipes," *Applied Thermal Engineering*, vol. 126, pp. 1156-1163, 2017/11/05/ 2017, doi: <https://doi.org/10.1016/j.applthermaleng.2017.01.090>.
- [11] N. Aprianingsih, A. Winarta, B. Ariantara, and N. Putra, "Thermal performance of Pulsating Heat Pipe on Electric Motor as Cooling Application," *E3S Web Conf.*, vol. 67, p. 03035, 2018.
- [12] K. McCarthy, A. Heltzel, E. Walters, J. Roach, S. Iden, and P. Lamm, "A Reduced-Order Enclosure Radiation Modeling Technique for Aircraft Actuators," 2010. [Online]. Available: <https://doi.org/10.4271/2010-01-1741>.
- [13] A. Bernot, "A high reliability natural convection airliner actuator permanent magnet motor," in 2016 XXII International Conference on Electrical Machines (ICEM), 4-7 Sept. 2016 2016, pp. 46-52, doi: 10.1109/ICELMACH.2016.7732504. [Online]. Available: <https://ieeexplore.ieee.org/ielx7/7592391/7732494/07732504.pdf?tp=&arnumber=7732504&isnumber=7732494&ref=>
- [14] S. Y. Jung, J. H. Park, S. J. Lee, and H. Park, "Heat transfer and flow characteristics of forced convection in PDMS microchannel heat sink," *Experimental Thermal and Fluid Science*, vol. 109, p. 109904, 2019/12/01/ 2019, doi: <https://doi.org/10.1016/j.expthermflusci.2019.109904>.
- [15] N. Zhan, L. Ding, Y. Chai, J. Wu, and Y. Xu, "Experimental study on natural convective heat transfer in a closed cavity," *Thermal Science and Engineering Progress*, vol. 9, pp. 132-141, 2019/03/01/ 2019, doi: <https://doi.org/10.1016/j.tsep.2018.11.009>.
- [16] A. I. Bashir, M. Everts, R. Bennacer, and J. P. Meyer, "Single-phase forced convection heat transfer and pressure drop in circular tubes in the laminar and transitional flow regimes," *Experimental Thermal and Fluid Science*, vol. 109, p. 109891, 2019/12/01/ 2019, doi: <https://doi.org/10.1016/j.expthermflusci.2019.109891>.
- [17] H. Gesell, V. Nandana, and U. Janoske, "Numerical study on the heat transfer performance and efficiency in a rectangular duct with new winglet shapes in turbulent flow," *Thermal Science and Engineering Progress*, vol. 17, p. 100490, 2020/06/01/ 2020, doi: <https://doi.org/10.1016/j.tsep.2020.100490>.
- [18] J. Chen, L. Li, G. Huang, and X. Xiang, "Numerical investigations of ducted fan aerodynamic performance with tip-jet," *Aerospace Science and Technology*, vol. 78, pp. 510-521, 7// 2018, doi: <https://doi.org/10.1016/j.ast.2018.05.016>.

- [19] C. Li, X. Li, P. Li, and X. Ye, "Numerical investigation of impeller trimming effect on performance of an axial flow fan," *Energy*, vol. 75, pp. 534-548, 2014/10/01/ 2014, doi: <https://doi.org/10.1016/j.energy.2014.08.015>.
- [20] C. Li, Q. Lin, X. Ding, and X. Ye, "Performance, aeroacoustics and feature extraction of an axial flow fan with abnormal blade angle," *Energy*, vol. 103, pp. 322-339, 2016/05/15/ 2016, doi: <https://doi.org/10.1016/j.energy.2016.02.147>.
- [21] X. Ye, J. Zhang, and C. Li, "Effect of blade tip pattern on performance of a twin-stage variable-pitch axial fan," *Energy*, vol. 126, pp. 535-563, 2017/05/01/ 2017, doi: <https://doi.org/10.1016/j.energy.2017.03.057>.
- [22] W. Wu, Y.-R. Lin, L. Chow, E. Gyasi, J. P. Kizito, and Q. Leland, "Electromechanical Actuator Cooling Fan Reliability Analysis and Safety Improvement," presented at the SAE Technical Paper Series, 2016.
- [23] W. Wu, Y. R. Lin, E. Gyasi, J. P. Kizito, Q. H. Leland, and L. C. Chow, "Design and Experiment on Aircraft Electromechanical Actuator Fan at Different Altitudes and Rotational Speeds," ed: SAE International, 2019.
- [24] W. Wu, Y.-R. Lin, L. Chow, E. Gyasi, J. P. Kizito, and Q. Leland, "Electromechanical Actuator Cooling Fan Blades Design and Optimization," presented at the SAE Technical Paper Series, 2016.
- [25] W. Wu, Y.-R. Lin, L. Chow, E. Gyasi, J. P. Kizito, and Q. Leland, "Electromechanical Actuator Cooling Fan Reliability Analysis and Safety Improvement," 2016. [Online]. Available: <https://doi.org/10.4271/2016-01-1997>.
- [26] W. Wu, Y. R. Lin, L. C. Chow, E. Gyasi, J. P. Kizito, and Q. H. Leland, "Electromechanical actuator fan failure analysis and safety-critical design," *IEEE Aerospace and Electronic Systems Magazine*, vol. 32, no. 4, pp. 18-25, 2017, doi: 10.1109/MAES.2017.150281.
- [27] W. Wu, Y.-R. Lin, L. C. Chow, and Q. Leland, "Fan Performance Characteristics at Various Rotational Speeds and Ambient Pressures," presented at the SAE Technical Paper Series, 2014.
- [28] J. J. J. Corona et al., "Testing of a Cooling Fan for Wing-Bay Electro-Mechanical Actuators," no. 51562, p. V002T14A016, 2018, doi: 10.1115/FEDSM2018-83480.
- [29] E. K. Gyasi, "Enhancement of Thermal Management in Air Cooled Systems Operating at Low-Pressure Conditions," Ph.D., North Carolina Agricultural and Technical State University, Ann Arbor, 10167865, 2016. [Online]. Available: <http://ncat.idm.oclc.org/login?url=https://search.proquest.com/docview/1845069609?accountid=12711>[Online].
- [30] O. P. H. Augustyn, S. J. van der Spuy, and T. W. von Backström, "Numerical and experimental investigation into the accuracy of the fan scaling laws applied to large diameter axial flow fans," *Proceedings of the Institution of Mechanical Engineers, Part A: Journal of Power and Energy*, vol. 230, no. 5, pp. 477-486, 2016, doi: 10.1177/0957650916633015.
- [31] M. S. El-Genk and T. M. Schriener, "A Review and Correlations for Convection Heat Transfer and Pressure Losses in Toroidal and Helically Coiled Tubes," *Heat Transfer Engineering*, vol. 38, no. 5, pp. 447-474, 2017/03/24 2017, doi: 10.1080/01457632.2016.1194693.
- [32] AMCA 210: Laboratory Methods of Testing Fans for Ratings, I. Air Movement and Control Association International, 30 West University Drive, Arlington Heights, Illinois, 1999.
- [33] Measurement of fluid flow by means of pressure differential devices inserted in circular cross-section conduits running full— Part 4: Venturi tubes, ISO, 2003.
- [34] A. A. Defense. Rotron PROPIMAX 2 Tubeaxial Fans. [Online]. Available: https://www.rottron.com/-/media/ametektoron/products/digital%20library/table%20of%20contents/tubeaxial%20fans/04-26_propimax_2.pdf?la=en.
- [35] I. Delta Electronics. Delta GFM0812DUB7S 252 Shang Ying Rd., Kuei San, Taoyan Hsein, 333 Taiwan R.O.C., 2016.
- [36] F. M. White, *Fluid mechanics, 8th edition in SI Units*. ed. (McGraw-Hill series in mechanical engineering). New Delhi, India: McGraw-Hill Education (in English), 2017.
- [37] Y. A. Çengel and J. M. Cimbala, *Fluid mechanics : fundamentals and applications, 2nd ed. ed. (Çengel series in engineering thermal-fluid sciences)*. Boston: McGraw-Hill Higher Education (in English), 2010.
- [38] FE Reference Handbook, Clemson, SC: NCEES, 2014.
- [39] R. S. Figliola and D. E. Beasley, *Theory and design for mechanical measurements, 4th ed. ed.* Hoboken, N.J.: John Wiley (in English), 2006.
- [40] OMEGA Inc. PX-409 High Accuracy Pressure Transducers

Nomenclature

Alphabet

A_t	Cross-sectional Area of Throat, m ²
C_d	Discharge Coefficient
D	System Diameter, m
I	Current, A
ΔP_f	Static Pressure Rise Across Fan, Pa
ΔP_v	Static Pressure Drop Across Venturi, Pa
Q	Volumetric Flow Rate, m ³ /min
Re	Reynolds Number
V	Fluid Velocity, m/s
V_e	Voltage, V
\dot{W}	Hydrodynamic Power, W
u_x	Uncertainty Parameter

Greek Symbols

β	Diameter Ratio
η	Fan Efficiency
ρ	Fluid Density, kg/m ³
μ	Fluid Viscosity, kg/m.s

APPENDIX G

UCF Project 1626-8282

Final
report
to

North Carolina A&T University

**THERMAL MANAGEMENT OF ELECTROMECHANICAL MACHINES FOR
AEROSPACE SYSTEMS**

University of Central Florida
Department of Mechanical and Aerospace Engineering
Orlando, FL 32816-2450

Louis Chow, PI
Osama Mesalhy
Mohamed Elsayed
Yeong-ren Lin

Date of report: February 27, 2020

In making the transition towards electric aircraft, electro-mechanical actuators (EMAs) have been used to move the flight control surfaces. This has numerous advantages such as (a) reduction in weight and volume of power transmission; (b) reliability and safety improvement; (c) less maintenance and lower operating costs; (d) better dynamic characteristics; and (e) higher energy efficiency. An EMA contains four main parts: electric motor, electronic box, gearbox, and drive train. One of the main issues in the use of EMAs in aircraft is the potential overheating that occurs in the electric motors and power electronics due to the high heat dissipation in them. In aerospace applications, air-cooling is preferable compared to liquid cooling because of the state instability (freezing) of liquids in a working environment, which could often become harsh. Besides, liquid cooling adds more weight and complication to the cooling system. Wing-bay air represents an attractive and economical medium for cooling. Using axial fans, this wing-bay air can be pushed/sucked over/through the heat sinks that cover the electric motor and electronics. In this project, we have focused on thermal management of EMA through:

- 1- Studying the performance of an axial fan in cooling a heat sink attached to the electric motor housing.
- 2- Studying the effect of using partial-shield/guide-plate on a parallel plate fin heat sink (PPFHS) attached on the electronics of an EMA.
- 3- Studying the availability of using two fans in series to add redundancy to the cooling system and increase its reliability.

In report #1 (Appendix H), we studied numerically the cooling performance of a fin structure attached to the electric motor housing. Different fin structure shapes were considered: continuous straight fins, interrupted fins in staggered arrangements and corrugated fins. A fan interface boundary was used to generate the pressure jump, which is equivalent to the real cooling fan pressure head. The characteristic fan curve of an actual Sunon fan running at 10,800 rpm was measured in an available fan loop and was utilized in this simulation. The results showed that the thermal resistance of straight fins is smaller than that of interrupted and corrugated fins.

In report #2 (Appendix I), a test rig was established to measure the cooling performance of a fin structure brazed on an aluminum cylinder. The air flow was introduced using a Sunon fan (model PF92381BX-000U-S99) that was attached to one end of the finned block. The thermal resistance was measured for different fan rotational speeds (6000, 9000 and 11200 rpm). The measurements were used to validate a numerical simulation carried out using ANSYS-Fluent software. The results showed that using $k-\omega$ SST turbulence model results in better agreement between numerical and experimental results compared to the $k-\epsilon$ and Transition $k-k\ell-\omega$ models.

In report #3 (Appendix J), we studied the performance of the Sunon fan in cooling a straight fin structure when the fan was operating at a rotational speed ranging from 6000 to 12000 rpm, and under an ambient pressure ranging from 0.2 to 1.0 atm. The results showed that there is an optimum value of the fin number that produces the minimum thermal resistance. The value of the optimum fin number changes with the fan speed and the ambient pressure. At lower ambient pressure, a lower fin number is preferred due to the rapid decrease in the air-cooling flow capacity as the number of fin increases. Also, the optimum number of fins increases with the fan rotational speed.

In report #4 (Appendix K), a manuscript for a paper submitted to Heat and Mass Transfer Journal by Springer was prepared to determine the optimum fin structure/fan combination that maximizes the heat transfer from fins mounted on the casing of electric motors. This paper has been accepted for publication under the title of “A parametric fin structure design study for cooling aerospace electro-mechanical actuators with high-speed axial fans” [1].

In report #5 (Appendix M), a manuscript for a paper submitted to International Journal of Heat and Mass transfer was prepared. This paper focused on studying the effect of altering the by-pass flow over a parallel plate fin heat sink using a partial shield and/or a guide plate. This heat sink is used to cool the EMA electronics. The results showed that when the flow is driven by a fan, a short partial shield with a slightly inclined guide plate yields a better thermal performance than the full shield. Furthermore, using a guide plate only with a small inclination angle gives a superior thermal performance as well. Changing the position of the guide plate was also investigated. This paper has been accepted for publication in Int. J. of Heat and Mass Transfer under the title of “Enhancement of a heat sink performance using a partial shield and/or a guide plate” [2].

In report #6 (Appendix N), a numerical simulation for the flow field in a dual-fan system was carried out. The considered configuration was a dual fan made by DELTA (Delta GFC0812DW). It consists of two fans: upstream fan of 7 blades and downstream fan of 5 blades. One of the fans is intended to be held stationary so it can be used as a backup when the running fan fails. The results showed that when the upstream fan is running and the downstream fan is stationary, the dual fan performance is much better than the case of running the downstream fan. This can be attributed to the blocking of the mass flow rate at the inlet when the upstream fan is kept stationary. So, several attempts have been tried to improve the dual fan performance when the downstream fan is running such as: removing the stator section, replacing the 5-blade downstream fan with a 7-blade fan, and using similar two 7-blade fans in back-to-back position or two reflected 7-blade fans.

In report #7 (Appendix O), the work in report #5 was extended to study the effect of using a guide plate on a parallel plate fin heat sink cooled by a fan at different altitudes from sea level to 12,000 m. The results showed that at high altitude operation, using the PPFHS only could lead to electronic failure due to the larger temperature increase compared to the PPFHS/guide plate configuration. The optimum fin number was determined to range between 20 to 28, which depends on the environmental pressure and fan speed. Also, it was shown that improper use of a PPFHS with highly dense fins may lead to inadequate electronic cooling while adding extra weight for high-altitude operation. This work has

been accepted for publication in Int. J. of Heat and Mass Transfer under the title of “High-altitude performance of a PPFHS with a guide plate for cooling electromechanical actuators” [3].

In report #8 (Appendix P), we studied the effect of changing the distance between two 7-blade fans and the effect of opening the circumferential area between the two fans on the performance of the dual-fan system. The results showed that operating the downstream fan with open wall results in a comparable performance as operating the upstream fan with closed wall. This means that using a movable wall to facilitate the opening and closure of the circumferential duct wall between the two fans can improve the reliability and effectiveness of the cooling system with two fans, with one serving as the backup. With this redundancy, the failure probability of the cooling system drops from 2×10^{-5} to 4×10^{-10} .

During the period of preparing this final report, the numerical model used in studying the performance of dual-fan system was validated with experimental measurements. In addition, the results in reports #6 and #8 were consolidated in a paper submitted to the Thermal Science and Engineering Progress journal under the title of “Study of a high-reliability dual-fan system for cooling aerospace electromechanical actuators” [4]. This manuscript is included below.

Publications

- [1] O. Mesalhy, C. Rath, D. Rini, J. Kizito, Q. Leland, L. Chow, A parametric fin structure design study for cooling aerospace electro-mechanical actuators with high-speed axial fans, Heat and Mass Transfer, (2019) 1-13. <https://doi.org/10.1007/s00231-019-02791-y>.
- [2] M.L. Elsayed, O. Mesalhy, R.H. Mohammed, J.P. Kizito, Q.H. Leland, L.C. Chow, Enhancement of a heat sink performance using a partial shield and/or a guide plate, International Journal of Heat and Mass Transfer, 134 (2019) 948-958. <https://doi.org/10.1016/j.ijheatmasstransfer.2019.01.096>.
- [3] M.L. Elsayed, O. Mesalhy, J.P. Kizito, Q.H. Leland, L.C. Chow, Performance of a guided plate heat sink at high altitude, International Journal of Heat and Mass Transfer, 147 (2020) 118926. <https://doi.org/10.1016/j.ijheatmasstransfer.2019.118926>.
- [4] O. Mesalhy, M.L. Elsayed, J.J. Corona, A.A. Kwarteng, J.P. Kizito, Q.H. Leland, and L.C. Chow, Study of a high-reliability dual-fan system for cooling aerospace electromechanical actuators, Submitted to Thermal Science and Engineering Progress.

APPENDIX H

Study of a high-reliability dual-fan system for cooling aerospace electromechanical actuators

Osama Mesalhy^{a,b}, Mohamed L. Elsayed^{a,b,1}, Corona, J. J. J.^c, Kwarteng, A. A.^c, John P. Kizito^c, Quinn H. Leland^d,

Louis C. Chow^a

^aDepartment of Mechanical and Aerospace Engineering, University of Central Florida, Orlando, FL 32816, USA ^bDepartment of Mechanical Power Engineering, Zagazig University, Zagazig 44519, Egypt

^cDepartment of Mechanical Engineering, North Carolina Agricultural and Technological State University,

Greensboro, NC 27411, USA

^dPower and Control Division, Aerospace Systems Directorate, Air Force Research Laboratory, Wright Patterson Air Force Base, OH 45433, USA

ABSTRACT

There is an increasing trend for incorporating Electro-Mechanical Actuators (EMAs) in aerospace applications to reduce weight and cost. Due to the high-power density required for EMAs in aircraft applications, they are prone to overheating. Pushing the wing-bay air on a finned EMA surface using axial flow fans is the most practical way to cool the EMAs used for flight control surfaces. The probability of failure of the commercial fans is 2×10^{-5} which is too high compared to the desired failure probability of 10^{-9} for the EMAs. This paper presents a validated numerical simulation to assess the performance of dual fans in cooling EMAs. The two fans are set in a series arrangement due to the space limitation in the wing bay. Only one fan is allowed to rotate, while the second backup fan is clamped to eliminate wear in its bearing. In case of failure of the running fan, the other fan will be switched on immediately. The results show that the performance of the dual fan is much better when the upstream fan is running. Due to flow blockage by the stationary upstream fan, the performance of the operating downstream fan decreases significantly. Different options have been explored to improve the performance in the case of running the downstream fan, such as removing the diffuser section, changing the distance between the two fans, and opening the circumferential duct wall between the two fans. It is found that

1 Introduction

In recent years, the aerospace and defense industry started to shift from hydraulic actuators to electro-mechanical actuators in a trend towards power-by-wire (PBW) actuation. This trend benefits the actuation system with a series of advantages such as (a) reduction in weight and

operating the downstream fan with open wall results in comparable performance as operating the upstream fan with closed wall. This means that using a movable wall to facilitate the opening and closure of the circumferential duct wall between the two fans can improve the reliability and effectiveness of the cooling system with two fans, with one serving as the backup. With this redundancy, the failure probability of the cooling system drops from 2×10^{-5} to 4×10^{-10} .

KEYWORDS: Air cooling; Electro-Mechanical Actuator; Aerospace; Dual fan.

volume of power transmission; (b) reliability and safety improvement; (c) less maintenance and lower operating costs; (d) better dynamic characteristics; and (e) higher energy efficiency. Electrical actuation is employed in PBW actuators such as electro-hydrostatic actuator (EHA) and electromechanical actuator (EMA) [1]. For example, EMAs are used as frontline actuators on commercial transport aircraft such as Boeing B787 for landing gear braking and secondary flight controls. For Airbus A380/A400M/A350, EHAs are employed as backup actuators for primary and secondary flight controls (ailerons and elevators) [3]. On the military side, EHA was tested as actuator for primary flight control systems on a F-18 research aircraft [4]. The PBW actuators achieve a significant reduction in fuel burn and maintenance costs on commercial (passenger) planes and may lead to a 30–50% reduction in ground service equipment [5]. For military aircraft, the take-off weight and the vulnerability of the fuselage area is significantly reduced [6].

Actuation using EMAs allows the elimination of hydraulic devices and the use of hydraulic fluids to drive the screw rods. This leads to significant maintenance reduction due to less energy conversion and provides a better leak-free option. Therefore, it is generally accepted that when sized for the same actuation requirements, the EMAs have a weight advantage over the EHAs [7]. Despite the above advantages, new challenges are delaying the development of EMA technologies for future aircraft applications. The principal problem in the extensive adoption of EMAs is the lack of accumulated knowledge and experience regarding reliability and the risk of failures due to jamming, health monitoring (HM) and assessment, and proper thermal management. Therefore, The EMA motor in safety-critical applications is designed with the increasing reliability requirements with a resort to the redundancy design technique to provide a system with tolerance to failure [8]. This includes duplicating system elements or adding backup channels. For instance, first, the complete redundancy system employs two or more sets of independent actuators forming dissimilar redundancy, which includes active/active mode, active/no-load mode, and active/passive mode [9, 10]. Second, the electrical redundancy system is backed up by two or more sets of motor and control devices. However, failure isolation cannot be fulfilled in the electrical redundancy system, thus resulting in decreased reliability. Another inevitable issue of the EMAs is the overheating due to the high heat dissipation requirement when replacing a traditional hydraulic system with a compact EMA system. So, developing reliable cooling systems for thermal management is

¹ E-mail: mlea@knights.ucf.edu, mlabelkrem@zu.edu.eg (Mohamed L. Elsayed).

a crucial task, especially for aerospace applications, which require the fulfillment of strict safety regulations.

Due to the continuous need to increase the power of electric motors, thermal analysis and management of electrical machines could become as challenging as electromagnetic analysis [11]. In this regard, many modern cooling techniques have been used to manage the temperature of electric motors. For example, Popescu et al. [11] reviewed most of the reported work in the literature related to various solutions for efficient heat extraction and thermal management of electrical machines. Several methods were reported, such as high thermal conductivity/high volume electric resistivity material [12] and high winding slot fill factors [13] to achieve heat extraction improvement through conduction. For low-power-density motors such as servo-motor, free convection is sufficient using housing fins. For many power-dense machines such as electrical racing cars, forced convection liquid cooling [14], spray cooling [15] and heat pipes coupled to a heat exchanger (fins with forced air) [16] are utilized using fluids such as water, aqueous glycol solutions, oil and ParathermTM LR [11]. Liquid cooling is used to cool the inner rotors of dualrotor motors [17], the motor shafts of interior permanent magnet motors (IPMs) [18], and oilimmersed electrical transformers [19]. While liquid rotor cooling is a very effective heat extraction method, proper seals, complex flow paths, frictional losses and pressure requirements, and potential leakage prevention must be carefully considered and addressed [14]. In parallel to conduction and convection heat extraction, radiation heat extraction occurs both outside and inside the motor. This phenomenon can be augmented by improving the housing emissivity and environment system absorptivity (surrounding walls) [20, 21].

The main heat sources in an actuator module are the copper loss of the stator winding and the iron loss of the stator iron core in the electric motor. Motors operating during the actuator holding periods present the most significant challenge to the thermal management of the EMA system, where all the electrical power is converted to heat [22]. Selection of the optimal cooling technique depends on the applications in which the EMAs are used. In aircraft applications, air cooling is far more preferable compared to liquid cooling because of the state instability of liquids in a working environment which could often become harsh. Besides, liquid cooling adds more weight and complication to the cooling system. Wing-bay air represents an attractive and economical medium for cooling EMAs used for aircraft flight control surfaces. Totally Enclosed Fan Cooled (TEFC) type motors are the preferred type where the windings are totally sealed within an enclosure and air is not permitted to flow through the enclosure. This offers increased protection against weather, dirt, and moisture. Farsane et al. [23] studied experimentally the cooling of a closedtype electric motor using three non-intrusive investigation methods. The combined results of these methods showed a strong relationship between the aerodynamic and thermal behaviors of the selected motor. The average temperature of the motor casing was considerably reduced by using enhanced heat transfer surface with air delivery across the casing surface. According to the data presented in McCarthy et al. [24], up to 600 W of heat can be generated in the electric motors and power electronics of EMAs used in aerospace applications. With this high heat generation, natural convection from an extended surface mounted on the electric motor or electronics is not sufficient to keep the temperature under the designated limits [25]. An axial flow fan should be used to enhance the heat transfer coefficient. Elsayed et al. [26] studied the effect of adding a shield/guide

plate on the thermal characteristics of parallel plate fins heat sink (PPFHS) in cooling the electronics of EMA using the wing-bay air driven by a state-of-the-art commercial SUNON fan. Although the study was directed to air-cooled EMA's electronics, no high-altitude conditions results were reported, and the heat transfer enhancement analysis was limited to a single PPFHS. Therefore, Elsayed et al. [27] extended their work done in [26] to high-altitude conditions and concluded that improper use of PPFHS with high fin density may lead to inadequate electronic cooling while adding extra weight for high-altitude operation. Mesalhy et al. [28] studied the effect of changing the fin shape (straight, offset-strip and corrugated), fin number and fin thickness on the performance of a heat sink mounted on an electric motor and cooled by a SUNON fan under different altitude environment. The performance of a fan produced by AMETEK of diameter 82 mm and volume flow rate 3 m³/min was studied by Wu et al. [29] and its blade design parameters had been modified to suit the operation at high altitudes where the ambient pressure is 0.2 atm.

Fan cooled electrical motors face overheating if the cooling fan fails. The cooling fan may fail due to electrical or mechanical causes. The mechanical causes include failure of bearings, lubricant, shaft, and fan blades. The electronic causes include failure of control circuitry, motor windings, power supply and power drives. Most fan manufacturers state that their products have an overall life-time of 50,000 hours under normal use. The fault probability is the reciprocal of the expected life-span in hours (2×10^{-5}). The probability of electronic failure is 2×10^{-5} and is the most likely cause of fan failure, while the probability of mechanical failure is 6×10^{-7} [30, 31]. The fault probability suggested by Defense Advanced Research Projects Agency (DARPA) solicitation (SB132-005) for electromechanical actuator was 1×10^{-9} [32]. So, the fault probability of the cooling fan must be reduced to meet the required restrictions of aerospace applications. Using fault-tree analysis, Wu et al. [31] studied the expected fault probability of the cooling fan for four cases: doubling the bearings; using dual winding for fan motor; using dual fan motor winding plus dual electronics; and using a dual fan system. The results showed that using a dual-fan system can achieve a fault probability of 4×10^{-10} compared to 2×10^{-5} for dual bearings and 6×10^{-7} for doubling the fan motor winding and the electronic system. A dual-fan cooling system can be achieved by placing two fans in series or parallel with one working at a time. The backup one will be switched on immediately if the operating fan fails.

Typically, the performance of a cooling fan depends on its type, dimensions, blade design, rotational speed, and tip clearance. For instance, Galloni et al. [33] developed a numerical model to study the performance a radial fan, which can be mounted on an electric motor shaft. The performance was monitored when the wheel aspect ratio and the number of blades were changed. A study of velocity and pressure fluctuations in the tip clearance flow of an axial fan was carried out by Bizjan et al. [34]. They showed that the rotor blade tip design with swept-back tip winglets can yield a significant noise level reduction. Redesign and optimization of a low-aspect-ratio transonic fan was implemented by Chen et al. [35] with a 7.5% increase in the fan total pressure ratio. For a dual fan system, Wang et al. [36] studied the noise source of two identical small axial flow cooling fans in series. Also, Wang et al. [37] studied the generated noise and the effect of adding a flow straightener between the two fans and obstructing the inlet on the performance of the two fans when the back pressure is equal to 120 Pa [37]. Kim et al. [38] numerically analyzed

an adjustable blade axial fan at forward and backward flow situations. The results showed the efficiency loss that occurred with the backward flow is caused by the shear stress increase which results in the total pressure loss. The performance of an axial dual-blade fan for indoor space ventilation in terms of flow rate, power consumption and noise were evaluated experimentally [39]. The power consumption and noise for an axial dual-blade fan were reduced by about 10% compared to the axial single-blade fan for the same flow rate. Wang et al. [40] studied experimentally a heat-sink cooling system using heat pipes and single/dual fans. The total thermal resistances of single fan operation are higher than those of dual-fan operation under identical heat source areas and fan speeds.

To the best knowledge of the authors and based on a careful literature search, there is a limited or a gap in the published literature dealing with an axial dual fan system for thermal management of air-cooled electric motors of the EMAs. Therefore, the current study focuses on a numerical study for the aerodynamic performance of a dual-fan system placed in a series configuration under different rotating speeds. The series arrangement is preferred because of the space limitation in the wing bay. The objective of using such an arrangement is to increase the reliability of the cooling system used in aerospace applications. One of the fans will be allowed to rotate while the second will be kept stationary as a backup. The backup fan is non-rotating to prevent any wear in its bearings which could occur if it is allowed to spin freely. By clamping the backup fan, the overall failure probability of the dual fan will be less than 10^{-9} . In the case of failure of the operating fan, the spare fan will be switched on immediately.

Two approaches have been employed in the current study to validate the numerical model built based on a commercial code ANSYS FLUENT. The first approach is through comparing the numerical results from the current model with the experimental results obtained using a fan loop for a single fan. The second approach is by comparing the numerical results obtained by using the model with the Delta GFC0812DW dual fan data provided by the manufacturer. After the numerical model has been validated, different fan arrangements are studied to find the configuration that produces the best dual fan performance when only one fan is operating while the other fan is stationary. The merits of using different arrangements are assessed by comparing the dual-fan characteristic curve associated with each case.

2. Mathematical model

Axial fans, in general, consist of two blade rows, one rotating (rotor) and the second row is stationary (stator). The Multiple Reference Frame (MRF) model available in ANSYS-FLUENT 18.2 is used to solve the flow field in both the rotating and stationary regions of the fan. Also, the flow domain is extended upstream and downstream of the fan. The computational domain is sliced into four different sections: inlet, fan rotor, fan stator and exit. A matching interface is created between every two contacting sections. This enables one to mesh each section individually. The flow is considered incompressible, turbulent, and steady. The standard κ - ϵ model is used in this simulation to model the turbulent fluctuations and the near-wall regions are treated using the nonequilibrium wall function. Based on these assumptions, the governing equations in the stationary and rotating sections take the following form.

Table 1 Governing equations for the stationary and rotating sections.

Governing equations	Stationary	Rotating
Continuity	$\nabla \cdot (\rho \mathcal{V}) = 0$	$\nabla \cdot (\rho \mathcal{W}) = 0$
Momentum	$\nabla \cdot (\rho \mathcal{V} \mathcal{V}) = -\nabla P + \nabla \cdot (\mu_{eff} \nabla \mathcal{V})$	$\nabla \cdot (\rho \mathcal{W} \mathcal{W}) = -\nabla P + \nabla \cdot (\mu_{eff} \nabla \mathcal{W}) + \mathcal{B}$
Turbulent kinetic energy, κ	$\nabla \cdot (\rho \kappa \mathcal{V}) = \nabla \cdot (\alpha_\kappa \mu_{eff} \nabla \kappa) + G_\kappa - \rho$	$\nabla \cdot (\rho \kappa \mathcal{W}) = \nabla \cdot (\alpha_\kappa \mu_{eff} \nabla \kappa) + G_\kappa - \rho$
Turbulence dissipation rate, ε	$\nabla \cdot (\rho \varepsilon \mathcal{V}) = \nabla \cdot (\alpha_\varepsilon \mu_{eff} \nabla \varepsilon) + C_{1\varepsilon} G_\kappa \frac{\varepsilon}{\kappa} - C_{2\varepsilon} \rho \frac{\varepsilon^2}{\kappa}$	$\nabla \cdot (\rho \varepsilon \mathcal{W}) = \nabla \cdot (\alpha_\varepsilon \mu_{eff} \nabla \varepsilon) + C_{1\varepsilon} G_\kappa \frac{\varepsilon}{\kappa} - C_{2\varepsilon} \rho \frac{\varepsilon^2}{\kappa}$

In Table 1, $\mathcal{W} = \mathcal{V} - \bar{r} \times \bar{\omega}$ is the relative velocity, $\mathcal{B} = -\rho(2\bar{\omega} \times \mathcal{W} + \bar{\omega} \times \bar{\omega} \times \bar{r})$ is the body force due to rotational motion, G_κ represents the turbulent kinetic energy generation due to the mean velocity gradient, α_ε and α_κ are the ε and κ inverse effective Prandtl numbers, respectively. The standard κ - ε model utilized constants are $C_{1\varepsilon}=1.92$, $C_{2\varepsilon}=1.92$ and $C_\mu=0.09$ [41]. The effective turbulent viscosity μ_{eff} is defined as $\mu_{eff} = C_\mu \kappa^{3/2}/\varepsilon$. The pressure-velocity coupling of the equations is solved using the SIMPLE algorithm and the convective terms are treated using the second-order upwind scheme. The solution is considered to have convergence when the residuals of the continuity, momentum and turbulence equations reach 10^{-4} .

3. Experimental and model validation

To validate the numerical model, the experimental facility presented in [42] is shown in Fig. 1 which is used to test a 7-blade fan. It consists of a 4-inch (10.16 cm) diameter tube in which the fan is fixed, a flow straighter, venturi meter and a cone throttling device to control the volume flow rate. The venturi flow meter and the flow straightener were designed following the ISO-5167-4 Standard for venturi flowmeters and ISO-5167 standards [43], respectively. These two components were 3D printed out of Acrylonitrile Butadiene Styrene (ABS) in order to achieve the best geometric qualities.

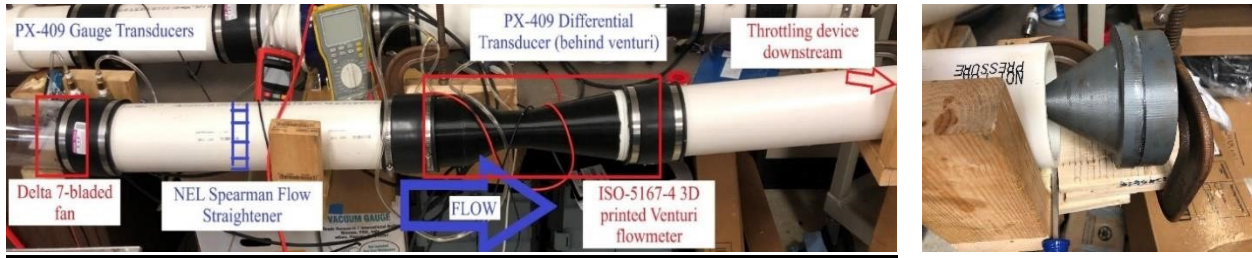


Fig. 1 Pictorial view of the experimental setup and the throttling cone.

OMEGA PX-409 pressure transducers with a range of 0 to 10 inches (25.4 cm) of water are used to measure the pressure one diameter upstream and downstream the fan as well as the differential pressure of the venturi meter. The flow straightener is located 3.5 diameters from the fan. The venturi flowmeter location is nine diameters from the entrance, and the throttling device is six diameters from the venturi flowmeter. Non-Contact digital tachometer unit 6208B by Protmex is used for measuring the fan rotational speed and for verifying the measured rpm by an Arduino UNO board. This board is used to control the fan speed, and to read the rotational speed of the fan through the pulse-width modulation (PWM) signal from the fan. Pressure transducers experience elemental errors such as linearity, hysteresis, sensitivity, drift, and temperature changes within the working environment. Taking those elemental errors into consideration, the overall uncertainty of the PX-409 pressure transducers is given by

$$u_P = [u_{BSL}^2 + u_z^2 + u_S^2]^{1/2} \quad (1)$$

where $u_{BSL} = 0.08\%$ of the full scale (FS) is the best standard line (BSL) which combines the linearity, hysteresis, and repeatability uncertainties, $u_z = 0.5\%$ FS is the zero-balance uncertainty, and $u_S = 0.5\%$ FS is the span setting uncertainty. The uncertainty of the pressure transducers in measuring gauge and absolute pressures is 0.712% FS, which represents 17.71 Pa and 736 Pa in gauge and absolute pressures, respectively. The uncertainty in the venturi meter is calculated based on the equation

$$Q = C_d A_t \sqrt{\frac{2\delta P}{\rho(1 - \beta^4)}} \quad (2)$$

where, A_t is the venturi throat area, δP is the venturi differential pressure and β is the diameter ratio. Following the method of error propagation described in Figliola and Beasley [44], it is found that the maximum uncertainty in the volume flow rate measurements is 0.375% .

The computational domain, as shown in Fig. 2, is cut 1.5 D upstream the fan and 1 D downstream the flow straightener. Zero total pressure is assigned at the flow inlet and pressure-outlet boundary condition is assigned at exit plane. A mesh of size 1.1×10^6 node

(4.8×10^6 element) is created where the grid is refined beside the walls, as shown in the figure. It was found that the change in the fan static pressure and fan flow rate become less than 0.2% when the grid size exceeds 1.1×10^6 node which ensures the solution insensitivity to the grid size. To produce the fan curve, the numerical simulation is carried out for different values of the pressure assigned at the pressure-outlet boundary condition and the mass flow rate driven by the fan is recorded for each case. Figure 3 shows the comparison between the measured and predicted fan static pressure jump versus the fan volume flow rate. It was found that the average difference between the measured and the numerically predicted fan static pressure jump is 30 Pa, which represents around 5% of the fan static pressure jump.

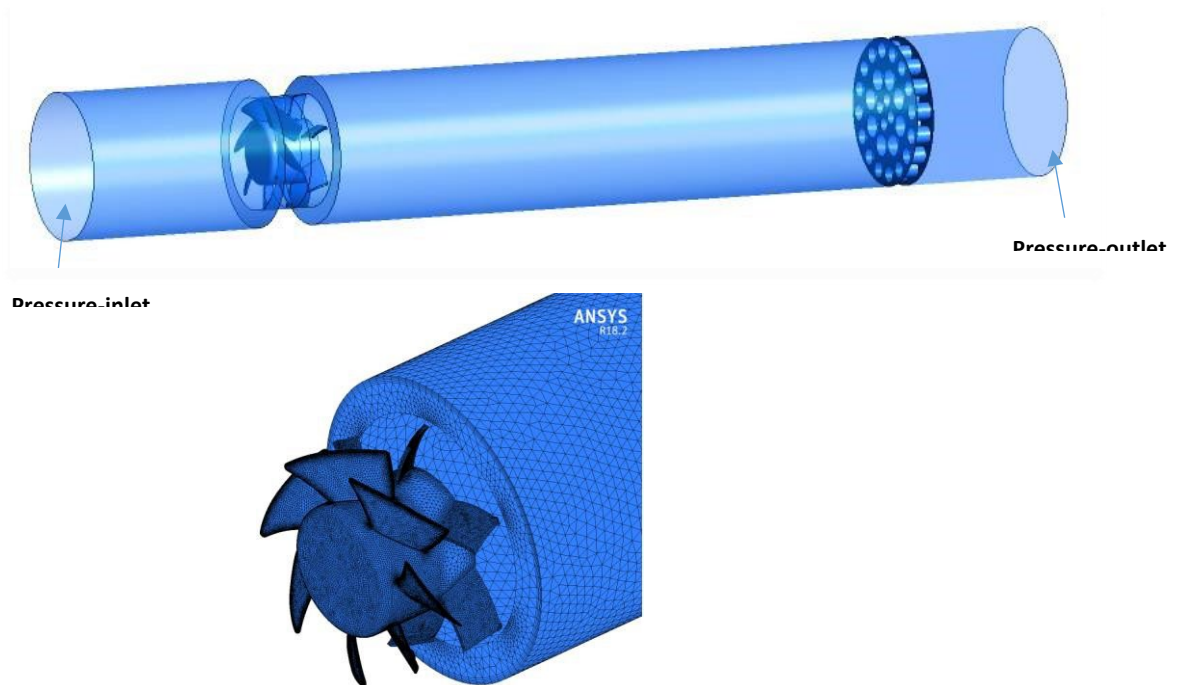


Fig. 2 Computational domain and surface mesh on the fan and 4-inch tube.

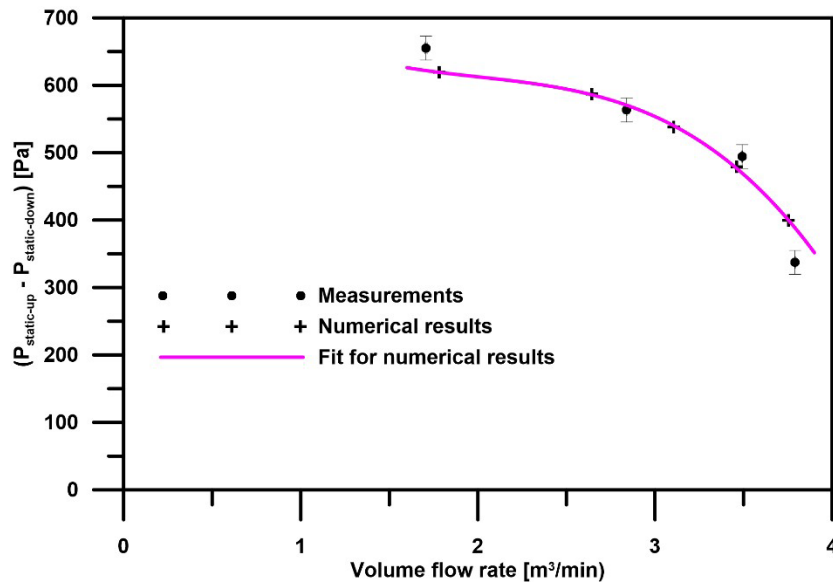


Fig. 3 Validation of the numerical model with the measurements of a single fan.

Also, the numerical model is applied to predict the performance of a commercial dual fan system (Delta GFC0812DW). This system has two sets of rotating blades. The first fan has 7 rotating blades, and the second fan has 5 rotating blades. The stator guide blades for the 7-blade fan are located downstream while the stationary guide blades of the 5-blade fan are located upstream. When the two fans are fixed together in the back-to-back position, the stator guide blades of the two fans form six diffusing passages between the two rotating blade sets, as shown in Fig. 4. The two fans are rotating counter to each other. When both fans are powered with 12 V power supply, the 7-blade fan runs at 13500 rpm while the 5-blade fan runs at 11000 rpm. Figure 4 shows the comparison between the manufacturer fan curve (static head versus volume flow rate) with the numerical results. The fan static head is defined as the static pressure at the fan exit minus the total pressure at the fan inlet. In the numerical simulation, the mass averaged static pressure and mass averaged total pressure are calculated at the fan exit and inlet planes, respectively. The figure shows that the numerical results match quite well with the manufacturer measurements. The average discrepancy of the numerical fan static head from the manufacturer curve is 52 Pa, which represents 4.7% of the zero-flow static head.

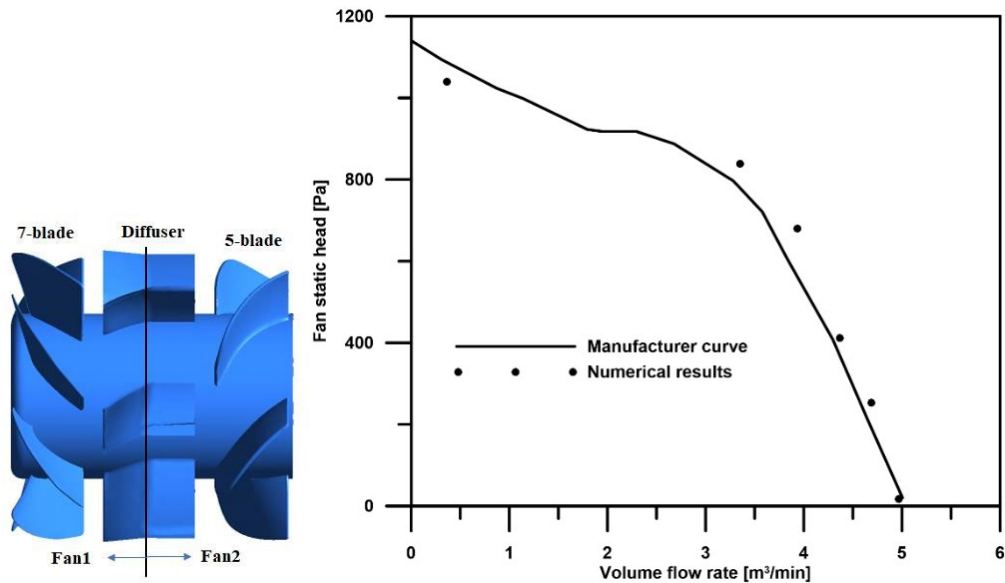


Fig. 4 Validation of the numerical model with Delta dual-fan manufacturer operating curve.

4. Results and discussions

4.1 Effect of keeping one of the two fans stationary

Starting with the Delta dual-fan as a base case, the effect of keeping one of its fans (7-blade or 5-blade) stationary is examined. So, the operation will follow two scenarios. The first case (case 1) is to run the upstream 7-blade fan while keeping the downstream 5-blade fan stationary to avoid bearing degradation of the downstream fan. The second scenario occurs when the upstream fan fails. In this case, the blades of this fan will be clamped stationary, and the downstream fan will be allowed to run (case 2). Figure 5 shows the streamlines and pressure contours for case 1 where the 7-blade fan is rotating at 13,000 rpm, and 5-blade fan is stationary. It can be seen that the flow enters axially to the dual fan system and after the flow passes through the 7-blade row, the diffuser section redirects the flow to the axial direction. The diffuser section converts the kinetic energy of the flow exiting the rotating fan into pressure. But since the 5-blade row is stationary, the exit flow from the diffuser strikes the suction side of the 5-blade fan, creating a low-pressure vortex beside the pressure side of the 5-blade row as shown in Fig. 5.

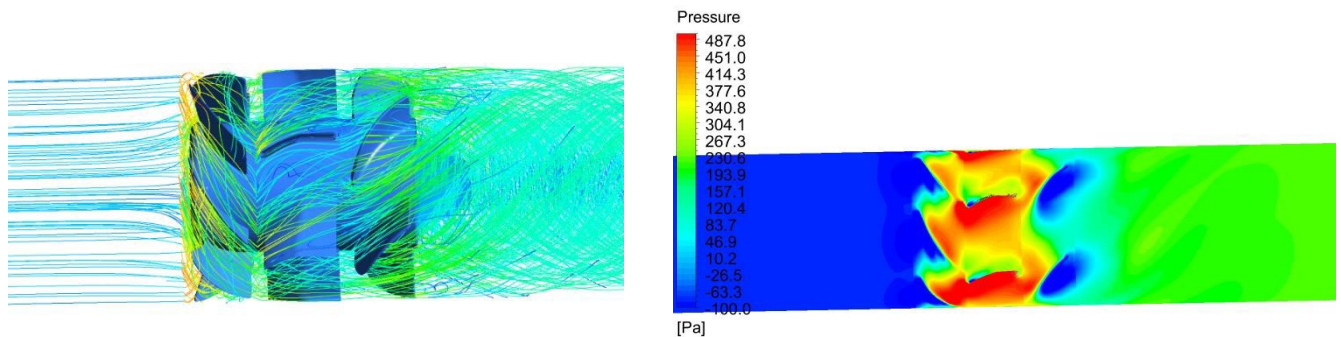


Fig. 5 Streamlines and pressure contours for case 1: the 7-blade fan is running at 13,000 rpm and the 5-blade fan is stationary

Figure 6 shows the streamlines and pressure contours for case 2: when the 7-blade fan is stationary, and the 5-blade fan rotates at 10,000 rpm. It can be seen that the upstream 7-blade fan blocks the inlet flow to the dual fan system and directs it in a direction that is not consistent with the diffuser inlet angle. This creates a big vortex beside the diffuser blades and generates a considerable pressure drop (in the order of 100 Pa) as the flow passes through the stationary 7-blade fan and the diffuser, as shown in Fig. 6.

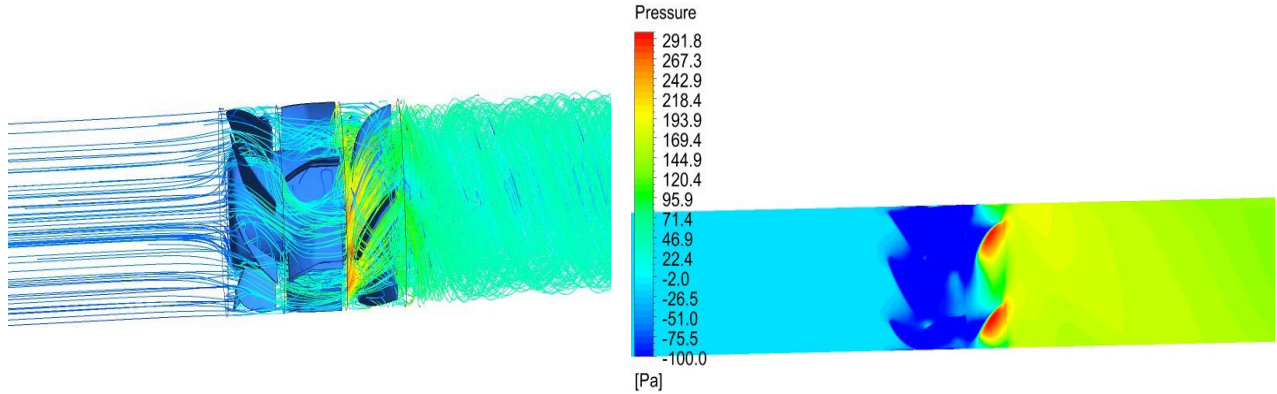


Fig. 6 Streamlines and pressure contours for case 2: the 7-blade fan is stationary, and the 5-blade fan is running at 10,000 rpm

Comparing the characteristic curves for the two cases, it can be seen from Fig.7 that when the upstream fan is running, and the downstream fan is stationary, the dual-fan performance is much better than the case of keeping the upstream fan stationary. This is because the upstream fan partially blocks the intake and directs the air in a direction that is inconsistent with how air should enter the downstream fan.

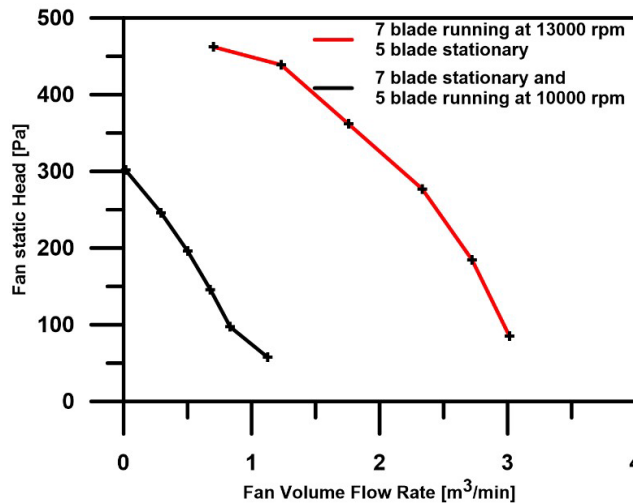


Fig.7 Dual fan curve for the two cases

4.2 Effect of removing the stator section

The diffuser section is removed from the dual fan assembly, as shown in Fig. 8. The flow direction is still from left to right and one fan is allowed to run while the second fan is stationary.

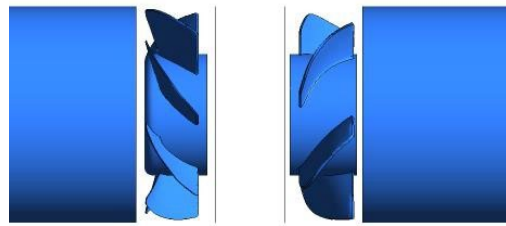


Fig. 8 The dual fan without the diffuser section

As shown in Fig. 9a, when the upstream 7-blade fan is running, the 5-blade downstream fan works as a diffuser and turns the exit flow from the 7-blade fan to the axial direction. So, the presence of the 5-blade fan does not cause a considerable pressure drop, as shown in the pressure contours. But when the downstream 5-blade fan is running, and the upstream 7-blade fan is stationary, the inlet flow to the 5-blade fan becomes quite distorted, as shown in Fig. 9b. This is due to the imparted tangential velocity to the flow when it passes through the 7-blade fan. By comparing the fan performance curve of the dual fan when the upstream 7-blade fan is running with and without the stator section, it can be seen from Fig. 10 that removing the stator section improves the dual-fan performance when the upstream fan is running. The dual fan system can deliver more mass flow rate and produce higher static pressure.

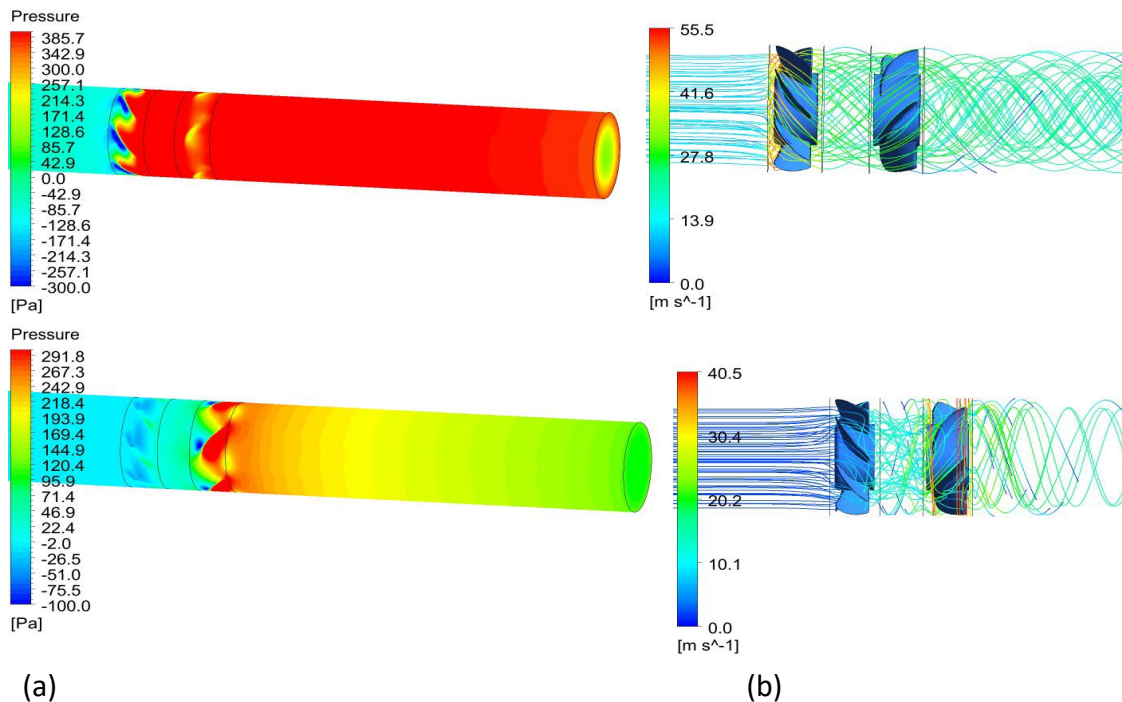


Fig. 9 Streamlines and pressure contours (a) 7-blade fan is running at 13000 rpm and blade fan is stationary (b) 5-blade fan is running at 10000 rpm and 7-blade fan is stationary

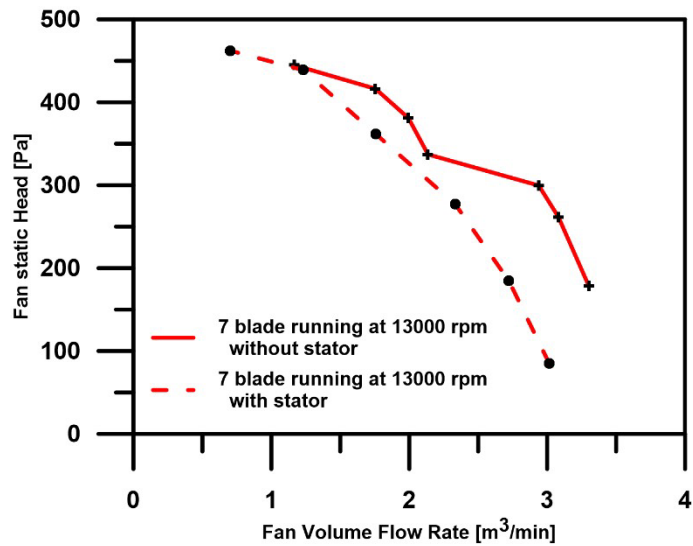


Fig. 10 Performance curve of the dual-fan system when the upstream 7-blade is running and the blade is stationary with and without the stator section

On the other hand, removing the stator section reduces the performance of the dual-fan when the 5-blade fan is running, as shown in Fig. 11. This is because the presence of the stator section helps in directing the flow to the 5-blade fan in the axial direction. The maximum volume flow rate which the dual fan system can produce when the downstream fan is running is about 1 m³/min compared to 3 m³/min when the upstream fan is running.

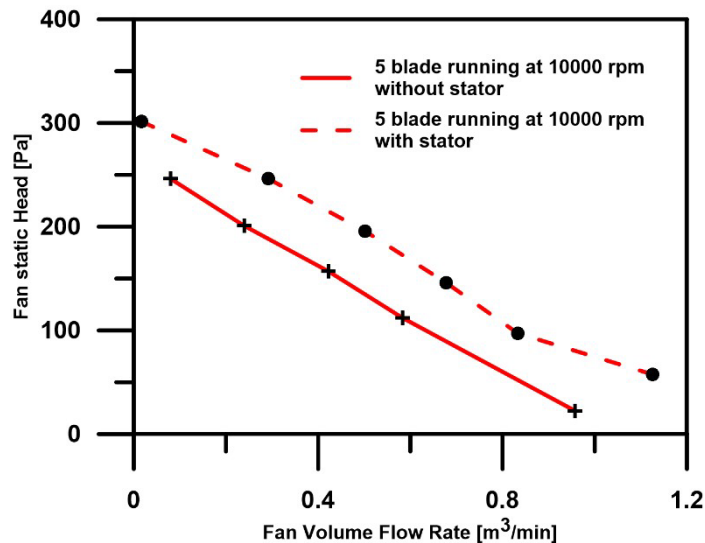


Fig. 11 Performance curve of the dual-fan system when the upstream 7-blade fan is stationary and the 5-blade fan is running at 10000 rpm with and without the stator section

4.3 Effect of replacing the 5-blade fan with a 7-blade fan and changing the distance between fans

To evaluate the performance of the 7-blade fan when it operates on the downstream side, the 5-blade fan is replaced with the 7-blade fan with the same design as the upstream one. However, the blades of the 7-blade downstream fan are set in such a way that when it

rotates in the counter direction to the upstream fan, it draws air from left to right. This is achieved by rotating the original upstream fan 180 degrees around the normal to the page then flipping the rotated image horizontally and adjusting the distance between the two fans as shown in Fig. 12. The results in Fig. 13 show the same conclusion of the superiority of the dual fan when the upstream fan is running. Also, it shows that in the case of running the downstream fan, the 7-blade fan has a better performance than the 5-blade fan. This is because the 7-blade fan runs at 13000 rpm while the 5-blade fan runs at 10000 rpm.

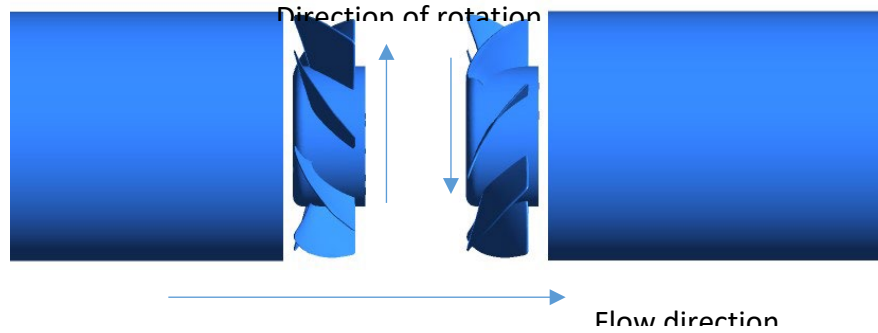


Fig. 12 Two 7-blade dual fan system

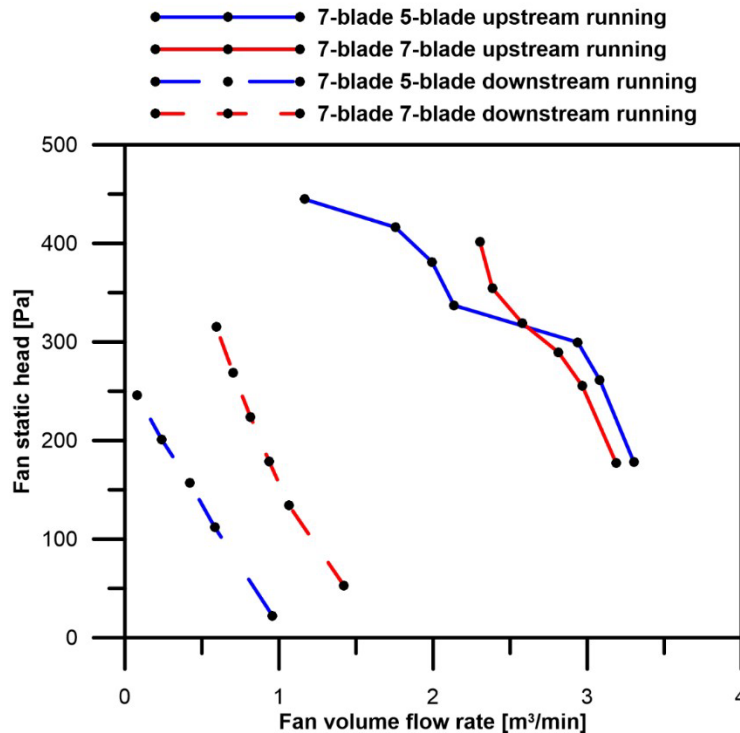


Fig. 13 Comparison between 7-5-blade and 7-7-blade systems

Next, the distance between the dual 7-blade fans is varied from 31 mm to 122 mm. The effect of changing the distance on the flow pressure and streamlines when the upstream fan (Fan1) is running is shown in Fig. 14. As seen from the pressure contours, the pressure at the exit of the dual fan system decreases with increasing the distance between the two fans. In the case of running the upstream fan, three components of pressure drop occur:

the pressure drop in the region between the two fans, the pressure drop due to the stationary downstream fan, and the pressure drop in the exit section. Keeping the distance between the two fans small minimizes the pressure drop occurred in the region between the two fans. In addition, the stationary downstream fan straightens the flow in the axial direction and reduces the tangential velocity component, which reduces the pressure drop in the exit section of the dual fan system. As can be noticed for the case of setting the distance between the two fans equal to 122 mm, a considerable part of the pressure drop occurs in the region between the two fans. This is due to the high tangential velocity in this long distance.

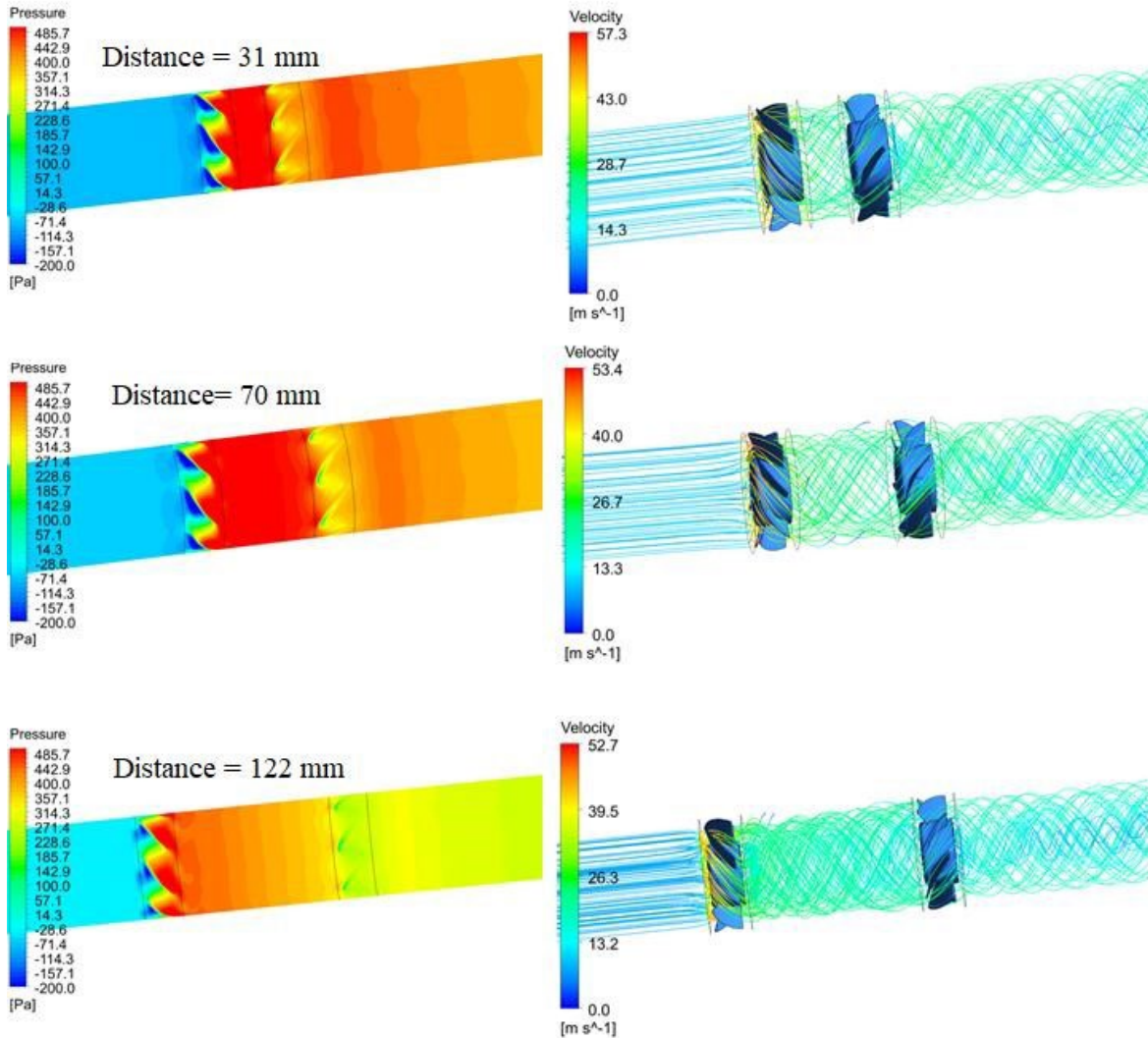


Fig. 14 Effect changing the distance between the two fans on the flow pressure and streamlines when the upstream fan (Fan1) is running

It can be noted from Fig. 15 that the performance of the dual-fan system decreases with increasing the distance between the two fans from 31 mm to 122 mm. In the same figure, the case of keeping the distance between the two fans to the smallest possible value of 6 mm is also shown. Keeping this distance to the smallest value does not improve the performance. This may be attributed to the friction between the air and the fan surfaces, which disturbs the flow in this small gap between the two fans. Therefore, for the current

configuration, there is an optimum distance between fans (~30 mm) that can maximize the performance of the dual 7-blade fan system with upstream fan (Fan1) running.

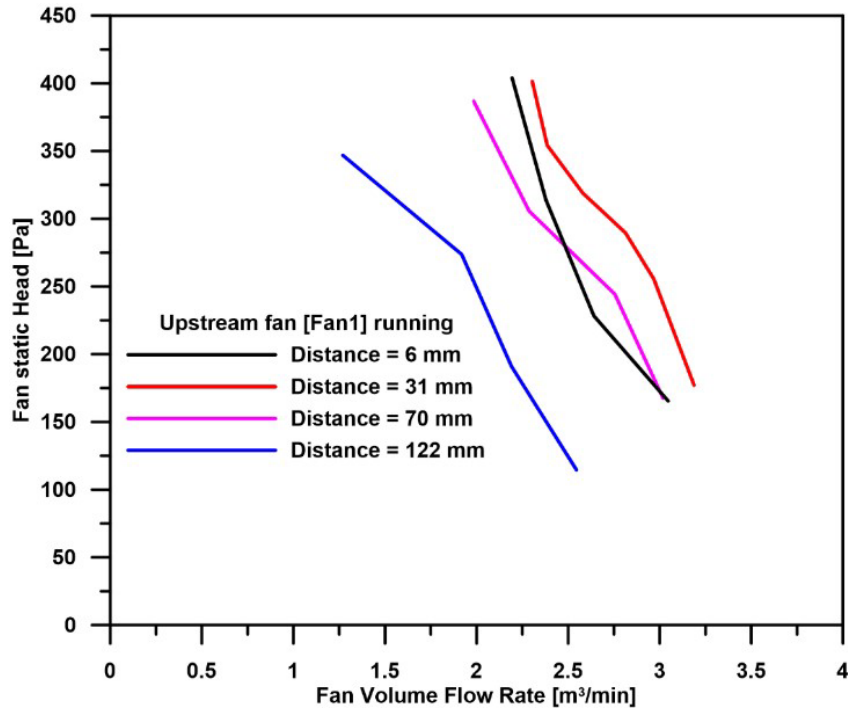


Fig. 15 Effect of changing the distance between the two fans on the performance of upstream fan (Fan1).

The effect of changing the distance between the two fans on the flow when the downstream fan (Fan2) is running is shown in Fig. 16. Keeping the distance between the two fans small does not allow the flow from the upstream fan to adapt to the downstream fan. The blade angles of the downstream fan are designed to receive the flow at its inlet in the axial direction. Since the distance between the two fans works as a flow straightener, it can be seen that increasing the distance from 31 mm to 70 mm increases the static pressure at the dual-fan exit at the higher flow rate. However, the pressure drop in the region between the two fans reduces the dual-fan static pressure rise when the distance increases to 122 mm.

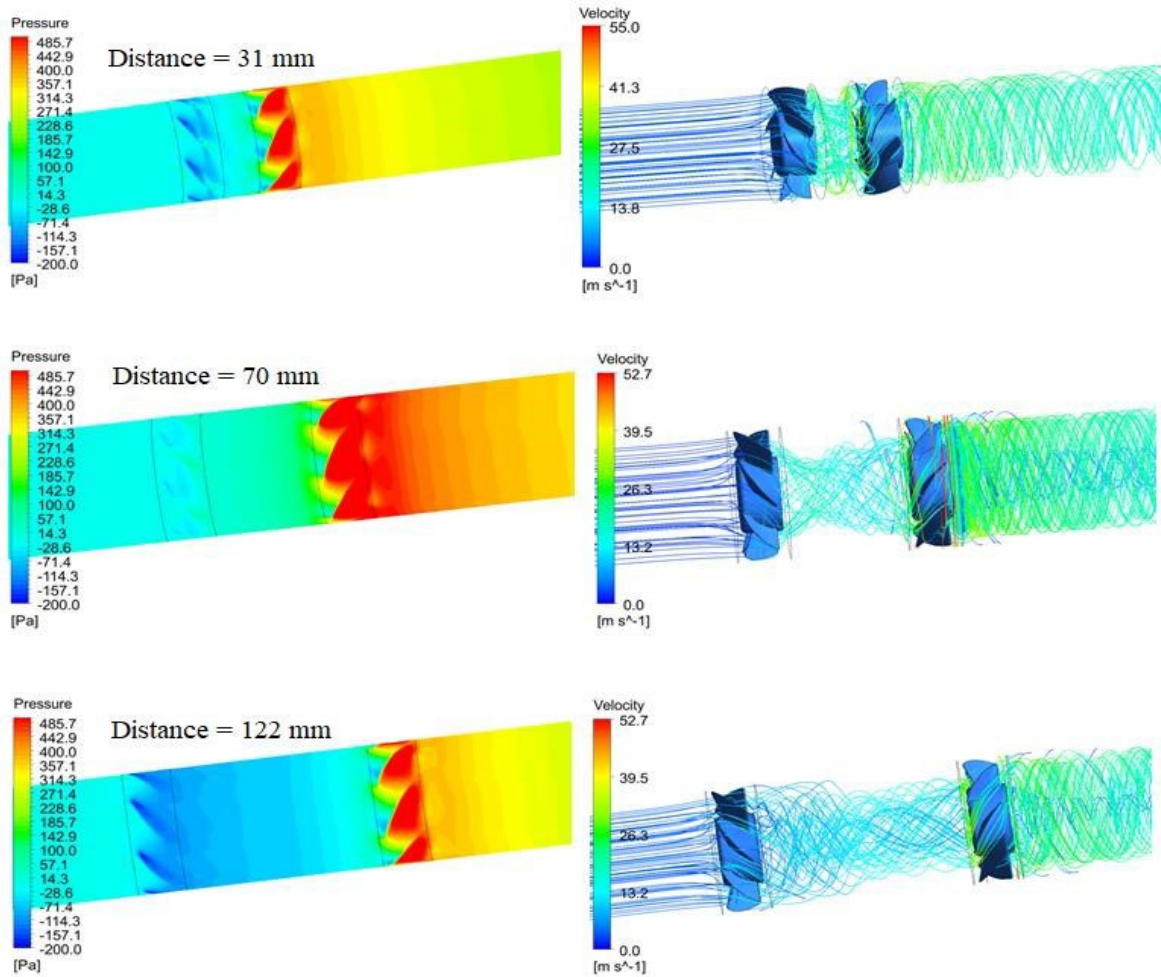


Fig. 16 Effect of changing the distance between the two fans on the flow pressure and streamlines when the downstream fan (Fan2) is running

Figure 17 shows the performance of the downstream fan for different fan spacing. When the dualfan is subjected to low back pressure (volume flow rate $> 1 \text{ m}^3/\text{min}$), the performance of the downstream fan is better when the distance between the two fans is 70 mm. But for high back pressure (volume flow rate $< 1.0 \text{ m}^3/\text{min}$), the performance is better when the distance is kept at 31 mm. This is attributed to the contradicting effects of increasing the distance between the two fans: pressure drop and flow straightening. The flow straightening effect is more pronounced at the higher volume flow rate region. In

general, the produced volume flow rate by the dual-fan system when the downstream fan (Fan2) is running is less compared to the case when the upstream fan (Fan1) is running.

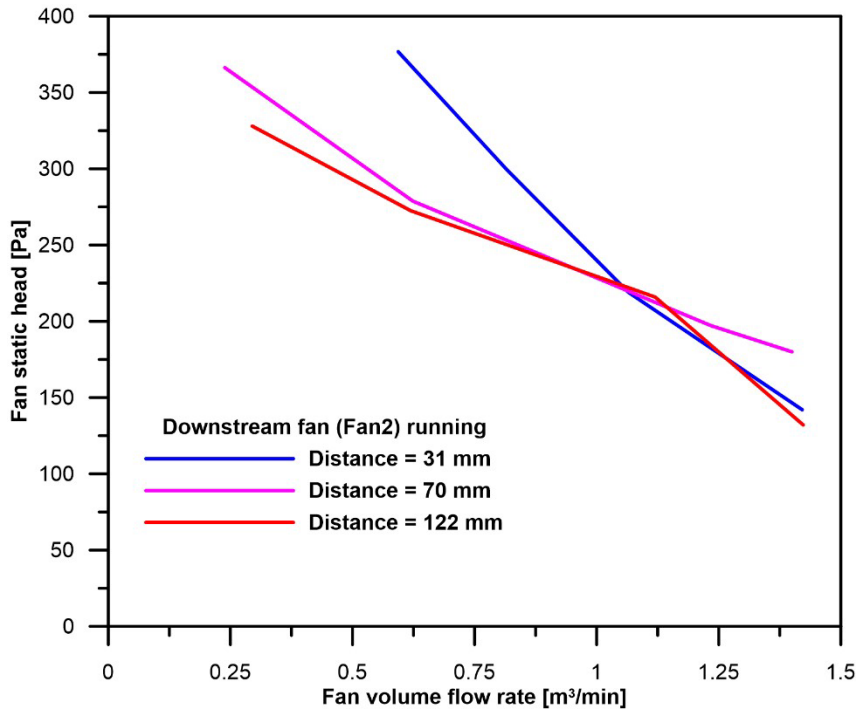


Fig. 17 Effect of changing the distance between the two fans on the performance of downstream fan (Fan2)

4.4 Effect of using a movable wall between the two fans

It can be seen from the previous results that the maximum air volume flow rate produced by the dual-fan system when the downstream fan is running is less than 50% of the maximum air volume flow rate produced by the upstream fan. This is mainly due to the effect of the stationary upstream fan in blocking the intake and directing the flow in a direction that is not consistent with the running downstream fan. So, in this section, we studied the effect of replacing the circumferential wall between the two fans with a movable wall which can be opened or closed, as shown in Fig.18. The distance between the two fans is kept at 31 mm which corresponds to the optimum performance of the dual-fan system with the upstream fan in operation. In the case of failure of the upstream fan, this movable wall can be opened, and the downstream fan sucks the air through the open circumferential area instead of sucking the air through the upstream fan.

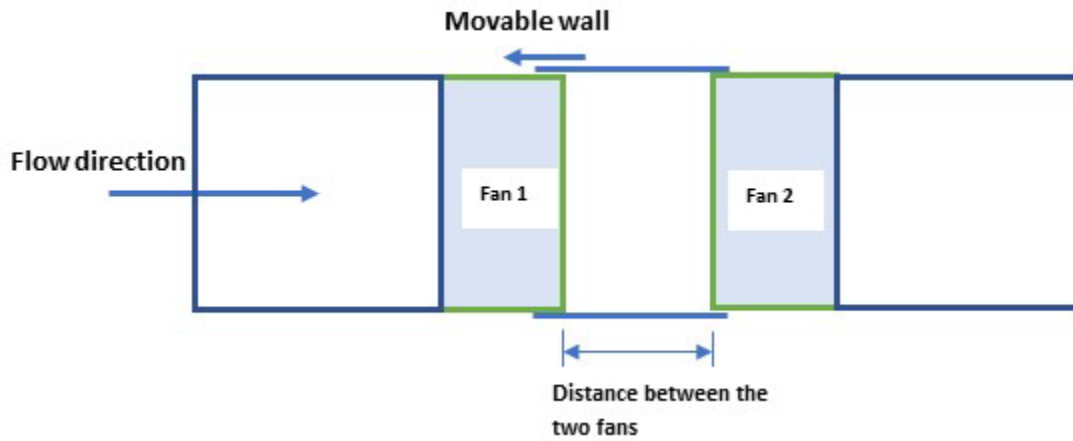


Fig.18 Movable wall between the two fans



Fig. 19 Computational domain and boundary condition for the open wall case

A numerical simulation has been carried out for the case of running the downstream fan at 13000 rpm while keeping the upstream fan stationary with the movable wall opened as shown in Fig. 19. The flow is allowed to enter the domain through two inlets: pressure-inlet1 and pressure-inlet2. Only 22.5 mm out of the distance between the two fans (31 mm) is opened. The total pressure at the two inlets is assumed to be equal to atmospheric pressure. Fig. 20 presents the streamlines and the pressure contours of the open wall case. The figure indicates that the downstream fan (Fan2) draws the air from the two pressure inlet boundaries. But the percentage of the air mass flow rate passing through pressure-inlet2 is much higher than that from pressure-inlet1. This can be observed from the low static pressure and high air velocity at pressure-inlet2. The numerical values of the mass flow rate indicate that the fraction of flow through pressure-inlet1 is approximate 9.5% of the total flow rate through the dual-fan system.

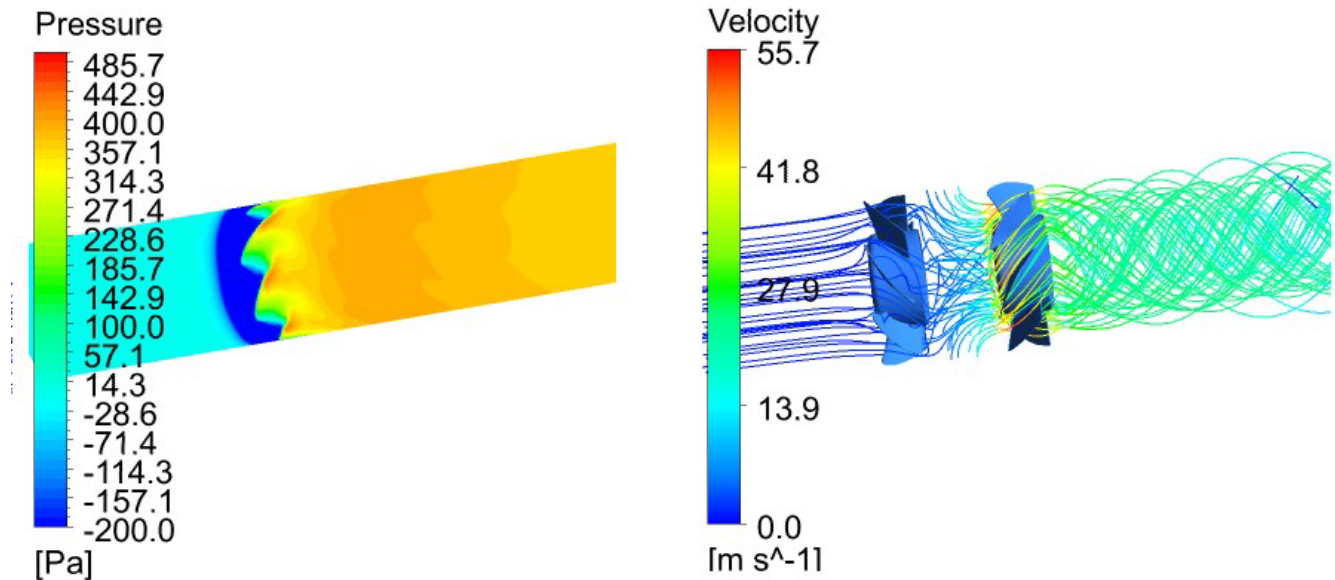


Fig. 20 Static pressure contours and streamlines when Fan2 is running with open wall

Figure 21 shows that in the case of running Fan2 with open wall, the dual-fan system performs better than running the upstream fan with closed wall, especially if the dual-fan system faces low back pressure at the outlet-pressure boundary. But if the dual-fan system faces higher back pressure (greater than 350 Pa), the performance of the two cases is comparable because in the case of running the upstream fan, the stationary downstream fan converts some of the kinetic energy into pressure head. So, the dual-fan system can be operated first by running the upstream fan (Fan1) and keeping the downstream fan (Fan2) as a spare (with its blades clamped stationary). During the operation of Fan1, the movable wall can be held in the closed position using a spring.

If the upstream fan fails due to any reason, the downstream fan can be used to produce air flow by releasing the movable wall to open the circumferential area. This can add double reliability to the cooling system without sacrificing the air flow rate when the downstream fan is running. Also, this arrangement requires no additional space compared to a single-fan system if the wing-bay space limitation is considered.

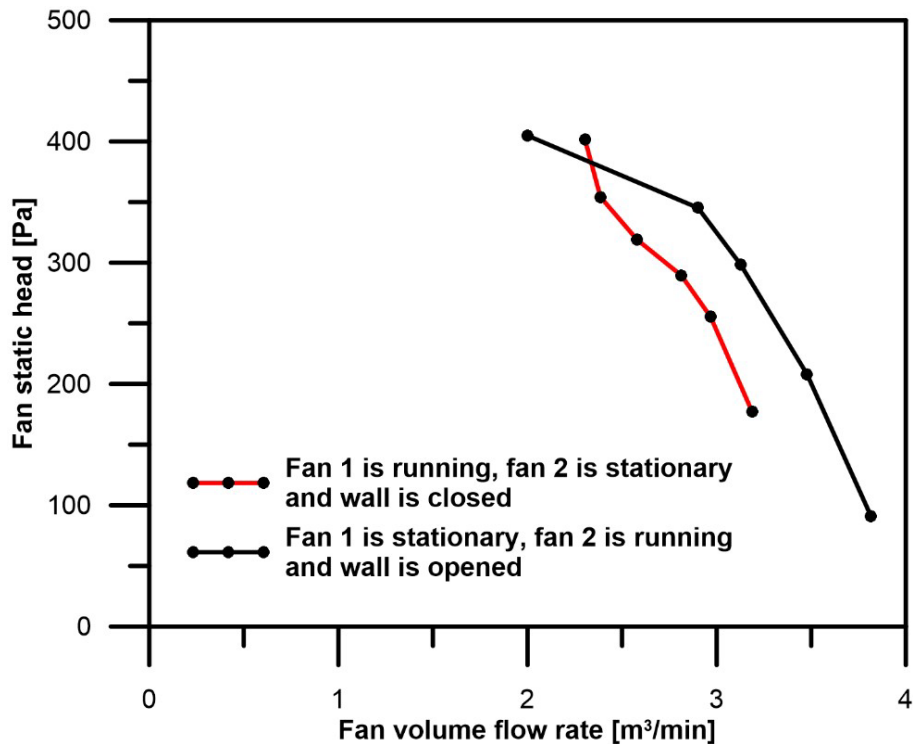


Fig. 21 The fan performance curve of Fan2 when the wall is opened compared to the performance of the upstream fan (Fan1) when the wall is closed

5. Conclusions

In this paper, a CFD model is developed to predict the performance of a dual fan system when only one fan is allowed to run while the second fan is kept stationary as a backup. The two fans are placed in series due to space limitation in the wing bay. The necessity of keeping one fan stationary with only the other one running is due to fault probability consideration. This system is proposed to be used in cooling electromechanical actuators in aerospace applications, which require very high level of reliability. The model is validated with experimental measurements and with the manufacturer data of the commercial 7-blade-5blade Delta GFC0812DW dual fan. Starting with the Delta dual fan system as a base case, the effect of keeping one of the fans stationary on the overall performance of the dual fan is examined. It was found that keeping the upstream fan stationary deteriorates the performance significantly because it partially blocks the intake of the downstream fan and directs the flow to the downstream fan in an undesirable direction. Delta dual-fan can provide a volume flow rate of 3 m³/min when the upstream fan is running compared to 1 m³/min when the downstream fan is running. Different arrangements have been tried to improve the performance of the dual fan system when the upstream fan is kept stationary. These arrangements include: removing the diffuser section; replacing the 5-blade with 7-blade and changing the distance between the two fans; and opening the circumferential area between the two fans using a movable wall. From the results, these conclusions can be drawn:

- 1- Removing the diffuser section improves the performance when the upstream fan is running and creates more deterioration to the performance when the downstream fan is running.
- 2- Replacing the 5-blade fan with a 7-blade fan improves the performance in the case running downstream fan. The dual fan can deliver up to 1.4 m³/min.
- 3- The performance of the dual fan decreases with increasing the distance between the two fans when the upstream fan is running.
- 4- Opening the circumferential area between the two fans improves the dual fan system significantly when the downstream fan is running. This is because more than 90% of the mass flow rate is drawn through the opened circumference area without passing through the upstream fan.

Conflict of interest

Authors declare that there is no conflict of interest.

ACKNOWLEDGMENT

This material is based on research sponsored by the United States Air Force under agreement number FA8650-17-2-2230. The U.S. Government is authorized to reproduce and distribute reprints for Governmental purposes notwithstanding any copyright notation thereon. The views and conclusions contained herein are those of the authors and should not be interpreted as necessarily representing the official policies or endorsements, either expressed or implied, of the United States Air Force or the U.S. Government.

REFERENCES

- [1] J. Rosero, J. Ortega, E. Aldabas, L. Romeral, Moving towards a more electric aircraft, IEEE Aerospace and Electronic Systems Magazine, 22 (2007) 3-9. <https://doi.org/10.1109/MAES.2007.340500>.
- [2] G. Qiao, G. Liu, Z. Shi, Y. Wang, S. Ma, T.C. Lim, A review of electromechanical actuators for More/All Electric aircraft systems, Proceedings of the Institution of Mechanical Engineers, Part C: Journal of Mechanical Engineering Science, 232 (2018) 4128-4151. <https://doi.org/10.1177/0954406217749869>.
- [3] J. Fu, J.-C. Maré, Y. Fu, Modelling and simulation of flight control electromechanical actuators with special focus on model architecting, multidisciplinary effects and power flows, Chinese Journal of Aeronautics, 30 (2017) 47-65. <https://doi.org/10.1016/j.cja.2016.07.006>.
- [4] R. Navarro, Performance of an electro-hydrostatic actuator on the F-18 systems research aircraft, TM-97206224(1997).
- [5] D. Blanding, Subsystem design and integration for the more electric aircraft, 5th international energy conversion engineering conference and exhibit (IECEC), (2007) 4828.
- [6] J.-J. Charrier, A. Kulshreshtha, Electric actuation for flight and engine control; evolution and current trend, 45th AIAA Aerospace Sciences Meeting and Exhibit, (2007) 1391.
- [7] I. Chakraborty, D.R. Trawick, D. Jackson, D. Mavris, Electric control surface actuator design optimization and allocation for the more electric aircraft, 2013 aviation technology, integration, and operations conference, (2013) 4283.
- [8] A. El-Refaie, Fault-tolerant permanent magnet machines: a review, IET Electric Power Applications, 5 (2011) 5974. <https://doi.org/10.1049/iet-epa.2009.0117>.

- [9] C. Shi, X. Wang, S. Wang, J. Wang, M.M. Tomovic, Adaptive decoupling synchronous control of dissimilar redundant actuation system for large civil aircraft, *Aerospace Science and Technology*, 47 (2015) 114-124. <https://doi.org/10.1016/j.ast.2015.09.012>.
- [10] L. Wang, J.-C. Mare, A force equalization controller for active/active redundant actuation system involving servohydraulic and electro-mechanical technologies, *Proceedings of the institution of mechanical engineers, Part G: Journal of aerospace engineering*, 228 (2014) 1768-1787. <https://doi.org/10.1177/0954410013504343>.
- [11] M. Popescu, D. Staton, A. Boglietti, A. Cavagnino, D. Hawkins, J. Goss, Modern heat extraction systems for electrical machines-A review, 2015 IEEE Workshop on Electrical Machines Design, Control and Diagnosis (WEMDCD), (2015) 289-296. <https://doi.org/10.1109/WEMDCD.2015.7194542>.
- [12] D. Staton, A. Boglietti, A. Cavagnino, Solving the more difficult aspects of electric motor thermal analysis in small and medium size industrial induction motors, *IEEE Transactions on Energy conversion*, 20 (2005) 620-628. <https://doi.org/10.1109/TEC.2005.847979>.
- [13] A.G. Jack, B.C. Mecrow, P.G. Dickinson, D. Stephenson, J.S. Burdess, N. Fawcett, J. Evans, Permanent-magnet machines with powdered iron cores and prepressed windings, *IEEE Transactions on industry applications*, 36 (2000) 1077-1084. <https://doi.org/10.1109/28.855963>.
- [14] W. Gerstler, E. Ruggiero, F. Ghasripoor, A. El-Refaie, H. De Bock, X. Shen, J. Alexander, A Liquid-Cooled Rotor for High Density Electric Machines, 47th AIAA/ASME/SAE/ASEE Joint Propulsion Conference & Exhibit, (2011) 5560. <https://doi.org/10.2514/6.2011-5560>.
- [15] M. Guechi, P. Desevaux, P. Baucour, C. Espanet, R. Brunel, M. Poirot, Spray cooling of electric motor coil windings, *The Journal of Computational Multiphase Flows*, 8 (2016) 95-100. <https://doi.org/10.1177/1757482X16653895>.
- [16] L. Fedoseyev, E.M. Pearce, Rotor assembly with heat pipe cooling system, in, Google Patents, 2016.
- [17] J. Bai, Y. Liu, Y. Sui, C. Tong, Q. Zhao, J. Zhang, Investigation of the cooling and thermal-measuring system of a compound-structure permanent-magnet synchronous machine, *Energies*, 7 (2014) 1393-1426. <https://doi.org/10.3390/en7031393>.
- [18] K.-H. Lee, H.-R. Cha, Y.-B. Kim, Development of an interior permanent magnet motor through rotor cooling for electric vehicles, *Applied Thermal Engineering*, 95 (2016) 348-356. <https://doi.org/10.1016/j.applthermaleng.2015.11.022>.
- [19] M. S. Mahdi, A. A. Khadom, H. B. Mahood, M. A. Yaqup, J. M. Hussain, K. I. Salih, and H. A. Kazem, Effect of fin geometry on natural convection heat transfer in electrical distribution transformer: Numerical study and experimental validation, *Thermal Science and Engineering Progress* 14 (2019) 100414. <https://doi.org/10.1016/j.tsep.2019.100414>
- [20] A. Boglietti, A. Cavagnino, M. Parvis, A. Vallan, Evaluation of radiation thermal resistances in industrial motors, *IEEE Transactions on Industry Applications*, 42 (2006) 688-693. <https://doi.org/10.1109/TIA.2006.873655>.
- [21] L. Seungjun, H. Uematsu, Cooling plate for electric motor with improved heat radiation capability, in, Google Patents, 2013.
- [22] E. Racine, Z. Lammers, S. Barnett, J. Murphy, Q. Leland, Energy analysis of electromechanical actuator under simulated aircraft primary flight control surface load, *SAE Technical Paper*, 0148-7191(2014). <https://doi.org/10.4271/2014-01-2182>.
- [23] K. Farsane, P. Desevaux, P. Panday, Experimental study of the cooling of a closed type electric motor, *Applied Thermal Engineering*, 20 (2000) 1321-1334. [https://doi.org/10.1016/S1359-4311\(99\)00094-0](https://doi.org/10.1016/S1359-4311(99)00094-0).
- [24] K. McCarthy, A. Heltzel, E. Walters, J. Roach, S. Iden, P. Lamm, A reduced-order enclosure radiation modeling technique for aircraft actuators, *SAE Technical Paper*, 0148-7191(2010). <https://doi.org/10.4271/2010-01-1741>.

- [25] Y.-R. Lin, Y. Hu, L. Zhou, D. Woodburn, T. Wu, L.C. Chow, Q. Leland, A reduced-order model for electromechanical actuator, SAE Technical Paper, 0148-7191(2012). <https://doi.org/10.4271/2012-01-2230>.
- [26] M.L. Elsayed, O. Mesalhy, R.H. Mohammed, J.P. Kizito, Q.H. Leland, L.C. Chow, Enhancement of a heat sink performance using a partial shield and/or a guide plate, International Journal of Heat and Mass Transfer, 134 (2019) 948-958. <https://doi.org/10.1016/j.ijheatmasstransfer.2019.01.096>.
- [27] M.L. Elsayed, O. Mesalhy, J.P. Kizito, Q.H. Leland, L.C. Chow, Performance of a guided plate heat sink at high altitude, International Journal of Heat and Mass Transfer, 147 (2020) 118926. <https://doi.org/10.1016/j.ijheatmasstransfer.2019.118926>.
- [28] O. Mesalhy, C. Rath, D. Rini, J. Kizito, Q. Leland, L. Chow, A parametric fin structure design study for cooling aerospace electro-mechanical actuators with high-speed axial fans, Heat and Mass Transfer, (2019) 1-13. <https://doi.org/10.1007/s00231-019-02791-y>.
- [29] W. Wu, Y. Lin, E. Gyasi, J. Kizito, Q. Leland, L. Chow, Design and Experiment on Aircraft Electromechanical Actuator Fan at Different Altitudes and Rotational Speeds, SAE International Journal of Aerospace, 12 (2019) 57-76. <https://doi.org/10.4271/01-12-01-0003>.
- [30] J. Bennett, B. Mecrow, D. Atkinson, G. Atkinson, Safety-critical design of electromechanical actuation systems in commercial aircraft, IET Electric Power Applications, 5 (2011) 37-47. <https://doi.org/10.1049/iet-epa.2009.0304>. [31] W. Wu, Y. Lin, L. Chow, E. Gyasi, J. Kizito, Q. Leland, Electromechanical actuator fan failure analysis and safety-critical design, IEEE Aerospace and Electronic Systems Magazine, 32 (2017) 18-25. <https://doi.org/10.1109/MAES.2017.150281>.
- [32] DARPA, Novel schemes for highly reliable aerospace electromechanical primary actuation systems, (2013). Defense Advanced Research Projects Agency solicitation (SB132-005) <https://www.sbir.gov/sbirsearch/detail/401746>
- [33] E. Galloni, P. Parisi, F. Marignetti, G. Volpe, CFD analyses of a radial fan for electric motor cooling, Thermal Science and Engineering Progress, 8 (2018) 470-476. <https://doi.org/10.1016/j.tsep.2018.10.003>.
- [34] B. Bizjan, M. Milavec, B. Širok, F. Trenc, M. Hočvar, Energy dissipation in the blade tip region of an axial fan, Journal of Sound and Vibration, 382 (2016) 63-72. <https://doi.org/10.1016/j.jsv.2016.06.036>.
- [35] H. Chen, Y. Qin, R. Wang, The optimization and flow diagnoses for a transonic fan with stage flow condition, Aerospace Science and Technology, 80 (2018) 247-260. <https://doi.org/10.1016/j.ast.2018.07.003>.
- [36] C. Wang, W. Zhang, L. Huang, Noise source analysis and control of two axial-flow cooling fans in series, Noise Control Engineering Journal, 64 (2016) 677-687. <https://doi.org/10.3397/1/376412>.
- [37] C. Wang, Noise source analysis for two identical small axial-flow fans in series under operating condition, Applied Acoustics, 129 (2018) 13-26. <https://doi.org/10.1016/j.apacoust.2017.07.010>.
- [38] H.-Y. Kim, S.-H. Yoon, S.-J. Moon, J.-H. Lee, H. Yoo, Y.-C. Im, A study on the fan efficiency decrease on the backward flow in an axial fan with adjustable pitch blade, International Journal of Air-Conditioning and Refrigeration, 18 (2010) 101-107. <https://doi.org/10.1142/S2010132510000216>.
- [39] H.-J. Kim, Y.-M. Lee, Experimental Study on Air Flow Characteristics of Axial Dual-blade Fan, Journal of the Korean Society of Manufacturing Process Engineers, 13 (2014) 113-120. <https://doi.org/10.14775/ksmpe.2014.13.4.113>.
- [40] R.-T. Wang, Y.-W. Lee, S.-L. Chen, J.-C. Wang, Performance effects of heat transfer and geometry on heat pipe thermal modules under forced convection, International Communications in Heat and Mass Transfer, 57 (2014) 140149. <https://doi.org/10.1016/j.icheatmasstransfer.2014.07.023>.
- [41] ANSYS FLUENT User's guide, Release 16.0., ANSYS Inc., Canonsburg, PA, 2016).

- [42] J. Corona, A. Kwarteng, G. Warwick, K. Kaddoura, O. Mesalhy, Q. Leland, L. Chow, J. Kizito, Testing of a Cooling Fan for Wing-Bay Electro-Mechanical Actuators, ASME 2018 5th Joint US-European Fluids Engineering Division Summer Meeting, (2018). <https://doi.org/10.1115/FEDSM2018-83480>.
- [43] ISO, Measurement of fluid flow by means of pressure differential devices inserted in circular cross-section conduits running full—Part 4: Venturi tubes. , International Organization for Standardization: Geneva, Switzerland, (2003) ISO 5167.
- [44] R.S. Figliola, D.E. Beasley, Theory and design for mechanical measurements, John Wiley & Sons, 2014.

NOMENCLATURE

Alphabet

A_t	Venturi throat area, m^2
B	Body force due to rotation, N
C_d	Venturi discharge coefficient
$C_{1\Omega}, C_{2\Omega}, C_\Omega$	Constants for Ω - Ω model
G_Ω	Turbulence generation rate, m^2/s^3
P	Pressure, Pa
Q	Volume flow rate, m^3/s
\bar{r}	Position vector in radial direction, m
u_p	Pressure uncertainty, Pa
V	Absolute velocity, m/s
W	Relative velocity, m/s

Greek symbols

α_k	Inverse Prandtl number for turbulent kinetic energy
α_ε	Inverse Prandtl number for turbulent dissipation
ε	Turbulent dissipation rate, m^2/sec^5
κ	Turbulence kinetic energy, m^2/s^2
μ_{eff}	Effective dynamic viscosity, Pa.s
$\bar{\omega}$	Rotational velocity, 1/s
ρ	Density, kg/m^3
β	Venturi diameter ratio

APPENDIX I

UCF Project 1626-8282

Quarterly Report # 1

to

North Carolina A&T University

**THERMAL MANAGEMENT OF ELECTROMECHANICAL MACHINES FOR
AEROSPACE SYSTEMS**

University of Central Florida

Department of Mechanical and Aerospace Engineering

Orlando, FL 32816-2450

Louis Chow, PI

Yeong-Ren Lin

Osama Mesalhy

Period: From September 12, 2017, to December 11, 2017

Date of report: December 13, 2017

1. Introduction

Permanent Magnet Synchronous Motors (PMSM) have the advantages of high-power density and high efficiency. In high performance aerospace electromechanical actuators (EMA), the PMSM drives can meet sophisticated requirements such as fast dynamic response, high power, and wide operating speed range. An air-cooling system utilizing wing bay air where the air is pushed over a finned surface attached to the motor housing with a cooling fan is the simplest and preferred way in cooling EMA. This is because of the following reasons: (i) least complicated (ii) light weight and reliable (iii) bay air can be effective if sufficient air flow to enhance heat transfer effectiveness is provided.

To enhance the heat transfer rate from the motor to the external air, a dense fin structure is desired to increase the surface area and consequently, enhance the heat removal. However, a dense fin structure also leads to high pressure drop and consequently a low volume flow rate from the fan. In this reporting period, we studied numerically the cooling performance of different fin structures which include continuous straight fins, interrupted fins in staggered arrangements, and corrugated fins. 2. Modeling of fan-finned surface cooling

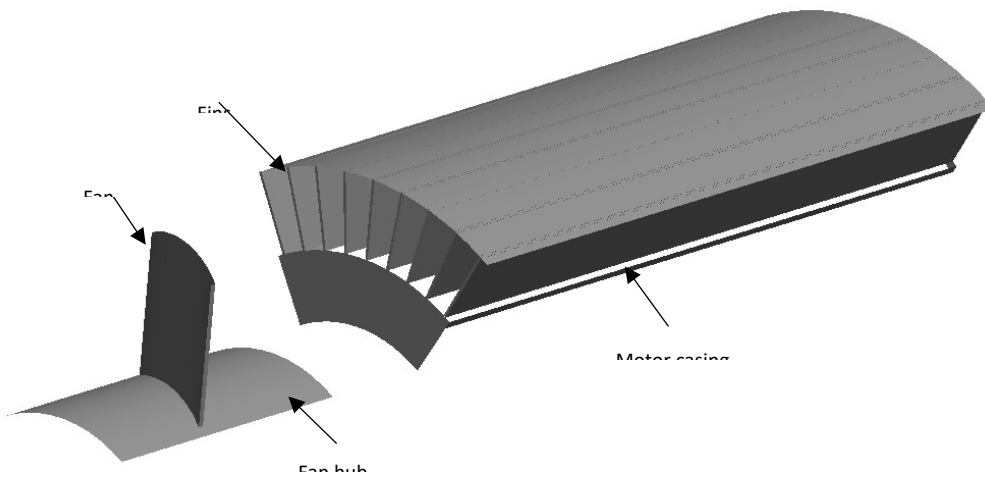


Figure (1) physical domain

As shown in Figure (1), the physical domain comprises a finned motor casing and a fan blowing air to flow through the inter-fin spacing. The fan rotation is not considered in this

model. Instead, a fan interface boundary is used to generate the pressure jump which is equivalent to the real cooling fan pressure head. The characteristic fan curve of a real Sunon fan running at 10,800 rpm has been measured in an available fan loop and is utilized in this simulation as shown in Figure (2). Due to the symmetry, only one axisymmetric repeated section is considered as the computational domain. The numerical model relies on solving the heat conduction in the solid regions as well as the flow over the finned frame using ASYS-FLUENT software. The flow is considered incompressible and turbulent. The standard k- ϵ turbulence model is selected to model the turbulent flow.

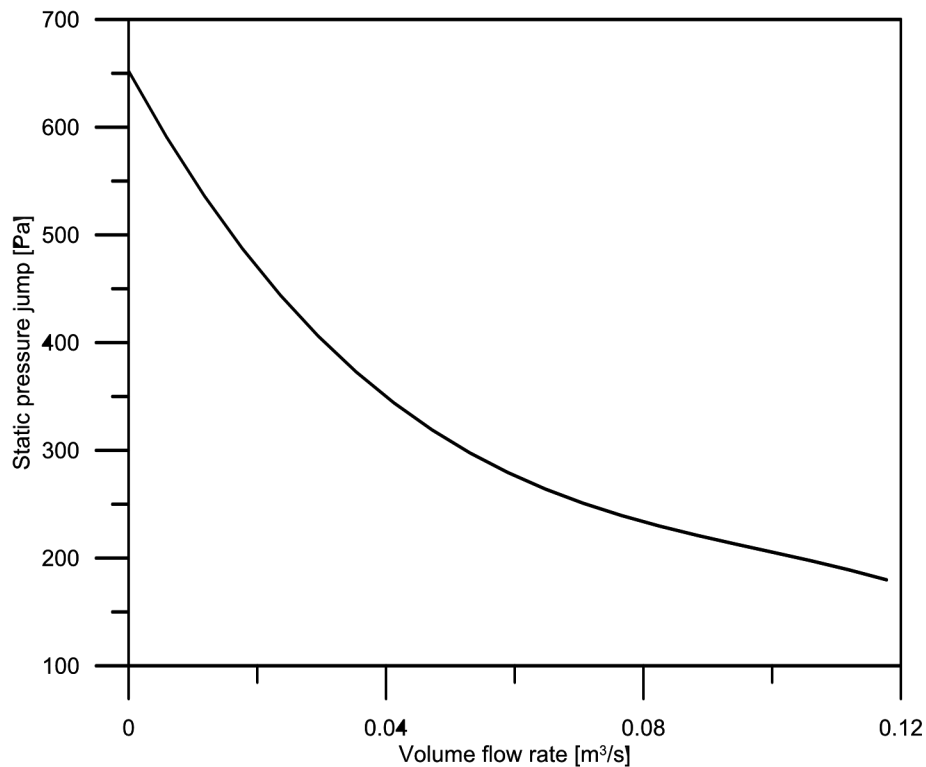


Figure (2): Static pressure jump for Sunon fan running at 10800 rpm and 1 atm ambient pressure

The considered dimensions of the motor finned casing are 70 mm in diameter and 120 mm in length [1]. The base thickness is assumed to be 1.5 mm. The fins attached to the casing is considered to be of 0.4 mm in thickness and 13.5 mm in height so the structure can be fitted in 100 mm tube. A total of 500 Watt is assumed to be generated inside the motor, which is assumed as a uniform heat flux at the bottom surface of the motor

housing. The performance of a finned structure of different configurations is studied. The considered configurations are shown in Figure (3) which include continuous straight fins, interrupted fins in staggered arrangement, and corrugated fins.

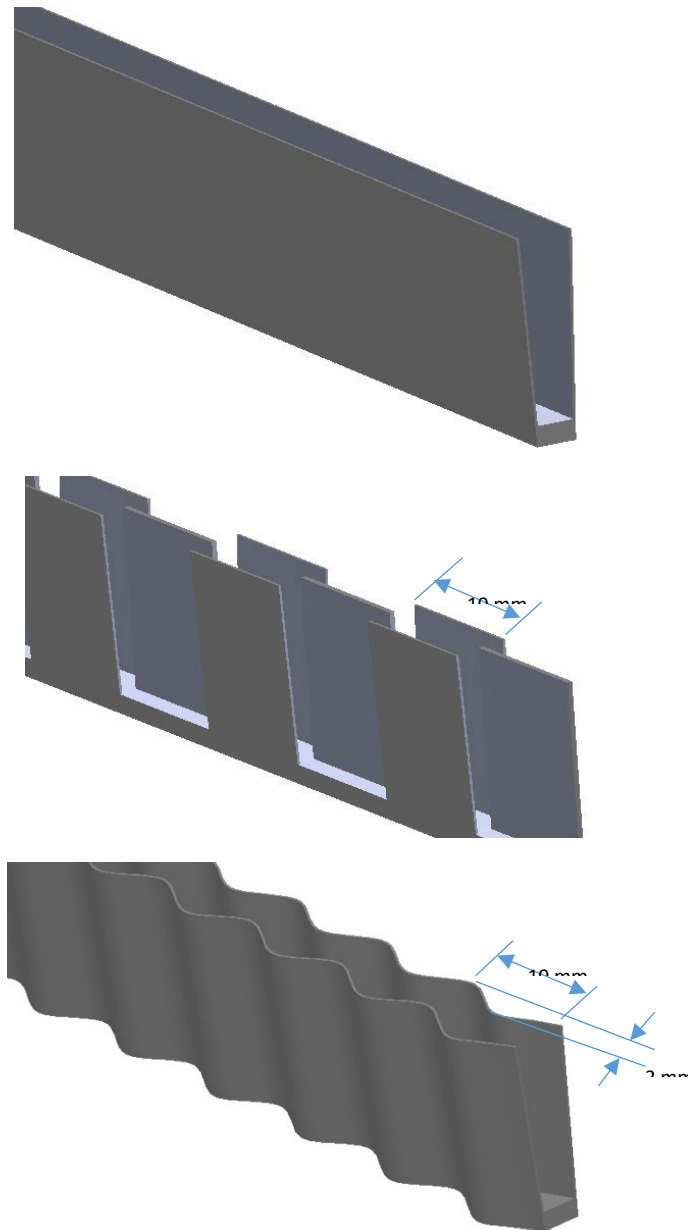


Figure (3) Fin configurations

2.1 Results for the different fin structures

Comparing the performance of the three fin configurations, it can be seen that the straight fins outperform both the interrupted and the corrugated fins. Straight fin configuration produces lower pressure drop and consequently allowing higher mass flow rate to flow through the fin structure. As shown in Table (1), straight fin is associated with the highest heat transfer coefficient and the lowest air

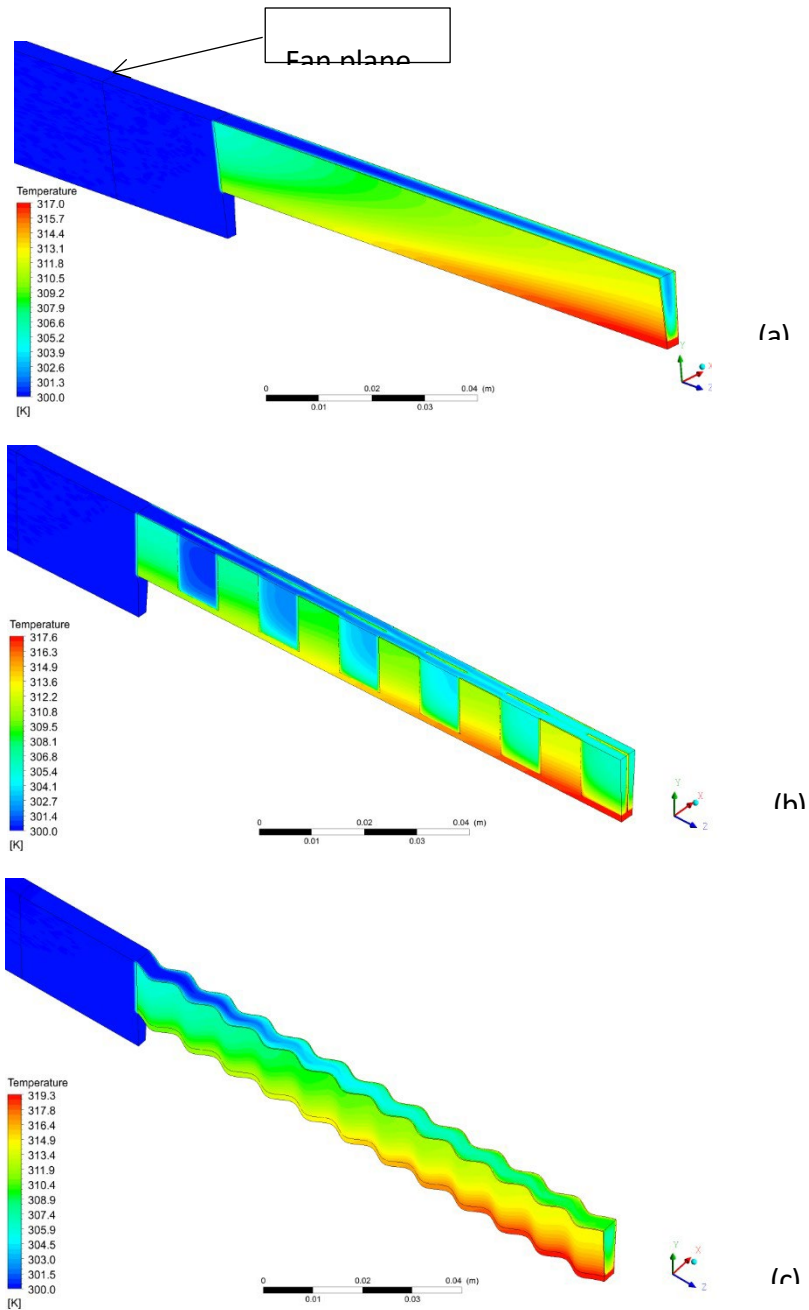


Fig. (4) Temperature contours (a) straight fins (b) interrupted fins (c) corrugated fins

exit temperature. Even with the higher surface area of the corrugated fin structure, its base temperature was considerably higher compared to the straight fin as shown in Figure 4. This is due to the higher pressure drop that is associated with the corrugated fin structure. Figure (5) shows the temperature at a line passing through the base of the motor housing

in the flow direction. It can be seen that the temperature along this line for interrupted and corrugated fins is distorted. This is due to the variation of the fin base location from this line for both interrupted and corrugated fins. Also, the figure shows that the base temperature at the flow exit is the maximum for the corrugated fin structure.

Table (1) Comparison between straight, interrupted, and corrugated fin structure of 72 fins

	Straight fins	interrupted	Corrugated
Air mass flow rate [kg/s]	0.10158	0.06826	0.05122
Average heat transfer coefficient [W/m ² K]	189.458	184.31	162.468
Maximum fin base temperature [K]	316.94	317.54	319.24
Mean air temperature at exit [K]	305.456	307.68	310.035

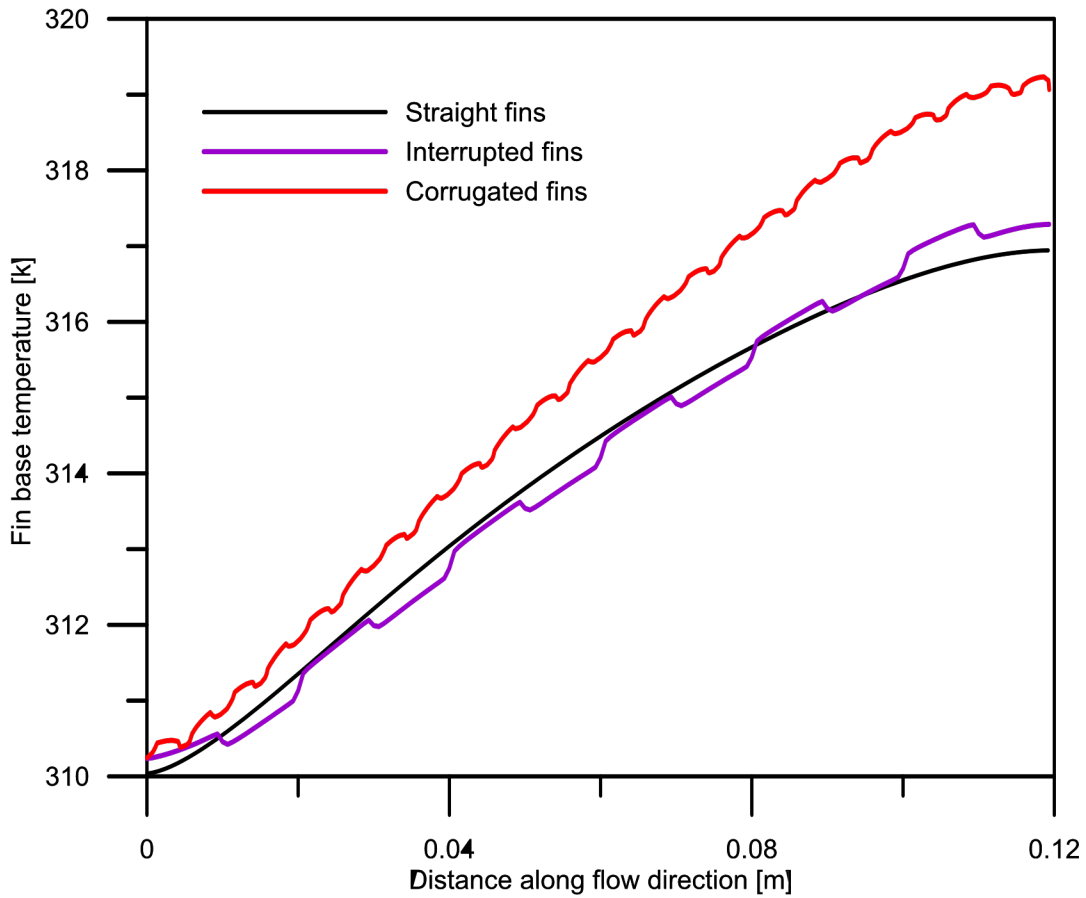


Figure (5) Fin base temperature along the flow direction

Table (2) Comparison between straight fin structures with different fin number

	Nf = 50	Nf =60	Nf =72	Nf =80	Nf=90	Nf=100
Air mass flow rate [kg/s]	0.112	0.106	0.101	0.09	0.086	0.08
Average heat transfer coefficient [W/m ² K]	201.1	195.3	189.4	178.6	173.28	167
Maximum fin base temperature [K]	321.5	319.1	317	316.4	315.6	314.9
Mean air temperature at exit [k]	305	305.25	305.4	306	306.3	306.6

2.2 Effect of fin number for straight fin structure

The simulation has been carried out for different fin number of straight fin structure to determine the optimum fin spacing. As shown in Table (2), it is found that the change in the maximum base temperature becomes less than 1oC as the fin number increases above 72. Increasing the fin number enhances heat transfer by adding more surface area but at the same time it adds more resistance to the fan air flow and more weight. As shown in Figure (6), the maximum base temperature reaches its minimum value at $N_f=150$. This means that without consideration of weight, the optimum fin spacing for this arrangement of straight fins with Sunon fan characteristics is 1.46 mm at the base and 2.09 mm at the tip.

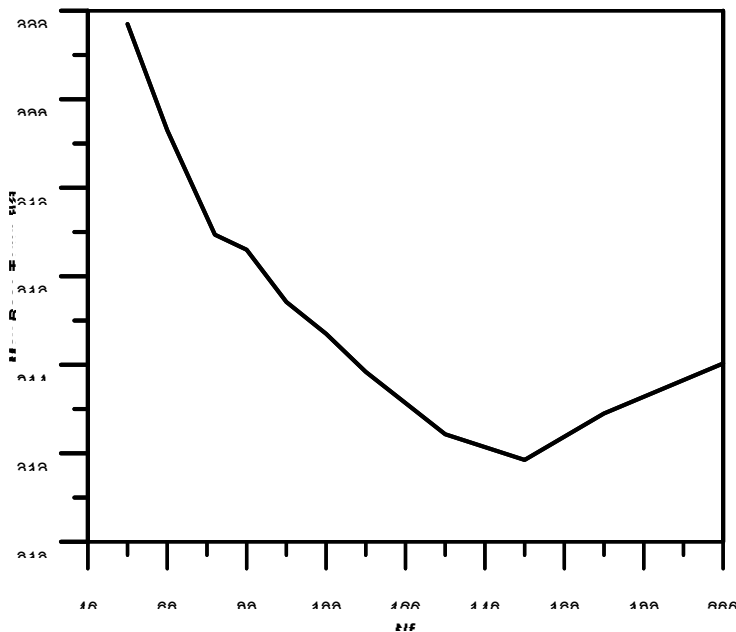


Figure (6) Variation maximum base temperature with fin number

3. Future work

Currently, we are working on designing and constructing a testing facility to measure the heat transfer characteristics of a finned structure cooled by a fan. These measurements will be used to

validate the numerical simulation to check the validity of the numerical model assumptions as well as the validity of the adopted turbulence model. In the meantime, more numerical simulations will be carried out to determine the optimum fin number for a Sunon fan when it runs at different rotating speeds and different ambient pressure.

Reference

- 1- K. McCarthy, A. Heltzel, E. Walters, J. Roach, S. Iden, and P. Lamm, " A Reduced-Order Enclosure Radiation Modeling Technique for Aircraft Actuators", SAE paper 10PSC-0093, 2010

APPENDIX J

UCF Project 1626-8282

Quarterly Report # 2
to
North Carolina A&T University

**Thermal Management of Electromechanical Machines for Aerospace
Systems**

University of Central Florida
Department of Mechanical and Aerospace
Engineering Orlando, FL 32816-2450

Louis Chow, PI
Yeong-Ren Lin
Osama Mesalhy

Period: From December 12, 2017, to March 11, 2018

Date of report: March 13, 2018

1. Introduction

Results of any proposed numerical model needs to be validated with experimental measurements for the purpose of checking the validity of the model assumptions. These assumptions include:

- Geometry simplification
- Position and type of the domain boundaries
- Adopted physical model especially the turbulence model in the case of modeling turbulent flow
- Grid size

In this reporting period, a test rig is established to measure the cooling performance of a fin structure brazed on an aluminum cylinder. The air flow is introduced using a Sunon fan of model PF92381BX-000U-S99 which is a DC brushless fan of dimensions 92X92X38 mm. The fan is attached to one end of the finned block as shown in Figure (1). The fan draws the air to flow through the fin structure. A DC power supply is used to introduce the DC power to the fan and Agilent Data Acquisition unit is used to read and record the output signal of the measured quantities.

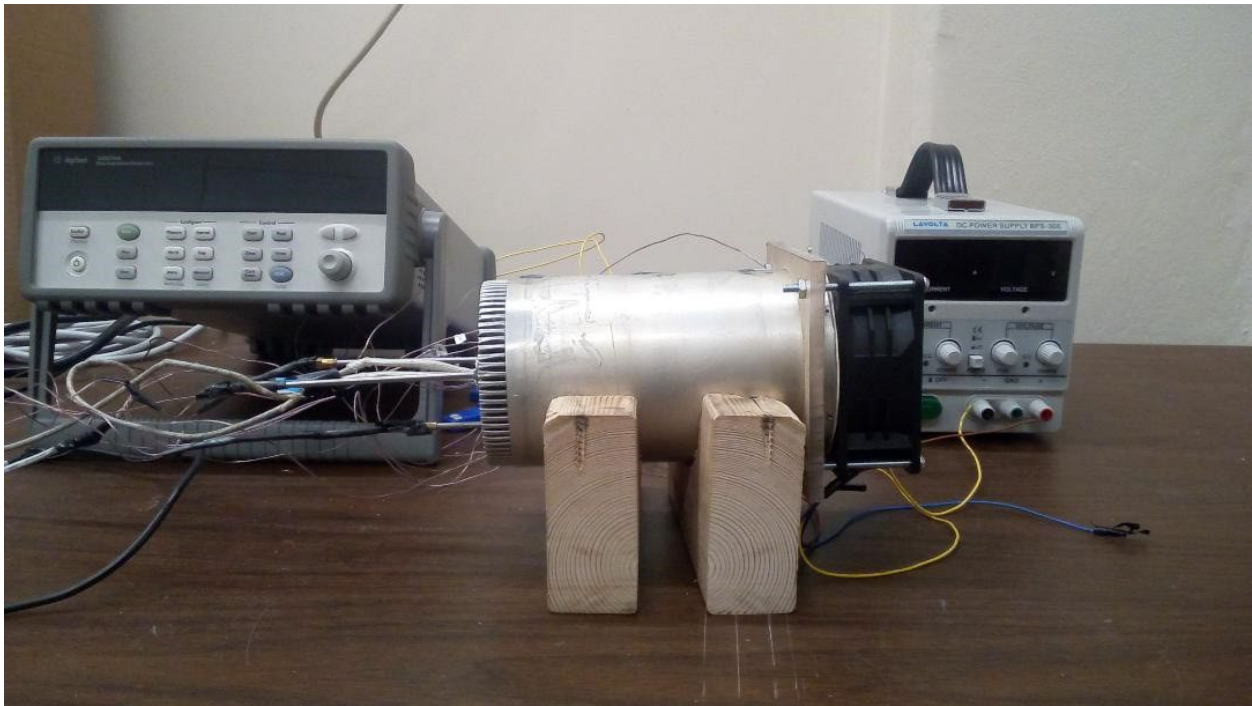


Figure (1) picture of the test-rig

2. Fin structure

The fin structure is made of a thin Aluminum sheet of thickness 0.2 mm, which is folded and brazed to a cylindrical block made of aluminum alloy 6061-T6. The dimensions of the Aluminum block is 66.5 mm in diameter and 152.4 mm in length. Then the whole structure is raped with an aluminum plate of thickness 1 mm as shown in Figure (2a). A cylindrical heater of rated power 300 W is fitted inside a drilled hole at the center of the aluminum block. Three holes are drilled in the block at different locations for the purpose of fixing the thermocouple wires for temperature measurements. The locations of the thermocouples are shown in Figure (2b).



(a)

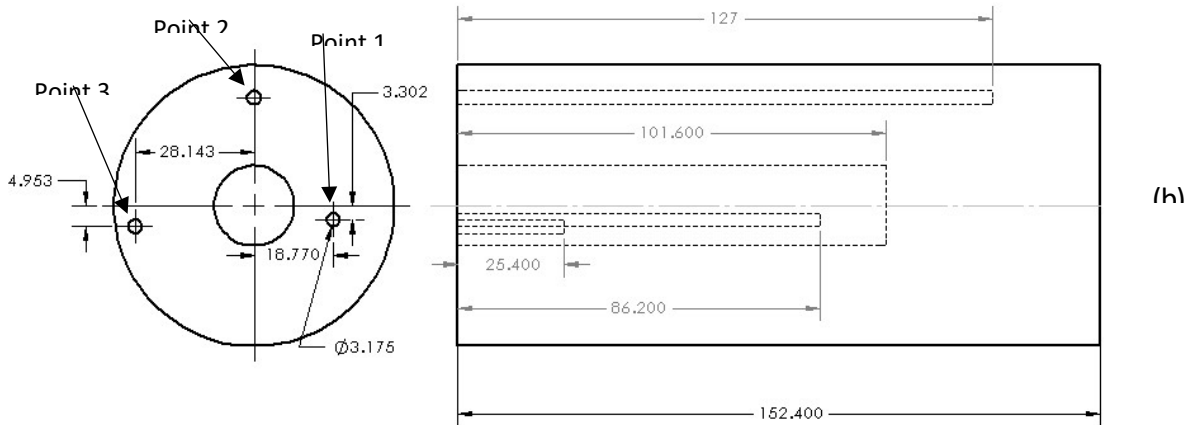


Figure (2) (a) Fin structure shape (b) locations of the thermocouples

3. Measured quantities

a) Fan static pressure head

The fan static pressure head is measured separately in a fan loop that is designed according to

ISO standards. The fan loop is equipped with pressure transducer and pitot tube to measure the fan static pressure jump and the velocity distribution at the loop cross-section, respectively. The velocity distribution is used to estimate the fan volume flow rate. Flow control valve is used to change the overall flow resistance inside the test loop

and hence change the fan volume flow rate. The pressure transducer output signal as well as the fan frequency generator signal are connected to data acquisition (DAQ) system in order to obtain and record the static pressure jump and the fan rotational speed. The rotational speed of the fan can be set to the desired value by the adjusting the delivered voltage and current from the power supply.

In this loop, the variation of the fan static pressure jump is measured versus the volume flow rate at different fan rotational speeds. The measured fan pressure jump is specified as a function of the fan volume flow rate. This function is set as a polynomial of the third order.

$$\Delta p = f_0 + f_1 Q + f_2 Q^2 + f_3 Q^3$$

where, Q is the volume flow rate across the fan plane.

b) Temperature measurements

Three T-type thermocouples are inserted at three locations inside the cylindrical block. In addition, two thermocouples are used to measure the air inlet and outlet temperature. The test is started by running the fan and adjusting its rotational speed. Then, at the same moment of supplying the power to the heater, the thermocouple signals are recorded with time. The test lasts until steady state condition is reached. The test is conducted for different fan speeds, 6000, 9000, and 11200 rpm.

4. Numerical model

To reduce the computational time, only one repeated sector is considered in the numerical solution as shown in Figure (3a). The grid is refined besides the walls that are in contact with the cooling air. To ensure grid independent solution, a grid of size 831,000 cell is adopted in this simulation. Figure (3b) shows the grid in x-y plane at flow entrance. The relation between static pressure jump and the volume flow rate, which is measured in the fan loop is applied at the fan plane. The heater power is assumed as a uniform heat generation in the heater material.

The numerical simulation assumes

- The thermo-physical properties of the solid material and the cooling air remain constant.
- The simulation is transient and the flow is incompressible and turbulent. - No slip condition is assumed at the solid-fluid interface.

Since the flow in the fin channel may make transition from laminar to turbulent, both low and high Reynolds number turbulence models have been tried. K-ε Realizable turbulence model is considered as a high Reynolds number model while Transition k-kl-ω and k-ω SST models are considered as low Reynolds number models. The results of each of the aforementioned models are compared with the experimental measurements to determine which model is more suitable.

ANSYS FLUENT is used to numerically solve the governing equations of the model. A second order upwind scheme is used to discretize momentum, energy, and turbulence equations. The transient terms in the equations are discretized using first order implicit technique. The coupling between continuity and momentum equations is treated with SIMPLE algorithm. In each time step, the solution is deemed to converge when the residuals in the flow equations reduce under 10^{-4} and the residuals in the energy equations reduces under 10^{-10} .

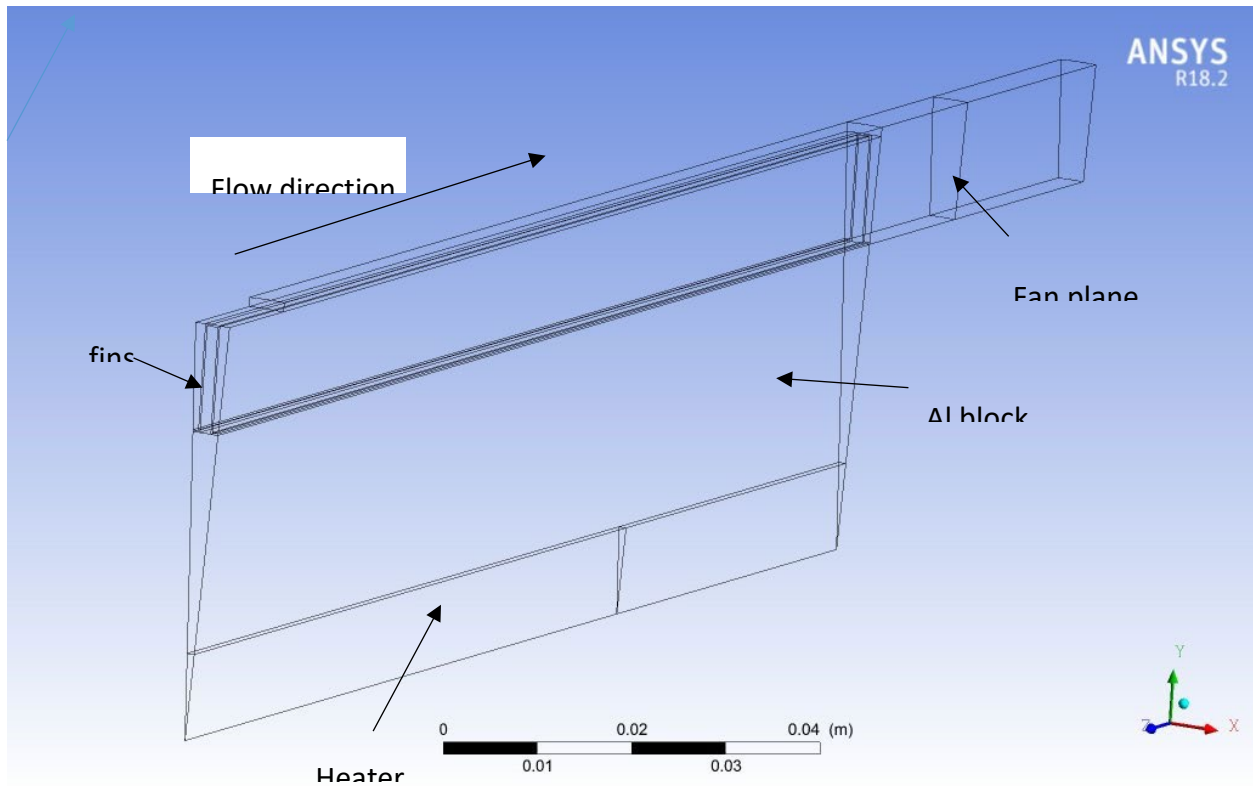


Figure (3a) Computational domain

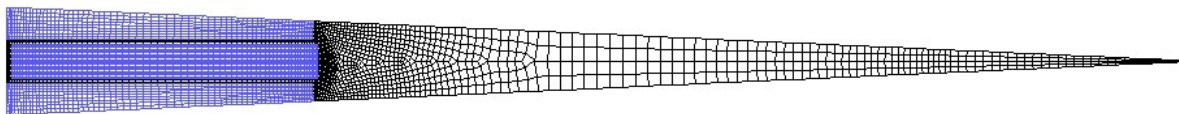


Figure (3b) Mesh in x-y plane

5. Results

During the numerical simulation of the repeated sector, the temperature is monitored at the radial and axial locations of the three thermocouples attached to the Aluminum block. The experimental temperature difference ($T-T_\infty$) is compared with the numerical values for three turbulence models: $k-\epsilon$ Realizable, Transition $k-k_l-\omega$, and $k-\omega$ SST (shear stress transport). The comparison is shown for fan speeds 6000, 9000, and 11200 rpm in Figures (4-6).

It can be seen that the results of the model $k-\omega$ SST matches better with the experimental results especially at higher fan speed.

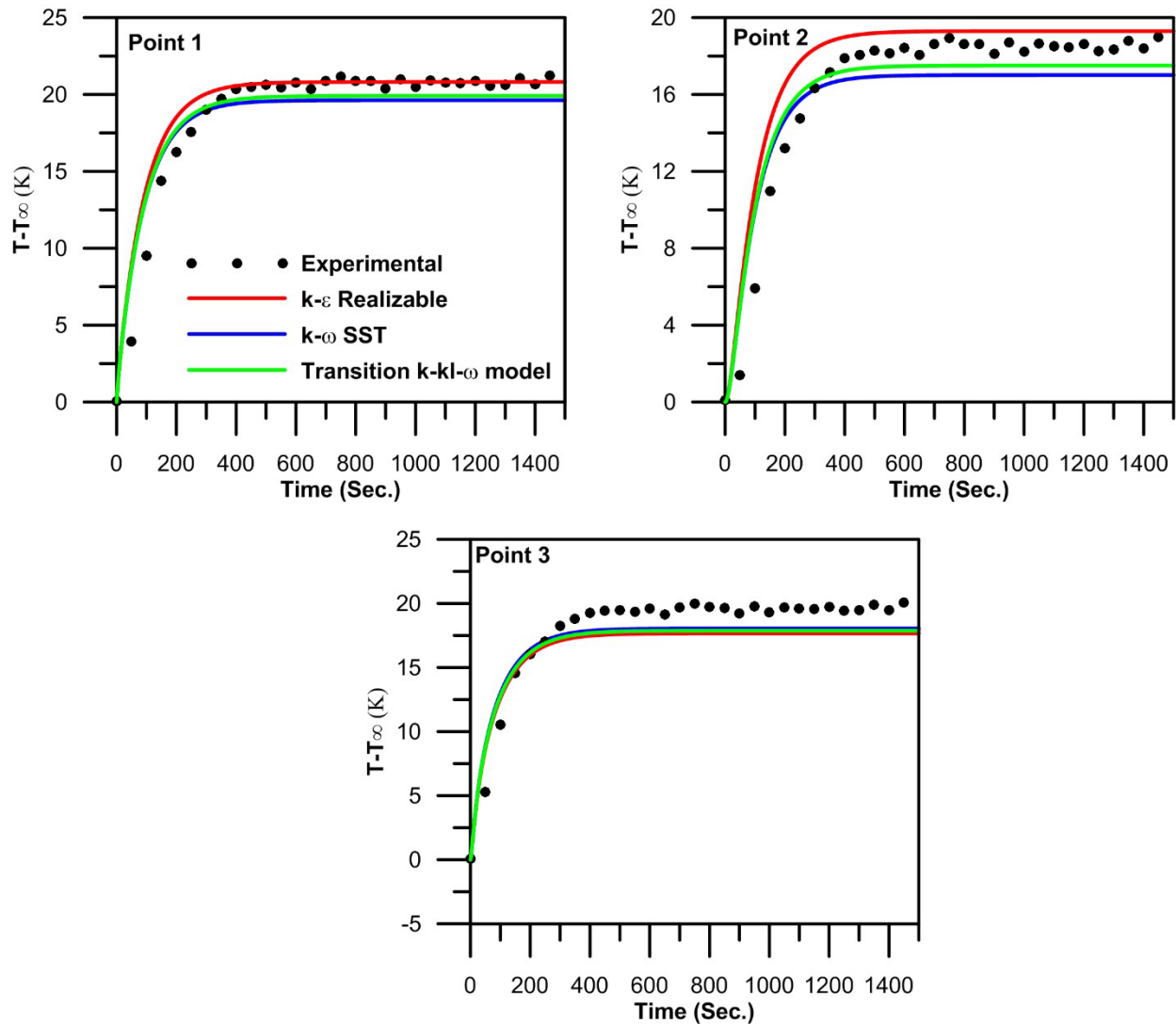


Figure (4) Monitored temperature difference ($T-T_\infty$) with time at three points in the Aluminum block for fan speed = 6000 rpm

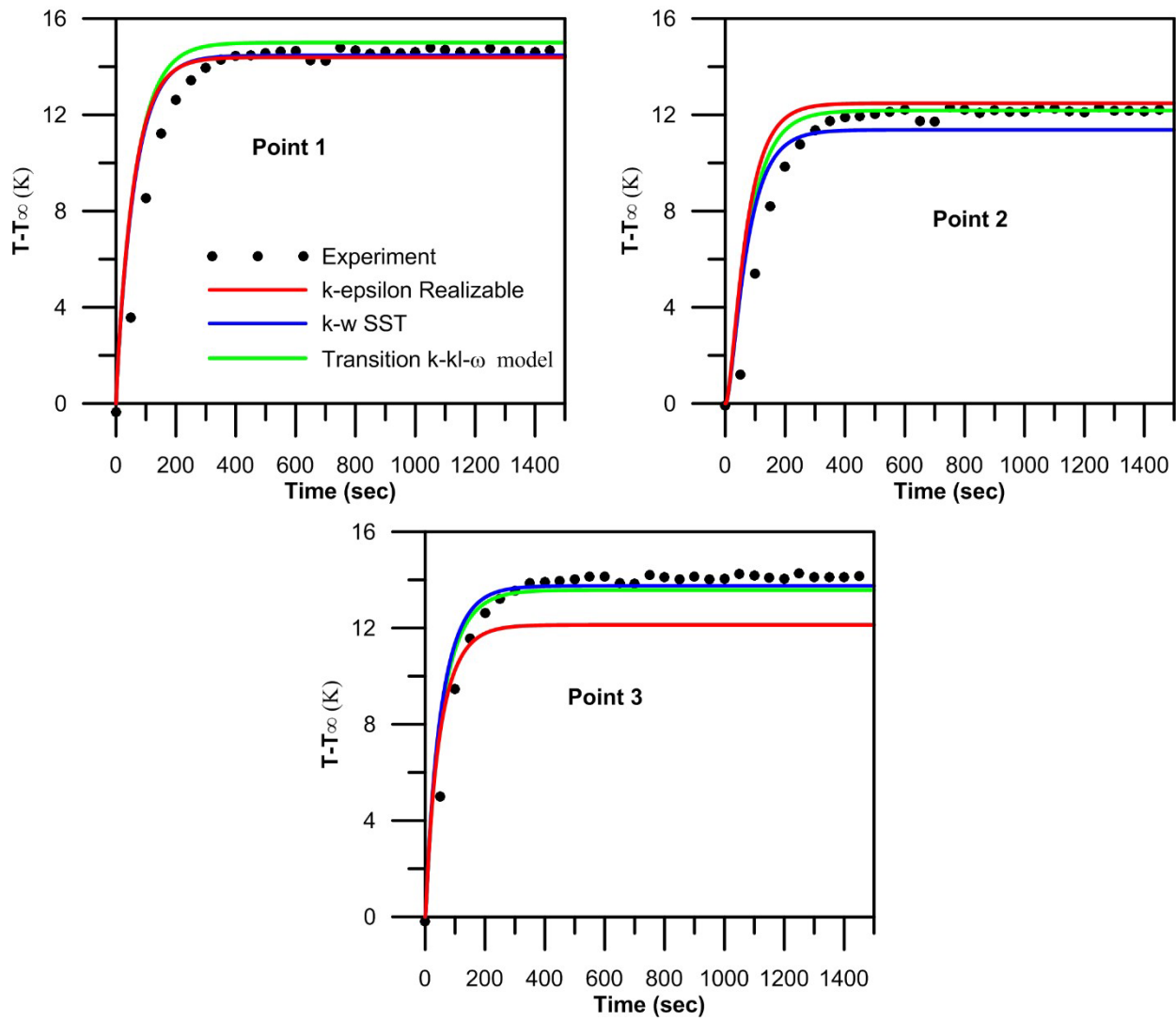


Figure (5) Monitored temperature difference ($T - T_{\infty}$) with time at three points in the Aluminum block for fan speed = 9000 rpm

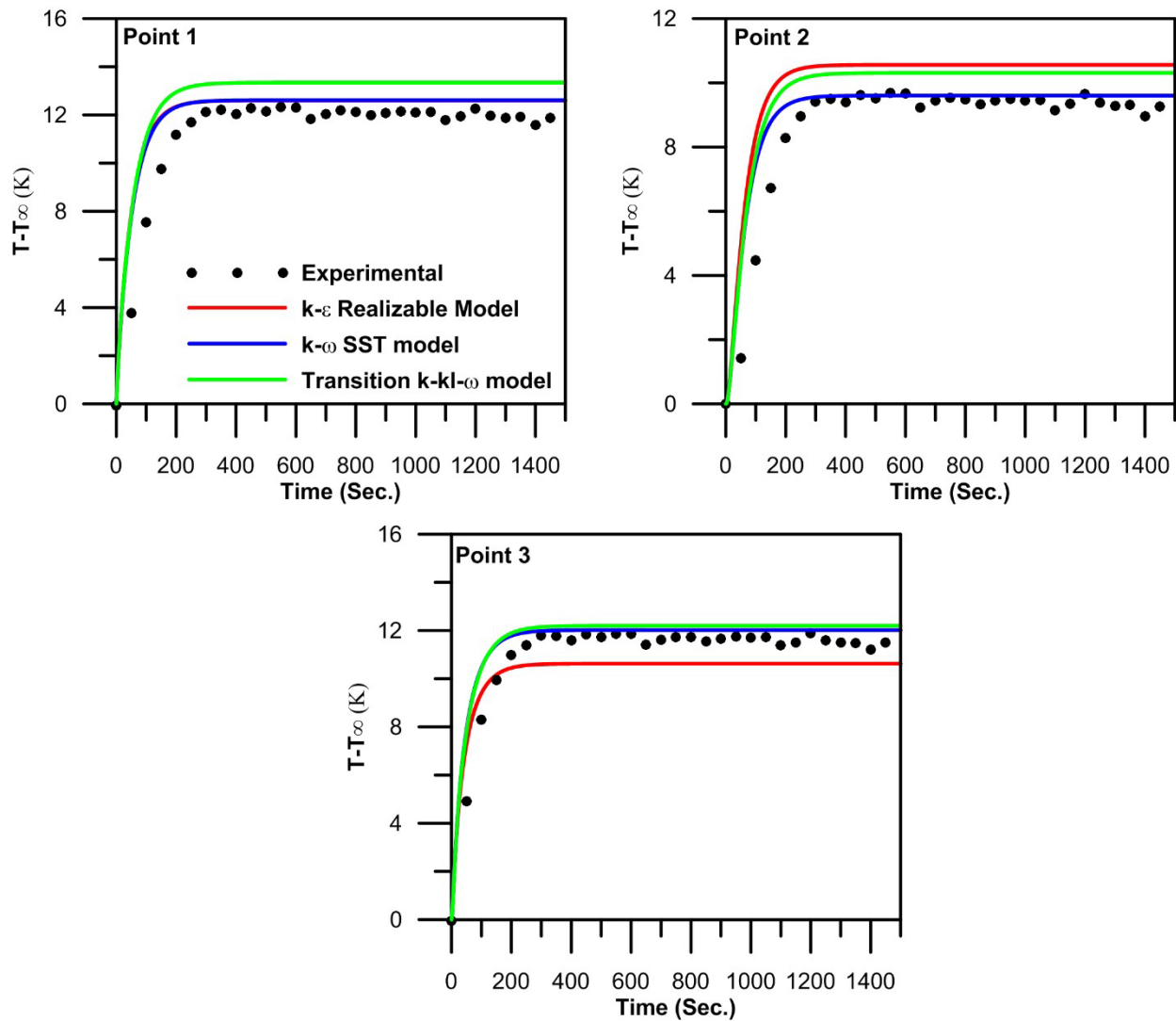


Figure (6) Monitored temperature difference ($T-T_{\infty}$) with time at three points in the Aluminum block for fan speed = 11200 rpm

Figure (7) shows the temperature contours at steady state condition for fan speed 9000 rpm for the three turbulence models. As shown from the figure, the $k-\epsilon$ realizable model overestimates the temperature in the Aluminum block. This can be explained due to the fact that the $k-\epsilon$ model is a high Reynolds number model which assumes that the inlet flow is fully turbulent. This leads to faster thermal boundary layer development which reduces the heat transfer coefficient due to the higher thermal boundary layer thickness. For $k-\omega$ SST and Transition $k-k1-\omega$ models, the thermal boundary layer as shown in the figure is thinner and the flow continues to thermally develop through an axial distance greater the heater length. This of course increases the heat transfer coefficient and reduces the temperature in the Aluminum block.

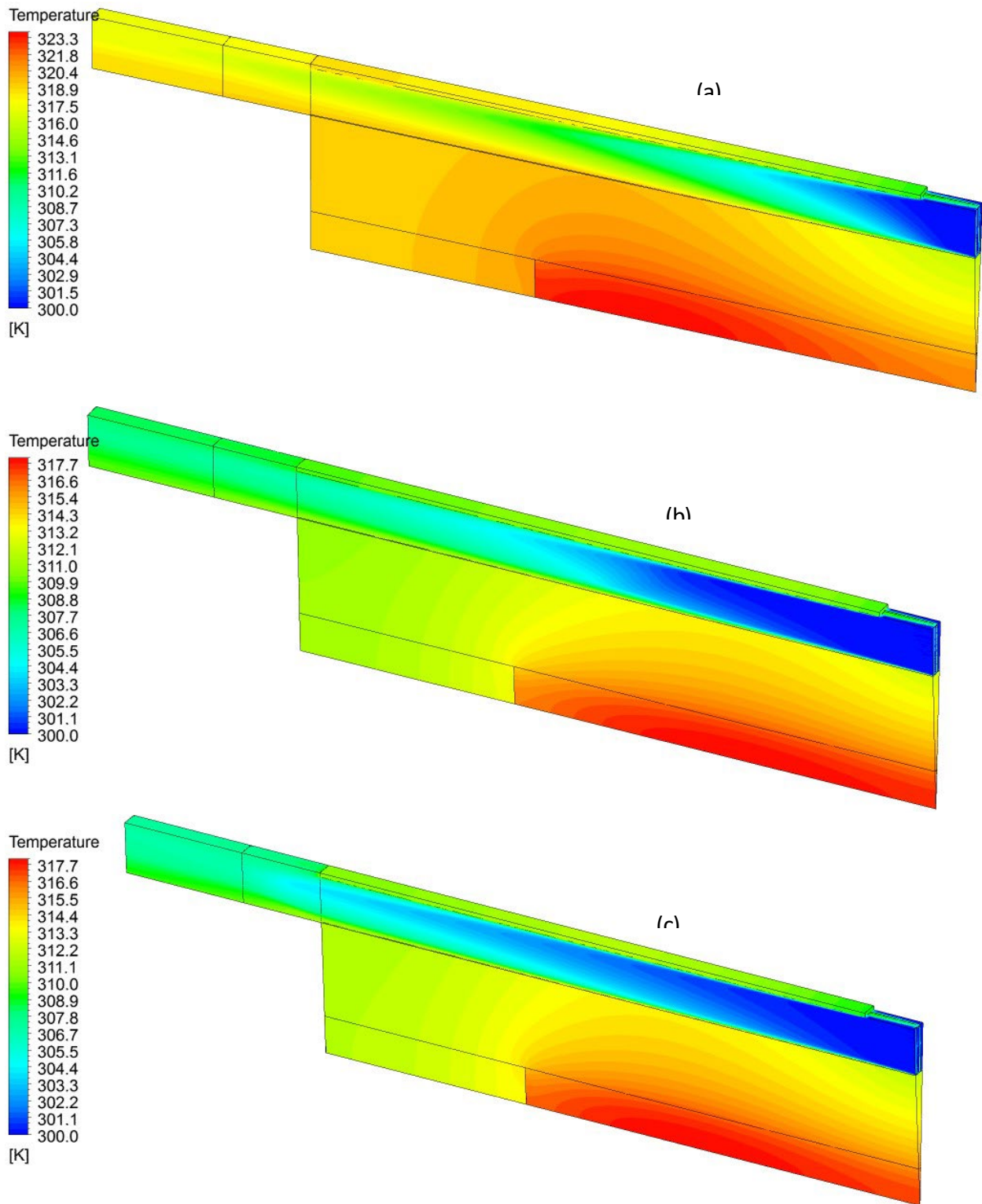


Figure (7) Temperature contours at steady state condition for (a) K-ε Realizable turbulence model (b) k-ω SST turbulence model and (c) Transition k-k1-ω turbulence model at Fan speed 9000 rpm

6. Future work

Currently, we are working on optimizing the fin structure. Different parameters of the fin structure will be studied such as the fin thickness, fin height, and fin spacing. Also interrupted fin structure and curved fins will be studied.

APPENDIX K

UCF Project 1626-8282

Quarterly Report # 3
to
North Carolina A&T University

**Thermal Management of Electromechanical Machines for Aerospace
Systems**

University of Central Florida
Department of Mechanical and Aerospace
Engineering Orlando, FL 32816-2450

Louis Chow, PI
Yeong-Ren Lin
Osama Mesalhy

Period: From March 12, 2018 to June 11, 2018

Date of report: June 18, 2018

Effect of ambient pressure and fan rotational speed on motor cooling performance

1. Introduction

In the last two reports, we have studied numerically the performance of a Sunon fan in cooling different fin structures situated on the motor surface of an electromechanical actuator. The studied fin structures include straight interrupted, and corrugated fin structures. The numerical results show that the straight fin structure outperforms the interrupted and the corrugated fins. This is attributed to the fact that straight fin configuration produces lower pressure drop and consequently allowing higher mass flow rate to flow through the fin structure. For straight fins, we have found that the most important parameter that affect the fin performance is the fin number. The fin number should be selected to enhance the surface area but without blocking the passage of the air from the fan. It is found that there is an optimum number of fins which can produce the minimum temperature rise (minimum thermal resistance). However, this analysis was restricted to the fan performance at only one rotational speed and at atmospheric ambient pressure. In real applications, the fan may work at different ambient pressures ranging from 0.2 up to 1 atm and at different rotational speeds.

In this report we studied the performance of the Sunon fan in cooling a straight fin structure when the fan is operating at a rotational speed ranging from 6000 to 12000 rpm and under an ambient pressure ranging from 0.2 to 1.0 atm.

2. Fan performance

The fan static pressure head is measured in a fan loop that is designed according to ISO standards. In this loop, the variation of the fan static pressure jump is measured versus the volume flow rate at different fan rotational speeds and different ambient pressures as shown in Figure (1). The measured fan pressure jump is specified as a function of the fan volume flow rate.

$$\Delta p = f_0 + f_1 Q + f_2 Q^2 + f_3 Q^3$$

where, Q is the volume flow rate.

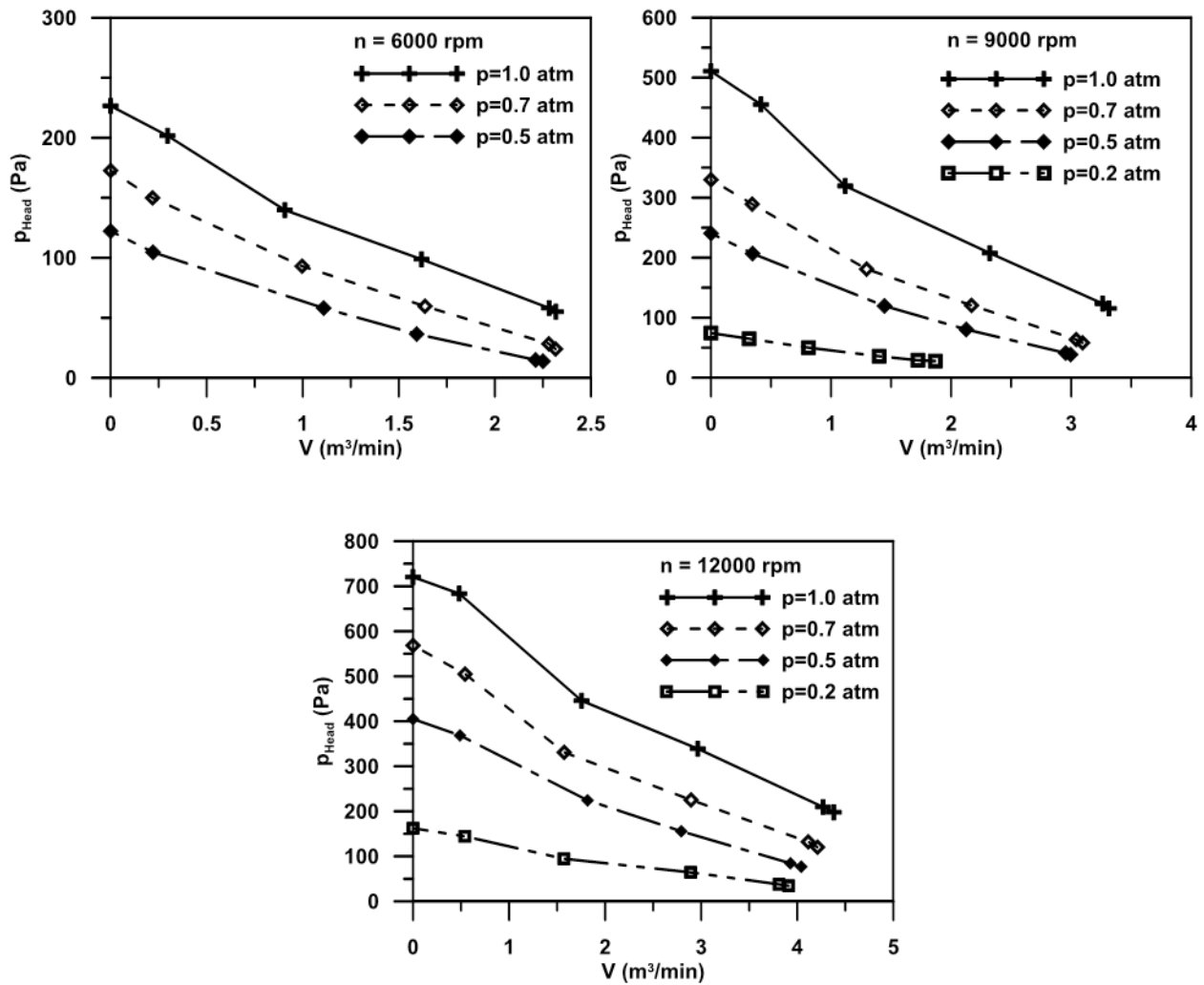


Figure (1) Sunon fan performance at different rotational speed and different ambient pressure

3. Selected fin structure

The fin structure is composed of radial straight fins attached to a cylindrical base of thickness 1.5 mm and inner diameter 70 mm, as shown in Figure (2) so a motor of diameter 70 mm can be fitted in this structure. The tips of the fins are attached to a cylindrical cover of thickness 1 mm and an outer diameter of 100 mm. The number of fins has been changed but with fixing the total mass of the fin structure since the weight represents an important issue in aerospace applications. The fin thickness is considered to be,

$$t_f = \frac{50}{N_f} \text{ mm}$$

where, N_f is the number of fins which is varied from 50 up to 210 and, consequently, the fin thickness has been changed from 1 mm to 0.238 mm.

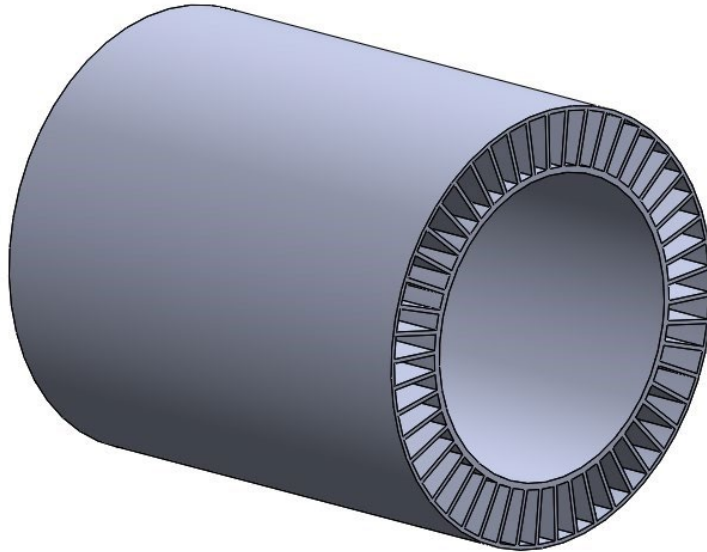


Figure (2) Radial straight fin structure

4. Numerical model

To reduce the computational time, only one repeated sector is considered in the numerical solution as shown in Figure (3). The relation between static pressure jump and the volume flow rate, which is measured in the fan loop is applied at the fan plane. The dissipated heat from the electric motor is assumed as a uniform heat flux at the inner surface of the fin structure base.

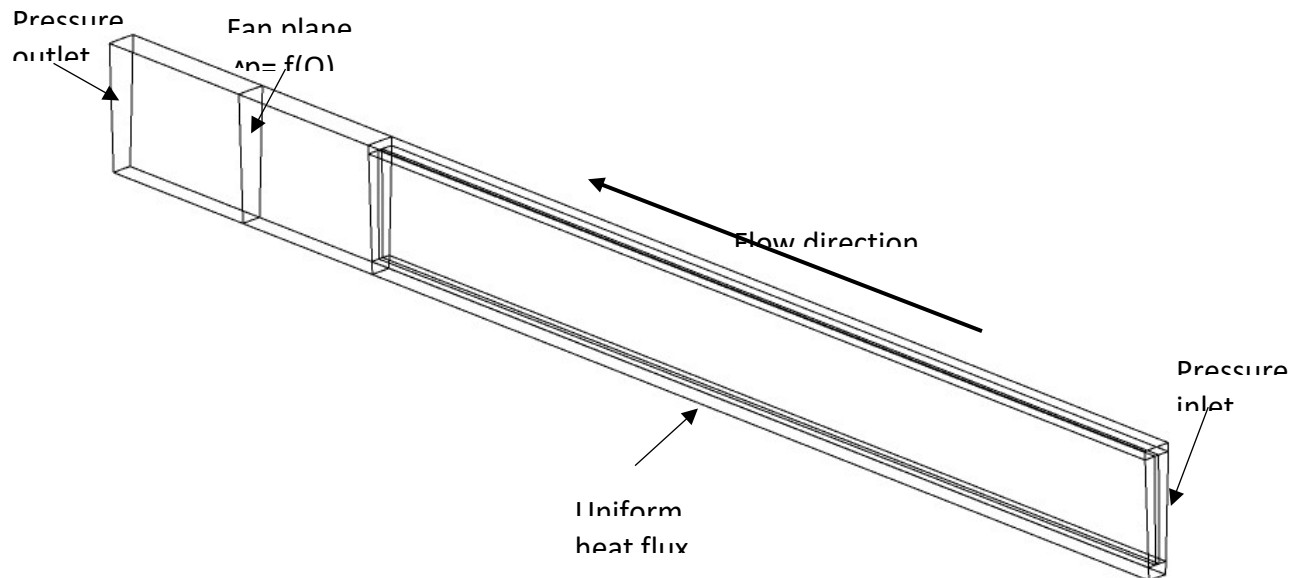


Figure (3) Computational domain

The numerical simulation assumes

- The thermo-physical properties of the solid material and the cooling air remain constant.
- The flow is three dimensional, steady, incompressible, and turbulent.
- Shear stress Transport SST $k-\omega$ model is used to simulate the turbulent flow

ANSYS FLUENT is used to numerically solve the governing equations of the model. A second order upwind scheme is used to discretize momentum, energy, and turbulence equations. The coupling between continuity and momentum equations is treated with SIMPLE algorithm. The solution is deemed to converge when the residuals in the flow equations reduce under 10^{-4} and the residuals in the energy equations reduces under 10^{-10} .

5. Results

The mass flow rate of the cooling air changes with fan ambient pressure, fan rotational speed, and number of fins of the fin structure. Figure (4) shows the volume flow rate variation with fin number at different ambient pressure and different rotational speeds. Increasing the fin number reduces the size of the flow

passage and results in higher pressure drop and consequently reduces the fan volume flow rate. However, increasing the number of fins adds higher heat transfer area which enhances the cooling process.

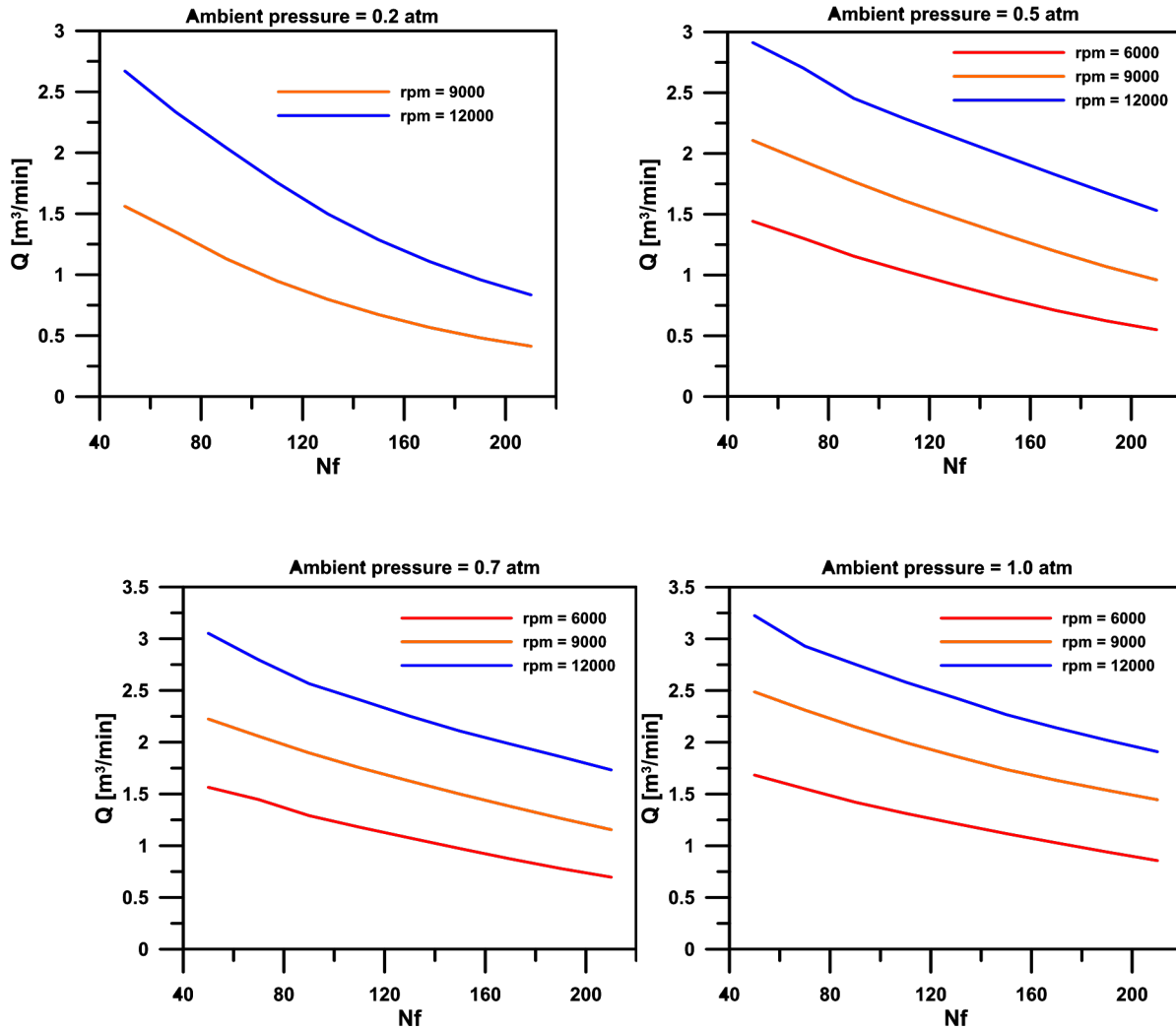


Figure (4) variation of fan volume flow rate with fin number

As shown from Figure (4), the reduction rate of the volume flow rate with fin number is higher at the lowest ambient pressure (0.2 atm). This means that when the fan operates at low ambient pressure its volume flow rate will be more sensitive to the changes in friction losses.

Thermal resistance is used as an indicator for thermal performance. The thermal resistance of the fin structure is defined as,

$$R = \frac{T_{base,max} - T_{\infty}}{Q}$$

The maximum base temperature is used in calculating the thermal resistance because this is more suitable for motor cooling application. Overheating the base at any spot may lead to motor failure.

Figure (5) shows the change of thermal resistance with fin number. It is clear from the figure that there is an optimum value of the fin number that can produce minimum thermal resistance. The value of the optimum fin number changes with the fan speed and the ambient pressure. For most cases, the optimum number of fins lies between 100-150. At lower ambient pressure, the optimum fin number shifts to the left due to the rapid decrease in the air cooling capacity as the number of fin increases. Also, the optimum number of fins increases with the fan rotational speed.

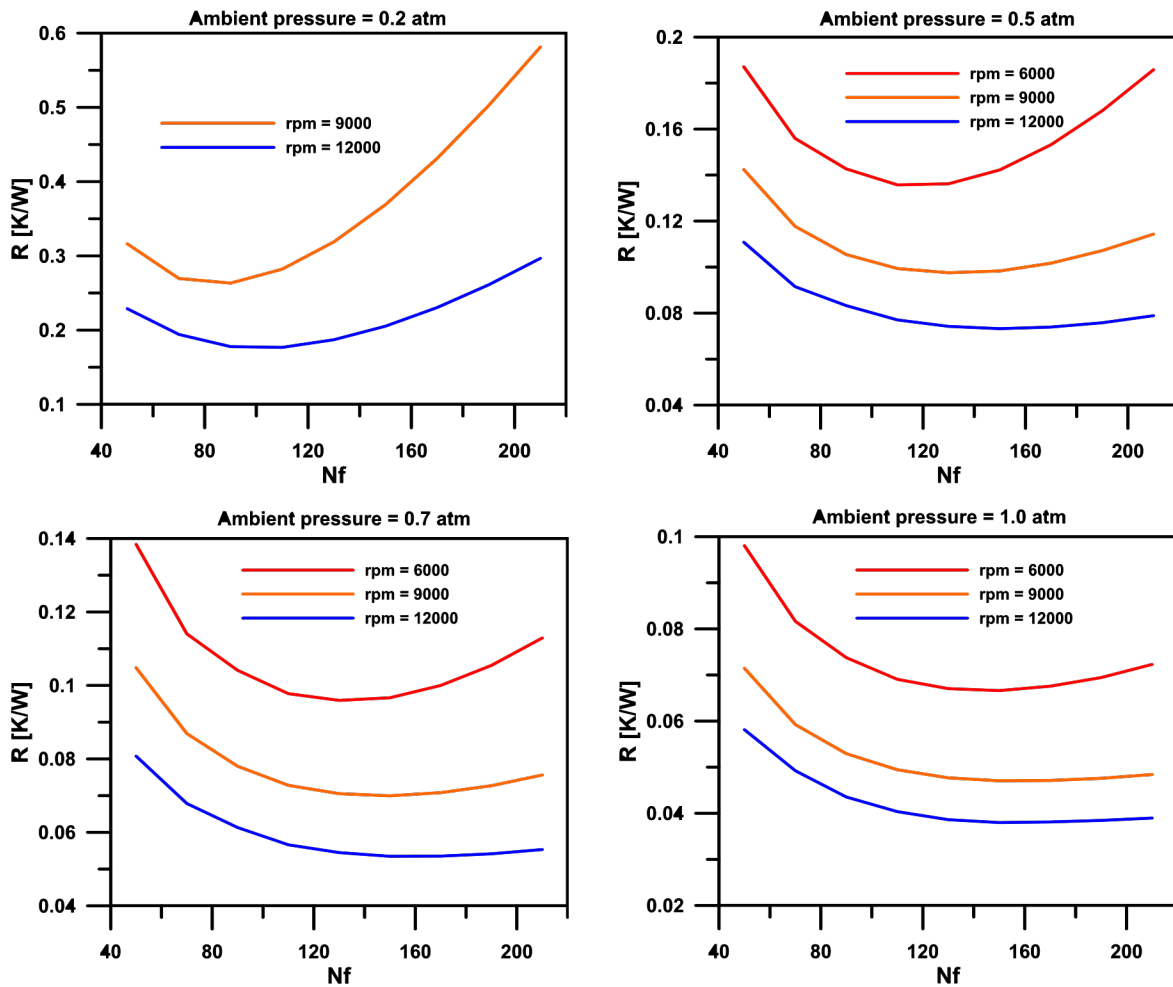


Figure (5) Variation of thermal resistance of the fin structures with number of fins

6. Future work

In the next period we'll try to study the effect of using fin structure of variable density in the flow direction. This configuration is expected to allow more mass flow rate and to concentrate the heat transfer surface area at the location of high temperature.

Flow direction



UCF Project 1626-8282

APPENDIX L

Quarterly Report # 4 to
North Carolina A&T University

Thermal Management of Electromechanical Machines for Aerospace Systems

University of Central Florida
Department of Mechanical and Aerospace
Engineering Orlando, FL 32816-2450

Louis Chow, PI
Yeong-Ren Lin
Osama Mesalhy

Period: From June 12, 2018, to September 11, 2018

Date of report: September 15, 2018

During the report period, the following manuscript was prepared. This completes Task 1.

- 1- To determine the optimum fin structure/fan combinations that maximize the heat transfer from fins on the casing of electric motors.

Optimum fin structure design for cooling aerospace Electro-Mechanical Actuators with high-speed axial fans

Osama Mesalhy^{ab*}, Cody Rath^c, Daniel Rini^c, John Kizito^d, Quinn Leland^e, Louis Chow^a

^aDepartment of Mechanical and Aerospace Engineering, University of Central Florida,
Orlando, FL
32816, USA

^bDepartment of Mechanical Power Engineering, Zagazig University, Zagazig
44519, Egypt ^cRINI Technologies, Inc., 582 S. Econ Circle, Oviedo, FL 32765,
USA

^dDepartment of Mechanical Engineering, North Carolina Agricultural and Technological State
University,
Greensboro, NC 27411, USA

^ePower and Control Division, Aerospace Systems Directorate, Air Force Research
Laboratory, Wright Patterson Air Force Base, OH 45433, USA

Abstract

Despite their advantages compared to hydraulic actuators, electric actuators are prone to overheating due to their high heat dissipation. So, developing reliable cooling systems for electric actuators is a crucial task especially for aerospace applications which require the fulfillment of high safety requirements. In this paper, an air-cooling system utilizing wing bay air is investigated. An axial fan sucks air to flow through a shrouded-fin surface attached to the motor housing. A CFD model is developed to study the heat transfer and air flow processes over the finned surface. The relation between the fan pressure jump with the volumetric flow rate of a high speed SUNON fan at different rotational speeds

and different ambient pressures is measured in a fan loop and incorporated in the model. To validate the CFD results, a test rig consisting of a finned surface brazed on a heated aluminum cylindrical block and attached to a fan is built. The predicted and measured temperatures at different locations in the aluminum block show good agreement when the numerical simulation is performed using the kw-SST turbulence model. Numerical simulation is performed to predict the effect of fin shape, fin number and fin thickness on the cooling performance of the fin structure. The results show that the straight plate fin configuration outperforms the offset-strip and corrugated fin. Also, it is found that there is an optimum value for the fin number, and this optimum fin number changes with the fan rotational speed and ambient pressure. Reducing the solidity of the fin structure by reducing its fin thickness results in improving the thermal performance when the fan operates at a low ambient pressure (0.2 atm).

1. Introduction

Hydraulic actuator systems have been used in the aerospace and defense industry because of their low cost and high-power density. But in recent years, attention has been focused on the limitations of hydraulic actuators including their weight, performance, and high maintenance requirements. One method of reducing weight is by changing from hydraulic to electro-mechanical actuators (EMA). This eliminates the weight of the components that perform the second conversion, including the hydraulic power unit, connections, and fluid. Boeing has performed analyses that show that electrically powered technology can provide a considerable weight and cost savings [1]. Despite their advantages compared to hydraulic and pneumatic actuators, electric actuators are prone to overheating due to their high dissipated heat. So, developing reliable cooling systems for electric actuators is a crucial task especially for aerospace applications, which require to fulfill stringent safety regulations.

In general, many cooling techniques have been used to manage the temperature of the electric motors. For low power density motors, just free convection is sufficient. For most power dense machines, liquid cooling [2] and spray cooling [3] are utilized. In the case of dual rotor motors, liquid cooling is used to cool the inner rotor [4] or the motor shaft in the case of interior permanent magnet motor (IPM) [5]. The selection of the cooling technique depends on the application in which the motor is used. For aerospace applications, liquid cooling is not preferred since it adds complication to the system and the cooling liquid may undergo phase change in the working environment. Wing-bay air represents an affordable and economic mean in cooling aerospace EMAs.

In air cooling, the flow of the cooling air in the motor differs according to the construction type of the motor: Open Drip Proof (ODP) type or Totally Enclosed Fan Cooled (TEFC) type. In ODP type, air is allowed to flow over the motor windings. But in TEFC, the windings are totally sealed with enclosure that does not permit air to flow through and a fan is used to force the air over the motor frame fins for cooling. TEFC type is preferred because this construction offers increased protection against weather, dirt, and moisture. In general, the

motor components which are most likely to fail as a result of thermal overload are the stator windings which must remain within its designated insulation class limits. So, the thermal management of a motor is important because the thermal characteristics of a motor are strongly related to its lifespan and efficiency [6,7]. K. Farsane et.al. [8] studied experimentally the cooling of an electric motor of closed type. Three non-intrusive investigation methods have been used, namely infrared thermography, laser tomography and laser Doppler anemometry. The results showed the correlation between the thermal and aerodynamic behaviors of an electric motor. A considerable reduction in the average temperature of the motor casing is achieved by enhancing the heat transfer surface and by better air distribution around the casing.

The heat generated inside an electric actuator faces two main thermal resistances: internal and external. The internal resistances are represented by contact resistances between the motor elements, material conduction resistance, and the convection resistance between the internal surfaces and the enclosed air. The external one is the thermal resistance between the motor frame and the outside cooling air [9]. The value of the external heat resistance depends on the heat sink adopted with electric motor. So, the design parameters of the heat sink have an important effect on motor thermal management. These design parameters include fin number, fin shape, and fin thickness. Different fin shapes have been used in designing heat sinks and heat exchangers such as flat plate fin, corrugated fins, and offset-strip fins. Ahmed et.al [10] presented an extensive review for the different approaches of optimizing the performance of parallel plate fin heat sinks.

Bejan [11] developed a correlation for the optimal spacing of parallel plates/fin number for the maximum cooling in forced convection using the method of intersecting the asymptotes. DongKwon Kim et.al [12] conducted thermal optimization of a plate-fin heat sink with the fin thickness varying in the direction normal to the fluid flow. It was shown that the thermal resistance of the plate-fin heat sink can be reduced by 15% by increasing the fin thickness in the direction normal to the fluid flow. A new design of the plate fin, namely, corrugated/vortex-generator plate-fin (CVGPF), is proposed and studied [13]. It is designed based on the corrugated plate-fin (CPF) and the vortex-generator plate-fin (VGPF) configurations. Xiangyang Zheng and Zhaogang [14] presented a review on the state-of-the-art of experimental and numerical research of offset strip fins and its applications.

Air cooling using axial flow fans is the most suitable and viable way in cooling aircraft (EMAs) where the wing bay air can be used. The main objective of the cooling fan is to deliver high static pressure head and high volumetric flow rate. W. Wu et.al [15] designed a cooling fan for (EMAs) in aerospace applications over all operating ambient conditions (ambient pressure =0.2-1.0 atm). The volume flow rate and the static pressure head are measured at different ambient pressures and different fan rotating speeds for the designed fan and the up to date Sunon fan in a fan loop. This loop is designed according to ASME standards [16].

When the flow is introduced to the fin structure via a fan, the flow rate adapts in an inverse relationship with the pressure loss along the fin structure [17]. As the pressure drop across the system increases due to changing the fin structure design (fin number or the fin thickness) the fan cooling air changes accordingly. Moreover, in aerospace

applications, the fan used to cool the EMA is working under different ambient pressures when the aircraft flies at different altitudes.

This of course affects the pressure head developed by the cooling fan. This paper focuses on studying the cooling performance of the up to date Sunon fan in cooling EMA when it is working under different ambient pressures. The attached fin structure to the fan will be optimized by studying the effect of changing fin shape, fin number, and fin thickness.

2. Test rig

A test rig is established to measure the cooling performance of a fin structure brazed on an aluminum cylinder block. The air flow is introduced using a Sunon fan of model PF92381BX000U-S99 which is a DC brushless fan of dimensions 92X92X38 mm. The fan is attached to one end of the finned block as shown in Figure (1). The fan draws the air to flow through the fin structure. A DC power supply is used to introduce the DC power to the fan. The fin structure is made of a thin Aluminum sheet of thickness 0.2 mm, which is folded and brazed to the cylindrical block. Both the block and the thin sheet are made of aluminum alloy 6061-T6. The dimensions of the Aluminum block is 66.5 mm in diameter and 152.4 mm in length. The whole structure is rapped with an aluminum plate of thickness 1 mm as shown in Figure (2a). A cylindrical heater of rated power 300 W is fitted inside a drilled hole at the center of the aluminum block. Three holes are drilled in the block at different locations for the purpose of fixing the thermocouple wires for temperature measurements where three T-type thermocouples are inserted. The locations of the thermocouples are shown in Figure (2b). In addition, two thermocouples are used to measure the air inlet and outlet temperature of the cooling air. The test is started by running the fan and adjusting its rotational speed. Then, at the same moment of supplying the power to the heater, the thermocouple signals are recorded with time. The test lasts until steady state condition is reached. The test is conducted for different fan speeds, 6000, 9000, and 11200 rpm. Aligent Data Acquisition unit is used to read and record the signal of the thermocouples as well as the fan frequency generator signal.

The fan static pressure head is measured separately in a fan loop that is designed according to ISO standards [15]. The fan loop is equipped with pressure transducer and pitot tube to measure the fan static pressure jump and the velocity distribution at the loop cross-section, respectively. The velocity distribution is used to estimate the fan volume flow rate. Flow control valve is used to change the overall flow resistance inside the test loop and hence change the fan volume flow rate. The rotational speed of the fan can be set to the desired value by the adjusting the delivered voltage and current from the power supply. In this loop, the variation of the fan static pressure jump is measured versus the volume flow rate at different fan rotational speeds and different ambient pressures. Vacuum pump is used to adjust the pressure to the desired value. The measured fan pressure jump is specified as a function of the fan volume flow rate. This function is set as a polynomial of the third order.

$$\Delta p_p = f_0 + f_1 Q + f_2 Q^2 + f_3 Q^3$$

where, Q is the volume flow rate across the fan plane.

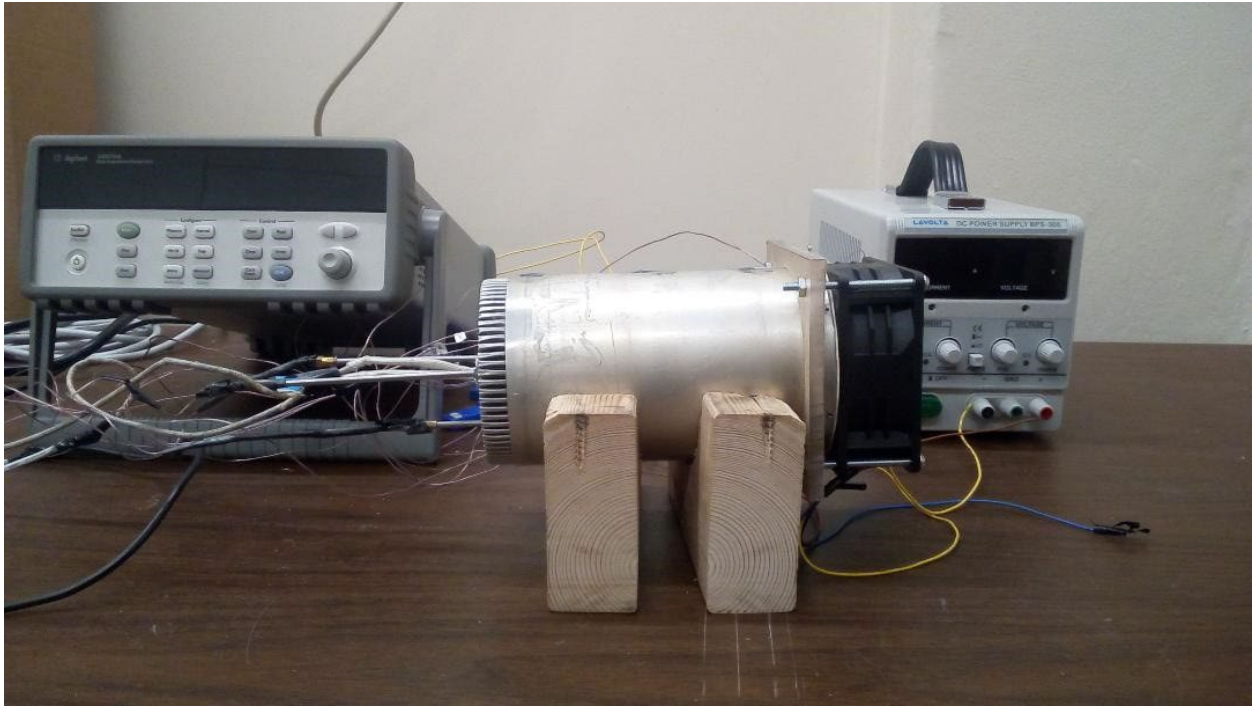


Figure (1) picture of the test-rig

3. Numerical model and validation

The domain of the fin structure fan arrangement is quite complicated. It includes a rotating fan, fluid moving around the finned surfaces, and the solid materials of the fins, Al block, and the heater. A 3-D model is generated for these domains. The fluid flow equations are solved in the fluid zones while the heat diffusion equation is solved in the solid regions.

To reduce the computational time, only one repeated sector is considered in the numerical solution as shown in Figure (3a). The grid is refined besides the walls that are in contact with the cooling air. To ensure grid independent solution, a grid of size 831,000 cell is adopted in this simulation. Figure (3b) shows the grid in x-y plane at flow entrance. Instead of solving the flow in the rotating fan, the fan is represented by an interface plane. At this plane, the relation between the static pressure jump and the volume flow rate which is measured in the fan loop is applied.

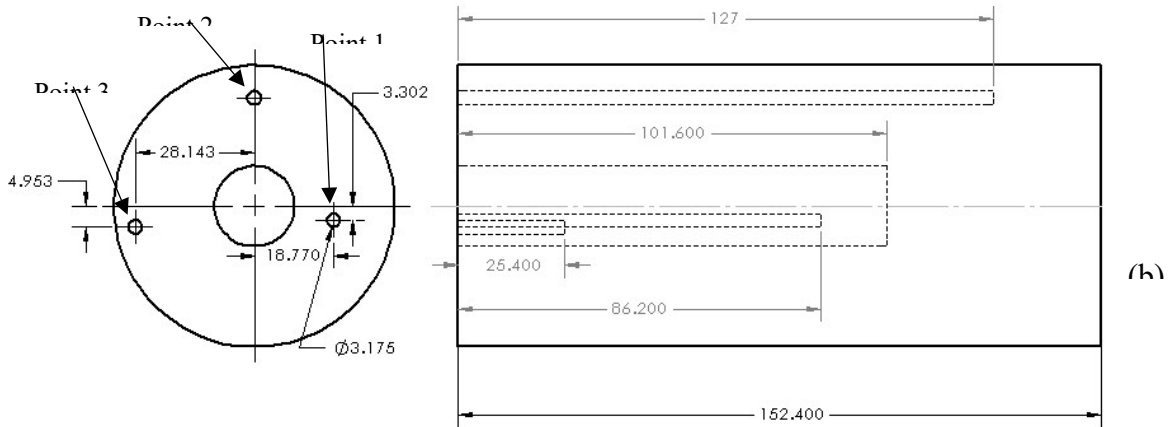
The heater power is assumed as a uniform heat generation in the heater material. The numerical simulation assumes,

- the thermo-physical properties of the solid material and the cooling air remain constant,
- the simulation is transient to validate the temperature development with time,

- the flow is incompressible and turbulent,
- no slip condition is assumed at the solid-fluid interface.



(a)



(b)

Figure (2) (a) Fin structure shape (b) locations of the thermocouples

Both low and high Reynolds number turbulence models have been tried. K- ϵ Realizable turbulence model is considered as a high Reynolds number model while Transition k-k ℓ - ω and k ω SST models are considered as low Reynolds number models. The results of each of the aforementioned models are compared with the experimental measurements to determine which model is more suitable.

ANSYS FLUENT 18.2 [18] is used to numerically solve the governing equations of the model. A second-order upwind scheme is used to discretize momentum, energy, and turbulence equations. The transient terms in the equations are discretized using first order implicit technique. The coupling between continuity and momentum equations is treated with SIMPLE algorithm. In each time step, the solution is deemed to converge when the residuals in the flow equations reduce under 10^{-4} and the residuals in the energy equations reduces under 10^{-10} .

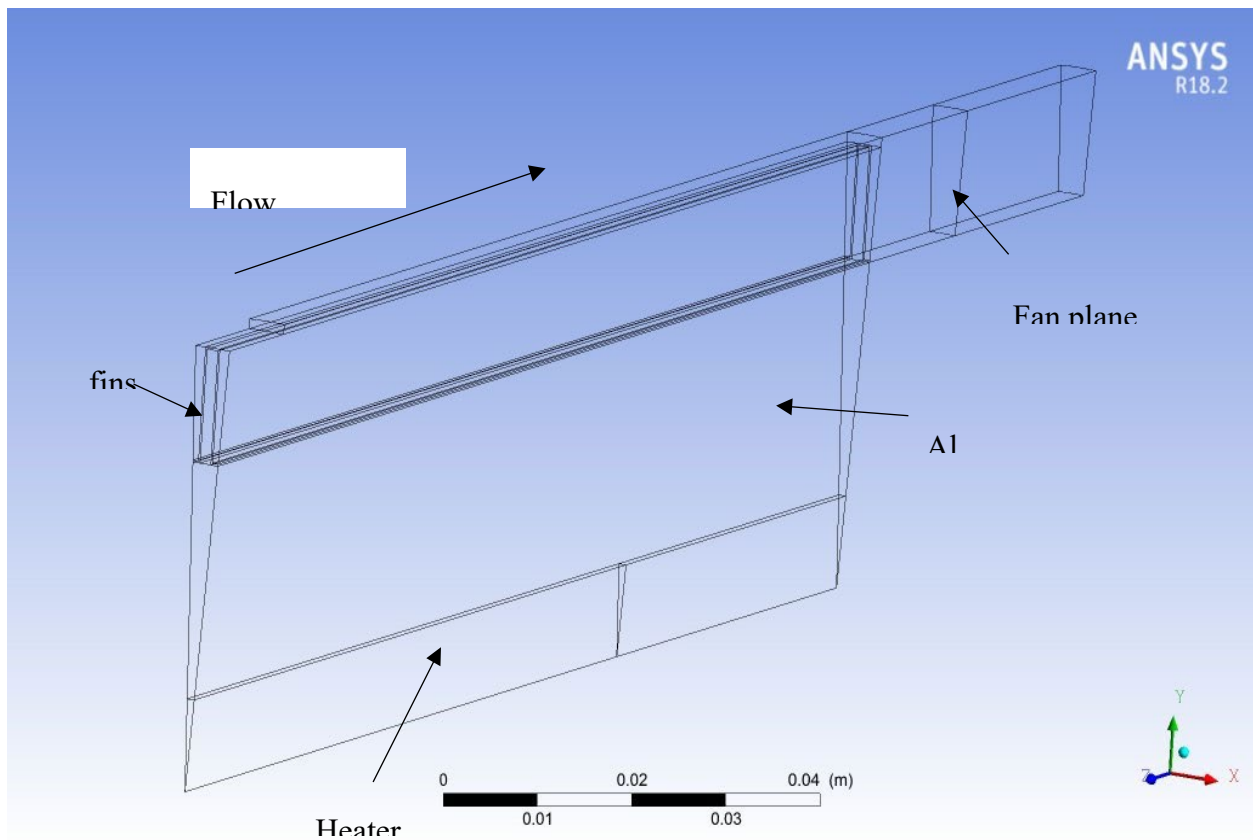


Figure (3a) Computational domain

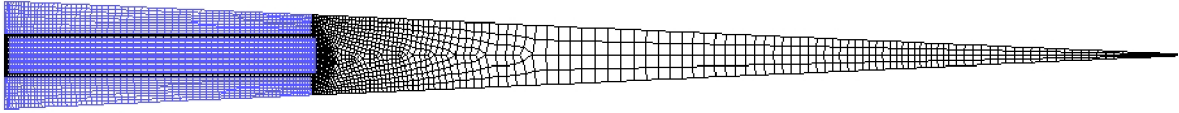
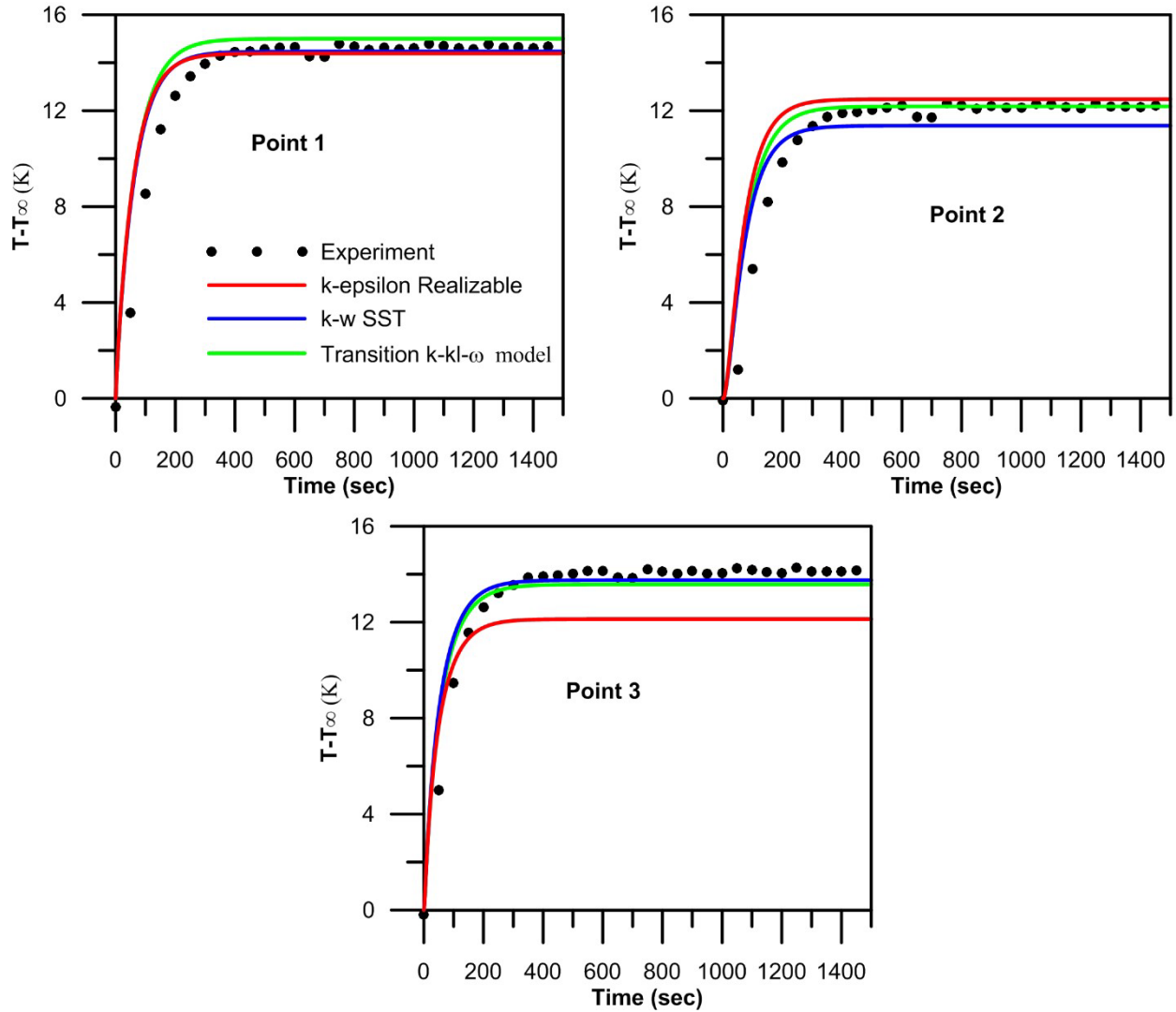
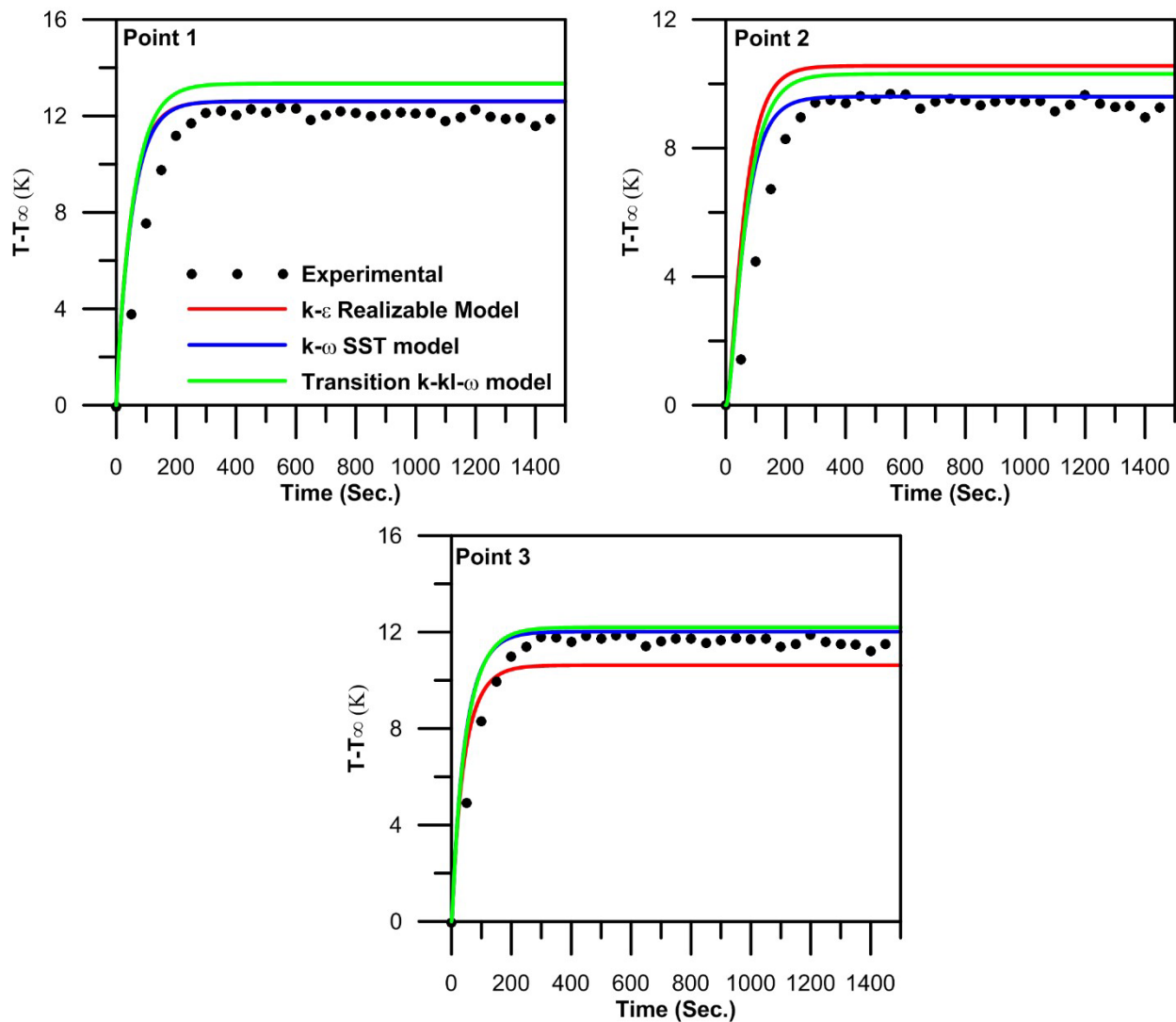


Figure (3b) Mesh in x-y plane



Figure(4) Monitored temperature difference ($T-T_{\infty}$) with time at three points in the Aluminum block for fan speed = 9000 rpm



Figure(5) Monitored temperature difference ($T-T_{\infty}$) with time at three points in the Aluminum block for fan speed = 11200 rpm

The experimental temperature difference ($T-T_{\infty}$) is compared with the numerical values for the three turbulence models: $k-\epsilon$ Realizable, Transition $k-k1-\omega$, and $k-\omega$ SST (shear stress transport). The comparison is shown for fan speeds 9000, and 11200 rpm in Figures (4 and 5). It can be seen that the results of the model $k-\omega$ SST matches better with the experimental measurements.

Figure (6) shows the temperature contours at steady state condition for fan speed 9000 rpm for the three turbulence models. As shown from the figure, the $k-\epsilon$ realizable model overestimates the temperature in the Aluminum block. This can be explained due to the fact that

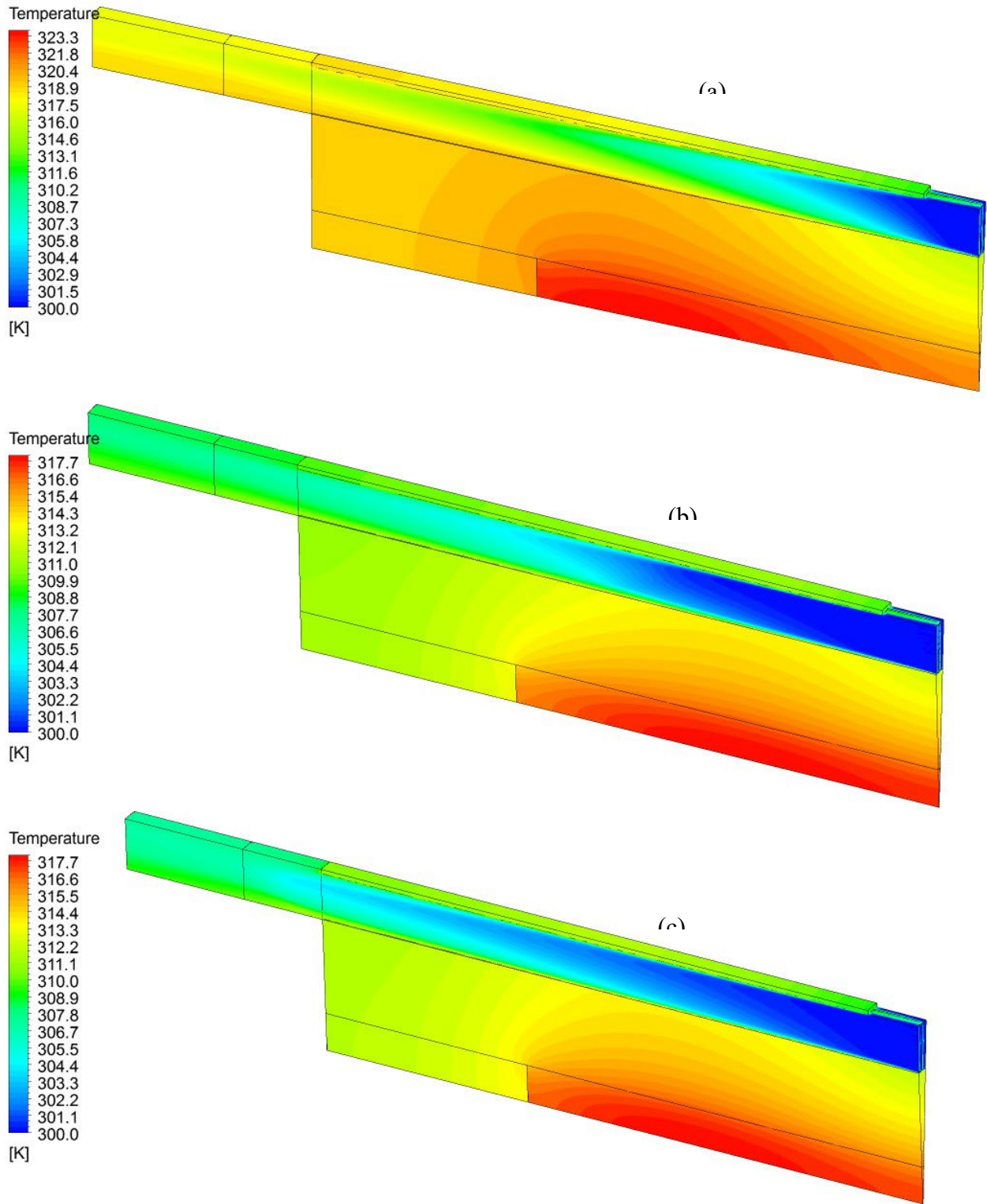


Figure (6) Temperature contours at steady state condition for (a) K- ϵ Realizable turbulence model

(b) k- ω SST turbulence model and (c) Transition k-k1- ω turbulence model at Fan speed 9000 rpm

the $k-\epsilon$ model is a high Reynolds number model which assumes that the inlet flow is fully turbulent. This leads to faster thermal boundary layer development which reduces the heat transfer coefficient due to the higher thermal boundary layer thickness. For $k-\omega$ SST and Transition $k-k_l-\omega$ models, the thermal boundary layer as shown in the figure is thinner and the flow continues to thermally develop through an axial distance greater the heater length. This of course increases the heat transfer coefficient and reduces the temperature in the Aluminum block.

4. Optimizing fin structure for fan cooling

An air-cooling system utilizing wing bay air where the air is pushed or sucked to flow over a finned surface attached to the motor housing with a cooling fan is the simplest and preferred way in cooling EMA used in aerospace applications. This is because of the following reasons: (i) least complicated (ii) light weight and reliable (iii) bay air can be effective if sufficient air flow is provided to enhance heat transfer. An electro-magnetic actuator of diameter 70 mm and 120 mm in length is considered [19]. Accordingly, the fin structure is assumed to compose of radial fins attached to a cylindrical base of thickness 1.5 mm and inner diameter 70 mm so the EMA can be fitted inside as shown in Figure (7a). The tips of the fins are attached to a cylindrical cover of thickness 1 mm and an outer diameter of 100 mm. The total heat dissipated by the electric actuator is considered as a uniform heat flux at the bottom surface of the fin base.

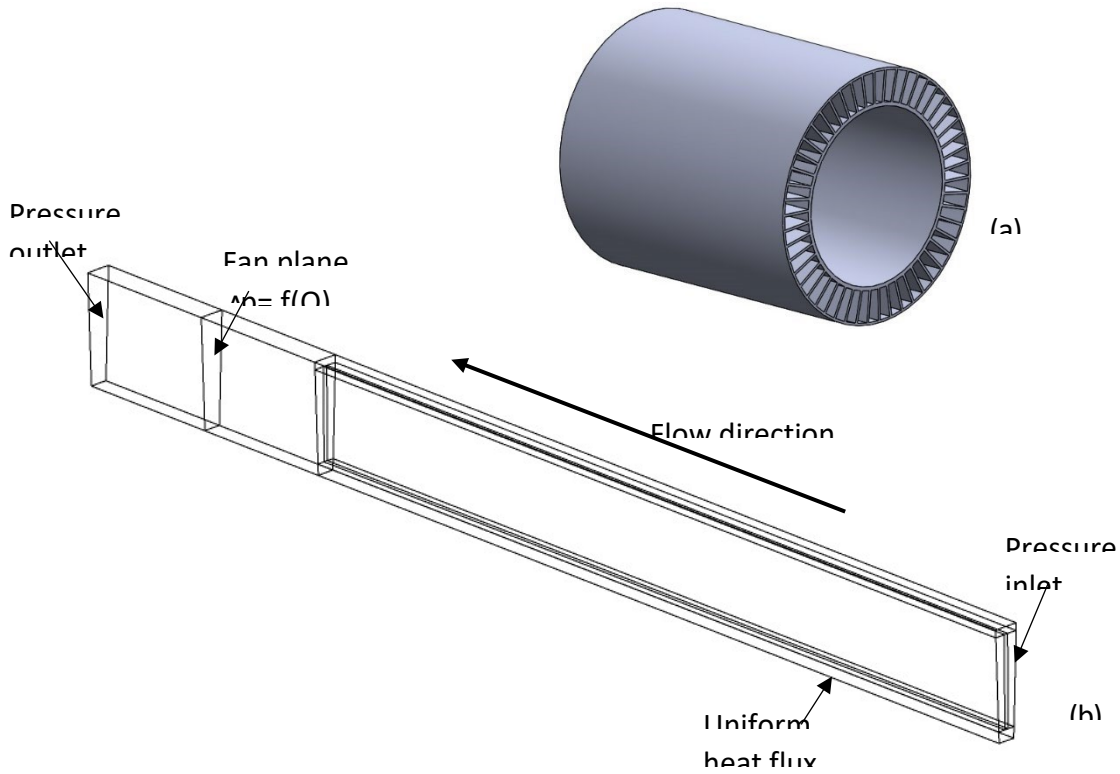


Fig. (7) Fin structure (a) and its computational domain (b)

The numerical model discussed in section 3 is used to simulate the fan cooling performance when it is attached to this fin structure. The simulation is considered to be steady state since the steady state temperature is the parameter required to estimate the fin performance. In aerospace applications, the cooling fan is working under different ambient pressures ranging from 0.2 atm to 1 atm. The fan pressure jump at different ambient pressures and rotational speed that is measured in ref. [15] has been applied at the fan plane.

The thermal performance of the fin structure is evaluated using the concept of thermal resistance. The fin structure thermal resistance is defined as the difference between the maximum base temperature and the cooling fluid temperature at the inlet per unit of heat flow rate.

$$R_{Total} = \frac{T_{max} - T_{\infty}}{q} = \frac{T_{max} - T_{f,o}}{q} + \frac{T_{f,o} - T_{\infty}}{q} = \frac{T_{max} - T_{f,o}}{q} + \frac{1}{\dot{m}c_p}$$

The thermal resistance can be decomposed into the capacitive resistance, which is responsible for the temperature rise of the coolant from the inlet to the exit,

$$R_{cap} = \frac{1}{\dot{m}c_p}$$

and the convective resistance, which is related to the heat transfer from the fins to the air,

$$R_{conv} = \frac{T_{max} - T_{f,o}}{q} = \frac{1}{hA_{tot}\eta}$$

where, A_{tot} is the total surface area and η is the overall surface efficiency. So, R_{Total} depends on fin surface area, fin shape, the cooling air mass flow rate, and fin efficiency.

4.1 Effect of fin shape

As shown in Fig. (8), three different fin configurations are considered: straight plate fin, offsetstrip fin, and corrugated fin. The fin number in each configuration has been varied from 50 to 200. For Offset-strip configuration, the length of each strip is assumed to be 10 mm and the ratio of the corrugation amplitude to corrugation length for corrugated fin configuration is kept at a value of 0.2. Since the weight represents an important issue in aerospace applications, the weight of all the tested fin structures is kept constant by changing the fin thickness. The fin thickness is considered to be,

$$t_f = \frac{50}{N_f} \text{ mm for straight plate and offset strip fins}$$

$$t_f = \frac{50}{N_f} * \frac{L_{straight}}{L_{corrugated}} \text{ mm for corrugated fins.}$$

where, N_f is the number of fins.

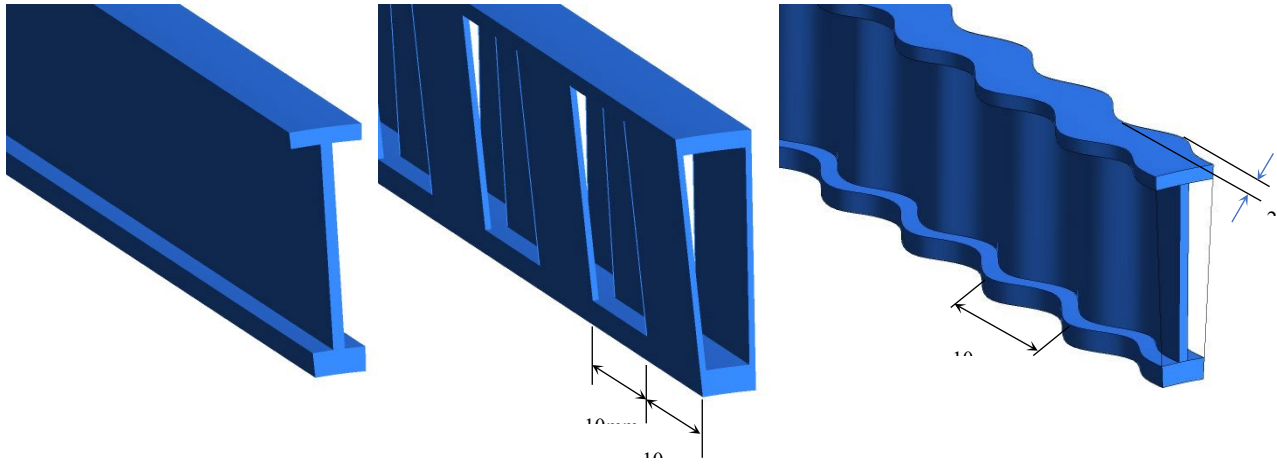


Fig. (8) Straight plate, offset-strip, and corrugated fin structures

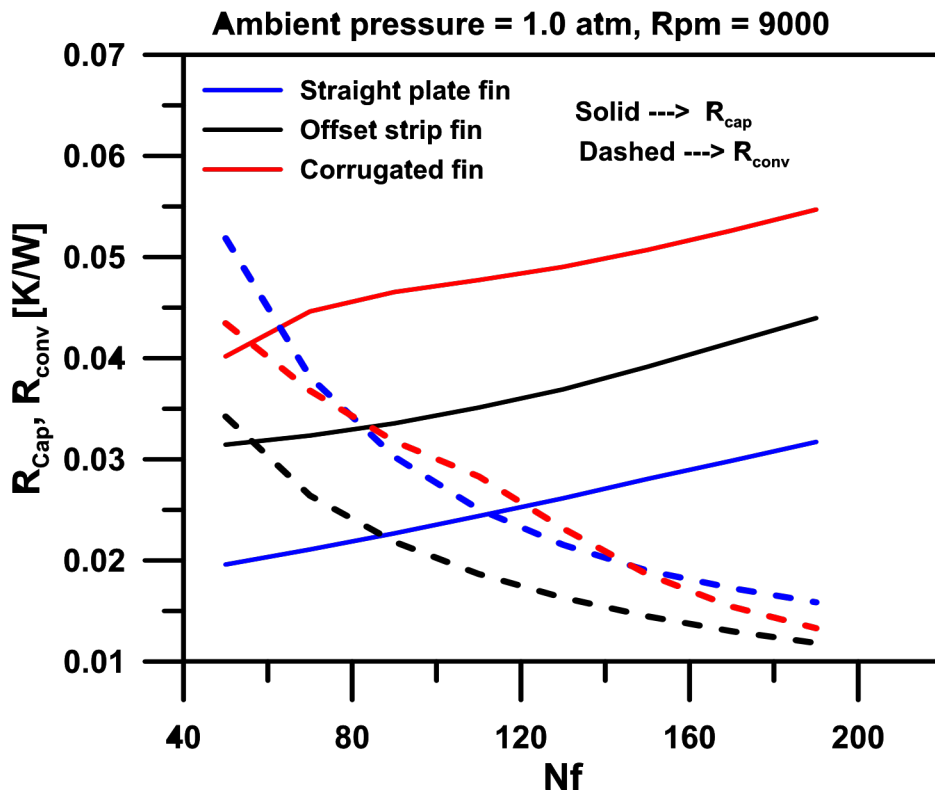


Fig. (9) Variation of R_{cap} and R_{conv} with fin number for different fin configurations

The cooling performance of the three fin configurations is tested when the cooling fan operates under ambient pressure 1 atm and with rotational speed of 9000 rpm. Fig.(9) shows the variation of both convective and capacitive resistances with fin number for the three fin configurations. As shown in the figure, it can be seen that the convective/capacitive resistance decreases/increases monotonically with fin number. This is due to the increase in surface area and friction resistances as a result of increasing fin number. The offset-strip fin structure shows the lowest convective resistance due to the interruption of the thermal boundary layer which enhances the heat transfer coefficient. By comparing the total thermal resistance of each fin

configuration as shown in Figure (10), it can be seen that straight plate fin outperforms the offset-strip when the fin number is greater than 70. Interrupting the fins enhances the heat transfer but at the same time it increases the friction which reduces the fan mass flow rate. However, straight fin configuration produces lower pressure drop and consequently allowing higher mass flow rate to flow through the fin structure. Even with the higher surface area of the corrugated fin structure, its total thermal resistance is the highest due to the higher pressure drop that is associated with the corrugated shape.

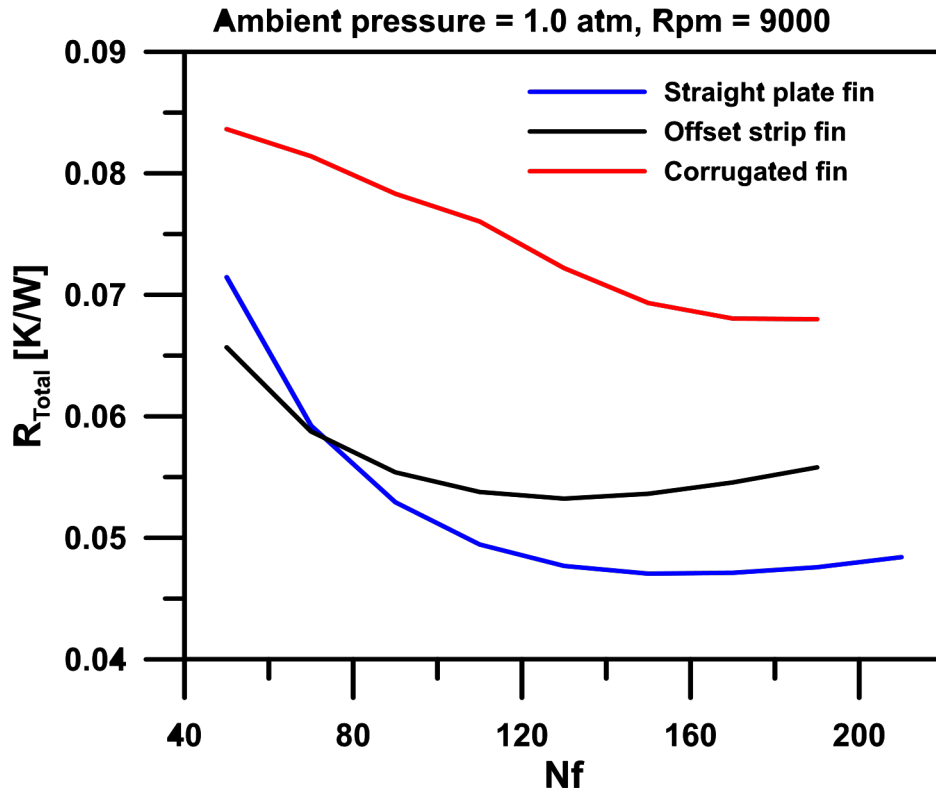


Fig.(10) variation of total thermal resistance with fin number for straight plate, offset strip, and corrugated fin structures

Also, it can be seen from the figure that there is an optimum fin number that can minimize the total thermal resistance. This optimum fin number ranges from 100 to 160 for this fan characteristic curve (1 atm, and 9000 rpm).

4.2 Effect of fan rotational speed and ambient pressure on fin optimum number

During the real fan operation, the mass flow rate of the cooling air changes with ambient pressure and fan rotational speed. Also, it changes with the fin number due to the change of pressure head required to push the air across the fin structure with fin number. It is shown that straight plate fin structure performs better than offset-strip and corrugated fin structures for fan operation at 9000 rpm and under 1 atm ambient pressure. So, in this

section, only straight plate fin structure will be investigated. The fan rotational speed has been varied from 6000 to 12000 rpm and the ambient pressure has been varied from 0.2 to 1 atm. Figure (11) shows the volume flow rate variation with fin number. Increasing the fin number reduces the size of the flow passage and results in higher pressure drop and consequently reduces the fan volume flow rate. As shown from Figure (11), the reduction rate or the slope of the volume flow rate with fin number is higher at the lowest ambient pressure (0.2 atm). This means that when the fan operates at low ambient pressure its volume flow rate will be more sensitive to the changes in friction losses. The volume flow rate reduces from 2.7 m³/min to 0.95 m³/min when the fin number changed from 50 to 200 at fan rotational speed 12000 rpm.

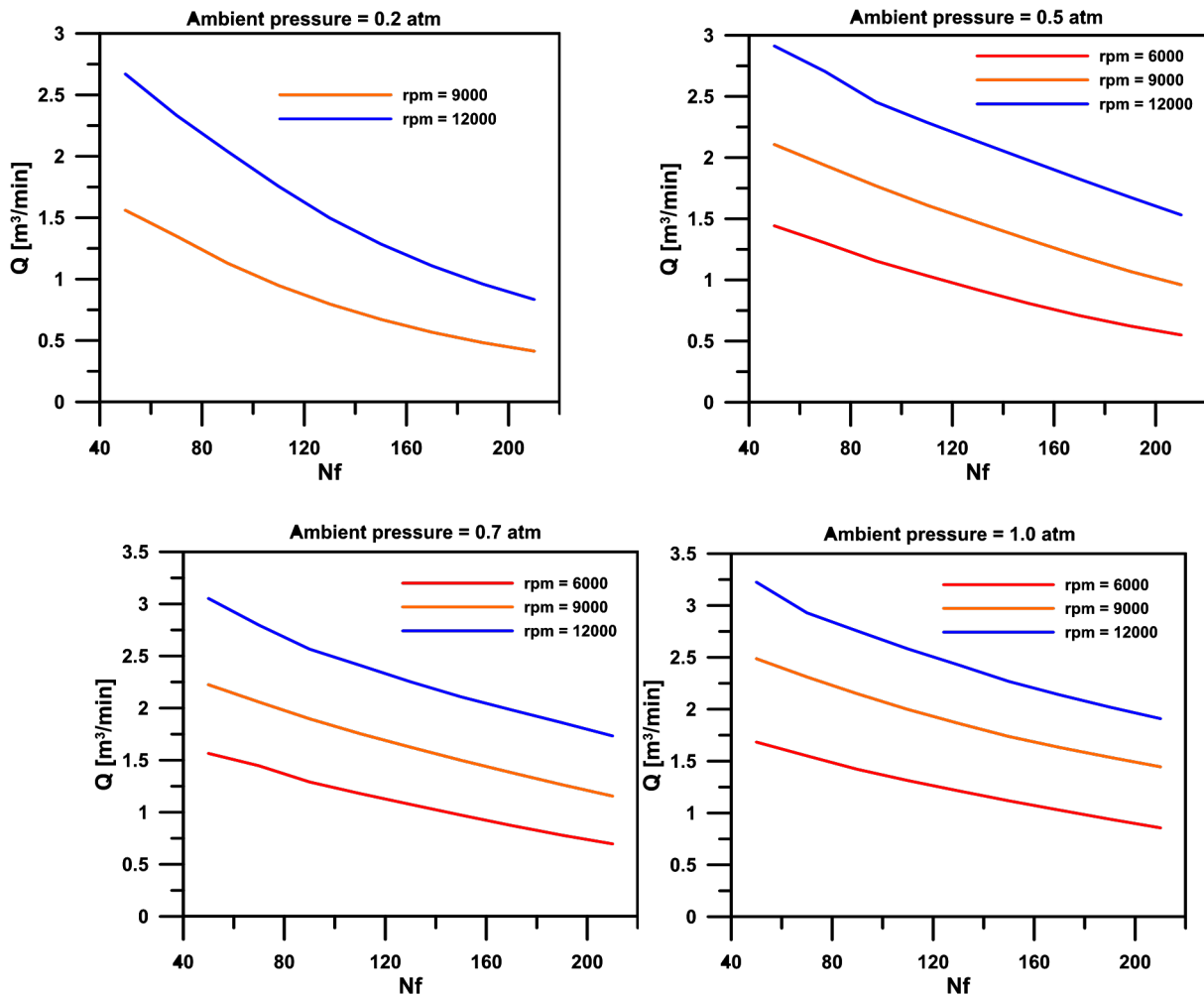


Figure (11) variation of fan volume flow rate with fin number for straight plate fin structure

Figure (12) shows the change of total thermal resistance with fin number for straight plate fin structure. It is clear from the figure that the value of the optimum fin number changes with the fan speed and the ambient pressure. For most cases, the optimum number of fins lies between 100-150. The optimum fin number shifts to lower values when the fan operates at lower ambient pressure. However, it increases with the fan rotational speed.

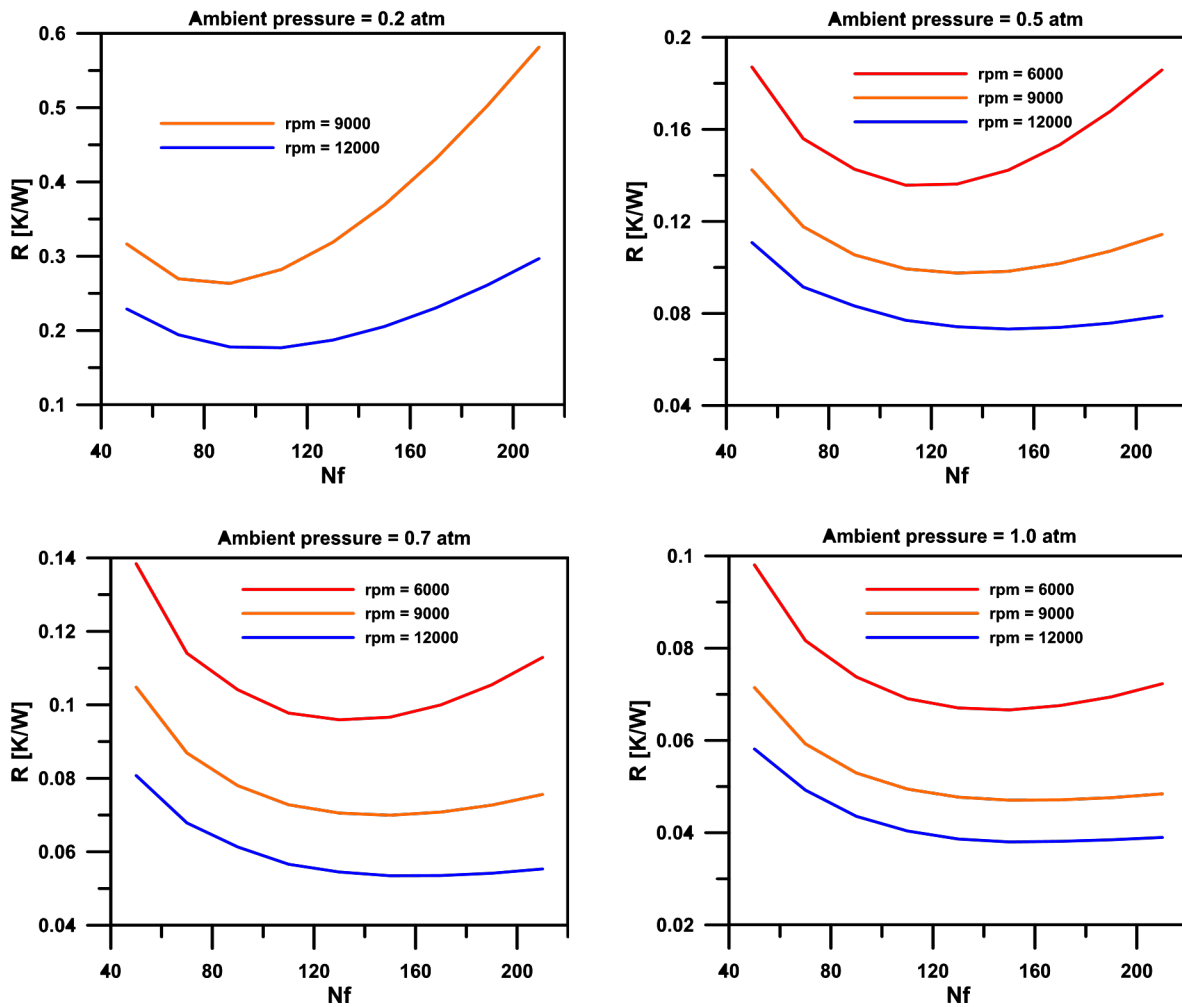


Figure (12) Variation of thermal resistance of the straight plate fin structure with fin number at different ambient pressure and fan rotational speed

4.3 Effect of fin thickness

For the purpose of minimizing the weight of the fin structure, the fin thickness effect on thermal performance is investigated. The fin thickness of straight plate fin structure has been changed from 0.2 up to 0.7 mm. Figure (13) shows the effect of fin thickness variation on the total thermal resistance of straight fin structure of different fin number when the fan operates at different ambient pressures. The figure shows that for fin structure of 70 fins, increasing the fin thickness improves the thermal performance monotonically for ambient pressure 0.5, 0.7, and 1.0 atm. But for ambient pressure 0.2 atm the optimum fin thickness for the 70-fin structure was about 0.5 mm. For fin structures of 110 and 150 fins, the optimum fin thickness ranges from 0.2 to 0.45 mm. This can be attributed to the fact that changing the fin thickness has two contradicting effects on the heat transfer process. Decreasing fin thickness allows bigger width for the cooling air passage while increasing the fin thickness improves the fin efficiency to conduct the heat along the fin length up to its tip. When the fan is operating at low ambient pressure, the heat transfer process is controlled by the pressure drop which is strongly dependent on the hydraulic diameter of the cooling air channel. However, at higher ambient pressures, the heat transfer process is controlled by both channel width and the fin efficiency which results in an optimum value for the fin thickness. So, reducing the fin thickness may lead to increasing the fin performance and at the same time it reduces the weight of the fin structure. For example, the total thermal resistance of 150-fin structure decreases monotonically when its fin thickness decreases from 0.5 to 0.2 mm which is equivalent to 35.5% reduction in the fin structure weight.

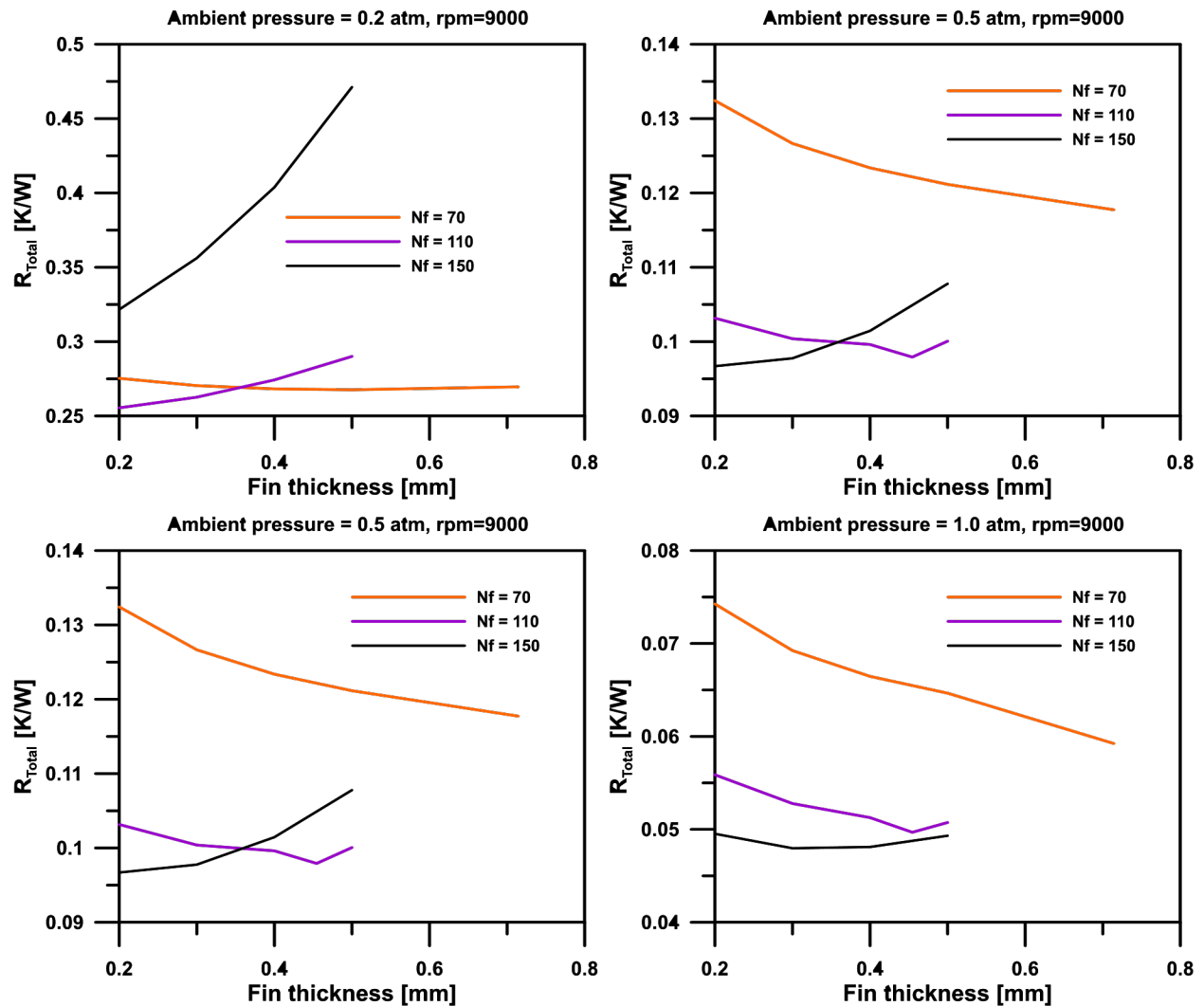


Fig. (13) variation of total thermal resistance with fin thickness

5. Conclusions

The thermal performance of a fin structure to cool aerospace EMAs with wing-bay air circulated by an axial fan is investigated. The fan performance is measured separately in a fan loop where the static pressure head is obtained as a function of volume flow rate at different rotational speeds and different ambient pressures. A numerical model is developed to predict the effect of fin shape, fin number and fin thickness on the thermal performance of the fin structure when the fan operates under different conditions. The results show that when applying the measured fan characteristic curves, the straight plate fin has a better performance than offset-strip and corrugated fins. Also, the optimum fin number changes under different fan operating conditions. It decreases significantly with decreasing fan ambient pressure. At the low ambient pressure of 0.2 atm, reducing the fin thickness of a fin structure with 150 fin results in a considerable thermal performance improvement. However, the performance of a structure of 70 fin improves with increasing

fin thickness when the fan operates at an ambient pressure greater than 0.5 atm. Also, the model predicts an optimum fin thickness which changes according to the fin number and fan ambient pressure from 0.2 to 0.5 atm.

ACKNOWLEDGMENT

This material is based on research sponsored by the United States Air Force under agreement number FA8650-17-2-2230. The U.S. Government is authorized to reproduce and distribute reprints for Governmental purposes notwithstanding any copyright notation thereon. The views and conclusions contained herein are those of the authors and should not be interpreted as necessarily representing the official policies or endorsements, either expressed or implied, of the United States Air Force or the U.S. Government.

References

- 1- D. Blanding, Subsystem design and integration for the more electrical aircraft, 25th Int. Congress of the Aeronautical Sciences, 2006.
- 2- W. D. Gerstler, E. J. Ruggiero, F. Ghasripoor, A. El-Refaie, H. P. De Bock, X. Shen, and J. P. Alexander, A Liquid-Cooled Rotor for High Density Electric Machines, 47th AIAA/ASME/SAE/ASEE Joint Propulsion Conference & Exhibit 31 July - 03 August 2011, San Diego, California.
- 3- MR Guechi, P. Desevaux, P. Baucour, C. Espanet, R. Brunel and M. Poirot, Spray cooling of electric motor coil windings, *The Journal of Computational Multiphase Flows*, 2016, Vol. 8(2) 95–100
- 4- J. Bai, Y. Liu, Y. Sui, C. Tong, Q. Zhao, and J. Zhang, Investigation of the Cooling and Thermal-Measuring System of a Compound-Structure Permanent-Magnet Synchronous Machine, *Energies* 2014, 7, 1393-1426.
- 5- Kea-Ho Lee, Hyun-Rok Cha, and Young-Bae Kim, Development of an interior permanent magnet motor through rotor cooling for electric vehicles, *Applied Thermal Engineering* 95 (2016) 348–356

- 6- T. Nakahama, D. Biswas, K. Kawano, and F. Ishibashi, Improved cooling performance of large motors using fans, *IEEE Trans. Energy Convers.*, 21 (2) (2006), pp. 324–331
- 7- Jer-Huan Jang, Han-Chieh Chiu, Wei-Mon Yan, M.C. Tsai, and Pin-Yuan Wang, Numerical study on electromagnetics and thermal cooling of a switched reluctance motor, *Case Studies in Thermal Engineering*, Vol. 6, 2015, 16–27
- 8- K. Farsane, P. Desevaux, and P.K. Panday, Experimental study of the cooling of a closed type of electric motor, *Applied Thermal Engineering* 20 (2000) 1321–1334
- 9- Y. Lin, Y. Hu, L. Zhou, D. Woodburn, T. Wu, L. Chow, and Q. Leland, A Reduced–Order Model for Electromechanical Actuator, 2012 SAE International, 2012-01-2230.
- 10- H. E. Ahmed, B.H. Salman, A.Sh. Kherbeet, and M.I. Ahmed, Optimization of thermal design of heat sinks: A review, *International Journal of Heat and Mass Transfer*, 118 (2018) 129–153
- 11- A. Bejan, Optimal Internal Structure of Volumes Cooled by Single-Phase Forced and Natural Convection, *Journal of electronic packaging*, ASME, 125(2003), 200-2007
- 12- Dong-Kwon Kim, Jaehoon Jung, and Sung Jin Kim, Thermal optimization of plate-fin heat sinks with variable fin thickness, *International Journal of Heat and Mass Transfer* 53 (2010) 5988–5995
- 13- M. Khoshvaght-Aliabadi, M. Khoshvaght, and P. Rahnama, Thermal-hydraulic characteristics of plate-fin heat exchangers with corrugated/vortex-generator plate-fin (CVGPF), *Applied Thermal Engineering* 98 (2016) 690–701

- 14- X. Zheng and Zhaogang Qi, A comprehensive review of offset strip fin and its applications,
Applied Thermal Engineering 139 (2018) 61–75
- 15- W. Wu, Y. Lin, O. Mesalhy, J. Kizito, Q. Leland, Design and Testing of a Cooling Fan for
Electro-Mechanical Actuators for Aerospace Applications, Int J Astronaut Aeronautical
Eng, 2 (2017)
- 16- W. Wu, Y. Lin, L. Chow, and Q. Leland, Fan Performance Characteristics at various
Rotational speeds and Ambient Pressures, SAE Technical Paper 2014-01-2219, 2014,
doi:10.427/2014-01-2219
- 17- J.R. Culham, Y.S. Muzychka, Optimization of plate fin heat sinks using entropy
generation minimization, IEEE Transactions on Components and Packaging
Technologies, 24 (2001)
159-165
- 18- Ansys Fluent User's Guide, Release 18.2, August 2017
- 19- K. McCarthy, A. Heltzel, E. Walters, J. Roach, S. Iden, and P. Lamm, A Reduced-Order
Enclosure Radiation Modeling Technique for Aircraft Actuators, SAE paper 10PSC-
0093, 2010

APPENDIX M

UCF Project 1626-8282

Quarterly Report # 5 to
North Carolina A&T University

Thermal Management of Electromechanical Machines for Aerospace Systems

University of Central Florida
Department of Mechanical and Aerospace Engineering
Orlando, FL 32816-2450

Louis Chow, PI
Yeong-Ren Lin
Osama Mesalhy

Period: From September 12, 2018, to December 11, 2018

Date of report: December 17, 2018

During the report period, the following manuscript was prepared.

Enhancement of a Heat Sink Performance Using a Partial Shield and/or a Guide Plate

Mohamed L. Elsayed ^{a,b,1}, Osama Mesalhy ^{a,b}, Ramy H. Mohammed ^{a,b}, John P. Kizito^c, Quinn H. Leland^d, Louis

C. Chow ^a

^aDepartment of Mechanical and Aerospace Engineering, University of Central Florida, Orlando, FL 32816-2450, USA. ^bDepartment of Mechanical Power Engineering, Zagazig University, Zagazig 44519, Egypt.

^cDepartment of Mechanical Engineering, North Carolina Agricultural and Technological State University, USA ^dPower and Control Division, Aerospace Systems Directorate, Air Force Research Laboratory, USA

ABSTRACT

The potential of using a full shield or partial shield with a guide plate to control the bypass cooling air flowing above a heat sink is numerically modeled using two different scenarios of inlet conditions – fixed mass flow rate and specified fan curve. Excellent agreement is observed when the simulation results are compared with available experimental data in the literature. Under the first inlet condition, the Nusselt numbers associated with the full shield installation are significantly higher than those without a shield, but with a significant pressure drop penalty. Friction factor increases with partial shield height till it reaches a maximum value with the full-shield configuration. Using an inclined guide plate with a partial shield alters the flow direction, forcing the air to impinge on the heat sink. This adds an extra cooling effect but without causing a considerable increase in the friction factor. In the case of fixed inlet mass flow rate, most of

¹ E-mail: mlea@knights.ucf.edu, mlabdelkrem@zu.edu.eg (Mohamed L. Elsayed).

the partial shield and guide plate cases show the lowest pressure drop when the ratio of the partial shield height to the total bypass height H_s/H_{BP} is between 0.35 and 0.5. The case with an inclination angle of $\theta_P=15^\circ$ has the highest thermal performance and the highest pressure drop. Correlations for the average Nusselt number and friction factor are developed to include the effect of Reynolds number, shield height, bypass height and guide plate inclination angle. For the second inlet condition, the test cases are repeated using a selected fan characteristic curve as an alternate to the fixed mass flow rate condition. The specified fan curve case shows that a short partial shield with a slightly inclined guide plate has a better thermal performance than the full shield case. Furthermore, using a guide plate only with a small inclination angle has a superior thermal performance. Changing the position of the guide plate is investigated as well and the optimal location is obtained.

KEYWORDS: Heat sink; hydraulic/thermal performance; partial shield; guide plate.

1. Introduction

Thermal management of electronic components has been an active area of research and development focus due to the evolution of microelectronics over the last few decades. The increase in power density in applications such as microelectronic packages and aircraft electro-mechanical actuation (EMA) has pointed to the need for using effective cooling methods. These cooling methods help to keep the operating temperature of electronic components at an acceptable level. Much attention has been given recently on the challenges that are encountered in flight actuation systems such as high-power-density electric motors and power electronics. Failure to manage the heat generated in the EMA systems may lead to mission objective failure and detrimental loss of the aircraft [1, 2]. McCarthy et al. [2] showed that the power electronics system has approximately 25% of the total heat load generated in a typical flight EMA system. At 200 W of heat load and without forced air cooling, the electronic substrate temperature can reach $\sim 107^\circ\text{C}$ which exceeds the imposed temperature limit to avoid overheating of the power electronics. To assure the reliability of the electronics and to lower the operating and maintenance costs of the flight actuation systems, an air-cooling system is considered as the primary cooling method for EMA system components [3].

Several studies have been undertaken on heat sink design for improved cooling of electronic components that include steady-state and transient models, simple analytical and empirical models, and experimental approaches. Morega et al. [4] carried out a study to minimize the thermal resistance (R_{th}) of a stack of parallel plate fin heat sink (PPFHS). The optimum heat transfer condition was determined for equal spacing between the plates. Furthermore, there is an optimal number of plates that minimizes the R_{th} for a specified free stream velocity when the overall dimensions of the PPFHS are specified. In comparison with other simple internal duct geometries, PPFHSs are thought to offer the best combination of high heat transfer and low pressure drop for high-performance heat sinks. This information was confirmed by the

experimental results conducted by El-Sayed et al. [5] who examined the thermal/hydraulic behavior of a PPFHS exposed to parallel flow, impinging and reverse-impinging flow. They concluded that parallel flow has the highest rate of heat transfer and the lowest pressure drop.

The performance of a PPFHS with the presence of flow bypass has been reported in the literature by several researchers. For instance, Lau and Mahajan [6] determined experimentally the effects of fin density and tip clearance on the PPFHS thermal and hydraulic performance. Their data indicated that significant gains in thermal performance can be obtained with high fin density heat sinks for a moderate increase in pressure drop. Tip clearances should be kept to a minimum for high thermal performance. Wirtz et al. [7] experimentally derived a correlation for inter-fin velocity as a function of approach free stream flow rate and heat sink fin density. They showed that the overall heat transfer coefficient of these fins can be obtained using the analytical solutions presented in [8] for developing flow between parallel plates. Moreover, their results showed that 60% of the air flow may bypass the PPFHS depending on the fin density of the heat sink and the geometry of the flow duct. This high level of air bypass results in approximately 50% reduction in the heat sink performance. Jonsson and Moshfegh [9] developed empirical bypass correlations for a PPFHS to predict the pressure drop and Nusselt number with an accuracy of $\pm 25\%$ and $\pm 10\%$, respectively. Leonard et al. [10] tested two PPFHSs with different channel/fin height ratios. A simple bypass model was used to estimate the average flow velocity inside the heat sinks with $\pm 8\%$ agreement with experimental data. Elshafei [11] theoretically and experimentally investigated the effects of the flow velocity, fin density, tip-to-shroud clearance (flow bypass) on the thermal performance and pressure drop across aluminum PPFHSs. Their results showed that the heat transfer rate decreases with an increase in the tip-to-shroud clearance. For instance, the thermal performance reduces by about 30% at a clearance ratio of 0.89 when compared to the fully shrouded case. Li and Chao [12] measured the thermal performance of PPFHSs with different fin density and flow velocity. They showed that the R_{th} decreases with the increase in the fin height and the optimal fin thickness was determined for different Reynolds numbers. Wu et al. [13] presented an analytical model to assess the thermal/hydraulic performance of a PPFHS with a wide range of Reynolds numbers. The model was able to predict the pressure drop within 8.4% to 13.9% compared to experimental results. Recently, Chingulpitak et al. [14] investigated the hydraulic/thermal performance of a PPFHS with crosscutted fin. Their results indicated that fin crosscutting can yield approximately a 16.2% decrease in the heat sink R_{th} for the same pumping power.

Computational fluid dynamics (CFD) approaches have been extensively applied to study heat transfer and flow behavior in heat sinks. Yuan [15] showed that the inter-fin velocity decreases with distance downstream which affects the heat transfer rate. Barrett and Obinelo [16] revealed that the augmentation in the heat sink heat transfer rate is due to surface area increase. Prstic et al. [17] numerically studied the bypass effects on the performance of a heat sink at different air flow rate, fin density and clearance area ratio. They concluded that the bypass flow increases with increase in fin density and clearance distance. Chen et al. [18] studied the performance of a PPFHS using an inverse method model and FLUENT software in conjunction with an experimental approach. Good agreement in the fin temperatures between the calculated values and the experimental data was obtained.

Recently, Ahmed et al. [19] reviewed different thermal and hydraulic optimization approaches for the PPFHS. Several studies were reported on the improvement of the performance of the PPFHS by promoting the turbulence of the flow through the inter-fin spacings [20, 21]. For example, Yang et al. [20] studied experimentally the performance of PPFHS with different types

of loose and dense vortex generators (VG). They concluded that vortex generators operating at a large fin pitch and a high frontal velocity are more effective than the plain PPFHS. The delta-winglet pair VG provides the optimal enhancement design as it can reduce by 12 to 15% the surface area at a frontal velocity of approximately 3–5 m/s. Ahmed et al. [21] optimized the thermal design of a PPFHS by inserting ribs at different locations and with different numbers and orientation in the space between fins. They concluded that a ribbed PPFHS can increase the thermal performance and decrease the pressure drop compared to conventional PPFHS. Ahmed et al. [19] also reported some papers that studied the characteristics of the flow through PPFHS if vortex generators or flow tabulators are installed through the tip clearance. For instance, Li et al. [22] experimentally investigated the effect of vortex generators attack angle and separating distance between the PPFHS and vortex generator on the thermal/hydraulic performance of PPFHS. The superior performance in terms of lower R_{th} and lower pressure is recorded at an attack angle of 30° and zero separating distance. For the lowest Re , the result showed that the R_{th} of the PPFHS with the vortex generator is 27% lower than that of the regular PPFHS. Prstic and Bar-Cohen [23] compared the performance of a partially/fully shrouded and a shielded heat sink experimentally and numerically. The fully shrouded heat sink has the best thermal performance, but this comes with a high pressure drop penalty. Adding a heat shield to a partially shrouded heat sink decreases the pressure drop while maintaining a thermal resistance comparable to the fully shrouded configuration. Li et al. [24] tested the installation of the vertical shield on PPFHS and found that more coolant fluid is forced to pass through the fin spacing. This promotes heat transfer, but the pressure drop across the heat sink rises. Furthermore, Tsai et al. [25] investigated the effect of the different shield inclination angle (θ) on the thermal/hydraulic performance of a PPFHS. They found that the variation of this angle can cause a substantial and complicated variation to the flow field both upstream and downstream of the heat sink. Correlations to assess the thermal/hydraulic performance of the heat sink with a shield were developed by Shaalan et al. [26]. They concluded that the inclination angle yielding the minimum R_{th} varies with the heat sink height. Zhang et al. [27] studied the effects of shield position and height on the thermal/hydraulic performance of a PPFHS experimentally. Their experimental data revealed that superior thermal performance occurs when the shield is half the height of the fins and is positioned at the top front of the heat sink. They developed correlations for the average Nusselt number and friction factor, and the predicted values fitted the experimental data with deviations less than $\pm 15\%$. Recently, Elsayed and Mesalhy [28] proposed a performance enhancement for a shield heat sink by making slots on the shield. The slots create jets that are able to eliminate the eddies and vortices generated by the solid shield. They reported the appropriate slot number and width to achieve the optimum thermal/hydraulic performance. For the highest Re number, a slotted shield offers an 80% lower pressure drop compared to a solid shield.

Most of the work available in the literature has focused on the effect of the geometrical variables of a PPFHS, such as fin height, fin thickness and fin density on the hydraulic/thermal performance. As the previous literature indicates, it is feasible to enhance the heat transfer of fin array by altering the bypass through the installation of a shield at different positions and inclination angles, and by forming slots in the solid shield. Shielding the entire bypass region produces an enhancement in heat transfer, but this causes a dramatic increase in the pressure drop at the same time. This study aims to investigate numerically the effect of using a partial shield with a guide plate to direct the bypass flow to impinge at the heat sink. Comprehensive performance evaluations of the heat sink with different partial shield heights and guide plate inclination angles are presented to find the optimum configuration that gives the maximum heat

transfer rate with low pressure drop. General correlations for the hydraulic/thermal performance of the PPFHS with partial shield and guide plate are obtained and compared with experimental correlations available in the literature.

To the best of the authors' knowledge, none of the literature mentioned above includes a fan performance curve as the inlet boundary condition which is a far more common scenario than the fixed inlet approach velocity. Therefore, an optimization analysis for the different installation is repeated using an actual fan operational curve. This analysis will establish the direct connection between the optimized pressure drop and flow rate with the system operating curve of the selected fan.

2. Numerical approach

2.1 Problem description and mesh generation

The assembly for the wing bay with an EMA installed is shown in Fig. 1a. The EMA consists of four main components including a motor, drivetrain, gearbox, and electronic box. The electronic box is simulated as a fixed heat source and the considered PPFHS with length L_{hs} (100 mm) and a baseplate thickness t_b of 5 mm is mounted at the bottom of the duct as shown in Fig. 1b. The figure also shows the boundary conditions for numerical simulation as well as the configurations of the PPFHS, partial shield and guide plate. Additional geometrical parameters are given in Table 1 as well. The total bypass height above the heat sink H_{BP} is set at 85 mm. The distance above the partial shield H_b can be determined as $H_b = H_{BP} - H_s$, where H_s is the height of the partial shield. The guide plate height H_p is equal to H_b . The assumptions made in the current numerical model include steady-state operation, three-dimensional flow, and heat transfer, temperature-independent thermophysical properties and negligible radiation heat transfer. These assumptions are valid in typical applications of EMA cooling. The upstream inlet and downstream exit are changed with respect to the heat sink length from $0.5L_{hs}$ to $3L_{hs}$. It is noted that the variations in the maximum baseplate temperature ($TT_{bb,mmmm} - TT_{mm}$) for different upstream and downstream lengths are within 2% of the $TT_{bb,mmmm} - TT_{mm}$ for $0.5L_{hs}$ case. Therefore, for all the simulation cases in the current work, the air inlet and outlet lengths are set to $0.5L_{hs}$.

Table 1 Values of geometrical and thermal parameters considered.

Value	Parameter	
25	Air inlet temperature (T_a), °C	
30	Heat Input (Q), W	
1, 3, 5 and 7	Duct air inlet velocity (V_d), m/s	
125	Duct hydraulic diameter (D_h), mm	
35	Fin height (H), mm	PPFHS Dimensions
1.5	Fin thickness (t_f), mm	
20	Fin number (N)	

5	Baseplate thickness (t_b),
100	Width (W), mm
100	Length (L_{hs}), mm
3.68	Fin spacing (S), mm
85	Total bypass height (H_{BP}), mm
20, 30, 40, 50, 60	Partial shield height (H_s), mm
15, 25, 35, 45, 55	Guide plate inclination angle (θ_p), degree

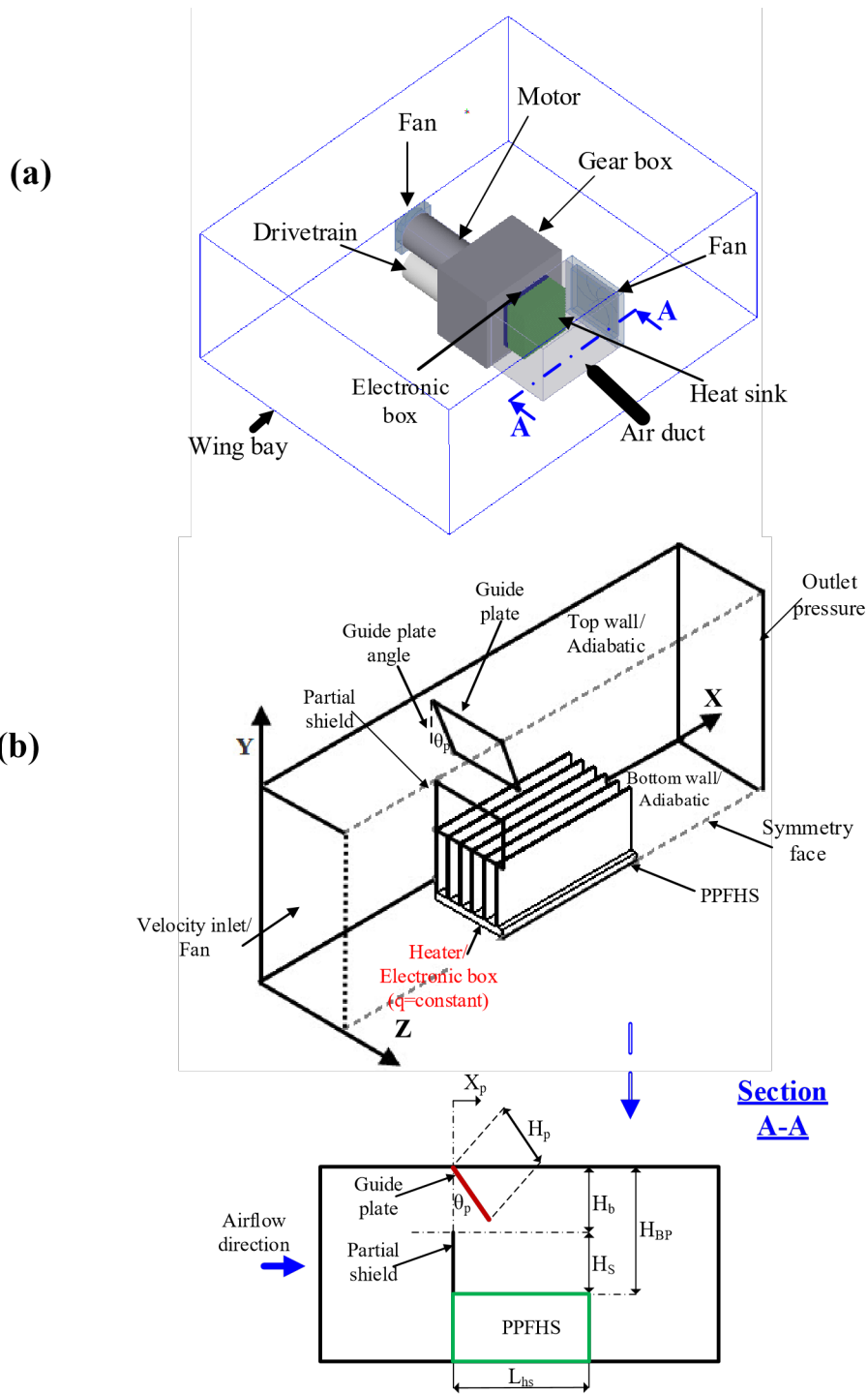


Fig. 1 . (a) Wing bay with EMA assembly, (b) Boundary conditions for heat sink with a partial shield and guide blade.

The temperature and flow fields were calculated numerically with the commercial CFD software ANSYS FLUENT 16 [29], under the following assumptions: steady state, incompressible, turbulent, constant thermophysical properties, and negligible gravitation and thermal radiation effects. The equations governing the fluid are the continuity equation,

Reynolds-averaged Navier–Stokes equation and the energy equation. Based on the assumptions above these equations can be expressed as:

$$\frac{\partial}{\partial x_i}(\rho V_i) = 0 \quad (1)$$

$$\frac{\partial}{\partial x_i}(\rho V_i V_j) = -\frac{\partial P}{\partial x_i} + \frac{\partial \tau_{ij}}{\partial x_j} \quad (2)$$

$$\frac{\partial}{\partial x_i}[V_i(\rho E + P)] = \frac{\partial}{\partial x_i}\left(K \frac{\partial T}{\partial x_i}\right) \quad (3)$$

where, i : is a tensor indicating 1, 2, and 3 and τ_{ij} is the viscous stress tensor.

The RNG (Reynolds Normalized Group) κ - ϵ turbulent model was used to solve the complex turbulent thermal flow field with enhanced wall function approach and viscous heating in the near-wall regions to fit the wall boundary conditions [29]. Equations 4 and 5 are for transport equations for the turbulence kinetic energy (k) and rate of dissipation ϵ , respectively. The numerical solution is assumed to have

converged when the scaled residual of the energy equation reached 10^{-7} , and the scaled residuals of other equations reached 10^{-4} .

$$\frac{\partial(\rho k u_i)}{\partial x_i} = \frac{\partial}{\partial x_j}\left(\alpha_k \mu_{eff} \frac{\partial k}{\partial x_i}\right) + G_k - \rho \epsilon \quad (4)$$

$$\frac{\partial(\rho \epsilon u_i)}{\partial x_i} = \frac{\partial}{\partial x_j}\left(\alpha_\epsilon \mu_{eff} \frac{\partial \epsilon}{\partial x_j}\right) + C_{1\epsilon} \frac{\epsilon}{k} (G_k) - C_{2\epsilon} \rho \frac{\epsilon^2}{k} - R_\epsilon \quad (5)$$

In these equations, G_k is the generation of k due to the mean velocity gradients. The quantities α_ϵ and α_k represent the inverse effective Prandtl number for ϵ and k , respectively. The production term is represented by R_ϵ . The model constants $C_{1\epsilon}$ and $C_{2\epsilon}$ are 1.42 and 1.68, respectively [29].

The Hex/Sub and hex/wedge meshing schemes are used in the current study for the computational domain with mesh refinement near the walls and along sharp or rough edges. To examine the dependence of the present numerical simulation results on the grid density, simulations were carried out with various mesh grid numbers in the X, Y and Z directions. As recommended by FLUENT [29], the y^+ values for the points approaching the walls were maintained between 1 and 5. The grid sensitivity analysis was performed to assure the grid independence of the results. When the grid number was increased above 740,000, only a 0.02% variation in thermal resistance was obtained.

2.2 Thermal and hydraulic performance parameters

In this section, the methods of calculating the parameters needed to evaluate the thermal and hydraulic performance of the PPFHS are described. The thermal performance of the PPFHS is evaluated by calculating the thermal resistance which is defined as:

$$R_{th} = \frac{T_{b,max} - T_a}{Q} \quad (6)$$

where $T_{b,max}$ is the maximum baseplate temperature, T_a is the inlet temperature of the cooling air, and Q is the heat dissipation rate by the PPFHS.

The heat transfer coefficient for the PPFHS is obtained using the Newton's law of cooling:

$$h = \frac{Q}{A_t(T_{b,max} - T_a)} = \frac{1}{R_{th}A_t} \quad (7)$$

The total heat transfer area (A_t) is calculated by

$$A_t = 2NL_{hs}H + (N - 1)SL.$$

The Reynolds number is given by:

$$Re_{Dh} = \frac{\rho V_d D_h}{\mu} \quad (8)$$

where D_h is the hydraulic diameter of the flow cross-section, and μ is the dynamic viscosity of air.

The Nusselt number is calculated as:

$$Nu_{Dh} = \frac{hD_h}{k_f} \quad (9)$$

where k_f is the thermal conductivity of the air.

The friction factor is defined as:

$$f = \frac{2\Delta P}{\rho(L/D_h)V_d^2} \quad (10)$$

where $\Delta\theta$ is the pressure drop across the PPFHS, L is the distance between the upstream and downstream pressure ports. The air thermophysical properties used in the parameters calculation are based on the average temperature of the air flow between the inlet and outlet test section.

2.3 Model Validation

To validate the computational model using the FLUENT software, a comparison between the numerically calculated performance parameters and actual experimental measurement data available in the literature is made and shown in Fig. 2. Several experiments on a PPFHS were done by Shaalan et al. [26]. The PPFHS is similar to the heat sink in the present study, with $N=12$ fins, $H_s=40$ mm and shield angle equals to 90° at various Reynolds numbers. Using the reported relative uncertainty in the experimentally

measured parameters, the calculated uncertainties in Nu_{Dh} and fRe_{Dh} are 2.01% and 3.97%, respectively. Figure 2 shows good agreement between the current numerical model calculations and the experimental measurements. The calculated root mean square discrepancies between the experimental data and

numerical values of Nu_{Dh} and fRe_{Dh} are 2.2 and 5.3%, respectively. With the current model validated, computations were conducted for a heat sink with a partial shield and guide plate with different inclination angles.

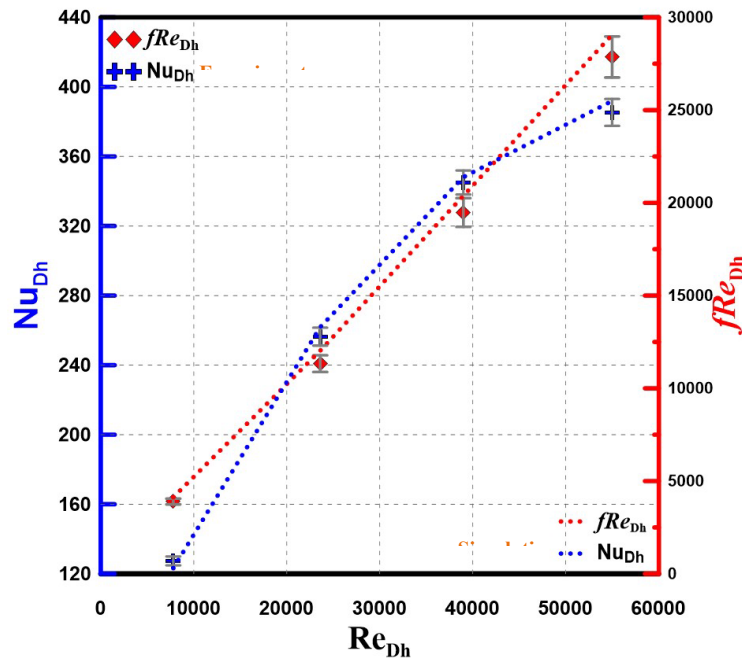


Fig. 2. Comparison of simulation with experimental data at different Reynolds numbers [26]

3. Results and discussion

Two different scenarios of forced convections are considered. For the first scenario, the volume flow rate is fixed at the inlet of the duct. Two sets of results are studied. In the first set, the performance of the heat sink with a partial shield is tested for different values of open area ratio. In the second set, the effect of inserting the guide plate with at different inclination angles is shown. For the second scenario, air flow is driven by a fan with the fan curve specified at the

inlet. The thermal performance of the PPFHS under different partial shield and guide plate configurations is studied and compared with the full shield configuration.

3.1 Partial Shield with different open area ratios

The open area ratio is defined as the ratio between the allowed open area above the partial shield and the total bypass area:

$$\beta = \frac{H_b}{H_b + H_s} = \frac{H_b}{H_{BP}} \quad (11)$$

For the case of the full shield, the values of H_b and β are both zero. With full open bypass the values of H_s and β are 0 and 1, respectively. To get a better understanding of the effect of using a partial shield with different β on the hydraulic/thermal performance of PPFHS, the Nusselt numbers and friction factors are determined for different Reynolds numbers and depicted in Fig. 3. It is clear that the Nusselt numbers for the full shield case are remarkably larger than those for the fully-open configuration (without a shield) for all Re_{Dh} numbers. The variation of the fRe_{Dh} with Re_{Dh} is relatively small for the cases without a shield and short partial shields. The fRe_{Dh} increases with decreasing open area β for cases with the partial shield installation till it reaches a maximum value in the full-shield case. This is attributed to the increase in the frictional losses as the Reynolds number increases and the open area ratio decreases.

This conclusion is similar to the results reported in [24-27].

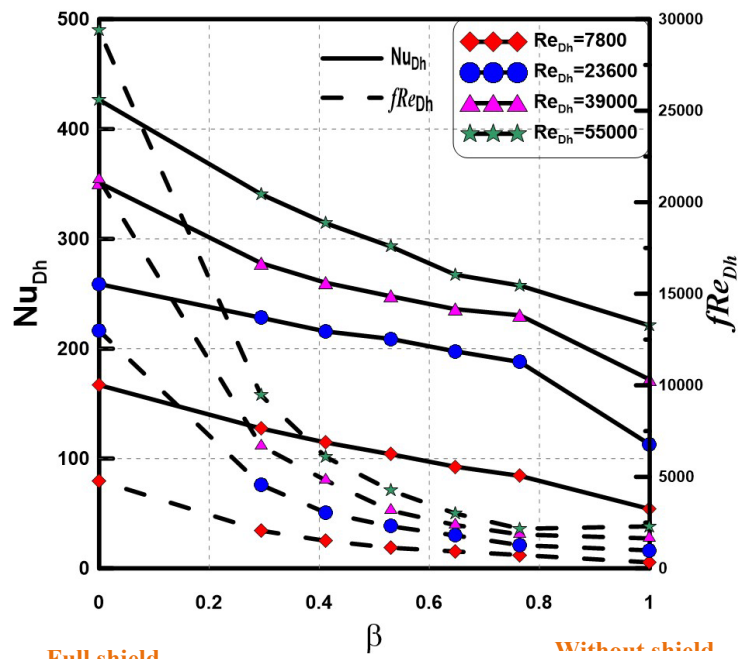


Fig. 3. Variation of Nusselt numbers and friction factors with different Re_{Dh} and β for partial shield cases

3.2 Partial Shield with Guide plate

i. Flow Streamlines

The pressure contours and velocity streamlines at $Re=55,000$ for the full-shield case and the partial shield with guide plate case ($H_s/H_{BP}=0.23$ and $\theta_P=15^\circ$) at the plane of symmetry that passes between two adjacent fins are portrayed in Fig. 4. For the full-shield case, the streamlines show that the blockage by the solid shield forces the cooling air to flow through the PPFHS and increases the air velocity between the fin channels. Nearly all the mass flow rate passes through the fin channels which enhances heat transfer. On the other hand, the blockage effect of the shield increases the upstream pressure which in turn increases the pumping power required for the cooling process. Two vortices are formed in the full shield case as shown in Fig. 4. The first vortex, which is the more significant one, is formed behind the shield while the smaller one is formed after the flow passes the heat sink. Reducing the blocked area can be achieved by using a partial shield only which in turn allows more fluid to bypass the heat sink and alleviate the high pressure formed upstream. It is clear that, adding a guide plate to the partial shield can direct the bypass flow to impinge onto the heat sink top surface and add an extra cooling effect as shown in the velocity contours in Fig. 4. From the pressure contours, the considerable difference in the upstream pressure between the two cases can be clearly noticed. Also, from the streamlines shape of the partialshield with guide plate case, the flow is rather complex. Two vortices are formed behind the partial shield and one additional vortex is created behind the guide plate. The vortex behind the guide plate decreases as the guide plate inclination angle increases which lead to a lower pressure drop. On the other hand the vortices behind the partial shield increase with the partial shield height increase till it reaches the size formed in the full shield case.

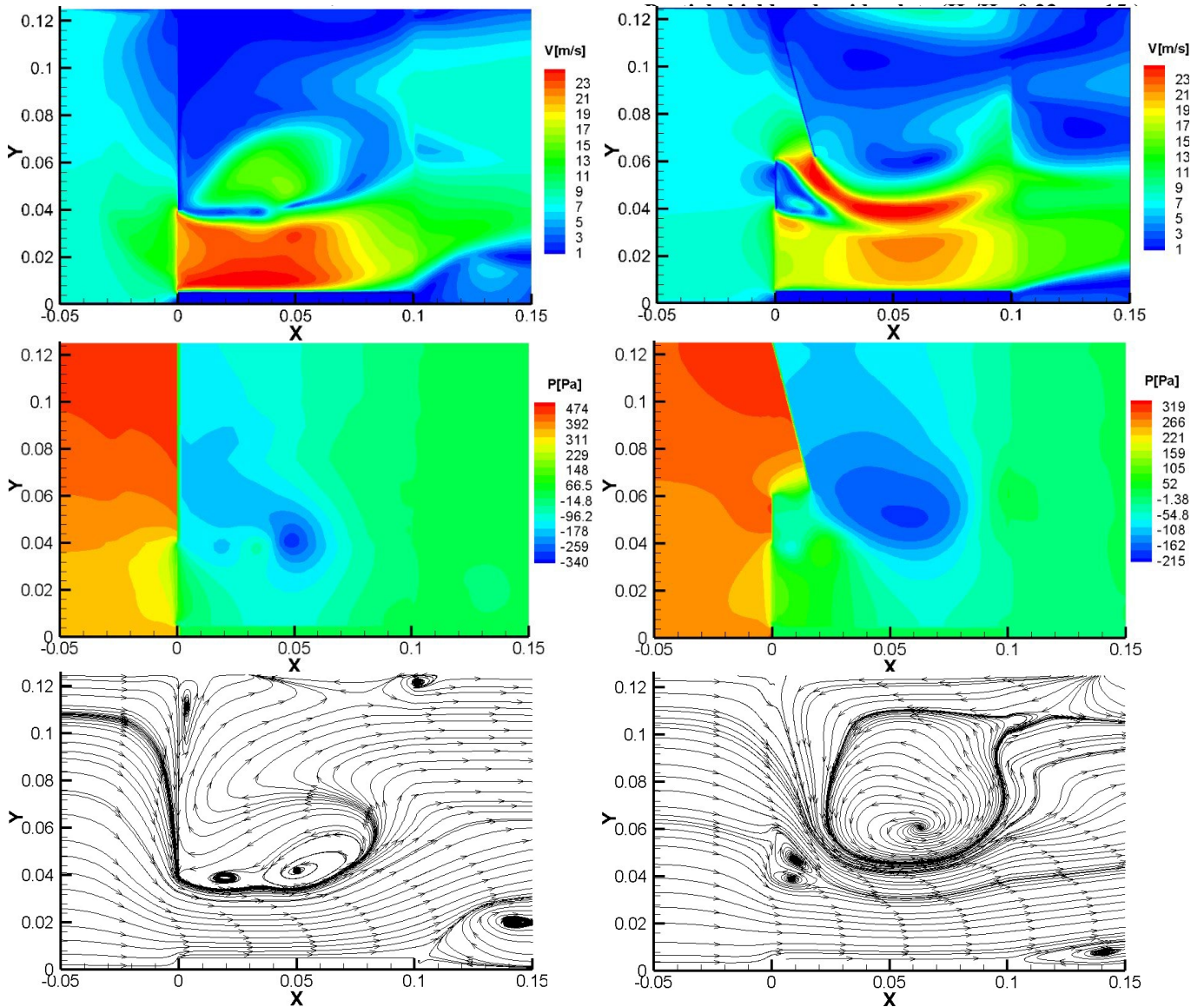


Fig. 4. Velocity contours, pressure contours and velocity streamlines at symmetry plane for $Re=55,000$. Axis dimensions are in m.

ii. Effect of shield height and guide plate inclination angle

The effect of the guide plate and partial shield combination on the thermal and flow performance of the heat sink operating at two different values of Reynolds number is shown in Fig. 5. It is worth to note that the shield height plus the distance above the shield is constant, which is the total bypass distance ($H_{BP}=85$ mm). So as the shield height decreases the guide plate gets closer to the heat sink. For most of the cases, the pressure drop reaches its minimum value when H_s/H_{BP} ranges approximately between 0.35 and 0.5. For higher values of this ratio ($H_s/H_{BP} > 0.5$) the pressure drop is high due to the blockage effect of the partial shield. On the other hand, for lower values ($H_s/H_{BP} < 0.35$) the pressure drop increases due to the flow impingement with the heat sink and the steep turn of the flow around the guide plate and the increased blockage of the guide plate. For the lower Reynolds numbers, similar trends are observed for Nusselt number for θ_p equal to 25° or higher while for the higher Reynolds

numbers, Nusselt number increases or stay nearly constant as the ratio H_s/H_{BP} increases. Also, the figure shows that both the friction factor and Nusselt number decrease significantly with increasing θ_p for all H_s/H_{BP} cases and for both Reynolds numbers. The case of $\theta_p=15^\circ$ has the highest thermal performance and the highest pressure drop. So, choosing the favorable operating conditions for the partial shield with guide plate should be decided by optimizing the shield height and the guide plate inclination angle that produces a higher heat transfer effect with a lower pressure drop penalty.

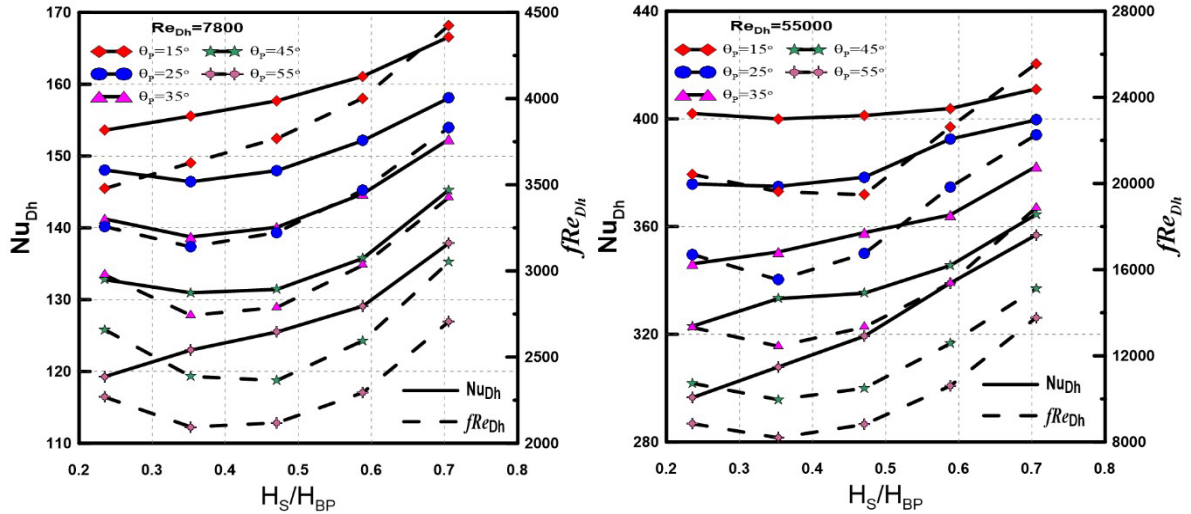


Fig. 5. Nusselt numbers and friction factors versus partial shield height at different guide plate angles

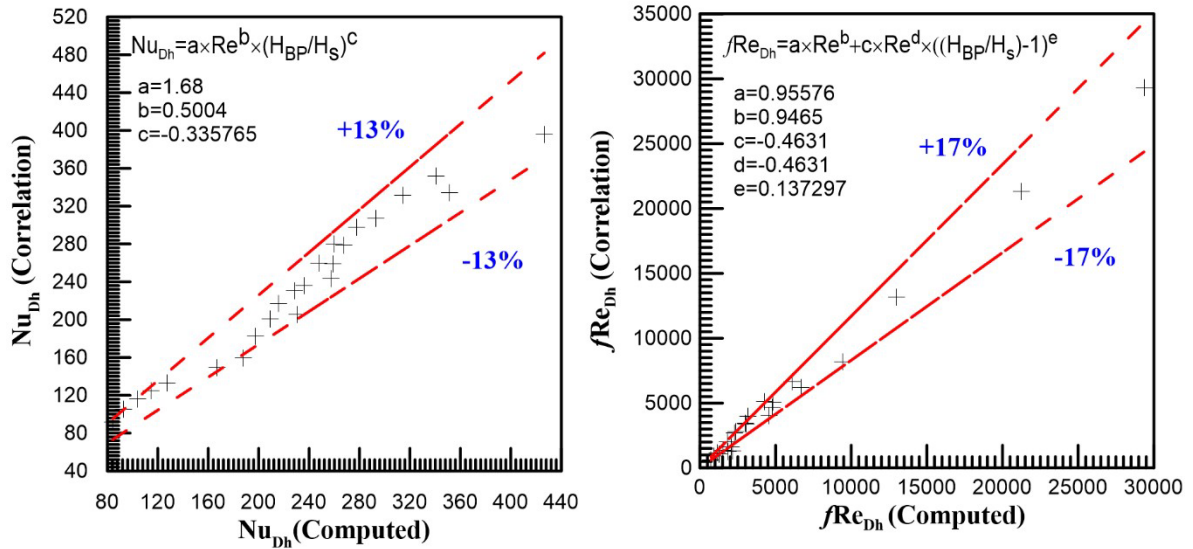
10.1.1.1 3.3 Empirical Correlation

According to the above discussion, the average Nusselt number and the friction factor are dependent on the Reynolds number, H_s and the inclination angle θ_p when a guide plate is used. Considering the previous parameters, correlations for Nu_{Dh} and fRe_{Dh} are derived and presented in Table 2 for both partial shield with and without guide plate. The deviation in Nusselt number correlations is about $\pm 13\%$ for the partial shield without guide plate configuration and $\pm 8\%$ for the partial shield with guide plate configuration. Also, the maximum deviation in the friction factor correlations is about $\pm 17\%$ for both cases. Table 2 shows all the constants and exponents (parameters) estimated for the Nu_{Dh} and fRe_{Dh} correlations for both cases of the partial shield and partial shield with the guide plate. The values of R^2 confirm the statistical goodness of the fit. The obtained correlations are applicable in the ranges mentioned. Also, the performances of the correlations for different cases are shown in Fig. 6.

Table 2 Nusselt number and friction factor correlations for partial shield only and partial shield with guide plate combination.

Correlations Equations	Range and case type	R^2	Error	
$Nu_{Dh} = 1.68(Re_{Dh})^{0.5} \left(\frac{H_{BP}}{H_s}\right)^{-0.336}$	Partial shield	0.964	13%	(12)
$fRe_{Dh} = 0.96(Re_{Dh})^{0.95} - 0.463(Re_{Dh})^{0.993} \left(\frac{H_{BP}}{H_s} - 1\right)^{0.137}$	$7800 \leq Re_{Dh} \leq 5.5 \times 10^4$ $0 \leq \frac{H_{BP}}{H_s} \leq 4.25$	0.993	17%	(13)
$Nu_{Dh} = 2.31(Re_{Dh})^{0.48} \left(1 + \frac{\theta_p}{\theta_{90^\circ}}\right)^{-0.602} \left(\frac{H_{BP}}{H_s} - 1\right)^{-0.041}$	Partial shield with the guide plate	0.991	8%	(14)
$fRe_{Dh} = 1.83(Re_{Dh})^{0.89} \left(1 + \frac{\theta_p}{\theta_{90^\circ}}\right)^{-2.273} \left(\frac{H_{BP}}{H_s} - 1\right)^{-0.162}$	$7800 \leq Re_{Dh} \leq 5.5 \times 10^4$ $0 \leq \frac{H_{BP}}{H_s} \leq 4.25$	0.976	16%	(15)
$15^\circ \leq \theta_{BB} \leq 55^\circ$				

Partial shield



Partial shield with guide plate

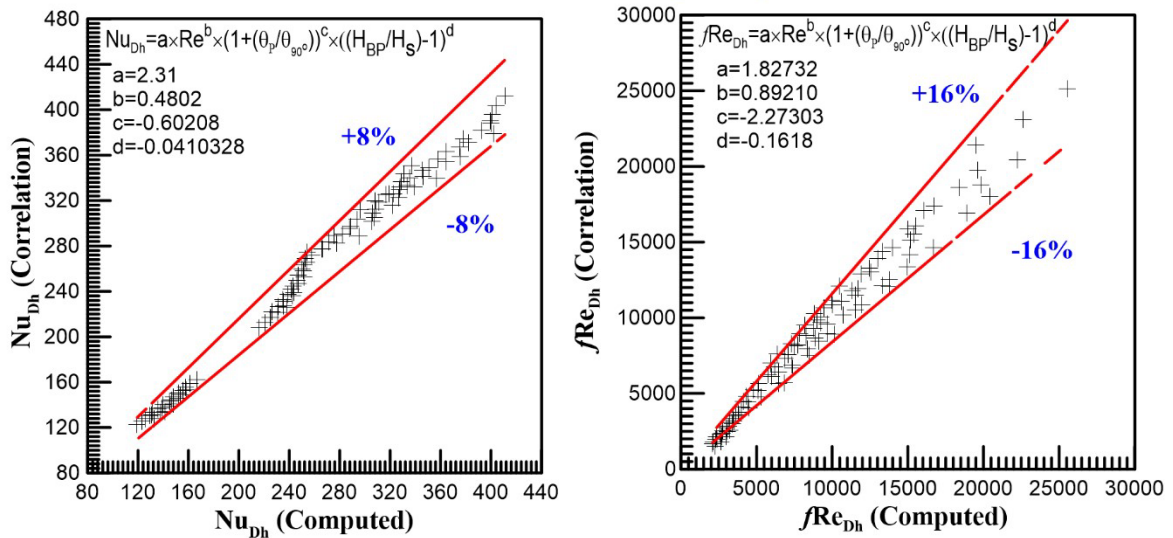


Fig. 6. Correlation performances obtained Nusselt number and friction factor versus computed values.

10.1.1.2 3.4 Performance using an operating fan

In the previous sections, optimization analysis and comparison between different partial shield configurations and partial shield/guide plate combinations are based on a fixed free stream inlet velocity. The inlet velocity approach assigns different inlet velocity values independently without considering the head loss produced. While such similar efforts were reported in numerous papers in the literature as discussed earlier, real applications are less likely to have a constant volume flow rate fan. A more realistic situation is to place a fan that adapts an inverse relationship between head loss and volumetric flow rate [30]. As the pressure drop across the system increases due to flow obstruction associated with lowering the bypass flow, the

volumetric flow rate and in turn the inlet stream velocity decreases. A comparison of thermal performance based on a fixed inlet velocity is therefore not appropriate. Perhaps a better comparison can be made by using an actual fan curve as the inlet boundary condition [31]. The analysis approach in the current section establishes the connection between the thermal performance of a PPFHS with different shield and guide plate installations as in the previous section using the system operating curve for a selected fan. A commercially available fan (Sunon PF92381) is chosen for the current simulation based on the size requirements for the wing bay, rotating speed range and the anticipated volume flow rate and pressure head requirements. The operating fan curve supplied from the manufacturer for the selected fan at its highest speed of 12,000 rpm is used with the fan operating at 12 V. The optimization approach used in the previous sections is repeated with the fan curve mentioned above set as the inlet boundary condition. The guide plate is anchored at the duct ceiling. The guide plate can be positioned at different inclination angles with a length equals the bypass height above the heat sink.

Thermal and hydraulic operating conditions of PPFHS without any installations is selected as the reference case in the present calculations. The different installation combinations are compared with the reference case to assess the overall performance enhancement in the thermal performance of the PPFHS. The variation of $R_{th}/R_{th,ref}$ with H_s/H_{BP} for partial shield only and partial shield/guide plate combination is shown in Fig. 7a and b for fan inlet boundary condition and fixed velocity inlet, respectively. For the cases of guide plate only or PPFHS without any partial shields, the value of H_s/H_{BP} is considered to be equal to zero. A value of $R_{th}/R_{th,ref}$ lower than 1 implies that the overall thermal performance is enhanced compared the reference case. For the installed shield only cases, the highest thermal performance for the PPFHS is attained when the lowest amount of air flow bypasses the heat sink (full shield case $\beta=0$ or $H_s/H_{BP}=1$). For the partial shield with guide plate combination, some important characteristics for different inclination angles can be concluded. For instance, If $\theta_P \geq 35^\circ$, decreasing the partial shield height raises the value of $R_{th}/R_{th,ref}$ which means lower thermal performance. On the other hand, a different situation occurs for $\theta_P < 35^\circ$ where the value of $R_{th}/R_{th,ref}$ increases as H_s decreases but then it decreases with further decrease in H_s . Finally, the $R_{th}/R_{th,ref}$ attains a minimum value for the shortest partial shield installed ($H_s=20$ mm). In this case, the thermal performance is better than the full shield case as shown in Fig. 7a which is attributed to the air flow directed by the guide plate onto the surface of the PPFHS. Figure 7a shows that using a guide plate with a height of $H_P=85$ mm only and the inclination angle of

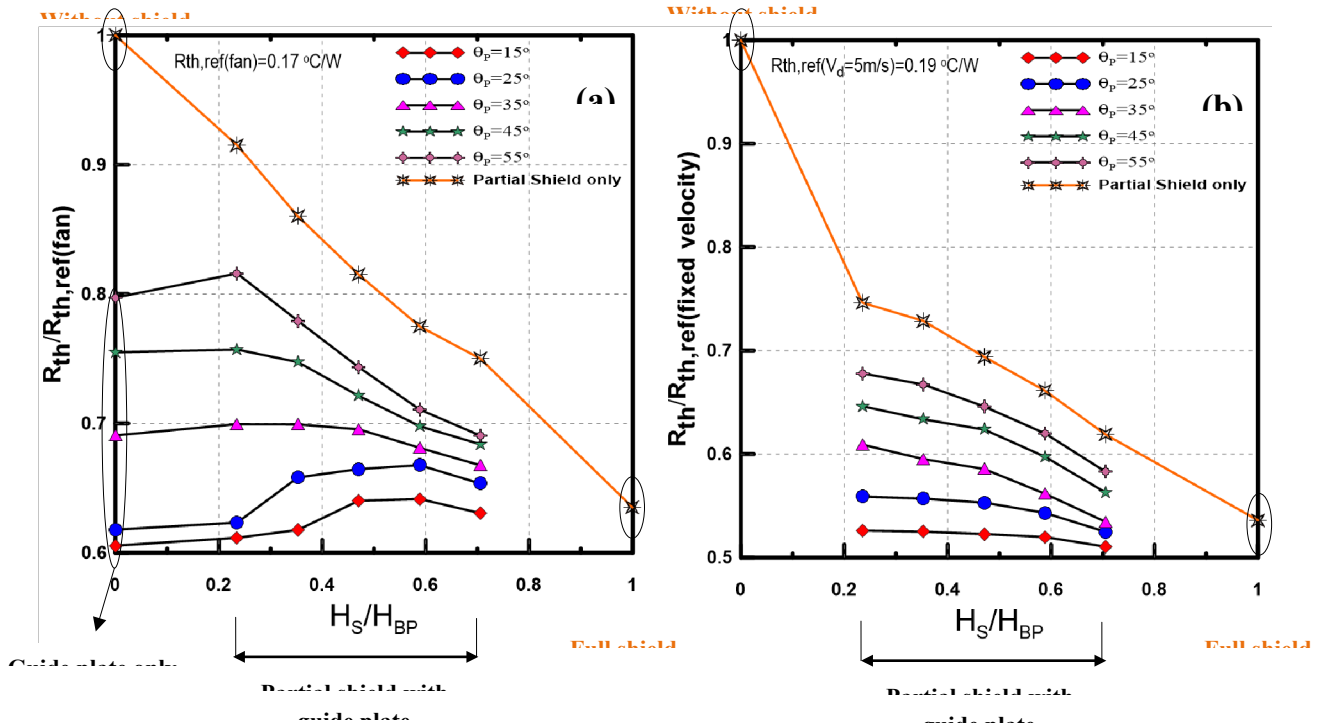


Fig. 7 Thermal performance enhancement due to partial heat shield installation and different guide plate inclination angles for (a) fan curve, (b) fixed velocity 5m/s

$\theta_p=15^\circ$ offers the best thermal performance compared to all tested cases. The air gap between the guide plate and the heat sink directs the bypass air to impinge onto the PPFHS top surface. The selected fan supplies air for all tested cases with an average velocity in the range between 4.2 to 5.4 m/s. To compare with a fixed velocity boundary condition, an inlet air velocity of 5 m/s ($Re=39,000$) is chosen. For the case of a fixed flow rate, the minimum thermal resistance occurs at the largest partial shield height of $H_S/H_{BP}=0.7$ as shown in Fig. 7b. Both inlet boundary conditions show that the $\theta_p=15^\circ$ case has the highest thermal performance at any given H_S/H_{BP} value. But the present analysis with the boundary condition associated with the selected fan to the PPFHS shows other optimal geometrical configurations as shown in Fig. 7a. It worth to note that the results are based on one characteristic curve of the selected fan. The results may change at different fan rotational speeds and different ambient pressure (different altitudes).

The calculated flow rate and the pressure drop (system operating point) the installed heat sink and different partial shield or guide plate combinations together with the Sunon operating fan curve supplied by the manufacturer are shown in Fig. 8. For the partial shield cases, the shorter shield height, the higher is flow rate and the lower is pressure drop. For the guide plate only cases, the larger the inclination angle, the lower is the pressure drop and the higher is the flow rate.

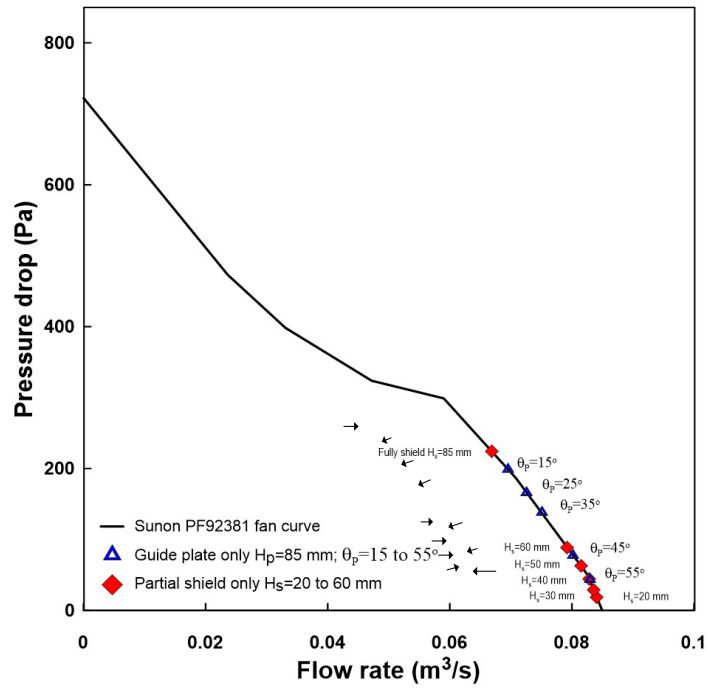
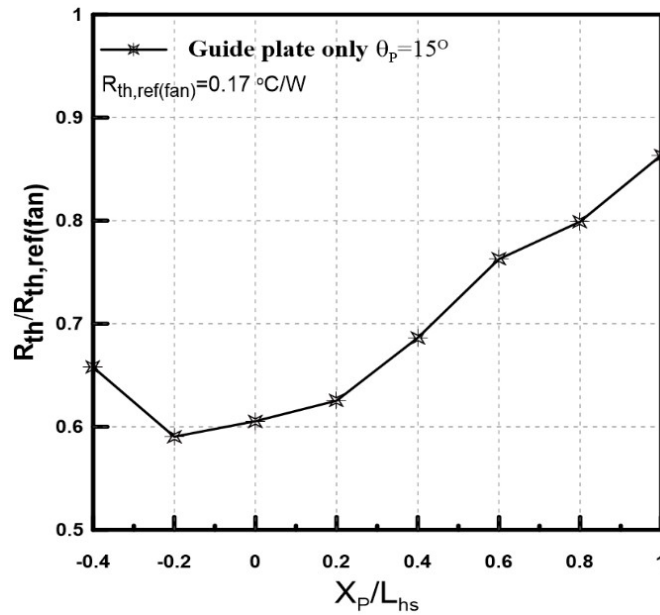
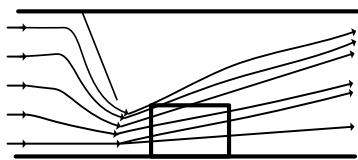


Figure 8 points for various guide plate and partial shield combination along with the fan curve

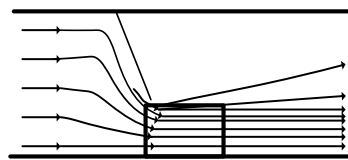


(a)

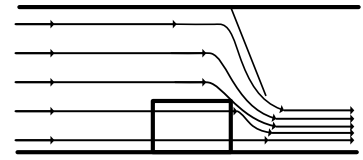
b



$X_p/L_{hs}=-0.4$



$X_p/L_{hs}=-0.2$



$X_p/L_{hs}=1.0$

Fig. 9 (a) Effect of guide plate with $\theta_p = 15^\circ$ on the thermal performance of the PPFHS.

(b) Flow direction for selected guide plate location.

Different positions for the guide plate are proposed and tested to study the effect of the guide plate location on the system thermal performance. Figure 9a depicts the effect of the guide plate ($\theta_p = 15^\circ$) dimensionless position X_p/L_{hs} on the thermal resistance ratio $R_{th}/R_{th,ref}$. The increase in the dimensionless value X_p/L_{hs} implies that the guide plate moves in the direction of the flow. As shown in the figure, the $R_{th}/R_{th,ref}$ ratio increases as the X_p/L_{hs} increases which is attributed to the increase in the flow that bypasses the PPFHS partially which lowers the overall heat transfer. Further increase in the X_p/L exposes the PPFHS to more air bypassing the heat sink and causes more deterioration in the thermal enhancement ratio. On the other side shifting the guide plate against the flow direction lowers the $R_{th}/R_{th,ref}$. However, the ratio increases if $X_p/L_{hs} < -0.2$. The first decrease in $R_{th}/R_{th,ref}$ is due to the maximum use of the air bypass obstruction with the guide plate. In this case, the air with lower temperature is obstructed and constrained to flow faster through the inter-fin channels. The reason for the increase in $R_{th}/R_{th,ref}$ when $X_p/L_{hs} < -0.2$ is because of the increasing gap for the air to bypass the heat sink. The approach flow will take the least resistance path below the guide plate trailing edge as shown in Fig. 9b. So, it is recommended to use a low plate inclination angle and position the guide plate so that the end of the guide plate points at the starting point of the heat sink.

4. Conclusions

The thermal and hydraulic performance of PPFHS is investigated for proper thermal control of the electro-mechanical actuation (EMA) electronics. The inlet conditions adopted are a fixed mass flow rate and a selected fan characteristic curve. For the fixed flow rate inlet condition, the effects of the partial shield height, partial shield and guide plate combinations are studied to obtain the optimal configuration in terms of thermal and hydraulic performance. The inlet velocity cases are repeated for the fan inlet condition and the guide plate only installation is proposed as a possible approach. Based on the detailed results of the current study, the following conclusions can be drawn:

1. Using only a partial shield decreases the large pressure drop caused by the full shield blockage, but this is accompanied by an increase in the thermal resistance. The Nusselt number and the friction factor increase with increase in Reynolds number and decrease in the dimensionless open area ratio.
2. Associating a guide plate with a partial shield directs the bypass air to impinge onto the heat sink and consequently adds an extra cooling effect with a moderate increase in the pressure drop.

3. The pressure drop reaches its minimum value for H_s/H_{BP} between 0.35 and 0.5. The same trend in Nusselt number occurs for low Reynolds numbers for guide plate inclination angles $\theta_P=25, 35$ and 45° , while for high Reynolds numbers, the Nusselt number decreases or stays nearly constant as the ratio H_s/H_{BP} decreases.
4. The friction factors and Nusselt numbers decrease significantly with increasing θ_P for all cases and all Reynolds numbers. For guide plate at $\theta_P=15^\circ$, the highest thermal performance and the highest-pressure drop are achieved.
5. Correlations of the average Nusselt number and friction factor are fitted based on the governing dimensionless parameters (Re_{Dh} , H_{BP}/H_s , $\theta_P/\theta_{90^\circ}$). The predicted values have a maximum deviation for the Nusselt number less than $\pm 17\%$ and the maximum deviation for the friction factor less than 13%.
6. When a Sunon fan curve is employed as the inlet condition, the results show a shorter shield with a small guide plate inclination angle has a better thermal performance compared to the full shield case.
7. Using a guide plate only with a small inclination angle has the best thermal performance among all the tested cases.
8. The effect of the guide plate location is investigated and the optimum location in terms of thermal performance is obtained where the dimensionless guide plate position is $X_P/L_{hs}=0.2$.

Conflict of interest

Authors declare that there is no conflict of interest.

ACKNOWLEDGMENT

This material is based on research sponsored by the United States Air Force under agreement number

FA8650-17-2-2230. The U.S. Government is authorized to reproduce and distribute reprints for Governmental purposes notwithstanding any copyright notation thereon. The views and conclusions contained herein are those of the authors and should not be interpreted as necessarily representing the official policies or endorsements, either expressed or implied, of the United States Air Force or the U.S.

Government.

REFERENCES

- [1] D. Woodburn, T. Wu, L. Chow, Q. Leland, W. Brokaw, J. Bindl, B. Jordan, Y. Ren Lin, L. Zhou, N. Rolinski, Dynamic heat generation modeling of high performance electromechanical actuator, 48th AIAA Aerospace Sciences Meeting Including the New Horizons Forum and Aerospace Exposition, (2010) 290-299. <https://doi.org/10.2514/6.2010-290>
- [2] K. McCarthy, A. Heltzel, E. Walters, J. Roach, S. Iden, P. Lamm, A reduced-order enclosure radiation modeling technique for aircraft actuators, SAE Technical Paper, (2010). <https://doi.org/10.4271/2010-01-1741>.
- [3] W. Wu, Y. Lin, O. Mesalhy, J. Kizito, Q. Leland, L. Chow, Design and Testing of a Cooling Fan for Electro-Mechanical Actuators for Aerospace Applications, Int J Astronaut Aeronautical Eng, 2 (2017).
- [4] A.M. Morega, A. Bejan, S. Lee, Free stream cooling of a stack of parallel plates, International journal of heat and mass transfer, 38 (1995) 519-531. [https://doi.org/10.1016/0017-9310\(94\)00123-D](https://doi.org/10.1016/0017-9310(94)00123-D).
- [5] S.A. El-Sayed, S.M. Mohamed, A.A. Abdel-latif, A.-h.E. Abouda, Experimental study of heat transfer and fluid flow in longitudinal rectangular-fin array located in different orientations in fluid flow, Experimental thermal and fluid science, 29 (2004) 113-128. <https://doi.org/10.1016/j.exptthermflusci.2004.02.006>.
- [6] K. Lau, R.L. Mahajan, Effects of tip clearance and fin density on the performance of heat sinks for VLSI packages, Components, Hybrids, and Manufacturing Technology, IEEE Transactions on, 12 (1989) 757-765. <https://doi.org/10.1109/33.49044>.
- [7] R.A. Wirtz, W. Chen, R. Zhou, Effects of flow bypass on the performance of longitudinal fin heat sinks, Journal of Electronic Packaging, Transactions of the ASME, 116 (1994) 206-211. <https://doi.org/10.1115/1.2905687>.
- [8] R. Shah, Laminar flow friction and forced convection heat transfer in ducts of arbitrary geometry, International Journal of Heat and Mass Transfer, 18 (1975) 849-862. [https://doi.org/10.1016/0017-9310\(75\)90176-3](https://doi.org/10.1016/0017-9310(75)90176-3).
- [9] H. Jonsson, B. Moshfegh, Modeling of the thermal and hydraulic performance of plate fin, strip fin, and pin fin heat sinks influence of flow bypass, Components and Packaging Technologies, IEEE Transactions on, 24 (2001) 142-149. <https://doi.org/10.1109/6144.926376>.
- [10] W. Leonard, P. Teertstra, J. Culham, A. Zaghlool, Characterization of Heat Sink Flow Bypass in Plate Fin Heat Sinks, ASME 2002 International Mechanical Engineering Congress and Exposition, (2002) 189-196. <https://doi.org/10.1115/IMECE2002-39566>.
- [11] E. Elshafei, Effect of flow bypass on the performance of a shrouded longitudinal fin array, Applied Thermal Engineering, 27 (2007) 2233-2242. <https://doi.org/10.1016/j.applthermaleng.2007.01.017>.

- [12] H.-Y. Li, S.-M. Chao, Measurement of performance of plate-fin heat sinks with cross flow cooling, *International Journal of Heat and Mass Transfer*, 52 (2009) 2949-2955. <https://doi.org/10.1016/j.ijheatmasstransfer.2009.02.025>.
- [13] H.-H. Wu, Y.-Y. Hsiao, H.-S. Huang, P.-H. Tang, S.-L. Chen, A practical plate-fin heat sink model, *Applied Thermal Engineering*, 31 (2011) 984-992. <https://doi.org/10.1016/j.applthermaleng.2010.10.014>.
- [14] S. Chingulpitak, N. Chimres, K. Nilpueng, S. Wongwises, Experimental and numerical investigations of heat transfer and flow characteristics of cross-cut heat sinks, *International Journal of Heat and Mass Transfer*, 102 (2016) 142-153. <https://doi.org/10.1016/j.ijheatmasstransfer.2016.05.098>.
- [15] T. Yuan, Computational modelling of flow bypass effects on straight fin heat sink in rectangular duct, *Semiconductor Thermal Measurement and Management Symposium*, 1996. SEMI-THERM XII. Proceedings., Twelfth Annual IEEE, (1996) 164-168. <https://doi.org/10.1109/STHERM.1996.545106>.
- [16] A.V. Barrett, I.F. Obinelo, Characterization of longitudinal fin heat sink thermal performance and flow bypass effects through CFD methods, *Semiconductor Thermal Measurement and Management Symposium*, 1997. SEMI-THERM XIII., Thirteenth Annual IEEE, (1997) 158-164. <https://doi.org/10.1109/STHERM.1997.566793>.
- [17] S. Prstic, M. Iyengar, A. Bar-Cohen, Bypass effect in high performance heat sinks, *ICHMT DIGITAL LIBRARY ONLINE*, (2000). <https://doi.org/10.1615/ICHMT.2000.TherSieProcVol2TherSieProcVol1.340>.
- [18] H.-T. Chen, S.-T. Lai, L.-Y. Haung, Investigation of heat transfer characteristics in plate-fin heat sink, *Applied Thermal Engineering*, (2012). <https://doi.org/10.1016/j.applthermaleng.2012.08.040>.
- [19] H.E. Ahmed, B. Salman, A.S. Kherbeet, M. Ahmed, Optimization of thermal design of heat sinks: A review, *International Journal of Heat and Mass Transfer*, 118 (2018) 129-153. <https://doi.org/10.1016/j.ijheatmasstransfer.2017.10.099>.
- [20] K.-S. Yang, S.-L. Li, Y. Chen, K.-H. Chien, R. Hu, C.-C. Wang, An experimental investigation of air cooling thermal module using various enhancements at low Reynolds number region, *International Journal of Heat and Mass Transfer*, 53 (2010) 5675-5681.
- [21] H.E. Ahmed, Optimization of thermal design of ribbed flat-plate fin heat sink, *Applied Thermal Engineering*, 102 (2016) 1422-1432. <https://doi.org/10.1016/j.applthermaleng.2016.03.119>.
- [22] H.-Y. Li, C.-L. Chen, S.-M. Chao, G.-F. Liang, Enhancing heat transfer in a plate-fin heat sink using delta winglet vortex generators, *International Journal of Heat and Mass Transfer*, 67 (2013) 666-677. <https://doi.org/10.1016/j.ijheatmasstransfer.2013.08.042>.
- [23] S. Prstic, A. Bar-Cohen, "Heat Shield"—An Enhancement Device for an Unshrouded, Forced Convection Heat Sink, *Journal of electronic packaging*, 128 (2006) 172. <https://doi.org/10.1115/1.2188955>.
- [24] H.-Y. Li, G.-L. Tsai, M.-H. Chiang, J.-Y. Lin, Effect of a shield on the hydraulic and thermal performance of a plate-fin heat sink, *International Communications in Heat and Mass Transfer*, 36 (2009) 233-240. <https://doi.org/10.1016/j.icheatmasstransfer.2008.11.012>.
- [25] G.-L. Tsai, H.-Y. Li, C.-C. Lin, Effect of the angle of inclination of a plate shield on the thermal and hydraulic performance of a plate-fin heat sink, *International Communications in Heat and Mass Transfer*, 37 (2010) 364-371. <https://doi.org/10.1016/j.icheatmasstransfer.2010.01.002>.
- [26] M.R. Shaalan, M.A. Saleh, O. Mesalhy, M.L. Elsayed, Thermo/fluid performance of a shielded heat sink, *International Journal of Thermal Sciences*, (2012). <https://doi.org/10.1016/j.ijthermalsci.2012.05.009>.
- [27] Y.-l. Zhang, J.-p. Liu, D.-t. Chong, J.-j. Yan, Experimental investigation on the heat transfer and flow performances of the fin array with shield in bypass, *International Journal of Heat and Mass Transfer*, 56 (2013) 674-682. <https://doi.org/10.1016/j.ijheatmasstransfer.2012.08.008>.
- [28] M.L. Elsayed, O. Mesalhy, Effect of a sotted shield on thermal and hydraulic performance of a heat sink, *J. Electronic Packaging*, 137 (2014) 1-6. <https://doi.org/10.1115/1.4027920>.
- [29] ANSYS FLUENT User's guide, Release 16.0., ANSYS Inc., Canonsburg, PA, (2016).

- [30] J.R. Culham, Y.S. Muzychka, Optimization of plate fin heat sinks using entropy generation minimization, IEEE Transactions on Components and Packaging Technologies, 24 (2001) 159-165. <https://doi.org/10.1109/6144.926378>.
- [31] A. Bhattacharya, R.L. Mahajan, Finned metal foam heat sinks for electronics cooling in forced convection, Journal of Electronic Packaging, 124 (2002) 155-163. <https://doi.org/10.1115/1.1464877>.

NOMENCLATURE

Alphabet- Upper Case

A_t	total convection area of a heat sink, m^2
B	heat sink footprint width, mm
D_h	duct hydraulic diameter, m
E	total energy per unit mass, J/kg
H	fin height, mm
H_s	shield height, mm
H_b	bypass height above the shield, mm
H_{BP}	total bypass height above the heat sink, mm
H_P	guide plate height, mm
L_{hs}	heat sink footprint length, mm
N	number of fins
Nu_{D_h}	Nusselt number using D_h
P_1	channel inlet pressure, N/m^2
Q	heat dissipation rate, W
R_{th}	total thermal resistance, K/W
Re_{D_h}	Reynolds number
T_b	base plate temperature, K
V_d	duct velocity, m/s
X_p	guide plate position

Alphabet- Lowercase h heat transfer coefficient, $W/m^2.K$ s fin spacing, mm f friction coefficient t_f fin thickness t_b baseplate thickness, mm

y^+ dimensionless wall distance. **Greek symbols**

ϵ turbulent dissipation rate, m^2/sec^5

μ absolute viscosity, Pa.s
 ρ density, kg/m³
 θ_{BB} guide plate inclination angle, degree
 ΔP pressure drop, N/m²

APPENDIX N

UCF Project 1626-8282

Quarterly Report # 6

to

North Carolina A&T University

**THERMAL MANAGEMENT OF ELECTROMECHANICAL MACHINES FOR
AEROSPACE SYSTEMS**

University of Central Florida

Department of Mechanical and Aerospace Engineering

Orlando, FL 32816-2450

Louis Chow, PI

Osama Mesalhy Yeong-

Ren Lin

Period: From December 12, 2018, to March 11th, 2019

Date of Report: March 16, 2019

1. Introduction

In this period, we have been able to simulate the flow field in the dual fan system. The considered configuration consists of two fans: upstream fan of 7 blades and downstream fan of 5 blades. When the two fans are attached together, the stator guide blades of the two fans form a diffusing passage between the two rotating blade sets as shown in Figure (1).

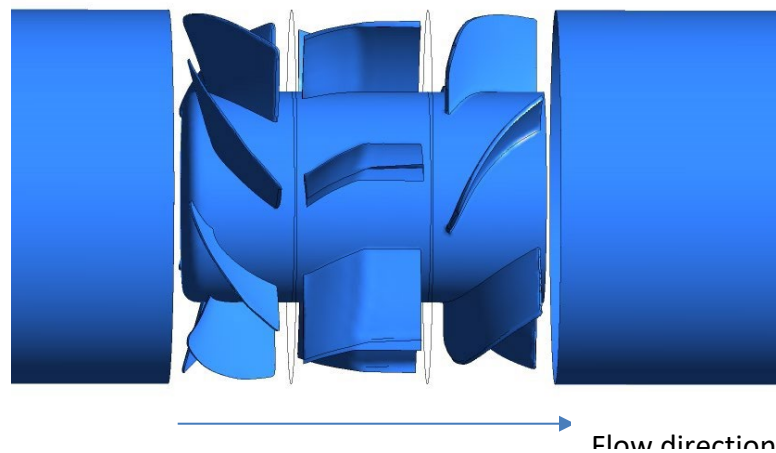


Figure (1) Original dual fan system

The results of the simulation showed that when the downstream fan is running, and the upstream fan is stationary the upstream fan blocks the inlet flow and directs it in a direction which is not consistent with the diffuser inlet angle. This creates a big vortex beside the diffuser blades and generates a considerable pressure drop as the flow passes through the stationary 7-blade and the stator section, as shown in Figure (2). This pressure drop is in the order of 100 Pa. By running the simulation at different back pressure at the flow domain exit, the fan characteristic curve (volume flow rate versus fan static head) can be produced. Figure (3) shows the fan characteristic curve of the dual fan for two cases:

case (1) the upstream 7-blade fan is running at 13000 rpm and 5-blade downstream fan is fixed

case (2) the upstream 7-blade fan is stationary, and the 5-blade fan is running at 10000 rpm

It can be seen from Figure (3) that when the upstream fan is running, and the downstream fan is stationary (case 1) the dual fan performance is much better than case (2). This can be attributed to the blocking of the mass flow rate at the inlet when the upstream fan is kept stationary.

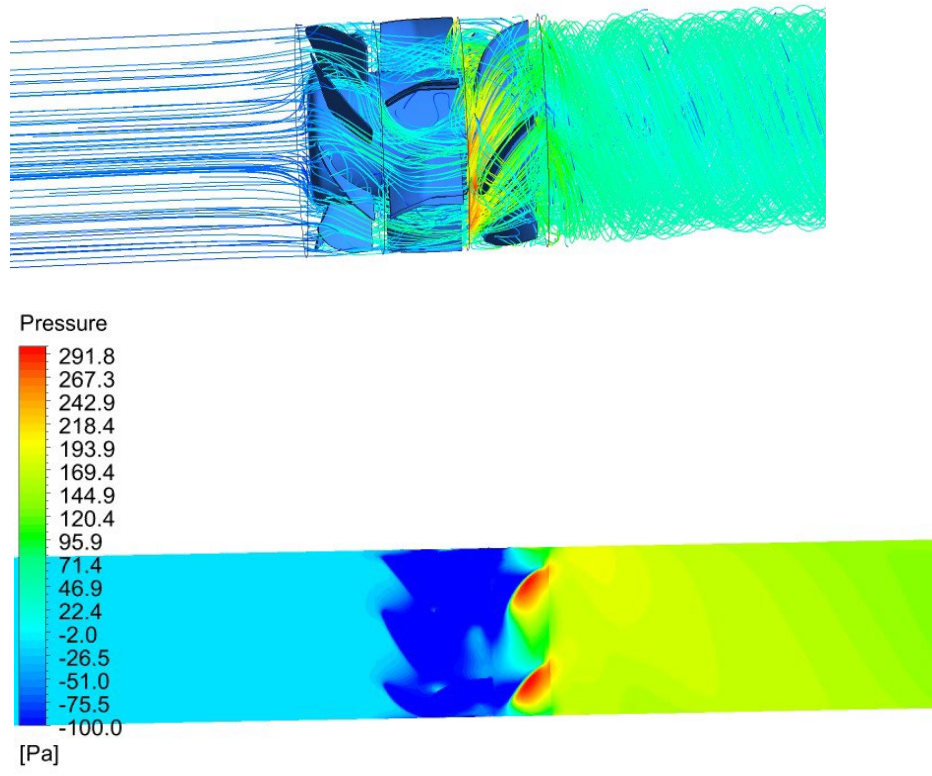


Figure (2) Streamlines and pressure contours for the dual fan system when the 7-blade fan is stationary, and the 5-blade fan is running at 10000 rpm

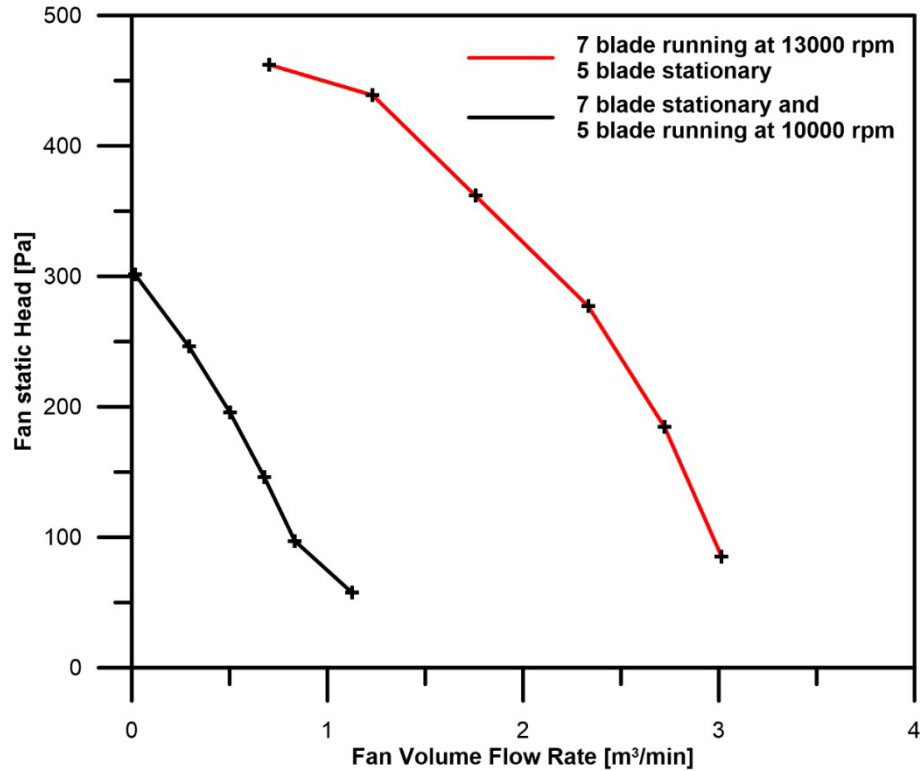


Figure (3) Dual fan curve for the two cases

So, we have tried to study the effect of:

- a- Removing the stator section
- b- Replacing the 5-blade downstream fan with a 7-blade
- c- Using similar two 7-blade fans in back-to-back position or two reflected 7-blade fans to ensure that the dual fan draws the air from the open side

2. Effect of removing the diffuser section from the 7-blade 5-blade dual fan system

The diffuser section is removed from the dual fan assembly as shown in Figure (4). The flow direction still from left to right and one fan is allowed to run while the second fan is stationary.

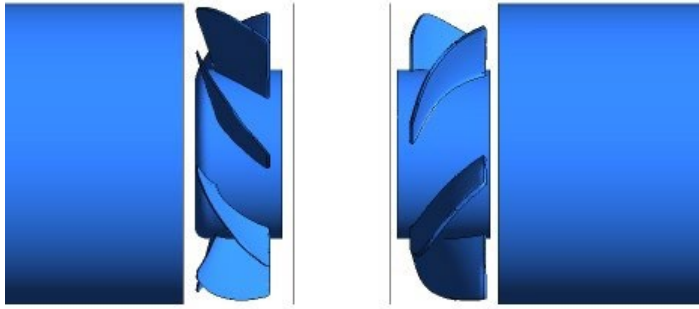


Figure (4) 7-blade 5-blade dual fan without the diffuser section

As shown in Figure (5), when the upstream 7-blade fan is running, the 5-blade downstream fan works as a diffuser and turns the exit flow from the 7-blade fan to the axial direction. So, the presence of the 5-blade fan does not cause a considerable pressure drop as shown in the pressure contours. By comparing the fan performance curve of the dual fan when the upstream 7-blade fan is running with and without the stator section, it can be seen from Figure (6) that removing the stator section improves the performance when the upstream fan is running. The dual fan system can deliver more mass flow rate.

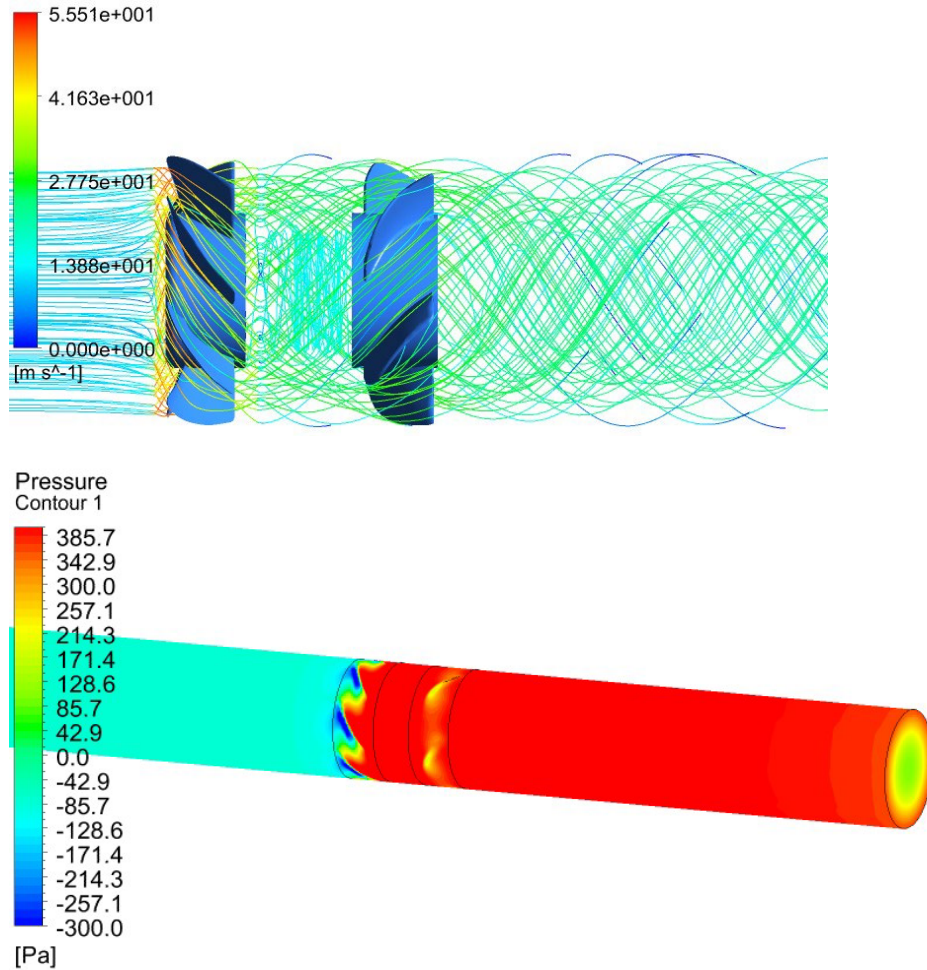


Figure (5) Streamlines and pressure contours when the 7-blade fan is running at 13000 rpm and 5-blade fan is stationary

When the downstream 5-blade fan is running and the upstream 7-blade fan is stationary, the inlet flow to the 5-blade fan becomes so distorted, as shown in Figure (7). This is due to the imparted tangential velocity to the flow when it passes through the 7-blade fan. This significantly reduces the fan performance as shown in Figure (8). The maximum volume flow rate which the dual fan system can produce when the downstream fan is running is about 1 m³/min compared to 3 m³/min when the upstream fan is running. Moreover, as shown in Figure (8), removing the stator section worsens the performance of the dual fan when the downstream fan is running because the presence of the stator section helps in directing the flow to the running fan in the axial direction.

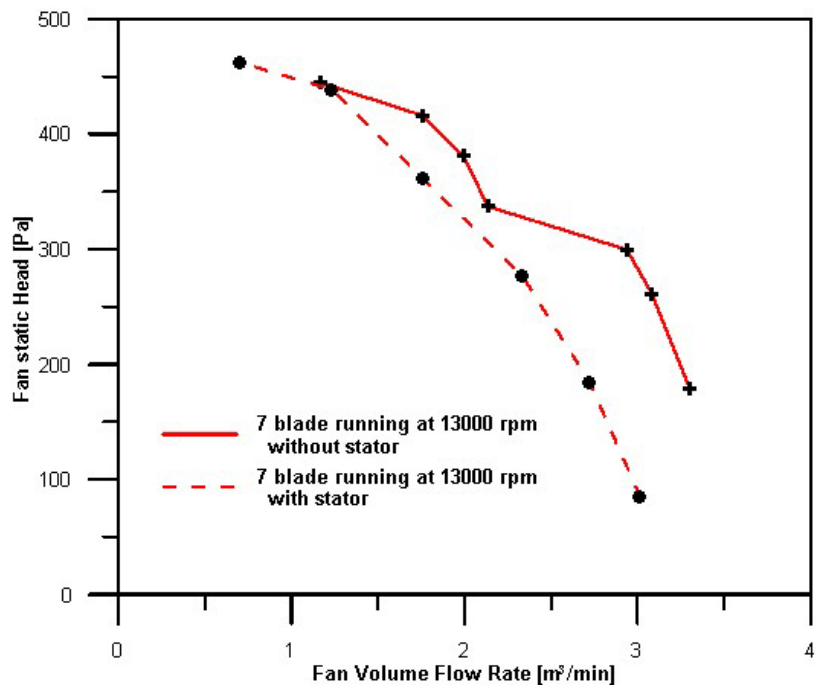


Figure (6) Performance curve of the dual-fan system when the upstream 7-blade is running, and 5-blade is stationary with and without the stator section

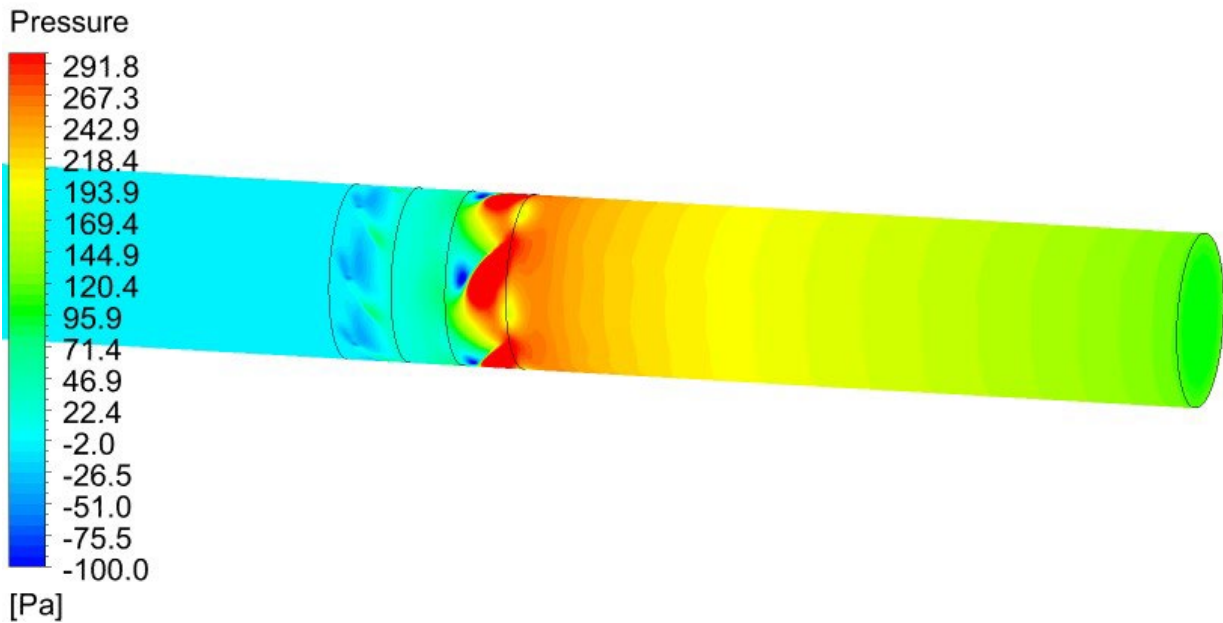
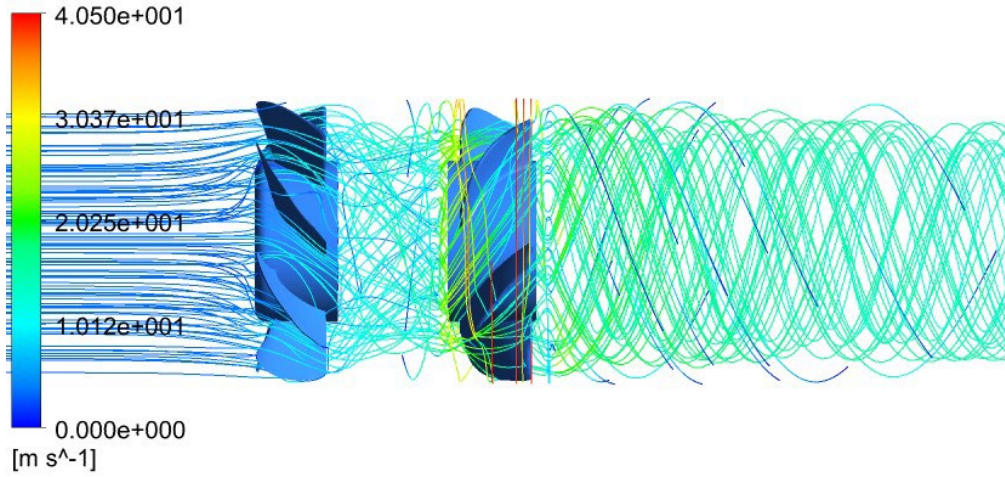


Figure (7) Streamlines and Pressure contours when the 7-blade fan is stationary and 5-blade fan is running at 10000 rpm

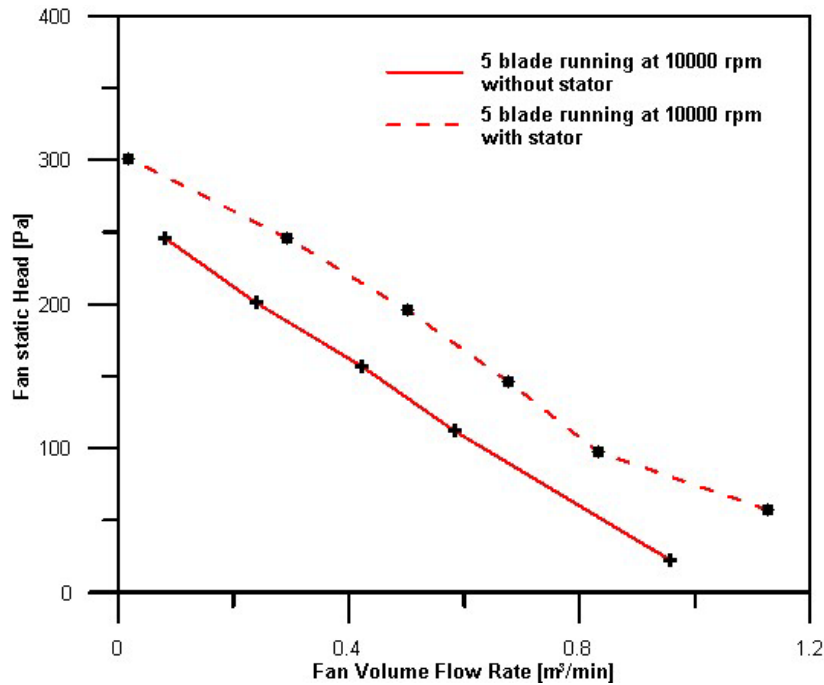


Figure (8) Performance curves of the dual-fan system when the upstream 7-blade fan is stationary and

5-blade fan is running at 10000 rpm with and without the stator section

3. Replacing the 5-blade downstream fan with a 7-blade fan

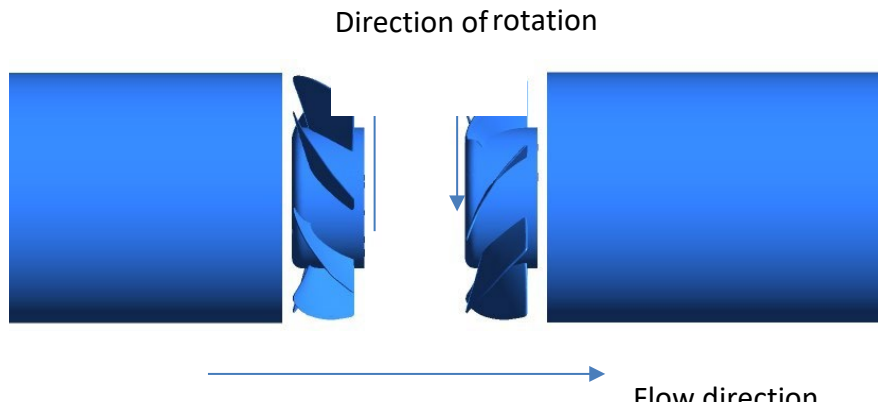


Figure (9) Two 7-blade dual fan system

To check the performance of the 7-blade fan when it operates in the downstream side, the blades of the 5-blade fan in the original system are replaced with seven blades of the same design parameters as the 7-blade fan. In this arrangement, when the two fans run in the counter direction to each other as shown in Figure (9), the direction of the flow will be from left to right. Figure

(10) shows the same conclusion of the superiority of the dual fan when the upstream fan is running. Also, it shows that in the case of running the downstream fan, the 7-blade fan has a better performance than the 5-blade fan. This is because the 7-blade fan runs at 13000 rpm while the 5-blade fan runs at 10000 rpm.

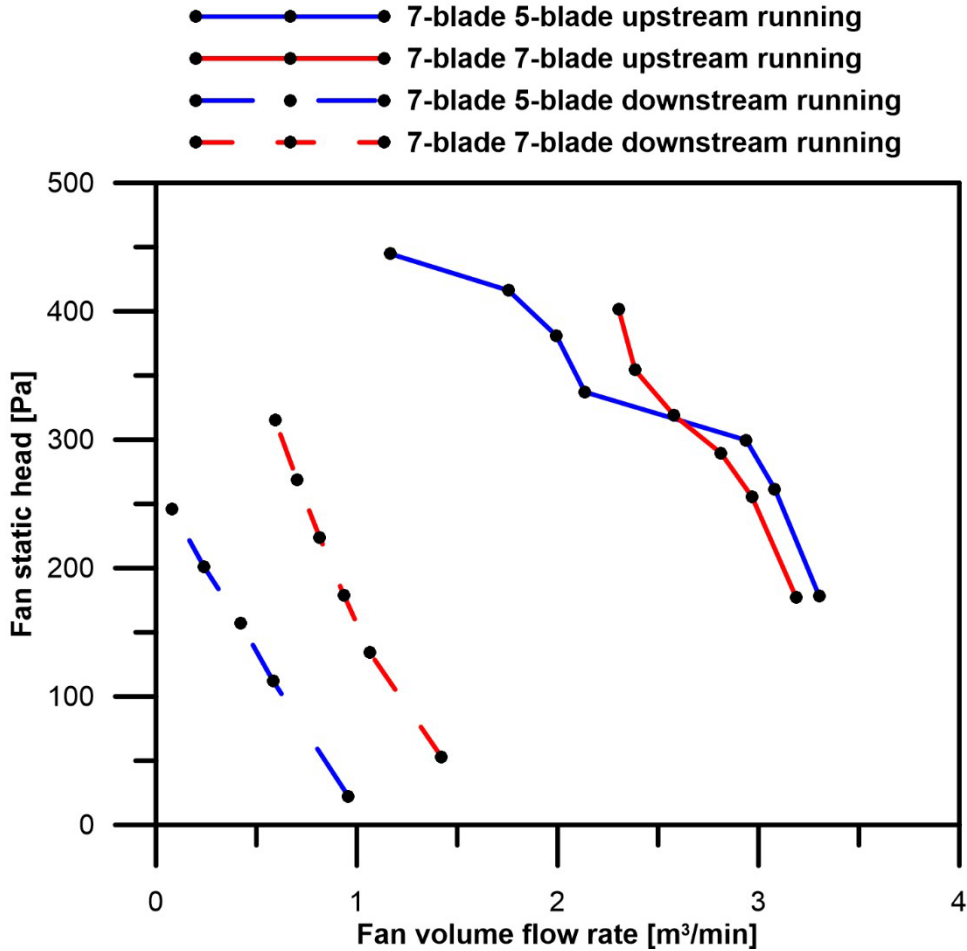


Figure (10) Comparison between 7-5-blade and 7-7-blade systems

4. Using two similar 7-blade fans in back-to-back position or two reflected 7-blade fans

As shown, the performance of the dual fan system deteriorates significantly when the downstream fan is running due to the blocking effect created by the presence of the upstream fan. So, two positions are proposed to ensure that each fan of the dual fan system draws the flow from the open end. These positions are shown in Figure (11). In this case, the flow direction will change from left-to-right and from right-to-left according to which fan is running and which is stationary. In addition, the performance of this system will be the same when any of the two fans runs.

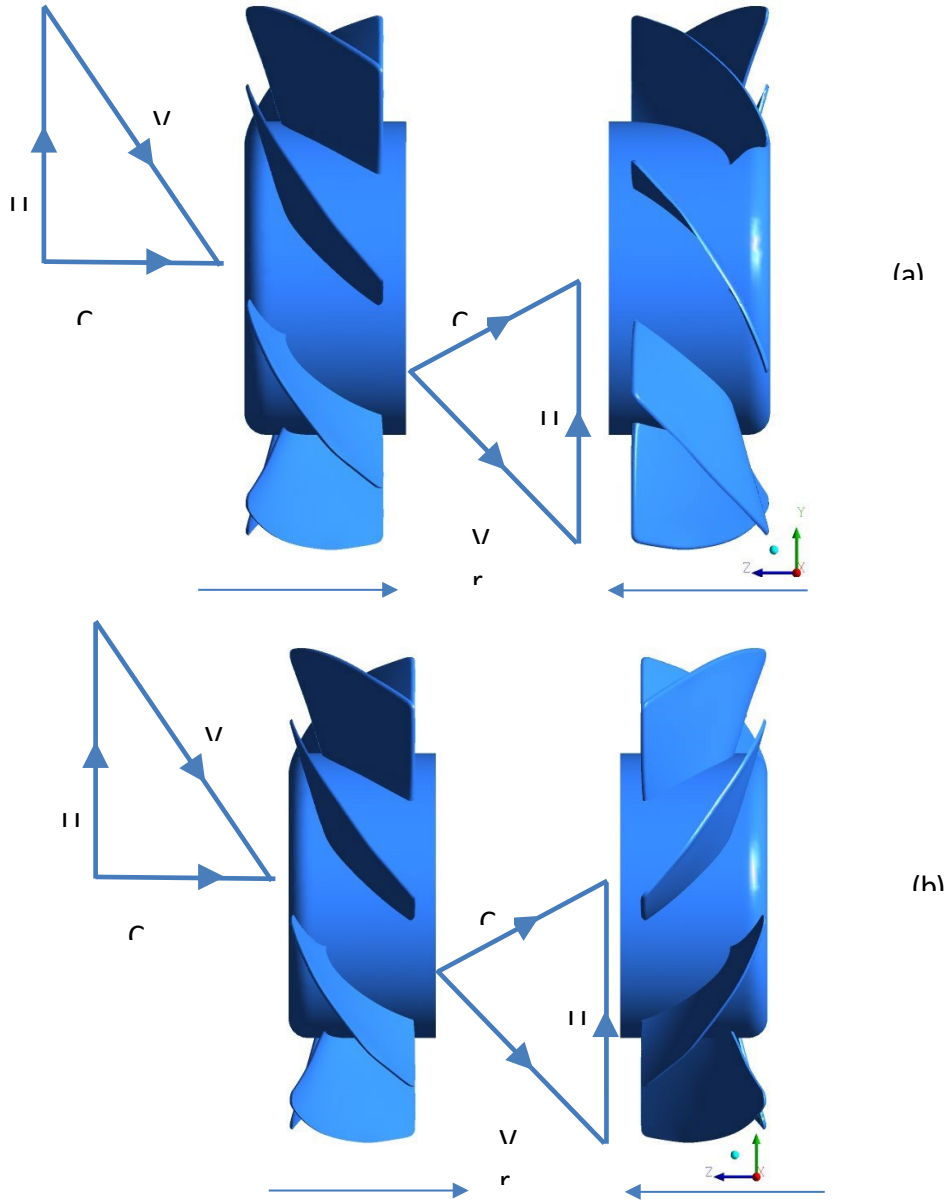
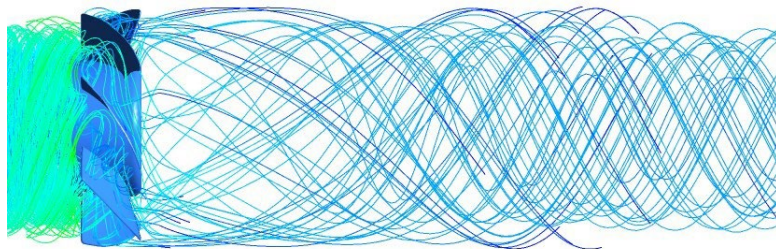


Figure (11) Two 7-blade fans in (a) back-to-back position (b) reflected to each other



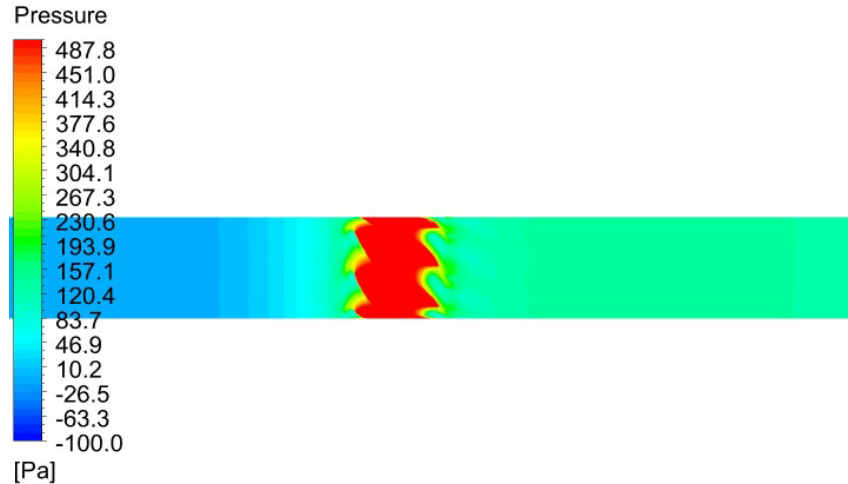
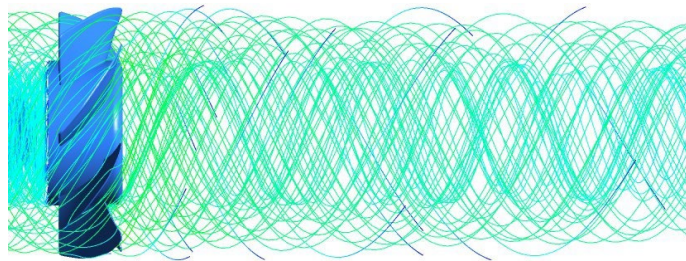


Figure (12) Flow streamlines around stationary fan and pressure contours for the two fans in back-to-back position

For the first arrangement (two 7-blade fans in back-to-back position), the absolute velocity at the exit of the running fan strikes nearly normal to the compression surface of the stationary one as shown from the streamlines in Figure (12) and as indicated by the approximate velocity triangle on Figure (11a). This makes the flow rebound in the opposite direction to the main flow and generates a very high pressure in the region between the two fans as shown in the pressure contours.

For the second arrangement (two reflected 7-blade fans), the absolute velocity at the exit of the running fan flows smoothly in the passages of the stationary fan as shown from Figure (13). However, the passage of the stationary fan behaves as a nozzle for the flow, which produces a pressure drop and a high swirl velocity component to the exit flow from the dual fan system. The high swirl motion generated by the stationary fan results in a higher rate of pressure drop as the air flows toward the flow exit end of the computational domain as shown in Figure (13).



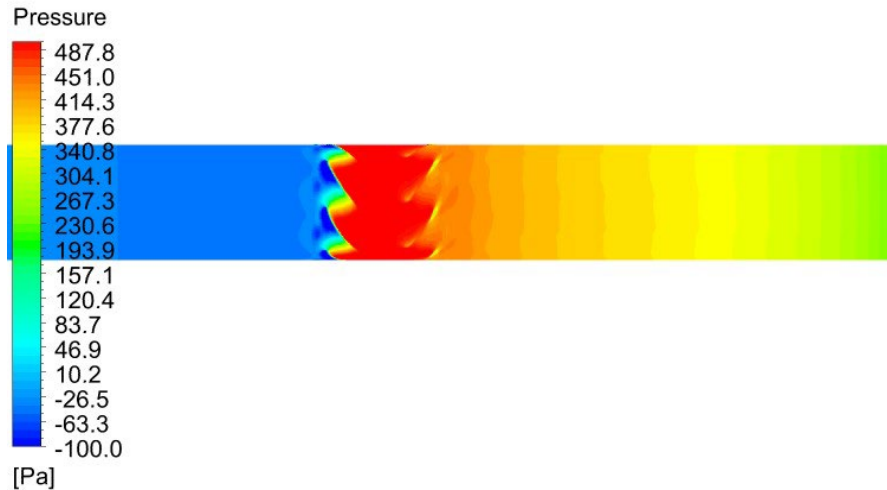


Figure (13) Flow streamlines around the stationary fan and pressure contours for the two reflected 7blade fans

Figure (14) shows the performance of the back-to-back and reflected 7-blade arrangement compared to the high performance two 7-blade dual fan system (when the upstream fan is running). The figure shows that the back-to-back position has the lowest performance. The two 7-blade in reflected position improves the performance but it cannot produce the same air mass flow rate produced by the two 7-blade dual fan when the upstream fan is running.

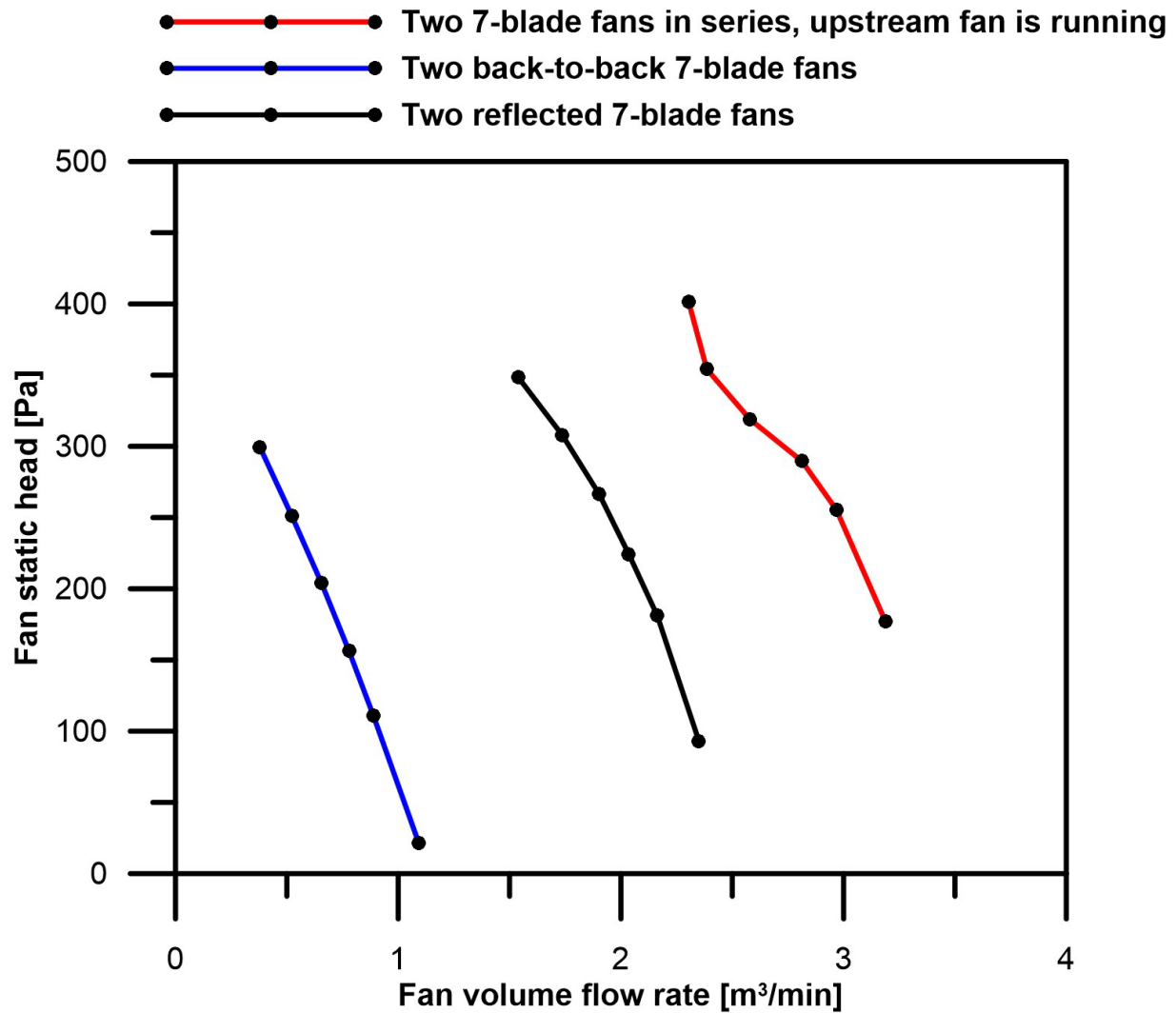


Figure (14) Performance curves of two 7-blade fans in back-to-back and reflected positions compared to two 7-blade fans in series with the upstream fan running

Next, we will try to investigate the effect of changing the distance between the two fans on the performance.

APPENDIX O

UCF Project 1626-8282

Quarterly Report # 7 to
North Carolina A&T University

Thermal Management of Electromechanical Machines for Aerospace Systems

University of Central Florida
Department of Mechanical and Aerospace Engineering
Orlando, FL 32816-2450

Louis Chow, PI
Mohamed Elsayed Osama
Mesalhy

Period: From March 12, 2019, to June 11, 2019

Date of report: June 18, 2019

During the report period, the following manuscript was prepared.

High-altitude Performance of a PPFHS with a Guide Plate for Cooling Electro-Mechanical Actuators

Mohamed L. Elsayed^{a,b,1}, Osama Mesalhy^{a,b}, John P. Kizito^c, Quinn H. Leland^d, Louis C. Chow^a

^aDepartment of Mechanical and Aerospace Engineering, University of Central Florida, Orlando, FL 32816-2450, USA.

^bDepartment of Mechanical Power Engineering, Zagazig University, Zagazig 44519, Egypt.

^cDepartment of Mechanical Engineering, North Carolina Agricultural and Technological State University, USA

^dPower and Control Division, Aerospace Systems Directorate, Air Force Research Laboratory, USA

ABSTRACT

In the present study, the thermal performance of an enhanced air-cooled heat sink system, comprising of a PPFHS with a guide plate installed to alter the bypass flow, was analyzed for forced air convection conditions at various altitudes from sea level to 12,000 m. Numerical simulations were performed in ANSYS Fluent 16.0 using the SST $k-\omega$ turbulence model accompanied by the enhanced wall treatment option to resolve the air flow and evaluate the heat transfer. Numerical results, which were validated with experimental data in the literature, were utilized to investigate the flow and the temperature fields for variable environmental operating pressure, variable operating fan speed and variable design parameters of the PPFHS. Using measured characteristic fan curves at different altitudes shows that the fan delivers approximately the same volume flow at the different altitude conditions. At high altitude operation, using the PPFHS only could lead to electronic failure due to the larger temperature increase compared to the PPFHS/guide plate configuration. For both configurations, the optimum fin number ranges between 20 to 28, which depends on the environmental pressure and fan speed. Improper use of highly dense PPFHS may lead to inadequate electronic cooling while adding extra weight for high-altitude operation. The optimal fin thickness depends on the operating fan speed, and the minimum thermal resistance occurs at low fin thickness at lower fan operating speeds.

KEYWORDS: Heat sink; hydraulic/thermal performance; Electro-Mechanical Actuator; guide plate.

1. Introduction

¹ E-mail: mlea@knights.ucf.edu, mlabelkrem@zu.edu.eg (Mohamed L. Elsayed).

Air-cooled electronic equipment are omnipresent and prevailing in our daily life as they provide many critical functions. For acceptable operational reliability, they should be controlled within a limited temperature range. Furthermore, they are required to operate over a wide range of ambient conditions. Reliable prediction of the operating temperature of electronics is crucial at the early stage of both the electrical and thermal design. For some applications such as avionics, the required high processing speed with consideration to volume and weight often result in an increase in component packaging and heat flux density [1]. This requires high heat dissipation rates for these devices to avoid localized hot spots around the devices which lead to high junction temperature and low reliability [2].

With the growth in dissipation rate, electronics cooling designers gravitate to several options in high-capacity cooling. Forced-air cooling is an attractive approach because of weight and ease of maintenance considerations. A fan is often used to force air to flow through the heat sink attached directly to the electronics to remove heat for the electronics [3]. Clearly, this method of acquiring and discarding heat to the ambient depends on the temperature and pressure of the ambient air. For aerospace applications such as cooling of the electronics and motors of electromechanical actuators (EMA) in aircraft, the ambient condition varies significantly with the altitude and geographical location of the aircraft. At high altitude, for the same fan speed, the low air density leads to a reduction in air mass flow rate passing through heat sinks which in turn degrades the convective cooling effectiveness. This results in an increase in the operating temperature of the electronics. Other applications where altitude is an important consideration include: (i) High-reliability, harsh-environment avionics, and airborne instrumentation; (ii) Global medical/industrial applications situated in high-mountain peaks such as observatories and highpower server systems. Experiments and investigations conducted at sea level environmental conditions may remarkably under predict the operating temperature at of electronics at high altitudes.

Thermal management of high-altitude electronics using air-cooled heat sink schemes has only been scarcely addressed in the literature. However, there is an extensive literature in sea-level thermal management of electronic systems in steady-state and transient situations using both experimental and numerical approaches. For instance, several researchers reported forced air cooling using parallel plate fin heat sink (PPFHS) with/without bypass which offer the best combination of high heat transfer and low pressure drop for high-performance heat sinks. The reported results using experimental, analytical, and numerical approaches are described in detail in [4-17]. Moreover, Khattak and Ali [18] and Ahmed et al. [19] reviewed most of the reported work in the literature related to PPFHS. They reported several PPFHS performance improvement methods such inter-fin spacing turbulence promoters using vortex generators (VG) [20], ribs insert [21] and tip clearance (bypass) flow turbulator [22-28]. On the other hand, there have been a gap in the published literature for thermal management of air-cooled PPFHS with any heat transfer improvement methods at high altitude such as 12,000 m above mean sea level (ASL).

One of the first contributions to the aircraft wing bay electronic equipment cooling to study the effect of environmental conditions was done by Steinberg [29]. Simple equations were used to analyze the performance of printed circuit board (PCB) with uniform heat flux. His results indicate that under highaltitude conditions, the density changes should be considered to avoid large pressure drop errors to ensure adequate cooling air flow. Failure to do this could dramatically increase the electronic components temperature when compared to sea-level conditions. Bar-Shalom [30] provided a guidance to determine the thermal design parameters to improve the performance of high-altitude avionics cooling systems and to identify the flight condition causing critical thermal conditions. However, the electronics and cooling systems geometrical information were not studied in detail. A simplified

numerical simulation was performed to predict the effect of reduction in air density on the performance of a desktop computer

PPFHS in [31]. However, there was no clarification for the method he used to adjust the environmental conditions to represent the altitude considered. Belady [32] studied the effect of variable air density on airflow impedance curve for a circular duct using fan scaling laws without performing any experiments or numerical simulation for altitude changes up to 3,000 m. He concluded that the component temperature increase between the inlet and outlet of a system is inversely proportional to the density ratio. Furthermore, the heat transfer coefficient for laminar flow remains constant with altitude change, but for turbulent flow it is a function of air density and volumetric flow rate to the 0.8 power. With the absence of costly 3D Computational Fluid Dynamic (CFD) resources, simple correction factors usually have been considered sufficient if large design margins were assumed to cater any unforeseen circumstances. Still, there are not as precise as a good CFD model or experimentally measured temperature at high altitude, and in many cases lead to overdesigned systems with lots of inefficiencies [33]. For instance, Rhee and Azar [34] proposed various correction multipliers analytically to predict temperature rise at different altitudes for high-altitude electronic cooling application. However, the altitude effect on fan performance was not considered. Xu [35] proposed correction factors through nondimensional correlations for any flow regimes to determine the impact of high-altitude conditions on high power CPU unit based on sea-level measured data. For a fixed volumetric air flow rate, thermal performance degradation is air flow rate dependent, and varies from 5% to 30%. At a low air flow rate, altitude change has a drastic impact on thermal resistance.

Mansuria [36] performed experiments on an entire IBM personal computer at different altitudes up to 2550 m. The reported maximum rise in the average temperature of various parts of the computer was 20% compared to sea level condition. Experiments conducted by Wong and Peck [37] extended the effect of altitude change up to 5,000 m at air speed from 1 to 5 m/s on the thermal performance of PCBs without heat sinks placed in wind tunnel. Their results show that the heat transfer coefficient decreases with increase in altitude and increases with increase in air velocity. They concluded that the heat transfer coefficient decreases by 2.8% per km increase in altitude. The effect of the altitude change on the fan performance was not discussed as the flow rate changes were compensated with air velocity increase.

Many people may be surprised that cooling at high altitude can be done without adding the great complexity of a pressurized system or liquid cooling. This paper describes fan cooling at high altitude although much of the information can be used with forced air-cooling systems at sea level. As mentioned above, a careful literature search reveals that the thermal/hydraulic performance assessment and optimization/improvement of the PPFHS are mainly focused on the development of air-cooled systems working at sea-level conditions. There is a scarcity of experimental data and correlations that describe/predict the performance of air-cooled systems under high-altitude operating conditions. This is especially true for turbulent/laminar flow in the presence of flow bypass. For this reason, this paper aims to study the thermal performance of PPFHS undergoing forced convection at different environmental operating conditions. Furthermore, the impact of the considered PPFHS geometrical variables such as fin thickness and fin density on the hydraulic/thermal performance are investigated as well. Following the trend in the literature to enhance the thermal performance of PPFHS, the tip clearance (bypass) is altered by installing a guide plate to direct the bypass flow to impinge at the PPFHS. The most recent work was presented by Elsayed et al. [38] in this regard, introduced and proved that installing a guide plate in comparison to shield plate direct the bypass flow to impinge at

the PPFHS which improves its thermal performance. Although this work was very promising, there were some restricting assumptions that led to a limitation regarding the information that could be obtained from the simulations. To address those major issues, we propose a new and more complete version of numerical model which is more representative to how real EMAs electronic are operated. Therefore, the merit of using the guide plate with PPFHS has been assessed compared to the stand alone PPDHS under the bypass flow condition at different environmental conditions. Comprehensive performance evaluations of the PPFHS with different fin thickness and fin numbers are presented to find the optimum configuration that gives the minimum thermal resistance. It is worth mentioning that the current optimization is focused on the air flow under selected fan curves as inlet boundary condition which is considered to be a much more realistic scenario than a specified inlet approach velocity used in the PPFHS optimization studies in the literature.

2. Problem description and numerical approach

Abrupt change in boundary condition can occur in minutes, still the avionics must operate over this wide range of ambient conditions. Therefore, the presence of varying (dynamic) boundary conditions, and the superfluity in power dissipation, have posed a major challenge on the design of a successful cooling system for the thermal management of military electronics. In addition to the aforementioned concerns, complexity to the design of the cooling solution is appended due to the unique reliability requirements of such electronics and the issue of weight. For a considerable number of air/space-borne electronic equipment, weight is a crucial consideration. Typically, an over-weighted payload means lower mission duration and higher operational costs, both of which play a pivotal role in a thriving mission launch. For example, hydraulic actuator systems are commonly used in aerospace and air-defense industries due to high-power density/reliability. However, recently, attention has been focused on their limitations that include weight and high maintenance requirements with the consideration of EMAs as a solution to these limitations. Analyses carried out by Boeing showed that electrically powered technology can provide considerable weight reduction, cost savings and greater reliability/efficiency [39]. Regardless of the benefits of EMAs, they are not without drawbacks such as exposure to overheating due to high heat dissipation. Therefore, the inability to handle the generated heat in this critical component may cause failure to the mission objective and loss of aircraft [40, 41]. Usually, an EMA and its internal components are housed in a wing bay which is an unpressurized enclosure detached from the air flow from the aircraft environmental control system (ECS). These wing bays are exposed to changes in the ambient conditions and the air condition inside resembles the ambient condition at a given altitude. For a typical flight wing bay EMA system without forced air cooling, overheating of the power electronics occurs when the temperature exceeds the designed operating temperature chosen to be 107°C for 200 W heat load [41].

2.1 Solution domains and boundary conditions

Figure 1 shows the main components of the EMA system for flight control which include motor, gearbox, drivetrain, and electronic box situated inside wing bay assembly. Most of the heat need to be dissipated is generated in the motor followed by the electronic box. The electronic box provides power and control to the motor of the EMA. For this type of electrical actuation system, the motor is a totally enclosed fan cooled (TEFC) motor where air is driven by a fan to flow over the fins situated on the circumference of the motor outside frame. Similar cooling approach is used to the electronic box which is considered as a fixed heat source and is placed on the side of the gearbox unit. In the present study, the PPFHS is selected due to simplicity in design, low pressure drop and high thermal performance. The geometrical parameters of the considered PPFHS are shown in Fig. 1a where the length, width,

height, and baseplate thickness are 100 mm, 100 mm, 40 mm, and 5 mm, respectively. The total bypass height above the heat sink H_{BP} is set at 60 mm which is equal to the guide plate height H_p . The remaining design parameters are given in [Table 1](#).

The heat sink and air computational domains are depicted in [Fig. 1a](#). The boundary conditions for the PPFHS and the guide plate are shown in [Fig. 1b](#). Three-dimensional fluid flow/heat transfer, incompressible flow and steady-state computation domain are considered as valid assumptions for the numerical solution of typical applications in air-cooling of EMAs. Furthermore, radiation heat transfer, buoyancy/body forces (natural convection) and viscous dissipation are neglected. No-slip and adiabatic conditions are assumed for the top/bottom/side walls and the guide plate placed in the bypass region as well. The symmetrical condition is assumed for the side wall passing through the middle of the PPFHS to reduce computational cost. A relative pressure of 0 Pa is set at the outlet boundary of the air domain. A fixed heat flux boundary condition was set at the bottom of the PPFHS to simulate the electronic box generated heat. The heating power for the entire PPFHS footprint is 100 W, which is 10^4 W/m² in terms of heat flux. The thermal contact resistance between the fin baseplate and the electronic box surface is neglected. The inlet boundary condition is provided by the fan curve condition which is considered to be a more realistic situation that adapts an inverse relationship between head loss and volumetric flow rate [[42](#), [43](#)]. This choice of inlet boundary condition is more applicable for fan-driven air flow as compared to assigning different inlet velocity values independently without considering the head loss produced. As the pressure drop across the system increases due to flow obstruction associated with lowering the bypass flow, the volumetric flow rate and in turn the inlet stream velocity decreases. A commercially available fan (Sunon PF92381) is chosen for the current simulation based on the size requirements for the wing bay, rotating speed range and the anticipated volume flow rate and pressure head requirements. The fan curve supplied by the manufacturer of the selected fan operating at its highest speed of 12,000 rpm and at 12 V is used for the sea-level condition, while the measured fan curves from [[3](#)] are used at different altitudes. The inlet fan boundary condition is defined by a piecewise-linear profile of pressure jump in terms of normal velocity and specific rotational speed.

The PPFHS is fabricated from extruded aluminum and has a thermal conductivity of 205 W/m.K. Based on air property data, we assume that the thermal conductivity and specific heat of air are only secondary order parameters. Therefore, assigned values for air thermal conductivity and specific heat capacity are fixed at 0.0261 W/m.K and 1.005 kJ/kg.K, respectively. The remaining thermophysical properties such as air density and viscosity are considered to be altitude, ambient pressure, and temperature dependent. The inlet section of the computational domain is extended by half of the PPFHS length to assure a developing velocity profile and the outlet section is also extended by a similar distance as the inlet portion to overcome the convergence related issues originated from the PPFHS outlet reversed flow. Therefore, for all simulations cases, the lengths of the upstream inlet and downstream exit are set relative to the

PPFHS length as $0.5 L_{hs}$.

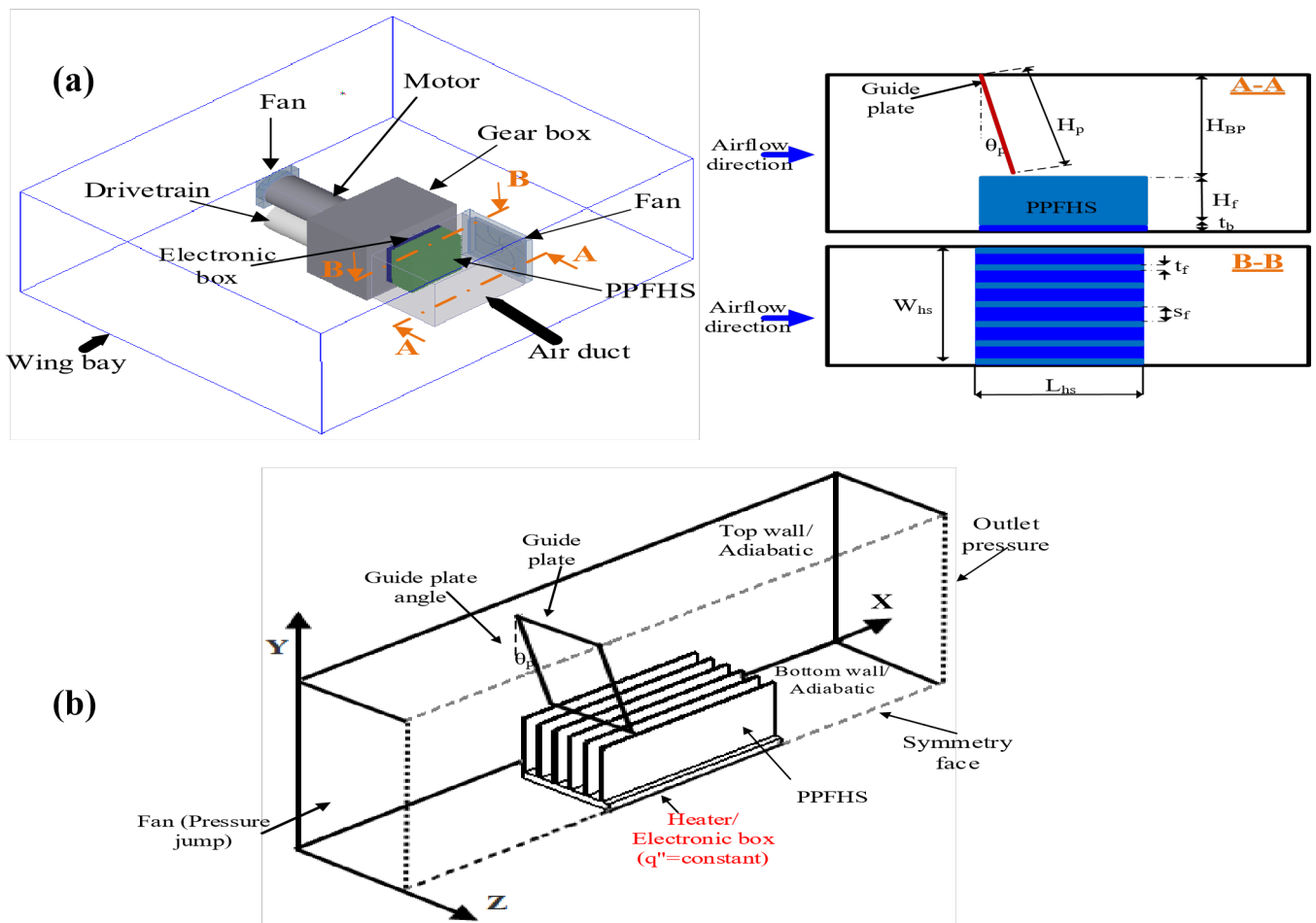


Fig. 1 . (a) EMA component assembly housed in aircraft wing bay and solution domain with geometrical parameters of the PPFHS, (b) Boundary conditions for heat sink with guide blade.

Table 1 Design parameters of PPFHS for numerical investigation. Unit: mm.

PPFHS		Duct		Guide plate, GP		
Thickness of base, t_b	5	Length of duct, L_d	200	Height of GP, H_p	60	
Width of base, W_{hs}	100	Height of duct, H_d	100	Angle of GP, θ_p	15°	
Length of base, L_{hs}	100	Width of duct, W_d	100	test matrix parameters		step
Length of fin, L_f	100	Hydraulic diameter of duct, D_h	100	Fin number, N_{fin}	12:40	4
Height of fin, H_f	35	Total bypass height, H_{BP}	60	Fin thickness, t_r	0.2:2	0.3

Fan speed, N_{fan}	6,000: 12,000 rpm	3000
Altitude-effect, P	1.0, 0.7, 0.5, 0.2 atm	

2.2 Governing equations

Based on the above mentioned assumptions, the simplified governing equations of continuity, momentum and fluid/solid domain energy under the selected boundary conditions can be expressed in tensor form, respectively as following;

$$\frac{\partial}{\partial x_i}(\rho u_i) = 0 \quad (1)$$

$$\frac{\partial}{\partial x_j}(\rho u_i u_j) = -\frac{\partial P}{\partial x_i} + \frac{\partial}{\partial x_j} \left(\mu \frac{\partial u_i}{\partial x_j} \right) \quad (2)$$

$$\frac{\partial}{\partial x_j}[\rho T u_j] = \frac{\partial}{\partial x_j} \left(\frac{\mu}{Pr} \frac{\partial T}{\partial x_j} \right) \quad (3)$$

$$\frac{\partial}{\partial x_j} \left[K_s \frac{\partial T}{\partial x_j} \right] = 0 \quad (4)$$

i : is a tensor indicating 1, 2, and 3.

Typically, for turbulent flow, most of the reported work in the literature employed $k-\epsilon$ and $k-\omega$ turbulence models, where the standard $k-\omega$ and the $k-\epsilon$ are able to predict the near-wall region flow in the near-wall region and to determine far-field free-stream independence, respectively. A refined model of $k-\epsilon$ named RNG $k-\epsilon$ is able to resolve the flow accurately not only at high, but also at low Reynolds numbers [44]. To merge the powerful and precise formulation of the previous models ($k-\omega$ and $k-\epsilon$), the shear stress transport (SST) $k-\omega$ turbulence model was proposed by Menter [45]. It is considered as a hybrid model or a combination between the standard $k-\omega$ model and the converted $k-\epsilon$ model to the $k-\omega$ model formulation. The SST $k-\omega$ model is more accurate and efficient for a broad type of flow conditions, such as flow over airfoils and adverse pressure gradient flows. Furthermore, the model was proven to be able to accurately solve the flow through rectangular ducts and the flow separation over smooth surfaces [46, 47] and has been selected in the current study. The SST $k-\omega$ models is based on Reynolds-averaged Navier–Stokes and the energy equations and has two transport equations for the turbulence kinetic energy (k) and the turbulence kinetic energy specific dissipation rate ω as shown in equations 5 and 6, respectively.

$$\frac{\partial(\rho k u_i)}{\partial x_i} = \frac{\partial}{\partial x_j} \left(\Gamma_k \frac{\partial k}{\partial x_j} \right) + \widetilde{G}_k - Y_k + S_k \quad (5)$$

$$\frac{\partial(\rho \omega u_i)}{\partial x_i} = \frac{\partial}{\partial x_j} \left(\Gamma_\omega \frac{\partial \omega}{\partial x_j} \right) + G_\omega - Y_\omega + D_\omega + S_\omega \quad (6)$$

In these equations, and G_ω are the k and ω mean velocity gradients generation; Γ_{kk} and $\Gamma_{\omega\omega}$ are the k and ω effective diffusivity; Y_{kk} and $Y_{\omega\omega}$ are the turbulence dissipation of k and ω ; S_{kk} and $S_{\omega\omega}$ are the k and ω source terms and are user defined and finally, $D_{\omega k}$ represents the cross-diffusion term. Further details about above terms and the required model constants are reported in [44]. Turbulent intensity and turbulent length scale were the method selected to define turbulence quantities at the fan intake side and the outlet side. The fan intake and backflow turbulent intensity was set to 10% whereas the fan intake and backflow turbulent length scale was set to 0.0095 and 0.01 m. There are no limiting conditions considered to describe turbulent quantities at the walls

2.3 Solver settings

The governing equations are solved to calculate the temperature and flow fields using the commercial CFD software ANSYS FLUENT 16 [44]. SIMPLEC algorithm was used for pressure-velocity coupling with second-order upwind differencing as the discretization scheme for the momentum, turbulent kinetic energy, and the turbulent dissipation rate. To discretize the governing equations, the high-resolution transient scheme is considered where the iteration of numerical solutions is repeated until the convergence is achieved. The convergence criterion was set when the scaled residual root mean square (RMS) errors of all parameters such as continuity, x-y-z velocities, k , ϵ , ω are less than 10^{-6} and less than 10^{-7} for the energy equation. In addition to the residuals convergence criteria, the outlet pressure/temperature weighted average values were assured to attain a steady state value before the termination of the calculations. Conducting these simulations using ANSYS Workbench 16.0 on Intel i7-7700HQ processor at 3.8 GHz with 4 cores, the simulations time varied between 4 to 10 h depending on the heat sink structure, guide plate presence and altitude effect. For instance, the simulations for PPFHS only with bypass condition converged faster at sea-level ambient conditions compared to the one with guide plate installation. Moreover, the total run time of the simulations for the PPFHS with guide plate installed was significantly longer at higher altitude and this could be attributed to the lower flow rate delivered by the fan which affects the convergence criterion.

2.4 Numerical data reduction

The temperatures and pressures of air at different simulations conditions were estimated using mass weighted averages reporting, while the PPFHS temperatures were estimated using area-weighted averages reporting of all the considered values of the cells at the considered boundaries. The ANSYS Fluent mass/area-weighted averaging methods for any parameter, ψ , is calculated as:

$$\psi_{mass-weighted} = \frac{\sum_{i=1}^n \psi_i \rho_i |\vec{u}_i \cdot \vec{A}_i|}{\sum_{i=1}^n \rho_i |\vec{u}_i \cdot \vec{A}_i|}, \quad \psi_{area-weighted} = \frac{1}{A} \sum_{i=1}^n \psi_i |A_i| \quad (7)$$

Following similar approach, the air mass flow rate is determined as follow at different section in the duct;

$$\dot{m}_{air} = \sum_{i=1}^n \rho_i \vec{u}_i \cdot \vec{A}_i \quad (8)$$

The thermophysical properties air employed in the calculation of the performance parameters are based on the mean temperature of the air flow between the inlet and outlet test section. Therefore, the average air velocity through any section of the duct is;

$$u_{d,avg} = \frac{\dot{m}_{air}}{\rho_{air@T_{mean\ air}} A_{flow\ cr\ sec}} \quad (9)$$

where for the duct inlet, the mean air temperature is considered the ambient condition at different altitudes

and the cross-sectional area is the duct area

$$A_{flow\ cr\ sec} = W_d \times H_d.$$

Thus, the average Reynolds number is calculated as:

$$Re_{Dh,avg} = \frac{\rho_{air@T_{mean\ air}} u_{d,avg} D_h}{\mu_{air@T_{mean\ air}}} \quad (10)$$

where D_h is the hydraulic diameter of the flow cross-section, and μ is the mean dynamic viscosity of air.

Newton's law of cooling is employed to determine the average heat transfer coefficient as:

$$h_{avg} = \frac{Q_{conv}}{A_t (T_{b,max} - T_a)} \quad (11)$$

where, A_t is the total heat transfer base area of the heat sink and is calculated by $A_t = NL_{hs}(2H + t) + (N-1)SL_{hs}$.

The convective heat dissipation rate (Q_{conv}) by the PPFHS to the air and the calculated as:

$$Q_{conv} = Q_{heater} - Q_{loss} \quad (12)$$

where, Q_{loss} represents the in energy through conduction and radiation. Throughout the entire simulated cases and different altitudes, the value of losses was assumed to be fixed as 4% of the supplied power to

the heater (Q_{heater}) as reported in [48].

Finally, the PPFHS thermal/hydraulic performance parameters, such as the thermal resistance, Nusselt number and dimensionless friction factor are calculated as:

$$Nu_{avg} = \frac{h_{avg} D_h}{K_{air@T_{mean\ air}}} \quad (13)$$

$$R_{th} = \frac{T_{b,max} - T_a}{Q_{conv}} = \frac{1}{h_{avg} A_t} \quad (14)$$

$$f = \frac{2\Delta P_{stat} D_h}{\rho_{air@T_{mean\ air}} u_{d,avg}^2 L_{stat}} \quad (15)$$

where K_{air} is the thermal conductivity of the air; $T_{b,max}$ is the maximum baseplate temperature, T_a is the inlet temperature of the cooling air; ΔP_{stat} is the pressure drop across the PPFHS, L is the distance between the upstream and downstream pressure ports.

2.5 Grid method and grid independence

For all computational domains, the hex/sub (structured) meshing scheme is employed except the domain above the PPFHS where the guide plate is located as the hex/wedge (non-uniform structured) mesh is used. Mesh refinement near the walls and along sharp or rough edges in contact with air are carefully considered to keep the y^+ values for the points approaching the walls < 0.5 to stratify the selected enhanced wall treatment (EWT) criteria and resolve the boundary layer. Therefore, layers of boundary layer mesh that is slowly growing was created with thickness that start at 0.01 mm. It worth to mention that due to the structure of PPFHS variation, this led to a change in the generated mesh size. Therefore, to obtain accurate simulation results with an adequate mesh points or elements (grid density), a comprehensive grid independence was conducted with different mesh grid numbers in X-Y-Z directions. This was implemented to attain the least number of cells in which the solution is considered established by monitoring the values of thermal resistance and friction factor, regardless the increase of the generated mesh size. When the utilized grid number increases above 5×10^5 elements a 0.1% variation was attained in thermal resistance for coarse PPFHS (less fin numbers). On the other hand, an increase in the grid numbers for dense PPFHS above 2×10^6 leads to a less than 0.13% change in the thermal resistance. Therefore, for the computational domain in the current work, the considered mesh counts were varied approximately between 5×10^5 and 3.2×10^6 .

2.6 Model Validation

As mentioned above in the introduction section, there is a dearth of published data available in the literature related to the high-altitude electronics cooling especially the real operation of these type of cooling systems. Manufacturers of these types of cooling systems, perhaps due to competition reason, are not revealing their systems performance or the sensitivity associated with the application. Therefore, unfortunately, the validation if the current proposed configuration of PPFHS with guide plate at different altitudes, is not possible because no air-cooling setup on the same layout of that under investigation has ever been experimented before. Two approaches were adopted, the first approach was to rely on the developed model which has been validated vs experimental data to study the current configuration of guide plate and PPFHS [38]. The second approach was to find the most suitable configuration of air-cooled system under various altitude operation. This approach led to a high-altitude lab-controlled experiment that simulates the electronic cooling using PPFHS without bypass (confined) flow [48]. Racine [48], performed several high-altitude experiments on coarse ($N=6$ fins) PPFHS with

comparable footprint dimensions as the one proposed in the present work ($L=10$ cm, $W=4.6$ cm, $H=3.2$ cm) to study forced convection cooling of EMA at high altitudes as shown in Fig. 2. Open-loop wind tunnel was constructed with a fan (AMETEK Rotron Propimax 2L 3715SF) installed at the inlet of the tunnel to supply air through and a heater/PPFHS at the bottom of the tunnel. To simulate the conditions of high altitude up to 12,000 m above sea level, the entire tunnel and associated equipment were situated in an environmental controlled chamber as shown in Fig. 2. The average reported relative uncertainty in the measured performance parameters such as R_{th} and fR_{Dh} are 2.95% and 1.2%, respectively. In order to rigorously test the model validity, two different operating velocities (Max/Min) were selected at various environmental operating pressure equal to 1.0, 0.8, 0.6, 0.4 and 0.2 atm. Firstly, Fig. 2 shows the measured performance parameters and the associated error bars due to uncertainty measurements which shows how high-altitude operation decreases the pressure drop and at the same time thermal resistance drastically increases. The surrounding figures to Fig. 2 were solely depicted for each operating pressure to clearly show the comparison between the current computational model simulation results using ANSYS FLUENT software and the experimental measurement data provided in [48]. The average absolute root mean square discrepancies between the experimental and simulated data are 2.2 and 5.3% for R_{th} and fR_{Dh} , respectively which indicates an excellent agreement between the simulation and the measured experimental data. After the validation of the present numerical model, further numerical computations were developed and performed for a PPFHS with a guide plate.

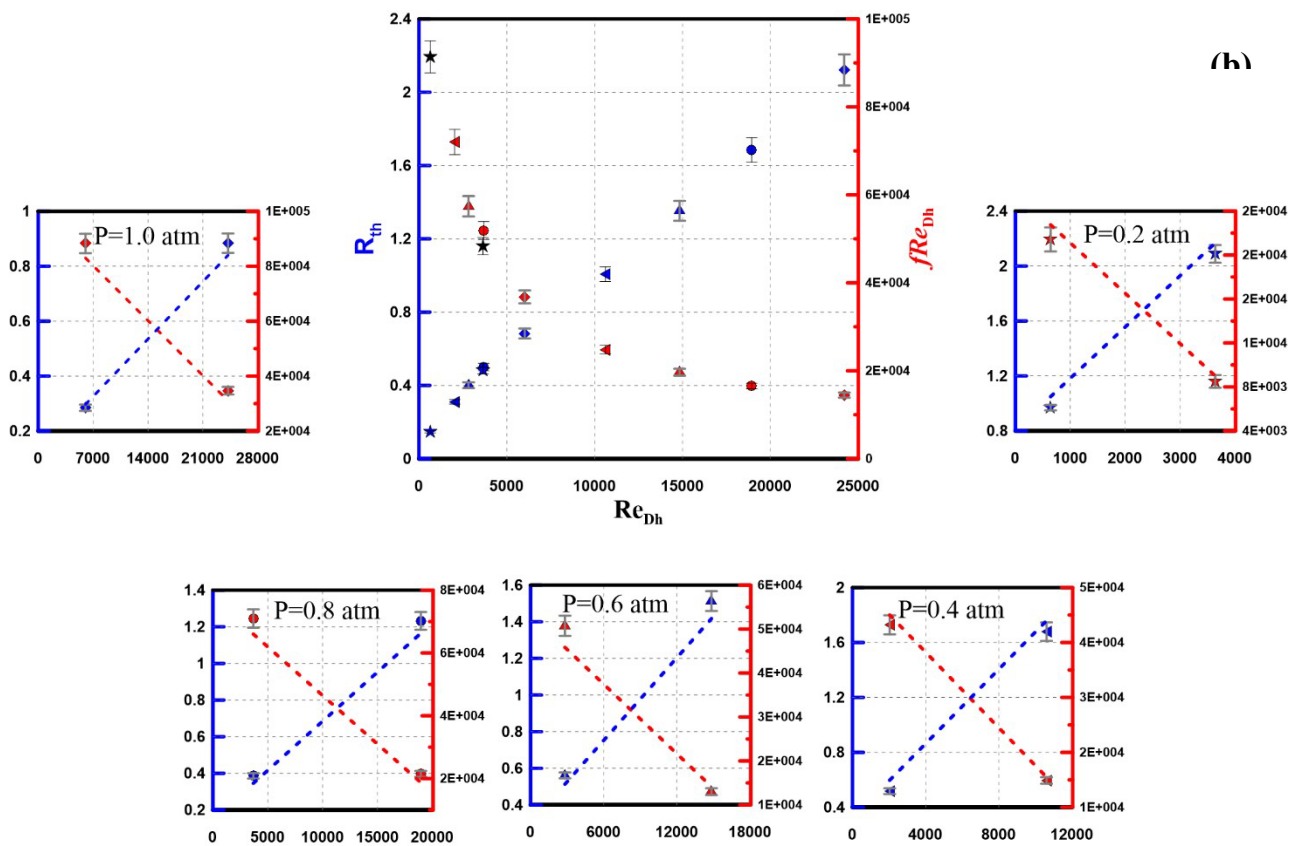
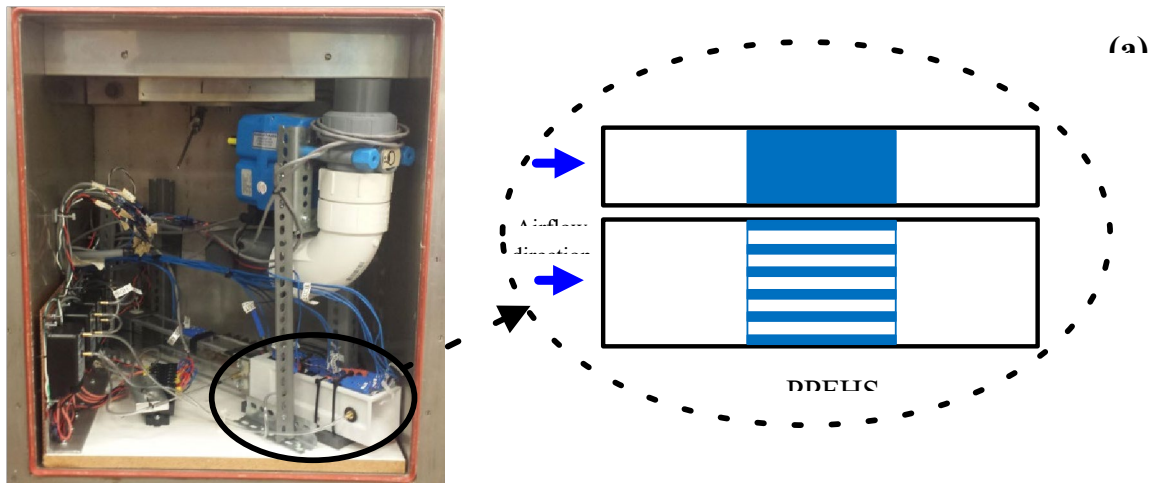


Fig. 2 . (a) Experimental setup and pictorial view of the test section (confined flow PPFHS), (b) Comparison of numerical results with experimental data at different Re [48].

3. Results and discussion

Two scenarios of forced convection over PPFHS are considered. For the first scenario, the PPFHS with tip-clearance is placed in tunnel where the air flow through and over the PPFHS. In the second scenario, the air is altered by placing inclined guide plate over the PPFHS. The geometrical parameters

of the PPFHS are optimized based on its thermal performance. Both scenarios are optimized for various environmental conditions (altitudes-effect) namely: sea-level, 0.7 atm, 0.5 atm, 0.2 atm. The operation is considered as uncontrolled- temperature environment which is the typical operation for EMAs. Beside exposure to lower air density at the higher elevations, the ambient temperature is lower at high elevation. However, this adverse effect is not able to improve the convective heat transfer capabilities of air and its overall heat capacity. Therefore, all electronics that rely on natural or forced convection to dissipate heat could experience greater air and component temperature rises for the same amount of power at high altitudes.

Thermal/hydraulic modelling of a conventional PPFHS/fan is a considered a Multiphysics problem which include: fluid dynamics, convective heat/mass transfers in fluid and heat conduction in solids. Fig. 3 shows the system level analysis for the proposed fan air-cooled system, considering two configurations. The first one is PPFHS with a certain dimension installed in a duct and then installing the guide plate represent the second configuration. For a defined PPFHS geometry ($N_f=28$, $t_f=0.2$ mm), the system

impedance characteristic $\Delta\theta_{ttfftt}VV$ is determined using defined inlet velocity. This curve correlates the fluid inlet and outlet static pressure difference across the PPFHS to the volume flow (V) as shown in Fig. 3a. The selected fan running at 12,000 rpm and sea-level condition (1.0 atm) provides characteristic curve that also correlates the static pressure drop versus volume flow $\Delta\theta_{ffmnnn}VV$. For the system level analysis, the intersection of the two characteristics curves $\Delta\theta_{ttfftt}VV$ and $\Delta\theta_{ffmnnn}VV$ defines the VV through the system and the system operating pressure drop. Also, the thermal resistance characteristic of the PPFHS could be determined as a function of the VV of the air flowing through the system $RR_{tth}VV$ as depicted in Fig. 3a. Following this approach, the system level analysis can be repeated for the PPFHS/guide plate configuration where the system impedance curve and $RR_{tth}VV$ are presented in Fig. 3 as well. Furthermore, a high-altitude condition (0.2 atm) has been investigated for the two-fixed system configurations and the resulting system impedance curve and $RR_{tth}VV$ are also drawn in Fig. 3a,b. Fig. 3a effectively shows that the system delivers approximately the same flow at the different altitude conditions for both systems. Due to the lower fluid density at altitude, this of course means that the mass flow is reduced at these altitudes. It worth to mention that the experiments done by Wu et al. [3] to determine the characteristic curves for the considered fan at lower-pressure environment have been used to describe the high-altitude conditions in the present study. As expected, increasing the VV for both systems cause a favorable decrease in the thermal resistance, and this is clearly significant for high-altitude case with PPFHS only. The ratio of the RR_{tth} between the PPFHS and PPFHS/guide plate cases shown in Fig. 3c illustrates that the improvement in the thermal performance of the PPFHS due to guide plate installation reaches its maximum values at lower VV . Despite the similar conclusion for the selected case of high-altitude condition, the high-altitude condition shows a range of operating VV in which the improvement level-off before reaching its maximum value.

Figure 4 shows effect of variation in fan rotational speed from 6000 to 12000 rpm and environmental operation pressure from 0.2 to 1 atm on the volume flow rate supplied from the fan for both configurations. It is clear that the fan delivers approximately fixed volume flow rate at different operating pressure. In the meantime, the volume flow rate substantially decreases when the rotational speed decreased which definitely will lower the mass flow rate a cross the system. This figure shows

how the volume flow rate delivered for the PPFHS is always higher than the PPFHS/ guide plate configuration which is attributed to the operation point of the former system with less pressure drop. However, to present the merit of using guide plate with PPFHS compared to PPFHS, variable altitude conditions range from sea-level up to 15 km has been simulated while the inlet air velocity is fixed to 3 m/s to simulate the selected fan operating condition. Fig. 5 shows the effect of altitude increase on the air density and the ambient air temperature. There is a continuous decrease in air density with altitude which at 15 km reaches approximately 15% of the actual value at sea-level. But the air temperature decreases with altitude up to nine kilometers and levels off. Below nine kilometers the ambient air temperature decreases more than density which causes the equipment temperature to be cooler than at sea level. For both cases, the thermal resistance increases with the altitude increase. However, there is a significant thermal resistance increase for the PPFHS case without the guide plate compared to the case where guide plate is installed. This dramatically causes the equipment temperature to exceed the allowable limits which may cause operation failure when the system is used to cool a 150 W load.

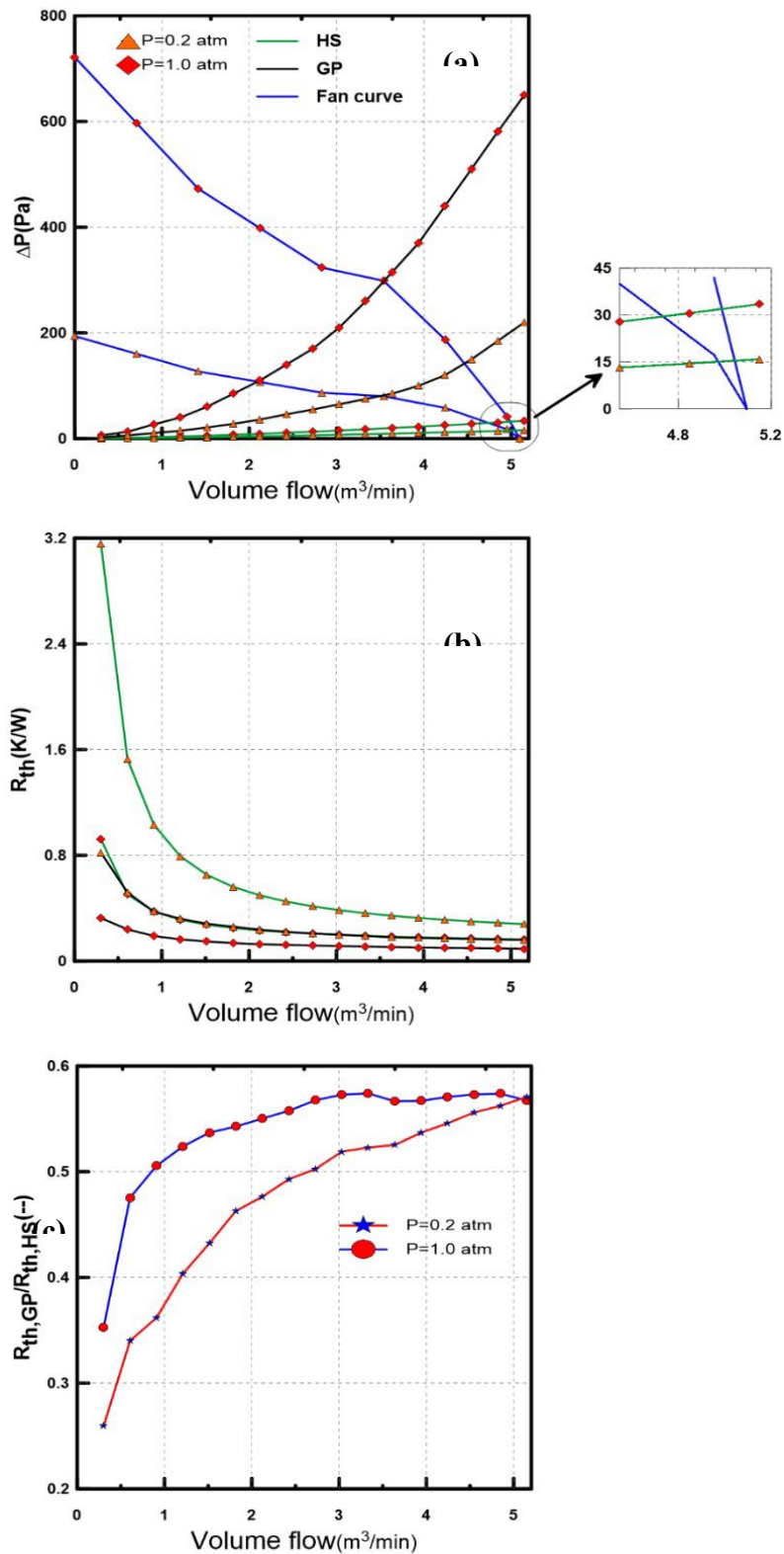


Fig. 3 . (a) Sunon PF92381 characteristic curve and the system impedance curve for PPFHS and PPFHS/guide plate. (b) RR_{th}

curve of the two systems as function of VV . (c) The improvement in thermal performance between the two systems.

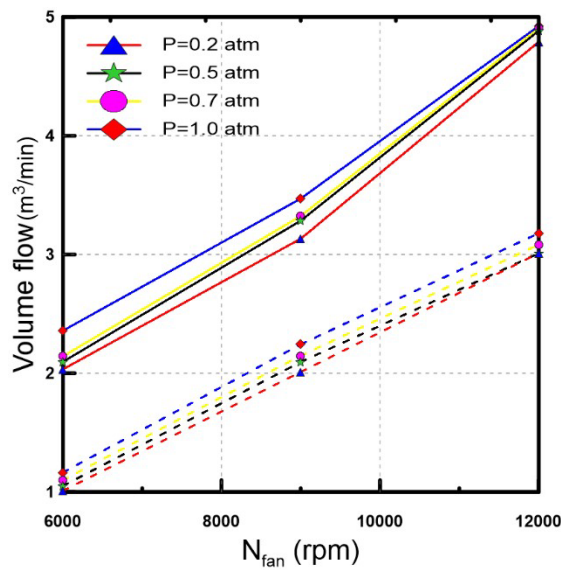


Fig. 4 . (a) Effect of fan rotational speed on the delivered volume flow rate for PPFHS and PPFHS/guide plate.

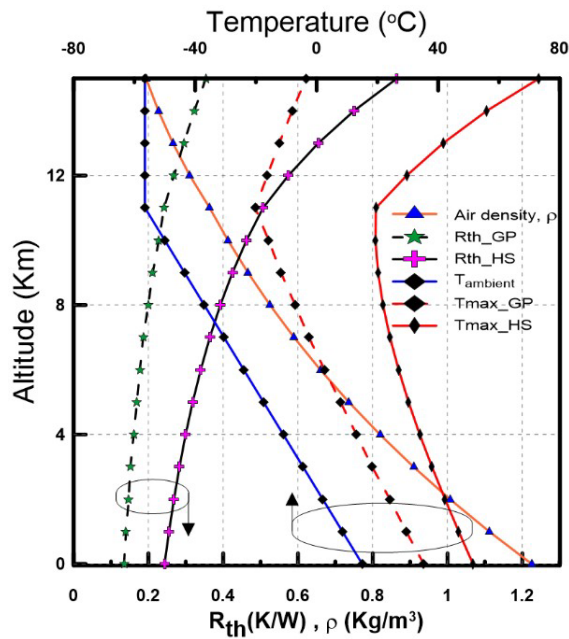


Fig. 5 . Altitude effect on air temperature/density, R_{th} and maximum temperature for PPFHS and PPFHS/guide plate.

Effect of ambient condition on PPFHS Structure optimization

In this section, a parametric study has been conducted to investigate the effect of changing the considered design parameters presented in Table 1 on the thermal performance of PPFHS and PPFHS/guide plate configurations. These design parameters are named as: fan speed N_{fan} , fin number N_{fin} , fin thickness t_f , and environmental operating pressure (altitude effect) P_{amb} .

i. fin density/fan rotation speed

Figure 5 shows the thermal resistance variation with fin number changes. The fin thickness equal to 1.5 mm has been selected based on the work done by Elsayed et al. [38]. Adding more fins while keeping fin thickness fixed results in fin spacing reduction which in turn causes pressure drop to increase. Therefore, the system operating point shifts to left on the fan characteristic curve and a reduction in the air volume flow rate supplied by the fan occurred. On the other side the heat transfer area increases and leads to PPFHS thermal capacity increase. Fig. 6 shows the effect of changing fin number on thermal resistance of PPFHS and PPFHS with guide plate installed at different operating fan speed and environmental pressure. The figure shows that lower environmental operational pressure has the maximum values of thermal resistance for all cases. For each fan rotational speed, a range of optimum fin number is noticed which is higher fin density at high operational pressure (sea-level). It is also noticed that this range shift to the left (lower fin density) when the fan exposed to lower operational pressure (high-altitude). Further shift to lower fin number to achieve the lowest thermal resistance is attained with fan speed reduction. This again is attributed to the lower volume flow rate delivered by the fan which lower the mass flow rate that flow across the system. For both configurations, the optimum fin number ranges between 20 to 28 which depends on the configuration, operational pressure, and fan speed. It is also worth to mention that, the obtained optimal fin number at sea-level operation does not lead to optimal fin number at high-altitude. Therefore, depending only on the sea-level optimization results may lead to insufficient thermal performance PPFHS and at the same time will increase the weight burden of the PPFHS on the cooling system. For instance, if the fan operates at 6,000 rpm, the optimal fin number for the PPFHS/guide plate case is 32 and 20 fins for the operational pressure equal to 1 and 0.2 atm, respectively. Using 24 fins instead of 32 fins for 0.2 operational pressure will lead to approximately 28% weight reduction and at the same time 33 % reduction in the PPFHS thermal resistance which means an overall improvement in the system thermal and structure performance

ii. fin thickness//fan rotation speed

Next, the optimum fin number for each case from the fin density study is selected and the effect of the fin thickness ranges between 0.2 to 2 mm is studied. This is done to attain the minimum weight for the PPFHS which will assure the optimal thermal performance of the system. Increasing fin thickness while fin number kept constant results in a reduction in the air-flow passages between fins which may lead to lower thermal performance. However, this adverse effect may be shifted by the increase in fin efficiency to transfer heat from the base due to thickness increase. Therefore, due to the two-opposite effects associated with fin thickness, an increase in the overall PPFHS performance with less weight could be attained. Fig. 7 shows the effect of changing fin thickness on thermal resistance of PPFHS and PPFHS/guide plate at different operating fan speed and environmental pressure. The figure also shows that the minimum thermal resistance depends only on the operating fan speed not the operating pressure. For lower fan operating speed lower fin thickness achieves the minimum thermal resistance. However very comparable fin thickness range gave minimum thermal resistance for different operational pressure.

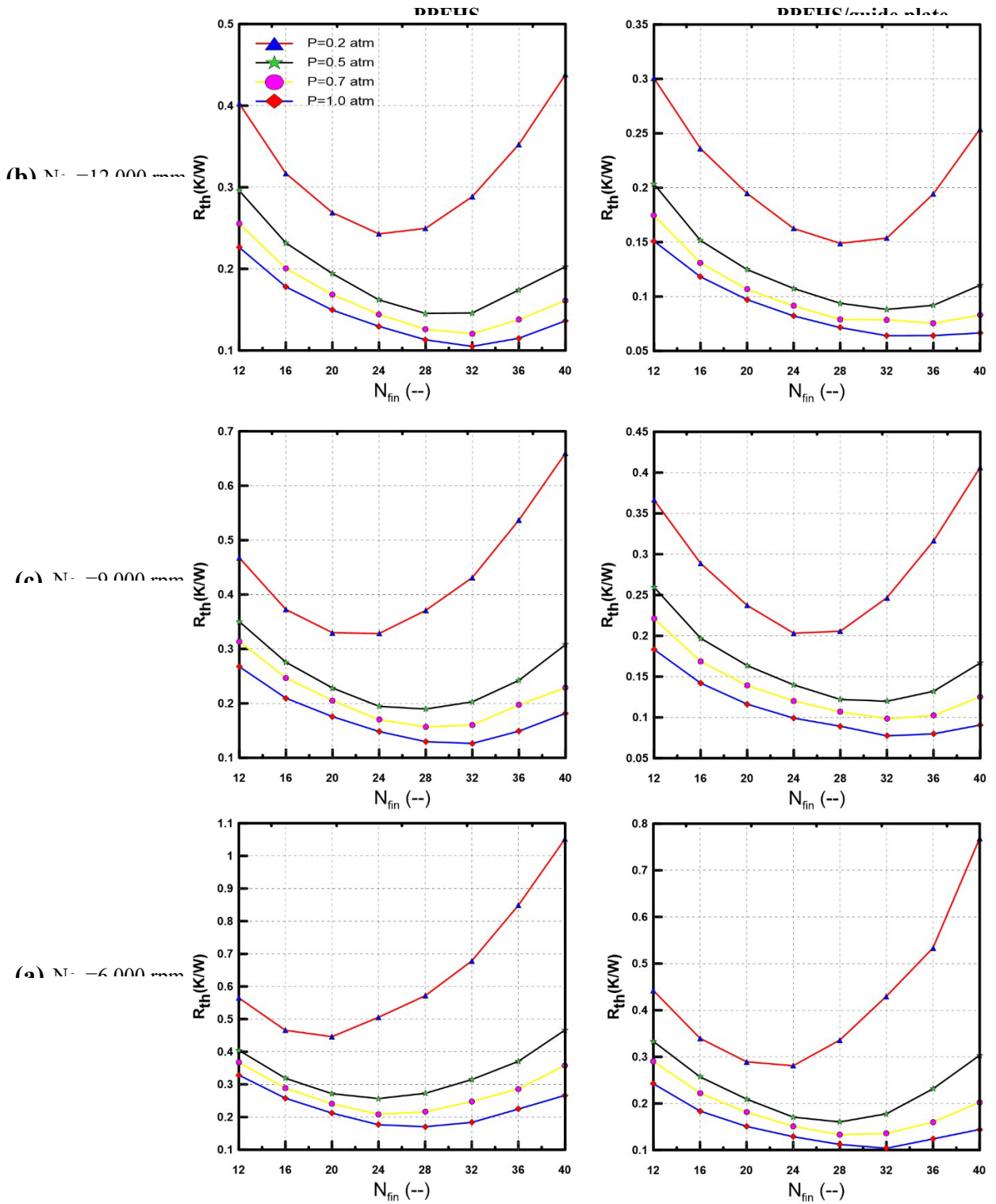


Fig. 6 . Effect of fin number on R_{th} for PPFHS and PPFHS/guide plate.

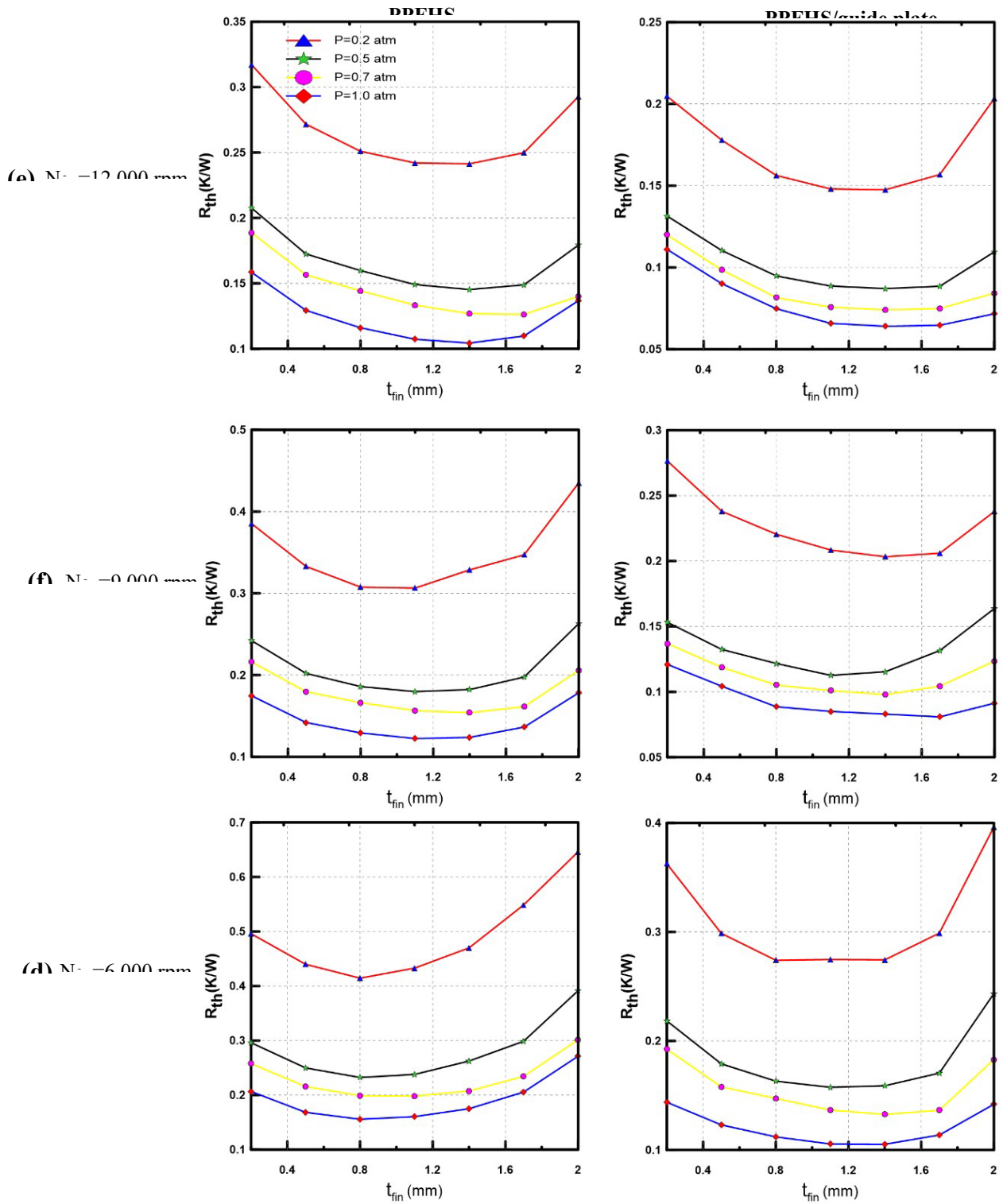


Fig. 7. Effect of fin thickness on R_{th} for PFHS and PFHS/guide plate.

4. Conclusions

An inclined guide plate anchored at the duct ceiling with a length equals the air-bypass height was proposed to improve the heat dissipating performance of an air-cooled PPFHS for the thermal management of electro-mechanical actuators (EMAs) operating at high altitude. The primary purpose of this work is to determine the optimal design parameters of the PPFHS when the fan operates under different speeds and environmental conditions. The current computational model is validated by comparing the simulation results with available experimental data. The average absolute error of the comparison results between a customized model of confined flow PPFHS and experimental results is less than 2.2% for the thermal resistance and 5.3% for the friction factor. Experimentally measured fan characteristic curves at high altitudes, different speeds and operational pressure were used as inlet condition to simulate the real operation of the EMA air-cooled system. The effects of using a guide plate with the PPFHS are presented and compared with using the PPFHS only. The following conclusions can be made:

1. For both PPFHS and PPFHS/ guide plate configurations, the fan delivers approximately the same volume flow at the different altitude conditions.
2. Increasing the volume flow rate leads to a favorable decrease in the thermal resistance and this is clearly significant for the high-altitude case with PPFHS only.
3. Up to 15 km operation, thermal resistance increases with the increase in altitude, which may lead to equipment failure due to exceeding the allowable temperature limits for the PPFHS case.
4. For different fan speed operation, a higher fin density results in a lower thermal resistance for sea-level operation. However, the number of fins shifts to a lower value for high-altitude operation which also leads to a lower weight.
5. For both configurations, the optimum fin number ranges between 20 to 28 which depends on the configuration, operational pressure, and fan speed.
6. Relying on the sea-level optimization results may lead to insufficient cooling effect and an increase in the total cooling system weight for high-altitude operation.
7. Using optimal fin numbers could lead to a substantial reduction in weight and a significant decrease in the thermal resistance.
8. For variable fin thickness, the minimum thermal resistance depends only on the operating fan speed, and not on the operating pressure.
9. A lower fin thickness results in the minimum thermal resistance at low fan operating speeds.

Conflict of interest

Authors declare that there is no conflict of interest.

ACKNOWLEDGMENT

This material is based on research sponsored by the United States Air Force under agreement number FA8650-17-2-2230. The U.S. Government is authorized to reproduce and distribute reprints for Governmental purposes notwithstanding any copyright notation thereon. The views and conclusions contained herein are those of the authors and should not be interpreted as necessarily representing the official policies or endorsements, either expressed or implied, of the United States Air Force or the U.S. Government.

REFERENCES

- [1] J.L. Baer-Riedhart, R.J. Landy, Highly integrated digital electronic control: Digital flight control, aircraft model identification, and adaptive engine control, (1987).
- [2] R.L. Webb, Next generation devices for electronic cooling with heat rejection to air, *Journal of heat transfer*, 127 (2005) 2-10. <https://doi.org/10.1115/1.1800512>.
- [3] W. Wu, Y. Lin, O. Mesalhy, J. Kizito, Q. Leland, L. Chow, Design and Testing of a Cooling Fan for ElectroMechanical Actuators for Aerospace Applications, *Int J Astronaut Aeronautical Eng*, 2 (2017).
- [4] A.M. Morega, A. Bejan, S. Lee, Free stream cooling of a stack of parallel plates, *International journal of heat and mass transfer*, 38 (1995) 519-531. [https://doi.org/10.1016/0017-9310\(94\)00123-D](https://doi.org/10.1016/0017-9310(94)00123-D).
- [5] R.A. Wirtz, W. Chen, R. Zhou, Effects of flow bypass on the performance of longitudinal fin heat sinks, *Journal of Electronic Packaging*, *Transactions of the ASME*, 116 (1994) 206-211. <https://doi.org/10.1115/1.2905687>.
- [6] S.A. El-Sayed, S.M. Mohamed, A.A. Abdel-latif, A.-h.E. Abouda, Experimental study of heat transfer and fluid flow in longitudinal rectangular-fin array located in different orientations in fluid flow, *Experimental thermal and fluid science*, 29 (2004) 113-128. <https://doi.org/10.1016/j.expthermflusci.2004.02.006>.
- [7] E. Elshafei, Effect of flow bypass on the performance of a shrouded longitudinal fin array, *Applied Thermal Engineering*, 27 (2007) 2233-2242. <https://doi.org/10.1016/j.applthermaleng.2007.01.017>.
- [8] H.-Y. Li, S.-M. Chao, Measurement of performance of plate-fin heat sinks with cross flow cooling, *International Journal of Heat and Mass Transfer*, 52 (2009) 2949-2955. <https://doi.org/10.1016/j.ijheatmasstransfer.2009.02.025>.
- [9] R. Shah, Laminar flow friction and forced convection heat transfer in ducts of arbitrary geometry, *International Journal of Heat and Mass Transfer*, 18 (1975) 849-862. [https://doi.org/10.1016/0017-9310\(75\)90176-3](https://doi.org/10.1016/0017-9310(75)90176-3).
- [10] H. Jonsson, B. Moshfegh, Modeling of the thermal and hydraulic performance of plate fin, strip fin, and pin fin heat sinks-influence of flow bypass, *Components and Packaging Technologies*, *IEEE Transactions on*, 24 (2001) 142-149. <https://doi.org/10.1109/6144.926376>.

- [11] W. Leonard, P. Teertstra, J. Culham, A. Zaghoul, Characterization of Heat Sink Flow Bypass in Plate Fin Heat Sinks, ASME 2002 International Mechanical Engineering Congress and Exposition, (2002) 189-196. <https://doi.org/10.1115/IMECE2002-39566>.
- [12] H.-H. Wu, Y.-Y. Hsiao, H.-S. Huang, P.-H. Tang, S.-L. Chen, A practical plate-fin heat sink model, Applied Thermal Engineering, 31 (2011) 984-992. <https://doi.org/10.1016/j.applthermaleng.2010.10.014>.
- [13] S. Chingulpitak, N. Chimres, K. Nilpueng, S. Wongwisets, Experimental and numerical investigations of heat transfer and flow characteristics of cross-cut heat sinks, International Journal of Heat and Mass Transfer, 102 (2016) 142-153. <https://doi.org/10.1016/j.ijheatmasstransfer.2016.05.098>.
- [14] T. Yuan, Computational modelling of flow bypass effects on straight fin heat sink in rectangular duct, Semiconductor Thermal Measurement and Management Symposium, 1996. SEMI-THERM XII. Proceedings., Twelfth Annual IEEE, (1996) 164-168. <https://doi.org/10.1109/STHERM.1996.545106>.
- [15] A.V. Barrett, I.F. Obinelo, Characterization of longitudinal fin heat sink thermal performance and flow bypass effects through CFD methods, Semiconductor Thermal Measurement and Management Symposium, 1997. SEMITHERM XIII., Thirteenth Annual IEEE, (1997) 158-164. <https://doi.org/10.1109/STHERM.1997.566793>.
- [16] S. Prstic, M. Iyengar, A. Bar-Cohen, Bypass effect in high performance heat sinks, ICHMT DIGITAL LIBRARY ONLINE, (2000). <https://doi.org/10.1615/ICHMT.2000.TherSieProcVol2TherSieProcVoll.340>.
- [17] H.-T. Chen, S.-T. Lai, L.-Y. Haung, Investigation of heat transfer characteristics in plate-fin heat sink, Applied Thermal Engineering, (2012). <https://doi.org/10.1016/j.applthermaleng.2012.08.040>.
- [18] Z. Khattak, H.M. Ali, Air cooled heat sink geometries subjected to forced flow: A critical review, International Journal of Heat and Mass Transfer, 130 (2019) 141-161. <https://doi.org/10.1016/j.ijheatmasstransfer.2018.08.048>.
- [19] H.E. Ahmed, B. Salman, A.S. Kherbeet, M. Ahmed, Optimization of thermal design of heat sinks: A review, International Journal of Heat and Mass Transfer, 118 (2018) 129-153. <https://doi.org/10.1016/j.ijheatmasstransfer.2017.10.099>.
- [20] K.-S. Yang, S.-L. Li, Y. Chen, K.-H. Chien, R. Hu, C.-C. Wang, An experimental investigation of air cooling thermal module using various enhancements at low Reynolds number region, International Journal of Heat and Mass Transfer, 53 (2010) 5675-5681. <https://doi.org/10.1016/j.ijheatmasstransfer.2010.08.015>.
- [21] H.E. Ahmed, Optimization of thermal design of ribbed flat-plate fin heat sink, Applied Thermal Engineering, 102 (2016) 1422-1432. <https://doi.org/10.1016/j.applthermaleng.2016.03.119>.
- [22] H.-Y. Li, C.-L. Chen, S.-M. Chao, G.-F. Liang, Enhancing heat transfer in a plate-fin heat sink using delta winglet vortex generators, International Journal of Heat and Mass Transfer, 67 (2013) 666-677. <https://doi.org/10.1016/j.ijheatmasstransfer.2013.08.042>.

- [23] S. Prstic, A. Bar-Cohen, "Heat Shield"—An Enhancement Device for an Unshrouded, Forced Convection Heat Sink, *Journal of electronic packaging*, 128 (2006) 172. <https://doi.org/10.1115/1.2188955>.
- [24] H.-Y. Li, G.-L. Tsai, M.-H. Chiang, J.-Y. Lin, Effect of a shield on the hydraulic and thermal performance of a plate-fin heat sink, *International Communications in Heat and Mass Transfer*, 36 (2009) 233-240. <https://doi.org/10.1016/j.icheatmasstransfer.2008.11.012>.
- [25] G.-L. Tsai, H.-Y. Li, C.-C. Lin, Effect of the angle of inclination of a plate shield on the thermal and hydraulic performance of a plate-fin heat sink, *International Communications in Heat and Mass Transfer*, 37 (2010) 364371. <https://doi.org/10.1016/j.icheatmasstransfer.2010.01.002>.
- [26] M.R. Shaalan, M.A. Saleh, O. Mesalhy, M.L. Elsayed, Thermo/fluid performance of a shielded heat sink, *International Journal of Thermal Sciences*, (2012). <https://doi.org/10.1016/j.ijthermalsci.2012.05.009>.
- [27] Y.-l. Zhang, J.-p. Liu, D.-t. Chong, J.-j. Yan, Experimental investigation on the heat transfer and flow performances of the fin array with shield in bypass, *International Journal of Heat and Mass Transfer*, 56 (2013) 674-682. <https://doi.org/10.1016/j.ijheatmasstransfer.2012.08.008>.
- [28] M.L. Elsayed, O. Mesalhy, Effect of a slotted shield on thermal and hydraulic performance of a heat sink, *J. Electronic Packaging*, 137 (2014) 1-6. <https://doi.org/10.1115/1.4027920>.
- [29] D.S. Steinberg, *Cooling techniques for electronic equipment*, New York, Wiley-Interscience, 1980. 387 p., (1980).
- [30] D. Bar-Shalom, *Altitude effects on heat transfer processes in aircraft electronic equipment cooling*, Master of Science in Aeronautics and Astronautics, Massachusetts Institute of Technology, (1988).
- [31] M.R. Vogel, *Thermal performance of air-cooled hybrid heat sinks for a low velocity environment*, Proceedings of 1994 IEEE/CHMT 10th Semiconductor Thermal Measurement and Management Symposium (SEMI-THERM), (1994) 17-22.
- [32] C.L. Belady, *Design considerations for air cooling electronic systems in high altitude conditions*, *IEEE Transactions on Components, Packaging, and Manufacturing Technology: Part A*, 19 (1996) 495-500.
- [33] E.K. Gyasi, *Enhancement of Thermal Management in Air Cooled Systems Operating at Low-Pressure Conditions*, Ph.D. Dissertation, North Carolina Agricultural and Technical State University, (2016).
- [34] J. Rhee, K. Azar, Adjusting temperatures for high altitude, *Electronics Cooling*, 5 (1999) 44-45.
- [35] G. Xu, *Thermal Performance Prediction for High Power Processors at High Altitude*, ASME 2005 International Mechanical Engineering Congress and Exposition, (2005) 549-554.
- [36] M. Mansuria, *Estimation of System Internal Air and Component Surface Temperatures at High Altitudes, Temperatures, and Relative Humidity*, Proceedings of the 1994 International Electronics Packaging Conference, (1994) 122-130.
- [37] H. Wong, R.E. Peck, Experimental evaluation of air-cooling electronics at high altitudes, *Journal of Electronic Packaging*, 123 (2001) 356-365.

- [38] M.L. Elsayed, O. Mesalhy, R.H. Mohammed, J.P. Kizito, Q.H. Leland, L.C. Chow, Enhancement of a heat sink performance using a partial shield and/or a guide plate, *International Journal of Heat and Mass Transfer*, 134 (2019) 948-958. <https://doi.org/10.1016/j.ijheatmasstransfer.2019.01.096>.
- [39] D. Blanding, Subsystem design and integration for the more electric aircraft, 5th international energy conversion engineering conference and exhibit (IECEC), (2007) 4828.
- [40] D. Woodburn, T. Wu, L. Chow, Q. Leland, W. Brokaw, J. Bindl, B. Jordan, Y. Ren Lin, L. Zhou, N. Rolinski, Dynamic heat generation modeling of high performance electromechanical actuator, 48th AIAA Aerospace Sciences Meeting Including the New Horizons Forum and Aerospace Exposition, (2010) 290-299. <https://doi.org/10.2514/6.2010-290>
- [41] K. McCarthy, A. Heltzel, E. Walters, J. Roach, S. Iden, P. Lamm, A reduced-order enclosure radiation modeling technique for aircraft actuators, SAE Technical Paper, (2010). <https://doi.org/10.4271/2010-01-1741>.
- [42] J.R. Culham, Y.S. Muzychka, Optimization of plate fin heat sinks using entropy generation minimization, *IEEE Transactions on Components and Packaging Technologies*, 24 (2001) 159-165. <https://doi.org/10.1109/6144.926378>.
- [43] A. Bhattacharya, R.L. Mahajan, Finned metal foam heat sinks for electronics cooling in forced convection, *Journal of Electronic Packaging*, 124 (2002) 155-163.
- [44] ANSYS FLUENT User's guide, Release 16.0., ANSYS Inc., Canonsburg, PA, (2016).
- [45] F.R. Menter, Two-equation eddy-viscosity turbulence models for engineering applications, *AIAA journal*, 32 (1994) 1598-1605.
- [46] A.K. Barik, A. Mukherjee, P. Patro, Heat transfer enhancement from a small rectangular channel with different surface protrusions by a turbulent cross flow jet, *International Journal of Thermal Sciences*, 98 (2015) 32-41. <https://doi.org/10.1016/j.ijthermalsci.2015.07.003>.
- [47] O.B. Kanargi, P.S. Lee, C. Yap, A numerical and experimental investigation of heat transfer and fluid flow characteristics of a cross-connected alternating converging–diverging channel heat sink, *International Journal of Heat and Mass Transfer*, 106 (2017) 449-464. <https://doi.org/10.1016/j.ijheatmasstransfer.2016.08.057>.
- [48] E.M. Racine, Experimental Study - High Altitude Forced Convective Cooling of Electromechanical Actuation Systems, Master of Science in Aerospace Engineering, University of Dayton, Dayton, United States, (2015).

NOMENCLATURE

Alphabet- Upper Case

A_t	total convection area of a heat sink, m^2
B	heat sink footprint width, mm
D_h	duct hydraulic diameter, m
E	total energy per unit mass, J/kg
H	fin height, mm
H_s	shield height, mm
H_b	bypass height above the shield, mm
H_{BP}	total bypass height above the heat sink, mm
H_p	guide plate height, mm
K_s	thermal conductivity
L_{hs}	heat sink footprint length, mm
N	number of fins
Nu_{D_h}	Nusselt number using D_h
P_1	channel inlet pressure, N/m^2
Q	heat dissipation rate, W
R_{th}	total thermal resistance, K/W
Re_{D_h}	Reynolds number
T_b	base plate temperature, K
S	fin spacing, mm
V_d	duct velocity, m/s
X_p	guide plate position
Y^+	Non-dimensional height, $(u^*.y/\nu)$

Alphabet- Lowercase

h heat transfer coefficient, $W/m^2.K$

f friction coefficient

t_f fin thickness

t_b baseplate thickness, mm

q'' Heat flux, W/m^2

y^+ dimensionless wall distance.

Greek symbols ε turbulent
dissipation rate, m^2/sec^5 μ
absolute viscosity, Pa.s

ρ density, kg/m^3

θ_{PP} guide plate inclination angle, degree

ΔP pressure drop, N/m^2

Abbreviations

GP Guide plate

HS Heat sink

APPENDIX P

UCF Project 1626-8282

Quarterly Report # 8

to

North Carolina A&T University

**THERMAL MANAGEMENT OF ELECTROMECHANICAL MACHINES FOR
AEROSPACE SYSTEMS**

University of Central Florida

Department of Mechanical and Aerospace Engineering Orlando,

FL 32816-2450

Louis Chow, PI

Osama Mesalhy

Mohamed Elsayed

Period: From June 12th, 2019, to September 11th, 2019

Date of Report: September 11th, 2019

In Quarterly Report # 6, we have shown the simulation of the flow field in the 7-blade 5blade dual fan system shown in Figure (1). The purpose of using this dual fan system is to increase the reliability of the fan cooling system by operating only one fan and keeping the other as a spare. The spare is used in case of failure of the first fan. So, the operation will follow two scenarios. The first is running the upstream fan while keeping the downstream fan stationary to avoid bearing degradation of the downstream fan. The second scenario occurs when the upstream fan fails. In this case, the blades of this fan will be clamped stationary, and the downstream fan will be allowed to run. The results of the simulation showed that the performance of the first scenario of operation is considerably better than the second. From the simulation results, it was found that when the upstream fan is stationary, it partially blocks the intake and directs the air in a direction which is inconsistent with how air should enter the downstream fan. Different modifications on the dual fan system have been conducted to improve the performance. It was found that removing the diffuser section and replacing the 5-blade fan with a 7-blade fan (which runs at 13000 rpm, see Figure (2)), improves the performance of the dual fan system for the two operation scenarios. However, the performance in the case of running the downstream fan is still lower than the performance when the upstream fan is running.

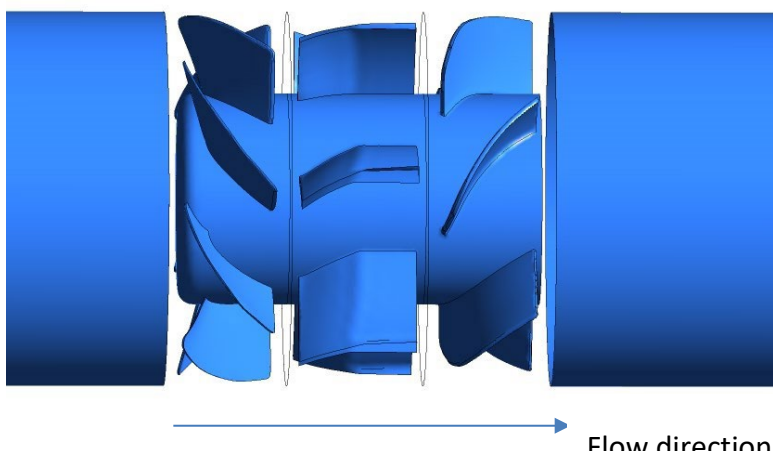


Figure (1) Original dual fan system

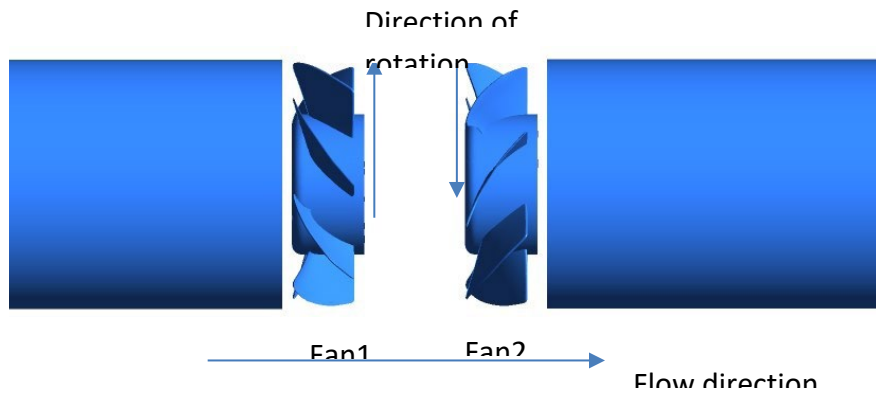


Figure (2) Two 7-blade dual fan system

In this period, we have studied:

- 1- The effect of changing the distance between the two 7-blade fans on the performance of both upstream and downstream fans;
- 2- The effect of opening the circumference area between the two fans on the downstream fan performance.

1. Effect of changing the distance between the two 7-blade fans

The distance between the two fans was varied from 31 mm to 122 mm. The effect of changing the distance on the flow pressure and streamlines when the upstream fan (Fan1) is running is shown in Figure (3). As seen from the pressure contours, the pressure at the exit of the dual fan system decreases with increasing the distance between the two fans. In the case of running the upstream fan, three components of pressure drop occur: the pressure drop in the region between the two fans, the pressure drop due to the stationary downstream fan, and the pressure drop in the exit section. Keeping the distance between the two fans small minimizes the pressure drop occurred in the region between the two fans. In addition, the stationary downstream fan straightens the flow in the axial direction and reduces the tangential velocity component which reduces the pressure drop in the exit section of the dual fan system. As can be noticed for the case of setting the distance between the two fans equal to 122 mm, a considerable part of the pressure drop occurs in the region between the two fans. This is due to the high tangential velocity in this long distance.

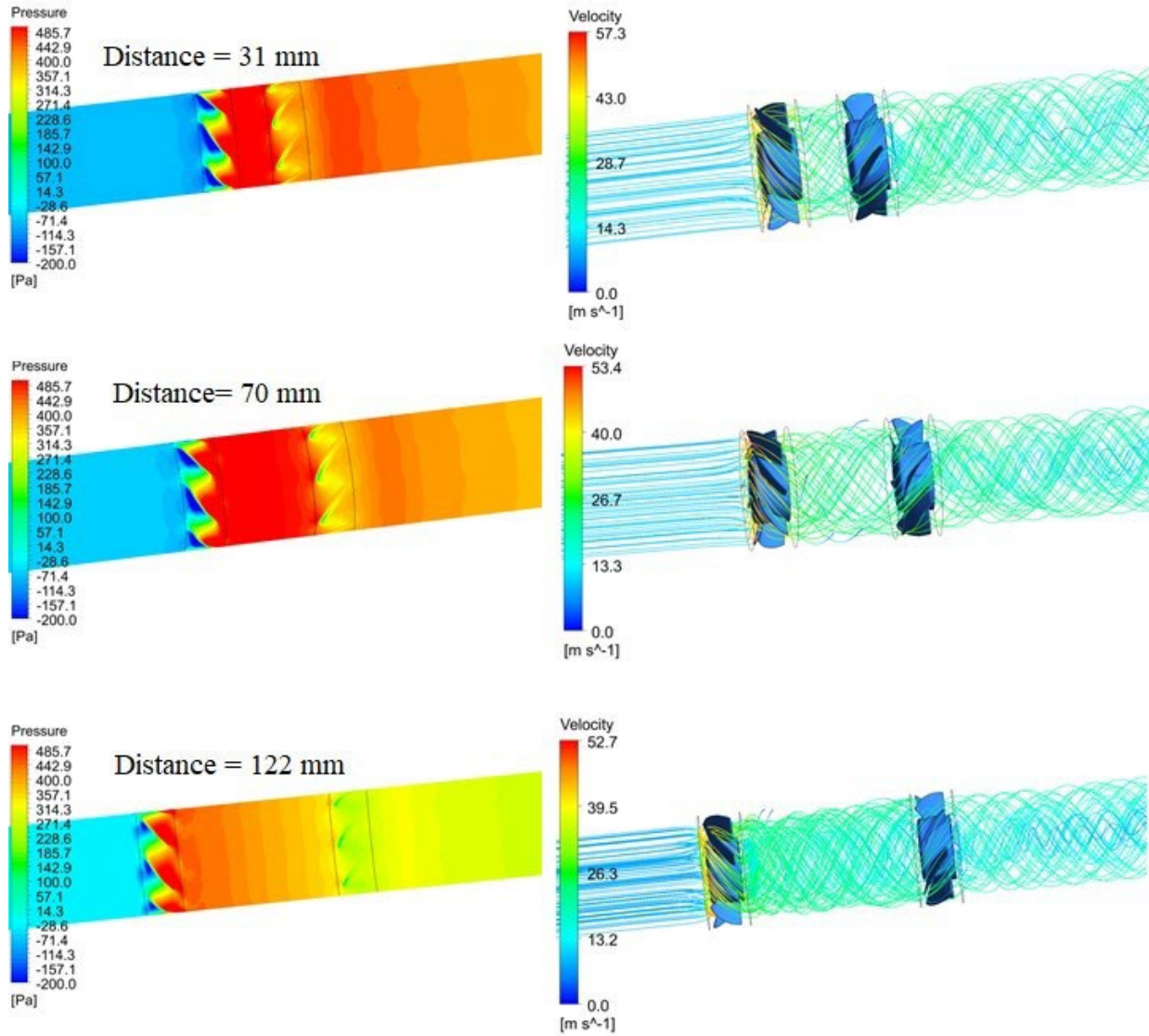


Figure (3) Effect changing the distance between the two fans on the flow pressure and streamlines when upstream fan (Fan1) is running

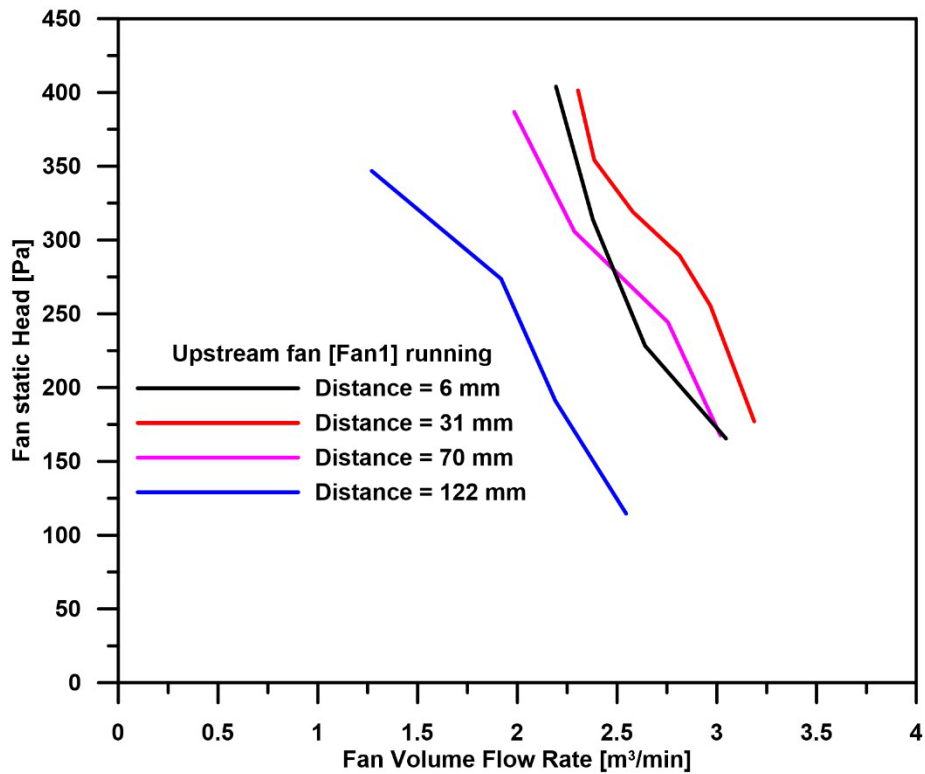


Figure (4) Effect of changing the distance between the two fans on the performance of upstream fan (fan1)

Comparing the performance of the upstream fan with changing the distance between the two fans, it can be noted from Figure (4) that the performance of the upstream fan decreases with increasing the distance between the two fans from 31 mm to 122 mm. In the same figure, the case of keeping the distance between the two fans to the smallest possible value, 6 mm, is also shown. It can be seen that keeping this distance to the smallest value does not improve the performance. This may be attributed to mismatch between the flow exit angle from the upstream fan and the angle of the blades of the stationary downstream fan. Also, the friction between the air and the fan surface disturbs the flow in this small gap between the two fans. So, we can conclude that there is an optimum distance which can maximize the performance of the upstream fan (Fan1). This distance is around 3 cm.

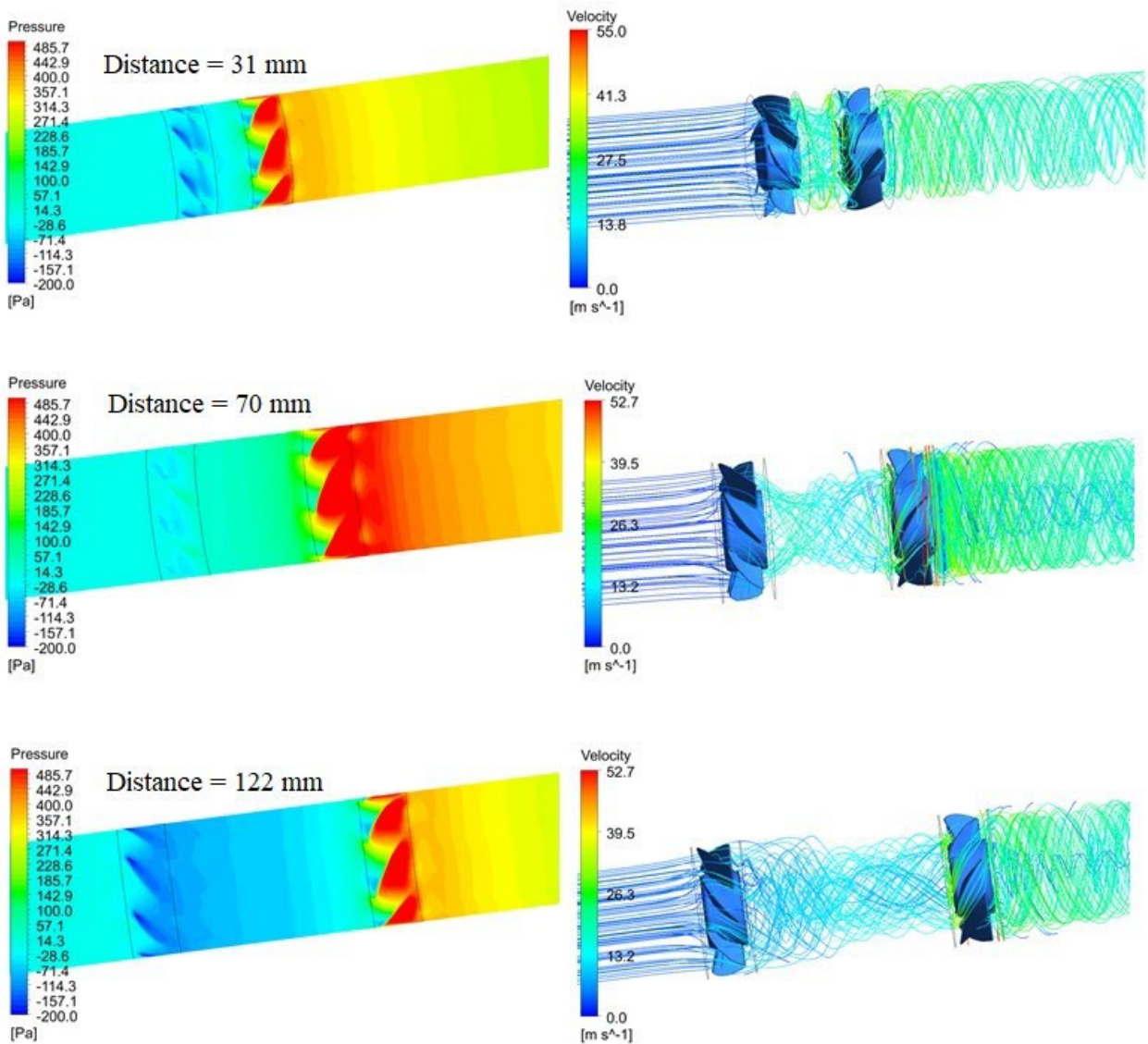


Figure (5) Effect of changing the distance between the two fans on the flow pressure and streamlines when downstream fan (Fan2) is running

The effect of changing the distance between the two fans on the flow when the downstream fan (Fan2) is running is shown in Figure (5). Keeping the distance between the two fans small does not allow the flow from the upstream fan to adapt with the downstream fan. The blade angles of the downstream fan are designed to receive the flow at its inlet in the axial direction. Since the distance between the two fans works as a flow straightener, it can be seen that increasing the distance from 31 mm to 70 mm results in an increase in the static pressure at the dual-fan exit at

the higher flow rate. However, the pressure drop in the region between the two fans reduces the dual-fan static pressure rise when the distance increases to 122 mm.

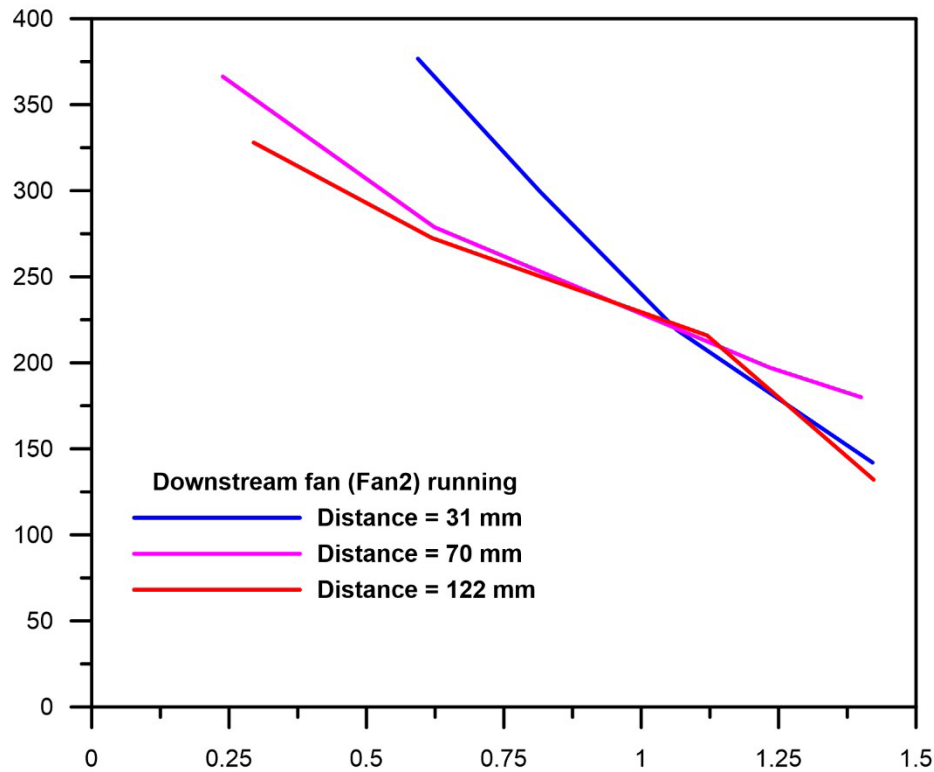


Figure (6) Effect of changing the distance between the two fans on the performance of downstream fan (fan2)

Figure (6) shows the performance of the downstream fan for different fan spacing. It can be seen that when the dual-fan is subjected to low back pressure (volume flow rate $> 1 \text{ m}^3/\text{min}$), the performance of the downstream fan is better when the distance between the two fans is 70 mm. However, for high back pressure (volume flow rate $< 1.0 \text{ m}^3/\text{min}$), the performance is better when the distance is kept at 31 mm. This is attributed to the contradicting effects of increasing the distance between the two fans: pressure drop and flow straightening. The flow straightening effect is more pronounced at the higher volume rate region. In general, the produced volume flow rate by the dual-fan system when the downstream fan is running is less than the volume flow rate that can be produced when the upstream fan is running.

2- The effect of opening the circumference area between the two fans

It can be found, by comparing Figures 4 and 6, that the performance of the downstream fan is much lower than that of the upstream fan. The maximum air produced by the downstream fan is less than 50% of the air produced by the upstream fan. This is mainly due to effect of the stationary upstream fan blocking the intake and directing the flow in a direction which is not

consistent with the running downstream fan. So, in this section, we studied the effect of replacing the circumferential wall between the two fans with a movable wall which can be opened or closed as shown in Figure (7). The distance between the two fans is kept at 31 mm which maximizes the performance of the upstream fan. In the case of failure of the upstream fan, this movable wall can be opened, and the downstream fan sucks the air through the open circumferential area instead of sucking the air through the upstream fan.

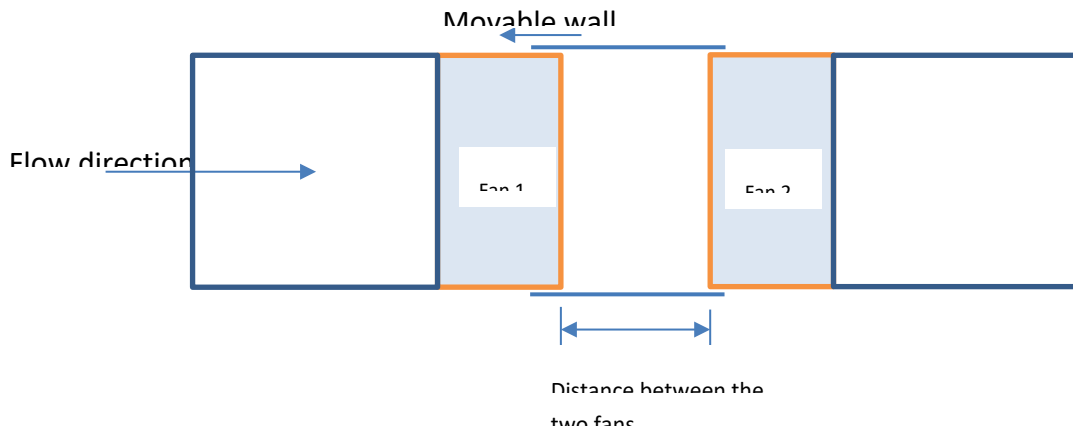


Figure (7) Movable wall between the two fans

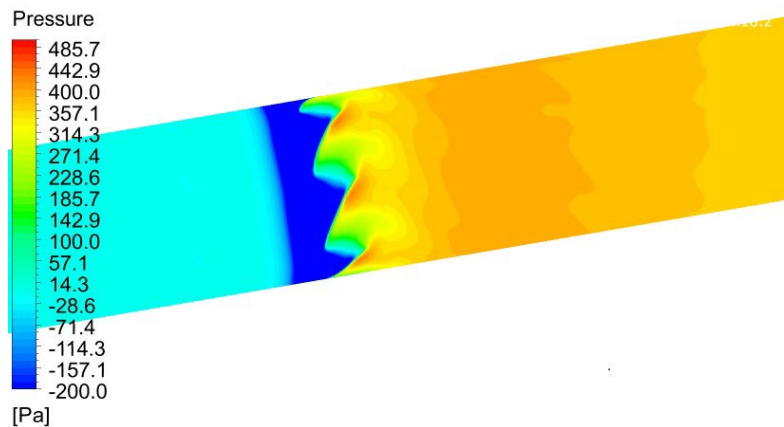
A numerical simulation has been carried out for the case of running the downstream fan at 13000 rpm while keeping the upstream fan stationary with the movable wall open. Figure (8) shows the boundary conditions for this simulation. It is considered that we have two inlets: pressure-inlet1 and pressure-inlet2. Only 22.5 mm out of the distance between the two fans (31 mm) is opened. The total pressure at the two inlets is assumed to be equal to atmospheric pressure and the static pressure at the pressure-outlet boundary has been changed from 0 to 300 Pa to produce the fan curve.



Fig. (8) Boundary conditions for the opened wall case

The results of the opened case are shown in Figure (9). The streamlines and the pressure contours shown in the figure indicate that the downstream fan (Fan2) draws the air from the two pressure inlet boundaries. But the percentage of the air mass flow rate coming from pressure-inlet2 is much higher than that coming from pressure-inlet1. This can be observed from the low static pressure and high air velocity at pressure-inlet2. The numerical values of the mass flow rate indicate that

$$\frac{\dot{m}_{\text{from pressure-inlet1}}}{\dot{m}_{\text{total}}} = 0.095$$



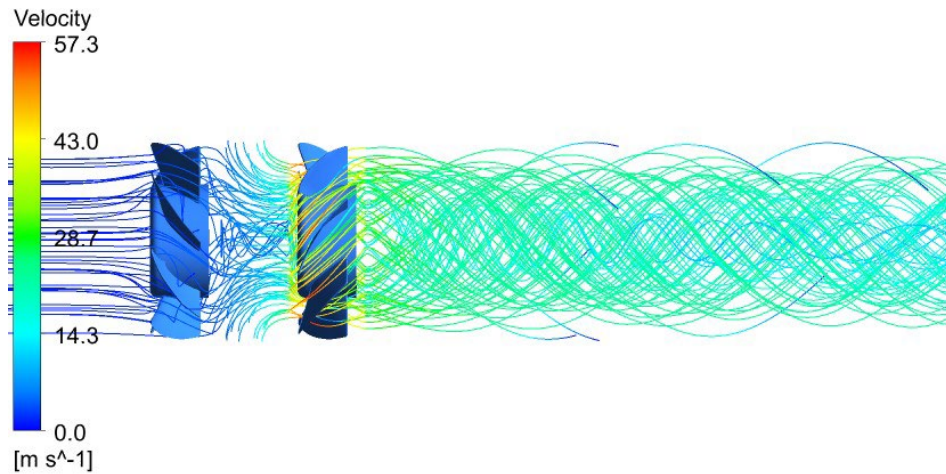


Figure (9) Static pressure contours and streamlines when Fan2 is running with open wall

Figure (10) shows that in the case of running Fan2 with open wall, the dual fan system performs better than running the upstream fan with closed wall, especially if the dual fan system faces low back pressure at the outlet-pressure boundary. But if the dual fan system faces higher back pressure (greater than 350 Pa), the performance of the two cases are comparable because in the case of running the upstream fan, the stationary downstream fan converts some of the kinetic energy into pressure head.

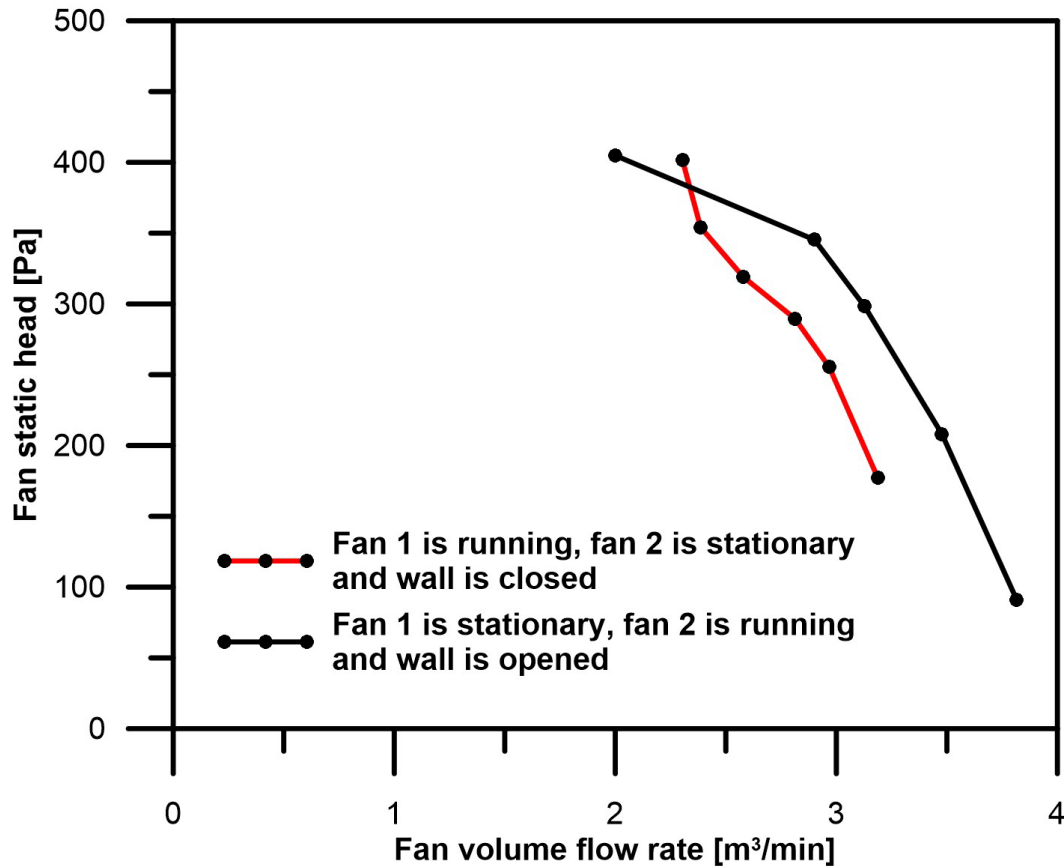


Figure (10) Fan performance curve of fan2 when the wall is opened compared to the performance of the upstream fan (fan1) when the wall is closed

So, the dual fan system can be operated first by running the upstream fan (Fan1) and keeping the downstream fan (Fan2) as a spare (with its blades clamped stationary). During the operation of Fan1, the movable wall can be held using a spring in the closed position. If the upstream fan fails due to any reason, the downstream fan can be used to produce air flow by releasing the movable wall to open the circumferential area. This can add double reliability to the cooling system without sacrificing the air flow rate when the downstream fan is running. Also, this arrangement will not need much additional space than a single-fan system if we have space limitation in the wing-bay.

In the next period we will work on optimization of the dual fan system and validating the numerical simulation with experimental measurements.